Aleksandar Rodić
Theodor Borangiu   *Editors*

# Advances in Robot Design and Intelligent Control

Proceedings of the 25th Conference on Robotics in Alpe-Adria-Danube Region (RAAD16)

# Advances in Intelligent Systems and Computing

Volume 540

*About this Series*

The series "Advances in Intelligent Systems and Computing" contains publications on theory, applications, and design methods of Intelligent Systems and Intelligent Computing. Virtually all disciplines such as engineering, natural sciences, computer and information science, ICT, economics, business, e-commerce, environment, healthcare, life science are covered. The list of topics spans all the areas of modern intelligent systems and computing.

The publications within "Advances in Intelligent Systems and Computing" are primarily textbooks and proceedings of important conferences, symposia and congresses. They cover significant recent developments in the field, both of a foundational and applicable character. An important characteristic feature of the series is the short publication time and world-wide distribution. This permits a rapid and broad dissemination of research results.

More information about this series at http://www.springer.com/series/11156

Aleksandar Rodić · Theodor Borangiu
Editors

# Advances in Robot Design and Intelligent Control

Proceedings of the 25th Conference on Robotics in Alpe-Adria-Danube Region (RAAD16)

Springer

*Editors*
Aleksandar Rodić
Robotics Laboratory
Mihajlo Pupin Institute
Belgrade
Serbia

Theodor Borangiu
Faculty of Automatic Control
  and Computers
University Politehnica of Bucharest
Bucharest
Romania

# Foreword

**Congratulations to the 25th anniversary of RAAD**

The most beautiful flowers grow in the absence of spotlights, and their full beauty unfolds only after having grown leaves and roots to store up energy for the upcoming bloom period. This picture comes in mind when looking at the history of the RAAD conferences. The beginning is closely connected with the political changes in South East Europe. The first RAAD meeting in 1992—in those days still considered as a "humble" workshop—was initiated by the Jožef Stefan Institute in Slovenia, two years after the first elections in that newly established country. Bearing in mind that the disintegration of former Yugoslavia just had started, accompanied by atrocities and NATO bombings, it was a heroic act to bring together roboticists in this region—which once was a "cradle" of European robotics! Humanoid robots of today still make reference to Miomir Vukobratović with his ground breaking theoretical work on biped locomotion at the Mihajlo Pupin Institute in Belgrade (1970). And based on theoretical and industrial excellence, several series of industrial robots (foremost the Goro, UMS, and Ivo Lola Ribor types) have been built between 1980 and 1988 and successfully installed in factories of Slovenia and Serbia.

It was not only heroic in those days to keep collaboration in the region alive, but it was also farsighted by transcending the horizon and encompassing now with "Alpe-Adria-Danube" a geographical "crescent" stretching from the French Alps to the Black Sea with more than 250 million inhabitants. Starting in 1992, RAAD left not a single year out—which shows the success of the concept.

Robotics is the next industrial revolution, permeating into all branches of daily life, at work and at home. This means: To participate in robotics will also decide about our economy and our welfare. However, robotics is a multidisciplinary endeavour. Most of the European states are too small to be excellent in all fields—advanced technologies require transnational cooperation.

As of today, the European Partnership in Robotics called SPARC is, with €700m funding from the European Commission and industrial obligations of three times

more, the largest civilian robotics programme in the world. As part of Horizon2020, SPARC is driven by a European roadmap on robotics which is developed by the community of European roboticists, coordinated by the European robotics association euRobotics in Brussels.

It is very likely that upcoming EU programmes will focus even more on economic growth, creating jobs, and concentrating on the equity of opportunities between all regions of Europe. Within the recent years, RAAD has developed into a network of experts who are very competent to develop regional roadmaps for robotics which identify opportunities for robotics around existing regional core competencies. This qualification underlines the growing strength of the RAAD community.

RAAD 2016 celebrates its 25th anniversary with a significant growth in quality and quantity: this Springer volume shows not only the high quality of the papers accepted, but also the growing diffusion of robotics into other sectors such as agriculture, health, and even architecture. With more than 80 registered participants from 25 nations, RAAD has gained a highly reputable share in the European robotics community. The organisers and committees of RAAD 2016 under the masterly leadership of Prof. Aleksandar Rodić are thanked for their excellent job in planning, organising, and performing this conference.

July 2016                                                                     Dr. Uwe Haass
                                            Former Secretary General euRobotics AISBL, Brussels

# Preface

The jubilee 25th International Conference on Robotics in Alpe-Adria-Danube Region, RAAD 2016 was held in the conference centre of the Best Western Hotel M, Belgrade, Serbia, from 30 June to 2 July 2016. The conference brought together academic and industry researchers in robotics from 25 countries, the majority of them affiliated to the Alpe-Adria-Danube region, and their worldwide partners in a collegial and stimulating environment.

According to its tradition, RAAD 2016 covered all important areas of research, development and innovation in robotics, including new trends such as bio-inspired and cognitive robots, visual servoing of robot motion, human–robot interaction, and personal robots for ambient assisted living. This year for the first time in the RAAD history, new topics such as cloud robots, legal and ethical issues in robotics as well as robots in arts were present in the technical programme of the conference.

Papers were solicited in topics related to new theories, advanced design of robot mechanics and intelligent control architectures and development of robot applications, including but not limited to the following:

- Novel design and applications of robotic systems
- Dexterous grasping, handling and intelligent manipulation
- Intelligent cooperating and service robots
- Advanced robot control—human–robot interfaces
- Robot vision systems and visual servoing techniques
- Mobile robots
- Humanoid and walking robots
- Bio-inspired and swarm robotic systems
- Towards micro- and nano-scale robots
- Aerial, underwater and spatial robots
- Robot integration in holonic manufacturing
- Personal robots for ambient assisted living
- Medical robots and bionic prostheses
- Intelligent information technologies for cognitive robots
- Education in robotics—history of automation and robotics

- Cognitive robots and emotional intelligence
- Cloud robotics
- Ethical, legal and social issues of robotic
- Construction robots

Human activities in many sectors are nowadays supported or replaced by robots, which range from standard robots for industrial or service applications to autonomous robots for complex activities, such as underwater and space exploration. The great versatility and flexibility of nowadays robots allows them to be employed in different sectors, to perform a diversity of tasks.

A number of papers included in this volume report advances in robot control and integration in production and services. Task-space control is an important approach to the control of complex robots; this control framework is of essential importance for redundant robot manipulators, especially for multi-arm robots or humanoid robots, which have more degrees-of-freedom than those required to fulfil a task, and have to perform the task in human-like way. Solving constraint satisfaction problems allows for robust, safe planning of multiple robots in manufacturing. The sustainability of robotized processes is analysed by monitoring energy consumption at operation level and consequently reconfiguring robot speed and acceleration or conducting robot allocation scenarios in an efficient way. In order to adapt themselves to the environment and characteristics of material flows, robot systems are often equipped with vision systems.

Vision-guided robot motion using look-and-move and visual servoing methods provide best performances in the generation of accurate, task-oriented motion patterns. Integrating Visual Quality Control services in manufacturing environments allows product traceability. In the context of agent-based manufacturing, some papers approach the problem of planning cooperative activities in robot teams. Theoretical principles and methods are addressed, implementing solutions and tools for visual servo control of robot manipulators in grasping tasks. Guidance vision is presented as an advanced motion control method, which provides flexibility to robots integrated in manufacturing cells with unstructured environment and in-line quality inspection.

Robotic coaching is a process of modifying the motion of a robot during execution through human intervention, in a manner of a coach. Thus, parts of the motion are changed depending on the instructions which can be provided through different approaches. Robotic coaching is treated in the conference, including methods relying on physical human robot interaction such as using compliantly controlled robots to different variations of position and force feedback.

There are also analysed new methods of using robots in interaction with humans (natural interaction) to provide assistance services. Using depth sensors, the robots are able to detect the human operator and to avoid collisions. Collision avoidance uses depth sensors which monitor the activity outside and inside the multi-robot system workspace using skeleton tracking (e.g. with the Kinect sensor), allowing the robot to detect collisions and stop the motion at the right time.

Papers in the conference address the development of software interfaces for natural-like interaction of humans with personal robots. This type of interaction is considered for communication (models of hand gestures are established that allow many natural gestures to be interpreted by the personal robot) and emulation of human skills, routine tasks (extracting reusable task knowledge from visual observation of human gestures, learning dexterous operations from human demonstration). These papers describe spatial and temporal modelling of communicative and manipulative gestures; hand gestures analysis and recognition based on multiple-image processing; reusable task knowledge extraction from visual observation of human performance and action reproduction (human tasks emulator); visual servoing for motion tuning.

Although today's robots are distinguished by an enviable degree of artificial intelligence, versatile perception and decision-making in real-time, this area is still in development. If the design approach of service robots is based on "technological copy" of the human, then we are placed in front of the impossible requirements for robots, expecting them to simultaneously solve a lot of complex numerical tasks such as planning developments and navigation, avoiding obstacles, pattern recognition, sound recognition, planning, visual-motor actions and making a decision in the absence of complete information. Performing such complex tasks in parallel (simultaneously) requires extremely powerful computing resources. In such cases, there is an alternative solution that promotes the so-called distributed ambient intelligence approach as technologically feasible, progressive approach to solving the problem of the accumulation of tasks and solving management problems in the system with simple distribution of tasks among agents. Cloud robotics is an emerging concept as real alternative to the built-in (embedded) management robot system, which overcomes the above-mentioned technological constraints in implementation.

Social interactive robot needs the same behaviours and capabilities as humans to be able to work in human daily life. Facial expressions is an examples of nonverbal cues used in inter-human interaction, that need to be recognised, possibly by deep learning techniques.

Together, the digital transformation and robotics open up new horizons for the design, construction and development of structures of modern avant-garde forms and systems. By coupling powerful CAD software tools and multitasking robot controllers, the most diverse and unusual forms in architecture and art can be today produced very accurately. This can be noticed by examining their stability and stresses in critical sections, aerodynamics, etc. When the robot is working, subjective factors of human fatigue, lack of motivation, etc. can be eliminated. For this reason, the robots in manufacturing have increased application and effectiveness and they have also a huge potential to be applied in design, construction and architecture.

The accepted papers have been grouped in ten technical sessions: (I) Intelligent Robot Motion Control, (II) Robot Vision and Sensory Processing, (III) Novel Design of Robot Manipulators and Grippers, (IV) Robot Applications in Manufacturing and Services, (V) Autonomous Systems, Humanoid and Walking

Robots, (VI) Human-Robot Interaction and Collaboration, (VII) Cognitive Robots and Emotional Intelligence, (VIII) Medical, Human-Assistive Robots and Prosthetic Design, (IX) Robots in Construction and Arts, and (X) Evolution, Education, Legal and Social Issues of Robotics.

All these aspects are treated in this book—**Advances in Robot Design and Intelligent Control**—Proceedings of the 25th International Conference on Robotics in Alpe-Adria-Danube Region of the Springer series *Advances in Intelligent Systems and Computing*, which we hope you will find useful reading.

Belgrade, Bucharest                                        Aleksandar Rodić
July 2016                                                    Theodor Borangiu

# Contents

## Robot Vision and Sensory Processing

## Novel Design of Robot Manipulators and Grippers

**Robot Applications in Manufacturing and Services**

# Intelligent Robot Motion Control

# Kinematic Control of Redundant Robots in Changing Task Space

Leon Žlajpah[(✉)]

Jožef Stefan Institute, Ljubljana, Slovenia
`leon.zlajpah@ijs.si`

**Abstract.** In the paper we propose a task-space kinematic velocity controller for tasks which do not require motion in all spatial directions and these directions also change over time. For that, the controller is mapped from the world space to the task space which may change during the task execution. To simplify the mapping we propose that the desired task location is the origin of the task frame. Effectiveness of the proposed control approach is illustrated by an experiment on a dual arm robot system performing a ring task.

**Keywords:** Kinematic control · Redundant robot · Task-space · Ring task

## 1 Introduction

The task-space control is an important approach to the control of complex robots. This control framework is of essential importance for redundant robot manipulators, especially for multi-arm robots or humanoid robots, which have more degrees-of-freedom (DOFs) than those required to fulfill a task, and have to perform the task in human-like way. The tasks are usually defined as a motion of the robot end-effectors or of some other points on the robot body. The importance of controlling directly the motion in the task space was recognized very early [3,10] and since then many control schemes for task-space control have been proposed [1,2,4,5,7]. Most of the proposed control schemes where the task requires/allows directional dependent behaviour of the robot rely on transforming the task requirements into the task space where the robot kinematics and dynamics are defined [3]. However, such an approach is not suitable when the task does not require the motion in all spatial directions. In the paper we propose an approach which overcomes this drawback and enables efficient control in reduced task space which can also change with task execution.

## 2 Task Space Specification

In robotics the task is usually related to the motion of some operational points. Depending on the task these points are required to move to a specified point,

to move along a specified path, or the robot has to exert a certain force at that point. These operational points can be any points on the robot structure. Typically they are assigned to the robot end-effectors [1,3,5]. The location of an operational point is in general represented by a homogeneous matrix

$$\mathbf{T} = \begin{bmatrix} \mathbf{R} \ \boldsymbol{p} \\ \mathbf{0} \ 1 \end{bmatrix}, \tag{1}$$

where $\mathbf{R}$ is a $3 \times 3$ rotation matrix representing the orientation of the operational point and $\boldsymbol{p}$ is a 3-dimensional position vector. In the following we will assume that the robot has only one operational point.

It is conveniently to describe the location of the operational point in a suitably defined task frame. Figure 1 shows a general situation where $\mathcal{S}_w$ is the world (or basic) frame with the origin in $O_w$ and $\mathcal{S}_t$ is the task frame with the origin in $O_t$. The location of the task frame in the world frame is defined by the translation vector $\boldsymbol{p}_t$ connecting the origins $O_w$ and $O_t$, and with the rotation matrix $R_t$ representing the rotation between both frames. It is easy to see that the end-effector location ${}^t\mathbf{T}$ in $\mathcal{S}_t$ can be expressed as
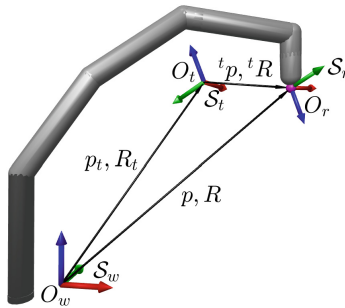


**Fig. 1.** Representation of task space, world space and corresponding frames

$$^t\mathbf{T} = \begin{bmatrix} {}^t\mathbf{R} \ {}^t\boldsymbol{p} \\ \mathbf{0} \ 1 \end{bmatrix} = \begin{bmatrix} \mathbf{R}_t^T \ -\mathbf{R}_t^T \boldsymbol{p}_t \\ \mathbf{0} \ 1 \end{bmatrix} \begin{bmatrix} \mathbf{R} \ \boldsymbol{p} \\ \mathbf{0} \ 1 \end{bmatrix} = \begin{bmatrix} \mathbf{R}_t^T \mathbf{R} \ \mathbf{R}_t^T(\boldsymbol{p} - \boldsymbol{p}_t) \\ \mathbf{0} \ 1 \end{bmatrix}, \tag{2}$$

where ${}^t\boldsymbol{p}$ and ${}^t\mathbf{R}$ are the end-effector position vector and orientation matrix defined in the task frame $\mathcal{S}_t$, respectively. Hereafter, we use the notation ${}^t(\cdot)$ to denote that the quantity is expressed in the frame $\mathcal{S}_t$, otherwise the quantity is expressed in the world frame $\mathcal{S}_w$.

How the task space is defined depends on the particular task the robot should perform. Typically, the task frame is selected to coincide with the fixed world frame ($\boldsymbol{p}_t = [0\,0\,0]^T$ and $\mathbf{R}_t = \mathbf{I}$). When the end-effector motion is constrained, the constraints restrict the motion (displacements and/or rotations) in some spatial directions. Therefore, it is convenient to align the task space with the

constraints [3,8]. If the constraints are not changing, the task frame can be fixed. On the other hand, when the task requires different behaviour in spatial directions and if these directions change during the task execution, the task frame $\mathcal{S}_t$ changes. For example, the task frame can be related to the path along which the robot is supposed to move. Hereafter, we focus on tasks where the task frame is changing, i.e. $\boldsymbol{p}_t = \boldsymbol{p}_t(t)$ and $\mathbf{R}_t = \mathbf{R}_t(t)$ or $\boldsymbol{p}_t = \boldsymbol{p}_t(s)$ and $\mathbf{R}_t = \mathbf{R}_t(s)$, where $s$ represents the task evolution.

The differential kinematics in task frame $\mathcal{S}_t$ can be obtained by differentiating Eq. (2). Let $\boldsymbol{v} = [\dot{\boldsymbol{p}}^T \ \boldsymbol{\omega}^T]^T$ be the operational point velocity in $\mathcal{S}_w$, $\boldsymbol{v}_t = [\dot{\boldsymbol{p}}_t^T \ \boldsymbol{\omega}_t^T]^T$ be the velocity of the task frame origin $O_t$ in $\mathcal{S}_w$, and ${}^t\boldsymbol{v} = [{}^t\dot{\boldsymbol{p}}^T \ {}^t\boldsymbol{\omega}^T]^T$ be the operational point velocity in $\mathcal{S}_t$. Then, differentiating Eq. (2) yields

$$ {}^t\boldsymbol{v} = \widetilde{\mathbf{R}}_t^T \boldsymbol{v} - \widetilde{\mathbf{R}}_t^T \mathbf{J}_t \boldsymbol{v}_t \,, \tag{3} $$

where $\widetilde{\mathbf{R}}_t$ is a $6 \times 6$ matrix

$$ \widetilde{\mathbf{R}}_t = \begin{bmatrix} \mathbf{R}_t & \mathbf{0}_{3\times3} \\ \mathbf{0}_{3\times3} & \mathbf{R}_t \end{bmatrix} \tag{4} $$

and $\mathbf{J}_t$ is the task frame Jacobian matrix defined as

$$ \mathbf{J}_t = \begin{bmatrix} \mathbf{I}_{3\times3} & -\mathbf{S}(\boldsymbol{p} - \boldsymbol{p}_t) \\ \mathbf{0}_{3\times3} & \mathbf{I}_{3\times3} \end{bmatrix} \tag{5} $$

and $\mathbf{S}$ the $3 \times 3$ skew-symmetric matrix operator performing the cross product [7]. If all positions and orientations of the operational point are important, then the task space dimension $m$ equals to 6. However, it is not necessary that the task requires motion or actions in all directions of the task frame $\mathcal{S}_t$. For such tasks, the dimension of the task space can be reduced, $m < 6$.

## 3   Modelling

The robotic systems under consideration are serial link manipulators consisting of links with rotational or prismatic joints. Let the configuration of the manipulator be represented by the $n$-dimensional vector $\boldsymbol{q}$ of joint positions. The robot end-effector position $\boldsymbol{p}$ and orientation $\mathbf{R}$ can be expressed as a function of joint coordinates using the direct kinematic equations

$$ \boldsymbol{p} = \boldsymbol{p}(\boldsymbol{q}) \qquad \text{and} \qquad \mathbf{R} = \mathbf{R}(\boldsymbol{q}). \tag{6} $$

The spatial end-effector velocity is in general expressed as a 6-dimensional vector $\boldsymbol{v}$, $\boldsymbol{v} = [\dot{\boldsymbol{p}}^T \boldsymbol{\omega}^T]^T$, where $\dot{\boldsymbol{p}}$ and $\boldsymbol{\omega}$ are the positional and rotational velocity, respectively. The differential forward kinematics of the robot is then given as

$$ \boldsymbol{v} = \mathbf{J}(\boldsymbol{q})\dot{\boldsymbol{q}}, \tag{7} $$

where $\mathbf{J}(\boldsymbol{q})$ is the $6 \times n$ geometric (or basic) Jacobian matrix.

In the case when the dimension of the configuration space $n$ is greater than the required task space dimension $m$, $n > m$, the robot is kinematically redundant. Under the assumption that the robot is kinematically redundant, the general inverse kinematic solution is given in the form

$$\dot{\boldsymbol{q}} = \mathbf{J}^{\#}\dot{\boldsymbol{x}} + \mathbf{N}\dot{\boldsymbol{q}}, \tag{8}$$

where $\mathbf{J}^{\#}$ is the generalized inverse of the Jacobian matrix $\mathbf{J}$ and $\mathbf{N}$ is a matrix representing the projection into the null space of $\mathbf{J}$, $\mathbf{N} = (\mathbf{I} - \mathbf{J}^{\#}\mathbf{J})$. Note that the above equations refer to the world coordinate system $\mathcal{S}_w$ in which kinematic and dynamic models of robots are usually formulated.

## 4   Kinematic Control

There are many different approaches to the kinematic control of robots. All kinematic controllers rely on some kind of inner-loop inverse dynamic control, and the kinematic controller in the outer-loop provides the necessary control signals for the inner-loop from the desired task-space velocities and accelerations [4]. In the present work, we assume that the inner-loop controller already compensates the nonlinear dynamics of the robot and that the robot motion is controlled by the joint velocity controller.

A natural way to describe the motion of the end-effector is to use the world space [3]. If the task space control system is also formulated in the world frame, no transformations of kinematic or dynamic models between the world frame $\mathcal{S}_w$ and the task frame $\mathcal{S}_t$ are necessary. When the task requires a special robot behaviour in some directions, then the common practice is to formulate the control constraints or requirements in a relevant task frame $\mathcal{S}_t$ and then transform these requirements to the world frame $\mathcal{S}_w$ [3]. However, such an approach is not suitable when the task-space control is not spanned over all six dimensions, i.e. when the task does not require a controlled motion in one or more spatial directions. In such situations we propose to define the control directly in the task space $\mathcal{S}_t$.

Classical task space velocity controllers are based on the following kinematic control law [9]

$$\dot{\boldsymbol{q}}_c = \mathbf{J}^{\#}\dot{\boldsymbol{x}}_c + \mathbf{N}\dot{\boldsymbol{q}}_n, \tag{9}$$

where $\dot{\boldsymbol{x}}_c$ is representing the task-space control velocity, and $\dot{\boldsymbol{q}}_n$ is an arbitrary joint velocity, which is projected into the null-space of $\mathbf{J}$ and can be used to perform some additional lower priority subtasks. Note that $\dot{\boldsymbol{x}}_c$ can represent the velocity in any space as long as the Jacobian matrix $\mathbf{J}$ relates the robot configuration space and the selected space.

The task-space control velocity $\dot{\boldsymbol{x}}_c$ in (9) can be selected as

$$\dot{\boldsymbol{x}}_c = \boldsymbol{v}_d + \mathbf{K}_p\boldsymbol{e}, \tag{10}$$

where $\boldsymbol{v}_d$ and $\boldsymbol{e}$, $\boldsymbol{e} = [\boldsymbol{e}_p^T \ \boldsymbol{\epsilon}^T]^T$, are the desired end-effector position/rotation velocity and the end-effector position/orientation error expressed in the world frame $\mathcal{S}_w$, respectively. $\mathbf{K}_p$ is a diagonal gain matrix.

The above control can be mapped into the task space using Eq. (3). To simplify the calculation of the control velocity $\dot{\boldsymbol{q}}_c$ and $\dot{\boldsymbol{x}}_c$, it is convenient to attach the task frame to the desired path of the operational point. So, we select $\boldsymbol{p}_t = \boldsymbol{p}_d$ and $\mathbf{R}_t = \mathbf{R}_d$. Then, using these in Eq. (3), the desired end-effector position/rotation velocity in frame $\mathcal{S}_t$ becomes

$$^t\boldsymbol{v}_d = \widetilde{\mathbf{R}}_t^T \boldsymbol{v}_d - \widetilde{\mathbf{R}}_t^T \mathbf{J}_t \boldsymbol{v}_d = \mathbf{0} \tag{11}$$

and using then in Eq. (2), the position and orientation errors in frame $\mathcal{S}_t$ become

$$^t\boldsymbol{e}_p = \mathbf{R}_t^T (\boldsymbol{p} - \boldsymbol{p}_d) = \mathbf{R}_t^T \boldsymbol{e}_p \qquad \text{and} \qquad {}^t\boldsymbol{\epsilon} = \mathbf{R}_t^T \boldsymbol{\epsilon}. \tag{12}$$

Rearranging Eqs. (11) and (12) and substituting them into Eq. (10) gives the the task space control velocity in the form

$$^t\boldsymbol{v}_c = \mathbf{K}_{p,t} \widetilde{\mathbf{R}}_t^T \boldsymbol{e}. \tag{13}$$

Note that the gain matrix $\mathbf{K}_{p,t}$ is now defining the close-loop behavior in the task space. Finally, we have to transform Eq. (9) to frame $\mathcal{S}_t$. Using Eq. (7) in Eq. (3) yields

$$^t\boldsymbol{v} = \widetilde{\mathbf{R}}_t^T \mathbf{J} \dot{\boldsymbol{q}} - \widetilde{\mathbf{R}}_t^T \mathbf{J}_t \boldsymbol{v}_d. \tag{14}$$

Rearranging it we obtain the kinematic velocity controller in the form

$$\dot{\boldsymbol{q}}_c = (\widetilde{\mathbf{R}}_t^T \mathbf{J})^{\#} \, {}^t\dot{\boldsymbol{x}}_c + (\mathbf{I} - (\widetilde{\mathbf{R}}_t^T \mathbf{J})^{\#} \widetilde{\mathbf{R}}_t^T \mathbf{J}) \dot{\boldsymbol{q}}_n, \tag{15}$$

where

$$^t\dot{\boldsymbol{x}}_c = \widetilde{\mathbf{R}}_t^T \mathbf{J}_t \boldsymbol{v}_d + \mathbf{K}_{p,t} \widetilde{\mathbf{R}}_t^T \boldsymbol{e}. \tag{16}$$

Here the term $\widetilde{\mathbf{R}}_t^T \mathbf{J}$ can be denoted as the task frame Jacobian. Comparing Eqs. (9) and (15) we can see that both controllers are similar. Actually, in the controller (15) only the Jacobian matrix and task velocities are mapped using matrix $\widetilde{\mathbf{R}}_t$. The only difference is a term $\mathbf{S}(\boldsymbol{e}_p)\boldsymbol{\omega}_d$ hidden in $\mathbf{J}_t$ and is depending on the task space positional error $\boldsymbol{e}_p$ and the task frame rotational velocity $\boldsymbol{\omega}_d$.

When the task does not require the controlled motion in all six spatial directions then instead of the control (15) we propose to use the following control law

$$\dot{\boldsymbol{q}} = \widehat{\mathbf{J}}^{\#} \, \dot{\widehat{\boldsymbol{x}}}_c + (\mathbf{I} - \widehat{\mathbf{J}}^{\#} \, \widehat{\mathbf{J}}) \dot{\boldsymbol{q}}_n, \tag{17}$$

where $\widehat{\mathbf{J}}$ is the Jacobian matrix consisting only of those rows of $\widetilde{\mathbf{R}}_t^T \mathbf{J}$ which correspond to the task frame directions to be controlled, and $\dot{\widehat{\boldsymbol{x}}}_c$ is a vector of control velocities in these directions. For example, if the orientation around z-axis in the task frame $\mathcal{S}_t$ should not be part of the task controller then

$$\dot{\widehat{\boldsymbol{x}}}_c = [{}^t\dot{\boldsymbol{p}}_{c,x}, \; {}^t\dot{\boldsymbol{p}}_{c,y}, \; {}^t\dot{\boldsymbol{p}}_{c,z}, \; {}^t\boldsymbol{\omega}_{c,x}, \; {}^t\boldsymbol{\omega}_{c,y}, \; {}^t\cancel{\boldsymbol{\omega}_{c,z}}]^T = [\mathbf{I}_{5\times5} \; \mathbf{0}_{5\times1}] \, {}^t\dot{\boldsymbol{x}}_c \tag{18}$$

and

$$\widehat{\mathbf{J}} = [\mathbf{I}_{5\times5} \; \mathbf{0}_{5\times1}] \widetilde{\mathbf{R}}_t^T \mathbf{J}. \tag{19}$$

## 5   Case Study

In order to show the performance of the proposed kinematic control we have
selected an illustrative task for a two-arm robot. The system consists of two
KUKA LWR robot arms operating as a two-arm robot. Figure 2 shows the model
of the two-arm robot system.



a) Configuration

b) Task motion

c) Self motion
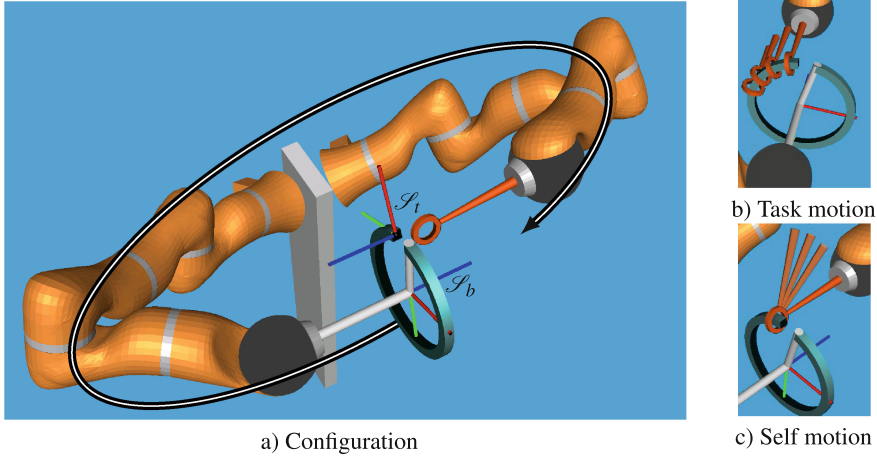
**Fig. 2.** Two-arm KUKA LWR robot system

The robots have to do the "ring" task, i.e. to move the ring, which is attached
to the left LWR robot arm end-effector, along the wire, which is attached to the
right LWR robot arm. For convenience, the wire is a hoop in a circular form
(diameter 0.25 m). The ring has to be moved so that the hoop is always in the
middle of the ring, and the ring orientation has to be perpendicular to the hoop
(see Fig. 2b). Note that the orientation of the ring regarding the hoop is not
important for the task, i.e. the ring can be freely rotated around the hoop (see
Fig. 2c).

To accomplish this task a coordinated motion of both robot arms is neces-
sary. Therefore, we have to find a suitable task description that allows coor-
dinated control of both robot arms. For this particular task only the relative
position/orientation between robot end-effectors is important. An effective for-
mulation of the kinematics for cooperative robot arms is to model both arms as
one kinematic chain. In contrast to usual formulation of the relative position,
which is the difference of end-effector positions in the fixed world frame [2], we
formulate the relative kinematics as a serial kinematic chain starting at the end-
effector of the right robot arm, going through both robot bases and ending at the
end-effector of the left robot (indicated with an arrow in Fig. 2a). According to
this formulation, the right robot arm end-effector frame $\mathcal{S}_b$ represents the basic

(world) frame, and the desired task motion is defined in frame $\mathcal{S}_b$ as

$$\boldsymbol{p}_d = 0.125[\cos(\varphi(t))\ \sin(\varphi(t))\ 0]^T \quad \text{and} \quad \mathbf{R}_d = \mathbf{R}_z(-\varphi(t))\mathbf{R}_x(\pi), \quad (20)$$

where $\varphi(t)$ represents the progression along the path. Matrices $\mathbf{R}_z$ and $\mathbf{R}_x$ are rotation matrices for rotations around $z$ and $x$ axis, respectively. As proposed before, the task frame $\mathcal{S}_t$ is at the desired position and is oriented so that the $y$-axis is pointing in the path direction (see Fig. 2a). We have used the controller (17) where the components corresponding to the rotation around $y$-axis have been removed from $\widetilde{\mathbf{R}}^T\mathbf{J}$ and $\dot{\hat{\boldsymbol{x}}}_c$.

To implement the proposed control on KUKA LWR robots we have used the Fast Research Interface (FRI) provided by KUKA, which allows external control of LWR robot [6]. As the FRI allows only independent control of each LWR robot arm, we have developed our own server, where we have implemented the kinematic control (17) of both arms as one robot system. The obtained joint positions have been then used as the desired joint positions for the joint position controller of each LWR robot [6].

The dual-arm experimental system has 14 DOF. To accomplish the proposed task only 5 DOF are necessary. Hence, the system offers 9 redundant DOF to perform some lower priority subtasks. For demonstration we have implemented the obstacle avoidance algorithm and the available redundant DOFs can been used to avoid obstacles in the workspace of the dual-arm robot system. The basic idea has been to define the obstacle avoiding motion using external forces caused when any of the robot arms is in contact with the environment [9]. These contact forces are provided by the KUKA LWR controller using internal joint torque sensors. Based on the Jacobian transpose formulation for the task motion control we propose to use the following simple null-space velocity control

$$\dot{\boldsymbol{q}}_n = -\mathbf{K_n}\,\boldsymbol{\tau}_{ext}(\boldsymbol{F}_{ext}), \quad (21)$$

where $\boldsymbol{\tau}_{ext}$ are external joint torques due to the external forces $\boldsymbol{F}_{ext}$ acting anywhere on the body of the robot arms. $\mathbf{K_n}$ is a suitable gain matrix. Figure 3
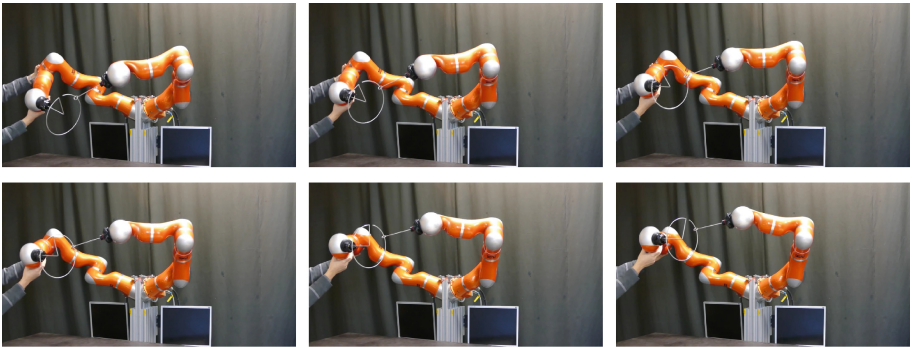


**Fig. 3.** Experimental results: dual-arm LWR robots performing the "ring" task and interacting with a human in the workspace

shows a motion sequence of the dual-arm robot performing the "ring" task while a human is disturbing the robot. We can see that the dual-arm robot system is performing the desired task and it is reconfiguring (using the redundant DOF) into the pose to which a human pushes the links. Note that the rotation of the ring around the wire is also utilized for the self motion.

## 6    Conclusion

Some tasks do not require all six spatial positions or orientations. We show how to augment the null-space motion with additional DOFs which are not necessary for performing the task. For that, it is convenient to implement the kinemtic control in the task space. Because the robot kinematics and dynamics are usually not defined in a particular task space but in the world space, it is necessary to map the kinematic and dynamic models from the world frame into a suitable task frame. Of course, if the task directions are changing then the task frame where the control is realized is also changing. To simplify the mapping we propose to select the desired task space location as the task frame for the control. Actually, it is necessary only to rotate the Jacobian matrix and the control velocities from the world frame into the task frame and then select the DOFs, which have to be controlled, to perform the main task. All remaining DOFs can be used then for additional lower priority tasks.

For the case study we have selected the ring task where it is not possible to exploit self-motion of the robot end-effector around the wire by using the classical kinematic control. With the proposed control approach the robot has successfully performed the ring task and simultaneously moved in the direction the human has pushed it. This "obstacle avoidance" subtask has taken advantage of the additional redundant DOF offered by the unused orientation axis.

## References

1. Brock, O., Kuffner, J., Xiao, J.: Motion for manipulation tasks. In: Siciliano, B., Khatib, O. (eds.) Springer Handbook of Robotics, pp. 615–645. Springer, Heidelberg (2008). Chap. 26
2. Caccavale, F., Uchiyama, M.: Cooperative manipulators. In: Siciliano, B., Khatib, O. (eds.) Springer Handbook of Robotics, pp. 701–718. Springer, Heidelberg (2008). Chap. 29
3. Khatib, O.: A unified approach for motion and force control of robot manipulators: the operational space formulation. IEEE J. Robot. Autom. **5**(3), 107–115 (1987)
4. Nakanishi, J., Cory, R., Mistry, M., Peters, J., Schaal, S.: Operational space control: a theoretical and empirical comparison. Int. J. Robot. Res. **27**, 737–757 (2008)
5. Russakow, J., Khatib, O., Rock, S.: Extended operational space formulation for serial-to-parallel chain (branching) manipulators (1995)
6. Schreiber, G., Stemmer, A., Bischoff, R.: The fast research interface for the kuka lightweight robot (2010)
7. Siciliano, B., Sciavicco, L., Villani, L., Oriolo, G.: Robotics - Modelling, Planning and Control. Springer, London (2009)

8. Stilman, M.: Global manipulation planning in robot joint space with task constraints. IEEE Trans. Rob. **26**(3), 576–584 (2010)
9. Žlajpah, L., Petrič, T.: Obstacle avoidance for redundant manipulators as control problem. In: Serial and Parallel Robot Manipulators - Kinematics, Dynamics, Control and Optimization, pp. 203–230. InTech, Rijeka (2012)
10. Whitney, D.E.: Resolved motion rate control of manipulators and human protheses. IEEE Trans. Man-Machine Syst. **10**, 47–53 (1969)

# Robot Force/Position Control Combined with ILC for Repetitive High Speed Applications

Herbert Parzer[1]([✉]), Hubert Gattringer[1], Andreas Müller[1], and Ronald Naderer[2]

[1] Institute of Robotics, Johannes Kepler University Linz, Altenbergerstraße 69, 4040 Linz, Austria
{herbert.parzer,hubert.gattringer,a.mueller}@jku.at
[2] FerRobotics Compliant Robot Technology GmbH, Altenbergerstraße 69, 4040 Linz, Austria
ronald.naderer@ferrobotics.at
http://www.robotik.jku.at, http://www.ferrobotics.at

**Abstract.** In this paper an approach for robot force/position control combined with an iterative learning control is proposed. Following high speed force trajectories in different repetitive robotic applications is a challenging field in robotics. Such applications require a desired contact force while following a position/orientation trajectory in the non-force controlled directions. For this a parallel force/position control is suitable, but when it comes to high speed tasks with varying contact stiffness along the trajectory such a method reaches its dynamical limit. The problem can be solved by using the parallel force/position control to learn the trajectory for a slowed down task and correct this trajectory step by step towards the original task speed. When the original task speed is reached an iterative learning control law combined with the force/position control is used to further reduce the force error.

**Keywords:** Robot force/position control · Iterative learning control · High speed applications · Non-linear contact stiffness

## 1 Introduction

In many industrial applications manipulators are used to perform repetitive force controlled tasks. Typically, such tasks are polishing, grinding, assembly as well as endurance testing of machine parts. The repetitive nature of such tasks allows for using iterative learning control (ILC) methods, see a brief survey in [2], or adaptive learning feed–forward control, as shown in [8]. While adaptive methods change controller parameters, classical ILC modifies the input of the stabilized system in a serial or parallel way, explained in [3]. Iterative learning control theory is a wide field with different approaches for iteratively minimizing an error between an actual and a desired control signal. These approaches or update laws start from simple proportional (P–type) over "PID–like" types to higher order

types (HOILC), see [1,5]. Such a "PID–like" ILC has typically the form

$$\mathbf{u}_j = \mathbf{u}_{j-1} + \boldsymbol{\Phi}\,\mathbf{e}_{j-1} + \boldsymbol{\Gamma}\,\dot{\mathbf{e}}_{j-1} + \boldsymbol{\Psi}\,\int \mathbf{e}_{j-1}\mathrm{dt}, \tag{1}$$

where $\boldsymbol{\Phi}$, $\boldsymbol{\Gamma}$ and $\boldsymbol{\Psi}$ are the learn gain matrices, $\mathbf{u}_j$ is the input vector of the system, $\mathbf{e}$ is the error and $j$ the trial index. Further there can be distinguished between *causal* or *non–causal* ILC methods, where the latter ones are able to include zero–phase filtering of the error signal and compensate the delay time of the system. Using such a *non–causal* P–type ILC method often leads to a fast convergence within a few iterations and then to a divergence of the error. This bad transients are explained by Longman in [4] because of the growth of high frequencies in the signals and can be overcome with signal filtering and the introduction of a linear phase–lead compensation. Iterative learning control was also successfully tested for a parallel robot with high speed motions in [1], using P–type as well as PID–type iterative learning.

This paper introduces a novel method of time scaled force/position control and iterative learning control for position controlled robotic manipulators following fast force trajectories.

## 2  Force/Position Control

Considering a periodic task, where a robot processes or tests the same kind of workpiece in a recurring manner, the end–effector of the robot has to provide a predefined contact force $_I\mathbf{f}_d$, given in the inertial frame ($I$), while following a trajectory along the workpiece. This trajectory is defined by the desired end–effector position $_I\mathbf{r}_{E,d}$ and the desired rotation matrix $\mathbf{R}_{IE,d}$ transforming the end–effector frame ($E$) into the inertial frame. To achieve this goal, a parallel force/position robot control, as suggested in [7], is best suited. Thereby, the force control manipulates a desired end–effector trajectory, of a position controlled system, in such a way that the desired force is reached. The force control law is described by the differential equation $\mathbf{K}_A\,{}_I\ddot{\mathbf{r}}_c + \mathbf{K}_V\,{}_I\dot{\mathbf{r}}_c = {}_I\mathbf{f}_d - {}_I\mathbf{f}$, where $\mathbf{K}_A$ and $\mathbf{K}_V$ denote positive definite controller parameters and the vector $_I\mathbf{f}$ represents the measured force. Using the parallel composition $_I\mathbf{r}_r = {}_I\mathbf{r}_{E,d} + {}_I\mathbf{r}_c$, with $_I\mathbf{r}_c$ as solution of the above differential equation, the reference trajectory $_I\mathbf{r}_r$ is calculated. This reference trajectory serves as input of the position controlled robotic system.

## 3  Iterative Learning Control

However, following a fast desired force trajectory leads to various difficulties. First of all, the exact contact position as well as the contact stiffness is not always known. Further, the stiffness is non–linear and may vary from one point on the surface to another. So, especially for fast trajectories it is difficult to adjust the controller parameter for stable force tracking. Inspired by ILC, the idea is to divide the task into an *on–line* task, where the robot is actually moving, and an *off–line* task, where the computation and trajectory adaptation is done.

### 3.1   Iterative Force Control

Different to classical ILC methods, the previous mentioned issues are overcome by controlling the task with stretched time by a factor $s_t \geq 1$, depending on the task. In this time stretched *on–line* task the robot is able to follow the desired position and force trajectory safely. So by adding in the actual step $j$ the stored and (*off–line*) non–causal filtered force controller output $F\left[{}_I\mathbf{r}_{c,j-1}\right]$ to the reference trajectory ${}_I\mathbf{r}_r$, the force controller only acts on small force errors, arising from contact damping and system dynamics. The learning law during the time stretched iterations can be written to

$$ {}_I\mathbf{r}_{m,j} = {}_I\mathbf{r}_{m,j-1} + F\left[{}_I\mathbf{r}_{c,j-1}\right], \tag{2} $$

where ${}_I\mathbf{r}_m$ is introduced as memory trajectory. To improve performance, the trajectory from the start to the contact point (and back from the last contact point to the start point) is calculated *off–line* using splines with continuous transition conditions at start and end. With each further iteration the factor $s_t$ is reduced step by step towards 1, representing the original trajectory. Assuming stable force control, the force error at original speed is close to zero and the memory trajectory is trained within a few iterations. Due to the limited dynamics of the force controller further learning will not improve the result. By comparing this method with a P–type ILC one can easily see, that the learning gain $\boldsymbol{\Phi}$ is equal to 1. So for long term learning this is rather aggressive and would lead to an unstable behaviour, as discussed in [4].

### 3.2   Anticipatory P–type Learning

If it is necessary to further decrease the error a combination of the modified force control learning law from Sect. 3.1 and an anticipatory P–type learning law can be used. Typically such an anticipatory P–type learning law is given with $\mathbf{u}_j\left(k\right) = \mathbf{u}_{j-1}\left(k\right) + \boldsymbol{\Phi}\left(k\right)\mathbf{e}_{j-1}\left(k+1+l\right)$, where $k$ is the time step and $l$ the linear phase–lead compensation. It is worth to notice, that it is also possible to have a time varying gain matrix $\boldsymbol{\Phi}$. In most cases of standard ILC the signal $\mathbf{u}$ and the error signal $\mathbf{e}$ are from the same type, e.g. joint positions of a robot, and there is no coupling resulting in a diagonal gain matrix. However, controlling contact forces with a position controlled robot system requires as input an end–effector position in the inertial frame, while the output is given by measured forces. So it is obvious that the relationship is defined by the contact stiffness. The contact force can be described by a non–linear function ${}_I\mathbf{f} = {}_I\mathbf{f}\left({}_I\mathbf{r}_E, \mathbf{R}_{IE}\right)$ depending on the end–effector position ${}_I\mathbf{r}_E$ and orientation $\mathbf{R}_{IE}$. Typically there is a desired force at a desired orientation required and so the function of the contact force can be linearized around this point to

$$ {}_I\mathbf{f} \approx \underbrace{{}_I\mathbf{f}\left({}_I\bar{\mathbf{r}}_{E,d}, \mathbf{R}_{IE,d}\right)}_{={}_I\mathbf{f}_d} + \underbrace{\left.\frac{\partial{}_I\mathbf{f}}{\partial{}_I\mathbf{r}_E}\right|_{\left({}_I\bar{\mathbf{r}}_{E,d}, \mathbf{R}_{IE,d}\right)}}_{=:\,\mathbf{C}_{local}\left({}_I\bar{\mathbf{r}}_{E,d}, \mathbf{R}_{IE,d}\right)} \Delta{}_I\mathbf{r}_E, \tag{3} $$

where $_I\bar{\mathbf{r}}_{E,d}$ is the desired end–effector position which will result in zero force error. Using this local contact stiffness matrix $\mathbf{C}_{local}$, which also depends on the orientation, would have a huge impact on the accuracy and also on the stability of the system. So, with additional iterations in the time stretched task and slightly changed desired force vectors, the estimated stiffness matrix $\hat{\mathbf{C}}_{local}$ can be identified from measurements. Substituting the estimated stiffness matrix in (3) a position correction for a measured force error can be calculated to $\Delta_I\mathbf{r}_{m,Pcorr} = \hat{\mathbf{C}}_{local}^{-1}\left(_I\mathbf{f} - _I\mathbf{f}_d\right) = -\hat{\mathbf{C}}_{local}^{-1}\Delta_I\mathbf{f}$. By using this in the P–type ILC the position correction

$$\Delta_I\mathbf{r}_{m,Pcorr,j-1}\left(k\right) = -\boldsymbol{\Phi}\,\hat{\mathbf{C}}_{local}^{-1}\left(\mathbf{R}_{IE,d}\left(k\right)\right)\,F\left[\Delta_I\mathbf{f}_{j-1}\left(k+1+l\right)\right] \qquad (4)$$

is derived, where $F$ is again a non–causal zero–phase filter to cutoff high frequencies. In this case the new update law reads in contrast to Sect. 3.1 $_I\mathbf{r}_{m,j} = _I\mathbf{r}_{m,j-1} + \Delta_I\mathbf{r}_{m,Pcorr,j-1}$. The additional linear phase–lead compensation $l$ is used to in increase the learning bandwidth. Without the knowledge of the local stiffness it would be critical to tune the ILC because a too high estimated stiffness will lead to a very poor convergence while a too low stiffness will cause instabilities, especially when the stiffness changes along the orientation. So, by using the system information of the contact stiffness in the ILC law the convergence is improved and the stability depends on the choice of the gain matrix, the cutoff frequency of the filter and the phase–lead compensator.

### 3.3   Combined ILC

With the *off–line* position correction from (4) a zero error convergence is not possible due to the filtering of the force error, but with well chosen parameters satisfying force tracking can be achieved. However, one big disadvantage of this method is that the learning control is only able to react on (periodic) disturbances after one trial, whereas the *on–line* force control method, which is used to create the basic memory trajectory, directly reacts on disturbances. In case of disturbances within the bandwidth of the force controller the force error is already in the actual trial reduced. Assuming a periodic disturbance the position correction will cancel out the remaining tracking error. A faster convergence can be achieved by taking the output of the force controller into account, like it is done by the P–type learning. To do this, a further correction of the memory trajectory can be done by

$$\Delta_I\mathbf{r}_{m,Fcorr,j-1}\left(k\right) = \boldsymbol{\Phi}\,F\left[_I\mathbf{r}_{c,j-1}\left(k+1+l\right)\right], \qquad (5)$$

where again the gain matrix, the filter and the phase–lead compensation are used.

All these corrections and controllers for a high speed force control can be summarized in the following statements. First of all, with the force control method and the time stretching a memory trajectory is trained to achieve good force tracking. In the time stretched trajectories the contact stiffness is identified for

the ILC and within a few iterations the original speed can be reached. To further improve performance an anticipatory P–type ILC weighted with the contact stiffness is used. Combined learning with the force controller is possible and the whole update law at the original speed is given by

$$_I\mathbf{r}_{m,j} = {_I}\mathbf{r}_{m,j-1} + \Delta_I\mathbf{r}_{m,Pcorr,j-1} + \Delta_I\mathbf{r}_{m,Fcorr,j-1}. \tag{6}$$

In the next section an example is shown, to clarify the theory above.

## 4   Example

The following example is based on an experiment published by the authors in [6], where only the time stretching method is introduced. Thereof the gained data are used to build a realistic simulation and so to test the combined ILC method.

### 4.1   Experiment

For the experiment a six–axis industrial robot (STÄUBLI TX90L) controlled by decentralized feed–back motor position controllers and by centralized trajectory generation and force control is used. At the end–effector of the robot a curved tool, see Fig. 1, with the radius $R$ is mounted. In the scenario the tool contacts the surface and moves with a smooth roll–over motion from $\beta_d = 25°$ to $\beta_d = -25°$ in $T = 0.75$ s over the surface and back. During the contact a desired force of $_I f_{z,d} = 100 \cos\left(\frac{\pi}{50}\beta_d\right)$ N in z–direction is required. For the time stretched trajectories the scaling factors $s_t = \{16, 16, 4, 1\}$ were used to track the desired force with a maximum force error of less than 3.5%. Figure 2 shows the desired and the measured force with learning force control from Sect. 3.1 (*FCTRL+MEM*, iteration 4) and with pure force control from Sect. 2 (*FCTRL*) at original speed.

### 4.2   Simulation

To test the above discussed update laws the simulation of the whole system is extended with the new control scheme and a position/orientation depended contact model is implemented. The contact model, see Fig. 3, is estimated by using the data from five measurements (blue lines) of the non–linear stiffness at discrete orientations $\beta$. This surface is described by B–splines in the $\beta$–$\Delta z$–plane, where $\Delta z$ is the difference between the end–effector point of the robot and the point on the elastic object in inertial $z$–direction. In Fig. 3 also the on the surface projected desired force $_I f_{z,d}$ (red line) is shown. Considering this, it is clear to see that the local stiffness around the desired force (marked with green) varies along this path. The continuous local stiffness function $c_{local}(\beta)$ is shown in Fig. 4. Figure 5 shows the robot control scheme for the simulation. First there is the *Trajectory* block, where the desired position and orientation for the roll–over
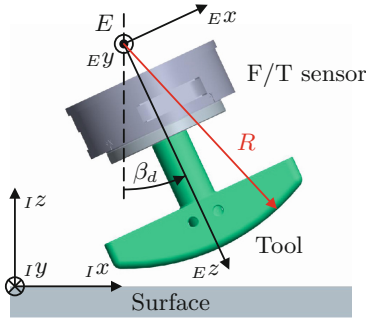
**Fig. 1.** Setup of the experiment
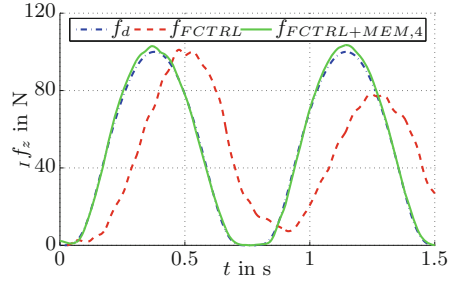


**Fig. 2.** Measurements from the experiment

motion is calculated. The *Inv. Kin.* block transforms task space coordinates $_I\mathbf{r}_r$ and $\mathbf{R}_{IE,d}$ to joints coordinates $\mathbf{q}_r$. They are passed to the position–controlled non–linear robot model, whose output is the actual end–effector position $_I\mathbf{r}_E$ and orientation $\mathbf{R}_{IE}$. The contact model from Fig. 3 is used to calculate the actual force $_I\mathbf{f}$ and the force controller modifies the desired trajectory, based on the force error. For the iterative learning control the modification as well as the force error is stored *off–line* and the thereof calculated memory trajectory is passed to the system *on–line* in the next trial.
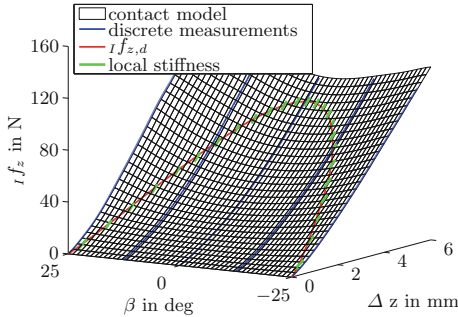


**Fig. 3.** Calculated contact model
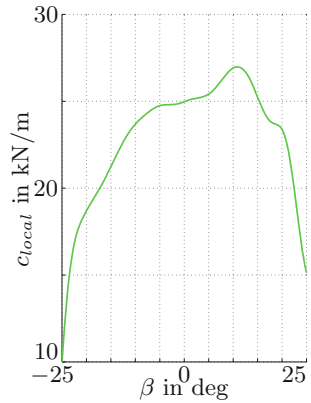


**Fig. 4.** Local stiffness

To study the learning behaviour the same desired trajectories as in the experiment are used and after 9 iterations a $\cos^2$–shaped periodic disturbance with an amplitude of $_I f_{z,dist} = 20$ N is added. This is done to compare three types of learning. The first type (*ILC*) is only learning with the weighted anticipatory P–type ILC from Sect. 3.2 while for the second type (*ILC+FCTRL*) additionally the force controller is switched on. Finally, the third type (*Combined ILC*) is the
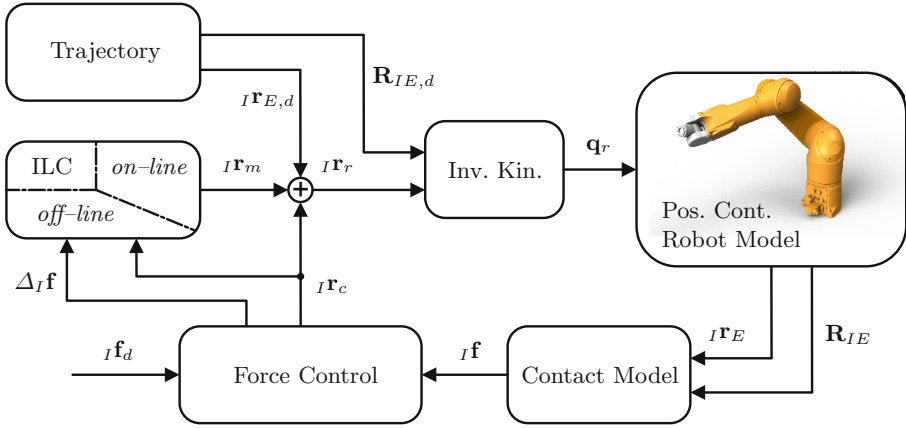
**Fig. 5.** Robot control scheme in the simulation

combined ILC, where also the output of the force controller is used to further train the memory trajectory, see (6). Identifying the local stiffness (Fig. 4) of the contact model is done during the time stretched iterations by simply following a slight changed desired force trajectory, as it would be done in reality. Figures 6 and 7 shows the convergence of the Euclidean norm of the force error from the first up to the 20th iteration and from the 20th to the 50th iteration, respectively. Thereby the iterations are counted since the original speed is reached. As one can see, additionally using the force controller can reduce the effect of the disturbance can be reduced. By also considering the output of the force controller in the combined learning strategy the convergence rate will be equivalent to that of the pure ILC. Not using this output results in a slower convergence rate of the second type. For all of these three types it is important to notice that
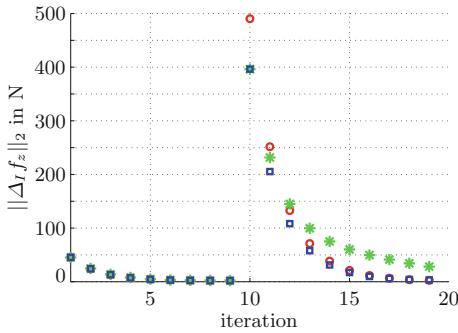


**Fig. 6.** Error norm (1–20)
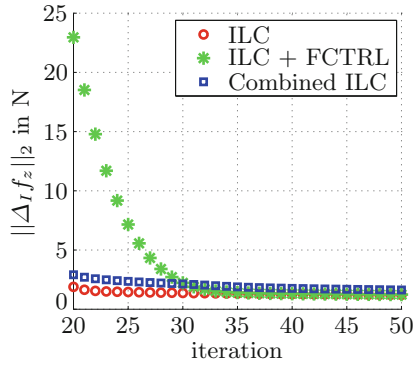


**Fig. 7.** Error norm (20–50)

if the local stiffness is not identified and estimated constant and too weak the stability of the ILC can not be guaranteed.

## 5   Conclusion

This paper introduces a promising combination of parallel force/position control for robotic systems and iterative learning control for repetitive high speed trajectories. While the force/position control has its limits in stability for fast force trajectories and varying contact stiffness, the approach of a time scaling iterative learning method shows best results. To further increase accuracy a combined method of anticipatory P–type learning weighted with system information and the force control itself is introduced. Simulation results shows good convergence and robustness, so that further research will focus on implementation and experiments.

## References

1. Abdellatif, H., Feldt, M., Heimann, B.: Application study on iterative learning control of high speed motions for parallel robotic manipulator. In: 2006 IEEE Conference on Computer Aided Control System Design, 2006 IEEE International Conference on Control Applications, 2006 IEEE International Symposium on Intelligent Control, pp. 2528–2533. IEEE (2006)
2. Ahn, H.S., Chen, Y., Moore, K.L.: Iterative learning control: brief survey and categorization. IEEE Trans. Syst. Man Cybern. Part C Appl. Rev. **37**, 1099 (2007)
3. Bristow, D.A., Tharayil, M., Alleyne, A.G.: A survey of iterative learning control. IEEE Control Syst. **26**, 96–114 (2006)
4. Longman, R.W.: Iterative learning control and repetitive control for engineering practice. Int. J. Control **73**, 930–954 (2000)
5. Owens, D.H., Hätönen, J.: Iterative learning control - an optimization paradigm. Ann. Rev. Control **29**, 57–70 (2005)
6. Parzer, H., Gattringer, H., Müller, A., Naderer, R.: Learning robot force/position control for repetitive high speed applications with unknown non-linear contact stiffness. PAMM **15**, 65–66 (2015)
7. Siciliano, B., Villani, L.: Robot Force Control. Springer Science & Business Media, New York (1999)
8. Velthuis, W.J., de Vries, T.J., van Amerongen, J.: Design procedure for a learning feedforward controller. In: Proceedings of the First IFAC Conference on Mechatronic Systems, pp. 955–960 (2000)

# On-Line Modifications of Robotic Trajectories: Learning, Coaching and Force Vs. Position Feedback

Andrej Gams[(✉)] and Tadej Petrič

Humanoid and Cognitive Robotics Lab, Department of Automatics,
Biocybernetics and Robotics, Jožef Stefan Institute, Ljubljana, Slovenia
{andrej.gams,tadej.petric}@ijs.si

**Abstract.** Robotic coaching is a process of modifying the motion of a robot during execution through human intervention, in a manner of a coach. Thus, parts of the motion are changed depending on the instructions which can be provided through different approaches. Methods and analyses of robotic coaching have been described in the literature, including methods relying on physical human-robot interaction. In this paper we analyze one such method, which uses a compliantly controlled robot, to different variations of position and force feedback. Our method is based on changing the motion by changing the dynamic motion primitives' (DMPs) weights. We qualitatively evaluate how such DMP based coaching methods can be made more responsive and what are the benefits of position vs. force feedback. Finally, through the use of position feedback on compliant robots, we show that the inherent properties of DMP learning itself can be used to achieve the same results as when coaching the robot. We present the results of a real-world experiment on a Kuka LWR-4 robot.

**Keywords:** Robotic coaching · Dynamic movement primitives · Learning · Force feedback

## 1 Introduction

In the last years several studies have focused on systems for robot coaching, tackling different approaches and tasks. The literature recognizes different methods of instructing the robots. For example, Gruebler et al. [7] combined voice commands and supervised learning, where voice commands served as the reward function. Verbal instructions of non-experts were similarly used to modify human demonstrated movements in [13]. On the other hand, Suzuki et al. [14] used facial expressions, measured with electromyography (EMG). Full body coaching based on motion capture was proposed in [2], where a motion capture suit was used. Motion capture is common for robotic motion imitation [3], and has also been applied for coaching. Gestures and obstacle avoidance algorithms were applied for coaching of dynamic movement primitives encoded motions in [12].

On the other hand, physical contact with a robot performing a motion has also been shown applicable for coaching. Lee and Ott [9] used kinesthetic teaching and iteratively updated the behaviour of a humanoid robot. Even more, physical human-robot interaction (pHRI) was combined with imitation learning in [10]. Compliant impedance control was utilized to limit the contact forces.

Since different methods are applicable for robotic coaching, it is not straight-forward which methods work best. Therefore, different analyses were performed. One such was published in [4]. In that paper the authors compared physical and visual feedback on a stiff and a compliant robot. A participant survey showed qualitatively, and the results showed quantitatively, that a method of using a compliant robot and position feedback worked best in the given case. Since only results for position feedback in combination with a compliant robot were presented, in this paper we extend that analysis with using force feedback on the compliant robot. Furthermore, we compare the results with respect to signals which represent an inverse of a DMP, thus linearizing the modification space. Finally, since compliant robots and position feedback can be used, we discuss how this differs from the learning of the motion in the framework of the periodic dynamic movement primitives (DMPs). This framework, serving as the backbone of the complete approach, provides favorable properties for robot control, but at the same time may introduce nonlinearities which can result in delays of robotic coaching. Figure 1 shows a person physically coaching the robot as part of the experiments of this study.
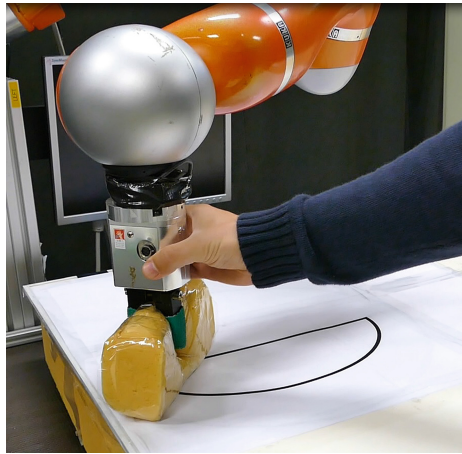


**Fig. 1.** A still image depicting the coaching of the robot through physical interaction.

This paper is organized as follows. In the next section we show how the learning of the DMPs is implemented, followed by applying that mechanism to robot coaching. The results of the real-world experiments are discussed next. A general discussion is finally included. For completeness of the paper, periodic DMPs are briefly explained in the Appendix.

## 2   Learning of Trajectories

In this section we introduce the learning of the weights of dynamic movement primitives. For details see [8]. A modification of this learning approach is used for coaching.

The waveform of the motion encoded in the DMP is given by the weights $\mathbf{w}$, which are used for the evolution of the forcing term $f(x)$. Typically, DMPs are employed for learning by demonstration, where the robot repeats a demonstrated motion. To learn the demonstrated motion, the weights of a periodic DMP are learned using incremental locally weighted regression (ILWR), see [1,5] for details. The target data for fitting, originating from (8)–(9) (see Appendix) is given as

$$f_{targ} = \frac{1}{\Omega^2}\ddot{y}_{\text{demo}} - \alpha_z\left(\beta_z\left(g - y_{\text{demo}}\right) - \frac{1}{\Omega}\dot{y}_{\text{demo}}\right). \tag{1}$$

Given $f_{targ}$, we can incrementally update the $i$-th weight $w_i$ for each timestep $j$ as

$$w_{i,j+1} = w_{i,j} + \Gamma_{i,j+1}P_{i,j+1}re_j \tag{2}$$

$$P_{i,j+1} = \frac{1}{\lambda}\left(P_{i,j} - \frac{P_{i,j}^2 r^2}{\frac{\lambda}{\Gamma_i} + P_{i,j}r^2}\right) \tag{3}$$

$$e_j = f_{\text{targ},j} - w_{i,j}r. \tag{4}$$

Here, $\Gamma_i$ are the kernel functions, with $P_i$ the inverse covariance of $w_i$ [11]. At the start of the recursion $w_i = 0$ and $P_i = 1$. $r$ is the amplitude gain. $\lambda \leq 1$ defines the forgetting factor, with useful range from 0.97 to 1. If $\lambda < 1$, more weight is given to recent data, i.e., forgetting older data.

## 3   Robot Coaching

### 3.1   Force Vs. Position Feedback

The robot in the used method is compliant in the direction that needs modification of motion through coaching, in our case this is the $x_p$ direction. Instead of making the weights of the DMP dependent on a demonstration, as in (4), in this case the adaptation is based on the difference between the robot's actual position and the robot's desired position. In this paper we evaluate if there is a difference, whether we use the actual measured force at the end effector, or what is in essence positional feedback. Because the reactive movement of the robot is linearly proportional to the external force, this should not be different.

The changing of DMP weights $w$, is for the position feedback, given by

$$e_j = K_p(x_{p,\text{des}} - x_{p,\text{act}}), \tag{5}$$

where $x_{p,\text{des}}$ stands for desired and $x_{p,\text{act}}$ for actual end effector position in $x_p$ direction and $K_p$ is the gain. For the force feedback it stands as

$$e_j = K_f F_{\text{act}}, \tag{6}$$

with $F_{\text{act}}$ being the measured force and $K_f$ a scaling factor.

### 3.2  Modified Feedback Signal

Besides the force-position feedback, in this paper we also evaluate whether we can improve the slow responsiveness of the coaching of this method, reported in [4]. We do this by modifying the feedback signal using the *Derived* method, introduced in [6]. In this method, the feedback signal is modified in the same manner as when making the target for the learning of DMPs,

$$e_j = \frac{1}{\Omega^2}\ddot{m} - \alpha_z \left( \beta_z \left( g - m \right) - \frac{1}{\Omega}\dot{m} \right), \tag{7}$$

where $m$ stands for either the force feedback, as in (6), or the position feedback given by (5). In this paper we also refer to this method as the *Derived* method.

Finally, we show what happens when filtering the derived signal from (7) with a low pass filter. This last method is termed in this paper as the *Filtered derived* method.

## 4  Experimental Evaluation and Results

We performed the experiment on a Kuka LWR-4 robot, controlled from a desktop PC, using the Kuka Fast Research Interface (FRI). The robot control algorithm and the coaching algorithm were both executed in a Matlab-Simulink scheme, running at 100 Hz. The Jacobian pseudo-inverse inverse kinematics was used so that the robot's end effector moves in the desired task-space direction and with a constant orientation in all directions. The range of motion in the robot's $x_p$ and $y_p$ directions was limited for safety.

The robot's task-space stiffness control mode was used, which also allowed joint control with appropriate FRI flags. The stiffness was set to 500 N/m for $x_p$ direction and 1500 N/m for all other directions and orientations. In the experiment the robot was using an environment adaptation technique described in [6] to maintain contact with a flat surface. A half-sphere shape was drawn on the surface as a guide to the user. A person coaching the robot is depicted in Fig. 1. The task of the user was to modify the initial motion to the half-sphere shape, leave it a few periods, and then try and achieve a straight left-right pattern. Only $x_p$ direction of motion was modified with coaching. The frequency of motion was constant.

The plots in Fig. 2 show the best achieved patterns for position and force feedback signals. In all the plots, green is the initial pattern, blue is the half-sphere intermediate pattern, and red is the final, straight line pattern.
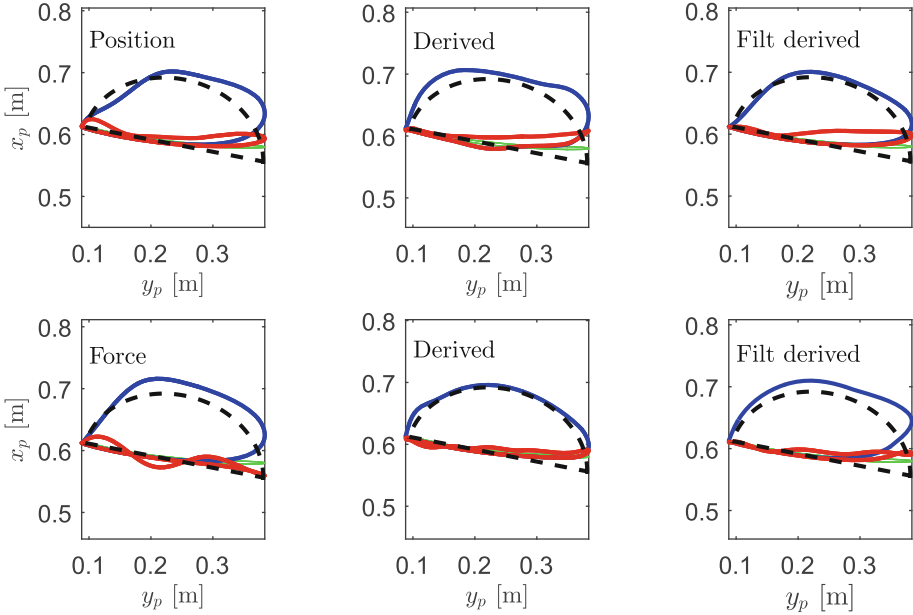
**Fig. 2.** Position feedback coaching results for all three variations (top) and force feedback coaching results for all three variations (bottom).

Analyzing the plots we can see that the derived force feedback (centre in bottom row) was the most closely following the referential motion. From the first plot in Fig. 2 we can see in the top right the same delay reported in [4]. On the other hand, in the first plot for force feedback one can notice oscillations at the straight pattern. Qualitatively, all other plots are similar. Similar behaviour
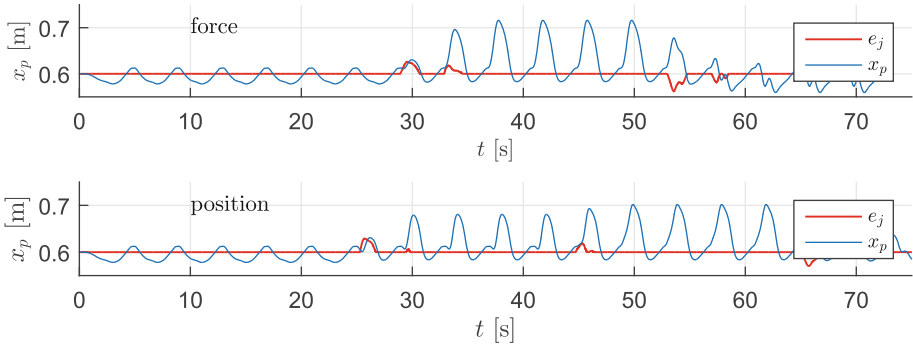


**Fig. 3.** $x_p$ direction signal during coaching and coaching signals for the position and force feedback methods.
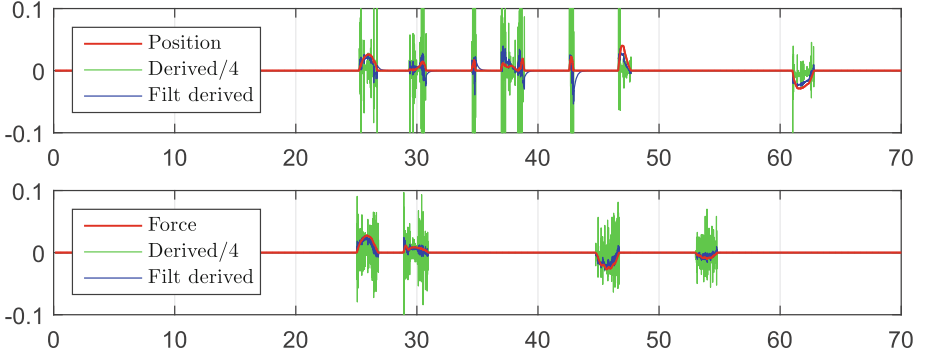
**Fig. 4.** Coaching signals for the derived position method (top), derived force method (bottom) and comparison with the coaching signal of the other two methods for each.
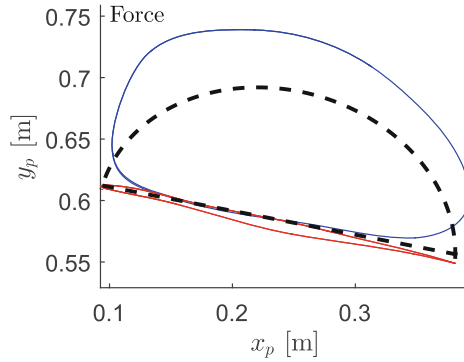


**Fig. 5.** The pattern after using DMP learning.

when using force or position feedback is also shown in Fig. 3, where the coached motion and the coaching signals are qualitatively the same.

Even though the motion results are similar, the derived coaching signal differs from the unchanged or the filtered ones. This is clearly seen in Fig. 4.

Finally, since position feedback is used in the position method, it is worth simply using DMP learning given with (2)–(4) and using the position of the end effector as the demonstrated trajectory, similar as in [5]. The results show qualitatively similar behaviour as shown in Fig. 5.

## 5  Discussion

Qualitatively, we can only observe a difference when using the derived force method, which clearly stands out from the other methods. On the other hand, we can also see that the derived position method suffers from a delay in learning, as reported in [4]. However, the derived position method does not suffer from

this, nor do any of the other methods, except for the filtered derived position method. It is clear that introducing position or velocity (filtered derived) signals at the acceleration level of a DMP will introduce delays.

The primary aspect of this paper, force vs. position feedback, has shown that there is qualitatively no difference between the two in the case of a compliant robot, where the compliance is linear with the force. The notoriously noisy force measurements, which we expected would make trouble with the derived method, have not manifested in any problems. Therefore, qualitatively, this method seems most accurate for both patterns. A thorough statistical analysis is required for confirmation of this conclusion.

Filtering the derived signal, as an engineering solution to the noise problem, has the same effect as simply introducing the velocity of the DMP to the acceleration level. While this has not clearly improved the behaviour, it has also not clearly degraded it.

Finally, in learning vs. coaching, one has to take into consideration several factors. For one, coaching has not been intended for learning of complete patterns. If patterns are complex, and only a small segment needs to be changed, coaching is clearly beneficial. For learning of complete patterns, on the other hand, coaching might do worse. This is seen also in Fig. 5, where another issue has to be taken into consideration; namely, only the $x_p$ direction was compliant. As shown in other publications, i.e., [5], such patterns are not problematic. It should be noted that the sponge used in the experiments was wide, and a person could only estimate the actual pattern of the robot.

In conclusion, we have shown that modifications of coaching signals can improve the behaviour, but a thorough statistical study would be required to determine the very best robotic coaching method based on dynamic movement primitives.

## Appendix

This Appendix describes periodic DMPs. For a complete DMP overview see [8]. The following description is limited to a single degree of freedom, denoted by $y_{\mathrm{DMP}}$, which stands for one of the task-space coordinates. This provides the referential position of the robot, $x_{p,\mathrm{des}} = y_{\mathrm{DMP}}$. Velocity with temporal scaling is given by $z_{\mathrm{DMP}}$.

A DMP in periodic form is defined by

$$\dot{z}_{\mathrm{DMP}} = \Omega \left( \alpha_z \left( \beta_z \left( g - y_{\mathrm{DMP}} \right) - z_{\mathrm{DMP}} \right) + f(\phi) \right), \tag{8}$$

$$\dot{y}_{\mathrm{DMP}} = \Omega z_{\mathrm{DMP}}. \tag{9}$$

$f(\phi)$ is comprised of a linear combination of $N$ radial basis functions $\Gamma_i(\phi)$.

$$f(\phi) = \frac{\sum_{i=1}^{N} w_i \Gamma_i(\phi)}{\sum_{i=1}^{N} \Gamma_i(\phi)} r. \tag{10}$$

Radial basis functions $\Gamma_i(\phi)$ are defined by

$$\Gamma_i(\phi) = \exp\left(h_i\left(\cos\left(\phi - c_i\right) - 1\right)\right). \tag{11}$$

The amplitude control parameter is given by $r$, $h_i > 0$ which are the widths of the kernels and $c_i$ spreads them equally along the phase $\phi$ from 0 to $2\pi$ in $N$ steps. The parameters $\alpha_z$, $\beta_z$, $> 0$ and $\alpha_z = 4\beta_z$ make the system (8)–(9) critically damped. The system oscillates around the goal $g$ with the waveform defined by $f(x)$.

The phase variable $\phi$ provides indirect dependency on time. It can increase with constant rate, where the parameter $\Omega$ denotes the frequency

$$\dot{\phi} = \Omega. \tag{12}$$

Constant frequency was used in the experiments in this paper.

## References

1. Atkeson, C.G., Moore, A.W., Schaal, S.: Locally weighted learning. AI Rev. **11**(1), 11–73 (1997)
2. Bogdanovych, A., Stanton, C., Wang, X., Williams, M.A.: Real-time human-robot interactive coaching system with full-body control interface. In: Roefer, T., Mayer, N., Savage, J., Saranli, U. (eds.) RoboCup 2011: Robot Soccer World Cup XV. LNCS, vol. 7416, pp. 562–573. Springer, Heidelberg (2012)
3. Demircan, E., Sentis, L., De Sapio, V., Khatib, O.: Human motion reconstruction by direct control of marker trajectories. In: Lenarčič, J., Wenger, P. (eds.) Advances in Robot Kinematics: Analysis and Design, pp. 263–272. Springer, Netherlands (2008)
4. Gams, A., Ude, A.: On-line coaching of robots through visual and physical interaction: Analysis of effectiveness of human-robot interaction strategies. In: IEEE International Conference on Robotics and Automation (ICRA) (2016)
5. Gams, A., Ijspeert, A.J., Schaal, S., Lenarčič, J.: On-line learning and modulation of periodic movements with nonlinear dynamical systems. Auton. Robots **27**(1), 3–23 (2009)
6. Gams, A., Petrič, T., Do, M., Nemec, B., Morimoto, J., Asfour, T., Ude, A.: Adaptation and coaching of periodic motion primitives through physical and visual interaction. Robot. Auton. Syst. **75**, 340–351 (2016)
7. Gruebler, A., Berenz, V., Suzuki, K.: Coaching robot behavior using continuous physiological affective feedback. In: IEEE-RAS International Conference on Humanoid Robots (Humanoids), pp. 466–471, October 2011
8. Ijspeert, A., Nakanishi, J., Pastor, P., Hoffmann, H., Schaal, S.: Dynamic movement primitives: Learning attractor models for motor behaviors. Neural Comput. **25**(2), 328–373 (2013)
9. Lee, D., Ott, C.: Incremental kinesthetic teaching of motion primitives using the motion refinement tube. Auton. Robots **31**(2), 115–131 (2011)
10. Lee, D., Ott, C., Yoshihiko, N.: Mimetic communication model with compliant physical contact in human-humanoid interaction. Int. J. Robot. Res. **29**(13), 1684–1704 (2010)

11. Ljung, L., Söderström, T.: Theory and Practice of Recursive Identification. MIT Press, Cambridge (1986)
12. Petrič, T., Gams, A., Žlajpah, L., Ude, A., Morimoto, J.: Online approach for altering robot behaviors based on human in the loop coaching gestures. In: IEEE International Conference on Robotics and Automation (ICRA), pp. 4770–4776 (2014)
13. Riley, M., Ude, A., Atkeson, C., Cheng, G.: Coaching: An approach to efficiently and intuitively create humanoid robot behaviors. In: IEEE-RAS International Conference on Humanoid Robots, pp. 567–574, December 2006
14. Suzuki, K., Gruebler, A., Berenz, V.: Coaching robots with biosignals based on human affective social behaviors. In: ACM/IEEE International Conference on Human-Robot Interaction (HRI), p. 419 (2013)

# Stabilization of Inverted Pendulum by Fractional Order PD Controller with Experimental Validation: D-decomposition Approach

Petar D. Mandić[1(✉)], Mihailo P. Lazarević[1], and Tomislav B. Šekara[2]

[1] Faculty of Mechanical Engineering, University of Belgrade, Belgrade, Serbia
{pmandic,mlazarevic}@mas.bg.ac.rs
[2] School of Electrical Engineering, University of Belgrade, Belgrade, Serbia
tomi@etf.rs

**Abstract.** This paper deals with the stability problem of two types of inverted pendulum controlled by a fractional order PD controller. Rotational inverted pendulum and cart inverted pendulum are under-actuated mechanical systems with two degrees of freedom and one control input. Detailed mathematical models of both pendulums are derived using the Rodriguez method. Fractional order PD controller is introduced for inverted pendulum stabilization. Stability regions in control parameters space are calculated using the D-decomposition approach, based on which tuning of the fractional order controller can be carried out. Numerical simulations and experimental realization are given to demonstrate the effectiveness of the proposed method.

**Keywords:** Inverted pendulum · Fractional order PID · D-decomposition · Asymptotic stability

## 1 Introduction

Many systems in nature are inherently under-actuated, with fewer actuators than degrees of freedom. However, even with reduced number of actuators, these systems are able to produce complex movements. To be capable of performing such motions, complex control algorithms must be implemented. This poses difficult challenges and open problems of designing controllers for under-actuated systems.

Classical benchmark examples for studying problems of this kind include pendulum systems among which the rotational inverted pendulum and cart inverted are very popular. These mechanical systems are nonlinear, unstable and with one unactuated degree of freedom. Stabilizing the system at an unstable equilibrium is one challenging control problems for systems of this type. Such studies help scientists to understand more complex problems encountered, for example, in biologically inspired legged and flying machines. Inverted pendulum can be employed to produce a very robust controller for walking motions [1]. More specifically, an inverted pendulum can mimic the trajectory of the centre of mass extracted from the human motion. Running motion can

be simulated by a smooth continuous trajectory of the cart inverted pendulum. So, basic concepts of human motion can be tackled and explained by using inverted pendulum model.

On the other hand, in recent years considerable attention has been paid to fractional calculus and its application [2]. In control theory fractional order controllers are used to improve the performance of closed loop systems. Among them, fractional order PID controllers are the ones most frequently used and were first introduced in [2]. In this paper, fractional order PD algorithm is used for stabilization of rotational and cart inverted pendulum, and it has been shown that this type of controller enhances the system control performance when compared with its integer order counterpart.

One of the basic requirements in control systems is their asymptotic stability. There are several methods for determining stability region of a closed loop system, and D-decomposition is one of them [3]. Herein, D-decomposition method is applied to the inverted pendulum case, and determining its stability regions in parameters space of a fractional order PD controller is presented. D-decomposition for linear fractional systems is investigated for the case of linear parameters dependence too. Some results of the D-decomposition procedure for inverted pendulum systems are given in [4–6]. This technique enables efficient computational method for determining the asymptotic stability region. When stability regions are known, tuning of the fractional order controller can be carried out.

The rest of the paper is organized as follows. First, mathematical models of rotational and cart inverted pendulum are presented. Then, a fractional order PD controller is introduced in order to stabilize the pendulum. A method for tuning the parameters of fractional order controller is given using the abovementioned D-decomposition method. At the end, both numerical simulation and experimental results are given in order to verify the validity of the proposed method.

## 2    System Modelling

Two different types of inverted pendulum systems are considered in this paper. Figure 1a depicts a schematic view of rotational inverted pendulum, also known in literature as Furuta pendulum. The cart inverted pendulum is shown in Fig. 1b. Herein, the Rodriguez method [7] is proposed for modelling the dynamics of the system where the configuration of the mechanical model with two degrees of freedom (2DOF) can be defined by generalized coordinates $q_1$ and $q_2$. The equations of motion of the inverted pendulum can be expressed in a covariant form of Lagrange's equation of second kind as follows:

$$\sum_{\alpha=1}^{n} a_{\gamma\alpha}\ddot{q}_\alpha + \sum_{\alpha=1}^{n}\sum_{\beta=1}^{n} \Gamma_{\alpha\beta,\gamma}\dot{q}_\alpha\dot{q}_\beta = Q_\gamma^g + Q_\gamma^v + Q_\gamma^a, \quad \gamma = 1, 2, \tag{1}$$

where the coefficients $a_{\alpha\beta}$ are the covariant coordinates of the basic metric tensor $[a_{\gamma\alpha}] \in R^{2\times2}$ and $\Gamma_{\alpha\beta,\gamma}\alpha, \beta, \gamma = 1, 2$ present Christoffel symbols of the first kind. The generalized forces $Q_\gamma^g, Q_\gamma^v, Q_\gamma^a$ denote the generalized gravitational, viscous and control forces, respectively.
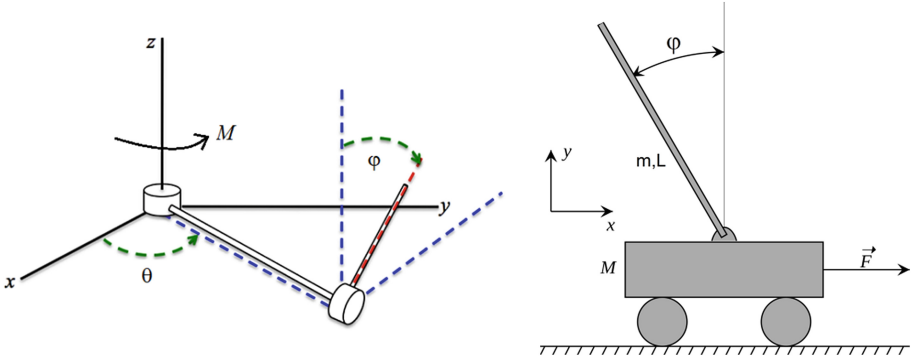
**Fig. 1.** A schematic view of the furuta pendulum (A) and cart pendulum system (B)

Furuta pendulum (Fig. 1A) is an underactuated 2DOF mechanical system, where angular position of the arm and the pendulum are denoted as $\theta$ and $\varphi$, respectively. The arm is driven with a torque, while no torque is applied directly to the pendulum. The system's parameters are: m1 - mass of the arm, m2 - mass of the pendulum $R_1$ - distance of the arm's pivot point to the pendulum's pivot point, $R_2$ - distance of the pendulum's pivot point to its end (extremity), $2r_1$, $2r_2$ - total length of the arm, and pendulum respectively, $J_{\zeta 1}$ - moment of inertia of the arm with respect to its centre of mass, $J_{\zeta 2}, J_{\eta 2}$ - axial moments of inertia of the pendulum with respect to its centre of mass.

Now, in the case of the Furuta pendulum, the equations of motion (1) can be rewritten in full form:

$$a_{11}\ddot{\theta} + a_{12}\ddot{\varphi} + 2\Gamma_{12,1}\dot{\theta}\dot{\varphi} + \Gamma_{22,1}\dot{\varphi}^2 = M, \quad a_{12}\ddot{\theta} + a_{22}\ddot{\varphi} - \Gamma_{12,1}\dot{\theta}^2 = Q_2^g, \quad (2)$$

where coefficients $a_{11}$, $a_{12}$, $a_{22}$, $\Gamma_{12,1}$, $\Gamma_{22,1}$ and $Q_2^g$ can be written as functions of the joint variable $\varphi$, i.e. $a_{11} = a_{11}(\varphi)$, $a_{12} = -K_3\cos(\varphi)$, $a_{22} = K_4$, $\Gamma_{12,1} = K_2\sin(2\varphi)$, $\Gamma_{22,1} = K_3\sin(\varphi)$, $Q_2^g = K_1\sin(\varphi)$. Physical parameters $K_1, K_2, K_3, K_4$ are defined in [6].

In the case of the cart pendulum system in Fig. 1B, the cart position and the pendulum angle are denoted as $x$ and $\varphi$, respectively. The system's control is by means of force $F$ applied horizontally to the cart. The equations of motion (1) are rewritten as:

$$(m+M)\ddot{x} - \frac{mL}{2}\ddot{\varphi}\cos(\varphi) + \frac{mL}{2}\dot{\varphi}^2\sin(\varphi) = F$$

$$-\frac{mL}{2}\ddot{x}\cos(\varphi) + \frac{mL^2}{3}\ddot{\varphi} = \frac{mgL}{2}\sin(\varphi) - k_v\dot{\varphi} \qquad (3)$$

where parameters of the system are: $M$ - mass of the cart, $m$ - mass of the pendulum, $L$ - total length of the pendulum, $0.5L$ - distance of the pendulum's pivot point to its center of mass, $J$ - moment of inertia of the pendulum with respect to its pivot point, $k_v$ - viscous damping coefficient.

## 3   Controller Design

Now, a control strategy is developed to stabilize the pendulum in upright position. First, we show the simplification of dynamic equations of the Furuta pendulum given by (2). A nonlinear technique known as inverse dynamic control is used for this purpose. It is basically a partial feedback linearization procedure [8], which simplifies the control design. If control input $M$ from (2) can be chosen as follows:

$$M = \frac{a_{11}}{a_{12}}\left(Q_2^g + \Gamma_{12,1}\dot{\theta}^2\right) + \left(a_{12} - \frac{a_{11}a_{22}}{a_{12}}\right)M_R\cos(\varphi) + 2\Gamma_{12,1}\dot{\theta}\dot{\varphi} + \Gamma_{22,1}\dot{\varphi}^2, \quad (4)$$

equations of motion now become:

$$\ddot{\theta} = -\frac{K_1}{K_3}\tan(\varphi) - 2\frac{K_2}{K_3}\sin(\varphi)\dot{\theta}^2 + \frac{K_4}{K_3}M_R, \; \ddot{\varphi} = M_R\cos(\varphi). \quad (5)$$

where $M_R$ stands for new control input. Using the same principle the simplified equations of motion for the cart pendulum system can be obtained by applying control force $F$ chosen as:

$$F = \left(m + M - \frac{3m}{4}\cos^2(\varphi)\right)F_R$$
$$- \frac{3mg}{4}\sin(\varphi)\cos(\varphi) + \frac{mL}{2}\dot{\varphi}^2\sin(\varphi) + \frac{3}{2}\frac{k_v}{L}\dot{\varphi}\cos(\varphi), \quad (6)$$

which transforms Eq. (3) in:

$$\ddot{x} = F_R, \qquad \ddot{\varphi} = \frac{g}{b}\sin(\varphi) - \frac{k_v}{J}\dot{\varphi} + \frac{1}{b}F_R\cos(\varphi), \quad (7)$$

where $g \approx 9.81\left[m/s^2\right]$, $b = 2L/3[m]$, and $F_R$ is new control signal. We can see that there is no influence from the motion of pendulum to cart position in these equations.

Now, we can linearize the system described by (5) around the equilibrium point $\left(\theta, \dot{\theta}, \varphi, \dot{\varphi}\right) = (0,0,0,0)$. A controller derived from a linearized system will work for a nonlinear system, provided that the region of attraction is not too large [8]. So, linearization around desired equilibrium point leads to:

$$\ddot{\theta} = -\frac{K_1}{K_3}\varphi + \frac{K_4}{K_3}M_R, \qquad \ddot{\varphi} = M_R. \quad (8)$$

Asymptotic stability for $\left(\varphi, \dot{\varphi}, \theta, \dot{\theta}\right)$ can be accomplished by the following control law:

$$M_R = -\left(K_{P\theta}\theta + K_{D\theta}\theta^{(\alpha)}\right) - \left(K_{P\varphi}\varphi + K_{D\varphi}\dot{\varphi}\right) + \frac{K_1}{K_4}\varphi, \tag{9}$$

where $K_{P\theta}, K_{D\theta}, K_{P\varphi}, K_{D\varphi}$ denote proportional and differential gains of the controller, and $\alpha$ is real differentiator parameter. After substituting (9) into (8), one obtains:

$$\ddot{\theta} + \frac{K_4}{K_3}K_{D\theta}\theta^{(\alpha)} + \frac{K_4}{K_3}K_{P\theta}\theta = -\frac{K_4}{K_3}K_{D\varphi}\dot{\varphi} - \frac{K_4}{K_3}K_{P\varphi}\varphi,$$

$$\ddot{\varphi} + K_{D\varphi}\dot{\varphi} + \left(K_{P\varphi} - \frac{K_1}{K_4}\right)\varphi = -K_{D\theta}\theta^{(\alpha)} - K_{P\theta}\theta. \tag{10}$$

Taking $\alpha = 1$ one obtains classical PD control. Five parameters $\left(K_{P\theta}, K_{D\theta}, K_{P\varphi}, K_{D\varphi}, \alpha\right)$ in (10) can be changed in order to achieve asymptotic or relative stability of closed loop system. Now, applying the same procedure, but for cart pendulum system, the control feedback law is chosen as:

$$F_R = -K_{P\varphi}\varphi - K_{D\varphi}\dot{\varphi} - K_{Dx}x^{(\alpha)} - K_{Px}x, \tag{11}$$

and Eq. (7) become now:

$$\ddot{x} + K_{Dx}x^{(\alpha)} + K_{Px}x = -K_{P\varphi}\varphi - K_{D\varphi}\dot{\varphi},$$

$$b\ddot{\varphi} + \left(K_{D\varphi} + \frac{k_v b}{J}\right)\dot{\varphi} + \left(K_{P\varphi} - g\right)\varphi = -K_{Dx}x^{(\alpha)} - K_{Px}x. \tag{12}$$

## 4  D-decomposition Method

### 4.1  Swing up and Asymptotic Stabilization of Furuta Pendulum

A control strategy is developed to stabilize the pendulum in upright position, and it consists of two different control problems. The first one is swinging the pendulum up from down to the upright position. Once the system is close to the desired position, with a simple change in the controller it is possible to bring the pendulum in the desired equilibrium. There are many ways to bring the pendulum to the upper half plane, when $|\varphi| < \pi/2$. One of the most popular is based on energy control. The energy of the uncontrolled pendulum ($M_R = 0$) is

$$E = \frac{1}{2}J\dot{\varphi}^2 + m_2 g(R_2 - r_2)(\cos(\varphi) + 1). \tag{13}$$

The energy is defined so that it is zero in downright rest position. If $E_0 = m_2 g$ $(R_2 - r_2)$ denotes potential energy of inverted vertical position of pendulum, then the following control law drives the pendulum towards its desired upright position:

$$M_R = -k\dot{\varphi}\cos(\varphi)\text{sgn}|E - E_0|, \; k = const > 0 \tag{14}$$

As for the stabilizing controller, using the classical D-decomposition method [3] the stability region in the parameter plane may be determined. The characteristic quasi-polynomial of the closed loop system described with (12) is given by:

$$f(s) = s^4 + s^2\left(K_4 K_{D\theta}s^\alpha/K_3 + K_{D\varphi}s\right) - K_1 K_{D\theta}s^\alpha/K_3 + s^2\left(K_4 K_{P\theta}/K_3 + K_{P\varphi} - K_1/K_4\right) - K_1 K_{P\theta}/K_3. \tag{15}$$

The plane $(K_{P\theta}, K_{D\theta})$ is decomposed by the boundaries of the D-decomposition into finite number regions D(k). Any point in D(k) corresponds to such values of $K_{P\theta}$ and $K_{D\theta}$ that polynomial (15) has exactly $k$ zeroes with positive real parts. The region D(0) represents the stability region. The stability boundaries are curves on which each point corresponds to polynomial (15) having zeroes on the imaginary axes. Substituting $s = j\omega$ in polynomial (15) and equating the real and imaginary part to zero, one obtains the following 2-D system:

$$\begin{bmatrix} U_1(\omega, \alpha) & U_2(\omega, \alpha) \\ V_1(\omega, \alpha) & V_2(\omega, \alpha) \end{bmatrix} \begin{pmatrix} K_{P\theta} \\ K_{D\theta} \end{pmatrix} = \begin{pmatrix} Q_1(\omega) \\ Q_2(\omega) \end{pmatrix}, \tag{16}$$

where $a = K_4/K_3$, $b = K_1/K_3$, and:

$$U_1(\omega, \alpha) = a\omega^2 + b, \; U_2(\omega, \alpha) = \left(a\omega^2 + b\right)\omega^\alpha \cos(0.5\alpha\pi),$$
$$V_1 = 0, \; V_2(\omega, \alpha) = \left(a\omega^2 + b\right)\omega^\alpha \sin(0.5\alpha\pi), \tag{17}$$
$$Q_1(\omega) = \omega^4 - \omega^2(K_{P\varphi} - b/a), \; Q_2(\omega) = -K_{D\varphi}\omega^3.$$

Equations (16) and (17) determine the stability boundaries in the parameter space $(K_{P\theta}, K_{D\theta})$ for the fixed values $K_{P\varphi}, K_{D\varphi}$ and $\alpha$.

## 4.2   Simulation Results

In this section, simulation results of system described with (10) are presented using the D-decomposition method. Physical parameters $K_1, K_2, K_3, K_4$ are taken from the real laboratory model of the Furuta pendulum. They have the following values: $K_1 = 6.514e - 2, K_2 = 9.186e - 4, K_3 = 1.428e - 3,$ and $K_4 = 1.837e - 3$. Also, controller gains $K_{P\varphi}$ and $K_{D\varphi}$ are predetermined and chosen as $K_{D\varphi} = 10$, $K_{P\varphi} = 41.48$. Now, the influence of $(K_{P\theta}, K_{D\theta})$ parameters on the stability property of system can be investigated using the Eqs. (16) and (17). For the case $\alpha \in [0.8, 1.2]$ stability regions are plotted as shown in Fig. 2.

By varying $\alpha$ and repeating the D-partition procedure, different stability regions are obtained. Stability region D(0) in all examples is chosen by testing an arbitrary point and checking the stability of quasi-polynomial (15). We can see stability region becomes larger as parameter $\alpha$ increases. Results of the swing up and stabilizing controller for $K_{P\theta} = -0.35$, $K_{D\theta} = -0.93$, $K_{P\varphi} = 41.48$, $K_{D\varphi} = 10$ and $\alpha = 1.1$ are shown in Fig. 3, which presents results for the change of pendulum angle and cart
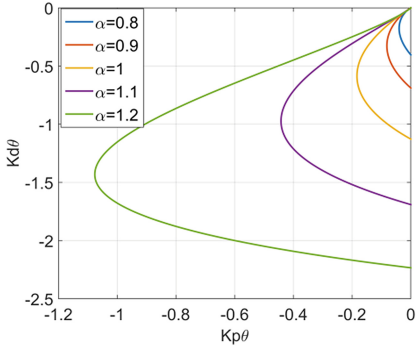
**Fig. 2.** Stability regions for α ∈ [0.8, 1.2]     **Fig. 3.** Swing up and stabilization simulation
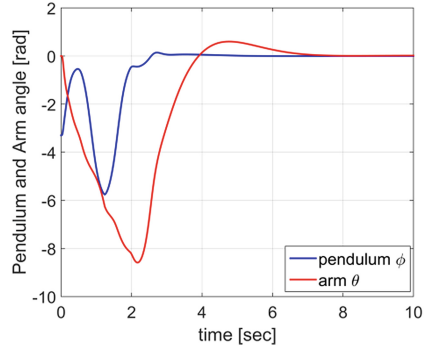
position with respect to time. Initial conditions are $\left(\theta, \dot{\theta}, \varphi, \dot{\varphi}\right) = \left(0, 0, 170°, 0\right)$. A change from swing up to stabilizing controller happens when $|\varphi| < 30°$.

## 5    Experimental Results: Cart Pendulum System

To show the practical implementation of the fractional order PD controller, we performed experiments for the asymptotic stabilization of the cart pendulum system given by (7). Some preliminary results regarding the fractional order PD control on the cart pendulum system (short pendulum case) are given in [9]. The laboratory setup of actual system is shown in Fig. 4, and consists of three subsystems: measurement, power and control supervision unit. The physical parameters of the system used in experiment (long pendulum case) are: $M = 0.75$ kg - mass of the cart, $m = 0.23$ kg - mass of the pendulum, $L = 0.64$ m - total length of the pendulum, $k_v = 0.0024$ Nms - viscous damping coefficient. The cart pendulum system used in experiments is equipped with two high resolution incremental encoders (4096 pulses per revolution) for the measurement of both cart and pendulum positions. The power amplifier provides the necessary power to drive the motor. The cart is driven by the force generated by the DC motor given by $F = c_m V_m - c_b \dot{x}$, where $V_m$ is a control input voltage, and $c_m = 1.0717$ N/V and $c_b = 4.809$ Ns/m are positive motor constants. Finally, the control supervision unit consists of a PC and *Quanser* Data Acquisition Board. The real time software is provided by *Quarc* running on *Matlab/Simulink*. The sample time used in experiments is 2 ms.

Since numerical differentiation usually introduces significant noise in velocity measurements, we estimate the corresponding velocities of the cart and pendulum from position measurements by utilizing a derivative filter given by the following fractional order transfer function $TF = (s/0.02\ s + 1)^{\alpha}$, where α represents the real differentiator parameter, having in mind that $\alpha = 1$ for pendulums derivative filter. In order to approximate this non-rational transfer function, a computationally efficient method for rational approximation of linear fractional order systems is used, as described in [10].

**Fig. 4.** Laboratory setup
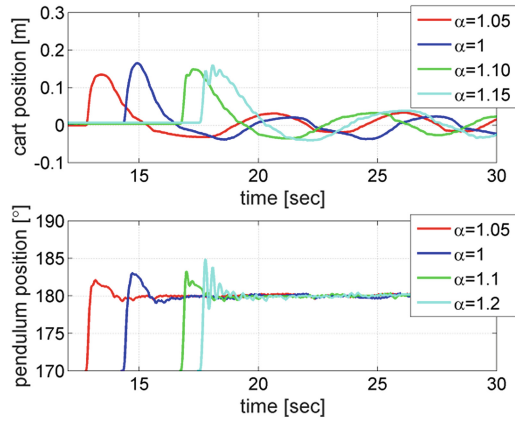


**Fig. 5.** Experimental results

The method proposed relies on the interpolation of the frequency characteristic of the system on a predefined set of target frequencies.

Figure 5 shows experimental results of the asymptotic stabilization of the actual cart pendulum system for different values of parameter $\alpha$, i.e. $\alpha \in [1.0; 1.05; 1.1; 1.15]$. Tests are performed for the following values of controller parameters: $K_{Px} = 14.14$, $K_{Dx} = 16.77$, $K_{P\varphi} = 79.57$, $K_{D\varphi} = 17.15$. The pendulum is manually brought to the initial position $(x, \dot{x}, \varphi, \dot{\varphi}) = (0, 0, 170°, 0)$ where the balancing controller catches and stabilizes it. One can see the best response is obtained for $\alpha = 1.05$, so fractional order controller gives better control performances when compared with its integer order counterpart.

## 6   Conclusion

In this paper, the stability problem of two types of inverted pendulum system is investigated. The mathematical models of Furuta pendulum and cart inverted pendulum are derived using the Rodriguez method, and a fractional order PD controller is introduced in order to stabilize it. The problem of asymptotic stability of closed loop system is solved using the D-decomposition approach. Based on this method, analytical forms expressing the boundaries of stability regions were determined for the Furuta pendulum case. Experimental results of cart pendulum system are given to demonstrate the effectiveness of the fractional order controller.

# References

1. Kwon, T., Hodgins J.: Control systems for human running using an inverted pendulum model and a reference motion capture sequence, In: 2010 ACM SIGGRAPH Eurographics Symposium on Computer Animation, July 2010
2. Podlubny, I.: Fractional Differential Equations. Academic Press, San Diego (1999)
3. Neimark, Y.I.: D-decomposition of the space of the quasi-polynomials. Appl. Math. Mech. **13**, 349–380 (1949). (in Russian)
4. Mandić, P.D., Lazarević, M.P., Šekara: T.B.: D-decomposition method for stabilization of inverted pendulum using fractional order PD controller. In: Proceedings of First International Conference on Electrical, Electronic and Computing Engineering (2014)
5. Mandić, P.D., Lazarević, M.P., Šekara, T.B.: Fractional order PD control of Furuta pendulum: D-decomposition approach. In: Proceedings of IEEE International Conference on Fractional Differentiation and its Applications (2014)
6. Mandić, P.D., Lazarević, M.P., Šekara, T.B.: D-decomposition technique for stabilization of Furuta pendulum : fractional approach. Bull. Poly. Acad. Tech. **64**, 189–196 (2016)
7. Čović, V., Lazarević, M.P.: Robot Mechanics, Faculty of Mechanical Engineering, Belgrade (2009). (in Serbian)
8. Khalil, H.: Nonlinear Systems. Prentice Hall, Upper Saddle River (2002)
9. Mandić, P.D., Lazarević, M.P., Šekara, T.B., Jovanović, R.Ž.: Stabilization of the cart pendulum system by fractional order control with experimental realization. In: Paper Submitted for ICFDA 2016 Conference, Novi Sad, 18–20 July 2016
10. Šekara, T.B., Rapaić, M.R., Lazarević, M.P.: An efficient method for approximation of non-rational transfer functions. Electronics **17**(1), 40–44 (2013)

# Virtual Compliance Control of a Kinematically Redundant Serial Manipulator with 9 DoF

Mathias Brandstötter[1](✉), Stephan Mühlbacher-Karrer[2], Dominik Schett[1], and Hubert Zangl[2]

[1] Institute for Robotics and Mechatronics, Joanneum Research,
Lakeside B08a, 9020 Klagenfurt am Wörthersee, Austria
{mathias.brandstoetter,dominik.schett}@joanneum.at
[2] Institute of Smart Systems Technologies, Sensors and Actuators,
Alpen-Adria-Universität Klagenfurt, 9020 Klagenfurt am Wörthersee, Austria
{stephan.muehlbacher-karrer,hubert.zangl}@aau.at

**Abstract.** Kinematically redundant serial manipulators are currently used in industry either to avoid singular configurations or to increase dexterity. However, the surplus degrees of freedom of such mechanisms can also be used to ensure, or at least increase safety in a human-robot collaborative scenario. In this work the behaviour of a serial manipulator with nine rotary joints is described where one joint module is equipped with a capacitive proximity sensor exemplarily. The compliance of the robot arm is realized by an impedance controller to achieve dynamic behaviour, which simulates a spring-mass-damper system at one point of the kinematics chain. Usually, this enables the robot-arm to avoid, or at least reduce contact with an approaching human body and to continue its primary task simultaneously.

**Keywords:** Serial robot · Inverse kinematics · Proximity sensor · Capacitive sensing · Human-robot collaboration

## 1 Introduction

The rigid parts of a robot are dangerous to a human if they move fast and collide with the human body. For this reason, they are either operated in enclosed areas or the application-related motion is subject to restrictions in order to minimize any damage. Since the beginning of 2016, the *Technical Specification ISO/TS 15066* [1] is available, which is devoted to the issue of collaborative robotics. The technical specification defines safety requirements for industrial robot systems and the related work environment. Two cases are distinguished: (a) a physical contact is permitted, and (b) is allowed. We will restrict ourselves to the contactless case in this work.

Amongst others, the sufficient separation distance $S_p$ is defined in the ISO/TS 15066, that adds up all essential distances influencing the lower bound of the safe distance between a human and a robot. This means that the distance between

the rigid parts of the robot arm and the human must be known within a certain time interval. To measure this quantity visual sensors (e.g., [5,7]) or proximity sensors (e.g., [10,11]) come into consideration.

In this sense, the main difference of the contribution to previous works is that a manipulator with 9 DoF is considered. Hence, depending on the task at least three degrees of freedom can be used for additional objectives, e.g., increasing the safety. A detailed null space analysis of the Schunk LWA 9 DoF manipulator on the basis of null space velocities can be found in [9].

## 2   Robot System Under Study

The robot system used in this work consists basically of an extended version of the Schunk 7 LWA 4D-arm, an internally manufactured proximity sensor, and essential packages of the ROS software framework running on a standard PC.

### 2.1   Design of the Robot Manipulator

As robotic testbed serves a serial manipulator with nine consecutive revolute joints, see Fig. 1(a). The construction of the arm corresponds to the Schunk 7 DoF LWA 4D-arm [12], however, the first two modules have been doubled. In Sect. 3 the kinematic model and further details of the manipulator are presented.

A capacitive sensor is mounted on joint 4 to study movement capacity and reactivity of the inner parts of the kinematic chain. In other words, humans



(a)                                      (b)
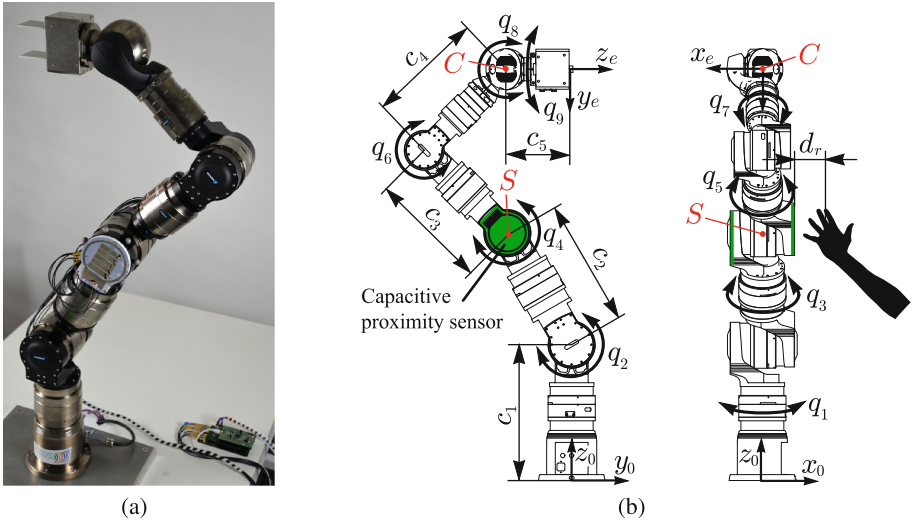
**Fig. 1.** Schunk LWA 9 DoF manipulator. (a) Image of the test bed. (b) Front and side view of the robot arm. The areas in green indicate the location of the proximity sensors which are able to detect parts of a humans body.

safety should be increased while the robot fulfills its task. To keep the goal of this work in focus and to gain insight into the behaviour of the redundant robot, the end effector is set to be always at rest. However, such a simplification does not lead to restrictions on general statements.

## 2.2  Sensor System

The sensor system utilizes a capacitive proximity sensor to determine the distance between the manipulator and the human body. The capacitive sensing principle is based on the measured distortion of the electric field caused by an object, while approaching the sensor front end. The capacitive proximity sensor measures the capacitance between an electrode and the far ground also known as the single end measurement mode. The measurement hardware [11] applies an AC excitation signal with $f_{ex} = 1\,\mathrm{MHz}$ in sequence on each electrode used to determine the change of the capacitance by measuring the displacement current on the transmitter electrode.

The capacitive proximity sensor front end consists of two electrodes tailored to the needs of the serial manipulator. The 4th joint module of the serial manipulator is equipped on two areas with the electrodes (see Fig. 1(a)) to determine the distance between the surface of the manipulator and an approaching human body. The electrodes consist of a four layer structure: a conductive layer at the bottom acting as active guard, an isolation layer, an electrode layer and an isolation layer on the top. The geometry of one electrode of the sensor front end is shown in Fig. 2. The sensing range and resolution of the capacitive proximity sensor obtained in the experimental setup are $s_{max} = 0.10\,\mathrm{m}$ and $s_{res} = 0.001\,\mathrm{m}$, respectively.
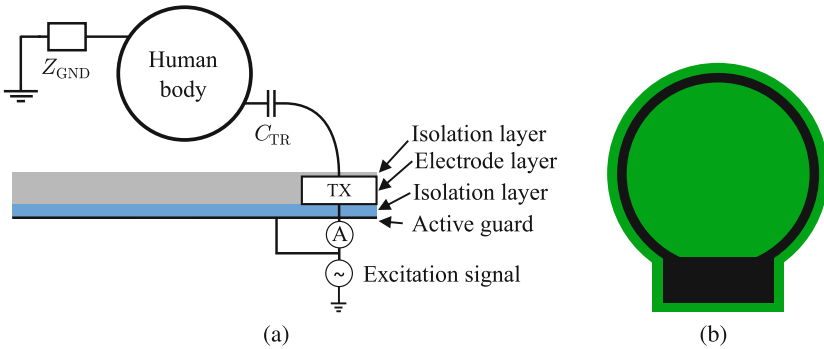


**Fig. 2.** Capacitive sensing principle and electrode geometry. (a) Single ended measurement mode comprising the transmitter electrode, the active guard, the isolation layers and the human body in the vicinity of the sensor front end. (b) Top view of the electrode design of the capacitive proximity sensor front end. The diameters of the electrode (black) and the active guard (green) are $d_e = 0.11\,\mathrm{m}$ and $d_{ag} = 0.12\,\mathrm{m}$, respectively.

### 2.3   Software Framework

The software framework consists of three ROS packages. The first package is the ROS package of the capacitive proximity sensor. The ROS software interface for capacitive sensors [8] is extended to fully support the measurement hardware used in [11] and to publish a sensor message containing the current distance between an approaching human body and the capacitive proximity sensor with an update rate of 38 Hz. The second implemented package contains the virtual torsion spring and damper system and the inverse kinematics of the manipulator publishing the trajectory control messages for the manipulator. The third package used from [6] is the ROS driver of the manipulator. Here, the commands are published with a loop rate of 70 Hz.

## 3   Kinematic Model

The Schunk LWA 9 DoF consists of nine joints with orthogonal joint axes. Hence, the manipulator is kinematically redundant for any given end effector task. A key objective of this work is to demonstrate the utility of the existing redundancy in the mechanical system. Therefore, a static end effector pose is chosen in order to place the focus on the null space motion. What can be figured out is that point $S$ (centre of the 4th joint) can move on a sphere, the so-called *redundancy sphere*, even if the end effector pose is fixed, see Fig. 3. However, $S$ can only lie on a restricted region of this sphere, shaped as a spherical cap. Its size depends on the location of the end effector and the length of the links.

The end effector pose $\mathscr{P}_e^{\Sigma_0}$ is defined as the position $\mathbf{t}_e^{\Sigma_0}$ and the orientation $\mathbf{R}_e^{\Sigma_0}$ of the end effector specified in the base coordinate system $(O; x_O, y_O, z_O)$, referred to as $\Sigma_0$:

$$\mathscr{P}_e^{\Sigma_0} := \begin{pmatrix} 1 & \mathbf{0}^T \\ \mathbf{t}_e^{\Sigma_0} & \mathbf{R}_e^{\Sigma_0} \end{pmatrix} = \begin{pmatrix} 1 & 0 & 0 & 0 \\ 0 & 1 & 0 & 0 \\ -100 & 0 & 0 & 1 \\ 1150 & 0 & -1 & 0 \end{pmatrix} \tag{1}$$

In (1) $\mathscr{P}_e^{\Sigma_0}$ is specified by a $3 \times 1$ position vector $\mathbf{t}_e^{\Sigma_0} = [t_x^{\Sigma_0} \ t_y^{\Sigma_0} \ t_z^{\Sigma_0}]^T$ and a $3 \times 3$ rotation matrix $\mathbf{R}_e^{\Sigma_0}$.

To solve the kinematics problem a geometry based technique is used. This means that the redundancy is resolved on the position level (pure inverse kinematics) in contrast to the conventional method which is bases on the velocity level (null space projection by generalized Jacobian inverse, see [4,9] for an overview). Therefore, the robot is split up into two consecutive kinematic chains (a serial 3R and a serial 6R arm) and the essential corresponding forward and inverse kinematics equations for this structures are presented in the following sections.
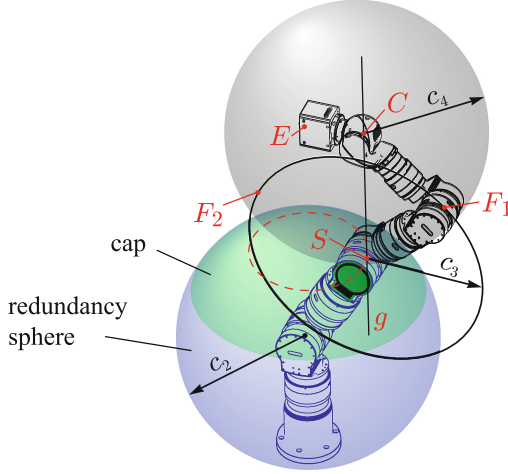
**Fig. 3.** An oblique projection of the 9 DoF robot. Its 3R substructure is highlighted in blue and the 6R orthogonal serial chain is drawn in black. The blue sphere symbolizes the redundancy sphere on which point $S$ must lie. If only joint 1 is actuated in the illustrated configuration, $S$ moves on the red dashed circle. The intersection ($F_1$ and $F_2$) of the gray-scaled sphere and the circle are possible locations for the 6th joint.

### 3.1   First Substructure (Serial 3R Chain)

The initial pose of the third joint $\mathscr{P}_s^{\Sigma_0}$ is assumed to be known by given $q_{1,\mathrm{init}}$ to $q_{3,\mathrm{init}}$. Due to the mechanical structure of the robot the intersection of the second and third joint axis (referred to as point $S$) is located on a sphere with radius $c_2$, see Figs. 1(b) and 3. This pose is computed to be

$$\mathscr{P}_{s,\mathrm{init}}^{\Sigma_0} = \mathbf{T}_x(c_1) \cdot \mathbf{R}_z(q_{1,\mathrm{init}}) \cdot \mathbf{R}_y(q_{2,\mathrm{init}}) \cdot \mathbf{R}_z(q_{3,\mathrm{init}}) \cdot \mathbf{T}_z(c_2).$$

Here, the well known homogeneous transformation matrices for rotations through an angle $\varphi$ about an $x$, $y$ and $z$ axis are notated in this work by $\mathbf{R}_x(\varphi)$, $\mathbf{R}_y(\varphi)$ and $\mathbf{R}_z(\varphi)$. Analogously $\mathbf{T}_x(d)$, $\mathbf{T}_y(d)$ and $\mathbf{T}_z(d)$ are understood to be translations along a known $x$, $y$ and $z$ axis by the distance $d$.

### 3.2   Second Substructure (Serial 6R Chain)

The special design of the second substructure allows to separate the problem into a *3R orthogonal* and a *3R wrist* subproblem. The computation steps are as follows: (i) point $C$ is computed by means of the known end effector pose, (ii) the sphere-circle intersections $F_1$ and $F_2$ are determined, (iii) the first three joint angles of the subproblem ($q_4, q_5, q_6$) are computed, (iv) the wrist angles ($q_7, q_8, q_9$) are ascertained.

In order to simplify the computation, the problem is considered independently of the first subsystem. From this it follows that joint 3 serves as basis and the end effector pose written in coordinate frame $(S; x_s, y_s, z_s)$, noted as $\Sigma_S$, is

$$\mathscr{P}_e^{\Sigma_S} = \left( \mathscr{P}_{s,\text{init}}^{\Sigma_0} \right)^{-1} \mathscr{P}_e^{\Sigma_0}. \tag{2}$$

**Coordinates of Point $C$.** For the computation of the inverse kinematics of the 3R orthogonal substructure the position of point $C$ in $\Sigma_S$ has to be known. The coordinates of point $C$ are obtained by a shift of the end effector position $\mathbf{t}^{\Sigma_S}$ into the negative $z_e$-direction of the end effector coordinate system $(E; x_e, y_e, z_e)$ by the distance $c_5$, see Fig. 1(b):

$$\begin{bmatrix} c_x^{\Sigma_S} \\ c_y^{\Sigma_S} \\ c_z^{\Sigma_S} \end{bmatrix} = \begin{bmatrix} t_x^{\Sigma_S} \\ t_y^{\Sigma_S} \\ t_z^{\Sigma_S} \end{bmatrix} - c_5\, \mathbf{R}_e^{\Sigma_S} \begin{bmatrix} 0 \\ 0 \\ 1 \end{bmatrix} = \begin{bmatrix} t_x^{\Sigma_S} \\ t_y^{\Sigma_S} - c_5 \\ t_z^{\Sigma_S} \end{bmatrix}$$

**Sphere-Circle Intersections.** It has to be noted in advance that in general the centre of the sphere (with radius $c_4$) will not meet the plane on which the considered circle (with radius $c_3$) lies. In any case, the sphere-circle intersections are located on a circle that can be found by the intersection of two spheres with the same midpoints and radii. This sphere-sphere intersection lies on a plane which is orthogonal to line $g$ (spanned by the midpoints $S$ and $C$, see Fig. 3). This plane intersects line $g$ in point $M$ and the coordinates of $M$ are given by:

$$\begin{bmatrix} m_x^{\Sigma_S} \\ m_y^{\Sigma_S} \\ m_z^{\Sigma_S} \end{bmatrix} = t \begin{bmatrix} c_x^{\Sigma_S} \\ c_y^{\Sigma_S} \\ c_z^{\Sigma_S} \end{bmatrix} , \quad \text{where } t = \frac{1}{2} \left( \frac{c_3^2 - c_4^2}{{c_x^{\Sigma_S}}^2 + {c_y^{\Sigma_S}}^2 + {c_z^{\Sigma_S}}^2} + 1 \right)$$

Now, the intersection of this plane and the circle will lead to two possible locations of the center of joint 5. The solutions can be found by

$$\begin{bmatrix} f_{x_{1,2}}^{\Sigma_S} \\ f_{y_{1,2}}^{\Sigma_S} \\ f_{z_{1,2}}^{\Sigma_S} \end{bmatrix} = \begin{bmatrix} \dfrac{k \cdot c_x^{\Sigma_S} \pm c_z^{\Sigma_S} \sqrt{c_3^2 \left( {c_x^{\Sigma_S}}^2 + {c_z^{\Sigma_S}}^2 \right) - k^2}}{{c_x^{\Sigma_S}}^2 + {c_z^{\Sigma_S}}^2} & 0 & \dfrac{k - c_x^{\Sigma_S} \cdot f_{x_{1,2}}^{\Sigma_S}}{c_z^{\Sigma_S}} \end{bmatrix}^T \tag{3}$$

where

$$k = \frac{1}{2} \left( c_3^2 - c_4^2 + {c_x^{\Sigma_S}}^2 + {c_y^{\Sigma_S}}^2 + {c_z^{\Sigma_S}}^2 \right).$$

**Solution of the 3R Orthogonal Subproblem.** By using the position coordinates of the 5th joint, given by (3), the possible joint angles can be calculated to be

$$q_{4;\text{i,ii}} = \text{atan2} \left( f_{x_{1,2}}^{\Sigma_S}, f_{z_{1,2}}^{\Sigma_S} \right).$$

The equations to compute the possible angles for joint 5 are

$$q_{5;i,ii} = \pm \mathrm{sgn}\left(c_y^{\Sigma_S}\right) \cdot \mathrm{acos}\left(\frac{\|\mathbf{n}_1 \cdot \mathbf{n}_2\|}{\|\mathbf{n}_2\| \cdot \|\mathbf{n}_2\|}\right)$$

where

$$\mathbf{n}_1 = \begin{bmatrix} m_x^{\Sigma_S} - c_x^{\Sigma_S} \\ m_y^{\Sigma_S} - c_y^{\Sigma_S} \\ m_z^{\Sigma_S} - c_z^{\Sigma_S} \end{bmatrix} \times \begin{bmatrix} c_x^{\Sigma_S} - f_{x_1}^{\Sigma_S} \\ c_y^{\Sigma_S} - f_{y_1}^{\Sigma_S} \\ c_z^{\Sigma_S} - f_{z_1}^{\Sigma_S} \end{bmatrix} \quad \text{and} \quad \mathbf{n}_2 = \begin{bmatrix} 0 \\ 1 \\ 0 \end{bmatrix}$$

are specific normal vectors. To determine the possible angles for the 6th joint

$$\mathbf{u} = \begin{bmatrix} f_{x_{1,2}}^{\Sigma_S} & f_{y_{1,2}}^{\Sigma_S} & f_{z_{1,2}}^{\Sigma_S} \end{bmatrix}^T$$

$$\mathbf{v} = \begin{bmatrix} c_x^{\Sigma_S} - f_{x_{1,2}}^{\Sigma_S} & c_y^{\Sigma_S} - f_{y_{1,2}}^{\Sigma_S} & c_z^{\Sigma_S} - f_{z_{1,2}}^{\Sigma_S} \end{bmatrix}^T$$

are defined and the joint angles are then:

$$q_{6;i,ii} = \pm \mathrm{atan2}\left(\|\mathbf{u} \times \mathbf{v}\|,\ \mathbf{u} \cdot \mathbf{v}\right)$$

**Solution of the 3R Wrist Subproblem.** The determination of the wrist angles is a well known problem and its solution can be found, e.g., in standard literature [2] or which is based mostly on the notation used in this work in [3].

The pose of the 6th joint $\mathscr{P}_c^{\Sigma_S}$ can be determined by the forward kinematics

$$\mathscr{P}_c^{\Sigma_S} = \mathbf{R}_y(q_4) \cdot \mathbf{R}_z(q_5) \cdot \mathbf{T}_z(c_3) \cdot \mathbf{R}_y(q_6) \cdot \mathbf{T}_z(c_4)$$

and together with (2) all possible angles $q_{7;i,ii,iii,iv}$, $q_{8;i,ii,iii,iv}$, and $q_{9;i,ii,iii,iv}$ defining a proper wrist orientation can be computed.

## 4    Virtual Compliance Control

The following desired model ignores the real physical limitations of the manipulator but all joint limits (including high-order derivatives) are taken into account when choosing the parameters of the virtual components.

The virtual compliance (inverse of the virtual spring rate) behaviour of the specific part of the robot arm can be modelled by the simple differential equation

$$I\ddot{\mathbf{q}} + d_\varphi\,\dot{\mathbf{q}} + k_\varphi\,\mathbf{q} = \boldsymbol{\tau},$$

where $I$ is the virtual moment of inertia ($I = m\,c_2^2$, where $m$ is the virtual mass), $d_\varphi$ is the virtual damper rate, $k_\varphi$ is the virtual torsion spring rate. $\tau$ is a virtual external torque which is proportional to the difference of the measured distances $d_r$ and $d_l$.

# 5   Experimental Results

Figure 4 shows a typical run of measuring a human hand and the resulting reaction of the robot arm according to the compliant behaviour. Because two opposing proximity sensors are used for this test, only a one-dimensional motion of joint 4 can be represented, see again the dashed circle illustrated in Fig. 3.
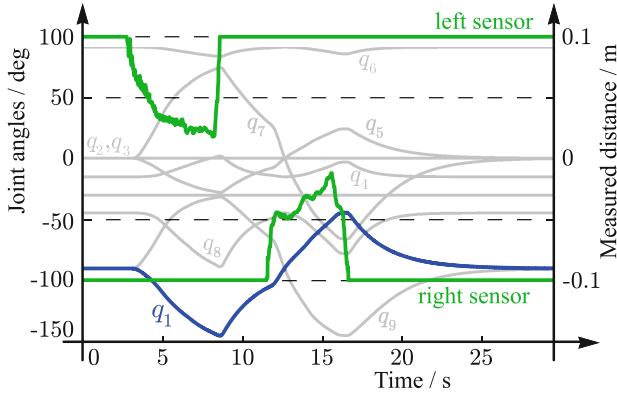


**Fig. 4.** Curves of all nine joint angles ($q_1$ is highlighted in blue) and the two proximity sensors (the green curves show the measurements of left and right sensor).

# 6   Conclusions

In order to analyze the suitability of a 9 DoF serial robot for human-robot collaboration such a system was equipped with a proximity sensor. The mobility of the centre of the 4th joint to move on a sphere was shown by an illustration and tested experimentally for a better idea. Moreover, the end point of the first substructure was modelled to be compliant and this behaviour was imposed via a controller. Here, the external influence of an object was modelled using the measured distance of a proximity sensor. Future works will include more sensitive and faster sensors. We also intend to cover more areas of the manipulator with a proximity skin to create a high redundant collaborative serial robot.

# References

1. ISO/TS 15066: 2016, robots and robotic devices - collaborative robots. Technical report, International Organization for Standardization (2016)
2. Angeles, J.: Fundamentals of Robotic Mechanical Systems: Theory, Methods, and Algorithms. Mechanical Engineering Series. Springer, Swizterland (2007)

3. Brandstötter, M., Angerer, A., Hofbaur, M.: An analytical solution of the inverse kinematics problem of industrial serial manipulators with an ortho-parallel basis and a spherical wrist. In: Proceedings of the Austrian Robotics Workshop (2014)

4. Dietrich, A., Ott, C., Albu-Schäffer, A.: An overview of null space projections for redundant, torque-controlled robots. Int. J. Robot. Res. **34**(11), 1385–1400 (2015)

5. Flacco, F., Kröger, T., De Luca, A., Khatib, O.: A depth space approach to human-robot collision avoidance. In: IEEE International Conference on Robotics and Automation (ICRA), pp. 338–345. IEEE (2012)

6. Ipa, F.: Schunk LWA 4D ROS driver (2016)

7. Morato, C., Kaipa, K.N., Zhao, B., Gupta, S.K.: Toward safe human robot collaboration by using multiple kinects based real-time human tracking. J. Comput. Inf. Sci. Eng. **14**(1), 011006 (2014)

8. Mühlbacher-Karrer, S., Faller, L.M., Zangl, H., Schlegl, T., Moser, M.: Short range capacitive proximity sensing. In: 2nd Workshop on Alternative Sensing for Robot Perception Beyond Laser and Vision, Hamburg, Germany, October 2015

9. Neythalath, N., Brandstötter, M., Hofbaur, M.: Redundancy resolution of a 9 DOF serial manipulator under hard task constraints. In: Parenti-Castelli, V., Schiehlen, W. (eds.) Romansy 21 - Robot Design, Dynamics and Control. CISM, vol. 569, pp. 31–38. Springer (2016)

10. Novak, J.L., Feddema, J.: A capacitance-based proximity sensor for whole arm obstacle avoidance. IEEE Int. Conf. Robot. Autom. **2**, 1307–1314 (1992)

11. Schlegl, T., Kroger, T., Gaschler, A., Khatib, O., Zangl, H.: Virtual whiskers - highly responsive robot collision avoidance. In: IEEE/RSJ International Conference on Intelligent Robots and Systems (IROS), pp. 5373–5379, November 2013

12. Schunk: Technical data - LWA 4D, dextrous lightweight arm. Schunk GmbH & Co., KG (2015)

# On the Vibration Control of a Flexible Metallic Beam Handled by an Industrial Robot Within an ARX-Based Synthetic Environment

Christos N. Kapsalas, John S. Sakellariou,
Panagiotis N. Koustoumpardis[(✉)], and Nikos A. Aspragathos

Mechanical Engineering and Aeronautics Department,
University of Patras, Rio Patras, Greece
chriskapsalas@gmail.com, {sakj,koust,
asprag}@mech.upatras.gr

**Abstract.** This study addresses the problem of vibration control of a flexible metallic beam which is transferred by an industrial robot. The control is designed in a special Matlab/Simulink synthetic environment that is founded on AutoRegressive with eXogenous (ARX) stochastic modelling of the robot-beam system through exclusively experimental data. Based on this, a simple closed-loop control system consisting of a feedforward typical Proportional-Integral (PI) controller and a feedback that enables the minimization of the induced force at the wrist of the robot is developed for beam vibration control. The data-based modelling of the robot-beam system allows for the precise design of the control system in offline mode, without interrupting normal production conditions, and achieves excellent performance in real time application.

**Keywords:** Industrial robot · Flexible beam · Vibration control · PI controller · ARX modelling · System identification · Force sensor

## 1 Introduction

A common, undesirable, characteristic in the manipulation of flexible metallic beams by industrial robots is the caused vibration at their free-end. In a production line this fact leads to longer cycle time and thus higher production cost, less precision in tasks like assembly and/or sliding of objects into slots as well as to reduced safety. The handling of such type of flexible objects is highly challenging and a proper control system should be capable of attenuating the stimulated vibrations at the free-end of a variety of beams very fast and without human intervention.

Chen and Zheng optimize robot's end-effector trajectory through open-loop vibration control of flexible beams by using a passive mechanism that is incorporated into the robot gripper [1]. This technique employs physics-based mathematical representations of the beam and the desired robot's end-effector trajectory. A fuzzy-based controller that eliminates the residual, undesirable, vibration at the free-end of a beam through active damping is presented in [2]. Alternatively, the suppression of the residual vibration of a deformable linear object (DLO) which is presented in [3], is

achieved through a force/torque sensor based method and a template matching technique. This is based on the period of the vibration that is determined through the embedded force sensor at the robot wrist while the DLO's stiffness is considered as known. On the other hand there are also techniques which based on extra vision sensors on the robot for treating the problem [4]. Similar vibration control techniques are also employed for crane anti-sway problems [9]. Yet, for most techniques, the need for detailed physics-based models representing the flexible object and its interaction with the robot, the significant time period with the robot out of production line for the design and tune-up of the control system and the set-up of additional, costly, equipment on the robot constitute important practical difficulties in real time application.

This study aims at the development of a *synthetic environment* in which the problem of vibration control of a flexible beam that is transferred by a robot manipulator is effectively tackled overcoming the above difficulties. The cornerstone of this environment is the AutoRegressive with eXogenous (ARX) *stochastic modelling* of the robot-beam system dynamics based on actual measurements that can be acquired even under *normal production conditions*. Based on the obtained ARX model, a closed-loop vibration control system consisting of a typical feedforward Proportional Integral (PI) controller and a feedback that enables the minimization of the induced force at the robot wrist is designed and automatically tuned through an *offline* procedure within a synthetic (simulation) environment of high precision. This procedure is suitable for various types of robots and flexible objects, avoiding the use of more involved physics-based models that necessitate intensive tuning based on actual measurements, also *minimizing* the robot idle time and the production line interruptions.

## 2    Problem Statement: The Industrial Robot, the Beam and the Experiments

The fast minimization of the vibrations caused at the free-end of a flexible metallic beam due to its rapid transfer by an industrial robot constitutes the general problem that is presently investigated (see Fig. 1). This leads to the beam's availability without delay and with precision with respect to its position for the next step of a production process, as for instance, the beam's sliding in a slot.
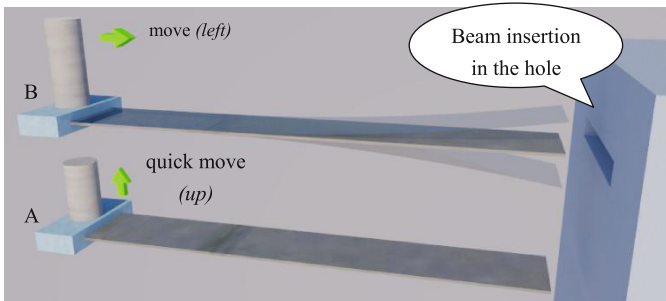


**Fig. 1.** Schematic representation of the investigated problem

In this study, an Adept Cobra s800 manipulator with 4 DoF (Fig. 2) equipped with a force sensor (ATI Industrial Automation, Gamma 65/5, resolution 0.05 N, baud rate 38400 bps or 150 Hz) which is mounted on the robot's wrist is used. The manipulated structure is a solid aluminium beam of dimensions 1000 mm × 50 mm × 3 mm (L × W × T), which is clamped to the robot gripper at the one end, while a lightweight accelerometer (PCB ICP 352C22) is mounted at the free-end for the monitoring of the vibration acceleration. It is noted that under normal operation only the force signal is used for the ARX modelling of the robot-beam system and the control design (see Sect. 3), while the acceleration measurement is solely used for the estimation of an ARX model representing the beam in various simulations for the controller's performance assessment (see Sect. 4).
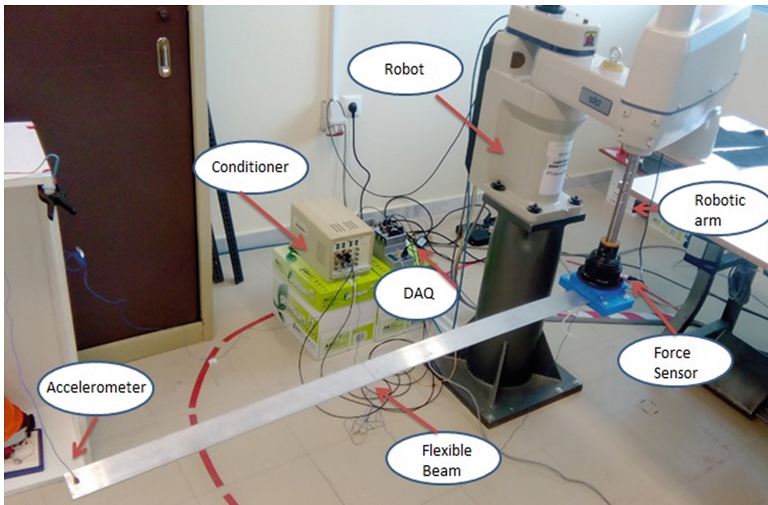


**Fig. 2.** The robot-beam system, the data acquisition (DAQ) unit with the signal conditioner and the accelerometer

Multiple experiments have been initially performed with the robot-beam system in order to study its dynamics as well as to confirm experimental repeatability of the certain investigated robot action. Yet, the signals of a single experiment are used with the robot end-effector to execute a rapid vertical movement between point A and point B of short duration (∼0.3 s) with maximum speed and acceleration inducing thus impulse-type excitation to the beam. More specifically, a signal of 3003 samples length (∼20 s) is acquired with a sampling frequency of 150 Hz via the force sensor of the robot. The measured acceleration response signal at the free-end of the beam is driven through a signal conditioner (PCB F482A20) into the data acquisition (DAQ) system (National Instruments 9234 module) with a sample frequency of 1651.6 Hz. All signals are normalized via sample mean subtraction and division by their sample standard deviation while the acceleration measurement is additionally filtered via a digital Chebyshev Type II filter (6th order, cut-off frequency = 75 Hz) and resampled at 150 Hz.

## 3   ARX-Based Synthetic Environment

The synthetic environment consists of: (i) the development of an ARX model representing the *robot-beam system dynamics* within the closed-loop control system and (ii) the *offline* design of a typical PI controller.

### 3.1   ARX Based Modelling of the Robot-Beam System

The stochastic modelling of the robot-beam system dynamics is achieved by using the given, trapezoidal-type velocity to the robot arm and the force measured at the wrist of the robot as the input-output signals in an AutoRegressive with eXogenous (ARX) input modelling procedure. Thus, a single-excitation single-response data-based ARX transfer function of the following form is obtained [5, pp. 81, 82]:

$$y[t] + \sum_{i=1}^{na} a_i y[t-i] = \sum_{i=0}^{nb} b_i x[t-i] + e[t], \quad e[t] \sim \text{iid } N(0, \sigma_e^2) \tag{1}$$

with t = 1, ..., N designating the normalized discrete time, $x[t], y[t]$ the force and acceleration response signals, respectively, na, nb the corresponding AR and X model orders, $a_i$, $b_i$ the i-th AR and X parameters, $e[t]$ the model residual (one-step-ahead prediction error) that is a white Gaussian zero-mean with variance $\sigma_e^2$ sequence and iid stands for independent identically distributed. The estimation of an ARX(na, nb) model involves parameter and structure estimation. The estimation of the parameter vector $\theta = [a_1 a_2 \ldots a_{na} | b_0 b_1 \ldots b_{nb}]^T$ is obtained based on a Least Squares (LS) estimator [5, pp. 203–207]. Model structure estimation, referring to the determination of the AR and X orders, is achieved by fitting increasingly higher order models to the signals until no further improvement is observed. Improvement may be judged via the combination of typical model order selection criteria, such as the Bayesian Information Criterion (BIC) and the RSS/SSS (Residual Sum of Squares/Signal Sum of Squares) criterion [5, pp. 498–514]. Final model acceptance is based on formal verification of the model's residual uncorrelatedness (whiteness) hypothesis [5, pp. 512, 513].

Using the backshift operator $\mathcal{B}(\mathcal{B}^i x[t] = x[t-i])$ the main expression of the discrete ARX model may be written in a transfer function form as:

$$A[\mathcal{B}]y[t] = B[\mathcal{B}]x[t] + e[t] \Rightarrow y[t] = \frac{B[\mathcal{B}]}{A[\mathcal{B}]} x[t] + \frac{1}{A[\mathcal{B}]} e[t] \tag{2}$$

with $A[\mathcal{B}] = 1 + \sum_{i=1}^{na} a_i \mathcal{B}^i$ and $B[\mathcal{B}] = \sum_{i=0}^{nb} b_i \mathcal{B}^i$.

The identification of an ARX model for the robot-beam system representation is based on the measured velocity (trapezoidal-type) - force signals of N = 3003 samples length ($\sim$20 s) and parameter estimation is based on Ordinary Least Squares with QR implementation [5, pp. 318–320]. Figure 3 depicts the BIC and the RSS/SSS criteria
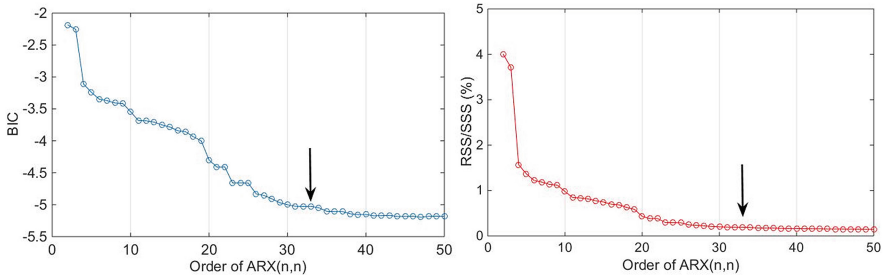
**Fig. 3.** BIC and RSS/SSS criteria for increasing model orders (n = na = nb)

for ARX models of increasing orders (n = na = nb) in the range of 2 up to 50 which reach a plateau for the model M1: ARX(33,33).

ARX(33,33) model validation is achieved by testing the model residual uncorrelatedness (whiteness) through a standard procedure with the normalized autocorrelation function mostly lying within the 99% confidence intervals (risk level of 1%) as shown in Fig. 4(a) indicating white residuals. In addition, the model one-step-ahead prediction of the force at the robot wrist is excellent as it is shown in Fig. 4(b) for a signal segment of ∼0.9 s (not used for model estimation). Thus, the ARX(33,33) model is used in the following for representing the robot-beam dynamics in the closed-loop control system of the synthetic environment.
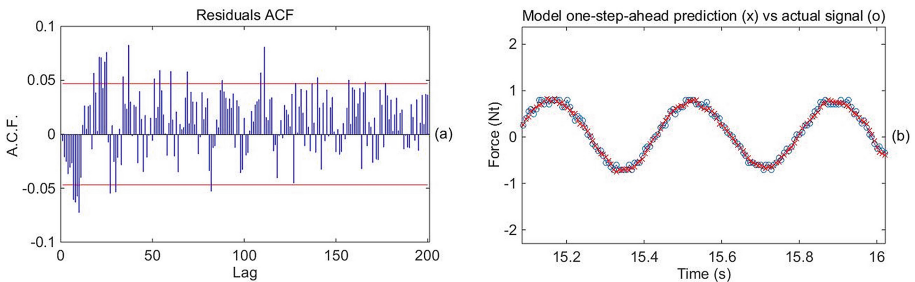


**Fig. 4.** ARX (33,33) model validation: (a) residual autocorrelation (blue bars) and confidence intervals (red solid lines; risk level of 1%); (b) force one-step-ahead predictions.

### 3.2 PI - Based Vibration Control

Figure 5 depicts the Proportional-Integral (PI) - based closed-loop control system that is designed for the attenuation of the vibration acceleration response at the free end of the beam based on the minimization of the oscillatory force at the robot wrist. The controller design is achieved through the *offline* procedure that is described below where the M1 model represents the actual robot-beam system. Thus, a position control command (e.g. move from point A to point B; see Fig. 1) - carried out by the robot internal controller - is given to the robot-beam system and the force at the robot wrist is compared through the feedback with the reference zero value. The discrete PI controller is of the Backward Euler form [6]:
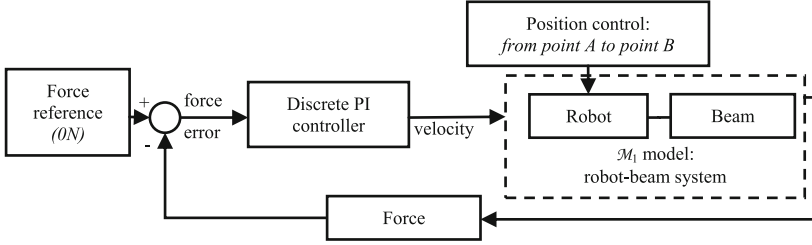
**Fig. 5.** Block diagram of the synthetic environment.

$$G(z) = K_P + K_I \frac{T_s z}{z - 1} \tag{3}$$

where $K_p$, $K_I$ are the corresponding gains of the Proportional and Integral parts of the controller, $z$ designates $z$-transform and $T_s$ (= 1/150 s) is the sampling period.

The controller receives the error signal and supplies the system with the necessary velocity that leads to the attenuation of the vibration acceleration at the beam's free-end. It is noted that although more advanced controllers were investigated a typical PI was found adequate for the fast minimization of the force preserving reasonable overshoot as shown in the next section (see Figs. 8 and 9). Once the controller tune-up procedure has been completed based on the typical Matlab/Simulink PID Controller block dialog [7], its real time application may be accomplished. Before this, its further assessment under various system operating conditions may be performed (see Sect. 4).

## 4   Vibration Control Simulation and Experimental Results

An additional ARX model representing the beam dynamics is obtained based on the procedure that is described in Subsect. 3.1. The measured force at the robot wrist is now used as the input (beam excitation) to the model, while the acceleration response at the free-end of the beam as the output. Thus, an M2: ARX(4,4) model is obtained and used only for the simulation of the beam vibration acceleration response. Such type of models may be used instead of approximated physics-based models for any type of flexible object achieving thus more realistic simulations. Figure 6 depicts the measured acceleration response at the free-end of the beam and the one simulated by the ARX (4,4) model. The excellent agreement is evident verifying the accurate representation of the beam's dynamics through the obtained model.

Based on this, the tuning of the PI controller within the synthetic environment (left part of Fig. 7) is initially activated. Once the PI controller gains have been obtained, the synthetic environment is connected with model M2 and the beam vibration acceleration response at its free-end is simulated for 20 s with and without the incorporation of the PI-based control system. Figure 8 depicts simulation and experimental[1] results for the

---

[1] https://youtu.be/QBJ-nUtPhys (vibration of the beam without control).
  https://youtu.be/fAVysBIFMYM (PI-based vibration control of the beam).
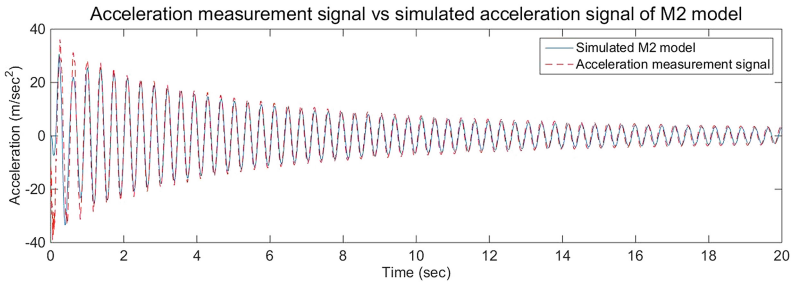
**Fig. 6.** Actual acceleration response signal at the free-end of the beam and its ARX(4,4) model based simulation
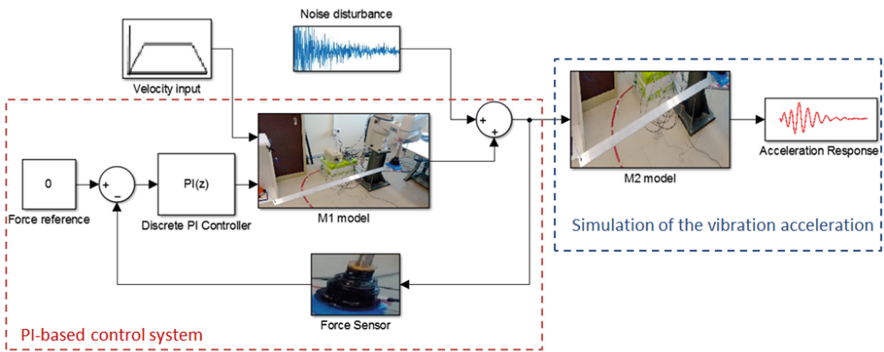


**Fig. 7.** Schematic representation of the simulation procedure
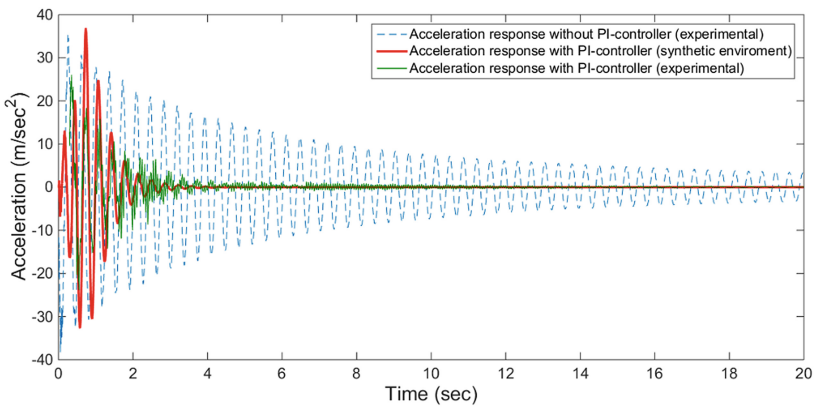


**Fig. 8.** Acceleration response at the free-end of the beam with and without the PI-based control system based on simulation and experimental results
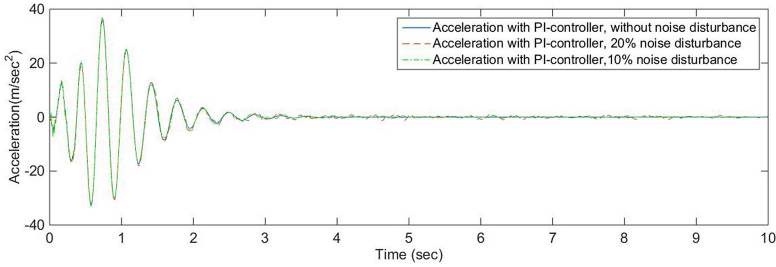
**Fig. 9.** PI-based vibration control of the acceleration response at the free end of the beam

vertical acceleration at the free-end of the beam where the effect of the control system is evident as in less than 4 s the induced acceleration becomes almost zero. The agreement between experimental and simulated results is remarkable and confirms the precise design of the control system within the synthetic environment.

Two additional simulations are performed with the control system activated while noise-corrupted force measurements are transferred by the feedback. The force signal is significantly corrupted by non-stationary uncorrelated noise at 10% and 20% noise-to-signal (N/S) local levels, in the standard deviation sense [8]. Figure 9 depicts the acceleration response at the beam's free-end with the force signal contaminated by measurement noise as well as without noise. It is obvious that the control system's performance is slightly affected by the added noise and suppresses rapidly the vibration acceleration although the PI controller is not re-tuned for the cases of added noise, indicating thus its robustness even under noisy industrial conditions.

## 5    Conclusions

The problem of vibration control of a flexible metallic beam, rapidly transferred by an industrial robot, was tackled in a novel Matlab/Simulink synthetic environment. This was based on ARX stochastic modelling of the robot-beam system dynamics and a closed-loop control system with a typical PI controller. All procedures were performed offline with even a single experiment with the actual robot-beam system being adequate for the design of the control system, minimizing thus the interruptions of the robot normal production activity. The results obtained through simulations and experiments with the robot-beam system demonstrated that the vibration acceleration at the free-end of the beam was attenuated very fast through the control of the induced force at the robot wrist in all considered cases. Furthermore, the excellent agreement between the simulation and experimental results indicate the precise design of the control system within the synthetic environment.

# References

1. Chen, M.Z., Zheng, Y.F.: Vibration-free movement of deformable beams by robot end-effectors. J. Robot. Syst. **12**(5), 331–347 (1995)
2. Yue, S.G., Henrich, D.: Manipulating deformable linear objects: fuzzy- based active vibration damping skill. J. Intell. Robot. Syst. **46**, 201–219 (2006)
3. Yue, S.G., Henrich, D.: Manipulating deformable linear objects: sensor-based skills of adjustment motions for vibration reduction. J. Robot. Syst. **22**(2), 67–85 (2005)
4. Bodenhagen, L., et al.: An adaptable robot vision system performing manipulation actions with flexible objects. IEEE Trans. Autom. Sci. Eng. **11**(3), 749–765 (2014)
5. Ljung, L.: System Identification: Theory for the User, 2nd edn. Prentice Hall PTR, Upper Saddle River (1999)
6. Dorf, R.C., Bishop, R.H.: Modern Control Systems, 11th edn. Prentice Hall, Upper Saddle River (2008)
7. The Mathworks Inc.: Natick, MA. http://www.mathworks.com/help/slcontrol/gs/automated-tuning-of-simulink-pid-controller-block.html
8. Sakellariou, J.S., Fassois, S.D.: Stochastic output error based damage detection and assessment in structures under earthquake excitation. J. Sound Vibr. **297**, 1048–1067 (2006)
9. Elbadawy, A.A., Shehata, M.M.G.: Anti-sway control of marine cranes under the disturbance of a parallel manipulator. Nonlinear Dyn. **82**, 415–434 (2015)

# Minimal Energy Cartesian Impedance Control of Robot with Bidirectional Antagonistic Drives

Branko Lukić[(✉)] and Kosta Jovanović

School of Electrical Engineering, Laboratory for Robotics,
University of Belgrade, Belgrade, Serbia
brankolukicl@gmail.com, kostaj@etf.rs

**Abstract.** This paper investigates how to split actuating torques between prime movers in bidirectional antagonistic actuators to obtain desired Cartesian stiffness with minimal energy store. Minimal energy in elastic elements during robot motion will ensure maximal energy storage capacity in case of a collision. The correlation between joint stiffness and energy stored in springs is demonstrated. A simulation case study targets a two DOF-s robot driven by QBMove maker pro actuator. Finally, a control scheme comprising impedance control and equal torque distribution between two bidirectional antagonistic drives is derived and validated through simulations.

**Keywords:** Impedance control · Bidirectional antagonistic actuators · Compliant actuators · QBMove maker pro · Minimal energy torque division

## 1 Introduction

Avoiding collisions and impacts without damage are crucial for successfully and reliably performing tasks in contemporary robotics. Collision between stiff object and robot driven by conventional rigid drives induces the energy into the mechanical system too fast. Thus, even if the robot is controlled to achieve active compliance, the controller cannot prevent possible damage and absorb an impact [1]. Therefore, contemporary service robots are deliberately designed as compliant, i.e. elastic deformation is planned to increase safety of the interaction between humans and robots and to increase energy efficiency by storing and recovering energy in compliant elements. Energy introduced into the system by collision, external forces or acceleration of the link inertia is converted to elastic energy by stretching the springs. Stored elastic energy can be observed as additional energy source. This source can be used to regain kinetic energy, and improve the dynamics of the system. Furthermore, stored energy in elastic elements allows compliant robots to outperform stiff robots dynamics. However, in order to exploit benefits of VSA, appropriate planning and control of compliance is of essential importance and therefore the topic is targeted in this paper.

The latest generation of robotic actuators, variable stiffness actuators (VSA), combines intrinsic compliant (passive) elements and actively controlled compliance to exploit benefits of both approach. Different types of VSA have been developed: Mechanical Control Stiffness [2], Structure Controlled Stiffness [3], and Antagonistic Controlled Stiffness [4].
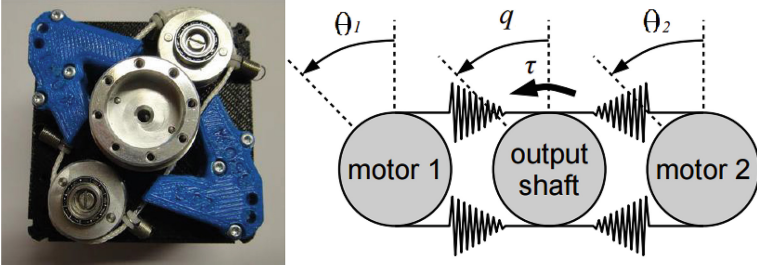
**Fig. 1.** QBMove maker pro: under the mask (left), functional scheme (right)

One of the newest VSA is QBMove Maker pro developed by The Natural Motion Initiative [5]. It is a low cost bidirectional spring antagonistic actuator design as open source, thus it is affordable and can be used for robotics research and educational purposes. The QBMove maker pro actuator and his structure, as a targeted actuation scheme of this paper, are shown in Fig. 1.

The idea for this work came out from previous research activities of the authors in the field of modelling [6] and control [7] of antagonistically driven robots and investigation of contribution of robot mechanical properties to control in contact tasks [8].

In Sect. 2, a general model for 2 DOF planar robots with bidirectional elastic actuators is derived. Section 3 describes a control strategy that minimizes overall system energy while performing desired Cartesian impedance. Simulation results are presented in Sect 4, while final remarks and directions for future work are pointed out in Sect. 5.

## 2  Model of a Robot Driven by Bidirectional Antagonistic Complaint Actuators

Let us consider the general structure of a 2-DOF robot shown in Fig. 2. The planar robot has two links connected by revolute joints. Links lengths are $l_1$ and $l_2$, masses $m_1$ and $m_2$ and moments of inertia $I_1$ and $I_2$, respectively. Lengths $l_{c1}$ and $l_{c2}$ denote distances from the rotating axes to the centres of mass of Link 1 and Link 2, respectively. Internal coordinates are denoted with $q_1$ and $q_2$, where $q_1$ is measured from $y$ axis and $q_2$ is measured relative to the extension of the Link 1 toward the Link 2, both being positive clockwise. The vector of joint positions is defined as $q = [q_1 q_2]^T$. The 2-DOF planar arm dynamics is given by:

$$Hq + Cq + G = \tau - J^T F int \tag{1}$$

$H$, $C$, $G$, $F_{int}$ and $\tau$ denote: robot inertia matrix, matrix of centrifugal and Coriolis forces, vector of gravitational forces, vector of interaction force between the robot and its environment, and joint drive torque respectively. Matrices $H$, $C$, $G$ and $\tau$ are:
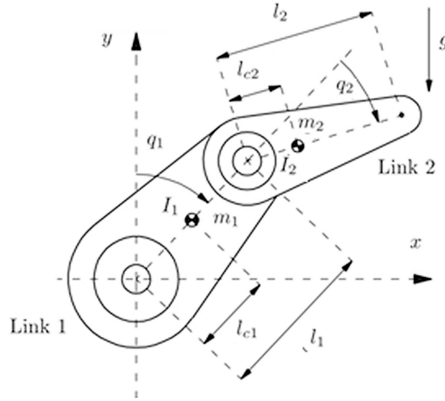
**Fig. 2.** Schematics of 2-DOF robot

$$H = \begin{bmatrix} m_1 l_{c1}^2 + m_2 \left( l_1^2 + l_{c2}^2 + 2l_1 l_{c2} \cos(q_2) \right) + I_1 + I_2 & m_2 \left( l_{c2}^2 + l_1 l_{c2} \cos(q_2) \right) + I_2 \\ m_2 \left( l_{c2}^2 + l_1 l_{c2} \cos(q_2) \right) + I_2 & m_2 l_{c2}^2 + I_2 \end{bmatrix}$$

(2)

$$C = \begin{bmatrix} -m_2 l_1 l_{c2} \sin(q_2) \, \dot{q}_2 & -m_2 l_1 l_{c2} \sin(q_2) \left( \dot{q}_1 + \dot{q}_2 \right) \\ m_2 l_1 l_{c2} \sin(q_2) \, \dot{q}_1 & 0 \end{bmatrix}$$

(3)

$$G = \begin{bmatrix} -g(m_1 l_{c1} + m_2 l_1) sin(q_1) - g \, m_2 l_{c2} sin(q_1 + q_2) \\ - g \, m_2 l_{c2} \sin(q_1 + q_2) \end{bmatrix}$$

(4)

$$\boldsymbol{\tau} = [\tau_1 \tau_2]^T$$

(5)

where $g$ is the gravity constant ($g = 9.81 \, \text{m/s}^2$).

The model of a robot joint driven by bidirectional springs is shown in Fig. 1. The mathematical model of the symmetric bidirectional motor-spring system in the case were friction is neglected is described by Eqs. (6), (7) and (8):

$$\tau_{m1/2} = \tau_{1/2} + I_m \ddot{\theta}_{1/2}$$

(6)

$$\tau_{1/2} = k \, \sinh \left( a \left( \theta_{1/2} - q \right) \right)$$

(7)

$$\tau = \tau_1 + \tau_2 = k(\sinh(a(\theta_1 - q)) + \sinh(a(\theta_2 - q)))$$

(8)

where $\tau_{m1}$ and $\tau_{m2}$ are actuation torques of motor 1 and motor 2, $\tau$ is the output shaft torque, $\tau_1$ and $\tau_2$ are torques developed in elastic springs, $\theta_1$ and $\theta_2$ are positions of motor 1 and motor 2, $I_m$ is the motor inertia, and $k$ and $a$ are drive parameters.

From now on, motor positions and actuation torques are labelled with $\theta_{ij}$ and $\tau_{mij}$ where $i$ and $j$ denote the $i$-th joint of the $j$-th motor.

From (1) through (8), the full dynamic model of the 2-DOF compliant driven robot can be obtained by calculating joint and motor accelerations:

$$\ddot{q} = H(q)^{-1}\left(\tau - J(q)^T F_{int} - C(q,\dot{q})\dot{q} - G(q)\right) \tag{9}$$

$$\ddot{\theta}_{ij} = I_m^{-1}\left(\tau_{m_{ij}} - k\,sinh\left(a\left(\theta_{ij} - q_i\right)\right)\right) \tag{10}$$

The stiffness for one QBmove maker pro joint is given by (11).

$$S = -\frac{d\tau}{dq} = ak(cosh(a(\theta_1 - q)) + cosh(a(\theta_2 - q))) \tag{11}$$

## 3   Control Strategy

The final control scheme proposed in this paper comprises the conventional impedance control which calculates desired joint torques and the algorithm for desired torque distribution between two antagonistic bidirectional drives.

Impedance control was first introduced by N. Hogan in [9, 10]. The principle of impedance control is to drive a robot in such way that the robot end effector exhibits desired impedance behaviour (12) – the second order mass spring damper system (Fig. 3), where **M** is the inertial mass matrix, **K** the Cartesian stiffness matrix, and **B** the Cartesian damping matrix:

$$\mathbf{F_{int}} = \mathbf{M}(\ddot{\mathbf{X}}_\mathbf{d} - \ddot{\mathbf{X}}) + \mathbf{B}(\dot{\mathbf{X}}_\mathbf{d} - \dot{\mathbf{X}}) + \mathbf{K}(\mathbf{X}_\mathbf{d} - \mathbf{X}), \tag{12}$$

where **X** is the actual and $\mathbf{X_d}$ the desired end effector position, and $\mathbf{F_{int}}$ represents the interaction force between the robot and its environment.

When interaction force is not measurable, the parameter **M** of the impedance controller is set to $\mathbf{M} = \Lambda(\mathbf{q})$. Thus, the desired torque is given by:

$$\tau_\mathbf{d} = \mathbf{J(q)^T}\left[\Lambda(\mathbf{q})\ddot{\mathbf{X}}_\mathbf{d} + \mathbf{B}(\dot{\mathbf{X}}_\mathbf{d} - \dot{\mathbf{X}}) + \mathbf{K}(\mathbf{X_d} - \mathbf{X}) + \Gamma(\mathbf{q},\dot{\mathbf{q}})\dot{\mathbf{X}} + \eta(\mathbf{q})\right] \tag{13}$$
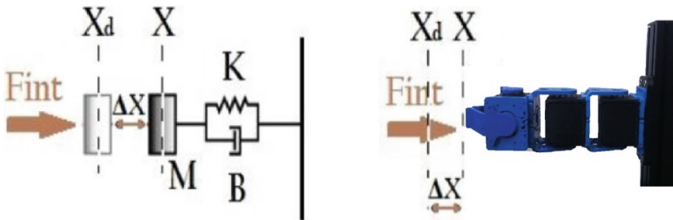


**Fig. 3.** Impedance control principle. The robot controlled by impedance controller behaves as second order mass spring damper system in Cartesian space.

$$\Lambda(\mathbf{q}) = \mathbf{J}(\mathbf{q})^{-\mathbf{T}}\mathbf{H}(\mathbf{q})\mathbf{J}^{-1}(\mathbf{q}) \tag{14}$$

$$\Gamma(\mathbf{q}, \dot{\mathbf{q}}) = \mathbf{J}(\mathbf{q})^{-\mathbf{T}}\mathbf{C}(\mathbf{q}, \dot{\mathbf{q}})\mathbf{J}^{-1}(\mathbf{q}) - \Lambda(\mathbf{q})\dot{\mathbf{J}}(\mathbf{q})\mathbf{J}^{-1}(\mathbf{q}) \tag{15}$$

$$\eta(\mathbf{q}) = \mathbf{J}(\mathbf{q})^{-\mathbf{T}}\mathbf{G}(\mathbf{q}) \tag{16}$$

The next task in the proposed control algorithm is desired torque division to portions of bidirectional antagonistic drives. To that end, we were interested in obtaining a desired Cartesian stiffness with minimal energy store. Minimal energy in elastic elements during robot motion will ensure maximal energy storage capacity in case of a collision. Thus, the correlation between joint stiffness and energy stored in springs is shown as follows.

The joint pulley ($r_j$) and prime mover pulleys ($r_p$) of QBmove maker pro are equal, $r_j = r_p = r$. According to Fig. 2, the expression (17) for elongation of elastic element stands. This expression combined with (7) represents the torque contribution of each prime mover given by (18):

$$\Delta l_{1/2} = r(\theta_{1/2} - q) \tag{17}$$

$$\tau_{1/2} = k \, \sinh\big(a(\theta_{1/2} - q)\big) = k \, \sinh\left(\frac{a\Delta l_{1/2}}{r}\right) \tag{18}$$

Thus, knowing pulley radius, the developed forces and torques and the energy stored in elastic springs, the total energy stored per one bidirectional antagonistic actuation unit are defined by (19), (20), and (21) respectively:

$$F_{1/2} = \frac{\tau_{1/2}}{r} \tag{19}$$

$$E_{1/2} = \int_0^{\Delta l_{1/2}} F_{1/2}(x)dx = \frac{k}{r}\int_0^{\Delta l_{1/2}} \sinh\left(\frac{ax}{r}\right)dx = \frac{k}{a}\left(\cosh\left(\frac{a\Delta l_{1/2}}{r}\right) - 1\right) \tag{20}$$

$$E = E_1 + E_2 = \frac{k}{a}\left(\cosh\left(\frac{a\Delta l_1}{r}\right) + \cosh\left(\frac{a\Delta l_2}{r}\right) - 2\right) = \frac{1}{a^2}(S - 2ak) \tag{21}$$

Since parameters $a$ and $k$ are constants, the minimal energy is obtained for minimal stiffness in every joint.

Our goal is to split the desired actuated torque $\tau_d$ between prime movers, where one motor contributes with $r\tau_d$ and the second with $(1 - r)\tau_d$ (so overall joint torque is $\tau_d$), while initial pretension $\tau_0$ is assumed. Accordingly, the equation for driving torques in each joint can be rewritten as:

$$\tau_1 = k \, \sinh(a(\theta_1 - q)) = r\tau_d + \tau_0 \tag{22}$$

$$\tau_2 = k \, \sinh(a(\theta_2 - q)) = (1 - r)\tau_d - \tau_0 \tag{23}$$

Equations (18) and (19) lead to equalities $a(\theta_1 - q) = asinh\left(\frac{r\tau_d + \tau_0}{k}\right)$ and $a(\theta_2 - q) = asinh\left(\frac{(1-r)\tau_d - \tau_0}{k}\right)$, so overall joint stiffness can be written in form (24):

$$S = ak\left(\cosh\left(asinh\left(\frac{r\tau_d + \tau_0}{k}\right)\right) + \cosh\left(asinh\left(\frac{(1-r)\tau_d - \tau_0}{k}\right)\right)\right) \quad (24)$$

In order to find the value of $r$ for $S$ to be minimal, Eq. (24) is differentiated over $r$ ($\frac{dS}{dr} = 0$), and the parameter $r$ which shows torque portions is calculated as:

$$\frac{dS}{dr} = a\left(\frac{(r\tau_d + \tau_0)\tau_d}{\sqrt{k^2 + (r\tau_d + \tau_0)^2}} - \frac{((1-r)\tau_d - \tau_0)\tau_d}{\sqrt{k^2 + ((1-r)\tau_d - \tau_0)^2}}\right) = 0 \Rightarrow r = \frac{1}{2} - \frac{\tau_0}{\tau_d} \quad (25)$$

The result (25) leads to the unambiguous conclusion that the desired joint torque should be equally distributed among two antagonistic bidirectional drives to minimize energy storage:

$$\tau_a = \tau_b = \frac{\tau_d}{2} \quad (26)$$

## 4  Simulation Results

According to labels in Fig. 1, the robot parameters used for simulations are: $m_1 = m_2 = 0.28$ kg and $I_1 = I_2 = 3 \times 10^{-6}$ kgm$^2$. Since links are created from lightweight plastic and the actuator's mass dominates, the approximations: $l_1 = l_2 = l_{c1} = l_{c2} = 0.09$ m are adopted. For simulation we adopted slightly different values of the parameters as compared to the ones given in technical specifications [11], identified as
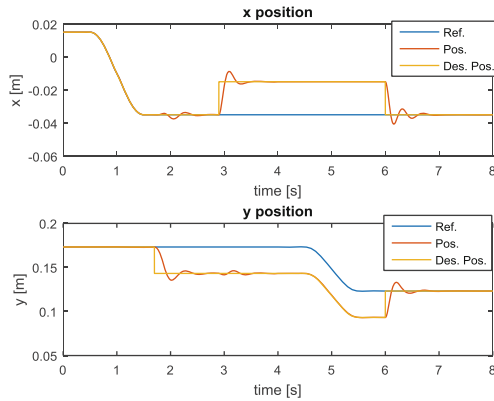


**Fig. 4.** Trajectory tracking in Cartesian coordinates comprising desired impedance behaviour

described in [12]. We assume that drive parameters are symmetric and their values are $a = 6.8465$ and $k = 0.02215$.

We consider the case when the interaction force is not measurable, thus the parameters adopted for the impedance controller are:

$$\boldsymbol{M} = \boldsymbol{\Lambda}, \quad \boldsymbol{B} = diag(4, 4)\frac{Ns}{m}, \quad \boldsymbol{K} = diag(100, 100)\frac{N}{m} \tag{27}$$

In the simulation, the desired trajectory comprises changes in $x$ coordinate at $t = 0.5$ s, and $y$ coordinate at $t = 4.5$ s. External force of $F_{int\_x} = 2N$ acts in $x$ direction during time interval $t_{Fx} = 1.7 \div 6$ s, and force of $F_{int\_y} = -3N$ in $y$ direction during time interval $t_{Fy} = 2.9 \div 6$ s. Simulation results are shown in Figs. 4, 5 and 6.
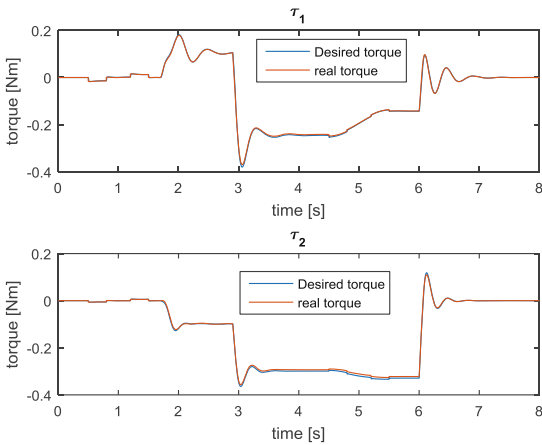


**Fig. 5.** Desired and actual joint torque
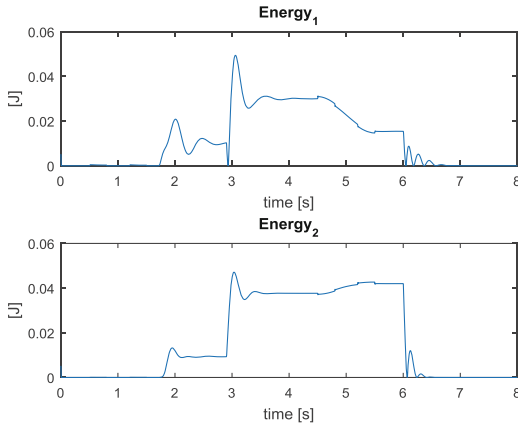


**Fig. 6.** Energy stored in elastic springs

Figure 4 confirms desired Cartesian impedance behaviour and good trajectory tracking. The desired and actual joint torques, obtained with the described control scheme, are given in Fig. 5. This small deviation is a consequence of neglecting prime mover inertia in the control strategy. Figure 6 depicts the energy stored in elastic elements of the joints. Although the algorithm keeps stored energy at low values and therefore reduces energy losses, the energy stored in springs increases when impact occurs.

## 5   Conclusion

This paper introduced impedance control for robots driven by bidirectional antagonistic compliant actuators. Desired joint torque division was done by minimal energy criterion which leads to minimal stiffness criterion on joint level, while still keeping desired Cartesian impedance behavior. Low stiffness and low level of stored energy in each joint enables higher energy storage in case of a collision.

Further research will include algorithm verification on a laboratory setup built from QBmove maker pro actuators. Furthermore, the algorithm will be applied to more complex redundant structure and influence of robot configuration and joint level stiffness to Cartesian stiffness will be examined.

## References

1. Haddadin, S., Albu-Schäffer, A., Hirzinger, G.: Safe physical human-robot interaction: measurements, analysis and new insights. In: Kaneko, M., Nakamura, Y. (eds.) Robotics Research, vol. 66, pp. 395–407. Springer, Heidelberg (2007)
2. Van Ham, R., Vanderborght, B., Van Damme, M., Verrelst, B., Lefeber, D.: MACCEPA, the mechanically adjustable compliance and controllable equilibrium position actuator: design and implementation in a biped robot. Robot. Auton. Syst. **55**(10), 761–768 (2007)
3. Migliore, S.A., Brown, E.A., De Weerth, S.P.: Biologically inspired joint stiffness control. In: Proceedings of IEEE International Conference on Robotics and Automation, ICRA 2005, Barcelona, pp. 4519–4524 (2005)
4. Tasch, A.D.U.: A two-DOF manipulator with adjustable compliance capabilities and comparison with the human finger. J. Robot. Syst. **13**(1), 25–34 (1996)
5. Catalano, M., Grioli, G., Garabini, M., Mancini, M., Tsagarakis, N., Bicchi, A.: VSA-CubeBot: a modular variable stiffness platform for multiple degrees of freedom robots. In: Proceedings of IEEE International Conference on Robotics and Automation, ICRA 2011, Shanghai, pp. 5090–5095 (2011)
6. Jovanovic, K., Potkonjak, V., Holland, O.: Dynamic modelling of an anthropomimetic robot in contact tasks. Adv. Robot. **28**(11), 793–806 (2014)
7. Potkonjak, V., Svetozarevic, B., Jovanovic, K., Holland, O.: The puller-follower control of compliant and noncompliant antagonistic tendon drives in robotic system. Int. J. Adv. Rob. Syst. **8**, 143–155 (2012)

8. Lukic, B., Jovanovic, K.: Influence of mechanical characteristics of a compliant robot on Cartesian impedance control design. In: 2nd IcETRAN Conference, Silver Lake, Serbia, pp. 1–6 (2015)

9. Hogan, N.: Impedance control: an approach to manipulation: Part I - theory. J. Dyn. Syst. Meas. Contr. **107**, 1–7 (1985)

10. Hogan, N.: Impedance control: an approach to manipulation: Part II - implementation. J. Dyn. Syst. Meas. Contr. **107**, 8–16 (1985)

11. http://www.qbrobotics.com/wp-content/uploads/2016/03/45c5a1_792590e00b134129b2b63 63a1ea7de45.pdf. Accessed 13 May 2016

12. Grioli, G., Wolf, S., Garabini, M., Catalano, M., Burdetk, E., Carloni, R., Friedl, W., Grebenstein, M., Laffranchi, M., Lefeber, D., Stramigioli, S., Tsagarakis, N., Vanderborght, B., Albu-Schaeffer, A., Bicchi, A.: Variable stiffness actuators: the user's point of view. Int. J. Robot. Res. **34**, 727–743 (2007)

# Robot Vision and Sensory Processing

# Robotic 3D Surface Laser Scanning for Feature-Based Quality Control in Holonic Manufacturing

Alexandru Dumitrache, Theodor Borangiu$^{(\boxtimes)}$, and Silviu Răileanu

Department of Automation and Industrial Informatics,
University Politehnica of Bucharest, Bucharest, Romania
{alex.dumitrache,theodor.borangiu,
silviu.raileanu}@cimr.pub.ro

**Abstract.** The paper describes an on line geometry control technique which uses a laser sensor hand-held by a 6 d.o.f.-vertical articulated robot and displaced along predefined scanning paths. The 3D surface of manufactured part is digitally reconstructed after the robot drives the laser sensor along a scanning motion pattern corresponding to the part type (prismatic, revolute) and geometric features to be checked (direct measurements: lengths, angles, signatures, depth map evaluation: local and global indicators) against reference part models. The robotized laser scanning system is integrated with a 2D vision platform allowing thus to perform an extended set of geometry inspection tasks on manufactured parts (processed on CNC machine tools, assembled by robots). The described quality control technology is applied to holonic manufacturing by including in the order holon the inspection sequence retrieved from the product holon and the laser scanner robot enabled by the resource holon. Implementing solutions and experimental results are reported.

**Keywords:** Laser scanning · 3D reconstruction · Image features · Robotized CAQC

## 1 Introduction

Manufacturing control systems have evolved in the last years; most significant is the emergence of semi-heterarchical systems dynamically switching between hierarchical (optimizing production at far, batch horizon) and heterarchical (robust at disturbances, adaptable and agile at environment and product changes) operating modes. The quest for safety, robustness, sustainability and agility requires a new type of smart control systems characterized by: (1) Distributed intelligence in MES (Manufacturing Execution System) and shop floor based on new ICT frameworks: control distributed over autonomous intelligent units (agents) [1], multi-agent systems (MAS), holonic organizations [2], product-driven automation [3]; (2) Service Oriented Architectures (SOA), increasingly used as implementation mean for MAS [4]; business and process information integration and interoperability at enterprise level will need the customized product as "active controller" of the enterprise resources – thus providing consistency between the material and informational flows; (3) Manufacturing Service Bus

(MSB 2.0) integration model: it introduces the principle of bus communication between the manufacturing layers acting an intermediary for data flows and assures loose coupling of manufacturing modules [5–7].

Input data and formats for mechanical part processing are subject to increased diversity, requiring: high-speed instrumenting with external sensors (range finder, vision, laser), intensive communication of dexterous robots with CNC machine tools and measuring devices, and easy reconfigurable, task-driven software systems capable to detect, recognize, locate, qualify, inspect complex objects and accurately represent in digital form their 3D shapes. This allows fast set up of production and control of products in response to customer orders (make-to-order) ranging from single complex parts to large batches [8].

The extension of traditional material-handling control to material-conditioning (recognizing, qualifying, locating, inspecting and manipulating) allows relaxation of material flow- and process constraints imposed to the transportation means, and:

- Rapid part surface scanning, accurate 3D digital representation, and further processing for $2^{1/2}$ descriptions to be used in CNC machining [9, 10];
- 2D and 3D geometry inspection of manufactured parts for on line computer aided quality control (CAQC) [11].

These functional extensions became possible in external sensor (vision, range)-robot-material processing systems (machining, assembly) by using: (i) effective descriptions of material flows through efficient sets of form-, surface-, and pose features of parts; (ii) scanning of complex part shapes with laser sensors along motion patterns generated by anthropomorphic robots, and (iii) applying Artificial Intelligence concepts and high level image processing techniques to the digital 3D representation of parts to evaluate quality descriptors (shape, surface, alignment) [12].

The rest of the paper is organized as follows: Sect. 2 presents the architecture of the robotized 3D part scanning system and defines the measuring primitives used to compute scalar, vector and domain descriptors of 3D surfaces. In Sect. 3, 3D scanning techniques are integrated with 2D high-level image processing to allow configuring geometry control in the holonic manufacturing approach. Implementing solutions and experimental results are reported in Sect. 4. Section 5 formulates conclusions and defines future research lines.

## 2   Robotized Part Scanning and Measuring Primitives

A hardware manufacturing platform with CAQC was developed; it integrates a short range, high-precision 3D laser scanning probe displaced by a 6-d.o.f. vertical articulated robot manipulator relative to: (a) part models to be digitized and reproduced on a 5-d.o.f CNC milling machine or (b) machined parts the geometry of which needs to be measured and compared with a set of predefined model shape features for in line quality control (Fig. 1). The laser probe can measure distances from 70 to 250 millimetres, with an accuracy of 30 μm. The anthropomorphic, 6-d.o.f. Viper 650 Adept robot has repeatability of 0.02 mm; the displacement domains of the 6 rotational joints are respectively 1: ± 170°, 2: −170°, + 45°, 3: −29°, +256°, 4: ± 190°, 5: ± 120°, 6: ± 360°.
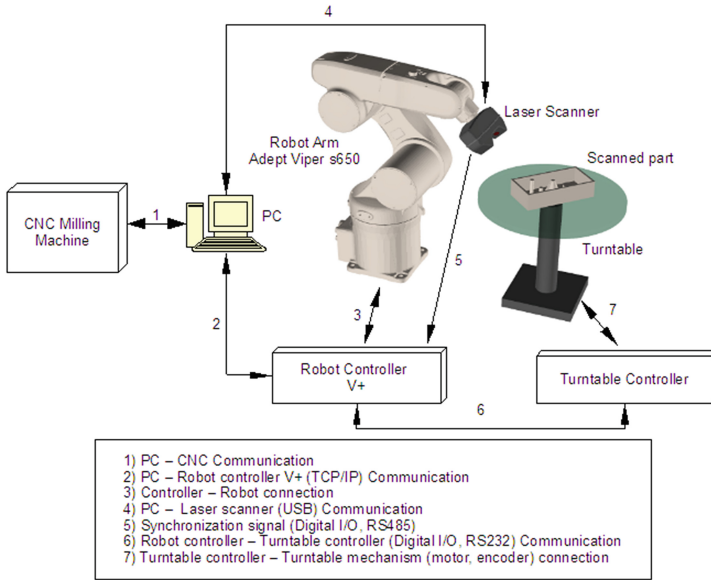
**Fig. 1.** Robotized laser scanner 3D shape reconstruction and inspection system

Products to be inspected (machined parts, assemblies) are placed on a rotary table with closed-loop position control of 0.05° resolution; a complete 360° digital representation of the object's 3D surface is obtained executing repeatedly the motion sequence: (i) the robot moves vertically the laser probe along the object's vertical axis between two predefined points a, b; (ii) the table rotates with a predefined angle, turning the object. This sequence is repeated until the object is rotated 360°. The laser sensor emits a laser beam focused into a plane; when this plane intersects the object's surface, the laser rays cast a line or a curve which is detected by two cameras. This curve is easily segmented due to its high intensity, and the coordinates of the points on a curve are transformed from pixels (in the image reference frame) to millimetres (in the sensor's frame) using nonlinear triangulation. Sensor data is synchronized with the robot's position, and then transformed as depth map into a fixed reference frame (Fig. 2).
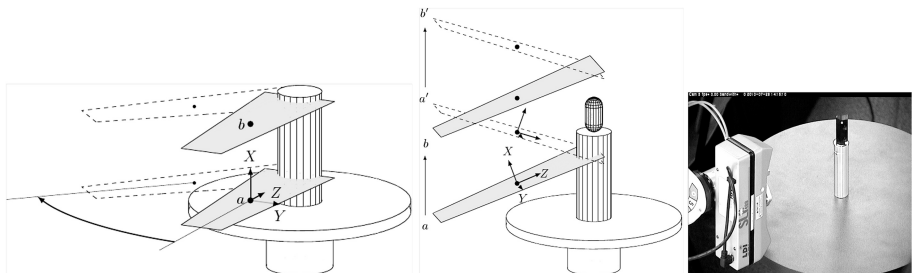


**Fig. 2.** Cylindrical exploration: constant (*left*)/variable (*middle*) orientation; the probe (*right*)

For more complex parts, point vectors can be defined with different sensor orientations; this allows acquiring more 3D shape details (from above and from beneath), at higher scan time and computing effort [13]. Cylindrical exploration is performed with the function `scan_rot` having the syntax `scan_rot (n,a,b,v)`, where:

- n: no. of positions of the rotating table necessary to cover 360°; for each position of the table, the robot displaces linearly the laser sensor between a and b;
- a, b: taught points between which the sensor is moved linearly in the C-space;
- v [mm/sec]: linear displacement speed of the laser sensor carried by the robot.

To integrate the laser scanning and range finder system with the robot system, the following software modules have been developed: (1) *Encoder Latching Server*: provides integration of the laser scanning control with the robot motion controller; the instantaneous Cartesian position of the robot is transmitted to the distance acquisition software, *Surveyor Scan Control*; (2) *Trajectory Planner*: computes the robot paths along which scanning of the surface of interest will be done, according to user defined exploring strategy - the motion pattern.

## 2.1 Direct Surface Measurements Using the Laser Sensor

Simple geometric surfaces (planar, spherical) can be analysed through shape measurements, which can be computed from a single scan line of the laser sensor; examples are: the diameter of an arc circle, the angle between two planar surfaces. In order to obtain accurate measurements, the laser plane must be positioned normal to the axis of the measured feature; for the above examples, the sensor should be perpendicular on the cylinder axis or on the edge between the two plane surfaces.

Angular measurements can be also applied to non-planar surfaces, their intersection with the laser plane resulting in two straight line segments. In this case, the intersection of the two surfaces will be an edge described by a spatial curve, and the sensor has to be positioned perpendicular to this curve to perform the measurement.

It is possible to automatically adjust the sensor orientation so that it becomes normal to the measured feature or edge, by estimating the tangent direction to this feature using small displacements of the laser sensor around the location manually taught by the user with low orientation accuracy [14]. For this, the user must place the scanning sensor almost perpendicular to the measured edge, with an error less than 30°.

The tangent to the measured feature is detected using a small scan pass ④ (Fig. 3), by fitting a straight line to the positions of the edge located with a 2D vision engine. After the tangent to the measured edge ③ is estimated, one can compute the rotation transformation necessary for correction ⑤. The rotation can be obtained in axis-angle format by computing the cross product between the current tangent vector ② (normal to the laser plane ①) and the desired one. This method of tangent estimation allows also automatic detection of the part contour and automatic generation of a scanning trajectory along this contour by automatic repositioning of the sensor.

*Measuring the angle between two straight lines* obtained from a single scan line consists of: (i) segmenting the scan line (and detecting the edge of interest); (ii) applying linear regression to the two detected segments; (iii) computing the angle.
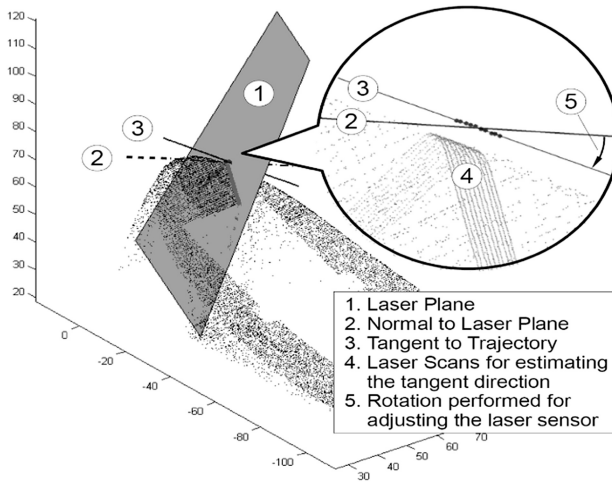
**Fig. 3.** Automatic orientation of the sensor by detecting the tangent to the measured edge

Segmentation can be performed by applying a single step of the well-known algorithm for polyline simplification, Douglas-Peucker [15], one of the most used algorithms for this task. This step will determine the farthest point from the segment joining the extreme points of the scan lines. However, if the scan lines contain other features, the segmentation has to be done with interactive help from the user.

To compute the orientation of straight line segments, it is recommended to use robust regression which reduces the influence of outliers (Fig. 4). A readily available implementation of robust regression is in Matlab with the `robustfit` function [16].



**Fig. 4.** Robust regression of straight line ignores outliers

*Measuring the diameter of a circular feature* is the same as determining the circle which approximates best the points on the scan line, under the hypothesis that these points are arranged on a circular arc (Fig. 5).

In this case, the regression equations are nonlinear, but the problem can be transformed in a linear regression problem with the Riemann method, which projects the points on a 3D paraboloid described by: $= x^2 + y^2$. After this transformation, the points previously placed on a circle or arc will describe a plane in the 3D space which can be easily identified by linear robust regression; this plane is: $ax + by + c = 0$.

The coordinates and the radius of the circle are: $r = \frac{\sqrt{a^2 + b^2 + 4c}}{2}, x_c = \frac{a}{2}, y_c = \frac{b}{2}$.

The method can be easily extended to obtain the centre and the radius of a sphere which approximates a set of 3D points. In this case, the 3D points will be projected on a
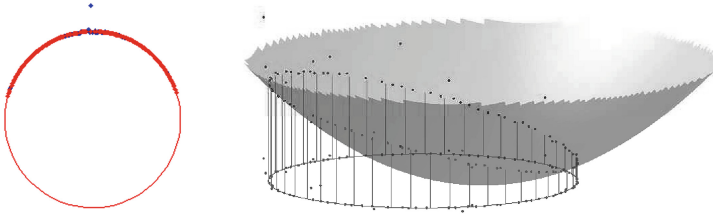
**Fig. 5.** Left: Robust regression for a circular arc, ignoring outliers; *Right*: Projection of circle points on a 3D paraboloid used for transforming the problem into a robust linear regression

4D paraboloid: $t = x^2 + y^2 + y^2$. The linear regression will result in a hyper plane of equation: $ax + by + cz + d = 0$. From the hyper plane one can recover the coordinates and the radius of the sphere {hip}: $r = \frac{\sqrt{a^2 + b^2 + c^2 + 4d}}{2}, x_c = \frac{a}{2}, y_c = \frac{b}{2}, z_c = \frac{c}{2}$.

## 2.2 Direct Comparison of Depth Maps

Machined parts having complex 3D surfaces can be inspected by point to point direct comparison of their depth maps with the model's depth map. The disadvantage of this method is that it may overvalue the dissimilarity between the two surfaces in the case of regions with steep slopes, such as vertical sides.

*Local indicators for depth maps comparison*: a local indicator describing the degree of similarity of two depth maps can be defined as: $\widetilde{Q}_1(x, y) = A(x, y) - B(x, y)$, where $A$ and $B$ are the two compared images, and $A(x,y)$, $B(x,y)$ are respectively the z coordinate of images $A$ and $B$ in point $(x,y)$ expressed in real coordinates (mm).

A more accurate comparison assumes computing the distance from each point of the reference depth map to the closest point in the verified map; this needs transforming the coded coordinates [pixels + grey level] in 3D ones $(X, Y, Z)$ A second local indicator for depths map comparison can be thus defined:

$$\widetilde{Q}_2(x_0, y_0) = \min_{x,y}\{\text{dist}([x_0, y_0, A(x_0, y_0)], [x, y, B(x, y)])\}$$
$$= \min_{x,y} \sqrt{(x - x_0)^2 + (y - y_0)^2 + (A(x_0, y_0) - B(x, y))^2}$$

One can observe that the value of $\widetilde{Q}_2(x_0, y_0)$ is upper bounded by $\widetilde{Q}_1(x_0, y_0)$, from which it results that to compute $\widetilde{Q}_2(x_0, y_0)$ it is sufficient to check a neighbourhood of point $(x_0, y_0)$ of radius equal to $\widetilde{Q}_1(x_0, y_0)$.

The processing time can be minimized by computing the value of $\widetilde{Q}_2$ starting from point $(x_0, y_0)$ and building progressively a neighbourhood around it. The computation stops when the neighbourhood radius overcomes the smallest value found until then.

These comparison methods can be used only if the two depth maps are acquired with the same orientation (*yaw*, *pitch*, *roll*) of the sensor relative to the measured part (the case of parts travelling on pallets). For parts having a plane base, their orientation differing only with a plane rotation, the alignment of the two depth maps to be

compared can be done only through a plane translation and rotation, which needs estimating 3 parameters: $(x, y, \theta)$.

*Global indicators for depth maps comparison*: local indicators, represented by depth maps, have the advantage to offer visual information about the difference between the compared models, but are difficult to use in an automated application taking decisions based on the inspection's result. A global indicator has the advantage to quantify the degree of similarity of two depth maps by a unique scalar value, and can be computed based on the values of a local indicator in a region of interest (ROI). The ROI can be defined as a binary image, of *selection mask* type, and will be noted by $M$.

The following are global indicators based on a local indicator $\widetilde{Q}(x_0, y_0), \widetilde{Q}_1$ or $\widetilde{Q}_2$:

- *Mean error in the ROI* (error sum for each pixel related to the pixel no. in the ROI)

$$G_{avg} = \frac{\sum_{(x,y)\in M} \widetilde{Q}(x,y)}{|M|}$$

- *Median error in the ROI*:

$$G_{med} = \varepsilon : |\{(x,y) : Q(x,y) > \varepsilon\}| = |\{(x,y) : Q(x,y) < \varepsilon\}|$$

- *Relative area of the regions in which the error is greater than an imposed tolerance $\varepsilon$ related to the ROI area*:

$$G_{area} = \frac{\left|\left\{(x,y) : (x,y) \in M \cap \widetilde{Q}(x,y) > \varepsilon\right\}\right|}{|M|}$$

- *Maximum error in the ROI*:

$$G_{max} = \max_{(x,y)\in M} \widetilde{Q}(x,y)$$

This last global indicator (max. error computed from an image) can be very easily affected by pixels having incorrect values (e.g., induced by specular reflexions). A more robust version of this indicator can be obtained if, before computing the max. value, the first $x$ pixels of maximum value are eliminated (the value of $x$ depends on the degree of accuracy of the depth maps which are used for comparison; for noiseless images acquired, this parameter has the value 0).

## 3 3D Laser Scanning Integration with 2D Image Processing

In order to extend product execution (part machining, product assembly) with in line quality control (geometry control, shape- and contour conformity, surface texture), the robotized laser scanning system is linked with a 2D vision platform and integrated in holonic manufacturing control with distributed intelligence [3].

By integrating the 3D laser scanning system with the AdeptSight 2D vision application, developed by Adept Technology Inc. for 2D image processing in robotics [17], the resulting platform is able to perform visual inspection tasks in 3D space from measurements carried out on shape depth maps of manufactured products.

A software interface between the AdeptSight vision software application and the 3D laser scanner surface digitization program has been created for depth map analysis of inspected products. The connectivity between the 3D scanning program and the 2D AdeptSight image processing involves the actions:

- The main program starts the scanning process along a predefined trajectory (geometric path + speed profile of the 6-d.o.f. robot) leading to a depth map saved in JPG format.
- The resulting depth map is loaded in AdeptSight by means of a driver created using Adept's SDK in C# language.
- The results produced by AdeptSight are saved in an implicit `results.txt` file which is read and interpreted by the main program.

The C# AdeptSight interface provides a 2D video camera driver capable to read the depth map; this driver includes the functions:

- *GrabImage*: reads the JPG depth map and converts it in bitmap format;
- *ShowProperties*: displays the configuring dialog to select the JPG used file;
- *GetResolution*: returns the depth map's resolution;
- *BitsPerPixel*: returns the colour depth (8 bits);
- *DeviceName*: returns the name of the driver (Image From JPEG);
- *OutputSource*: returns the image type, here OutputSourceType.Grayscale.

Figure 6 shows the AdeptSight operations sequence used to compute a global indicator based on the median value of the Z coordinate in a current depth map:

- *Image acquisition*: the plug-in Image From JPEG, configured to download a depth map acquired by laser scanning, is used;
- *Histogram computing in a ROI*: this tool allows evaluating the statistical indicators such as average value, median value or standard deviation;
- *Support to decision*: establishing the part acceptance/rejection criteria; in the example, the condition for part acceptance is that the median value of the Z coordinate in the ROI lies between two pre-established limits, and the standard deviation is less than a defined threshold. Such specifications need adding conditional expressions in the dialog box "*Result Inspection Tool*".

To automatize this process, the inspection operation is coordinated by a main program running in Matlab. Having access to the robot system (Adept V+), this program can communicate with the robot controller and sends the results of the inspection to the Resource Holon (Robot Vision) application used as CAQC task by the holonic manufacturing control. The sequence of CAQC operations is:

- AdeptSight and Scan Control are used in ActiveX form initialized by the Matlab application; this allows automatizing these applications and using them as software libraries (not as standalone applications);
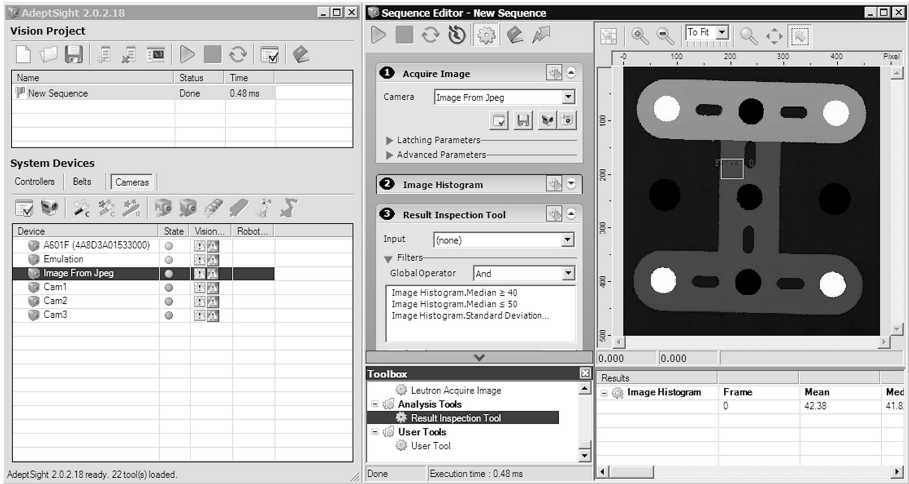
**Fig. 6.** Defining part inspection operation based on the median value of depth map Z coordinate

- The Matlab application will initialize AdeptSight and Surveyor Scan Control applications;
- The Matlab application will ask Surveyor Scan Control to acquire a scan data set;
- Based on the obtained scan data set, a depth map will be constructed and saved in a location from which it can be read by AdeptSight;
- The Matlab application will ask AdeptSight application to run the inspection operation sequence; the computed result will be saved in a text file named *Results. log* containing the results of the AdeptSight inspection's tools;
- The *Results.log* file is read, the data of interest are extracted (the inspection's results) and sent to the robot controller through the ActiveX library.

The scope of this quality control operation is to verify whether part processing/ assembling is properly executed; the result of this operation is used as decision support for further product routing: intermediate verification passed and authorization to start next operation, intermediate verification failed and command to repeat operation, final control passed/failed and product validated/returned for further processing. The CAQC application has a server role, i.e., the inspection operation will be requested by the program running on the robot controller; the advantage of local/global depth map comparison is that, for correction purpose, only non-conformity affected areas of the part must be re-machined – reducing thus the supplementary execution duration.

The described quality control technology is applied to holonic manufacturing by including in the *order holon* (OH) the inspection sequence retrieved from the *product holon* (PH) and the integrated [3D laser scanner + 2D vision] robot represented by the *resource holon* (RH). Holons are the information counterparts respectively of: product execution and inspection recipes (PH), available resources (RH) and scheduled orders with assigned execution means (OH).

The product holon extends the operation set for product execution with one (the final operation) or more (after specified manufacturing operations) inspection operations, with predefined precedencies. For any such inspection task there are defined:

1. The part scanning motion pattern: parameters n, a, b, v of the combined motion of the 6-d.o.f. vertical articulated robot and the turntable.
2. The precedencies (machining/assembly) relative to the 3D inspection operations.
3. The set of geometry features to be measured and checked against pre-taught model ones: (a) scalars (length, angle, hole details); (b) coordinate transformations (relative position and orientation of points, edges, faces); (c) vectors (linear and radial signature) and (d) depth maps (local and global indicators: degree of ROI's similarity, mean, median, and max. error in the ROI).
4. The types of alerts and decisions that must be issued following the inspection operation: product accepted/rejected, additional machining to correct errors, a.o.

## 4   Implementing Solution and Experimental Results

The software system developed in C# for robotized surface scanning and depth map image processing integrates the laser scanning and range finder system with the 6-d.o.f. vertical articulated Adept Viper s650 robot system using the V+ programming environment and AdeptSight 2D vision library, and the 8-bit RISC microcontroller AVR ATMega64 of the PWM turntable's position and speed control. The motion of the turntable is planned with a trapeze speed profile (Fig. 7). The robot controller sees the turntable as a slave device, and the designed communication protocol provides synchronization of the robot manipulator and turntable.
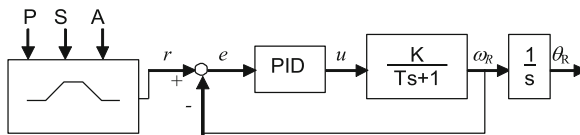


**Fig. 7.** Closed loop position and speed control of the turntable with ATMega64

The speed profile, from which the reference value for the PID loop results, is computed based on the destination angular position P, the maximum speed S and the acceleration A, and the PID algorithm computes the command sent to the motor (u) based on the error signal e (difference between the reference speed $r$ and the current motor speed $\omega_R$), estimated from the encoder signal. When the table's angular position $\theta_R$ reaches the planned position P, the motion is stopped. The application does not impose the table to stop exactly in the required position, because the matrices of 3D data alignment are computed from the position read from the encoder and not from the ideal position (requested through the program).

The scanning provides 3D data in "Point Cloud" format; cylindrical scanning was optimized by simultaneously rotating the table and moving the robot [13] with automated avoidance of singular points that might affect the accuracy and safety of the scanning process.

When the scanning is finished, the 3D data are in the Surveyor Scan Control application in point cloud form. This format cannot be directly used because the number of points is very high (order of millions) and the information cannot be processed by 3D graphics or CAD/CAM programs. To use the 3D digitized model, the reconstruction of a surface-type model of the digitized object is needed; this model is created in the form of partial depth maps which will be joined in a triangular mesh-type model that builds up a closed surface without discontinuities.

The 3D reconstruction operation `reconst3d(resolution)` will create one depth map for each layer in Surveyor. These maps are transformed in triangular meshes saved as .PLY (Polygon File Format) files; the depth map is also saved as image (JPG or PNG on 16 bits). These .PLY files can be post processed in MeshLab, then aligned and joined in several partial views; the result can be exported in 3DS or STL formats that can be imported by CAD or 3D graphics programs. The scanning passes may be not perfectly aligned, because the Iterative Closest Point algorithm solves the problem.

The next step is surface smoothing with the Poisson Reconstruction filter.

Figure 8 shows a direct map depth comparison between a miniature sport car machined with a round head mill, and its model. The difference between the two images leads to the decision of local remanufacturing using either a same type of mill with smaller diameter or a cylindrical mill, in the area of near vertical sides of the object.



(a)                          (b)                          (c)



(d)                                        (e)
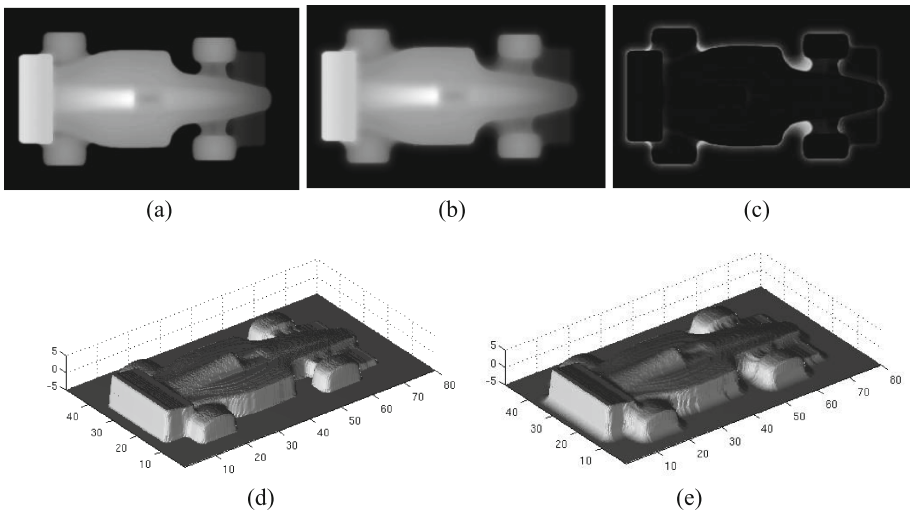
**Fig. 8.** Product inspection using direct comparison of depth maps: (a) Ideal mini car model; (b) Model resulting from machining; (c) Model difference; (c, d) 3D representation of (a, b) models, putting in evidence the machining defect

# 5  Conclusions

The reported research refers to on line geometry control technique which uses a laser sensor hand-held by a 6 d.o.f.-vertical articulated robot and displaced along predefined scanning paths; geometrical measurement primitives (linear and circular measurements, signature analysis, plane and sphere detection, direct depth map comparison of 3D shapes and bodies alignment) of machined/assembled products from 3D scan data post processed using robust linear regression are performed by transforming the problem into linear regression, for which robust fitting can be applied to ensure rejection of outliers. A software system was developed to synchronize the 7-d.o.f. robot + turntable mechanism with the laser scanning along motion pattern depending on the product's shape; the ensemble was integrated with a 2D vision system.

The description of part shape in depth map format allows automated generation of machining paths only in the "out of conformity" areas of the executed product relative to its reference model, minimizing thus correction time. The steps of direct depth map comparison for part correction are: (1) Global depth map indicators detect conformity errors between the machined part and its model; (2) Local indicators establish the defect area; (3) Remanufacturing decision; (4) CNC paths computed for the defect area.

# References

1. Novas, J.M., Bahtiar, R., Van Belle, J., Valckenaers, P.: An approach for the integration of a scheduling system and a multiagent manufacturing execution system. Towards a collaborative framework. In: Proceedings of the 14th IFAC Symposium INCOM2012, IFAC PapersOnLine, Bucharest, 23–25 May, pp. 728–733. Elsevier (2012)
2. Băbiceanu, R.F., Chen, F.F., Sturges, R.H.: Framework for the control of automated material-handling systems using the holonic manufacturing approach. Int. J. Prod. Res. **42** (17), 3551–3564 (2004)
3. Borangiu, T., Răileanu, S., Berger, T., Trentesaux, D.: Switching mode control strategy in manufacturing execution systems. Int. J. Prod. Res. **53**, 1950–1963 (2015). doi:10.1080/00207543.2014.935825
4. Morariu, C., Morariu, O., Borangiu, T.: Customer order management in service oriented holonic manufacturing. Comput. Ind. (2013). ISSN 0166–34615, doi:10.1016/j.compind.2013.07.007
5. Keen, M., Bishop, S., Hopkins, A., Milinski, S., Nott, C., Robinson, R., Adams, J., Verschueren, P., Acharya, A.: Patterns: Implementing an SOA using an Enterprise Service Bus, IBM Redbooks. ISBN 0738490008 (2004)
6. Morariu, C., Morariu, O., Borangiu, T.: Manufacturing service bus integration model for implementing highly flexible and scalable manufacturing systems. In: Proceedings of the 14th IFAC INCOM2012 Symposium, PapersOnLine, Part 1, vol. 14, pp. 1850–1855 (2012)
7. Boyd, A., Noller, D., Peters, P., Salkeld, D., Thomasma, T., Gifford, C., Pike, S., Smith, A.: SOA in Manufacturing Guidebook, MESA International, IBM Corporation and Capgemini co-branded white paper, 05.21.08
8. Borangiu, T., Gilbert, P., Ivănescu, N.A., Rosu, A.: An implementing framework for holonic manufacturing control with multiple robot-vision stations. Eng. Appl. Artif. Intell. **22**(4–5), 505–521 (2009). Elsevier

9. Lefebvre, P., Lauwers, B.: 3D morphing for generating intermediate roughing levels in multi-axis machining. Comput.-Aided Des. Appl. **2**(1–4), 115–123 (2005)
10. Chuang, C.-M., Chen, C.-Y., Yau, H.-T.: A reverse engineering approach to generating interference-free toolpaths in three-axis machining from scanned data of physical models. Int. J. Adv. Manuf. Technol. **19**, 23–31 (2002). doi:10.1007/PL00003965
11. Batchelor, B.: Intelligent Image Processing in Prolog. Springer, Berlin (1991)
12. Ma, Y., Soatto, S., Kosecka, J., Sastry, S.: An Invitation to 3-D Vision: From Images to Geometric Models. Springer, New York (2003)
13. Borangiu, T., Dogar, A., Dumitrache, A.: A heuristic approach for constrained real time motion planning of a redundant 7-dof mechanism for 3D laser scanning. In: INCOM 2009 – 13th IFAC Symposium on Information Control Problems in Manufacturing, Moscow, Part. 1, IFAC PapersOnLine, vol. 1. Elsevier (2009)
14. Borangiu, T., Dogar, A., Dumitrache, A.: Flexible 3D trajectory teaching and following for various robotic applications. In: IFAC Syroco 2009, part 1, Gifu, Japan, vol. 9 (2009)
15. Bresenham, J.: Algorithm for computer control of a digital plotter. IBM Syst. J. **4**(1), 25–30 (1965)
16. Frühwirth, R., Strandlie, A., et al.: A review of fast circle and helix fitting. Nucl. Instrum. Methods Phys. Res., Sect. A **502**, 705–707 (2003)
17. Adept Technology Inc., AdeptSight User's Guide, v3.2.x, updated: 23 August 2012. http://www1.adept.com/main/ke/data/pdf_web/AdeptSight_UG.pdf. Accessed 21 Feb 2016

# Design and Shape Optimization
# of Novel Load Cell

Jaroslav Hricko[(✉)]

Institute of Informatics, Slovak Academy of Sciences, Banská Bystrica, Slovakia
`hricko@savbb.sk`

**Abstract.** The novel approach of contactless measurement of small deformations requires new design of load cell. The design and shape optimization of deformable part of load cell is discussed in this paper. Functional requirements and requirements connected with manufacturing of sensors have been taken into account in optimization process.

**Keywords:** Load cell · Shape optimization · Compact compliant mechanism · Robotic · Sensor

## 1 Introduction

Integration of sensors into industry applications can add enhancement with proven effectiveness. For instance, force sensors can be applied to robotic systems as feedback elements to control velocity, or they can allow adding other functionalities to robotic systems (haptic touch of gripper, etc.). The wide range of sensors used in robots is discussed in [1, 2]. In case of flexible production lines where cooperation of several manipulators and CNC machines is required, a powerful sensor system should be proposed [3].

The miniaturization of robotic devices leads to the utilization of compact compliant robotic structures [4, 5]. This requires new approaches to sensing mechanical quantities (force, torque, displacement, etc.). Considering that, such devices are usually composed from one piece of material and work on principles of elastic deformation. Using sensors in small robotic devices requires their integration with minimal negative influence to functional characteristics of these devices. An example of this approach is presented in [6], where between the electromagnetic actuator and the micro-gripper a compliant structure of force sensor is inserted; this approach of building small robotic devices is not expedient for getting e.g. high precise robotic devices. Each other flexure is placed for getting rid of unwanted parasite deformations that cause lower positioning accuracy. In case of bigger compliant devices (order of mm) it is possible to use classical approaches based on applying strain gauges; however, one disadvantage of this approach is the high number of "wires" enabling data transfer (sending the information about the measured value).

The design and shape optimization of deformable parts of novel force/displacement sensors is discussed in this paper. The sensor will utilize contactless displacement measurement, where the whole micro-robotic device works under the influence of

electromagnetic field. The basic idea and some simulations have been described in [7, 8]. Specific restrictions and requirements must be taken into account in optimized design of deformable parts. The proposed solution will be used to realize initial measurements and design of electronic components of the whole sensor.

## 2  Formulation of Input Requirements

The design of novel solutions for contactless measurement of small deformations requires the formulation of additional requirements imposed to deformable parts of the sensor. The proposed physical prototype should be suitable for initial verification of physical principles in laboratory tests. Due to this, some requirements have not direct connection with performance characteristics of the force/displacement sensor.

The main input requirements and boundary values are formulated as follows:

- The material of the deformable part
- The manufacturing process of the structure
- The maximal dimensions
- The requirements related to the output displacement of the structure
- The functional requirements (linearity, frequency range, etc.)

Since the final design of the force sensor will be minimized, the deformable part should be produced from one piece of material, using the elastic deformation (compliant structure). The materials used for such devices require the highest ratio between Yield strength and Young's modulus, in other words they should have good flexural characteristics [4]. The most known materials are metals like aluminium, steel, etc., plastics like polyethylene, nylon, etc. and ceramics like piezoelectric/ferroelectric ceramics, e-glass, aluminium oxide, etc. In our case, the whole structure should be made from dielectric material, because it will be located close to the influence of electromagnetic fields and other types of materials that can alter the output information about displacement. For the physical prototype, the plastic material has been chosen. In next design stage (miniaturization, functional tests in applications) this material will be replaced with another one – ceramics, which will provide in smaller dimensions better flexural characteristics and longer lifetime.

In principle, for the manufacturing of such complex form and dimensions there are two technologies that can be used: precise machining or 3D printing. Standard 3D printers support only specific types of materials like PLA or ABS, but these materials exhibit small flexibility. A suitable material that can be processed by 3D printers seems to be the polyamide. In case of precise machining (production of the first prototype), Teflon (PTFE) was chosen as material for the physical realization. Both manufacturing methods have one important restriction: the minimum thickness of the wall has to be of 1 mm. The minimum thickness of wall corresponds to the dimension of flexure hinges/links that produce the output movement.

As was mentioned, in the actual stage of the design process, the force sensor was developed for initial laboratory tests. Consequently, the dimensions of the deformable part are relative bigger than the final version. The maximal dimensions are 50 mm × 10 mm × 10 mm (width × height × depth). The advantage of compliant

structures development is that this same physical principle works similarly without any restriction in dimensions from millimetres to micro/nanometres.

One important constraint is represented by the formulation of the output displacement. The novel contactless measurement method is based on getting information from an LC (inductor - capacitor) circuit located under influence of an electromagnetic field. It is thus possible to consider that the deformable part of sensor should be composed from two (capacitor) parallel plates, their surface being big enough. The deformations of the moving plates are unwanted and should be minimized.

Important requirements imposed to the design of the compliant structure are the functional ones. One such requirement is the linearity of the output displacement, which can be obtained by minimizing the number of flexure components enabling thus the measurement of small forces. It is clear that the smallest measured force will be the force which produces the minimal deformation of the compliant structure. In general, the sensor should have a prescribed accuracy in a supposed frequency range of force/displacement changes. A high limit of the natural frequency of mechanical oscillations is required.

## 3  Design of Load Cell Deformable Part

Load cells are well-known 1-axis force sensors [9]. The deformable part of the proposed sensor is based on this simple structure. The initial approach to design was based on the modification of this well-known structure. In case that the bottom of sensor is fixed and the load is acting on the top surface, the material used being plastic (PTFE, PA2200), then the deformation of the moving plate is significant: more than 0.15 mm (7.5 % of the entire movement). This type of sensor load leads to the minimum utilization of the flexure joints located at the bottom of structure. Last but not least important, the output characteristic of sensor is non-linear (the dependence between input force and output displacement).

Consequently, another six modifications have been analysed (see Fig. 1). In Fig. 2 (a) the output characteristic of the modified load cell is shown (the point located in the middle of the moving plate has been taken as output point of the sensor). Figure 2(b) shows the deformation of the moving plate.
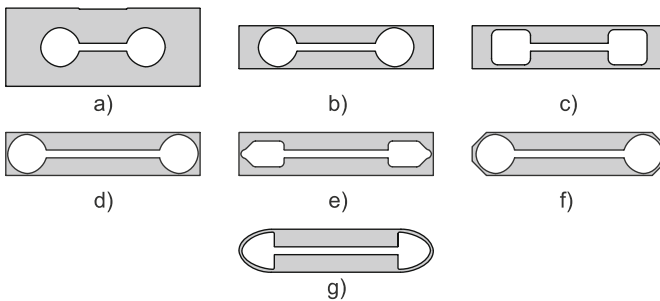


**Fig. 1.** (a) Classical load cell, (b) – (g) proposed modifications of classical load cell (mod01 – mod06, respectively)

# 4   Shape Optimization

From the results presented in Fig. 2, the last modification for shape optimization of the proposed compliant structure has been derived. The reason is that it was possible to use minimal input force with acceptable characteristics. The optimization procedure has been focused on three important goals:

- Maximize the deformation with minimal force.
- Distribute the stress on the entire flexure area.
- Maximize the capacitor plate's surface with no change of dimensions, keeping the parallelism of plates, etc.
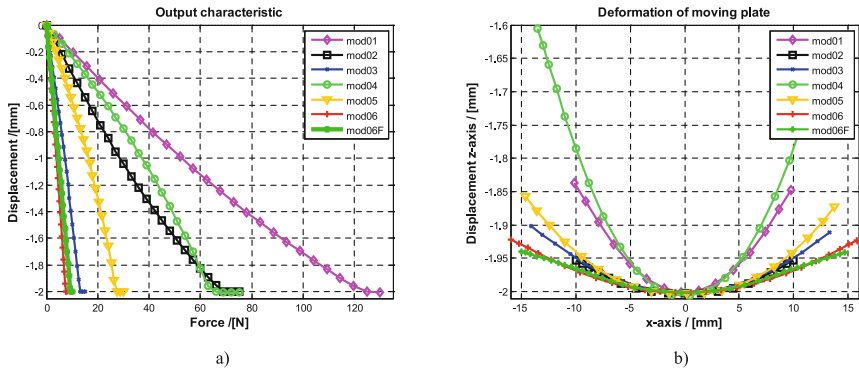


**Fig. 2.** (a) Output characteristic of analysed structures, (b) Deformation of moving plate

The second requirement is clear from Fig. 3(a), where the stress distribution in the flexure part of the proposed force/displacement sensor is shown. The stress which appears is higher as the available stress (Yield strength) and is located only on small areas of the flexure element. Other requirements are closely connected with input design requirements and were described before.

Figure 3(c) shows the optimized structure of the proposed deformable part of the force/displacement sensor designed according to the novel contactless approach of deformation measurement. The output characteristic of the designed sensor and the deformation of the output plate are shown in the Fig. 3(b).

The proposed deformable part of this sensor is 50 mm width, 11 mm height and has a depth of 5 mm. The first physical prototype has been manufactured by precise laser cutting, the material used for the whole structure being PTFE with Young's modulus 0.7 GPa and Yield Strength 30 MPa.

a)                                                    b)



c)
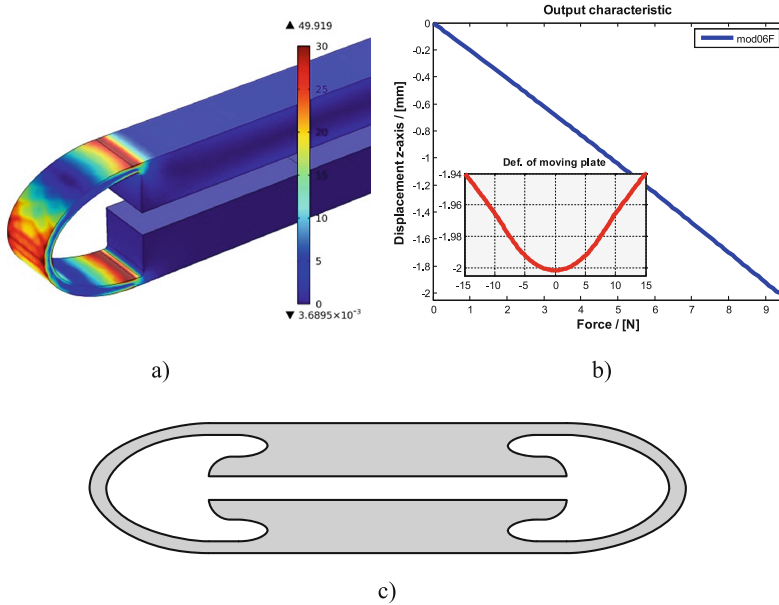
**Fig. 3.** (a) Stress distribution (mod6), (b) Output characteristics (c) Optimized design

## 5  Stiffness Model

Stiffness (compliance) plays an important role in the design and utilization of sensors which are working on the principle of elastic deformation. The knowledge of stiffness provides a basis for the characterization of static, modal and dynamic behaviour of the deformable part of sensors. The most known method for modelling compliant structures is their description as mass-spring-damping system. As a consequence of the minimization process the influence of mass can be neglected and damping depends on properties of the material used for the structure, whereas the stiffness should be calculated.

To establish a complete stiffness modelling approach it is necessary to evaluate the deformations (in terms of bending, torsion, and tensile/compression) of each component of the mechanism that can be performed. Such a model can be derived effectively by the matrix method under the assumption of Hooke's law of materials [10, 11]. The basic dependence between external load and deflection is expressed as

$$\mathbf{u} = \mathbf{CF} \rightarrow \mathbf{F} = \mathbf{Ku} \tag{1}$$

where $u$ is the vector of deflection $u = [u_x,\ u_y,\ u_z,\ \theta_x,\ \theta_y,\ \theta_z]^T$, $C$ is the compliance matrix which is the inverse matrix of stiffness $K$, $K = C^{-1}$ and $F$ is the vector of external load $F = [F_x,\ F_y,\ F_z,\ M_x,\ M_y,\ M_z]^T$.

The calculation of compliance/stiffness of elastic components like joints, hinges and links must be done to create the complete stiffness model of the whole device. In
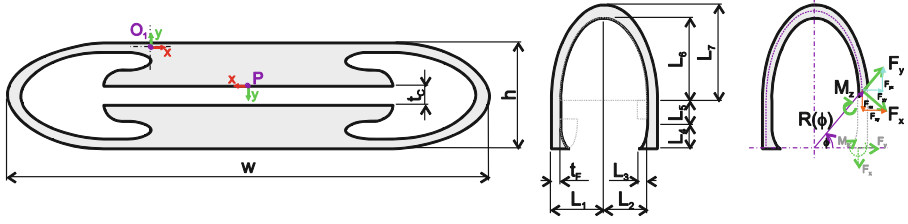
**Fig. 4.** Dimensions and orientation of local coordinate systems in observed points

our case the compliance/stiffness of curved beam with variable thickness must be derived. Figure 4 depicts the dimensions and orientation of the local coordinate systems which are used for calculations.

For simplification of calculations, all lengths depend on the height $h$ and the width $w$ of the proposed load cell. The variables $t_C$ and $t_F$ are the thicknesses between capacitor plates and the minimal thickness of flexure respectively. The thickness of the structure will be denoted by $t_S$. The dimensions of the flexure are: $L_1 = h/2$; $L_2 = h/2 - t_F$; $L_3 = h/12$; $L_4 = 0.0484w$; $L_5 = 0.05w$; $L_6 = w/5 - 1.4t_F$; $L_7 = w/5$. The variable thickness of the flexure will be substituted by a constant value equal to $t_F(\phi) = 1.2t_F$. The simplified piecewise function (two straight lines and half of ellipse) described by the radius of curved beam $R(\phi)$ is

$$
R(\phi) = \begin{cases}
\dfrac{L_1 - 0.5t_F}{\cos(\phi)} & -\arctan\dfrac{L_4 + L_5}{L_1} \leq \phi < 0 \\[3mm]
\dfrac{(L_1 - 0.5t_F)(L_7 - 0.7t_F)}{\sqrt{(L_1 - 0.5t_F)^2 \sin^2(\phi) + (L_7 - 0.7t_F)^2 \cos^2(\phi)}} & 0 \leq \phi < \pi \\[3mm]
\dfrac{-L_1 + 0.5t_F}{\cos(\phi)} & \pi \leq \phi \leq \pi + \arctan\dfrac{L_4 + L_5}{L_1}
\end{cases}
\tag{2}
$$

The internal in-plane forces and the moment at any point on $R(\phi)$ may be expressed as follows:

$$
\begin{aligned}
\sum F_x = 0: \quad & F_x(\phi) = F_x \sin(\phi) - F_y \sin(\phi) \\
\sum F_y = 0: \quad & F_y(\phi) = -F_x \cos(\phi) + F_y \cos(\phi) \\
\sum M_z = 0: \quad & M_z(\phi) = M_z + F_x R(\phi)\cos(\phi) + F_y R(\phi)\cos(\phi) + F_x R(\phi)\sin(\phi) - F_y R(\phi)\sin(\phi)
\end{aligned}
\tag{3}
$$

The strain energy in the beam can be expressed as:

$$
U = \frac{1}{2E} \int_{-\arctan\frac{L_4 + L_5}{L_1}}^{\pi + \arctan\frac{L_4 + L_5}{L_1}} \left( \frac{F_x(\phi)^2}{A_k} + \frac{F_y(\phi)^2}{A_k} + \frac{M_z(\phi)^2}{I_{zk}} \right) d\phi
\tag{4}
$$

where $A_k$ and $I_{zk}$ are the area of cross-section an the second moment of the area, respectively.

Using Castigliano's theorem, the deformation components are obtained from (4):

$$u_x = \frac{\partial U}{\partial F_x(\phi)}; \quad u_y = \frac{\partial U}{\partial F_y(\phi)}; \quad \theta_z = \frac{\partial U}{\partial M_z(\phi)} \tag{5}$$

Now, it is possible to calculate the stiffness/compliance of the whole load cell with respect to the coordinate system located in the point P:

$$K_P = 2\left(T_{1P}T_{01}C_0T_{01}^{-1}T_{1P}^{-1}\right)^{-1} \tag{6}$$

where $C_0$ is the compliance matrix expressed from (1) and (5), and $T_{ij}$ are transformation matrices between $i$-th and $j$-th local coordinate systems.

## 6   Conclusions

The proposed load cell uses a novel approach of contactless measurement of small distances. Such an approach requires compliance with a number of constraints, but it enables contactless measurement of displacements of small robotic devices working under the influence of electromagnetic fields.

Throughout the design process six modification of classical load cell have been analysed. The design and shape optimization of the novel deformable part of the force/displacement 1-axis sensor has been focused on two main requirements. The first requirement was related by the parallel movement of capacitor plates (minimal deformation). The second requirement was related to the sensor's manufacturing; in our case precise machining or 3D printing technology were assumed. In both manufacturing methods the minimal wall thickness should be of 1 mm, which does not allow applying classical flexure hinges (e.g., half circular flexure hinge).

The proposed compliant structure using the novel contactless (distance) measurement approach, allows measuring forces up to 9 N with high sensitivity because deformation of 100 μm is represented in a range of about 7.5 MHz (see Fig. 5(b)).



a)                                    b)
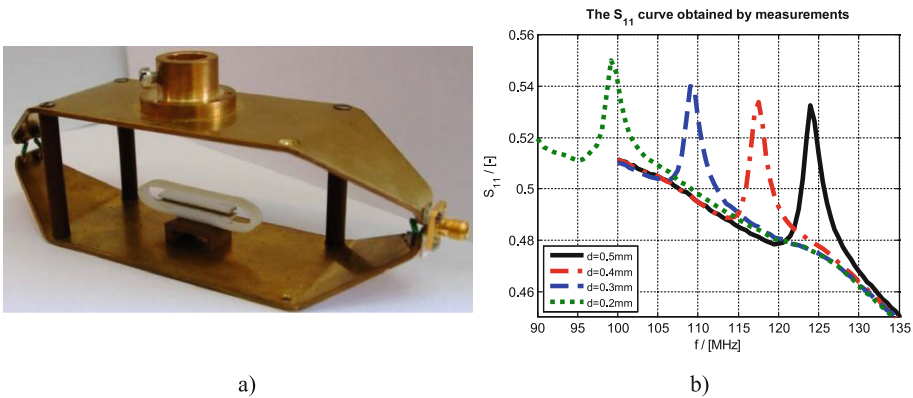
**Fig. 5.**   (a) Real model of proposed sensor, (b) the $S_{11}$ curve obtained by measurements

# References

 1. Henderson, T.C. (ed.): Traditional and Non-Traditional Robotic Sensors. Springer, Heidelberg (1990). ISBN 978-3-642-75984-0
 2. Vagaš, M., Baláž, V., Semjon, J., Sukop, M.: The measurement and prevent errors of 3D position and posture. In: International Scientific Herald, vol. 3, no. 2, pp. 230–233 (2012). ISSN 2218-5348
 3. Vagaš, M.: Sensors for robotized workplaces. In: Ukraine - EU. Modern Technology, Business and Law, Chernihiv National University of Technology, Chernihiv, pp. 42–43 (2015)
 4. Howell, L.L.: Compliant Mechanisms. Wiley-IEEE (2001). ISBN 047138478X
 5. Smith, T.S.: Flexures: elements of elastic mechanisms, p. 448. Gordon and Breach Science Publishers (2000). ISBN 90-5699-261-9
 6. Kim, D.-H., Lee, M.G., Kim, B., Sun, Y.: A superelastic alloy microgripper with embedded electromagnetic actuators and piezoelectric force sensors: a numerical and experimental study. In: Smart Materials and Structures, vol. 14 (2005). ISSN 1265–1272
 7. Maršalka, L., Harťanský, R.: Proposal of novel sensor applicable to contactless displacement measurement. In Measurement 2013: Proceedings of the 9th International Conference on Measurement, Smolenice, Slovakia, 27–30 May 2013, pp. 287–290. Slovak Academy of Sciences, Bratislava (2013). ISBN 978-80-969672-5-4
 8. Maršalka, L., Harťanský, R.: Electromagnetic method for distance measurement on MEMS structures. In: MM Science Journal Special Edition: Proceedings of the RAAD 2011, 20th International Workshop on Robotics in Alpe-Adria-Danube Region (RAAD), 5–7 October 2011, Brno, Czech Republic, p. 48 (2011). ISBN 1805-0476
 9. Load cell Handbook - A Comprehensive Guide to Load Cell Theory, Construction and Use. Rice Lake Weighing Systems (2007)
10. Sciavicco, L., Siciliano, B.: Modeling and Control of Robot Manipulators, McGraw-Hill International Editions. Electrical Engineering Series (1996). ISBN 0-07-114726-8
11. Xu, Q., Li, Y.: Stiffness modeling for an orthogonal 3-PUU compliant parallel micromanipulator. In: Proceedings of the 2006 IEEE International Conference on Mechatronics and Automation, 25–28 June 2006, Luoyang, China (2006)

# 3-Axis Contact Force Fingertip Sensor
# Based on Hall Effect Sensor

Mirko Raković$^{(\boxtimes)}$, Miroslav Beronja, Aleksandar Batinica, Milutin Nikolić,
and Branislav Borovac

Faculty of Technical Sciences, University of Novi Sad,
Trg Dositeja Obradovića, 21000 Novi Sad, Serbia
{rakovicm,batinica,milutinn,borovac}@uns.ac.rs,
mickochelsea1234@gmail.com

**Abstract.** The paper describes the prototype of a novel embedded
3-axis force sensor which is intended to be used for detecting and measur-
ing the contact forces at the fingertips of a robotic hand when grasping
and manipulating objects. The sensor is composed of three main parts: a
printed circuit board with Hall effect sensors, a neodymium magnet and
a elastic silicon layer. The dimensions of the sensor that should be placed
at the fingertip are minimized to fit the size of a human inspired robotic
hand. The signal processing of the data obtained from the Hall effect sen-
sors is completely done with an ARM Cortex-M4 micro-controller with
implemented neural network. The target data which is used for training
the neural network is obtained from reference precise 6 axis force/torque
sensor. The experimental setup as well as the procedure for acquiring
the training data set, learning and implementing the neural network on
embedded platform are presented.

**Keywords:** Robotic hand · Hall effect sensor · 3-axis force sensing

## 1 Introduction

The humanoid robotics today is continuously expanding toward the goal of effi-
cient operation in complex human centric environments such as offices, homes,
schools and hospitals. The human working environment is dynamic and unstruc-
tured, thus, to coexist with humans the robot should act in a way that is efficient
similar to humans. To achieve this basic requirements, these humanoid robots
have to be equipped with many versatile sensors to confer them sufficient auton-
omy sufficient to perform tasks in such environment. One of the essential tasks
exposed to humanoid robots is dexterous manipulation of grasped objects. To
make robots capable to do the same, two basic facts have to be kept in mind. The
first is that the objects in human's surrounding are mainly designed for humans.
The second is that, when manipulating these objects humans are heavily relying
on the feedback from tactile sensors. The same should happen for the robots.
The tactile sensory system is of paramount importance, providing information
to the robot about physical interaction with the surrounding objects.

The requirements imposed to tactile sensor can be found in [13,16] where tactile sensors are defined as a devices that can measure a given property of an object or can measure continuously variable contact forces. Out of many properties that can be measured, 3-axis contact forces are of the greatest importance because this is essential in grasping and can be used as force feedback in control loop. The papers [8,19] give an excellent review of the current state-of-the-art in different designs of tactile sensors and the analytical comparison between them. Furthermore, paper [12] reviews the techniques for handling tactile data in robotic manipulation covering approaches and applications of tactile sensors in the control of multi-fingered robotic hands.

In [9] a set of sensor design parameters was introduced, making a list which is still widely used by researchers today. The prototypes of tactile sensors for contact force measurement are utilizing different technologies such as resistive, piezoelectric, capacitive, magnetic and optoelectronic. In [4] a cylindrical sensor that can measure three-dimensional applied force is proposed. The main components of the sensor are three coils and a dielectric medium. In [15] the overall design of the Sandia Hand which is equipped with a variety of proprioceptive and exteroceptive sensors is presented. In Sandia Hand, the finger pads can sense the normal contact forces by measuring the deflection of the soft inner layer. In [10] a fingertip for the hands of the iCub robot, where each fingertip consists of 12 sensors is presented. The sensing elements of the fingertip are based on change of capacitance. They are made from a flexible PCB, and a multi-layer fabric that includes the dielectric material and the conductive layer. Authors in [18] designed a flexible and multilayer capacitive microfluidic normal force sensor with a $5 \times 5$ sensing elements grid. The sensor uses liquid metal-filled microfluidic channels as capacitive plates and conductive interconnects. In [17] authors have proposed a dome shaped sensor. For measuring the displacement of the dome centre three methods are considered: magnetic, optical and pressure sensors. The authors of [11] designed the sensor that consists of a silicone body in which a small magnet is immersed and a Hall-effect sensor placed below the silicone body can measure the magnetic field generated by the magnet. This sensor can be used to estimate 1-axis normal force applied to the silicone body. The authors in [6] proposed a tactile sensor based on the use of LED-phototransistor couples and a deformable elastic layer.

In [7] the design of BioTac sensor, which consists of a rigid core surrounded by an elastic skin filled with a liquid is described. The skin of the BioTac possesses texture and thickness similar to the properties of human skin. This sensor is capable of detecting cutaneous sensory information that human fingers can detect, i.e. forces, microvibrations, and temperature [7]. The BioTac sensor can be mounted on different robotic hands, as illustrated in [14]. Besides the BioTac fingertip sensor, other tactile sensors for robotic applications can be found such as 3D Force Sensor from OptoForce [1], the FlexiForce from Tekscan [3], and QTC from Peratech [2]. However, the price of these sensors is still relatively high and the performances are not always suitable for the desired implementation. Since the tactile sensor is usually an integrated part of the robotic finger it is not easy to use the existing sensors, and the only possibility is to develop a particular solution.

In this paper the design, development and realization of a tactile sensor that can measure 3 components of the applied force is described. The base of the sensor is a PCB with 4 Hall effect sensors interfaced with ARM Cortex M4 controller that has a 12-bit AD converter. Above the Hall effect sensors the neodymium magnet is placed with the silicon layer in between. The applied force pushes the magnet whose displacement has been recorded by Hall sensors. The complete sensor was placed on top of precise 6 axis force torque sensor used to measure the applied force. To find the relationship between the output of Hall effect sensor and the output of force/torque sensor, i.e. to estimate the 3-axis force based on the output from 4 Hall effect sensors, a neural network (NN) is utilized. The trained NN is implemented in ARM Cortex M4 controller which gives a embedded solution for measuring 3-axis contact force at the fingertip.

## 2   Structure of the Sensor

The basic measuring element of the proposed 3-axis force sensor is a Hall effect sensor. The Hall effect sensor varies its output voltage in response to the intensity and direction of a magnetic field. The first examples of using Hall-effect sensor for tactile sensing can be found in [5]. Authors in [11] have shown that this concept for measuring the contact force gives high sensitivity, low hysteresis and good repeatability. To measure 3-axis contact force, we used 4 Hall effect sensors and placed them on a PCB as shown in the Fig. 1. The distance between sensors in both x and y direction is approximately 3.2 mm.

As a source of magnetic field, one neodymium disc magnet of 3 mm in radius and 1 mm thickness is positioned above the centre of the PCB. The positioning of the magnet is done manually, but care is taken that the distance from all four Hall sensors is equal. As a consequence, the output voltage of the Hall effect sensor varies with respect to the displacement of the magnet. Since the contact force has to be measured, the distance between the magnet and the Hall sensor should correspond to the intensity of applied force. Thus, a space between magnet and Hall effect sensors is filled with elastic material, i.e. silicone (see Fig. 2). This will allow the displacement of the magnet with respect to sensors once the external force is applied.

An external force $F_{ext}$ applied to the deformable body displaces the magnet from its initial position causing the change of the output voltage of the Hall
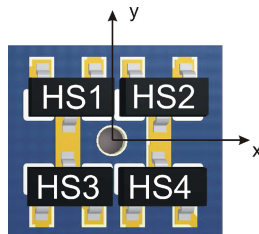


**Fig. 1.** Position of the Hall effect sensors HS1, HS2, HS3 and HS4 on the PCB board
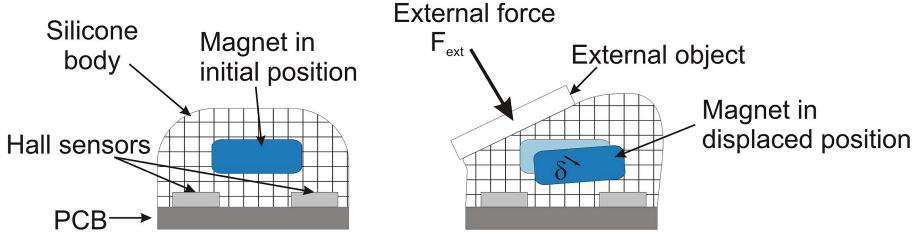
**Fig. 2.** Working principle of 3-axis sensor

effect sensors. In particular, these deformations produce the change in direction and intensity of the magnetic field with respect to a coordinate frame fixed to the PCB. The deformations can be such as to decrease or increase the magnetic field sensed by the Hall effect sensor.

## 3    Sensor Characterization as 3-DOF Force Sensor

The magnet motion is not restricted in any direction. It is free floating in silicone body and can rotate or translate. The relationship between the applied force $F_{ext}$ and the 6 degrees of freedom displacement $\delta$ as well as the output voltage of the Hall effect sensor against the displacement of the magnet are not linear. This means that the estimation of the external force based on the output voltage of the Hall effect sensors is hard to be determined analytically. For this purpose either a lookup table or some nonlinear regression tool are of great help. For the proof of concept, in this research a classical two layered feed forward neural network is used. In order to collect reference data paired with the output voltage of the Hall effect sensors, the data from precise 6 axis force torque sensor is acquired. For collecting reference data two approaches can be used. The first is to use 6 axis F/T sensor to apply external force. In this case the force intensity is known, but to define its components with respect to the tactile sensor coordinate system is not easy. The second possibility is to place the tactile sensor on top of the 6 axis F/T sensor. If a force is applied it will deform silicon body and will be simultaneously measured by the 6 axis F/T sensor below. In this research, the second approach is adopted. The setup for collecting the paired output from the Hall effect sensors and 6 axis F/T sensor is shown in Fig. 3.

A layer of silicone rubber with magnet on top has been placed on the PCB with mounted Halls sensors. During the data gathering, a plastic stick is used to press the magnet and apply the force manually. The synchronized unfiltered samples from the 6 axis F/T sensor and Hall effect sensors are taken every 10 ms.

As it can be seen from the Fig. 4, the force measured at the reference sensor is in the range of approximately 3 N in x and y direction and 12 N in z direction. The direction and intensity of the force applied to the magnet were varied manually. In total of 6000 samples of data were collected, out of which 70% were used for training and 30% for testing and validation.
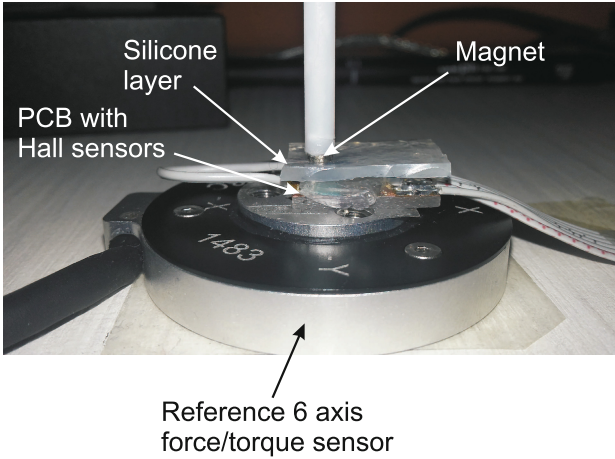
**Fig. 3.** Setup for collecting the paired output from the Hall effect sensors and 6 axis F/T sensor
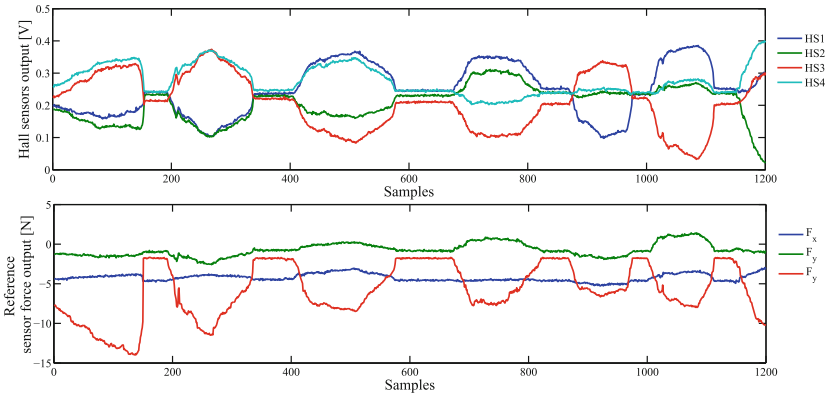


**Fig. 4.** Samples of paired output from 4 Hall effect sensors HS1, HS2, HS3 and HS4, and three components of the force from the reference sensor

To find the unknown relationship between the outputs from Hall effect sensors and reference force, a feed-forward 2-layer neural network was used. The transfer function of hidden and output layer was set to tangent sigmoid and linear function respectively. For training the neural network, Levenberg-Marquardt backpropagation algorithm was used. Figure 5 shows the comparison between the measured forces from reference sensor and the output from the learned neural network when the data used during training, testing and validation is provided as input.

The obtained NN model was implemented in C code for ARM Cortex-M4 controller, which is the same controller used to read the values from Hall effect sensors. The values from Hall effect sensors are set as input to implemented neural network, thus providing the estimated 3-axis force as output.
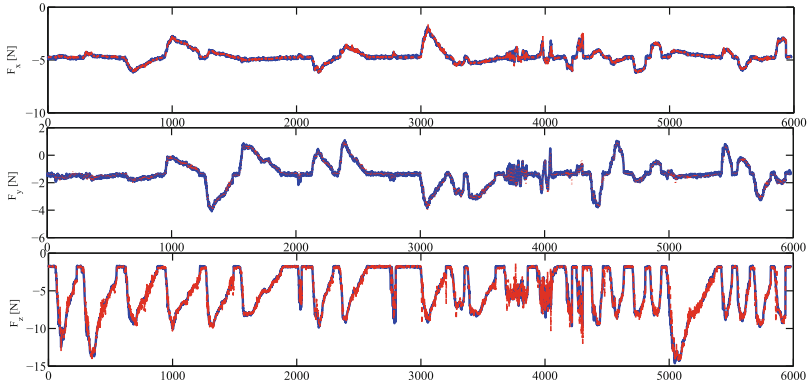
**Fig. 5.** Compared forces measured by reference sensor (blue lines) and estimated forces obtained by neural network (red lines) when the data used for training, testing and validation is applied as input
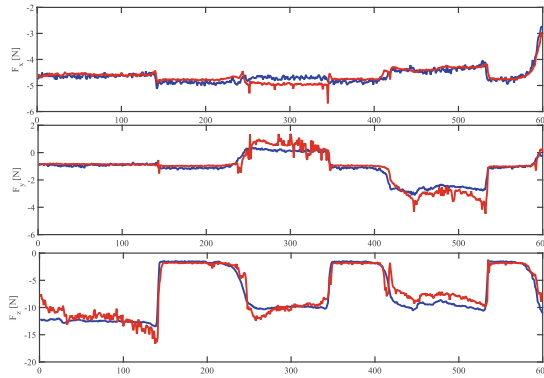


**Fig. 6.** Compared forces measured by reference sensor (blue lines) and estimated forces obtained by an embedded neural network (red lines) when previously unknown data is applied as input

The estimated output forces and the forces measured from the reference sensor are collected. Figure 6 compares between the estimated forces obtained from embedded neural network model, and the applied forces. It can be seen that there are certain unwanted oscillations of the forces estimated from embedded neural network. The reasons for this can be the over-fitting of the neural network, an insufficiently dense training data set, noisy training data etc.

## 4   Conclusion

The paper described the concept, realization and experimental characterization of a 3-axis force sensor based on Hall-sensors suited for use as a integral part

of a robotic finger. The mechanical structure of the sensor has been designed so as to allow the device to work as a 3-axis force sensor. As reference sensor a precise 6 axis force/torque sensor is used. To establish the nonlinear relationship between the output from the 4 Hall effect sensors and the output from the reference sensor the neural network is modeled and trained. The training of the NN model is carried out in MATLAB, and after the validation process the final neural network with the identical structure is implemented in ARM Cortex M4 controller. This allowed an embedded and relatively cheap solution for measuring the 3-axis contact force.

Further development will be multi-fold. We will work on the integration of the sensor into the fingertips of a robotic hand in order to use in real-time feedback control systems. More focus will be put on the process of data gathering and filtering the input data. Also, other methodologies for force estimation will be considered.

# References

1. Optoforce 3D force sensor. http://optoforce.com/3dsensor/
2. Peratech QTC touch processing unit. https://www.peratech.com/touch-development-kit.html
3. Tekscan flexiforce. https://www.tekscan.com/flexiforce-load-force-sensors-and-systems
4. Chi, Z., Shida, K.: A new multifunctional tactile sensor for three-dimensional force measurement. Sens. Actuators A: Phys. **111**, 172–179 (2004)
5. Clark, J.J.: A magnetic field based compliance matching sensor for high resolution, high compliance tactile sensing. In: Proceedings of the 1988 IEEE International Conference on Robotics and Automation, 1988, pp. 772–777. IEEE (1988)
6. De Maria, G., Natale, C., Pirozzi, S.: Force/tactile sensor for robotic applications. Sens. Actuators A: Phys. **175**, 60–72 (2012)
7. Fishel, J., Lin, G., Loeb, G.: Biotac® product manual. SynTouch LLC, February 2013
8. Girão, P.S., Ramos, P.M.P., Postolache, O., Pereira, J.M.D.: Tactile sensors for robotic applications. Measurement **46**, 1257–1271 (2013)
9. Harmon, L.D.: Tactile sensing for robots. In: Brady, M., Gerhardt, L.A., Davidson, H.F. (eds.) Robotics and Artificial Intelligence, pp. 109–157. Springer, Heidelberg (1984)
10. Jamali, N., Maggiali, M., Giovannini, F., Metta, G., Natale, L.: A new design of a fingertip for the iCub hand. In: 2015 IEEE/RSJ International Conference on Intelligent Robots and Systems (IROS), pp. 2705–2710. IEEE (2015)
11. Jamone, L., Natale, L., Metta, G., Sandini, G.: Highly sensitive soft tactile sensors for an anthropomorphic robotic hand. IEEE Sens. J. **15**, 4226–4233 (2015)
12. Kappassov, Z., Corrales, J.A., Perdereau, V.: Tactile sensing in dexterous robot hands—review. Robot. Auton. Syst. **74**, 195–220 (2015)

13. Lee, M.H., Nicholls, H.R.: Review article tactile sensing for mechatronics—a state of the art survey. Mechatronics **9**, 1–31 (1999)
14. Navarro, B., Kumar, P., Fonte, A., Fraisse, P., Poisson, G., Cherubini, A.: Active calibration of tactile sensors mounted on a robotic hand. In: IROS: Intelligent Robots and Systems. IEEE/RSJ (2015)
15. Quigley, M., Salisbury, C., Ng, A.Y., Salisbury, J.K.: Mechatronic design of an integrated robotic hand. Int. J. Robot. Res. **33**, 706–720 (2014)
16. Righetti, L., Kalakrishnan, M., Pastor, P., Binney, J., Kelly, J., Voorhies, R.C., Sukhatme, G.S., Schaal, S.: An autonomous manipulation system based on force control and optimization. Auton. Robots **36**, 11–30 (2014)
17. Torres-Jara, E., Vasilescu, I., Coral, R.: A soft touch: compliant tactile sensors for sensitive manipulation
18. Wong, R.D.P., Posner, J.D., Santos, V.J.: Flexible microfluidic normal force sensor skin for tactile feedback. Sens. Actuators A: Phys. **179**, 62–69 (2012)
19. Yousef, H., Boukallel, M., Althoefer, K.: Tactile sensing for dexterous in-hand manipulation in robotics—a review. Sens. Actuators A: Phys. **167**, 171–187 (2011)

# One Approach to Detection and Extraction of On-Road Obstacles Based on Image Processing

Mourad Bendjaballah[1,2] and Stevica Graovac[3(✉)]

[1] Ministry of National Defence, Algiers, Algeria
mourad.bendjaballa@hotmail.com
[2] University of Defence, Belgrade, Serbia
[3] School of Electrical Engineering, University of Belgrade, Belgrade, Serbia
graovac@etf.rs

**Abstract.** The process of automatic control and guidance of robots and autonomous vehicles is frequently based on the processing of image sequences obtained by a camera mounted on robot/vehicle. The first step in all algorithms of autonomous guidance of this type of devices consists in the analysis of scene contents and detection and extraction of obstacles that exist in the camera's field of view. In the particular case of this research work, the extraction of "on-road" obstacles, which are generally moving, is done in order to track them from frame to frame and to adjust the device's motion according to obstacles' positions and relative velocity (incoming, outgoing, stationary ones). An initial segmentation oriented toward extraction of a road region is based on the Support Vector Machine (SVM) method of classification and learning. The following step consists in the extraction of "non-road" objects over the road area in order to mark the obstacles to be tracked later. The verification of this algorithm is done using typical scenes including the images of structured roads, urban environment and country roads.

**Keywords:** Machine vision · Image processing · Image segmentation · Pattern recognition · Support vector machines

## 1 Introduction

The self-anti-collision systems are rapidly developing in order to prevent traffic accidents, as well as to enable the autonomous guidance of road vehicles. The recognition of road obstacles can at least improve the safety of driving by issuing the proper alerts. A completely autonomous motion control of a vehicle requires very precise and reliable detection, extraction, tracking, and classification of the road obstacles.

The existing methods in obstacle detection might be classified into three categories [1]: (1) The usage of a monocular static camera; this method detects obstacles based on the optical flows that are incompatible with the main direction of the vehicle's orientation/movement [2–5]. This method requires rather huge calculations and is sensitive to vehicle changes in movement. Since it is basically used for static cameras, it only detects the moving obstacles. (2) The second method uses a monocular moving camera.

This method detects obstacles based on the analysis of characteristics like the shape [6–8] or symmetry [9, 10]. It can only be used to detect a specific type of objects, such as pedestrians or vehicles. (3) The third method is based on the stereo vision [11–13]. Images are captured using two or more cameras at the same time from different angles, and then obstacles are detected by matching. This method requires a lot of time to do the necessary calculations and it is sensitive to vehicle movement.

The fact that the camera is moving itself as it is mounted on the vehicle, causes that all the elements of the scene are moving from frame to frame. Also, the task of detecting and extracting the obstacles that are really of interest is rather a complex one. In order to provide the basis of future real-time implementation, our choice was to use single camera, but to make the detection and extraction task as complex as it is needed for reliable operation. Actually, the algorithm should provide that: (1) objects that are outside the road are eliminated; (2) irregularities on the road surface that are not affecting the driving are not considered; (3) static obstacles on the road are properly recognized in order to be avoided; (4) vehicles on the road are detected in order to adjust the vehicle's own motion according to their relative distances and velocities.

The algorithm starts with detecting the road-region using the SVM (Support Vector Machine) method (Sect. 2). The analysis was made by comparing the cases where the colour components are used only with those where they are combined with texture descriptors. The comparison between the cases where SVM is used in "Off-line" and "On-line learning" version is made in Sect. 3. The extraction of the objects that belong to the road region but are located over the road region is done as a final step, before the obstacles are prepared in standard rectangular form in order to be tracked later (Sect. 4). Final conclusions which include the comments regarding the actual limits in application and ideas about the future work are given in Sect. 5.

## 2 Road Region Extraction

The first step of the algorithm consists in the segmentation of an image into the road region and the other region that includes the remaining part of image ("non-road"). In order to classify one pixel as a member of a class "road", there are a number possible segmentation methods based on colour, texture descriptors based on statistic parameters, structure, or frequency spectrum, etc. While some acceptable results have been obtained when only the colour components have been used, even three decades ago [14], or by using the best candidates among texture statistics and structure descriptors [15], our reasoning was oriented toward a more complex approach where the colour and the texture are simultaneously considered [16]. The flowchart shown on Fig. 1 illustrates this algorithm.

As an initial operation, the populations of "road" and "non-road" pixels are indicated by an operator (driver) action, by marking the appropriate rectangular regions on the image and creating thus an initial content of a dynamic Image Training Database (ITD).

In order to reduce the calculations, the number of pixels inside the rectangle is limited to 1000. If the total of encompassed pixels is greater, 1000 of them will be chosen in a random manner. This ITD is going to be continually updated in order to
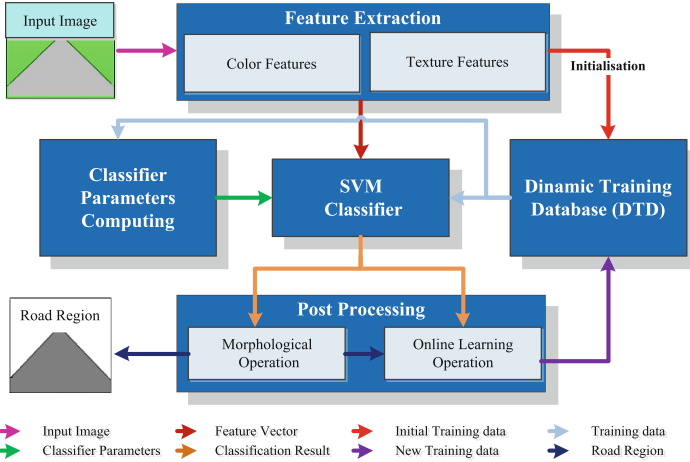
**Fig. 1.** Flowchart of the road segmentation algorithm [16]

follow the changes in the road scene. The selected set of classifying parameters is calculated for every subsequent image. The process of segmentation is based on the SVM method. The final classification step consists in morphological processing of the binarized image. After the final segmentation is done, the upgrade consisting in on-line updating of ITD is the final step before the acquisition of a new image.
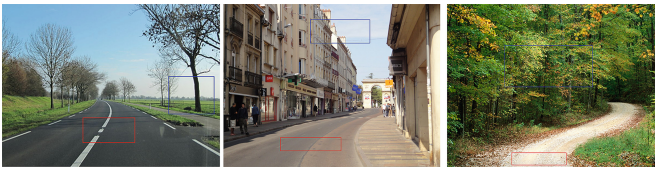


**Fig. 2.** ITD initialization. Red rectangles are used for "positive" training (road class) and blue ones for "negative" training (non-road class). The examples include the cases of structured road, urban environment, and country road

The features vector is 8-dimensional. The first 5 elements are Haralick's statistical features, Eqs. (2)–(4), while the remaining 3 are pixel USV colour components.

$$F_{i,j} = \left[ f_{t_1(i,j)}, f_{t_2(i,j)}, f_{t_3(i,j)}, f_{t_4(i,j)}, f_{t_5(i,j)}, f_{c_1(i,j)}, f_{c_2(i,j)}, f_{c_3(i,j)} \right] \quad i = 1, \ldots, H \quad j = 1, \ldots, W \tag{1}$$

$$Energy = \sum_u \sum_v \{p(u,v)\}^2, \; Entropy = \sum_u \sum_v \{p(u,v)\} \log\{p(u,v)\} \tag{2}$$

$$Contrast = \sum_{n=0}^{N_g-1} n^2 \left\{ \sum_{u=1}^{N_g} \sum_{v=1}^{N_g} p(u,v) \right\}, \ |u-v| = n,$$

$$Corellation = \frac{\sum_u \sum_v (uv)p(u,v) - \mu_x \mu_y}{\sigma_x \sigma_y} \tag{3}$$

$$Inverse\ Moment\ of\ Differences = \sum_u \sum_v \frac{1}{1+(u-v)^2} p(u,v) \tag{4}$$

where: $p(u,v)$ is an element of Gray Level Co-occurrence Matrix - (GLCM), and $\mu_x, \mu_y$ i $\sigma_x, \sigma_y$ are mean values and Co-variances calculated using this matrix.

It is natural to suppose that the features space of "road" and "non-road" classes are in a nonlinear relation and that obtaining some linear hyper-plane which distinguishes these two classes in the original feature space is not expected. Following the results given in [17], a Gaussian radial basis function (RBF) kernel is used as SVM kernel function. There are two classifying parameters, maximum value and standard deviation. It should be found which one is more appropriate for this discrimination. In order to do so, the parallel validation relative to these two parameters is done on the image belonging to ITD. Due to the continuous dynamic changes of the road contents as a result of camera motion, ITD should be updated from time to time. It was chosen that after each ten frames, the training databases for both classes are refreshed by replacing 100 stochastically chosen old members by 100 new ones, among the population of pixels already classified in the particular class. Larger numbers of updated elements lead to excessive impact of incorrectly classified pixels, while for too low numbers of replaced sampled pixels one can expect low adaptation abilities. After this classification step it is usual that there would be a number of small unconnected groups of pixels around the road, classified as the "road", as well as the number of "holes" over the road region. In order to eliminate such small aggregations of pixels, the algorithm includes morphological operations "opening" and "filling the holes". The final results of the road region extraction are shown on the Fig. 3. The examples from Fig. 2 have been analysed.

The initialization of ITD should select possible road markers (ex. lane separators) as a part of the road region. Similarly, when some areas in the image are initially designated as the road environment, the representative pixels of both near and far environment should be included. These were the criteria to be used for the image, while the shape and size of rectangles are of no particular importance because the selection of 1000 points inside the rectangle is used. It is obvious that some morphological erosion procedures are needed in all cases, while the need for holes filling on the road was not really present. The third row on Fig. 3 illustrates final classification results superimposed onto the original image. In order to show the superiority of the classification method used, the 4th row represents the final classification results if the colour feature is used only (initialization and morphological processing have been the same).

## 3    Segmentation Based on On-Line Learning Option of SVM

On-line training upgrade of the SVM method [16] is optional, but very useful in the context of this application. Besides the already mentioned updating the ITD includes the evaluation of the performance of current classification. This process is based on the basic assumption that the road region consists from connected pixels. Consequently, "road" pixels detected outside the main region of a road as well as the "non-road" pixels located over the road image are the sources of how the classifier should be modified. In order to evaluate the effectiveness of the proposed road detection method, we compared the classification result with a priory known information about the number of pixels in this class, using the performance parameters:

$$\text{Recall } = \frac{N_{TP}}{N_{GT}} \times 100[\%] \text{ , Precision } = \frac{N_{TP}}{N_{TP} + N_{FP}} \times 100[\%] \qquad (5)$$

where $N_{TP}$ is the number of correctly classified pixels, $N_{GT}$ is an overall number in the class, and $N_{FP}$ is a number of incorrectly classified pixels.
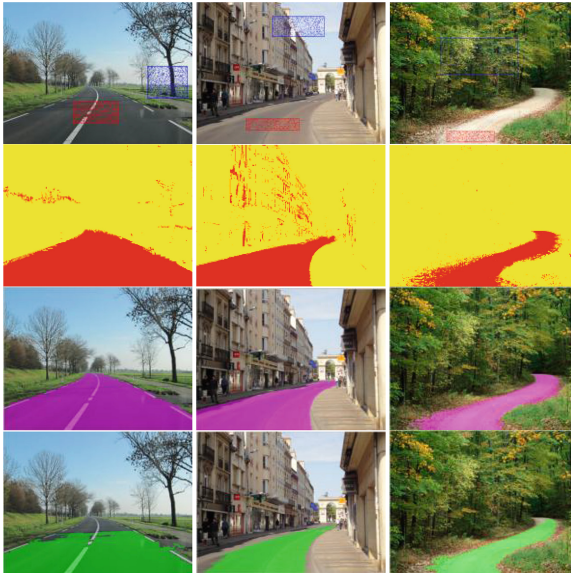


**Fig. 3.** The road detection algorithm and comparison of results between SVM and the colour method. (a) The classification results (red is road class - yellow is non-road class). (b) The results of morphological filtration after SVM classification (the regions labelled in pink - road). (c) The results obtained only with the method based on colour.

The results for three typical images shown in Fig. 4 give a proof of the performance of self-supervised online learning process in our algorithm. In each experiment, two small sampling windows are selected on the image to initialize the ITD; this can be

seen as offline learning. The suggested algorithm restudies from the poor classification result, then retrains the classifier and reclassifies the road image. The first example shows the results of different learning processes in the shadowed road situation. From the offline learning results (left side), some road marks and tree shadows are misclassified as non-road. After online learning process, the number of misclassified points is getting smaller. The second example shows the results in the unstructured road situation. Almost all the points in the sky used to be misclassified as road as a result of offline learning. With the process of online learning, the results become more accurate. From the third example we can see slightly better segmentation of the street area in the situation where the choice of sampling windows is very sensitive because of the similarities in colour and texture between the street and surrounding walls.
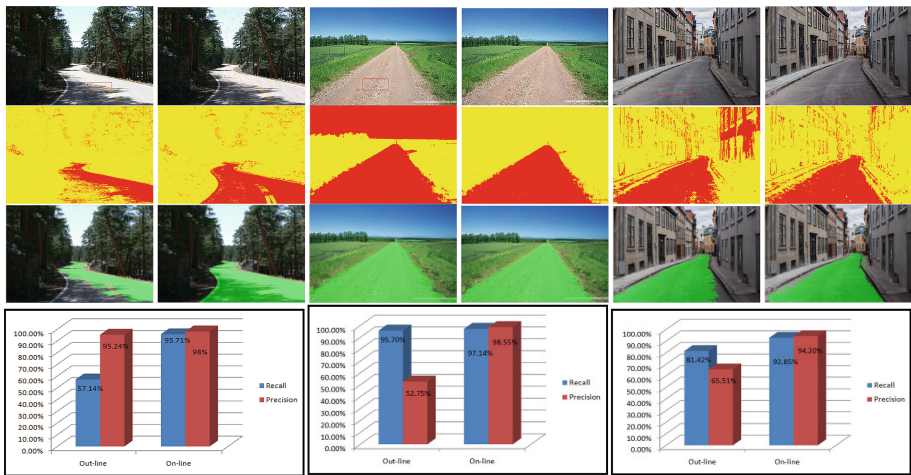


**Fig. 4.** Comparison of results between segmentations based on off-line learning and on-line learning

## 4 Extraction of Obstacles

To extract the obstacles on the road, one has to remove two kinds of image objects: the marks on the road and the environment outside the road. It is supposed that the markers on the road are going to be associated to the road region in the previous process of road detection.

The environment around the road has been already classified as "non-road" region at the first step of classification. This step of the algorithm is oriented toward the separation of the whole "non-road" region into two subclasses: the "obstacles on the road" and "everything else existing outside the road".

### 4.1    Classification Inside the "Non-road" Region

Figure 5 shows the result of detecting the road region (a), and the template image of the road region (b) where the black pixels are representing the road. After analysing a particular row in the image, one obtains a profile as shown in Fig. 6. Based on this line profile, white line segments that have two adjacent black segments on both the left and right sides are the line segments that belong to the road obstacles. By checking each row in the template image of the road this classification can be done. Figure 5(c) shows the results of this classification. The overall class of obstacles on the road is represented by grey pixels in Fig. 5(d).



(a)                    (b)                    (c)                    (d)
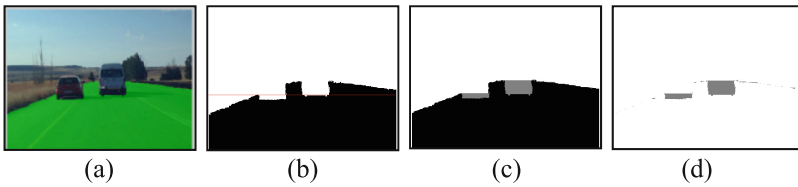
**Fig. 5.**  (a) The result of road region detection. (b) Road region template image. (c) The result of region classification. (d) Obstacle region.
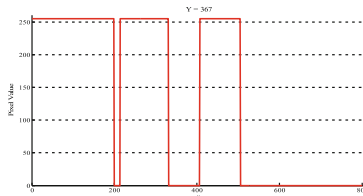


**Fig. 6.**  Line profile of pixel intensity values ($367^{th}$ row in the road region image)

### 4.2    Obstacles' Detection and Marking

After the classification phase, three regions (classes of pixels) are obtained: road region, obstacles on the road, and environment region, while the road-obstacle class is important only. This class consists from multiple objects of different sizes (Fig. 5(d)), but the small objects (less than 50 pixels) are eliminated as false ones. The extracted obstacles should be tracked continuously in the sequence of incoming frames. In order to prepare this tracking phase, some areas of interest should be specified - the detected obstacles should be marked by specifying some tracking windows encompassing each of them.

Figure 7 shows the different steps of marking the obstacles on the road. Figure 7a shows the region of the real obstacles after filtering unwanted objects. Red rectangle around this region is shown in Fig. 7b which will be replaced in the next step by the green square of width equal to the base of red rectangle as in Fig. 7c. The final representation of a search area superimposed to the original image is shown in Fig. 7d.
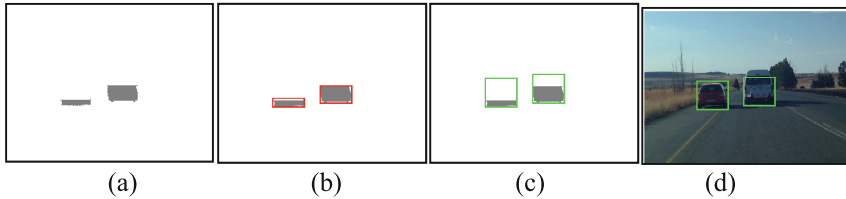
**Fig. 7.** Phases of road-obstacle marking

Some tall vehicles like trucks are not going to be fully encompassed by this type of tracking window, while some low-profile cars would not fill the tracking window completely, but the choice of square-shaped tracking window seems a reasonable compromise.

## 5   Conclusion

The algorithm of automatic detection and extraction of on-road obstacles is discussed here as a prerequisite for obstacles tracking and their automatic avoidance. The first step consists in image segmentation in order to distinguish all pixels belonging to the road area. This task is a rather complex one, having in mind that a variety of roads types and surrounding scene environments can be expected. That was the reason why we choose to use the SVM method based on 8-dimension vector of features including 3 colour components as well as 5 texture descriptors, showing the advantages in comparison to the case where only colour information is used.

On the other hand, the road area is dynamically changing and some on-line adaptation to these changes must be made. We used the opportunity of SVM method to provide "On-line Learning" ability and have shown visible advantages of it. After the whole image is segmented in "road region" and "non-road region", the next step consists in detecting the pixel aggregations that belong to the class "non-road", but surrounded by elements of the "road" class. Such groups of pixels can be detected by analysing the line profiles; after that they were marked by standard rectangular shape, and dimensionally adjusted according to the obstacle's actual size. In this way, it becomes possible to track the obstacles and calculate their positions and velocities relative to the moving camera. The results of this obstacle detection and extraction algorithm have been successfully applied for their tracking in the sequence of frames, but there is still a lot of verifications to be done, having in mind the variety of visibility conditions and traffic situations.

# References

1. Demonceaux, C., Kachi-Akkouch, D.: Robust obstacle detection with monocular vision based on the motion analysis. In: Proceedings of the IEEE Intelligent Vehicles Symposium, pp. 527–532 (2004)
2. Kruger, W., Enkelmann, W., Rossle, S.: Real-time estimation and tracking of optical flow vectors for obstacle detection. In: Proceedings of the IEEE Intelligent Vehicles Symposium, pp. 304–309 (1995)
3. Braillon, C., Pradalier, C., Crowley, J., Laugier, C.: Real-time moving obstacle detection using optical flow models. In: Proceedings of the IEEE Intelligent Vehicle Symposium, pp. 466–471 (2006)
4. Braillon, C., Pradalier, C., Crowley, J., Laugier, C.: Real-time motion tracking using optical flow on multiple GPUs. Bull. Pol. Acad. Tech. Sci. **62**(1), 139–150 (2014). doi:10.2478/bpasts-2014-0016
5. Leffaix, G., Marchand, E., Bouthemy, P.: Motion-based obstacle detection and tracking for car driving assistance. In: Proceedings of Pattern Recognition, pp. 74–77 (2002)
6. Broggi, A., Bertozzi, M., Fascioli, A., Sechi, M.: Shape-based pedestrian detection. In: Proceedings of the IEEE Intelligent Vehicles Symposium, pp. 215–220 (2000)
7. Lutzler, M., Dickmanns, E.D.: Road recognition with merveye. In: Proceedings of the IEEE Intelligent Vehicles Symposium, pp. 341–346 (1998)
8. Kuehnle, A.: Symmetry-based vehicle location for AHS. In: Proceedings of SPIE Transportation Sensors and Controls: Collision Avoidance, Traffic Management, and ITS, vol. 2902, pp. 9–27 (1998)
9. Teoh, S., Bräunl, T.: Symmetry-based monocular vehicle detection system. Proc. Mach. Vis. Appl. **23**(5), 831–842 (2012)
10. Bertozzi, M., Broggi, A., Gold, A.: A parallel real-time stereo vision system for generic obstacle and lane detection. In: Proceedings of IEEE Image Processing, pp. 62–81 (1998)
11. Yu, Q., Araújo, H., Wang, H.: A stereovision method for obstacle detection and tracking in non-flat urban environments. Proc. Auton. Robots **19**(2), 141–157 (2005)
12. Bernini, N., Bertozzi, M., Castangia, L., Patander, M., Sabbatelli, M.: Real-time obstacle detection using stereo vision for autonomous ground vehicles: A survey. In: IEEE 17th International Conference on ITSC, pp. 873–878. IEEE (2014)
13. Labayrade, R., Aubert, D.: Robust and fast stereo vision based obstacles detection for driving safety assistance. In: Proceedings of Machine Vision Applications, pp. 624–627 (2004)
14. Kuan, D., Phipps, G., Hsueh, A.C.: Autonomous robotic vehicle road following. IEEE Trans. Pattern Anal. Mach. Intell. **10**(5), 648–658 (1988)
15. Graovac, S., Goma, A.: Detection of road image borders based on texture classification. Int. J. Adv. Robotic Syst. **9**, 1–12 (2012)
16. Zhou, S., Gong, J., Xiong, G., Chen, H., Iagnemma, K.: Road detection using support vector machine based on online learning and evaluation. In: Proceedings of IEEE Intelligent Vehicles Symposium, pp. 21–24 (2010)
17. Chang, C., Lin, C.: LIBSVM: a Library for Support Vector Machines (2008). http://www.csie.ntu.edu.tw/~cjlin/papers/libsvm.pdf. Accessed 20 Nov 2008

# Development and Implementation of Orthogonal Planes Images Method for Calibration of Tool Centre Point

Zaviša Gordić[1(✉)] and Claudio Ongaro[2]

[1] School of Electrical Engineering, University of Belgrade, Belgrade, Serbia
zavisa@etf.rs
[2] Advanced Automation Technologies s.r.l, Conegliano, TV, Italy
claudio@adatsrl.it

**Abstract.** This paper presents a system for automated calibration of the robot's tool centre point (TCP). The main aim is to present innovative solutions and procedures developed and implemented in order to overcome theoretical and practical challenges encountered during realization of the calibration unit. The idea to analyse images from two orthogonal planes in order to identify TCP serves as a foundation for all features and procedures and offers a number of advantages to the system. Using a camera system, the TCP's calibration can be performed in very short time, which enables frequent checks to ensure production quality without losing valuable time resources. The calibration unit and all procedures are designed and developed as a self-sufficient fully automated system that does not require any additional components or operator intervention in normal operation. This makes the system suitable for integration in highly automated production facilities such as factories of the future.

**Keywords:** Robot TCP calibration · Camera system · Industrial application

## 1 Introduction

Accurate and reliable identification of tool centre point (TCP) parameters is one of the crucial preconditions for proper functioning of the robot. Without it, the robot does not possess any information about its end-effector, and therefore cannot perform any reasonable operation with it.

Many solutions and approaches have been developed to help identifying tool parameters, the problem being well known both in theory and in practice [1–3]. Contactless automated procedures are of key importance for advanced robotic application, since they have the potential to be fully integrated into highly autonomous production facilities that require little or no human intervention.

Solutions like ABB's BullsEye and Leoni's advintec use a technique that requires the robot to intersect infrared beams in order to calibrate the TCP [2]. Although the principle can achieve good precision performance, it requires several steps and can be time consuming. Camera based systems such as the one presented in [3] can provide good and inexpensive 6-dimension calibration results when working in optimal

conditions. However, the solution is susceptible to various disturbances such as lighting, dust and humidity and requires previous knowledge about the tool.

The motivation for this paper was to present a system for the calibration of robot's TCP, developed for real life application. The working principle is based on the analysis of images from two orthogonal planes, a concept developed and proven in earlier phases of the project [4]. This paper presents procedures and algorithms designed to implement the concept into a calibration unit which can be fully integrated into working environments.

The Sects. 2 and 3 offer a short overview of designing of the calibration unit and the calibration principle, described in more details in [4]. They also present explanations and conclusions from previous phases of testing. The procedure used to align coordinate systems of the robot and calibration unit is presented in the Sect. 4. It explains the theoretical principle of the alignment algorithm as well as the steps needed to implement it in a manner suitable for operation with different brands of robots and various types of tools. The Sect. 5 describes a procedure that is used to acquire information about the coordinates of points inside the image acquisition area in the robot's frame. It is explained how the algorithm calibrates the TCP without any prior knowledge about the tool, and how it uses this information to determine coordinates of points inside the image acquisition area. The procedure used in daily operations is described in the Sect. 6. It presents a routine designed to enable fast check of proper TCP calibration, as well as to recalibrate the tool if some modifications were made to it, or to define a completely new tool. The discussion and conclusion sections explain how procedures were tested, and present main observations and conclusions. They also provide some recommendations for optimal operating performance and give an overview of the system's main advantages.

## 2    Calibration Unit Design

The calibration unit was designed to be suitable for installation in industrial environment, so all components are packed into a single case made of sturdy materials. The image acquisition area is located on the top of the unit, in form of an open-top cuboid.

Two vertical neighbouring sides of the image acquisition area serve as background panels, while the other two are transparent (Fig. 1). Background panels are illuminated with LED strips which can be triggered by cameras. Each transparent side has a mirror placed behind it at 45° angle which is used to redirect the image vertically downwards to cameras which are mounted on the vertical sides of the unit. The mirrors are placed in sealed chambers to prevent dust or humidity interference. Power supply, fanless PC, cables, and other components are housed inside the unit, and they can easily be accessed by removing the corner panel of the box.
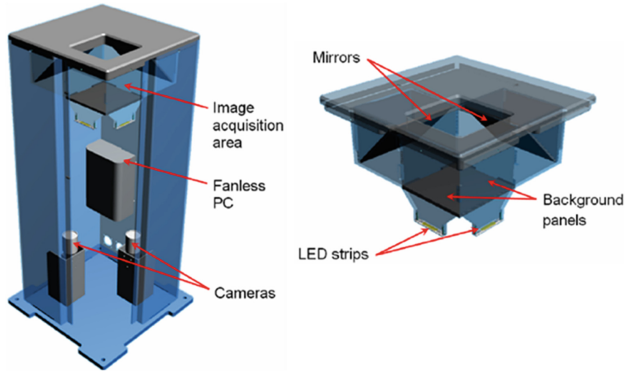
**Fig. 1.** Layout of the calibration unit with access cover removed and image acquisition area

## 3 Calibration Principle

In order to start calibration procedure, the tool must be placed inside the image acquisition area, after which its identification is assigned to National Instruments' software. Due to appropriate lighting conditions, the software can identify the TCP, longitudinal axis of the tool, and determine angles and positions of interest for further processing.

The calibration principle has two steps. The first step consists in orientating the longitudinal axis of the tool in such way that it is parallel to the reference longitudinal axis. This step places the tool in favourable orientation, where the TCP can be properly identified with high level of accuracy. The second step aligns these two axes, which means guiding the TCP to a reference point whose coordinates are known in the robot's base frame. The position and orientation of the robot's flange are also known in the robot's base frame, which means the coordinates of the tool can be calculated using simple transformations of coordinate systems.

One of the issues related to this method concerns perspective distortion. In order to orientate the tool in a desired way, it was necessary to determine the rotation angles in both image planes. The problem is that angles seen on images are not equal to those that are needed to perform the rotation. Namely, if the current orientation is the result of two sequential rotations of the tool around two mutually perpendicular axes, the second rotation angle can correctly be seen on the image, while the first angle's projection on the image plane is distorted. This is because the plane in which the first rotation occurs is no longer parallel to the image plane. Therefore, the angle of the first rotation can be seen correctly only after the movement which compensates the second rotation is performed. In order to eliminate the need for two cycles of measurement and orientation movement, a formula was derived (1) which calculates the real value of the second angle based on the measurements of angles in two image planes, thus speeding up the process.

$$\alpha = \arctan(\tan(\alpha') \cos(\beta)) \tag{1}$$

where $\alpha$ and $\beta$ are the real angles, and $\alpha'$ and $\beta' = \beta$ are angles seen on images between the longitudinal axis of the tool and the vertical axis on images. After rotating the tool with $(\alpha, \beta')$, it will be orientated vertically, which is chosen as the default reference orientation. Any other desired orientation can be achieved using a similar procedure.

The derived Eq. (1) assumes that images provided to it are orthographic which would require using telecentric lenses, but their size, cost and implementation requirements greatly surpass desirable characteristics of a system intended for practical application in industry.

The solution is to use regular lenses with greater distance between the camera and the observed object to reduce distortion. In order to keep small dimensions, while increasing distance, two mirrors were placed to reflect the image vertically downwards from the image acquisition area located on top towards the cameras installed at the bottom of the calibration unit. This solution presents a compromise between required small area footprint and adequate quality of provided images.

Although functional as a concept, in order to perform the steps of the described calibration principle, further elaboration was needed. The concept assumes that the robot can be guided by the calibration unit in any position and orientation, and that coordinates of a point inside the image acquisition area are known. The robot possesses no information about the location of the image acquisition area, orientation of its axes, nor about coordinates of points inside it. Therefore, it is necessary to design algorithms that will create preconditions for implementing the calibration principle.

## 4   Local Coordinate System

In order to guide the tool according to the information obtained from analysed images, it is necessary to establish a relation between the coordinate system defined by cameras, and the coordinate system of the robot's base. In essence, a transformation matrix between the two coordinate systems must be obtained using only the calibration unit and any tool that can fit its TCP within the image acquisition area.

The cameras' coordinate frame consists of the horizontal axes of two orthogonal images which form its $x$ and $y$ axes, while the vertical axis is represented by the $z$ axis. If the coordinates of a point in the reference frame of robot's base are $C_b = [x_b\ y_b\ z_b]^T$, and coordinates of the same point in reference frame of cameras $C_c = [x_c\ y_c\ z_c]^T$, the relation (2) connects them.

$$C_c = T_{cb}(C_b - V_{cb}), \tag{2}$$

where $T_{cb}$ is a matrix that performs orientation alignment of axes, and $V_{cb}$ is a column-vector that represents the translational offset between origins of the two frames.

When the origins of two reference frames are matched, by analysing the transformation matrix, it is possible to identify that columns in matrix $T_{cb}$ represent projections of respective unit vectors in robot's the base frame onto axes in the cameras' frame, as shown in (3). First column represents projections of $[1\quad 0\quad 0]_b^T$ onto $x$, $y$ and $z$ axis of cameras' frame, second column of $[0\quad 1\quad 0]_b^T$, and third of $[0\quad 0\quad 1]_b^T$,

where subscript $b$ denotes that these are coordinates of unit vectors in the reference frame of robot's base.

$$T_{cb} = \left\lfloor \begin{bmatrix} 1 & 0 & 0 \end{bmatrix}_b^T proj. \quad \begin{bmatrix} 0 & 1 & 0 \end{bmatrix}_b^T proj. \quad \begin{bmatrix} 0 & 0 & 1 \end{bmatrix}_b^T proj. \right\rfloor \qquad (3)$$

With this perspective in mind, it is possible to perform unit movements of the robot along each axis of its coordinate system, and observe their projections in coordinate system of cameras. The idea is to assume that the first point where the robot's TCP is located in the cameras' frame represents the origin of coordinate system that is aligned with cameras. Then, upon performing unit movement of the TCP along the $x$ axis of the robot's frame, it is possible to measure the offset between the new position and the position of the origin in each axis. The offsets represent projections of the first unit vector onto the axes of coordinate systems of cameras, and give the first column of the transformation matrix. A similar procedure is applied for unit movement along $y$ axis and second column, and along $z$ axis for third column of the transformation matrix $T_{cb}$.

From the implementation point of view, it is important to determine which distance should be considered as a unit movement. Although most logical, movement of 1 millimetre is not big enough because of limited resolution of cameras, and accuracy issues of the robot. The solution is to perform longer movements, and then normalize the obtained results.

Using the acquired matrix $T_{cb}$, it is possible to determine the Euler angles of transformation between two coordinate systems, needed by the robot's controller to define a new coordinate system. For this purpose, it is necessary to know the order of elemental rotations, and in this case, the X-Y-Z order was used. Therefore, matrix $T_{cb}$ is equal to matrix $T$ containing Euler angles $R_x$, $R_y$ and $R_z$ is given by (4)–(8).

$$T = \begin{bmatrix} \cos(R_y)\cos(R_z) & \cos(R_y)\sin(R_z) & -\sin(R_y) \\ T_{2,1} & T_{2,2} & \cos(R_y)\sin(R_x) \\ T_{3,1} & T_{3,2} & \cos(R_x)\cos(R_y) \end{bmatrix} \qquad (4)$$

$$T_{2,1} = \cos(R_z)\sin(R_x)\sin(R_y) - \cos(R_x)\sin(R_z) \qquad (5)$$

$$T_{2,2} = \cos(R_x)\cos(R_z) + \sin(R_x)\sin(R_y)\sin(R_z) \qquad (6)$$

$$T_{3,1} = \sin(R_x)\sin(R_z) + \cos(R_x)\cos(R_z)\sin(R_y) \qquad (7)$$

$$T_{3,2} = \cos(R_x)\sin(R_y)\sin(R_z) - \cos(R_z)\sin(R_x) \qquad (8)$$

The Euler angles can be calculated using Eqs. (9)–(11) obtained from (4):

$$R_x = \arctan(T_{2,3}/T_{3,3}) \qquad (9)$$

$$R_y = \arcsin(-T_{1,3}) \qquad (10)$$

$$R_z = \arctan(T_{1,2}/T_{1,1}). \qquad (11)$$

The transformation matrix $T_{cb}$ and angles obtained can be used to transform coordinates from the robot's frame to the cameras' frame. Since the transformation matrix $T_{cb}$ is real, symmetric and orthogonal, the inverse matrix is equal to transposed matrix. Therefore, in order to transform from cameras' to robot's base reference frame, expression (12) can be used:

$$C_b = T_{cb}^{-1} C_c + V_{cb} = T_{cb}^{T} C_c + V_{cb} \qquad (12)$$

The described procedure offers the theoretical background for acquiring matrix $T_{cb}$, therefore performing alignment of coordinate systems of the camera and robot's base. However, it is not described how to obtain the offset vector $V_{cb}$.

Due to the fact that the tool used to perform alignment is unknown, the coordinates of the TCP seen on images are also unknown, and the whole procedure is performed using coordinates of the robot's flange. While the axes of the coordinate system defined in this way are parallel to the respective axes of cameras' reference frame, the offset introduced by the tool between them is not compensated. The next Section will provide the means for calculation of the complete offset $V_{cb}$.

The procedure was designed such as to enable alignment using any tool that can fit its tip into the image acquisition area, making it easy to implement and adapt without any changes to the system. The procedure needs to be executed only once, when the relative position of the robot and calibration unit are determined and fixed. All the movements and calculations are performed automatically, so the operator only needs to guide the tool into the image acquisition area, and run the procedure.

## 5   Initial Calibration of the TCP

Once the alignment of coordinate systems is performed, the TCP can be moved along the axes of the cameras frame at any desirable distance in any direction. However, at this point, the origin of the newly defined reference frame (and therefore coordinates of points within image acquisition area) is unknown in the robot's base reference frame. This section will describe the TCP calibration procedure which does not require any prior information about the tool, and which will later be used to acquire coordinates of points inside the camera's reference frame, and the vector $V_{cb}$.

In order to define a tool, it is usually required to define a 6-dimension vector that contains positions and orientations of the TCP relative to the coordinate system of the robot's flange. One solution of determining tool parameters without any previous information is to guide the TCP in the same point several times, from different directions. In theory, it is enough to approach the same point from only two directions, but they need to be different at least in two angles. In that way, it is possible to find position coordinates of the TCP relative to the flange. Position and orientation coordinates of the flange in both positions are known, since they can be obtained from the robot's controller, and the point $TCP_b$, where the tool's tip is guided, is the same in both cases. By assuming that the tool is rigidly fixed to the flange, it is possible to write (13):

$$T_1^{-1}TCP_f + V_1 = T_2^{-1}TCP_f + V_2 = TCP_b \qquad (13)$$

Subscripts $f$ and $b$ of TCP signify that these are TCP coordinates in the reference frames of the robot's flange and base, respectively; $T_1$ and $T_2$ are transformation matrices between the coordinate system of robot's base and flange in the first and second position, and $V_1$ and $V_2$ are offsets between the reference frames of the robot's base and flange in these two positions. $T_1$, $T_2$, $V_1$, $V_2$ are all known parameters provided by the robot's controller in form of 6-dimension vector of the flange's positions and orientations. $T$ matrices are acquired by substituting respective $R_x$, $R_y$ and $R_z$ angles of the flange orientation into (4), and $V$ matrices consist of flange offsets from the origin of the robot's base coordinate system, $V = [x_{offset}\ y_{offset}\ z_{offset}]^T$.

An analytical solution to the problem of finding the TCP position can be obtained using (13). However, in practice this solution requires very high precision, and it is highly unlikely that it would work mainly because of two reasons. The first reason originates from inaccuracies of the robot's structural parameters which lead to direct kinematics inaccuracy [1, 5], which means that position and orientation information obtained from the robot is usually not accurate enough. The second reason is that it is very difficult to guide the TCP in exactly the same point due of finite resolution of measuring and guiding devices. These two issues, although irrelevant in most practical applications, can lead to a situation where two directions do not intersect, and therefore the solution does not exist. In reality, the solution would be to take the points where direction axes are closest to each other.

A suboptimal solution can be implemented using a numerical solving algorithm. Although in theory it could work with only two points, it is advised to use at least four points for improved accuracy, (Fig. 2a). The solution is a point $TCP_f$ from the search region $R_f$ in the flange's coordinate system, for which the sum (14) is the smallest.
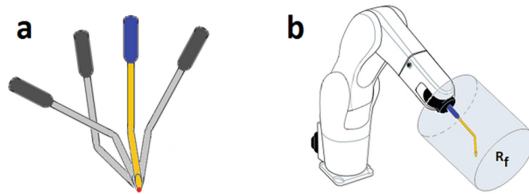


**Fig. 2.** Example of positions for TCP calibration (a) and search region $R_f$ (b)

$$\sum \left(T_i TCP_f - T_j TCP_f\right)^2, \quad i = \overline{1, n} - 1, \quad j = \overline{i, n}, TCP_f \in R_f \qquad (14)$$

It is evident that the search region $R_f$ (Fig. 2b) must be big enough to enable wide variety of tools, but the algorithm must also provide sufficient accuracy. Time and computational resources needed to meet these two conditions at the same time are very high. The solution is in an iterative algorithm, which uses relatively low search resolution in the first iterations, when the search region is big, and gradually increases the resolution while narrowing the search region as iterations progress.

The process of guiding the robot into the same point from several directions is done by the vision system, being enabled by previously performed axes alignment. Once at least four flange coordinates are obtained, the calibration unit performs the calculations using the previously described principles, and defines the TCP position.

Using the tool defined with this procedure, the coordinates of any desired point in image acquisition area can simply be requested from the robot and used as vector $V_{cb}$.

## 6    Fast Calibration Procedure

This procedure practically implements the calibration principle and algorithm explained in the Sect. 3 and in [4], since all its preconditions are fulfilled. Tool parameters are typically coordinates of the TCP in the robot's flange coordinate frame. If the TCP is guided into a point in space whose coordinates are known the robot's base frame, and the position and orientation of the robot's flange are also known in the same coordinate system, the tool parameter calculation is a matter of transformation of coordinate systems (15):

$$TCP_f = T(TCP_b - V),\qquad(15)$$

where $TCP_b$ represents the position of the TCP in the robot's base frame, $V$ stands for position coordinates of the robot's flange in its base frame, and $TCP_f$ are coordinates of the TCP in the coordinate system of robot's flange.

Evidently, this procedure requires far less time and computational resources than the previous one. It is used in regular operation, and it performs two main tasks. The first task is to check whether the position and orientation of the tool are within tolerances relative to the reference position when the flange is in its reference position. If the result is true, the robot will continue its normal routine. The second task is to orientate and guide the tool to the reference position and orientation if it is not there, and recalibrate it using the new position of the flange, after which the robot can again proceed with normal operation. The design of this technique additionally simplifies the implementation, since the same routine verifies and corrects the tool parameters. As a result, the TCP is always calibrated and the robot can resume with its regular operation after running this procedure.

## 7    Main Observations and Discussion

The evaluation of the calibration principle was performed and presented in [4], and it is not in focus of this paper. The recommendations to set the reference position of the TCP close to centre of the image acquisition area and the reference orientation close to the vertical axis in both images, should be followed to reduce distortion and achieve optimal performance.

The procedure for axis alignment, as well as other procedures, was tested using a DENSO VS-087 6-axis industrial robot and information obtained from the camera system. After the alignment was performed, the movement was attempted along axes of the camera system. Although the axes were aligned with adequate precision, the results

of the test also demonstrated that the movement on longer distances resulted in offsets of less than 2% of attempted distance in axes that should have remained unchanged. A greater positioning accuracy can be achieved by introducing positioning check. If the position recorded after the movement is not within set tolerances, additional correction can be performed. It is reasonable to set positioning tolerance to be at least as big as the robot's declared repeatability. The robot used for testing has very good repeatability of 0.02 mm. Considering the maximum percentage of error, and the size of the image acquisition area, in order to guide the TCP within tolerances, no more than two movements must be performed. The main reason for this positioning imperfection lays in the fact that the image is not orthographic, but slightly distorted because of the finite distance between the camera and the observed object. However, this effect is only notable in areas that are close to the borders of the image acquisition area, and does not affect the robot's guidance in regular operation. The procedure was repeated for various relative orientations between the calibration unit and the robot, and conclusions were consistent.

The procedure for initial calibration of the TCP was tested in order to verify its accuracy. The first step was to compare its performance with the performance of built-in TCP calibration functionality of the Denso robot. The functionality uses a similar principle, and requires identical type inputs, being therefore suitable to compare them. When identical coordinates were used for both algorithms, the difference in obtained tool parameters was less than 0.1 mm. The second testing phase was to identify potential sources of inaccuracy. The procedure was performed for various angles, and it was concluded that calibration results were more accurate when angles of rotation were bigger.

However, it is not recommended to perform big angle rotations because of high risk of collision with the calibration unit. The reason is that at the start of the procedure, the robot has no information about the tool, and therefore rotations have to be made around the centre of the robot's flange. In that way, if the tool is long, even small angle rotation would result in big offsets of the tip of the tool. The solution is to perform two sequential calibrations. The first calibration uses small rotation angles, and therefore does not result in big movement of the tool's tip, but results in lower accuracy. However, the accuracy is good enough to provide initial information about the tool parameters. It is possible and recommended to repeat the procedure with bigger angles, but this time around previously provided TCP information. The result of the second iteration is calibration with higher accuracy without the risk of collision with the calibration unit. Testing was performed with various shapes and sizes of tools, which proved that the initial calibration of the tool can be successfully performed in two steps with different tools.

The procedure for fast calibration uses the result of axes alignment and initial calibration to check and correct the tool parameters. In this procedure, a position tolerance is set to take into account small deviations of TCP's position caused by minor tool deformations or robot's repeatability issues. The procedure was tested with different levels of distorted tools, ranging from untampered tool to realistic impact scenario where both position and posture of the tool have been changed. In some tests, changes were made to the extent where such deviations would indicate serious tool damage.

However, in all cases the procedure was performed according to expectations and managed to recalibrate all the necessary parameters. In order to ensure correct positioning in all circumstances, a check was also introduced to verify whether the position and orientation were properly corrected. If they were not, an additional correction iteration is going to be performed.

## 8   Conclusion

The intention of this paper was to present theoretical and practical concepts and procedures implemented during the development of a solution for robot TCP calibration. The idea to use images from orthogonal planes to acquire TCP information, conceived in earlier phases of research, served as a basis for development of calibration unit. The presented algorithms and routines serve as crucially important links between theoretical concepts and practical realization ready for implementation in industry. The procedure for axes alignment uses a simple and reliable algorithm to enable the calibration unit to guide the robot's tool. The routine used for the initial calibration of the tool additionally serves as a mean to determine coordinates of the points within the image acquisition area and therefore enables a faster algorithm to be used in subsequent tool identifications or TCP checks in regular operations.

The fast calibration procedure is the only one used in regular operation, and it can perform checks of proper calibration, or recalibrate the tool if its parameters have changed. The important benefit of this procedure it that its outcome is always a calibrated tool, which means that the robot can continue with regular operation without human-assisted recovery. This is especially important in environments where tools are frequently switched using an automatic changing station in order to perform different operations.

From the beginning, the system was practically oriented, and therefore its construction and all the algorithms were designed to be accurate, reliable and robust. All procedures are independent from other devices, and none of them requires any modifications of the system, or some specially developed tool, which makes them easy to implement. Human intervention is only needed to guide the new tool into the unit and run the procedure during the installation phase, or when introducing an entirely new tool. This means that the system is completely automated, and therefore it can be integrated in facilities that rarely require human presence. The short time needed for calibration checks means they can be performed more frequently, which ensures higher quality of production. From the versatility point of view, one calibration unit can be used by multiple robots, if it is in their working range, and it is universal to all robot brands.

# References

1. Cheng, F.S.: Calibration of robot reference frames for enhanced robot positioning accuracy. In: Robot Manipulators, INTECH 2008, Chap. 5, Sect. 1, Rijeka, Croatia, pp. 95–112 (2008)
2. BullsEye Application Manual, Revision G. ABB Robotics, Västerås, Sweden (2012)
3. Hallenberg, J.: Robot tool center point calibration using computer vision. M.Sc. thesis, Department of Electrical Engineering, Linköping University, Linköping, Sweden (2007)
4. Gordić, Z., Ongaro, C.: Calibration of robot tool centre point using camera-based system. Serb. J. Electr. Eng. **13**(1), 9–20 (2016)
5. Conrad, K.L., Shiakolas, P.S., Yih. T.C.: Robotic calibration issues: accuracy, repeatability and calibration. In: Proceedings of the 8th Mediterranean Conference on Control & Automation (MED 2000), Rio, Patras, Greece, 17–19 July 2000
6. Ongaro, C.: Dispositivo e metodo di calibrazione di una torcia di saldatura robotizzata, Pat. pend. N.: TV2014A000165, 25 November 2014

# Novel Design of Robot Manipulators and Grippers

# Design, Construction and Testing of a Gripper for Horticulture Products

Matteo Russo[1(✉)], Marco Ceccarelli[1], Burkhard Corves[2],
Mathias Hüsing[2], Michael Lorenz[2], and Giuseppe Carbone[1]

[1] LARM: Laboratory of Robotics and Mechatronics – DiCEM,
University of Cassino and South Latium,
Via di Biasio 43, 03042 Cassino, FR, Italy
`{matteo.russo,ceccarelli,carbone}@unicas.it`
[2] IGM: Institut für Getriebetechnik und Maschinendynamik RWTH Aachen,
Kackertstraße 16-18, 52072 Aachen, Germany
`{corves,huesing,lorenz}@igm.rwth-aachen.de`

**Abstract.** This paper describes the design of a gripper for grasping and manipulating horticulture products. The design solution has been achieved by means of a systematic approach, by evaluating all the possible architectures to get an optimal one. The proposed structure is numerically designed and simulated and then a prototype has been built and successfully tested in laboratory.

**Keywords:** Robot design · Grasping · Horticulture products Grippers

## 1 Introduction

The end-effector is the most important component of a robot when it deals with horticulture products, since it acts as interface between the robotic system and the product. Since fruits and vegetables have irregular changeful shapes and low mechanical properties, the end-effector must be designed properly to manipulate them. Robotics applied to horticulture products handling has been studied for more than twenty years. Research results have been focused on single-product applications and end-effectors have been designed only for specific targets, such as tomatoes [1–3], strawberries [4] and cucumbers [5]. Current grippers are not flexible enough to adapt the grasp to the wide variety of shapes and sizes of horticulture products [6].

An important aspect in grippers for horticulture products is the use of compliant components since non-rigid materials are able to adapt passively to the irregular shape of horticulture products. Furthermore, compliance increases contact surfaces and reduces the stress on manipulated objects. This solution in grippers can deal with a wide variety of objects in a wide range of shape and dimension (instead of a single fruit/vegetable).

This paper presents the development of a gripper that is able to manipulate medium-sized spherical fruits with careful grasp and release.

**Table 1.** Horticulture products sizes [8]

| Product | Min. size [mm] | Max. size [mm] |
|---|---|---|
| Apple | 60 | 110 |
| Apricot | 30 | 60 |
| Clementine | 35 | 60 |
| Lemon | 45 | 90 |
| Orange | 53 | 120 |
| Peach | 56 | 100 |
| Tomato | 35 | 105 |

**Table 2.** Average mechanical properties of common fruits and vegetables [9–11]

| Product: | Young's Modulus average [MPa] | Young's Modulus deviation [MPa] | Poisson's ratio [-] |
|---|---|---|---|
| Tomato – Ripe | 2.32 | – | 0.74 |
| Tomato – Unripe | 4.07 | – | 0.55 |
| Pear | 5.80 | 0.50 | 0.25 |
| Apple | 12.89 | 2.43 | 0.32 |
| Carrot | 6.86 | 0.46 | 0.25 |

**Table 3.** General features of grasping solutions for horticulture products

| Requirement | Grippers | Hands | Pneum. devices |
|---|---|---|---|
| Geometry: | | | |
| Radius: 20-50 mm | Yes | Yes | Yes |
| Forces: | | | |
| Firm grasp | Yes | Yes | No |
| No damage | Yes | Yes | No |
| Materials: | | | |
| Non-toxic material | Yes | Yes | Yes |

## 2 Requirements for Horticulture Products Handling

Object analysis is required to design the end-effector of a robotic unit [7]. This work deals with medium-sized spherical products, such as apples, tomatoes, citrus fruits and peaches. Since 1961, the OECD sets international standards for fruits and vegetables [8], as shown in Table 1. The mechanical properties of apples, pears and tomatoes were measured by several research groups [9–11] and summarized in Table 2.

The possible end-effector can be identified through general considerations among the architectures in Table 3:

- *Gripper*, composed by two or more rigid fingers and a mechanism to move them against an object, with 1 to 3 degrees-of-freedom and suitable force control.
- *Artificial hand*, which is composed of multiple fingers to adapt to most shapes, but with several actuators, requiring a control with complex features.
- *Pneumatic device with suction cups*, which use partial vacuum to lift objects by using traditional electro-pneumatic technologies.

The finger can be designed with the following characteristic solutions:

- *Rigid fingers*, which perform firm grasp mainly by using friction.
- *Articulated fingers*, which perform firm grasp mainly by adapting to the manipulated object's shape.
- *Compliant fingertips*, based on compliant material, which adapt to irregular shapes and decrease the grasping force needed to lift the object.

The design solution has been determined through a systematic approach with a design procedure for grippers as in [7, 12]. A 1-DoF gripper with compliant fingers and an electric actuator has been developed.

## 3   Gripper Design

The proposed solution is a three-fingered gripper with a crank-slider mechanism as actuating mechanism, as in Fig. 1. Even if high-compliance fingers can be used, a rigid mechanism is preferred, since it is easier to analyse, to build and to test for a proper grasping operation.

Compliance can be restrained to the fingertips. Several different rubbers could be used as compliant material, as long as they do not contain toxic plasticizers such as phthalates. The Grasping Index in [12] is used as design criterion in the form:

$$\text{G.I.} = \frac{F \sin\zeta}{P} \tag{1}$$

in which P is the force exerted by the actuator, F the grasping force and $\zeta$ represents the configuration angle of the mechanism at grasp. The Grasping Index can be written as a function of the design parameters shown in Fig. 1 as:

$$\text{G.I.} = \frac{l_1}{h} \text{tg}\phi \, \cos\left(\phi + \psi - \frac{\pi}{2}\right) \tag{2}$$

Since the Grasping Index is configuration-dependent, it must be evaluated for as many configurations as possible. Then a mechanism solution can be defined in two different ways [12], namely by using:
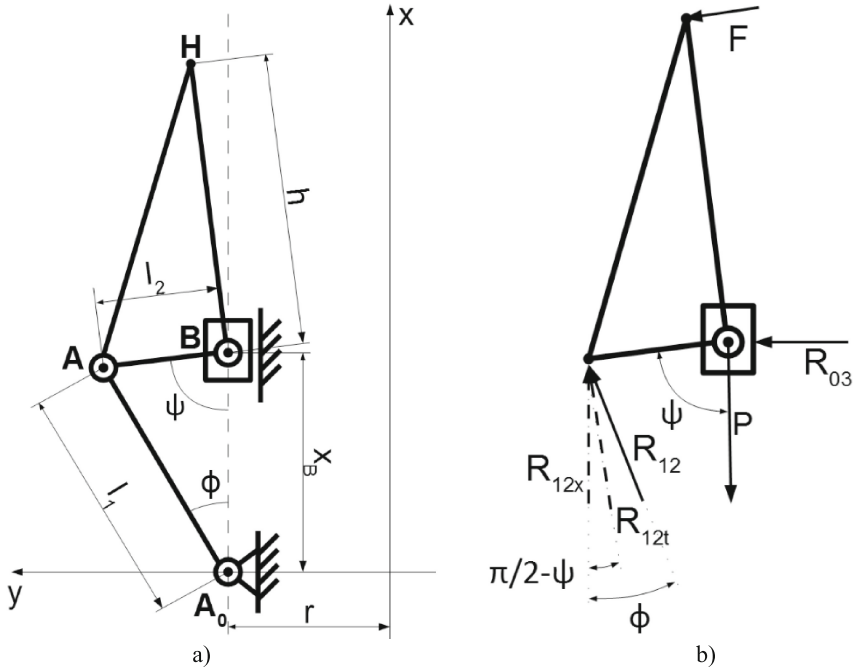
**Fig. 1.** The proposed finger mechanism with design parameters: (a) A kinematic diagram; (b) Free-body diagram for finger (body 2) and slider (body 3).

- Maximized Mean Grasping Index through the expression:

$$\max G.I._{mean} \, subject \, to \, l_{i,min} < l_i < l_{i,max} \, for \, i = 1, 2. \tag{3}$$

- Minimized Grasping Index deviation with:

$$\min \frac{G.I._{max} - G.I._{min}}{G.I._{mean}} \, subject \, to \, l_{i,min} < l_i < l_{i,max} \, for \, i = 1, 2. \tag{4}$$

A simulation has been worked out to evaluate G.I. for different configurations and geometries. Table 4 describes the assigned ranges for the design parameters of the gripper, while the design results are shown in Table 5. Since the first solution is only marginally better than the second in mean G.I. (6.2%) but significantly worse (108.5%) in deviation, the one with minimum deviation can be considered more efficient. The peak actuation force $P_{max}$ has been computed as equal to 106.66 N. A rotational motor is chosen to actuate the gripper, adding a lead screw in the system so that the maximum required torque is equal to 0.2186 Nm. The CAD model of the gripper is based on both the results of optimization problems in (3) and (4) and in operation simulation and it is aimed at 3D printing manufacturing [13]. Figure 2 shows the mechanical design that has been implemented in the 3D printer.

**Table 4.** Assigned ranges for design parameters of gripper mechanism in Fig. 1

| Variable | $l_1$ | $l_2$ | h | r |
|---|---|---|---|---|
| Min. [mm] | 30 | 15 | 70 | 30 |
| Max. [mm] | 60 | 20 | – | 30 |

**Table 5.** Results of the gripper optimization problem

| $l_1$ [mm] | $l_2$ [mm] | G.I.$_{mean}$ | Deviation | Criterion |
|---|---|---|---|---|
| 30 | 20 | 0,316308 | 0,126631 | Max. mean G.I. |
| 42 | 20 | 0,297702 | 0,060774 | Min. deviation |



a)                                        b)
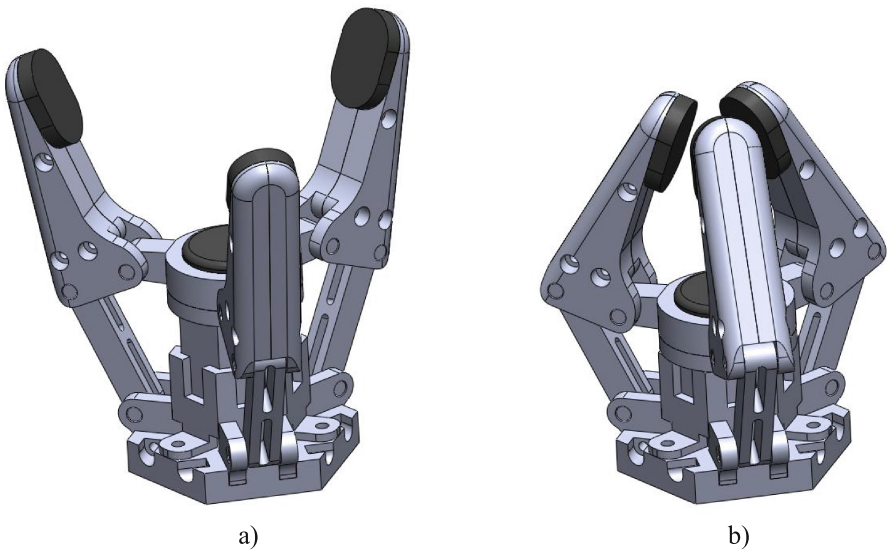
**Fig. 2.** CAD model of the designed gripper: (a) Gripper open; (b) Gripper closed.

## 4 Prototype and Experimental Tests

The designed gripper has been built using a Stratasys Dimension Elite 3D Printer [14]. The material used by the printer is ABS+ plastic. In order to get a smooth motion with low friction, backlash among moving parts has been designed equal to 0.3 mm. The printed prototype with an additional connection flange and a socket for the motor is shown in Fig. 3. The compliant parts were made out of Polyurethane foam rubber, using a layer with thickness equal to 10 mm.

Electric switches have been used to keep the control as simple as possible: they send a signal when the trigger is below a critical position. Three different switches were used to send the following signals:
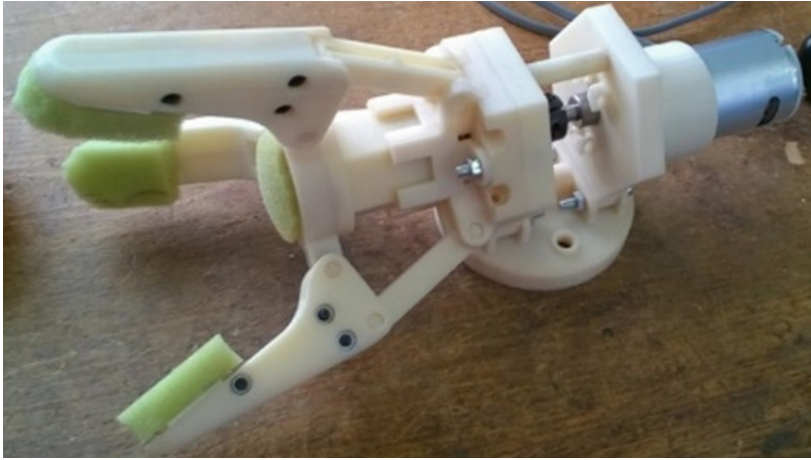
**Fig. 3.** The gripper prototype built through 3D printing



a)                                                    b)
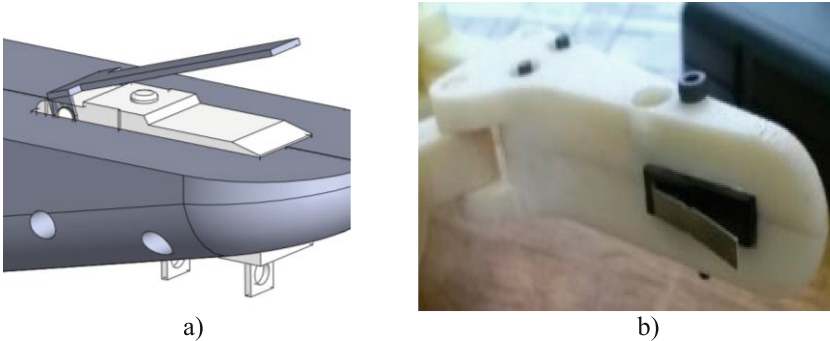
**Fig. 4.** The finger switch encased in the structure: (a) CAD model; (b) The prototype solution

- A *fingertip switch*, to stop the motor at the grasp operation. It is encased in the finger as shown in Fig. 4.
- A *security stop switch*, to stop the grasp if the gripper close command is given while there is no object between the fingers.
- A *fingerbase switch*, needed to stop the motor after a gripper open command. The switch is triggered for a critical relative position of the rocker and finger.

A gear motor and a UR5 arm of Universal Robots [15] have been used for laboratory tests. The UR5 has been controlled through its own control interface. The prototype has been tested in several different pick and place operations, with different products (ripe tomatoes, unripe tomatoes, peaches, apples). The basic pick & place task for a single product is described in Table 6, where elementary actions are detected and classified, such as: transport (T), movement (M), active pause (A) and passive pause (P) [12]. The layout of the testing environment is shown in Fig. 5. During several tests,

**Table 6.** Pick & Place task analysis via elementary actions

| Pick & Place task | T | M | A | P |
|---|---|---|---|---|
| Manipulator moves in the grasping position | | X | | |
| The product is grasped | | | X | |
| The manipulator lifts up the object | X | | | |
| The manipulator moves in the release point | X | | | |
| The manipulator goes down to the first release position | X | | | |
| The object is released | | | X | |
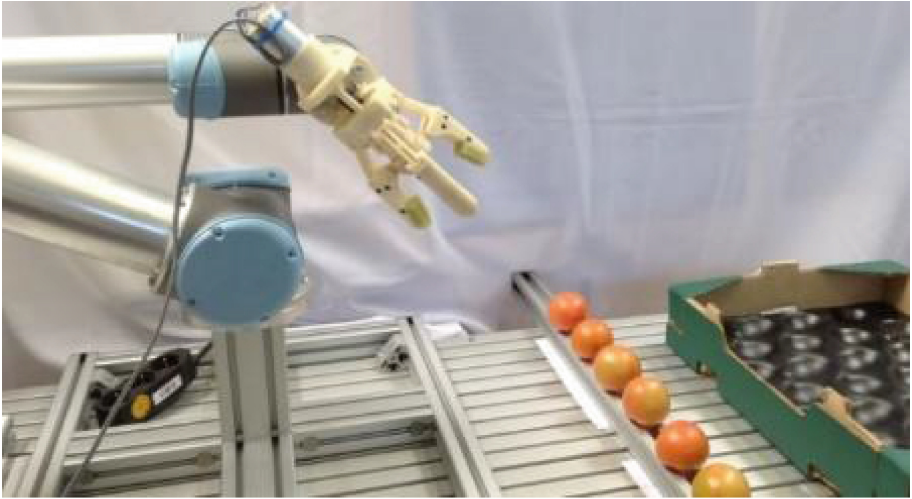


a)



b)                         c)                         d)

**Fig. 5.** Layout of the testing environment: (a) System layout; (b) Grasping position; (c) Transport; (d) Release.

each product has been lifted from the initial position, transported onto a socket of the final package and released into it.

No horticulture products have been damaged by the manipulation, when the rigid grasp does not allow the object to move. The cycle time for a single pick & place task is 2.0 s, while the maximum actuation torque is equal to 0.0981 Nm.

## 5   Conclusions

In this paper, a new gripper for horticulture products is proposed as result of a design procedure. Its kinematics and dynamics have been studied and the mechanism has been optimized through numerical simulations. The gripper design has been modelled for prototyping through 3D printing. The prototype has been tested using a UR5 robot arm in several pick & place operations to demonstrate that the proposed gripper is able to fulfil all requirements for the task. It grasps firmly medium-sized horticulture products without damaging them. Future developments include the optimization of compliant fingertips and the development of a force-based control system.

## References

1. Ceccarelli, M., Figliolini, G., Ottaviano, E., Mata, A.S., Criado, E.J.: Designing a robotic gripper for harvesting horticulture products. Robotica **18**(1), 105–111 (2000). Cambridge University Press
2. Zhi-Guo, L., Ji-Zhan, L., Ping-Ping, L., Jian-Jun, Y.: Study on the collision-mechanical properties of tomatoes gripped by harvesting robot fingers. Afr. J. Biotechnol. **8**(24), 7000–7007 (2009)
3. Carbone, G., Gherman, B.G., Ceccarelli, M., Pisla, D., Itul, T.P.: A robotization for packaging of horticulture products. Robotica Manage. Romania **12**(2), 13–20 (2007)
4. Dimeas, F., Sako, D.V., Moulianitis, V.C., Aspragathos, N.A.: Towards designing a robot gripper for efficient strawberry harvesting. In: Proceedings of 22nd International Workshop on Robotics in Alpe-Adria-Danube Region – RAAD, Portoroz, Slovenia, pp. 220–226 (2013)
5. Van Henten, E.J., Hemming, J., Van Tuijl, B.A.J., et al.: An autonomous robot for harvesting cucumbers in greenhouses. Auton. Robots **13**, 241–258 (2002). Kluwer publishing
6. Carbone, G.: Grasping in Robotics. Springer, Dordrecht (2013)
7. Pahl, G., Beitz, W., Feldhusen, J., Grote, K.H.: Engineering Design: A Systematic Approach. Springer, Dordrecht (2007)
8. OECD: Fruit and Vegetables standards. http://www.oecd.org/. Accessed 10 Oct 2015
9. Williams, S.H., Wright, B.W., Van den Truong, V., Daubert, C.R., Vinyar, C.J.: Mechanical properties of foods used in experimental studies of primate masticatory function. Am. J. Primatol. **67**, 329–346 (2005)

10. Gladyszewska, B., Ciupak, A.: Changes in the mechanical properties of the greenhouse tomato fruit skins during storage. Tech. Sci. **12**, 1–8 (2009)
11. Babarinsa, F.A., Ige, M.T.: Young's Modulus for packaged Roma tomatoes under compressive loading. Int. J. Sci. Eng. Res. **3**(10), 314–320 (2012)
12. Ceccarelli, M.: Fundamentals of Mechanics of Robotic Manipulation. Kluwer Publishing, Dordrecht (2004)
13. Ceccarelli, M., Carbone, G., Cafolla, D., Wang, M.F.: How To Use 3D Printing for Feasibility Check of Mechanism Design. Advances in Intelligent Systems and Computing, vol. 371, pp. 305–313. Springer, Dordrecht (2015)
14. Stratasys. http://www.stratasys.com/3d-printers/. Accessed 09 June 2015
15. Universal Robots. http://www.universal-robots.com. Accessed 05 June 2015

# A Real-Time Serial Approach for Solving the Forward Kinematic Model of Spherical Parallel Manipulators

Margot Vulliez, Houssem Saafi$^{(\boxtimes)}$, and Said Zeghloul

Department of GMSC, PPRIME Institute, CNRS, ENSMA, UPR,
University of Poitiers, 3346 Poitiers, France
{margot.vulliez,houssem.saafi,said.zeghloul}@univ-poitiers.fr

**Abstract.** This paper discusses a serial approach to solve the forward kinematic of a spherical parallel manipulator (SPM). The SPM is used as master device in minimally invasive surgery to control a slave robot. The orientation of the moving platform of the SPM is determined by solving the forward kinematic of one serial leg. The forward model is very simple compared to the classical way of solving the forward model using three sensors placed on the base of the SPM and also it does not suffer from parallel singularities which amplify the classic forward model. The serial way of solving the forward model needs a short calculation time which is suitable for real-time applications.

**Keywords:** Forward kinematic model · Spherical parallel manipulator · Real-time · Singularity · Model accuracy

## 1 Introduction

Parallel manipulators are more and more used as haptic devices to provide low inertia, high stiffness and compactness. That way Spherical Parallel Manipulators (SPM) have been designed to provide three rotational degrees of freedom (DoFs) with a fixed centre of rotation. SPM are found in several haptic applications in the literature. For example, Birglen et al. [2] use a SPM as a system to control the orientation of a camera. SPM provide the three rotational DoFs in several medical applications such as in laparoscopic surgery in [8,9]. It is also used as haptic device to control autonomous submarine vehicles like in [4].

However parallel manipulators have complex kinematic models and can suffer from important parallel singularity issues. The parallel singularities amplify errors in solving the forward kinematic model which make difficult the control of the slave robot.

The studied spherical parallel manipulator presented in this paper was developed to control a surgical robot. However, this manipulator suffers from the parallel singularity and also has a complex forward model. In previous work [10], we improved the forward model resolution by the use of an extra sensor placed

on the moving platform. This technique has reduced booth the error of the resolution and the calculation time of the forward model of the SPM. However, it requires the use of four sensors instead of three.

In this paper, a new approach to solve the forward kinematic model FKM of the SPM is studied. This approach is based on the serial way to solve the FKM, where three sensors are installed on one leg of the SPM. This solution aims to ensure a fast calculation time suitable for real-time applications and to eliminate the effect of the parallel singularity for the FKM. The new serial approach is compared to the classic method where the sensors are installed on the base, and to the improved method where an extra-sensor is used.

The paper is organized as follows. In Sect. 2, the PROMIS tele-operation system is presented. The three forward kinematic models are studied in Sect. 3. In Sect. 4, a comparison between calculation times of the three model is carried out. Section 5 presents an experimental validation of the forward kinematic model.

## 2 PROMIS Tele-Operation System Overview

The Spherical Parallel Manipulator studied in this paper is part of the haptic master device of the PROMIS (Pprime RObot for Minimally Invasive Surgery) tele-operation system represented in the Fig. 1.

This system is designed to assist the surgeon with more security and accuracy in his gestures in minimally invasive operations. The motions of the instruments are limited to three rotations around the incision point and one translation along the instrument axis. The 3-RRR SPM provides the three rotational DoFs in the haptic interface. The useful workspace for these medical interventions has been determined in Chaker et al. [6] to be a cone with an apex angle of 26°.

The haptic device must reproduce the surgeon movements faithfully and with high accuracy. For this purpose the SPM is equipped with sensors measuring joint angles ($\theta_{1A}$, $\theta_{1B}$, $\theta_{1C}$) to compute the platform orientation, described by



(a)                                          (b)
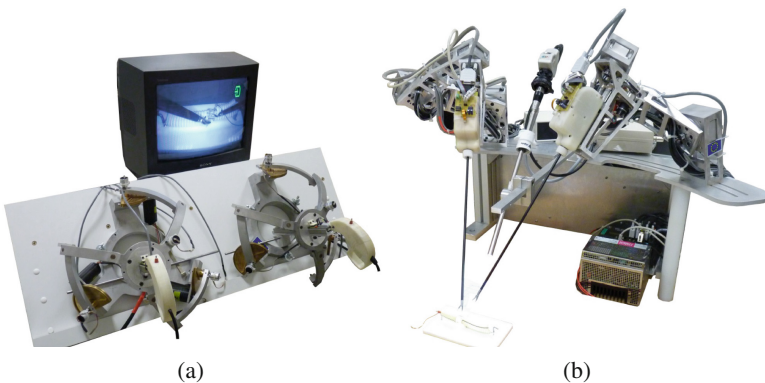
**Fig. 1.** Master station **(a)** and slave station **(b)** of the PROMIS system
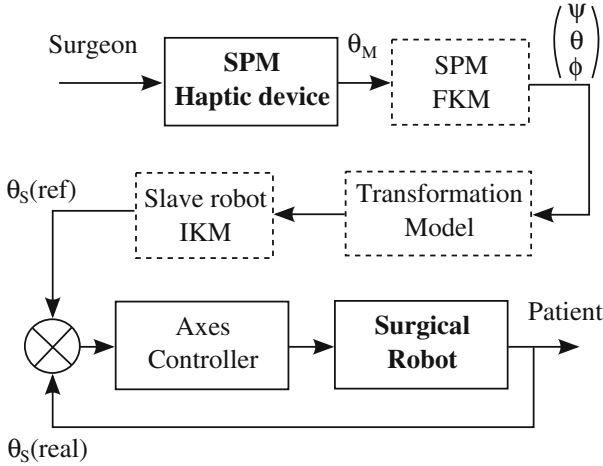
**Fig. 2.** Control system architecture
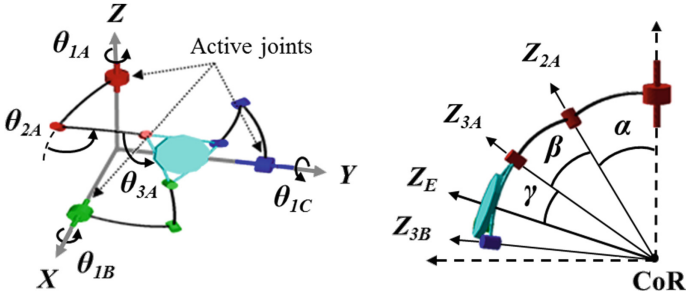


**Fig. 3.** SPM structure and parameterisation

ZXZ Euler angles $(\psi, \theta, \phi)$, by solving the Forward Kinematic Model (FKM). The slave surgical robot is then controlled knowing its Inverse Kinematic Model (IKM) and the platform orientation.

The control system architecture is shown in Fig. 2 and underlines the importance of the FKM of the haptic interface in the control scheme. The implementation of SPM in such real-time applications involves the need for fast and accurate calculation.

The studied SPM consists of three serial legs, composed by one active and two passive R-joints, connecting the base to the moving platform (Fig. 3a).

All the joint axes intersect in a common point, the Centre of Rotation (CoR), that matches the incision point for the surgical robot. The joint base axes are located in the reference orthogonal frame $XYZ$. The parametrization of the SPM is represented in Fig. 3b. The design geometric parameters $\alpha$, $\beta$ and $\gamma$ were optimized in [6] to obtain the adequate workspace excluding serial singularities outside. The design vector is $[\alpha = 39.3°, \beta = 34.1°, \gamma = 18.2°]$. However, the

self-rotation is not studied in [6] which yields to the presence of parallel singularity in the workspace of the SPM. The parallel singularity amplifies the error while solving the forward kinematic model which makes impossible the motion control of the surgical robot. The high error values and the error fluctuations provoke vibrations that can damage the actuators. For this reason, in [10] we added an extra sensor on the moving platform to eliminate the effect of parallel singularities and also to reduce the calculation time. In the next section, different ways to solve the FKM are presented.

## 3   Different Forward Kinematic Models

### 3.1   Classical FKM

The classical forward model computes the platform orientation $(\psi, \theta, \phi)$ according to the measurement of the actuated-joint angles $(\theta_{1A}, \theta_{1B}, \theta_{1C})$.

Different methods are proposed in the literature to solve the FKM using a classic way. Gosselin et al. [7] introduce an 8-degree polynomial to describe the direct model that has the 8 possible solutions of the problem. Yet the resolution needs a complex and high-time consuming numeric iterative method. Celaya [5] proposes an alternative solving method based on interval propagation. But this method appears to be very sensitive to the size of the initial intervals and also requires a high computation time. Bai et al. describe in [1] a procedure to obtain a simplified FKM equation by studying two spherical four-bar linkages. This equation is then transformed to an 8th order polynomial solved with a numeric iterative method as the Newton-Raphson method. The study presented in [10] shows that this method suffers from two main issues. The first issue is that the accuracy of the solution depends on how far is the SPM from the parallel singularity. The resolution error exceeds $1°$ close to singular configurations. The second issue is that the classic FKM admits multiple solutions while only one corresponds to the real configuration. It is not possible to guarantee that the given solution is the good one.

In the next paragraph, an improved method is presented and discussed. This method eliminates the issues of the classical FKM.

### 3.2   Improved FKM

The simple way to eliminate effects of parallel singularity on the resolution of the FKM is the use of an extra sensor. Vertechy and Parenti-Castelli [11] justify the use of extra sensors for the following reasons: to obtain a closed form solution by turning the FKM into a linear problem, to speed-up the calculation, to be robust against singularities and to improve the solution accuracy. The number and the optimal location of extra-sensors on general parallel manipulators have been analyzed by Bonev et al. [3] according to the FKM complexity. Such extra-sensors have been installed on a 3-RRR planar robot by Zubizarreta et al. [12].

For the SPM, we proposed in [10] to simplify the FKM resolution of the SPM by adding an extra-sensor measuring the passive joint angle $\theta_{3A}$. Thus, the

improved FKM allows to calculate the platform orientation $(\psi, \theta, \phi)$ knowing the sensor measurements $(\theta_{1A}, \theta_{1B}, \theta_{1C}, \theta_{3A})$. The method transforms the four sensors configuration FKM in an explicit problem with a closed form solution. It eliminates the effects of the parallel singularities, reduces its complexity and its computing time. In addition, it makes it robust and highly improves the accuracy of the solution. However, this solution requires the use of a fourth sensor instead of three.

In the next paragraph, we present a new way to solve the forward model which requires the use of only three sensors.

### 3.3   Serial Positioning of the Sensors

The new proposed approach consists in placing the three sensors on one leg to determine the platform orientation $(\psi, \theta, \phi)$ by considering a simple serial kinematic model. The sensors are placed on the leg A and measure the angles $(\theta_{1A}, \theta_{2A}, \theta_{3A})$. In this way the solution can be calculated by evaluating the direct kinematic transformation of the equipped leg as described in Eq. (1).

$$
\begin{aligned}
T_0^3 = & \ Rot(Z, \theta_{1A}) \times Rot(X_{1A}, \alpha) \times Rot(Z_{2A}, \theta_{2A}) \\
& \times Rot(X_{2A}, \beta) \times Rot(Z_{3A}, \theta_{3A}) \times Rot(X_{3A}, \gamma)
\end{aligned}
\tag{1}
$$

Then the platform orientation is evaluated by using the expression of the ZXZ Euler transformation matrix (Eq.(2)).

$$
T_0^3 = Rot(Z, \psi) \times Rot(X', \theta) \times Rot(Z'', \phi)
\tag{2}
$$

The Euler angle expressions are:

$$
\begin{cases}
\theta = acos(Z_E(3)) \\
\psi = atan2(\dfrac{Z_E(1)}{sin\theta}, \dfrac{-Z_E(2)}{sin\theta}) \\
\varphi = atan2(\dfrac{X_E(3)}{sin\theta}, \dfrac{Y_E(3)}{sin\theta})
\end{cases}
\tag{3}
$$

The serial FKM is very simple and should strongly speed-up the problem resolution. It also has a direct closed-form solution that avoids the use of iterative numeric solving methods harmful for real-time applications.

## 4   Computing Time Comparison

The three models are implemented in C language on an industrial computed. Table 1 details the average calculation time of FKMs for 1000 random orientations.

The execution time must be very small to be adapted to real time control. Such a constraint is not verified by the classic model because the numeric method of resolution of the problem leads to a combinatorial explosion in computation time. The extra-sensor addition allows a lower calculation time because

**Table 1.** FKM computing time

| FKM | Computing time |
|---|---|
| Serial | $\approx 5\,\mu s$ |
| Four sensors | $\approx 20\,\mu s$ |
| Classic | $\approx 100\,\mu s$ |

it provides a direct solution to the kinematic equation of the parallel structure. However, four sensors instead of three sensors are required. The serial configuration leads to a simpler direct model that is solved in a very small computing time suitable for real-time applications.

The new serial approach of the Forward Kinematic Model highly improves the computing time of the SPM platform orientation that is a major point for real-time applications such as medical haptic devices. The next section presents experiments made on the master device.

## 5 Experiments

The three sensors are installed on the leg A as presented in Fig. 4.
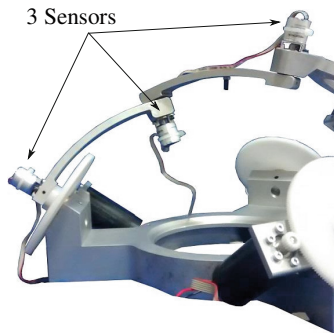


**Fig. 4.** Leg A with three sensors.

The Serial model was implemented to determine the orientation of the moving platform. The orientation of the master device was varied. The angles $\psi$ and $\varphi$ were kept constants. Figure 5 shows the variation of the joint angles.

The orientation of the moving platform solved using the serial model is presented in Fig. 6. The experiments show that FKM can calculate faithfully the orientation of the SPM.

The new model is used successfully to control the surgical robot.
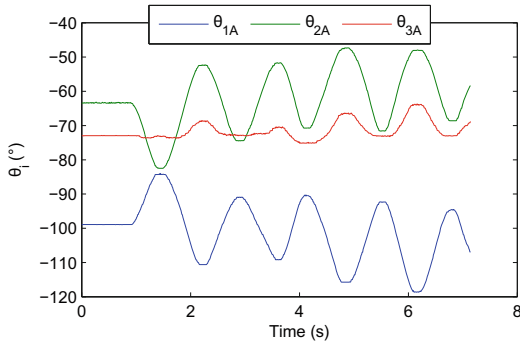
**Fig. 5.** Evolution of the joint angles $(\theta_{1A}, \theta_{2A}, \theta_{3A})$.
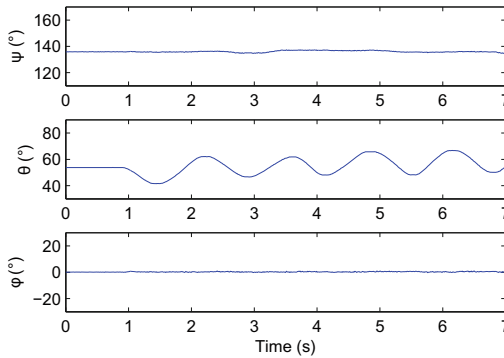


**Fig. 6.** Orientation of the moving platform.

## 6    Conclusion

In this paper, a serial method to solve the forward kinematic model of a 3-RRR spherical parallel manipulator. This method was compared to the classical way to solve the FKM where three sensors are installed on the base and an improved method where three sensors installed on the base and an extra sensor installed on the moving platform are used to solved the FKM. The study shows that the serial way to solve the FKM gives the best calculation time ($5\,\mu s$) compared to the other models. Experiments were carried out to validate the serial model. This model was used successfully to control the surgical robot.

# References

1. Bai, S., Hansen, M.R., Angeles, J.: A robust forward-displacement analysis of spherical parallel robots. Mech. Mach. Theor. **44**, 2204–2216 (2009)
2. Birglen, L., Gosselin, C., Pouliot, N., Monsarrat, B., Laliberté, T.: Shade, a new 3-dof haptic device. IEEE Trans. Robot. Autom. **18**, 166–175 (2002)
3. Bonev, I.A., Ryu, J., Kim, S.G., Lee, S.K.: A closed-form solution to the direct kinematics of nearly general parallel manipulators with optimally located three linear extra sensors. IEEE Trans. Robot. Autom. **17**, 148–156 (2001)
4. Cavallo, E., Michelini, R.: A robotic equipment for the guidance of a vectored thrustor AUV. In: 35th International Symposium on Robotics ISR 2004. Citeseer (2004)
5. Celaya, E.: Interval propagation for solving parallel spherical mechanisms. In: Lenarčič, J., Thomas, F. (eds.) Advances in Robot Kinematics, pp. 415–422. Springer, Heidelberg (2002)
6. Chaker, A., Mlika, A., Laribi, M., Romdhane, L., Zeghloul, S.: Accuracy analysis of non-overconstrained spherical parallel manipulators. Eur. J. Mech. A. Solids **47**, 362–372 (2014)
7. Gosselin, C., Sefrioui, J., Richard, M.J.: On the direct kinematics of spherical three-degree-of-freedom parallel manipulators of general architecture. J. Mech. Des. **116**, 594–598 (1994)
8. Li, T., Payandeh, S.: Design of spherical parallel mechanisms for application to laparoscopic surgery. Robotica **20**, 133–138 (2002)
9. Ma, A., Payandeh, S.: Analysis and experimentation of a 4-DOF haptic device. In: 2008 Symposium on Haptic Interfaces for Virtual Environment and Teleoperator Systems. pp. 351–356. IEEE (2008)
10. Saafi, H., Laribi, M.A., Zeghloul, S.: Forward kinematic model improvement of a spherical parallel manipulator using an extra sensor. Mech. Mach. Theor. **91**, 102–119 (2015)
11. Vertechy, R., Parenti-Castelli, V.: Robust, fast and accurate solution of the direct position analysis of parallel manipulators by using extra-sensors. INTECH Open Access Publisher (2008)
12. Zubizarreta, A., Marcos, M., Cabanes, I., Pinto, C., Portillo, E.: Redundant sensor based control of the 3RRR parallel robot. Mech. Mach. Theor. **54**, 1–17 (2012)

# Computer Simulation of Bounded Error Algorithm for Iterative Learning Control

Kaloyan Yovchev[1(✉)], Kamen Delchev[2], and Evgeniy Krastev[1]

[1] Faculty of Mathematics and Informatics, Sofia University, Sofia, Bulgaria
{k.yovchev,eck}@fmi.uni-sofia.bg
[2] Institute of Mechanics, Bulgarian Academy of Sciences, Sofia, Bulgaria
kamen@imbm.bas.bg

**Abstract.** This paper uses simulation to investigate the convergence and the accuracy of the Bounded Error Algorithm (BEA) for Iterative Learning Control (ILC). The BEA resolves the problem of transient growth of the tracking error that appears as one main problem of the nonlinear ILC procedure. This algorithm ensures that trajectory-tracking errors are constrained by an upper limit of a given error norm. The results from a computer simulation of a PUMA 560 robot arm are hereby analysed. The overall convergence rate of the learning control method is evaluated subject to the precision of the differential equation solver and the influence of deterministic disturbances. The numerical procedures of this method are presented in a way suitable for implementation in real industrial robotics.

**Keywords:** Nonlinear iterative learning control · Transient growth · Robotic manipulator · Computer simulation

## 1 Introduction

A large number of industrial robotic arms are executing repeating trajectories during their everyday operation. The accuracy of their movement can be improved by using an Iterative Learning Control (ILC) procedure.

ILC for robotic arms is a class of self-tuning algorithms, which repeatedly implement assigned tasks of robot motions in order to minimize positioning or trajectory-tracking errors, implementation time, power costs or improve other motion characteristics. The trajectory-tracking ILC uses the data from the previous trial of a robot arm motion to update the feed-forward term of the control law for improving the trajectory tracking in the next trial [1–5].

In classical ILC the following postulates are required [2, 4], although some recently reported ILC algorithms eliminate or relax these postulates [3, 6]:

- Every trail has a fixed duration. In this paper we present a new bounded-error learning algorithm which does not satisfy this postulate.
- Repetition of the initial setting (initial state coordinates) is satisfied. This postulate has been also weakened by Heinzinger et al. in [3].

- Invariance of the system dynamics is ensured throughout the repetition.
- The system output is measured in a deterministic way.

The main advantage of a classical offline ILC is that it compensates trajectory errors caused by the imprecise dynamics model of the system (errors in the estimated dynamics parameters), and its deterministic disturbances. This control can automate the process of fine-tuning of the actual controllers. Another big advantage is that this method is performed offline, avoiding thus real-time computation of the updated input signals and simplifying the update law. There are, however, some disadvantages which can even make ILC inapplicable in real life operations. The first one relates to the convergence rate of the method. It is proven [3] that the convergence rate strictly depends on the choice of the learning operator in the ILC update law. The second problem which must be considered is the transient growth error. Despite the convergence of the ILC, the tracking performance at early iterations can result in a significant increase in tracking errors related to violating the constraints in the motion of the joints of the robotic arm. The ILC procedure cannot compete successfully in this case. Figure 1 shows the transient growth error problem in the computer simulation of ILC for PUMA 560.
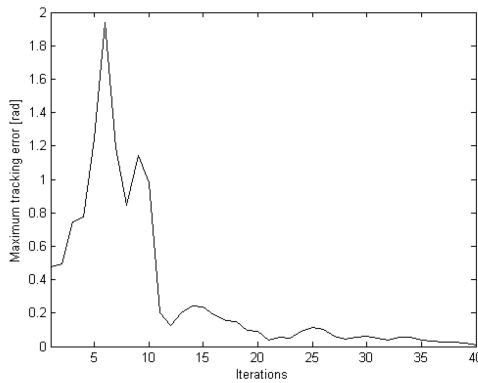


**Fig. 1.** Simulated PUMA 560 transient growth error

This paper proposes the Bounded Error Algorithm (BEA) [6] which can effectively resolve the transient growth problem in ILC. The convergence and the accuracy of this algorithm are thoroughly analysed by means of computer simulation.

The paper is organized as follows: Sect. 2 describes the mathematical model of PUMA 560 used for the creation of the computer simulation and formulates the problem. Section 3 proposes a solution by using BEA. Section 4 presents the results of the computer simulation.

## 2   Problem Formulation

Let us consider the well-known Puma 560 robot manipulator with 6 DOF (Fig. 2).
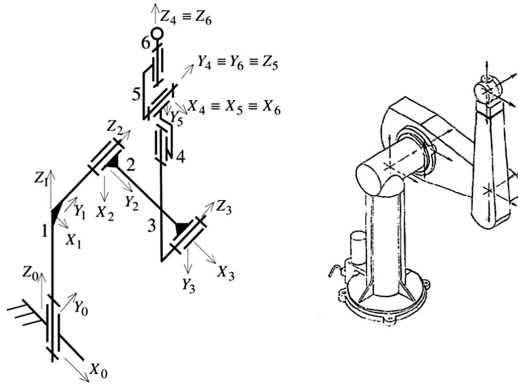
**Fig. 2.** Kinematic and design scheme of PUMA 560 robot [6]

Its nonlinear dynamic model based on the Lagrange's formulation of equation of motion in the space of generalized coordinates [6] is:

$$A(q)\ddot{q} + b(q, \dot{q}) + D\dot{q} + g(q) + f = u \tag{1}$$

where $q$ is the $6 \times 1$ vector of generalised coordinates (joint angles); $A(q)$ is the $6 \times 6$ symmetric positive-definite inertia matrix; the $6 \times 1$ vector $b(q, \dot{q})$ takes into account the Coriolis and centrifugal torques; $D = diag\{\delta_1, \cdots, \delta_6\}$ denotes the diagonal $6 \times 6$ matrix of the coefficients of viscous friction; $g(q)$ is the $6 \times 1$ vector representing gravity torques; $f = [f_1 sign(\dot{q}_1) \ldots f_6 sign(\dot{q}_6)]^T$ is the vector of coefficients of Coulomb friction, and $u = u_l + u_c$ is the $6 \times 1$ vector of generalized torques where $u_l$ and $u_c$ are feed-forward and feedback terms, respectively. The allowable set of generalized torques is a rectangular hyper-parallelepiped, where $u_i \in [-U_i^{max}, U_i^{max}]$. The modified Denavit–Hartenberg method [8] is applied to the structure in Fig. 2 to define the coordinate frames in the joints of the PUMA560 robot arm.

The control system shown in Fig. 3 is used for the purpose of simulation of the robot arm motion. It is based on a traditional computed torque control combined with an ILC scheme proposed in [6].

In Fig. 3, $P$ represents the robot arm; $C$ and $L$ are feed-back and feed-forward controllers, respectively; $M$ is the memory of the control system; the input trajectory $u_l$ is the feed-forward term of the control law $u$ in (1), and $l = 1, \ldots, N$ is the current
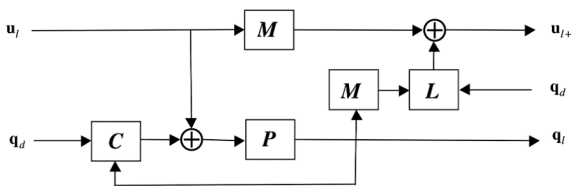


**Fig. 3.** Computed torque control scheme with ILC

iteration number; $q_l$ is the actual output trajectory; and $q_d$ is the desired output trajectory. The offline computed feed-forward term $u_{l+1}$ decreases the tracking error of the robot's motion on the next iteration.

The realization of the considered ILC scheme requires the specification of feed-forward and feedback controllers, respectively. The feed-forward controller is based on the update control law that improves the feed-forward control term:

$$u_{l+1} = u_l + L(q_l)[\ddot{q}_d - \ddot{q}_l + L_v(\dot{q}_d - \dot{q}_l) + L_p(q_d - q_l)] \qquad (2)$$

where $L(q_l(t)), l = 0, 1, \ldots, N$ is a learning operator; $u_0(t) \equiv 0$ is the initial feed-forward control input; the learning gains $L_p$ and $L_v$ are positive constants, $t \in [0, T]$ denotes time, where $[0, T]$ is the robot tracking time interval [6].

The feedback term is considered to be:

$$u_c = \widehat{A}(q)\left[\ddot{q}_d + K_v(\dot{q}_l - \dot{q}_d) + K_p(q_l - q_d)\right] + \hat{b}(q,\dot{q}) + \widehat{D}\dot{q} + \hat{g}(q) + \hat{f} \qquad (3)$$

where $q_l$ and $\dot{q}_l$, $l = 1, \ldots, N$ are respectively the feedback generalized coordinates and velocities of output trajectory; $\widehat{A}, \hat{b}, \widehat{D}, \hat{g}$ and $\hat{f}$ are the corresponding estimates of $A, b, D, g$ and $f$ from (1). The feedback gains $K_v$ and $K_p$ are positive constants [6].

The robustness and convergence of the ILC update law (2) is proven [3]. This learning controller will later be referred to as classical (standard) ILC. Previously established results [6, 9] show that good convergence rate will be achieved if the learning operator $L(q)$ is chosen to be the estimated inertia matrix of the robot $\hat{A}(q)$.

Let us consider the transient growth error problem in ILC. In the computer simulations of ILC it is common for the learning process to start with a fast increase of the trajectory error before it converges to a small value (Fig. 1), Most often this happens when controlling a real manipulator. It will actually stop the learning process because the robot will not be able to execute the desired trajectory. In this paper, this problem is solved by using the proposed BEA [9].

## 3 Bounded Error Algorithm

One possible way to solve the transient growth problem is to modify the standard ILC scheme and make use of the below defined BEA [6, 9]. Given an attainable target trajectory $y_d(t)$ and an error bound $\varepsilon$ the new algorithm for the implementation of the NILC procedure can be formulated as follows:

1. Set the initial iteration number $l$ to zero and begin the iterative procedure.
2. Starting from the initial position $y_l(0)$, the system is tracking the desired trajectory under the control $u_l(t)$ until $\left\|y_l(T_l^s) - y_d(T_l^s)\right\| \geq \varepsilon$ or the end position $y_l(T)$ is reached. In case the end position is not reached for $t = T_l^s$, $T_l^s \in (0; T]$, otherwise $T_l^s$ is equal to $T$ and the tracking process in the current iteration ends.
3. After the tracking has finished, the learning operator updates the feed-forward control term according to this new update law:

$$\boldsymbol{u}_{l+1}(t) = \boldsymbol{u}_l(t) + \boldsymbol{u}_l^* \tag{4}$$

$$\boldsymbol{u}_l^*(t) = \begin{cases} \widehat{\boldsymbol{A}}\,(\boldsymbol{q}_l(t))\,[\ddot{\boldsymbol{q}}_d(t) - \ddot{\boldsymbol{q}}_l(t) + L_v(\dot{\boldsymbol{q}}_d(t) - \dot{\boldsymbol{q}}_l(t)) \\ \quad + L_p(\boldsymbol{q}_d(t) - \boldsymbol{q}_l(t))], & t \in [0; T_l^s] \\ 0, & t \in (T_l^s; T] \end{cases} \tag{5}$$

4. If the output error is less than or equal to an acceptable value, exit from the learning process, else set $l = l + 1$ and go to step 2.

The execution time of each one of the iterations may vary although all the controls $\boldsymbol{u}_l(t)$ are defined over the whole interval of time $t \in (0; T]$ where the motion control takes place. This algorithm effectively solves the problem of the transient growth of the error by preventing it from occurring. The convergence of this method is proven in [9] and it can be used not only in the computer simulation but also in real life operations.

## 4 Simulation Results

A computer simulation of PUMA 560 was done to evaluate the performance of the Bounded Error Algorithm. This robot is widely used in research as common basis for comparison of the results obtained by testing the performance of algorithms for robot arm motion control. A couple of different estimations of the parameters of its dynamics are available.

Our simulation for motion control and the learning procedure make use of a slightly modified version of the dynamics parameters initially proposed by Armstrong in 1986 [7]. The modification of the dynamics parameters is introduced by Tarn [10]. This allows taking in consideration the errors due to imprecise modelling of the robot arm dynamics in a simulation procedure applying BEA for resolving the transient growth error problem [6].

The convergence of this algorithm for presented simulation parameters of PUMA 560 model is proven in [6].

The computer simulation of the algorithm was done on MATLAB R2013a. The first objective of the simulation was to investigate whether the choice of an ordinary differential equation (ODE) solver integrated in MATLAB influences the convergence rate of the algorithm. The examined solvers are "ode45", "ode23" and "ode113". As stated in the MATLAB documentation [11] the first two are based on Runge-Kutta's method, and the third one is Adams' method and they provide different order of accuracy.

The second test examines the convergence rate of the algorithm when the motion control is subject to disturbances. The simplest way to estimate it is to run the procedure in the presence or absence of Coulomb friction. The third test investigates the convergence rate subject to different values of the learning gains.

The initial values of the feedback and learning gains are: $K_p = 9$, $K_v = 3$, $L_p = 1$ and $L_v = 5$. The iteration number during all tests was limited to 40 and unless stated otherwise the value of $\varepsilon$ for the BEA is 0.5 rad. The desired trajectory is set to:

$$\left| \begin{array}{l} q_{d,1}(t) = q_{d,6}(t) = 0, q_{d,2}(t) = -2\cos(t) + 2 \\ q_{d,3}(t) = -\cos(t) + 1, q_{d,4}(t) = -3\cos(t) + 3 \\ q_{d,5}(t) = -1.5\cos(t) + 1.5, t \in [0; 2\pi] \end{array} \right. \tag{6}$$

The maximum tracking error for iteration $l$ is equal to $\max_{t\in[0;2\pi]} ||\boldsymbol{q_d}(t) - \boldsymbol{q_l}(t)||$.

Figure 4a shows a comparison between the simulation implementations of the classical ILC and the BEA. Their convergence rate is almost the same. The maximum tracking error of the classical ILC, however, is almost 2 radians. This may cause violation of the constraints of the generalized coordinates of the robot arm and make impossible in practice the further continuation of the standard ILC procedure.
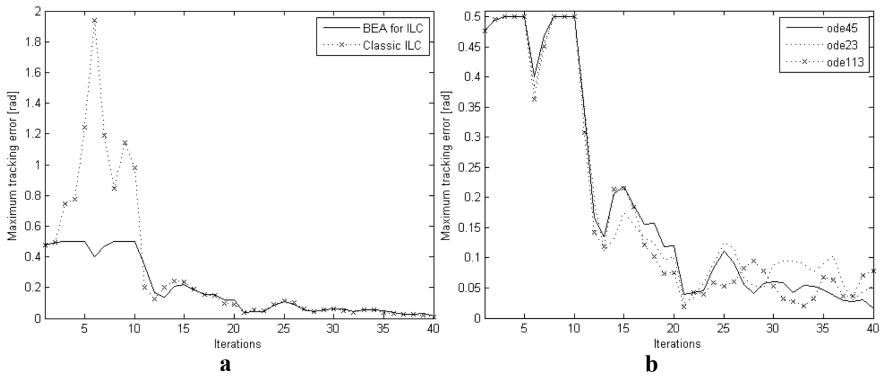


**Fig. 4.**  a. BEA vs. classical ILC; b. ODE solvers comparison

The result from the test of the influence of the ODE solver choice in MATLAB over the convergence rate of BEA is shown in Fig. 4b; the simulation procedure demonstrates that the convergence rate is independent on the choice of an ODE solver. All the three ODE solvers available in MATLAB achieve low error at iteration 12, whereas the maximum tracking error gets below 0.05 at iteration 21. It is noteworthy that when there are disturbances the ILC never converges to true zero, and the error increases in the subsequent iterations. This illustrates the importance of step 4 in the BEA, where the execution of the algorithm ends in case the desired accuracy is achieved. Higher absolute and relative accuracy of the ODE solvers result in increased computing time; however there are no significant changes in the convergence rate. In addition, here is a rather subjective statement - the "ode23" takes a lot more time for computing than the others.

The next objective in our investigation is to compare how the standard ILC and the BEA learning methods deal with disturbances. The friction forces are an example of the deterministic disturbances that exist in any real robot manipulator. The test results, shown in Fig. 5a, prove that the transient growth problem has negligible effect on the motion control when the disturbances are ignored. In such case the tracking errors are smaller and the convergence rate is higher.
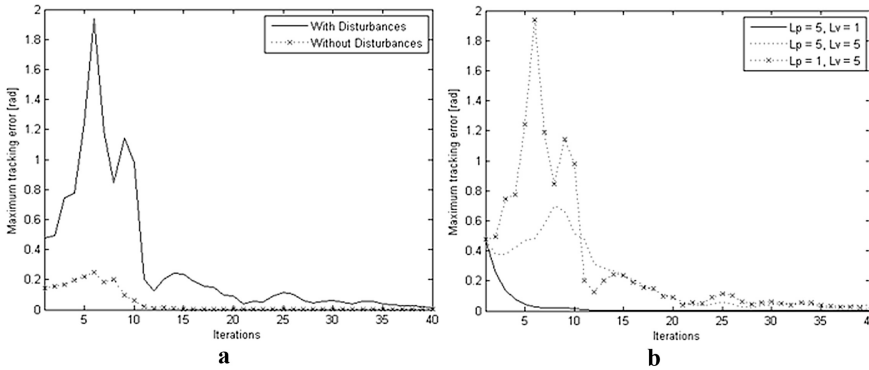
**Fig. 5.** (a) Classical ILC convergence in presence or absence of disturbances (b) Different values of the learning gains for ILC

Next, the influence of the different values of $L_p$ and $L_v$ for the convergence of both the standard ILC and the BEA are simulated by using the ideas proposed in [12]. The simulation results prove that the ILC convergence rate is monotonically increasing and faster when the value of $L_p$ is significantly larger than the value of $L_p$ (Fig. 5b). Additionally, we observe transient growth error problems when $L_v$ is larger than $L_p$. In all three test cases the ILC proves to be convergent and the desired accuracy is obtained for a finite number of iterations.

## 5    Conclusion

This paper presents MATLAB simulation results proving that the proposed Bounded Error Algorithm can effectively reduce the maximum trajectory error and resolve the transient growth problem inherent to ILC implementations. It enables the use of the ILC in real life applications. The computer simulations establish that the convergence rate of the BEA is not influenced substantially by the choice of the MATLAB ODE solver in the simulation procedure. A comparison of simulation tests with different MATLAB ODE solvers show that the "ode45" ODE solver provides the highest ILC convergence rate. This solver will be used in further tests and simulations.

Another important point is that when there are any deterministic disturbances the learning procedure must be stopped once the desired accuracy is achieved (as stated in Step 4 of the algorithm). Otherwise, the execution of the procedure starts to oscillate around the achieved average error. Obviously, the tracking error will be nonzero in the presence of disturbances (Coulomb friction). Another very important point for the learning process in order to be efficient is how the learning gains are chosen if the proposed learning operator is used. For the test scenarios in this computer simulation best results are achieved when the value of $L_p$ is significantly larger than the value of $L_v$.

Finally, in order to achieve applicability, greater convergence rate and accuracy of the ILC procedure, there is reasonable compliance with the following conclusions:

- Despite of the ILC robustness the deterministic disturbances, like Coulomb friction, should be minimized.
- The learning gains $L_P$ and $L_v$ could be tuned by computer simulation [12].
- By using the Bounded Error Algorithm, the Iterative Learning Control can be applied easily and safely on a real robotic manipulator system to reduce unacceptable initial or transient errors.

# References

1. Arimoto, S., Kawamura, S. and Miyazaki, F.: Bettering operation of dynamic systems by learning: a new control theory for servomechanism of mechatronics systems. In: Proceedings of 23rd Conference on Decision and Control, Las Vegas, NV, pp. 1064–1068 (1984)
2. Ahn, H.-S., Moore, K.L., Chen, Y.: Iterative Learning Control Robustness and Monotonic Convergence for Interval Systems. Springer, London (2007)
3. Heinzinger, D., Fenwick, B., Paden, B., Miyazaki, F.: Robust learning control. In: Proceedings of 28th Conference on Decision and Control, Tampa, FL, pp. 436–440 (1989)
4. Ahn, H.-S., Bristow, D.A.: Special issue on iterative learning control. Asian J. Control **13**(1), 1–2 (2011)
5. Longman, R.W.: Iterative learning control and repetitive control for engineering practice. Int. J. Control **73**(10), 930–954 (2000)
6. Delchev, K.: Iterative learning control for robotic manipulators: a bounded-error algorithm. Int. J. Adap. Control Signal Process. **28**, 1454–1473 (2014)
7. Armstrong, B., Khatib, O., Burdick, J.: The explicit dynamic model and inertial parameters of the Puma 560 arm. In: Proceedings of IEEE International Conference on Robotics and Automation, vol. 1, pp. 510–518, San Francisco, USA (1986)
8. Craig, J.J.: Introduction to Robotics: Mechanics and Control. Addison-Wesley, Reading (1985)
9. Delchev, K.: Iterative learning control for nonlinear systems: a bounded-error algorithm. Asian J. Control **15**(3), 1–8 (2013)
10. Tarn, T.J., Bejczy, A.K., Han, S., Yun, X.: Inertia parameters of puma 560 robot arm, Technical report SSMRL-85-01, Washington University, St. Louis, MO, September 1988
11. Ordinary Differential Equations from MATLAB Online Documentation; Available at http://www.mathworks.com/help/matlab/math/ordinary-differential-equations.html. Accessed 24 January 2016
12. Delchev, K.: Simulation-based design of monotonically convergent iterative learning control for nonlinear systems. Arch. Control Sci. **22**(**LVIII**)(4), 371–384 (2012)

# Dynamical Modeling and Swing-Up Control of a Self-balancing Cube

Hubert Gattringer[1(✉)], Alexander Reiter[1], Christoph Stöger[1], Matthias Jörgl[1,2], Philip Hörmandinger[1], and Andreas Müller[1]

[1] Institute of Robotics, Johannes Kepler University Linz,
Altenbergerstraße 69, 4040 Linz, Austria
{hubert.gattringer,alexander.reiter,christoph.stoeger,
matthias.joergl,philip.hoermandinger,a.mueller}@jku.at
[2] Trotec GmbH, 4614 Machtrenk, Austria
http://www.robotik.jku.at

**Abstract.** In this paper a balancing cube is presented. Driven flywheels are used as actuators for the balancing control. The cube is additionally equipped with an IMU measuring the orientation and rotational velocity of the cube. The control is done on an embedded control system. Based on the kinematical and dynamical modelling, two methods for swing-up of the cube are presented. The first one makes use of pre-defined trajectories, while for the second one a time/energy optimal solution subject to technological constraints is performed. Proportional control laws based on velocities and orientation measurements are used for stabilization. To demonstrate the effectiveness of the test bench, experimental results are shown.

**Keywords:** Dynamical modelling · Robotics · Optimal control · Inverted pendulum

## 1 Introduction

Inverted pendulums are interesting devices in robotics and are often used as reference models in control theory. These models can be realized as a rotating unit (Furuta) or as a pendulum on a moving cart. However, also flywheels can be utilized for the stabilization of such under-actuated devices. These reaction wheels are typically used, for instance, for attitude control in spacecrafts and satellites. Therein, three wheels are mounted with mutually perpendicular axes. By varying the speed of a wheel, a reaction torque is applied to the supporting structure. In this work, we employ a similar approach to stabilize a cube. In our case, the inverted wheel cube serves as test hardware for non-linear control theory and optimization enabling use in education as well as research. The cube combines many sophisticated topics like non-linear dynamics, unstable positions, under-actuation, non-holonomic velocities, gyroscopic and inertia effects, amongst others. Similar cube stabilization projects are realized at ETH-Zürich [5],

(Cubli project) and in Stanford [4] (Hedgehog project), where the cube should be used for exploration of planets. Both of these two cubes use friction-based brakes to decelerate the flywheels. In contrast to that, our cube decelerates with the electrical motors, the mechatronic design of which can be found in [7]. With the three flywheels, the cube is able to apply a three dimensional torque vector. Therefore a mobile robotic device can be built by surrounding the cube with a ball.

## 2  Hardware Setup

A photo of the balancing cube in different situations can be seen in Fig. 1. The main parts of the hardware setup are three inertia wheels driven by 70 W EC45 Maxon motors. The motors are driven by custom-made power electronics since for swing-up experiments high current (up to 40 A) is required. Such devices are not available on the market. The orientation in terms of roll-pitch-yaw angles and the rotational velocity of the cube are measured with an Xsens MTi-30 inertial measurement unit. All the trajectory planning, control, communication, input output channels are done on a central computational unit (Beagle Bone Black) composed of a 1 GHz ARM processor. The implementation of the control concept is done with automatic code generation in the X2C-tool framework, see [1]. This allows for fast prototyping and protects against coding errors. The power supply is a 7-cell LiPo battery pack. All the parts are embedded in a carbon fiber-reinforced 3D printed frame. The result is a cube with a length of 0.16 m and an overall mass of 2 kg.
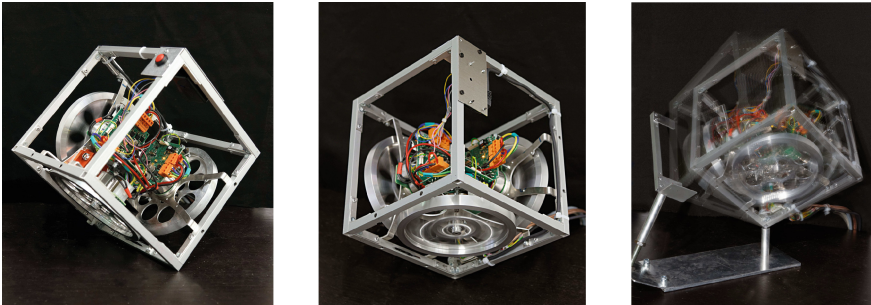


**Fig. 1.** Cube in different situations: (left) stabilizing on an edge, (middle) stabilizing on the tip, (right) swinging up from its rest position.

## 3  Mathematical Modelling

This section is divided into kinematic and dynamical modelling. The goal is to calculate the Equations of Motion (EoM) in a structured way. A basic assumption of the modelling is that the lower tip of the cube is fixed to the ground, see Fig. 2.

## 3.1   Kinematics

Due to the above assumption, the cube's pose can be fully described by its orientation. Here, roll $R$, pitch $P$, yaw $Y$ angles are used for a parametrization

$$\mathbf{q}_C = (R, P, Y)^T \qquad (1)$$

and serve as minimal coordinates of the cube. This parametrization is defined by a subsequent rotation about the $z$-axis (rotation matrix $\mathbf{R}_z$, angle $Y$), followed by the $y$-axis ($\mathbf{R}_y$,$P$) and the $x$-axis ($\mathbf{R}_x$,$R$) leading to a rotation matrix

$$\mathbf{R}_{CI} = \mathbf{R}_x(R)\mathbf{R}_y(P)\mathbf{R}_z(Y) \qquad (2)$$

that transforms vectors from the inertial frame $I$ to the cube-fixed frame $C$. Note, wheel angles do not enter the EoM and are therefore not part of the minimal coordinates (1). The choice of minimal velocities $\dot{\mathbf{s}}$ is not unique. In this paper we use the rotational velocity of the cube $\omega_C$ and the wheel velocities $\dot{\mathbf{q}}_W = (\dot{q}_{W,x}, \dot{q}_{W,y}, \dot{q}_{W,z})$
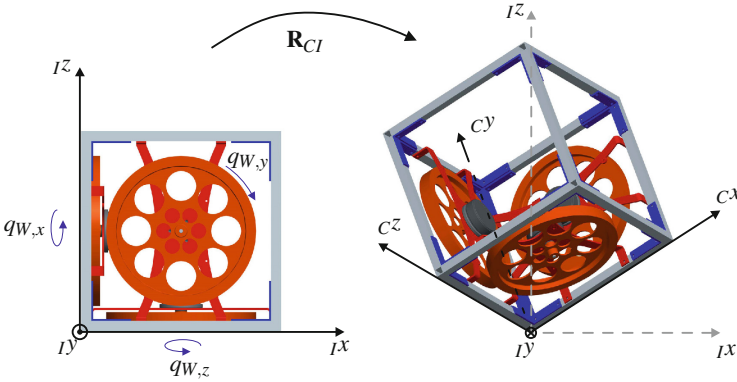


**Fig. 2.** Kinematic model

$$\dot{\mathbf{s}} = \begin{pmatrix} \omega_C \\ \dot{\mathbf{q}}_W \end{pmatrix}. \qquad (3)$$

The angular velocity $\omega_C$ is related to $\dot{\mathbf{q}}_C$ by the non-linear transformation

$$_C\omega_C = \underbrace{[\mathbf{e}_1 \quad \mathbf{R}_x(R)\mathbf{e}_2 \quad \mathbf{R}_x(R)\mathbf{R}_y(P)\mathbf{e}_3]}_{\mathbf{T}(\mathbf{q}_C)} \dot{\mathbf{q}}_C, \qquad (4)$$

($\mathbf{e}_i$..$i$th unit vector) resulting from the chosen sequence of rotation for RPY-angles. Note, rotational velocities $\omega_C$ are non-integrable. Therefore also $\dot{\mathbf{s}}$ are non-holonomic velocities which has to be considered in the dynamical modelling when choosing an appropriate method.

## 3.2   Dynamics

There are several methods to calculate the EoM for multibody systems. Bremer [2] gives a good overview. When using non-holonomic velocities, the Projection Equation (PE)

$$\sum_{i=1}^{N} \left[ \left( \frac{\partial_R \mathbf{v}_c}{\partial \dot{\mathbf{s}}} \right)^T \left( \frac{\partial_R \omega_c}{\partial \dot{\mathbf{s}}} \right)^T \right]_i \left( \begin{array}{c} (_R\dot{\mathbf{p}} +_R \widetilde{\omega}_{IR} \ _R\mathbf{p} - _R\mathbf{f}^e)_i \\ (_R\dot{\mathbf{L}} +_R \widetilde{\omega}_{IR} \ _R\mathbf{L} - _R\mathbf{M}^e)_i \end{array} \right) = 0 \qquad (5)$$

is well-suited, since non-holonomic velocities can be included a priori. The balance of linear $\mathbf{p} = m\mathbf{v}_c$ and angular momenta $\mathbf{L} = \mathbf{J}\omega_c$ are projected into the free motion directions via the appropriate Jacobians. Velocities $\mathbf{v}_c, \omega_c$ (translational, rotational) are expressed w.r.t. the centre of gravity of the bodies. $\omega_{IR}$ is the absolute rotational velocity of the chosen reference frame. In our case all values are associated with the cube fixed frame $C$, $R = C$. Since constraint forces do not influence motion they can be neglected a priori and only impressed forces $\mathbf{f}^e$ and torques $\mathbf{M}^e$ enter the PE. The sum over all $N$ bodies (wheels, IMU, battery, cube frame,...) delivers the EoM of the cube as

$$\underbrace{\begin{bmatrix} \mathbf{M}_1 \ \mathbf{M}_2 \\ \mathbf{M}_2 \ \mathbf{M}_2 \end{bmatrix}}_{\mathbf{M}} \underbrace{\begin{pmatrix} \dot{\omega}_C \\ \ddot{\mathbf{q}}_W \end{pmatrix}}_{\ddot{\mathbf{s}}} + \underbrace{\begin{pmatrix} \mathbf{h}_1(\mathbf{q}_C, \dot{\mathbf{s}}) \\ \mathbf{D}\dot{\mathbf{q}}_W \end{pmatrix}}_{\mathbf{h}(\mathbf{q}_C, \dot{\mathbf{s}})} = \underbrace{\begin{pmatrix} 0 \\ \mathbf{M}_{Mot} \end{pmatrix}}_{\mathbf{Q}} \qquad (6)$$

with the positive definite, symmetric mass matrix $\mathbf{M}$, the non-linear terms $\mathbf{h}$ and the generalized forces $\mathbf{Q}$. Due to our choice of the minimal velocities, this model has some interesting properties. First of all, the mass matrix is constant and consists of the two parts

$$\mathbf{M}_1 = {}_C\mathbf{J}^0 = {}_C\mathbf{J}_C{}^c + m_C\tilde{\mathbf{r}}_C\tilde{\mathbf{r}}_C^T + \sum_1^3 m_W\tilde{\mathbf{r}}_{W,i}\tilde{\mathbf{r}}_{W,i}^T \qquad (7)$$

$$\mathbf{M}_2 = \mathrm{diag}[J_W \ \ J_W \ \ J_W]. \qquad (8)$$

Matrix $\mathbf{M}_1$ is basically the inertia tensor of the overall system with respect to the lower tip of the cube $\mathbf{J}^0$, while $\mathbf{M}_2$ has diagonal form that contains the inertia parameter $J_W$ of the wheels in rotating direction. $\mathbf{J}_C^c$ is the inertia tensor of the cube w.r.t the centre of gravity. $m_C$ and $m_W$ are the masses of the cube and the wheels, respectively. Coriolis, centrifugal and gravitation forces are summarized in $\mathbf{h}_1$

$$\mathbf{h}_1(\mathbf{q}_C, \dot{\mathbf{s}}) = \tilde{\omega}_C[\mathbf{M}_1 \ \ \mathbf{M}_2]\dot{\mathbf{s}} + m_0\tilde{\mathbf{r}}_G\mathbf{g}, \qquad (9)$$

where $m_0$ is the overall mass, $\mathbf{r}_G$ the position vector to the centre of gravity and $\mathbf{g}$ represents the gravity vector. Viscous friction is included with damping matrix $\mathbf{D}$ and $\mathbf{M}_{Mot}$ are the driving motor torques of the three wheels. The second row in (6) is mainly the dynamics of the three wheels that is coupled to the under-actuated cube DoF (first row) via $\mathbf{M}_2$ in the mass matrix.

# 4   Trajectory Planning for Swing-Up

In the following, two methods for the swing-up of the cube are presented. Both methods are strongly model-based and use the mathematical models of the previous section.

## 4.1   Pre-defined R,P,Y Trajectories

Within the first method, trajectories for desired roll-pitch-yaw angles (index $d$) are defined

$$\mathbf{q}_{C,d} = \begin{pmatrix} R_d \\ P_d \\ Y_d \end{pmatrix} = \begin{pmatrix} R_S \\ P_S \\ Y_S \end{pmatrix} + \begin{pmatrix} R_E - R_S \\ P_E - P_S \\ Y_E - Y_S \end{pmatrix} \frac{t^3}{t_E^3}\left(10 - 15\frac{t}{t_E} + 6\frac{t^2}{t_E^2}\right), \qquad (10)$$

where $t_E$ is the chosen swing-up time. Each of the angles is planned from a start position $S$ to the end position $E$ (upper rest position) with e.g. polynomial functions. Appropriate bounds for velocities and accelerations have to be respected. With this pre-defined trajectories (10) and derivatives w.r.t time, rotational velocities $\omega_{C,d}$ and accelerations $\dot{\omega}_{C,d}$ of the cube can be evaluated with the kinematic model (4). In a next step, the desired accelerations of the wheels to bring the cube from the start to the end position can be calculated with the help of the EoM (first row)

$$\ddot{\mathbf{q}}_{W,d} = -\mathbf{M}_2^{-1}(\mathbf{h}_1(\mathbf{q}_{C,d}, \omega_{C,d}, \dot{\mathbf{q}}_{W,d}) + \mathbf{M}_1\dot{\omega}_{C,d}). \qquad (11)$$

Solving this differential equation by time integration (e.g. ode45 solver) delivers the desired wheel velocities $\dot{\mathbf{q}}_{W,d}$. Thus, feedforward torques required for swing-up can be computed from the EoM (second row) to

$$\mathbf{M}_{Mot,d} = \mathbf{M}_2\dot{\omega}_{C,d} + \mathbf{M}_2\ddot{\mathbf{q}}_{W,d} + \mathbf{D}\dot{\mathbf{q}}_{W,d}. \qquad (12)$$

Therefore, all necessary values $\mathbf{q}_{C,d}, \omega_{C,d}, \mathbf{q}_{W,d}, \mathbf{M}_{Mot,d}$ are evaluated and can be used for feedback control. Plots for $\mathbf{q}_{C,d}$ and $\mathbf{M}_{Mot,d}$ can be seen in Fig. 3. The swing-up time $t_E = 0.9$ s is chosen so that the maximum torque of 1 Nm (dashed line in Fig. 3) is not violated.
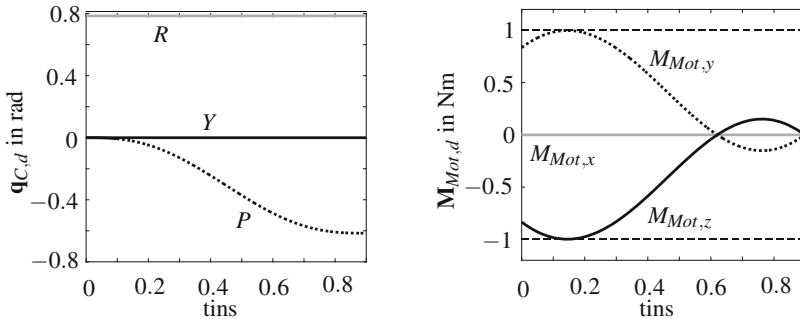


**Fig. 3.** Desired pre-defined trajectories for swing-up

### 4.2   Optimal Swing-Up Trajectories

In Sect. 4.1 a strategy for swing-up of the cube is presented. It is based on pre-defined trajectories and a chosen swing-up time not to exceed physical constraints. This method can be improved using optimization techniques. Therefore we are looking for time/energy optimal swing-up trajectories subject to constraints. The following optimization problem can be formulated:

$$\underset{\mathbf{M}_{Mot}, t_E}{Minimize} \int_0^{t_E} 1 + k\mathbf{M}_{Mot}^T \mathbf{M}_{Mot} \; dt \tag{13}$$

subject to

$$|\dot{\mathbf{q}}_W| \leq \dot{\mathbf{q}}_{W,max} \tag{14}$$

$$|\mathbf{M}_{Mot}| \leq \mathbf{M}_{Mot,max} \tag{15}$$

$$\frac{d}{dt}\begin{pmatrix} \mathbf{q}_C \\ \dot{\mathbf{s}} \end{pmatrix} = \begin{pmatrix} [\mathbf{T}^{-1}(\mathbf{q}_C) \; 0]\dot{\mathbf{s}} \\ \mathbf{M}^{-1}(\mathbf{Q} - \mathbf{h}(\mathbf{q}_C, \dot{\mathbf{s}})) \end{pmatrix} \tag{16}$$

$$\mathbf{q}_C(0) = \mathbf{q}_{C,0} \qquad \dot{\mathbf{q}}_C(0) = 0 \qquad \dot{\mathbf{q}}_W(0) = \text{free} \tag{17}$$

$$\mathbf{q}_C(t_E) = \mathbf{q}_{C,E} \qquad \dot{\mathbf{q}}_C(t_E) = 0 \qquad \dot{\mathbf{q}}_W(t_E) = \text{free.} \tag{18}$$

The cost functional in Eq. 13 is a trade-off between time and energy optimal solution, weighted with parameter $k$. Inequality constraints (14) and (15) are the maximum wheel velocities $\dot{\mathbf{q}}_{W,max}$ and motor torques $\mathbf{M}_{Mot,max}$. Equality constraints are the EoM (6), and initial and final values for the cube pose, cube velocity and the wheel velocities. Note, the wheel velocities are chosen to be free within the constraints. We use MUSCOD II optimization software developed at the university Heidelberg. The software uses the well established direct multiple shooting method, see e.g. [6] for details. Figure 4 shows the optimized solution for the wheel velocities and the motor torques. The cube orientation looks similar to Fig. 3 and is therefore not depicted. The result is that two wheels start with a quite high velocity and are abruptly decelerated by the appropriate motor torques (right picture). The swing-up time for this optimized motion is $t_E = 0.6$ s.
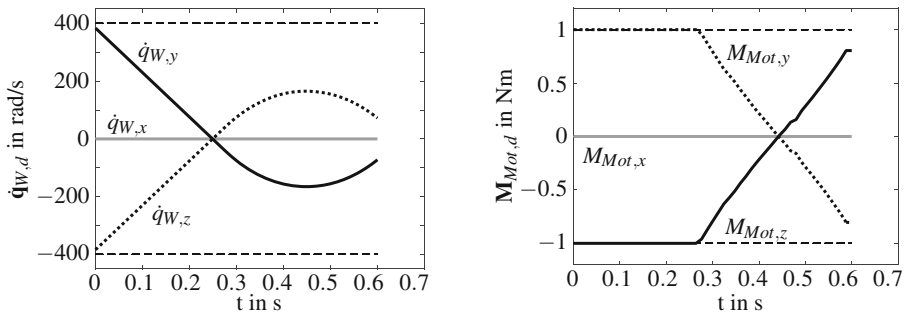


**Fig. 4.** Desired time/energy optimized trajectories for swing-up

## 5   Control

With the trajectory planning from the last section, desired values are available and can be used for control. Figure 5 shows the used control concept. The blocks *trajectory generation*, *feed forward control*, *trajectory calculation* have to be calculated offline.
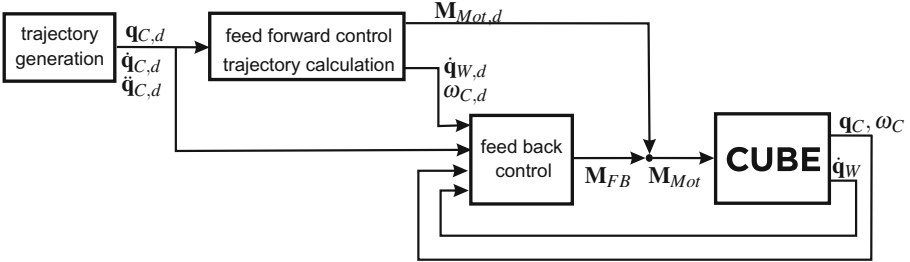


**Fig. 5.** Control scheme

The feedback control part consists of three parts

$$\mathbf{M}_{FB} = K_\omega(\omega_{C,d} - \omega_C) + K_D(\dot{\mathbf{q}}_{W,d} - \dot{\mathbf{q}}_W) + K_o\mathbf{e}_o. \tag{19}$$

The first two parts are proportional control for the cube velocity and the wheel velocities. $K_o\mathbf{e}_o$ introduces an rotational stiffness regarding the orientation of the cube. The orientation error $\mathbf{e}_o = \sin\varphi_e\mathbf{u}_e$ is the angle/axis representation $(\varphi_e, \mathbf{u}_e)$ of the rotation error matrix $\mathbf{R}_e = \mathbf{R}_{CI}\mathbf{R}_{IC,d}$ between actual and desired orientation, see [3] for details. Stability proof of the non-linear system is challenging. A linearisation of the non-linear controlled system (6) and (19) about the upper unstable position and calculation of the eigenvalues show that they have negative real parts and therefore stabilization is shown for this position.

## 6   Experimental Results

For the experiment, the cube starts from a rest position of $\mathbf{q}_{C,S} = (0.5, -0.6, 0)^T$ (realized by a starting ramp) and moves to an end position of $\mathbf{q}_{C,E} = (0.9, -0.6, 0)^T$ with the help of the trajectory planning method from Sect. 4.1. The results (measured orientation $\mathbf{q}_C$ and motor torques $\mathbf{M}_{Mot}$) can be seen in Fig. 6. The swing-up phase starts at $t = 1$ s and is followed by a stabilization phase. The experiment works satisfactorily.
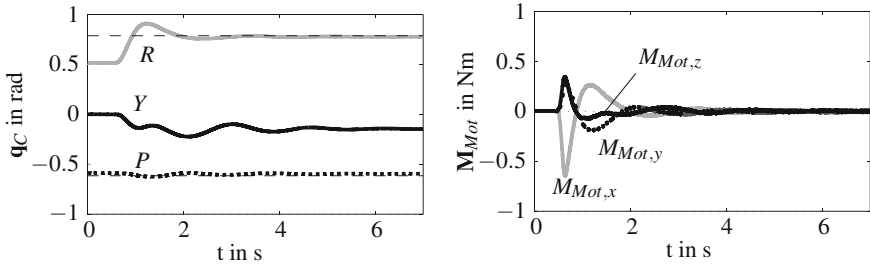
**Fig. 6.** Experimental results for swing-up

## 7   Conclusion

In this paper, a novel balancing cube is presented. The kinematical and dynamical EoM are analyzed and used for trajectory generation. Two methods for the swing-up from a start position to a unstable end position are compared. A spatial stiffness controller stabilizes this position very well as can be seen in the experimental results. Future work will be done in the design of further non-linear control concepts, mainly passivity based control. Additionally, the battery management for the swing-up procedure is an interesting topic and will be included in the optimization problem.

## References

1. X2c. www.mechatronic-simulation.org
2. Bremer, H.: Elastic Multibody Dynamics. Springer, Berlin (2008)
3. Caccavale, F., Natale, C., Siciliano, B., Villani, L.: Six-dof impedance control based on angle/axis representations. IEEE Trans. Robot. Autom. **15**, 289–300 (1999)
4. Falker, J.M.: Spacecraft/rover hybrids for the exploration of small solar system bodies. Ph.D. thesis, nasa (2012)
5. Gajamohan, M., Muehlebach, M., Widmer, T., D'Andrea, R.: The cubli: a reaction wheel based 3d inverted pendulum. IMU (2013)
6. Leineweber, D.: Efficient reduced sqp methods for the optimization of chemical processes described by large sparse dae models (1999)
7. Mayr, J., Spanlang, F., Gattringer, H.: Mechatronic design of a self-balancing three-dimensional inertia wheel pendulum. Mechatronics **30**, 1–10 (2015)

# A Synthesis of a Six Bar Mechanism with Nonlinear Stiffness for Prismatic Compliant Joint

Y. Ayoubi[1], M.A. Laribi[1(✉)], F. Courrèges[2], S. Zeghloul[1], and M. Arsicault[1]

[1] Department of GMSC, Prime Institute, CNRS, University of Poitiers, ENSMA, UPR 3346, Poitiers, France
{med.amine.laribi,said.zeghloul, marc.arsicault}@univ-poitiers.fr
[2] Xlim Institute – Team Mechatronics, University of Limoges, Limoges, France
fabien.courreges@unilim.fr

**Abstract.** A prismatic compliant joint (PCJ) composed of a linear spring and a six-bar mechanism is proposed in this paper. The operating principle of the PCJ is discussed and its mathematical model is established. The main contribution of the proposed PCJ lies in its nonlinear stiffness capability achieved thanks to only passive mechanical elements. An optimal synthesis of the six-bar mechanism with nonlinear stiffness is presented. A genetic algorithm approach (GA) is used in order to explore and identify optimal design solutions. A CAD model and a first prototype of the PCJ are presented.

**Keywords:** Six-bar mechanism · Optimal synthesis · Genetic algorithm · Nonlinear stiffness · Prismatic compliant joint

## 1 Introduction

Compliant devices generally consist of rigid links with compliant joints added in strategic locations in order to control the force or displacement. These devices present important advantages over traditional designs of rigid-body articulated joints, as they can: (i) store energy and provide restoring force and (ii) reduce the damage caused by accidental impact. Compliant devices with variable stiffness are preferable compared to those with a constant stiffness due to their safety aspect. This explains the increasing demand on compliant joints. Therefore, several types of compliant joints and flexible links have been proposed for safety. The compliance can be achieved either by passive or active variable stiffness. Active compliance based approach suffers from the relatively low bandwidth because it involves sensing and actuation in response to dynamics collision [1]. On the other hand, passive compliance is usually composed of completely mechanical elements such as a spring and a link to store energy and restore force. This approach does not utilize sensor or actuator, which can lead to a fast and reliable response.

In the literature, several variable stiffness mechanisms based on passive compliance have been developed. A popular method is to arrange two nonlinear springs in the

antagonistic setup [2, 3]. However, systems based on such springs tend to become complex and bulky. Torres-Jara and Banks [4] proposed a scalable force actuator with a simple transmission mechanism which consists of two pre-compressed springs connected to a motor with a cable. A variable stiffness actuator with nonlinear torque transmitting system composed of a spring and a 4-bar mechanism was developed in [5]. A compliance method in the drive system which mechanically decouples the heavy actuator inertia from the link inertia was also introduced in [6]. A safe joint mechanism (SMJ) in two versions was proposed by Jung-Jun Park [7, 8]. The SMJ is composed of linear springs and a double-slider mechanism. Other effective mechanisms are introduced in [9]. We notice that the most variable stiffness mechanisms developed in the literature are of rotary type; they are usually dedicated to revolute joints. The previously introduced approaches could be adapted to be of linear type with variable stiffness but this issue remains underexplored. The prismatic joint is rarely addressed. Only few linear variable stiffness mechanisms have been proposed [10–12]. This paper focuses on the development of mathematical formulations that allow the synthesis of planar six-bar mechanism associated with a linear spring in the aim to propose a new prismatic compliant joint. In particular, the main contributions are linked to the association of six-bar mechanism with a linear spring and the use of force transmission relationship in a mono-objective optimization.

The paper is organized as follows. The prismatic compliant joint definition is discussed in detail in Sect. 2. Section 3 presents the optimal synthesis of the six-bar mechanism with nonlinear stiffness, for which the objective function and the constraints are presented. In Sect. 4, a Genetic Algorithm approach is used to solve the synthesis problem. The CAD model as well as the first prototype of the PCJ are presented and discussed. Finally, Sect. 5 presents some conclusions and future work.

## 2 Prismatic Compliant Joint Definition

The prismatic compliant joint proposed in this paper is composed of a spring and a six-bar mechanism. This section deals with the kinematic model of the PCJ and the static study and behaviour law of the bars system in presence of an external force.

### 2.1 Kinematic Model

Figure 1 shows a general six-bar mechanism. When an external force $F_e$ acts on the output slider (link 5) along the y-axis, an appropriate force $F_R$ exerted on the input slider (link 1) is required for static equilibrium of this mechanism. Table 1 includes all parameters and variables that are used for detailed analysis of the six-bar mechanism.

All relationships between the input and output displacements are analysed by solving the set of following closed loop equations:

$$l_2 e^{i\theta_2} + l_3 e^{i\theta_3} = l_1 + a_4 e^{i\theta_4} \tag{1}$$

$$l_1 + a_4 e^{i\theta_4} + (d_4 - a_4 \sin\alpha) e^{i\left(\theta_4 + \alpha - \frac{\pi}{2}\right)} + b_4 e^{i(\theta_4 + \alpha)} = x_5 + iy_5 \tag{2}$$
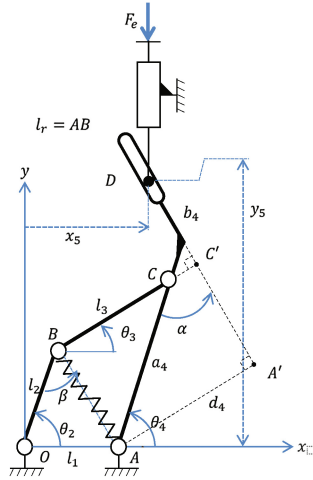
**Fig. 1.** Geometry of the six-bar mechanism

**Table 1.** The parameters and variables of the Prismatic Compliant joint

| | |
|---|---|
| $l_0$ | The initial length of the spring |
| $l_1$ | The distance between points O and A |
| $l_2$ | The crank |
| $l_3$ | The coupler |
| $a_4, d_4, \alpha$ | The rocker |
| $x_5, y_5$ | The position of point D |

If a value of the displacement $y_5$ (the input variable) of the slider is given, Eqs. (1) and (2) become the set of non-linear simultaneous equations with three unknown variables $\theta_2$, $\theta_3$ and $\theta_4$. The Forward Kinematic Model (FKM) of the six-bar mechanism can be defined by the angle $\theta_2$ as output and the displacement $y_5$ as input. The input displacement is defined by the following expression using the dyad equations:

$$y_5 = \left[ (x_5 - l_1) - \frac{d_4}{\cos(\theta_4 + \alpha)} \right] \tan(\theta_4 + \alpha) \tag{3}$$

Then, the angle $\theta_4$ can be expressed using the input variable $y_5$ as follows:

$$\theta_4 = -\alpha + atan2(l_1 - x_5, y_5) \pm acos\left( \frac{-d_4}{\sqrt{y_5^2 + (l_1 - x_5)^2}} \right) \tag{4}$$

Using Eq. (1), one can obtain two equations:

$$l_2 \cos \theta_2 + l_3 \cos \theta_3 = l_1 + a_4 \cos \theta_4 \qquad (5)$$

$$l_2 \sin \theta_2 + l_3 \sin \theta_3 = a_4 \sin \theta_4 \qquad (6)$$

In order to eliminate the passive joint variable $\theta_3$, we square and add these equations:

$$l_3^2 = l_1^2 + a_4^2 + l_2^2 - 2l_1 a_4 \cos(\theta_4) - 2l_2(l_1 + a \cos \theta_4) \cos \theta_2 - 2a_4 l_2 \sin \theta_4 \sin \theta_2 \qquad (7)$$

which can be written as:

$$A_1 \cos \theta_2 + B_1 \sin \theta_2 = C_1 \qquad (8)$$

with, $A_1 = -2l_2(l_1 + a_4 \cos \theta_4)$, $B_1 = -2l_2 a_4 \sin \theta_4$ and $C_1 = l_1^2 + a_4^2 + l_2^2 - l_3^2 + 2l_1 a_4 \cos \theta_4$

From the displacement of point D, the values of angle $\theta_2$ (see Fig. 1) can be obtained as follows:

$$\theta_2 = atan2(2l_2 a_4 \sin \theta_4, 2l_2(l_1 + a_4 \cos \theta_4)) \pm acos\left(\frac{C_1}{\sqrt{A_1^2 + B_1^2}}\right). \qquad (9)$$

The ($\pm$) sign corresponds to the two possible solutions for the crank OB. The values of angle $\theta_3$ can be obtained using the Eqs. (5) and (6) as follows:

$$\theta_3 = atan2(-l_2 \sin \theta_2 + a_4 \sin \theta_4, l_1 + a_4 \cos \theta_4 - l_2 \cos \theta_2) \qquad (10)$$

## 2.2 Static Force Analysis

This section presents a force analysis of the six-bar mechanism. It is important to understand how the mechanism will function under loaded conditions in practice. The force transmission relationship from the input link to the output link will be investigated in this section. Static force analysis makes direct use of static force equilibrium equations.

For an analytical solution formulation, the free-body diagram of each rigid body must be drawn. The unknown forces must also be identified. The system is in equilibrium under the action of the external force $F_e$ and the spring force $F_R$. The magnitude and direction of the force $F_e$ are known. In the next, we determine the relationship between forces acting on different links of the mechanism.

All free-body diagrams of the moving links are shown in Figs. 2, 3 and 4. On each diagrams the unknown joint force components are shown acting in the positive $x$ and $y$ directions.
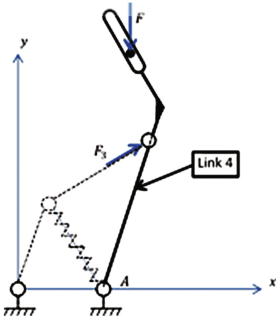
**Fig. 2.** The free-body diagrams of link 4
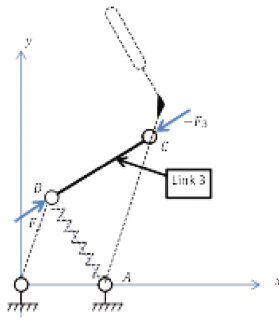


**Fig. 3.** The free-body diagrams of link 3
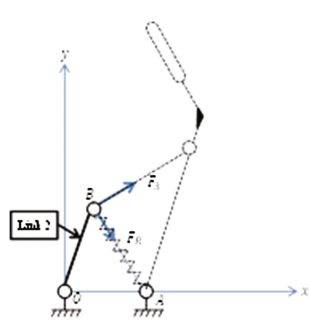


**Fig. 4.** The free-body diagrams of link 2

For link 4:

$$F_e \cos(\pi - \theta_4 - \alpha)(a_4 \cos \alpha + b_4) = F_3 a_4 \sin(\theta_4 - \theta_3) \tag{11}$$

For link 3, $F_3$ on C $\Leftrightarrow -F_3$ on B, and for link 2:

$$F_3 \sin(\theta_2 - \theta_3) = F_R \sin(\beta) = F_R \frac{l_1 \sin \theta_2}{l_R} \tag{12}$$

with, $l_R = l_1^2 + l_2^2 - 2l_1 l_2 \cos \theta_2$.

The relation between the external force and the spring force can be written as follows:

$$F_e = -F_R \frac{a_4}{a_4 \cos \alpha + b_4} \cdot \frac{l_1}{l_R} \cdot \frac{\sin(\theta_4 - \theta_3)}{\cos(\theta_4 + \alpha)} \cdot \frac{\sin \theta_2}{\sin(\theta_2 - \theta_3)} \tag{13}$$

with, $F_R = k(l_R - l_0)$, where k is the spring constant, $l_0$ the initial length of the spring and $l_R$ the length of the spring. If the pre-compressed spring is installed between points A and B, the spring force can offer the resisting force $F_R$, which resists the movement of slider caused by the external force $F_e$. When the external force is balanced against the spring force, the external force can be described in terms of the variable angles and the other geometric parameters as follows:

$$F_e = k(l_0 - l_R) \frac{a_4 l_1}{(a_4 \cos \alpha + b_4)l_R} \cdot \frac{\sin(\theta_4 - \theta_3)}{\cos(\theta_4 + \alpha)} \cdot \frac{\sin \theta_2}{\sin(\theta_2 - \theta_3)} \tag{14}$$

Also, $l_R$ is directly related to $\theta_2$ by the relation $l_R = l_1^2 + l_2^2 - 2l_1 l_2 \cos \theta_2$.

## 3   Optimal Synthesis of a Six-Bar Mechanism

### 3.1   Formulation of the Optimization Problem

The following optimization problem is considered for the desired function generated by the PCJ (six-bar mechanism + linear spring): find optimal dimensions of the mechanism so that the objective function has the minimum value. This defined optimization problem can be given by the following general mathematical formulation:

Minimise: $F(\mathbf{X}) = f(\mathbf{X}) + G(\mathbf{X}, \lambda_j)$

where $G(\mathbf{X}, \lambda_j)$ are the penalty functions which can be presented as:

$$G(\mathbf{X}, \lambda_j) = \left[ \sum_{j=1}^{n_g} \lambda_j \left( \max\left(0, g_j(\mathbf{X})\right) \right)^2 \right] \tag{15}$$

where $n_g$ is the total number of constraints, $g_j$ introduced in the objective function and $\mathbf{X} = [x_1, \ldots, x_N]^{\mathbf{T}}$ represents the design vector composed of $N$ design variables.

Design variables are the values that should be defined during the optimization procedure. Each design variable is defined by its lower and upper boundary. When the solution is found outside the region considered, then the current values of the constraints are squared and multiplied by large positive numbers (penalty factors) $\lambda_j$, and then added to the numerical value of the objective function.

### 3.2   The Objective Function and the Constraints

The objective function (the function to minimize) is defined by the expression:

$$f(\mathbf{X}) = f_e(\mathbf{X}) + \lambda_1 g_1^2 + \lambda_2 g_2^2 \tag{16}$$

The first member $f_e(\mathbf{X})$ in the given expression for the objective function represents a sum of squares of deviations, the second member $\lambda_1 g_1^2$ refers to the argument conditions verifying that a solution exists for the kinematic model, and the third member $\lambda_2 g_2^2$ refers to the Grashof conditions.

The objective function value $f_e(\mathbf{X})$ is defined as the sum of the squared distances between the i-th desired position of the reference point $(x_{5i}^d, F_i^d)$ and the respective position of the slider point D $(x_{5i}, F_{ei})$, computed according to the following equation:

$$f_e(\mathbf{X}) = \frac{1}{n} \sqrt{ \sum_{i=1}^{n} \left( F_i^d - F_{ei} \right)^2 + \left( x_{5i}^d - x_{5i} \right)^2 } \tag{17}$$

where $n$ is the number of selected points in an operating cycle. The constraints are defined as declared below.

(1) *Argument Conditions.*

If one structure is able to accomplish a configuration on the workspace, then the inverse kinematic expression of each arm has a solution for the considered

position of the slider. Using the Eqs. (4) and (8), we study the existence conditions on the argument of the inverse cosine as follows:

$$g_{11} = \begin{cases} H_{11} & \text{if } \left| \dfrac{d_4}{\sqrt{d_1^2 + (l_1 - x_5)^2}} \right| \leq 1 \\ 0 & \text{otherwise} \end{cases} \tag{18}$$

$$g_{12} = \begin{cases} H_{12} & \text{if } \left| \dfrac{C_1}{\sqrt{A_1^2 + B_1^2}} \right| \leq 1 \\ 0 & \text{otherwise} \end{cases} \tag{19}$$

Here, $H_{11}$ and $H_{12}$ are large positive constants.

(2) *Grashof Conditions*

The sum of lengths of the shortest and the longest members of the basic four-bar linkage (OBCA) must be smaller than the sum of lengths of the two remaining members.

The constraint referring to the Grashof conditions in Eq. (16) is $g_2$ and defined as:

$$g_2 = \begin{cases} |l_{\max} + l_{\min} - l_{r1} - l_{r2}| & \text{if } L > 0 \\ 0 & \text{otherwise} \end{cases} \tag{20}$$

where, $L = l_{\max} + l_{\min} - l_{r1} - l_{r2}$, $l_{\max} = \max(l_1, l_2, l_3, a_4)$, $l_{\min} = \min(l_1, l_2, l_3, a_4)$, $l_{r1}$ and $l_{r2}$ the lengths of the two remaining members.

## 4  Results and Discussion

### 4.1  Genetic Algorithm Method

To find the optimal design vector we suggest in this work the use of Genetic Algorithm (GA), method [13]. The idea for GA is originated from natural evolution consisting of generation, selection and mutation; GA is successfully applied in optimization tasks.

*Example*

The desired behaviour curve is given by the coordinates of 24 points, Table 2, corresponding to the values of the external force and the slider displacement respectively.

The parameters of the GA used in this work are shown in Table 3. They have been tested in the current simulation and seem reasonable considering the optimization results. The bounding intervals for each design variable are shown in Table 4.

**Table 2.** The external force $F_e$ as a function of $y_5$

|  | 1 | 2 | 3 | 4 | 5 | 6 | 7 | 8 | 9 | 10 | 11 | 12 |
|---|---|---|---|---|---|---|---|---|---|---|---|---|
| $y_5$[mm] | 0.6 | 1.3 | 2.4 | 3.7 | 5.3 | 7.2 | 9.2 | 11.4 | 13.7 | 16.2 | 18.7 | 21.2 |
| $F_e$[N] | 0.06 | 0.2 | 0.4 | 0.7 | 1 | 1.5 | 2.2 | 3 | 3.9 | 5 | 6.5 | 8.3 |
|  | 13 | 14 | 15 | 16 | 17 | 18 | 19 | 20 | 21 | 22 | 23 | 24 |
| $y_5$[mm] | 23.7 | 26.1 | 28.4 | 30.6 | 32.7 | 34.5 | 36.1 | 37.4 | 38.5 | 39.3 | 39.8 | 40 |
| $F_e$[N] | 10.4 | 12.8 | 15.7 | 18.9 | 22.5 | 26.5 | 30.6 | 34.7 | 38.6 | 42 | 44.3 | 45.1 |

**Table 3.** Parameters used for the GA

| Population size | Maximal generation number | n° of variables | Crossover fraction | Mutation rate |
|---|---|---|---|---|
| 100 | 250 | 9 | 0.7 | 0.03 |

**Table 4.** Bounding interval for design variables

| $l_0$[mm] | $l_1$[mm] | $l_2$[mm] | $l_3$[mm] | $a_4$[mm] | $x_5$[mm] | $d_4$[mm] | $\alpha$[°] | $k$[N/mm] |
|---|---|---|---|---|---|---|---|---|
| [10, 100] | [10, 100] | [10, 100] | [10, 100] | [10, 100] | [−50, 50] | [0, 100] | [0, 60] | [1, 10] |

The optimal mechanism obtained through GA optimization is presented in Table 5

**Table 5.** Optimization result for the six-bar mechanism

| **X** | $l_0$[mm] | $l_1$[mm] | $l_2$[mm] | $l_3$[mm] | $a_4$[mm] | $x_5$[mm] | $d_4$[mm] | $\alpha$[°] | $k$[N/mm] |
|---|---|---|---|---|---|---|---|---|---|
|  | 57 | 40 | 40 | 40 | 40 | 25 | 39 | 45 | 2.4 |

## 4.2 Prototype

To validate our proposed method, we present an example solved on a 2.7 GHz processor and implemented in Matlab®. In this proposed mechanism, the external force required to balance the spring force is defined as the critical force. For a given displacement $y_5$, a static balance is maintained when the external force equals the critical force equal to 0.06 N, as shown in Fig. 5, but the spring is rapidly compressed once the external force acting on this mechanism becomes greater than this critical value. Compliant behaviour of the PCJ is raised once the external force reaches the critical force. The modulation of the critical force value will be investigated in future work.

The external force and position signals are used to get, numerically under SimMechanics, the evolution curve of the mechanism stiffness, shown in Fig. 5, as a function of the linear actuator displacement, by using the following formula: $S = \frac{dFe}{dy_5}$.

A solid representation of PCJ, the six-bar mechanism with a linear spring, is shown in Fig. 6. The prototype of PCJ shown in Fig. 6 was constructed to conduct experiments related to the performance of PCJ and validate the desired behaviour.
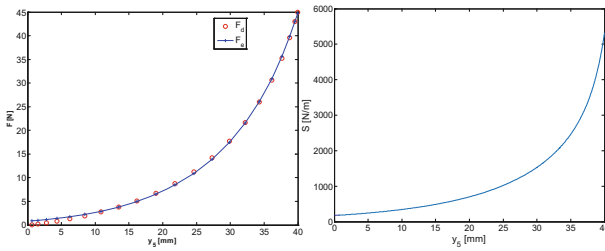
**Fig. 5.** $F - y_5$ curve of the proposed PCJ (left), $S - y_5$ curve of the proposed PCJ (right)
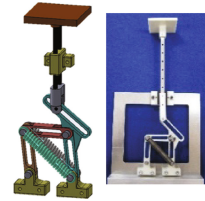


**Fig. 6.** A solid representation of PCJ (left); a prototype of PCJ (right).

## 5    Conclusion

This paper has presented the design and analysis of a prismatic compliant joint (PCJ) composed of a linear spring and a six-bar mechanism. The main contribution of this work is to propose a prismatic compliant joint rarely discussed up to now in the literature as compared to those producing rotary motion. The operating principle of the PCJ has been presented as well as its mathematical model. In addition, the nonlinear stiffness capability of PCJ is achieved only by passive mechanical elements.

An optimal synthesis formulation of the six-bar mechanism with nonlinear stiffness, solved using genetic algorithm approach was presented in the paper. The CAD model as well as the first prototype of the PCJ was realized and it behaves as expected.

Our future work includes static, dynamic, and control experiments to evaluate the variable stiffness performance. We expect the proposed mechanism to be applied in a device that requires nonlinear stiffness.

## References

1. Park, J.-J., Kim, B.-S., Song, J.-B., Kim, H.-S.: Safe link mechanism based on passive compliance for safe human-robot collision. In: 2007 IEEE International Conference on Robotics and Automation, pp. 1152–1157, 10–14 April 2007
2. Koganezawa, K., Inaba, T., Nakazawa, T.: Stiffness and angle control of antagonistically driven joint. In: Proceedings of the IEEE/RAS-EMBS International Conference on Biomedical Robotics and Biomechatronics, pp. 1007–1013 (2006)
3. English, C., Russell, D.: Mechanics and stiffness limitations of a variable stiffness actuator for use in prosthetic limbs. Mech. Mach. Theory **34**(1), 7–25 (1999)
4. Torres-Jara, E., Banks, J.: A simple and scalable force actuator. In: Proceedings of the 35th International Symposium on Robotics (2004)

5. Schiavi, R., Grioli, G., Sen, S., Bicchi, A.: VSA-II: a novel prototype of variable stiffness actuator for safe and performing robots interacting with humans. In: Proceedings of the IEEE International Conference on Robotics and Automation, pp. 2171–2176 (2008)
6. Zinn, M., Khatib, O., Roth, B., Salisbury, J.K.: A new actuation approach for human-friendly robot design. Int. J. Robot. Res. **23**(4/5), 379–398 (2005)
7. Park, J.-J., Kim, H.-S., Song, J.-B.: Safe robot arm with safe joint mechanism using nonlinear spring system for collision safety. In: IEEE International Conference on Robotics and Automation ICRA 2009, pp. 3371–3376, 12–17 May 2009
8. Park, J.-J., Kim, B.-S., Song, J.-B., Kim, H.-S.: Safe link mechanism based on nonlinear stiffness for collision safety. Mech. Mach. Theory **43**(10), 1332–1348 (2007)
9. Van Ham, R., Sugar, T., Vanderborght, B., Hollander, K., Lefeber, D.: Compliant actuator designs. IEEE Robot. Autom. Mag. **16**(3), 81–94 (2009)
10. Rodríguez, A.G., Chacón, J.M., Donoso, A.: Design of an adjustable-stiffness spring: Mathematical modeling and simulation, fabrication and experimental validation. Mech. Mach. Theory **46**, 1970–1979 (2011)
11. Wu, Y.-S., Lan, C.-C.: Linear variable-stiffness mechanisms based on preloaded curved beams. ASME J. Mech. Des. **136**(12), 122302 (2014)
12. Wu, T.-H., Lan, C.-C.: Design and analysis of a linear elastic mechanism with adjustable stiffness. In: The 14th IFToMM World Congress, Taipei, Taiwan, 25–30 October 2015
13. Goldberg, D.E.: Genetic Algorithms in Search, Optimization, and Machine Learning. Addison-Wesley Publishing, Massachusetts (1994)

# About the Accuracy of Fast Moving Robotic Devices Based on Compliant Mechanisms

Štefan Havlík[(✉)] and Jaroslav Hricko

Institute of Informatics, Slovak Academy of Sciences, Banská Bystrica, Slovakia
{havlik, hricko}@savbb.sk

**Abstract.** This paper deals with small and micro - size robotic devices with strict requirements on the accuracy of prescribed motions/trajectories. The kinematic mechanisms of such positioning devices are usually made as compact elastic structures and the key problem is to guarantee the desired accuracy especially in high frequency modes of operation. The deflection effects and influence of different stiffness and damping coefficients in particular d.o.f. are analysed. The dynamics of a case system is simulated and performance characteristics are discussed.

**Keywords:** Compliant mechanisms · Accuracy · Dynamics · Modelling · Simulation

## 1 Introduction

Several applications of robotic systems, mainly in microelectronics and optoelectronics, require new task oriented robotic devices that exhibit specific performance features. There is especially high accuracy of motion trajectory at high frequency of motions that can reach several tents, or, hundreds of cycles per second.

As obvious, the classic constructions of such devices are hardly realizable. The single solution lies in designing elastically compliant mechanisms and using appropriate manufacturing technology. The mechanisms made from one piece of elastic material allow miniaturizing dimensions and making small or micro scale structures. Naturally, the design of compliant mechanical structures supposes using techniques for force and compliance analysis, modelling and simulation of their characteristics and performances in static and dynamic modes of operations.

There are books and numerous papers dealing with description, design and analysis of elastic joints arms and compliant kinematic mechanisms [1–3, 7, 9]. A great number of mechanisms were designed for purposes of high-accuracy positioning devices [7–9]. A specific class represents the x−y mechanisms for task-oriented positioning devices [10–12]. On the other hand, there is relatively rare literature analysing devices and their complex performance characteristics from the mechatronic point of view.

This paper deals with problems of accuracy of multi degrees of freedom (d.o.f) devices at higher frequency modes of motions. The study evaluates characteristics that describe errors of the end part and influence of different stiffness and damping parameters in particular directions.

## 2   Accuracy Errors

Comparing compliant mechanisms with classic robotic mechanisms there are a number of possible sources of errors that should be taken into account. Here, the end position is given by deflections of particular joints/links and the flexural characteristics of the mechanical structure as a whole. A crucial problem in designing precise mechanisms lies in not exactly knowing flexural effects that deteriorate the final accuracy of the end element. Thus, the compliance/stiffness characteristics of the kinematic flexure have dominant influence on the behaviour, kinematic accuracy and dynamics of the whole mechanisms.

For the calculation of flexural displacement of any part and the whole mechanism, one accepts the basic assumption that all local strains are small and fit within the validity of Hooke's low. Then, the flexure behaves as a linear force – deflection system with validity of the superposition principle.

The flexural characteristics of a joint/segment in the structure can be expressed

$$d = C \cdot L \text{ or } L = K \cdot d \tag{1}$$

where, in general, d is the six-component deflection vector, L is the load vector that consists of force and torque components, C and K = $C^{-1}$ are the $(6 \times 6)$ compliance and stiffness matrices respectively, all related to the joint reference system Oj(x,y,z) [1, 4].

Based on the superposition principle the end deflection/positional error will respect arrangements of the kinematic structure. Thus, the end position/deflection for serial chains will be:

$$e_H = \sum_{(j)} T_{jH} \cdot d_j = \sum_{(j)} T_{jH} \cdot C_j \cdot (T_{jH})^T \cdot L_H \tag{2}$$

and for parallel arrangement of elastic segments (see Fig. 2b):

$$e_H = \left[ \sum_{(j)} T_{jH}^T \cdot K_j \cdot T_{jH} \right]^{-1} \cdot L_H \tag{3}$$

where $T_{jH}$ is the transformation matrix that relates the joint j - reference system to the references in H.

The expression for errors in a compound structure combines calculations of errors for both serial and parallel parts of the mechanisms related to the end reference system. Under the above assumptions, applying the SVD (Singular Value Decomposition) method it is possible to evaluate and to compare "the kinematic quality" of particular joints, elastic segments and the mechanisms, as a whole [5].

For slowly moving mechanisms the errors mainly due to cross compliance effects represent quasi-static departures from desired positions and can be easily compensated by feed-forward modes using compliance models of the mechanisms [5, 6].
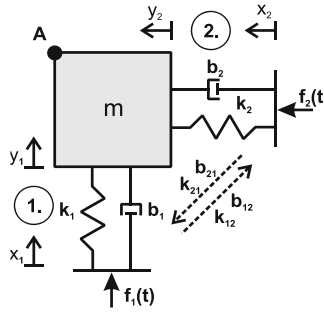
**Fig. 1.** The scheme of the 2-d.o.f. mechanical system

A more complex situation arises in the case of fast moving mechanisms, where in addition to the stiffness and damping parameters their mutual couplings in particular d.o.f. should be considered.

To show this dependence, the brief and simple simulation of the 2-d.o.f. mechanisms, as depicted in Fig. 1, is discussed below. The mechanically coupled system is represented by the parameters: $m$ - mass, $k_1$ and $k_2$ - the stiffness coefficients and $b_1$, $b_2$ - the damping coefficients in equations for particular directions of motion; $y_1$, $y_2$ and $k_{12}$, $k_{21}$ and $b_{12}$, $b_{21}$ are coefficients that represent mutual couplings.

Let us consider this mechanical system with two input variables x1 and x2 described by the equation:

$$\begin{bmatrix} m & 0 \\ 0 & m \end{bmatrix} \begin{bmatrix} y_1''(t) \\ y_2''(t) \end{bmatrix} + \begin{bmatrix} b_1 & b_{12} \\ b_{21} & b_2 \end{bmatrix} \begin{bmatrix} y_1'(t) \\ y_2'(t) \end{bmatrix} + \begin{bmatrix} k_1 & k_{12} \\ k_{21} & k_2 \end{bmatrix} \begin{bmatrix} y_1(t) \\ y_2(t) \end{bmatrix}$$
$$= \begin{bmatrix} b_1 & b_{12} \\ b_{21} & b_2 \end{bmatrix} \begin{bmatrix} x_1'(t) \\ x_2'(t) \end{bmatrix} + \begin{bmatrix} k_1 & k_{12} \\ k_{21} & k_2 \end{bmatrix} \begin{bmatrix} x_1(t) \\ x_2(t) \end{bmatrix} \tag{4}$$

in matrix form

$$m\ddot{y} + B\dot{y} + Ky = B\dot{x} + Kx \tag{4'}$$

where $K$ is the stiffness matrix and $B$ is the damping matrix where non-diagonal elements represent the cross/transversal sensitivities.

Performing simulation, actual positions and the end/output trajectory of $A$ point are observed and departures from the desired input variables are evaluated. As input variables x1(t), x2(t) two trajectories in rectangular (Fig. 2a, b) and circular (Fig. 3) forms were chosen. For the purpose of this simulation the same control parameters were chosen in both directions respecting the given range of operation frequency/time period. The transmit functions are on top of Fig. 2a, b. The motion trajectories of the x −y positioning system for different speeds of motions/decreasing time period T are depicted in Fig. 2a. For the same system working with motion period T = 8 s the influence of different stiffness and damping coefficients in particular directions are shown in Fig. 2b.
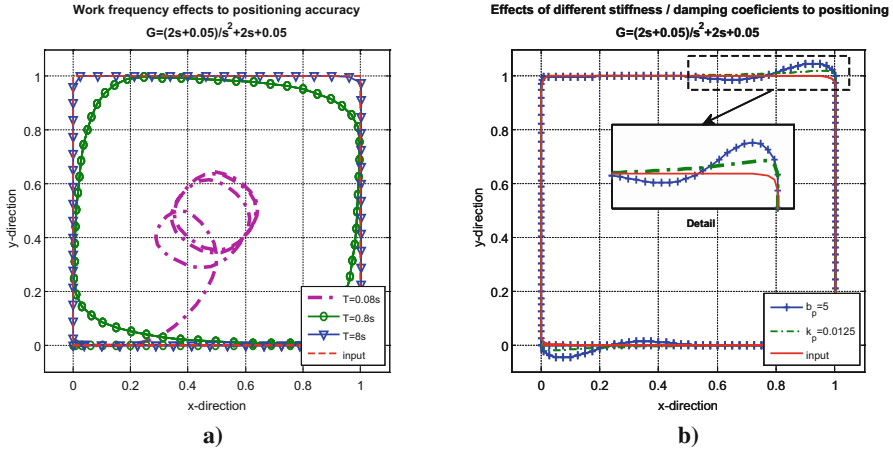
**Fig. 2.** Motion trajectories: (a) Decreasing time period; (b) Influence of different stiffness and damping coefficients; $k_p = k_1/k_2$, $b_p = b_1/b_2$
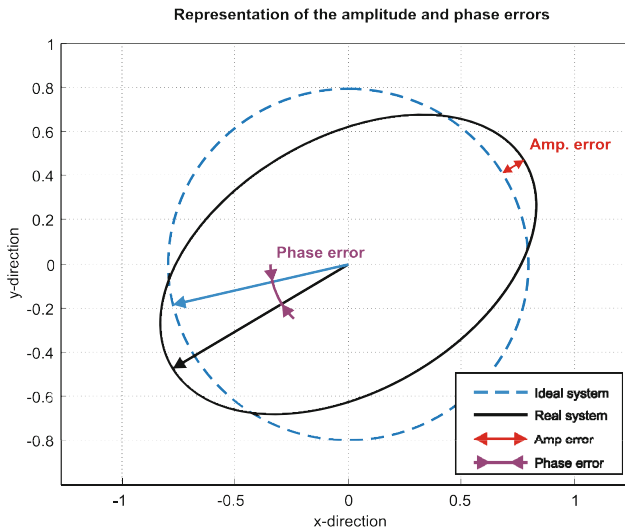


**Fig. 3.** Representation of the amplitude and phase errors

For the first simulation experiment, the parameters of the mechanisms in both directions are equal. As can be seen in Fig. 2a, the change of the operation speed towards the higher values (smaller time period T) results in increasing errors and the system will collapse approximately at T = 0,08 s.

Another situation appears when parameters of the mechanism are different in x and y directions, as shown in Fig. 2b. It is observed that the big differences between stiffness and damping coefficients in particular directions result in non-negligible errors that deteriorate the accuracy of the motion trajectories in higher speed modes. This fact,

especially the influence of different damping parameters, is not satisfactory solved in literature and it is frequently neglected in the design process.

In reality, due to cross flexural effects of elastic segments the compliant mechanisms should be considered as mechanically coupled systems, i.e. the coupling coefficients $k_{12}$, $k_{21} \neq 0$ and $b_{12}$, $b_{21} \neq 0$. This means practically that any desired displacement of the mechanisms is corrupted by other superimposed static and dynamic errors. In order to minimize this influence, the complex compliant mechanisms are usually designed symmetrically. As discussed below, the influence of cross flexural effects and differences of stiffness and damping parameter should be taken into account.

Let us express now the errors due to system dynamics. For examination of dynamic behaviour, frequency transfer functions are frequently used. The frequency transfer function $G(j\omega)$ that consists of an amplitude part $A(\omega)$ and phase part $\varphi(\omega)$ has the general form:

$$G(j\omega) = A(\omega)e^{j\varphi(\omega)} \tag{5}$$

In this paper, the errors in the frequency domain are taken as the differences between amplitudes and phases of the desired "ideal mechanical system" (index $i$) and a real system (index $0$) under acting the same harmonic input signals

$$e_A = A_0(\omega) - A_i(\omega), \text{ and } e_\varphi = \varphi_0(\omega) - \varphi_i(\omega) \tag{6}$$

The amplitude and phase errors for a planar mechanism are depicted in Fig. 3. The ideal system (dashed line) represents the mechanisms where corresponding stiffness and damping coefficients in both moving axes have exactly the same values, i.e. when for both ratios: $k_p = k_1/k_2 = 1$, $b_p = b_1/b_2 = 1$, and $k_{12}$, $k_{21} = 0$, $b_{12}$, $b_{21} = 0$.

## 3  Modelling Compliant Mechanisms

In general, the multi d.o.f. positioning mechanisms can be considered as the "mass-spring-damper" system represented by linear matrix Eq. (5).

Following previous discussion the task is to study the behaviour of such a complex system performing desired trajectories at higher frequency modes.

### 3.1  Mathematical Models

Using accepted notations for an "ideal" – mechanically decoupled mechanism one can state in Eq. (5): $k_{12} = k_{21} = 0$; $b_{12} = b_{21} = 0$. Then, Eq. (5) will be in form of transfer functions

$$\begin{bmatrix} (ms^2 + b_1 s + k_1) & 0 \\ 0 & (ms^2 + b_2 s + k_2) \end{bmatrix} \cdot \begin{bmatrix} Y_1(s) \\ Y_2(s) \end{bmatrix}$$
$$= \begin{bmatrix} (b_1 s + k_1) & 0 \\ 0 & (b_2 s + k_2) \end{bmatrix} \cdot \begin{bmatrix} X_1(s) \\ X_2(s) \end{bmatrix} \tag{7}$$

Solving this matrix equation is

$$\mathbf{Y}(s) = \mathbf{G}(s) \cdot \mathbf{X}(s) \tag{8}$$

where G(s) is the matrix of transfer functions

$$\mathbf{G}(s) = \begin{bmatrix} G_{11} & 0 \\ 0 & G_{22} \end{bmatrix} = \begin{bmatrix} \frac{b_1 s + k_1}{ms^2 + b_1 s + k_1} & 0 \\ 0 & \frac{b_2 s + k_2}{ms^2 + b_2 s + k_2} \end{bmatrix} \tag{9}$$

Consider now a "real" - mechanically coupled planar system with non-zero values of cross-coupling coefficients represented by (4). Applying the same procedure the matrix of transfer functions will be in full form:

$$\mathbf{G}_P(s) = \begin{bmatrix} G_{11P} & G_{12P} \\ G_{21P} & G_{22P} \end{bmatrix} \tag{10}$$

with four transfer functions:

$$\begin{aligned}
G_{11P} &= [(ms^2 + b_2 s + k_2) \cdot (b_1 s + k_1) + (b_{21} s + k_{21}) \cdot (-b_{12} s - k_{12})]/D \\
G_{12P} &= [(ms^2 + b_2 s + k_2) \cdot (b_{12} s + k_{12}) + (b_2 s + k_2) \cdot (-b_{12} s - k_{12})]/D \\
G_{21P} &= [(ms^2 + b_1 s + k_1) \cdot (b_{21} s + k_{21}) + (b_1 s + k_1) \cdot (-b_{21} s - k_{21})]/D \\
G_{22P} &= [(ms^2 + b_1 s + k_1) \cdot (b_2 s + k_2) + (b_{12} s + k_{12}) \cdot (-b_{21} s - k_{21})]/D
\end{aligned} \tag{11}$$

$$D = (ms^2 + b_2 s + k_1).(ms^2 + b_2 s + k_2) - (b_{12} s + k_{12}).(b_{21} + k_{21})$$

To see how the different stiffness and damping parameters will influence the final accuracy in particular directions the amplitude and phase errors in cases of transfers of an 'ideal' (7) and the real - mechanically coupled system (4) were calculated. For this simulation the following values of parameters are taken: $m = 1.10^{-3}$ kg; $k_1 = 2.5$ Nm; $b_1 = 2.5$; $k_{12} = 0.01$ Nm; $b_{12} = 0.05$.
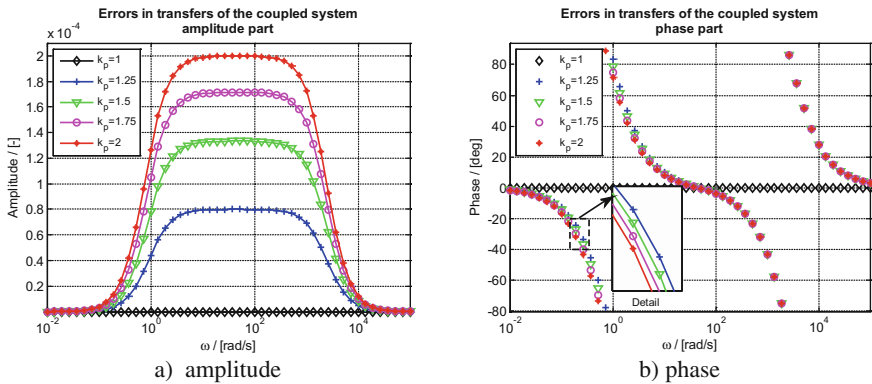


a) amplitude

b) phase

**Fig. 4.** Errors in transfers of the coupled system due to different stiffness coefficients $k_1$, $k_2$
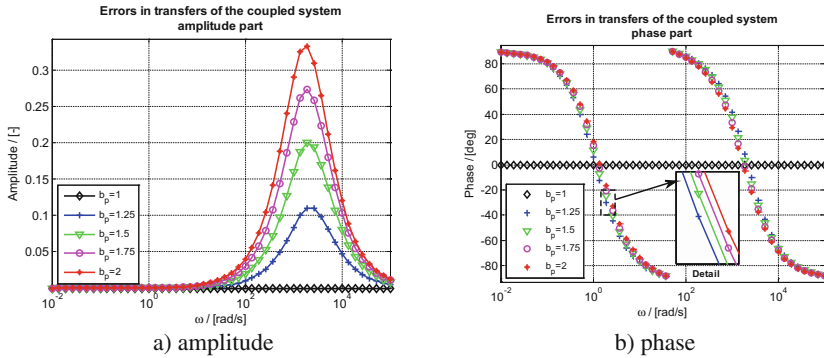
**Fig. 5.** Errors in transfers of the coupled system due to different damping coefficients $b_1$, $b_2$

These errors in amplitudes (a) and phases (b), in Figs. 4 and 5, are calculated for five ratios of stiffness kp = k1/k2 and damping coefficients bp = b1/b2.

When evaluating Figs. 4a and 5a, one can see that the difference of damping coefficients exhibits much more influence on the final amplitude errors/accuracy especially at higher frequency modes.

## 3.2    System Dynamics

Beside the description of the system dynamics in form of the transfer functions as amplitude phase frequency characteristics, the Bode transfer characteristic is used too.
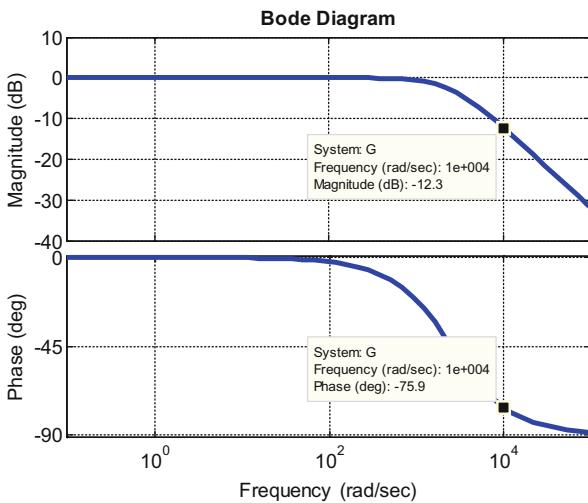


**Fig. 6.** Bode characteristics of the transfer function $G_{11}$

More frequently, the description of the amplitude and phase-frequency parts are expressed in logarithmic measures. From both these characteristics one can determine the amplitude and phase shifts of the system at a specific frequency.

$$\ln G(j\omega) = \ln|G(j\omega) + j\varphi(\omega)| \tag{15}$$

For our system the Bode characteristics are plotted in Fig. 6. As shown, the desired amplitude will keep until frequency approx. $10^3$ rad/s and the zero phase shifts until $10^2$ rad/s.

## 4    Conclusion

The small and micro mechanisms based on compliant elastic structures are applied in a broad class of electro-mechanical systems, especially in precise multi degrees of freedom positioning devices or sensors for mechanical quantities. The principal requirement for this kind of devices is to reach maximal positioning or sensing accuracy under desired frequency modes of operation. The final accuracy of these electro-mechanical systems is mainly influenced by cross flexural effects of deformable parts in static and dynamical modes of operations. These effects in quasi static modes of operations result in errors in positioning accuracy and could be compensated by feed-forward control solutions.

The study presented in this paper concentrates on the influence of different stiffness and damping parameters in particular control axes and performance evaluation of the positioning system under high frequency modes of operation. Considering the harmonic motion of a planar mechanical x−y system the amplitude and phase errors are calculated for various values of stiffness and damping parameters and the behaviour of such mechanisms is simulated. It is shown that the amplitude errors in transfers are mainly influenced by differences of damping parameters in particular motion axes. As follows from the above analysis the high accuracy mechanisms should exhibit physical symmetry in particular motion axes, i.e. forms, masses and dimensions must be identical.

## References

1. Lobontiu, N.: Compliant Mechanisms: Design of Flexure Hinges. CRC Press (2003). ISBN 0849313678
2. Howell, L.L.: Compliant Mechanisms. John Wiley & Sons (2001). ISBN 047138478X
3. Schotborgh, O.W., et al.: Dimensionless design graphs for flexure elements and a comparison between three flexure elements. Precis. Eng. **29**, 41–47 (2005)

4. Havlík, Š.: Analysis and modeling flexible robotic (micro) mechanisms. In: Proceedings of the 11th World Congress in Mechanism and Machine Science, Tianjin, PRC, vol. 3, pp. 1390–1395, 1–4 April 2004
5. Havlík, Š.: Improving accuracy of compliant robotic (micro) devices. In: Szakál, A. (ed.) Proceedings of the RAAD 2010, Budapest, pp. 385–389. IEEE (2010). ISBN 978-1-4244-6884-3
6. Hricko, J.: Modeling compliant mechanisms – comparison of models in MATLAB/sim-mechanics vs. FEM. In: Proceedings of the 21th International Workshop on Robotics in Alpe-Adria-Danube Region, Napoli, Italy, pp. 57–62 (2012). ISBN 978-88-95430-45-4
7. Yong, Y.K., Lu, T.F.: Kinetostatic modeling of 3-RRR compliant micro-motion stages with flexure hinges. Mech. Mach. Theory **44**, 1156–1175 (2009)
8. Yi, B.-J., et al.: Design and experiment of a 3-dof parallel micromechanism utilizing flexure hinges. IEEE Trans. Robot. Autom. **4**(19), 604–612 (2003)
9. Ouyang, P.R.: A spatial hybrid motion compliant mechanism: design and optimization. Mechatronics **21**, 479–489 (2011)
10. Li, Y., Xu, Q.: Design and analysis of a totally decoupled flexure-based x-y parallel micromanipulator. IEEE Trans. Robot. **3**(25), 645–657 (2009)
11. Li, Y., Xu, Q.: Optimal design of a novel 2-dof compliant parallel micromanipulator for nano manipulation. In: Proceedings of the 2005 IEEE International Conference on Automation Science and Engineering, Edmonton, Canada, 1–2 August 2005
12. Awtar, S., Slocum, A.H.: Design of parallel kinematic x–y flexure mechanisms. In: Proceedings of IDETC/CIE 2005, ASME 2005 International Design Engineering Technical Conferences & Computers and Information in Engineering, Long Beach, California, USA, pp. 89–99, 24–28 September 2005

# Inverse Kinematics of Six - DOF
# Three - Limbed Parallel Manipulator

Zhumadil Baigunchekov[1(✉)], Maksat Kalimoldaev[2],
Muratulla Utenov[3], Myrzabai Izmambetov[1],
and Talgat Baigunchekov[1]

[1] K.I. Satpayev Kazakh National Research Technical University,
Almaty, Kazakhstan
{bzh47,myrza_62}@mail.ru,
talgat.baigunchekov@gmail.com
[2] Institute of Informatics and Computing Technologies, Almaty, Kazakhstan
mnk@ipic.kz
[3] Al - Farabi Kazakh National University, Almaty, Kazakhstan
umu57@mail.ru

**Abstract.** Most of 6-DOF parallel manipulators (PM) consist of six limbs.
These PM possess the advantages of high stiffness, low inertia and large payload
capacity. However, such six – limbed fully PM have a limited workspace and
complex kinematic singularities. In this paper the method of inverse kinematics
of six-DOF three – limbed PM is presented. This PM is formed by connection of
a moving platform with a base by three spatial dyads with cylindrical joints.
Each of the three active cylindrical joints located on a base of this PM 3CCC has
actuators of P-R type. The inverse kinematics of the PM 3CCC is solved on the
basis of position analysis of the spatial dyads with cylindrical joints. The
analysis shows that 8 sets of inverse kinematic solutions exist for PM 3CCC.

**Keywords:** Parallel manipulator · Cylindrical joint · Inverse kinematics

## 1 Introduction

6 - DOF fully parallel manipulators (PM) consist of six limbs, and have a limited
workspace [1–3]. Therefore, in robotics literature [4, 5] a great interest to the PM with
fewer limbs and larger workspace is observed. For 6-DOF PM with symmetrical limbs
there are two practical solutions - with three or six limbs. The following types of limbs
of 6-DOF PM with three symmetrical limbs are known: USR type (where U denotes a
universal joint, S denotes a spherical joint, R denotes a revolute joint) [6], RSPR type
(where P denotes a prismatic joint) [7], RES type (where E denotes a plane joint) [8],
PPSP type [9], and others.

In this paper a six - DOF three – limbed PM with only cylindrical joints is con-
sidered. This PM of 3CCC type (where C denotes a cylindrical joint) is formed by
connection of a moving platform 3 with a base 0 by three spatial dyads *ABC*, *DEF* and
*GHI* of type CCC as shown in Fig. 1. In the PM 3CCC the variable parameters
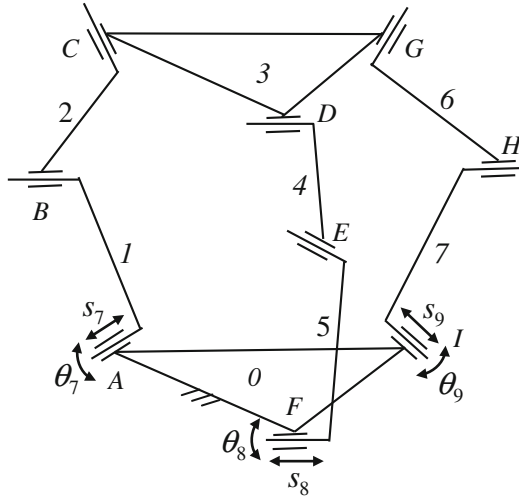
**Fig. 1.** Parallel manipulator with cylindrical joints

$s_7, \theta_7, s_8, \theta_8, s_9, \theta_9$ of the active joints *A, F, I* are generalized coordinates, and the joints *B, C, D, E, G, H* are passive joints. A patent for this PM has been received [10].

For the definition of constant and variable parameters of the PM 3CCC characterizing the geometry of links and relative motions of elements of the joints respectively, the right-hand Cartesian coordinate systems *UVW* and *XYZ* have been attached to each element of each joints [11]. The *W* and *Z* axes of the coordinate systems *UVW* and *XYZ* are directed along the axes of rotation and translation of the cylindrical joints. The transformation matrix $\mathbf{T}_{jk}$ between the coordinate systems $U_j V_j W_j$ and $X_k Y_k Z_k$ attached to the ends of the binary link with the *j*-th and *k*-th joints has been formed

$$\mathbf{T}_{jk} = \mathbf{T}_{jk}(a_{jk}, b_{jk}, c_{jk}, \alpha_{jk}, \beta_{jk}, \gamma_{jk},) = \begin{bmatrix} t_{11} & t_{12} & t_{13} & t_{14} \\ t_{21} & t_{22} & t_{23} & t_{24} \\ t_{31} & t_{32} & t_{33} & t_{34} \\ t_{41} & t_{42} & t_{43} & t_{44} \end{bmatrix}, \qquad (1)$$

where

$$t_{11} = 1, \, t_{12} = t_{13} = t_{14} = 0, \, t_{21} = a_{jk} \cdot \cos \gamma_{jk} + b_{jk} \cdot \sin \gamma_{jk} \cdot \sin \alpha_{jk},$$

$$t_{22} = \cos \gamma_{jk} \cdot \cos \beta_{jk} - \sin \gamma_{jk} \cdot \cos \alpha_{jk} \cdot \sin \beta_{jk},$$

$$t_{23} = -\cos \gamma_{jk} \cdot \sin \beta_{jk} - \sin \gamma_{jk} \cdot \cos \alpha_{jk} \cdot \cos \beta_{jk},$$

$$t_{24} = \sin \gamma_{jk} \cdot \sin \alpha_{jk}, \, t_{31} = a_{jk} \cdot \sin \gamma_{jk} - b_{jk} \cdot \cos \gamma_{jk} \cdot \sin \alpha_{jk},$$

$$t_{32} = \sin \gamma_{jk} \cdot \cos \beta_{jk} + \cos \gamma_{jk} \cdot \cos \alpha_{jk} \cdot \sin \beta_{jk},$$

$$t_{33} = \cos \gamma_{jk} \cdot \cos \alpha_{jk} \cdot \cos \beta_{jk} - \sin \gamma_{jk} \cdot \sin \beta_{jk},$$

$$t_{34} = -\cos \gamma_{jk} \cdot \sin \alpha_{jk}, \, t_{41} = c_{jk} + b_{jk} \cdot \cos \alpha_{jk},$$

$$t_{42} = \sin \alpha_{jk} \cdot \sin \beta_{jk}, \, t_{43} = \sin \alpha_{jk} \cdot \cos \beta_{jk}, \, t_{44} = \cos \alpha_{jk},$$

$a_{jk}$ denotes the distance from axis $W_j$ to axis $Z_k$ which is measured along the direction of $t_{jk}$; $t_{jk}$ is a common normal between axes $W_j$ and $Z_k$; $\alpha_{jk}$ denotes the angle between positive directions of axes $W_j$ and $Z_k$ which is measured counter clockwise relatively to positive direction of $t_{jk}$; $b_{jk}$ denotes a distance from the direction of $t_{jk}$ to the direction of the axis $X_k$ which is measured along the positive direction of an axis $Z_k$; $\beta_{jk}$ denotes an angle between positive directions of $t_{jk}$ and axis $X_k$ which is measured counter clockwise relatively to positive direction of axis $Z_k$; $c_{jk}$ denotes the distance from the direction of axis $U_j$ to the direction of $t_{jk}$ which is measured along positive direction of axis $W_j$; $\gamma_{jk}$ denotes an angle between positive directions of axis $U_j$ and $t_{jk}$ which is measured counter clockwise relatively to the positive direction of axis $W_j$.

In comparison with the Denavit – Hartenberg transformation matrix having four parameters, the transformation matrix (1) has six parameters fully characterizing the relative locations of the coordinate systems $U_j V_j W_j$ and $X_k Y_k Z_k$.

Constant and variable parameters of the first limb $ABC$ of the PM 3CCC are shown in Fig. 2, where $s_7$ and $\theta_7$ are the generalized coordinates of the active joints $A$; $s_2, \theta_2$ and $s_3, \theta_3$ are variable parameters of the passive joints $B$ and $C$; all other parameters are the constant values characterizing the geometry of links. Constant and variable parameters of two other symmetrical limbs are defined similarly. In [11] the geometry of the PM 3CCC is described and its direct kinematics is solved. The results of singularity analysis of the PM 3CCC are presented in [12]. In this paper an inverse kinematics of the PM 3CCC is considered.

## 2   Inverse Kinematics

For the inverse kinematics of the PM 3CCC, shown in Fig. 1, variable parameters $s_7, \theta_7, s_8, \theta_8$ and $s_9, \theta_9$ of the active joints $A$, $F$ and $I$ are defined by the given positions of the coordinate system $X_P Y_P Z_P$, attached to the moving platform 3, with respect to the absolute coordinate system $U_0 V_0 W_0$. Let us define the variable parameters $s_7$ and $\theta_7$ of the active joint $A$ of the first limb shown in Fig. 2. Variable parameters $s_8, \theta_8$ and $s_9, \theta_9$ of active joints $F$ and $I$ of the other two limbs are defined similarly.

We can determine the radius vectors $\mathbf{r}_{O_7}$ and $\mathbf{r}_{O_2'}$ of the points $O_7$ and $O_2'$ with respect to the absolute coordinate system $U_0 V_0 W_0$ by the following equations, respectively

$$\begin{bmatrix} 1 \\ \mathbf{r}_{O_7} \end{bmatrix} = \mathbf{T}_{07} \cdot \begin{bmatrix} 1 \\ {}^7\mathbf{r}_{O_7} \end{bmatrix} = \mathbf{T}_{07} \cdot \begin{bmatrix} 1 \\ 0 \\ 0 \\ 0 \end{bmatrix} = \begin{bmatrix} 1 \\ a_{07} \cos \gamma_{07} \\ a_{07} \sin \gamma_{07} \\ c_{07} \end{bmatrix}, \tag{2}$$

$$\begin{bmatrix} 1 \\ \mathbf{r}_{O_2'} \end{bmatrix} = \mathbf{T}_{0P} \cdot \begin{bmatrix} 1 \\ {}^P\mathbf{r}_{O_2'} \end{bmatrix} = \mathbf{T}_{0P} \cdot \mathbf{T}_{P2} \cdot \begin{bmatrix} 1 \\ 0 \\ 0 \\ 0 \end{bmatrix} = \mathbf{T}_{0P} \cdot \begin{bmatrix} 1 \\ a_{P2} \cos \gamma_{P2} \\ a_{P2} \sin \gamma_{P2} \\ c_{P2} \end{bmatrix}, \tag{3}$$
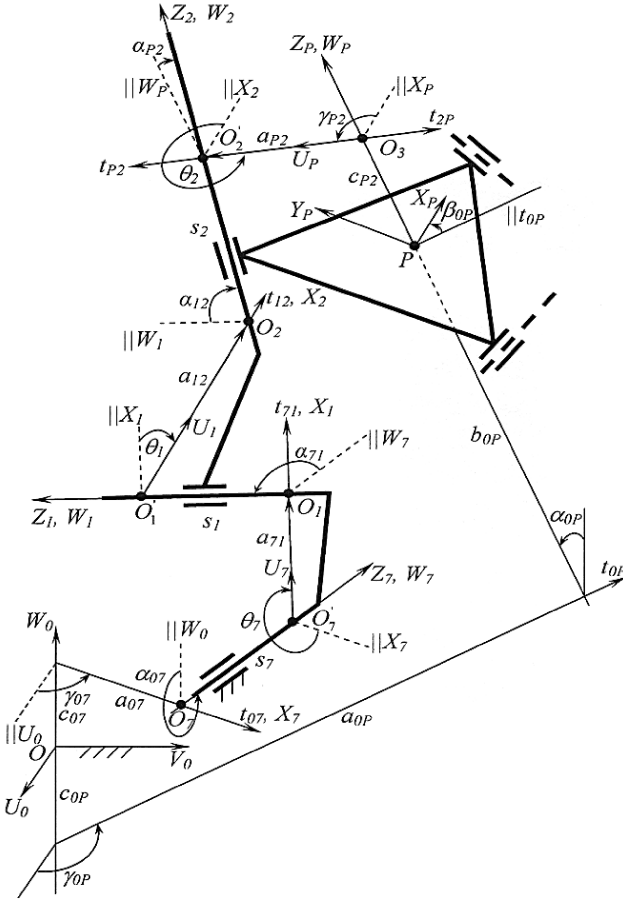
**Fig. 2.** The first limb of PM 3CCC

where $\mathbf{T}_{07} = \mathbf{T}_{07}(a_{07}, 0, c_{07}, \alpha_{07}, 0, \gamma_{07})$ is a transformation matrix between the absolute coordinate system $OU_0V_0W_0$ and the coordinate system $O_7X_7Y_7Z_7$, attached to the fixed element of the cylindrical joint 7; $\mathbf{T}_{0P} = \mathbf{T}_{0P}(a_{0P}, b_{0P}, c_{0P}, \alpha_{0P}, \beta_{0P}, \gamma_{0P})$ - a transformation matrix between the absolute coordinate system $OU_0V_0W_0$ and the local coordinate system $PX_PY_PZ_P$ of the moving platform 3; $\mathbf{T}_{P2} = \mathbf{T}_{P2}(a_{P2}, 0, c_{P2}, \alpha_{P2}, 0, \gamma_{P2})$ - a transformation matrix determining the location of the cylindrical joint 2 with respect to the local coordinate system $PX_PY_PZ_P$.

The unit vectors $\mathbf{e}_7$ and $\mathbf{e}_2$ of the rotation axes of cylindrical joints $A$ and $C$ with respect to the absolute coordinate system $U_0V_0W_0$ are defined by the equations

$$\begin{bmatrix} 0 \\ \mathbf{e}_7 \end{bmatrix} = \mathbf{T}_{07} \cdot \begin{bmatrix} 0 \\ {}^7\mathbf{e}_7 \end{bmatrix} = \mathbf{T}_{07} \cdot \begin{bmatrix} 0 \\ 0 \\ 0 \\ 1 \end{bmatrix} = \begin{bmatrix} 0 \\ \sin\gamma_{07} \cdot \sin\alpha_{07} \\ -\cos\gamma_{07} \cdot \sin\alpha_{07} \\ \cos\alpha_{07} \end{bmatrix}, \qquad (4)$$

$$\begin{bmatrix} 0 \\ \mathbf{e}_2 \end{bmatrix} = \mathbf{T}_{0P} \begin{bmatrix} 0 \\ {}_P\mathbf{e}_2 \end{bmatrix} = \mathbf{T}_{0P} \cdot \mathbf{T}_{P2} \begin{bmatrix} 0 \\ {}_2\mathbf{e}_2 \end{bmatrix} = \mathbf{T}_{0P} \cdot \mathbf{T}_{P2} \begin{bmatrix} 0 \\ 0 \\ 0 \\ 1 \end{bmatrix} = \mathbf{T}_{0P} \begin{bmatrix} 0 \\ \sin\gamma_{P2} \cdot \sin\alpha_{P2} \\ -\cos\gamma_{P2} \cdot \sin\alpha_{P2} \\ \cos\alpha_{P2} \end{bmatrix}.$$

$$(5)$$

The parameters $s_7$ and $\theta_7$ of the PM 3CCC are defined by the solution of the position of the spatial dyad 1–2 with cylindrical joints. For the dyad 1–2 the unit vectors $\mathbf{e}_7$ and $\mathbf{e}_2$ of the cylindrical joints $A$ and $C$, coordinates $U_{O_7}$, $V_{O_7}$, $W_{O_7}$ and $U_{O'_2}$, $V_{O'_2}$, $W_{O'_2}$ of the points $O_7$ and $O'_2$ with respect to the coordinate system $U_0V_0W_0$, parameters $a_{71}$ and $a_{12}$ are given. It is necessary to define the parameters $s_7 = l_{O_7O'_7}$, $s_1 = l_{O_1O'_1}$, $s_2 = l_{O_2O'_2}$ and the unit vector $\mathbf{e}_1$ of cylindrical joint $B$ axis.

The direction and module of the vector $\mathbf{e}_{O_7O'_2}$ are defined by the expressions

$$\left.\begin{aligned} e_{O_7O'_2,U} &= \cos(U_0, {}^\wedge l_{O_7O'_2}) = (U_{O'_2} - U_{O_7})/l_{O_7O'_2} \\ e_{O_7O'_2,V} &= \cos(V_0, {}^\wedge l_{O_7O'_2}) = (V_{O'_2} - V_{O_7})/l_{O_7O'_2} \\ e_{O_7O'_2,W} &= \cos(W_0, {}^\wedge l_{O_7O'_2}) = (W_{O'_2} - W_{O_7})/l_{O_7O'_2} \end{aligned}\right\}, \quad l_{O_7O'_2} = [(\mathbf{r}_{O_7} - \mathbf{r}_{O'_2})^2]^{\frac{1}{2}}, \quad (6)$$

From the loop-closure equation of kinematic chain $O_7O'_7O_1O'_1O_2O'_2O_7$ we have

$$\left.\begin{aligned} s_7\mathbf{e}_7 + a_{71}\mathbf{e}_{71} + s_1\mathbf{e}_1 + a_{12}\mathbf{e}_{12} + s_2\mathbf{e}_2 - l_{O_7O'_2}\mathbf{e}_{O_7O'_2} = 0 \\ \mathbf{e}_7 \cdot \mathbf{e}_1 = \cos\alpha_{71}, \quad \mathbf{e}_1 \cdot \mathbf{e}_2 = \cos\alpha_{12}, \quad \mathbf{e}_1^2 = 1 \end{aligned}\right\}, \quad (7)$$

where $\alpha_{71}$ - the given angle between directions of the unit vectors $\mathbf{e}_7$ and $\mathbf{e}_1$; $\alpha_{12}$ - the given angle between the directions of the unit vectors $\mathbf{e}_1$ and $\mathbf{e}_2$.

We use a rule of vector multiplication for vectors perpendicular to two given vectors. Then the system (7) will become

$$s_7\mathbf{e}_7 + a_{71}(\mathbf{e}_7 \times \mathbf{e}_1) + s_1\mathbf{e}_1 + a_{12}(\mathbf{e}_1 \times \mathbf{e}_2) + s_2\mathbf{e}_2 - l_{O_7O'_2}\mathbf{e}_{O_7O'_2} = 0, \quad (8)$$

$$\mathbf{e}_7 \cdot \mathbf{e}_1 = \cos\alpha_{71}, \, \mathbf{e}_1 \cdot \mathbf{e}_2 = \cos\alpha_{12}, \, \mathbf{e}_1^2 = 1. \quad (9)$$

To determine the unit vector $\mathbf{e}_1$ we will write the system (9) in the form

$$\left.\begin{aligned} e_{7U}e_{1U} + e_{7V}e_{1V} + e_{7W}e_{1W} &= \cos\alpha_{71} \\ e_{2U}e_{1U} + e_{2V}e_{1V} + e_{2W}e_{1W} &= \cos\alpha_{12} \\ e_{1U}^2 + e_{1V}^2 + e_{1W}^2 &= 1 \end{aligned}\right\}. \quad (10)$$

From the system (10) one can see that it consists of two linear and one quadratic equations containing the unknown projections $e_{1U}$, $e_{1V}$, $e_{1W}$ of the unit vector $\mathbf{e}_1$ to the axes of the coordinate system $U_0V_0W_0$. The system (10) has two solutions. It is necessary to find the solution of the system (9) or (10), and also to choose the necessary solution. Let us transform the first two equations of (10) to the form

$$
\left.
\begin{aligned}
e_{7V}e_{1V} + e_{7W}e_{1W} &= \cos\alpha_{71} - e_{7U}e_{1U} \\
e_{2V}e_{1V} + e_{2W}e_{1W} &= \cos\alpha_{12} - e_{2U}e_{1U}
\end{aligned}
\right\}. \tag{11}
$$

Solving the system of Eq. (11) with respect to the unknown parameters $e_{1V}$, $e_{1W}$ yields

$$
e_{1V} = \frac{1}{A_U}(A_V e_{1U} + D_W), \quad e_{1W} = \frac{1}{A_U}(A_W e_{1U} - D_V), \tag{12}
$$

where

$$
A_U = e_{7V}e_{2W} - e_{7W}e_{2V}, \quad A_V = e_{7W}e_{2U} - e_{7U}e_{2W}, \quad A_W = e_{7U}e_{2V} - e_{7V}e_{2U},
$$
$$
D_V = e_{2V}\cos\alpha_{71} - e_{7V}\cos\alpha_{12}, \quad D_W = e_{2W}\cos\alpha_{71} - e_{7W}\cos\alpha_{12}.
$$

Substituting the expressions (12) to the third equation of the system (10) we obtain

$$
A^2 e_{1U}^2 + 2B_U e_{1U} + C_U = 0, \tag{13}
$$

where $A^2 = A_U^2 + A_V^2 + A_W^2$, $\quad B_U = A_V D_W - A_W D_V$, $\quad C_U = D_V^2 + D_W^2 - A_U^2$.
Then solving Eq. (13) yields

$$
e_{1U} = (-B_U + \varepsilon \cdot R_U)/A^2, \tag{14}
$$

where $R_U = \sqrt{B_U^2 - A^2 C_U}$ and $\varepsilon = +1$ or $-1$. A choice of the numbers $+1$ or $-1$ is dependent of the configuration of the spatial dyad 1–2. Expression (14) means that the inverse kinematics problem for one limb has at most two sets of solutions. Then at most eight sets of inverse displacement solutions exist for a complete 3-limbed 6-DOF 3CCC parallel manipulator. The vector Eq. (8) in the projections leads to the following system of linear equations:

$$
\mathbf{A} \cdot \mathbf{x} = \mathbf{B}, \tag{15}
$$

where

$$
\mathbf{A} = \begin{bmatrix} e_{7U} & e_{1U} & e_{2U} \\ e_{7V} & e_{1V} & e_{2V} \\ e_{7W} & e_{1W} & e_{2W} \end{bmatrix}, \quad \mathbf{x} = \begin{bmatrix} s_7 \\ s_1 \\ s_2 \end{bmatrix}, \quad \mathbf{B} = \begin{bmatrix} l_{O_7 O_2'} e_{O_7 O_2', U} - a_{71}(e_{7V} \cdot e_{1W} - e_{7W} \cdot e_{1V}) \\ - a_{12}(e_{2V} \cdot e_{1W} - e_{2W} \cdot e_{1V}) \\ l_{O_7 O_2'} e_{O_7 O_2', V} - a_{71}(e_{7W} \cdot e_{1U} - e_{7U} \cdot e_{1W}) \\ - a_{12}(e_{2U} \cdot e_{1W} - e_{2W} \cdot e_{1U}) \\ l_{O_7 O_2'} e_{O_7 O_2', W} - a_{71}(e_{7U} \cdot e_{1V} - e_{7V} \cdot e_{1U}) \\ - a_{12}(e_{2U} \cdot e_{1V} - e_{2V} \cdot e_{1U}) \end{bmatrix}.
$$

Because the vectors $\mathbf{e}_7$, $\mathbf{e}_1$ and $\mathbf{e}_2$ are linearly independent, the matrix $\mathbf{A}$ is not singular. The matrix $\mathbf{A}$ is invertible and the parameters $s_7$, $s_1$, $s_2$ can be determined from the system (15)

$$\mathbf{x} = \mathbf{A}^{-1} \cdot \mathbf{B}. \tag{16}$$

We note that some results of the singularity analysis of the PM 3CCC are presented in [12], where the possibility of a linear dependence of vectors $\mathbf{e}_7$, $\mathbf{e}_1$ and $\mathbf{e}_2$ is considered as a consequence of degeneracy of inverse-kinematics Jacobean matrix.

The second generalized coordinate $\theta_7$ is defined from the following expressions

$$\cos \theta_7 = \frac{\mathbf{f}_{07} \cdot (\mathbf{e}_7 \times \mathbf{e}_1)}{\sin \alpha_{71}}, \quad \sin \theta_7 = \frac{(\mathbf{e}_7 \times \mathbf{f}_{07}) \cdot (\mathbf{e}_7 \times \mathbf{e}_1)}{\sin \alpha_{71}}, \tag{17}$$

where $\mathbf{f}_{07}$ is a unit vector of the axis $t_{07}$, and it is defined as

$$\begin{bmatrix} 0 \\ \mathbf{f}_{07} \end{bmatrix} = \mathbf{T}_{07} \cdot \begin{bmatrix} 0 \\ {}^7\mathbf{f}_{07} \end{bmatrix} = \mathbf{T}_{07} \cdot [0, 1, 0, 0]^T = [0, \cos \gamma_{07}, \sin \gamma_{07}, 0]^T. \tag{18}$$

The angles $\theta_1$ and $\theta_2$ are defined from the following expressions, respectively

$$\cos \theta_1 = \frac{(\mathbf{e}_7 \times \mathbf{e}_1) \cdot (\mathbf{e}_1 \times \mathbf{e}_2)}{\sin \alpha_{71} \cdot \sin \alpha_{12}}, \quad \sin \theta_1 = \frac{[\mathbf{e}_1 \times (\mathbf{e}_7 \times \mathbf{e}_1)] \cdot (\mathbf{e}_1 \times \mathbf{e}_2)}{\sin \alpha_{71} \cdot \sin \alpha_{12}}, \tag{19}$$

$$\cos \theta_2 = \frac{(\mathbf{e}_1 \times \mathbf{e}_2) \cdot \mathbf{f}_{2P}}{\sin \alpha_{12}}, \quad \sin \theta_2 = \frac{[\mathbf{e}_2 \times (\mathbf{e}_1 \times \mathbf{e}_2)] \cdot \mathbf{f}_{2P}}{\sin \alpha_{12}}, \tag{20}$$

where $\mathbf{f}_{2P}$ is a unit vector of the axis $t_{2P}$ and is defined as

$$\begin{bmatrix} 0 \\ \mathbf{f}_{2P} \end{bmatrix} = \begin{bmatrix} 0 \\ -\mathbf{f}_{P2} \end{bmatrix} = \mathbf{T}_{0P} \cdot \begin{bmatrix} 0 \\ -{}^P\mathbf{f}_{P2} \end{bmatrix} = \mathbf{T}_{0P} \cdot [0, -\cos \gamma_{P2}, -\sin \gamma_{P2}, 0]^T. \tag{21}$$

## 3   Conclusions

A new symmetrical 6-DOF parallel manipulator with cylindrical joints PM 3CCC was described; it has three identical limbs and offers an intermediate performance (workspace, accuracy and stiffness) between a serial robot and a six-legged fully parallel manipulator. This parallel manipulator is formed by connection of a moving platform with a base by three spatial dyads with cylindrical joints of CCC type. Constant and variable parameters of the PM 3CCC are defined on the basis of two coordinate systems which are attached to each element of the joints. Constant parameters characterize geometry of links, and variable parameters characterize relative motions of elements of joints. The inverse kinematics of the PM 3CCC is solved on the basis of position analysis of spatial dyads with cylindrical joints. The analysis shows that eight sets of inverse kinematic solutions exist for the PM 3CCC. These analytical results can be used for trajectory planning and control of the PM 3CCC.

# References

1. Merlet, J.-P.: Parallel Robots. Kluwer Academic Publishers, Dordrecht (2000)
2. Angeles, J.: Fundamentals of Robotic Mechanical Systems. Theory, Methods and Algorithms. 4th edn. Springer (2014). doi:10.1007/978-3-319-01851-5
3. Ceccarelli, M.: Fundamentals of Mechanics of Robotic Manipulation. Kluwer Academic Publishers, Dordrecht (2004)
4. Yang, G., Chen, I.M., Chen, W., Lin, W.: Kinematic design of six-DOF parallel-kinematics machine with decoupled-motion architecture. IEEE Trans. Rob. **20**(20), 876–884 (2004)
5. Jin, Y., Chen, I.M., Yang, G.: Kinematic design of a family of 6-DOF partially decoupled parallel manipulators. Mech. Mach. Theory **44**(5), 912–922 (2009)
6. Cleary, K., Ubel, M.: Jacobean formulation for a novel 6 – DOF parallel manipulator. In: Proceedings of the IEEE Conference on Robotics and Automation, vol. 3, pp. 2377–2382 (1994)
7. Alizade, R.I., Tagiyev, N.R.: A forward and reverse displacement analysis of a 6 – DOF in-parallel manipulator. Mech. Mach. Theory **29**(1), 115–124 (1994)
8. Ebert, U., Gosselin, C.M.: Kinematic study of a new type of spatial parallel platform mechanism. In: ASME Design Engineering Technical Conference, Atlanta, 13–16 September (1998)
9. Byun, Y.K., Cho, H.S.: Analysis of a novel 6 – DOF 3 – PPSP parallel manipulator. Int. J. Robot. Res. **16**(6), 859–872 (1997)
10. Baigunchekov, Z., Ceccarelli, M., et al.: Parallel manipulator. Patent No. 20725. Republic of Kazakhstan
11. Baigunchekov, Z., Kalimoldaev, M., Utenov, M., Baigunchekov T.: Geometry and direct kinematics of six – DOF three – limbed parallel manipulator. In: ROMANSY 2016 21st CISMIFToMM Symposium on Robot Design, Dynamics and Control, 20–23 June 2016, Udine, Italy (2016)
12. Baigunchekov, Z., Izmambetov, M.: Singularity analysis of parallel manipulator with cylindrical joints. In: Proceedings of the World Congress on Engineering WCE 2012, London, UK, 4–6 July, vol. 3, pp. 1733–1737 (2012)

# The Variable Position of the Load's Centre of Mass Relative to the Load's Hanging Point of the CPR System

Mirjana Filipovic[1(✉)], Ljubinko Kevac[2,4], and Ana Djuric[3]

[1] Mihajlo Pupin Institute, University of Belgrade,
Volgina 15, 11060 Belgrade, Serbia
mira@robot.imp.bg.ac.rs
[2] School of Electrical Engineering, The University of Belgrade,
Bulevar Kralja Aleksandra 73, 11000 Belgrade, Serbia
ljubinko.kevac@ic.etf.rs
[3] Wayne State University, 4855 Fourth Street, Detroit, MI 48202, USA
ana.djuric2@wayne.edu
[4] Innovation centre of School of Electrical Engineering,
The University of Belgrade, Bulevar Kralja Aleksandra 73,
11000 Belgrade, Serbia

**Abstract.** This paper deals with the analysis of the position of the load's centre of mass relative to the load's hanging point during the motion in the workspace of Cable-suspended Parallel Robot – CPR system. It will be proven that the distance between the load's centre of mass and the hanging point is variable during the motion. Also, their relative positions are variable as well. This phenomenon can be present at any type of CPR system, whose workspace can have a shape of: parallelepiped, triangle or line (planar example). The CPR system carries the load via pulleys and ropes. This analysis is valid for any construction of the CPR system where the load is carried with ropes and each rope is wound (unwound) on the corresponding system motor – winch. The ropes are hanged on highest points of the CPR system's workspace.

**Keywords:** Cable-suspended parallel robot · Load's centre of mass · Load's hanging point

## 1 Introduction

The researchers deal with the analysis and synthesis of Cable-suspended Parallel Robots – CPR systems for more than three decades. The first papers appeared at the beginning of 1980 s. The analysis of cable – driven parallel robot has attracted the interest of researchers since the very beginning of the study of parallel robots in [1].

The authors of [2] have presented the kinematic design of a planar three-degree-of-freedom parallel manipulator. The workspace conditions and the dynamics of the manipulator were described in details. Because of all the problems with workspace conditions, it is hard to conceive a good trajectory tracking algorithm, so the authors of [3] have presented algorithms that enable precise trajectory control of the Networked

Info Mechanical Systems – NIMS, and under constrained 3D cabled robot intended for use in actuated sensing. Several prototypes of the wire-driven parallel robots, with different actuation schemes have been presented in [4]. Two of them have been evaluated through extensive tests and showed unexpected kinematic problems. An auto calibration method for over constrained cable-driven parallel robots using internal position sensors located in the motors has been presented in paper [5]. Nonlinear dynamic analysis of the suspended cable system is carried out with some sensible results in [6–8] that could be useful for the real engineering of LSRT (Large Spherical Radio Telescopes). Regardless of intensive development and diversity of application of the CPR system, this topic is still very interesting for researchers, because a lot of characteristics and phenomena of CPR systems were not yet discovered and explained. One of these phenomena is the main topic of this paper and it points out the importance of analysis of variable load's centre of mass in respect to the load's hanging point of the CPR system. This topic is a result of many years of research in the field of CPR systems. During these years a lot of various constructions were designed. The construction of CPR system, called CPR–A, was presented in [9, 10]. In paper [11], the authors describe the CPR–C system. The development and advantages, as well as kinematic and dynamic models of another modern construction of the CPR system, named RSCPR, were presented in the paper [12]. RFCPR system also presents a modern structure in the class of CPR systems. This system is similar to the RSCPR system only by appearance; their difference is confirmed by their kinematic and dynamic models, as well as by the simulation results, see [13, 14]. Also, in [15] a novel CPR-D system was defined and presented.

Each of these constructions has specifications that were presented in detail in the mentioned publications. In this paper we will not deal with any of these constructions nor any other already known construction, but we will deal with the effect of the phenomena of variable load's centre of mass in respect to the load's hanging point of the CPR system. This feature characterizes all constructions of CPR systems which were published and developed until now. In Sect. 2 of the paper we will present the geometric analysis of variable position of the load's center of mass relative to the load's hanging point of the CPR system. Experimental confirmation of this phenomenon will be shown in the Sect. 3. The last Section presents our conclusions and observations.

## 2    Geometric Distance Between the Load's Centre of Mass and the Load's Hanging Point

The development of CPR systems has an upward trend for more than thirty years. Still there are many unknown phenomena for these systems. In this work we have discovered one of these phenomena, which can have a big influence on a future of CPR system's development. In widely available literature, it was usually presumed that the load carrier's centre of mass overlapped with the carrier's hanging point. In this paper, we will show that this presumption is correct only in one position of the carrier's workspace, and in all other positions this presumption is not valid. It can be seen that the nature of the system is like that that these two points have significant distance when the load carrier is near the boundary planes of the workspace.
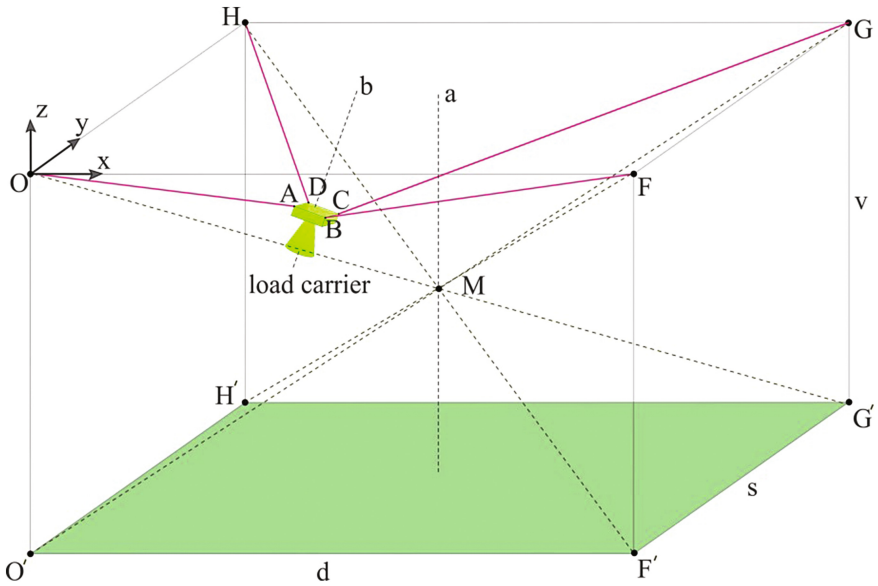
**Fig. 1.** CPR system in 3D space
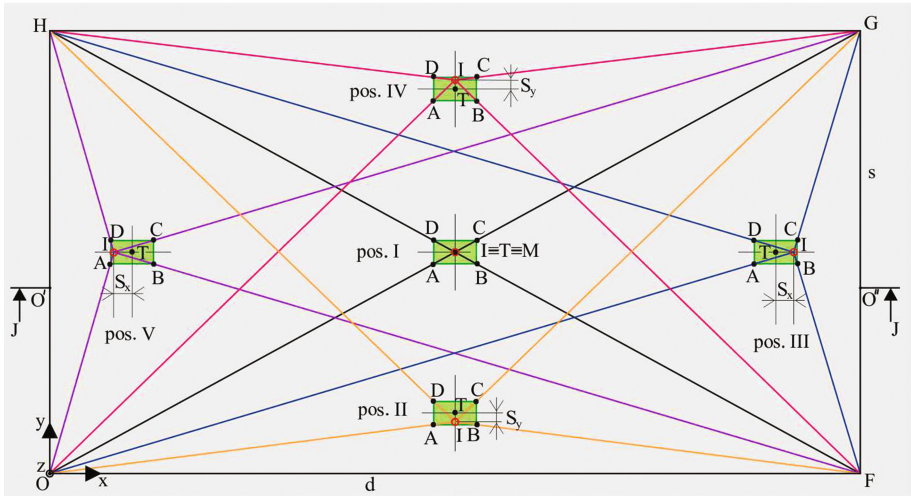


**Fig. 2.** CPR system – view from above, random position of the load (idealized case)

In this Section we will present the geometric analysis of the position of load's hanging point of CPR system relative to the load's centre of mass. The problem is presented in general, so we will not relate to any specific construction of the CPR system or to a specific situation. In order to generalize this problem, we will observe the load's motion in the CPR system's workspace of parallelepiped shape, see Fig. 1.

The upper hanging points are labelled O, F, G, H, while points labelled O', F', G', H' define the bottom of the workspace. The load carrier is shaped as a parallelepiped as well and its upper points are A, B, C, D (see Figs. 1 and 2). The ropes which guide the load in CPR system's workspace are connected with the load at points A, B, C, D, while the hanging points of these ropes are O, F, G, H, as shown on Fig. 1.

The view from above of the workspace is shown in Fig. 2. For us to understand this spatial problem it is not enough to just analyse the above view of the system; we need to consider the vertical view of the CPR system as well, which is presented in Fig. 3. In Figs. 2 and 3 we show the idealized position of the load when its central axis $b$ is vertical regardless of the load's position in the CPR system's workspace. We have labelled the load's centre of mass as point T. We will observe the relative motion of point T and because of that we show 5 different positions of the load in Fig. 2. These are the positions I, II, III, IV, V.
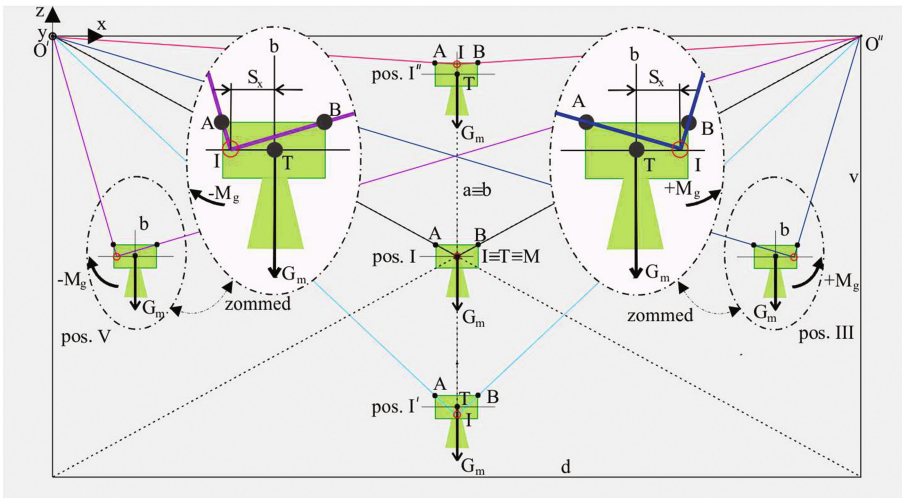


**Fig. 3.** The intersection JJ of the CPR system from Fig. 2, idealized case of vertical load's position

Position I is characterized by the fact that it presents the intersection of main diagonals of the workspace, i.e. intersection of lines OG', FH', GO' and HF'. The intersection point is labelled M, see Fig. 1.

The central vertical axis of the workspace is labelled $a$ and has coordinates $x = d/2$ and $y = s/2$ for any $z$ coordinate. The central vertical axis of the load is labelled $b$. Let us consider what happens when the load is lowered from the point M along the line $a$. The load's hanging (carrying) point I is lowered along the axis $a$ somewhat faster that the point T is lowered. If the load is lower, these two points are more distant.

This case is shown with the load's position I' in Figs. 3 and 4. In the case when the load is lifted above the point M, i.e. when $z > -v/2$ and $z < 0$, the point I rises faster than the point T along the line $a$. These two points are more and more distant. For $z \approx 0$, the distance between points T and I is maximal. Because both points are on the
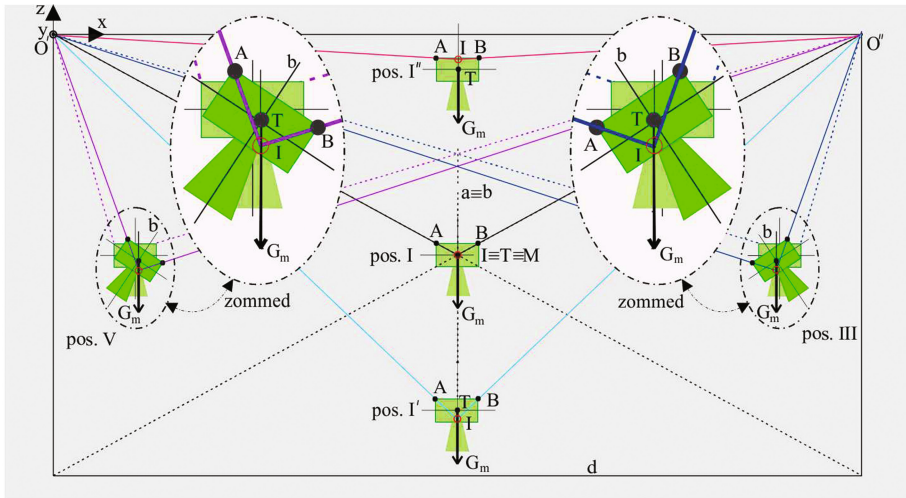
**Fig. 4.** The intersection JJ of the CPR system from Fig. 2, load's equilibrium position

line $a$ in these cases, there is no disturbance torque which would rotate the load, see Figs. 3 and 4.

All the time during the motion of the load along the line $a$, the disturbance torque is $M_g = 0$, and we have balanced motion when the load axis $b$ overlaps with the workspace axis $a$. During the motion of the load along axis $a$, the distances between points I and T are: in direction of $x$ axis $S_x = 0$ and in direction of $y$ axis $S_y = 0$. For all the other positions of the load in the CPR system's workspace, points I and T are not on the same vertical line. Let us consider the relative deflection of the point I relative to point T. In Fig. 2 we can see the above view of the CPR system's workspace. In this figure, we can see the load positions I, II, III, IV, V which are at the same level, in this case for $z = -v/2$. From this figure, we can notice the fact that with the motion of the load from the point:

- M towards the plane which is characterized by $y = 0$ (pos. II) or
- M towards the plane which is characterized by $x = d$ (pos. III) or
- M towards the plane which is characterized by $y = s$ (pos. IV) or
- M towards the plane which is characterized by $x = 0$ (pos. V),

point I is more distant to point T. When the load carrier is closer to CPR system's workspace boundaries, point I is more distant to point T and at distance $\sqrt{S_x^2 + S_y^2}$ from point I, the disturbance torque $M_g = G_m \cdot \sqrt{S_x^2 + S_y^2}$ occurs. In Fig. 3 we show the intersection J – J where we can see the direction of the torque in this vertical plane. The torque $M_g$ rotates the load in any considered position of the load carrier as can be seen in Figs. 1 and 4. When the hanging point is closer to the vertical boundary surfaces, the vertical load axis $b$ is more inclined with respect to the line $a$.

Each equilibrium point of the load, where load axis $b$ is inclined relative to the vertical, is characterized by the fact that in that equilibrium the load's centre of mass T

is at the same vertical in comparison to the hanging point I. For the system to come to the equilibrium point, the following condition needs to be satisfied: $\sqrt{S_x^2 + S_y^2} = 0$, i.e. the disturbance torque in that point must have the value $M_g = 0$.

It can be concluded that the disturbance torque is always present at different positions of load carrier in the CPR system's workspace before the load enters the equilibrium state. The torque is not present only during the motion along the line $a$. The torque $M_g$ grows when the distance from the central axis $a$ is growing and when the load is closer to the boundary positions of the CPR system's workspace. In this
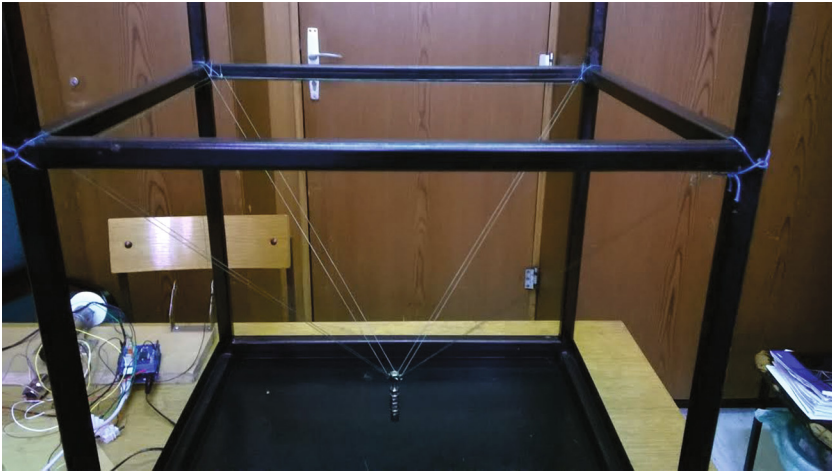


**Fig. 5.** Load carrier position at line a – experimental setup
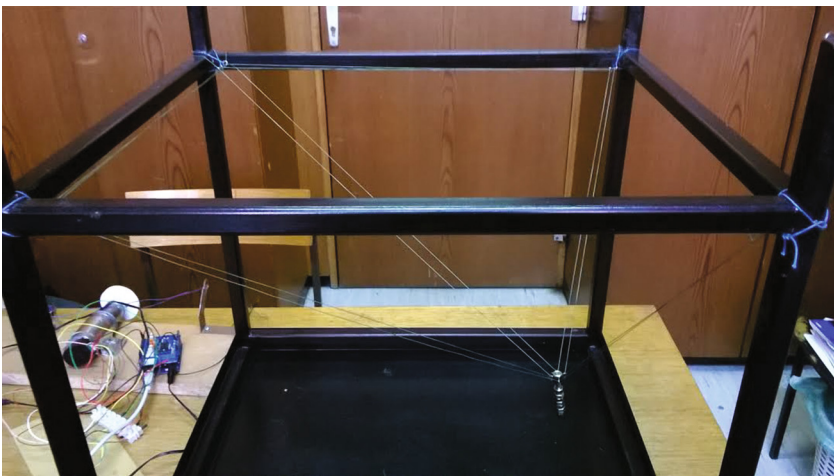


**Fig. 6.** Load carrier position near right boundary – experimental setup

**Fig. 7.** Load carrier position near left boundary – experimental setup

Section we have defined the geometric formulation of the phenomenon of deflection between the carrier's hanging point I and its centre of mass T.

In the next Section, we will provide the experimental confirmation of this formulation.

## 3   The Experiment

The experimental proof of the theoretical analysis from previous Section is shown in Figs. 5, 6 and 7. In this case, the carrier load has a different shape than the carrier presented in examples from previous Section. Because of its shape, the load carrier's centre of mass T is always beneath the carrier's hanging point I. From this statement, one can conclude that the carrier load's shape, i.e. its centre of mass, needs to be considered and analysed for each different case by using theoretical observations presented in Sect. 2.

In Fig. 5 we show the load's position when the hanging point I is on the central axis $a$. The load carrier's centre of mass T is on line $a$ as well. We can see that in this position the load stands vertically, i.e. there is no inclination of axis $b$ of the load carrier. This position is comparable with position I from Figs. 2, 3 and 4.

In Fig. 6 we present the position of the load carrier near the right boundary, when $x \approx d$. We can see that the load carrier's axis $b$ is inclined in positive mathematical direction with respect to the vertical axis $a$. Compare this position with the position III from Fig. 4.

In Fig. 7 we show the equilibrium of the load carrier's position when the load is near the left vertical boundary $x \approx 0$. We can see that the load carrier's $b$ axis is inclined in negative mathematical direction in respect to the vertical axis $a$. Compare this position with position V from Fig. 4.

With the experiments presented in Figs. 5, 6 and 7 we have confirmed the theoretical presumptions formulated in Sect. 2. The phenomenon analysed in this paper is important for generation of the kinematic model of CPR system which presents a prerequisite for its dynamics model. Also, this phenomenon, as far as we are informed, was not published in the previous literature.

## 4    Conclusion

In this paper, we have analysed the phenomenon which characterizes the load carrier's motion of the CPR system, i.e. the variable position of load's centre of mass T in comparison with the load's hanging point I. Until now the researchers did not deal with this problem; they have always assumed that the hanging point overlaps with the load's centre of mass. In this paper, we have shown exactly the opposite, i.e. these two points do not overlap during the load's motion and the distance between them changes in time. In the case when the load moves along the central axis of its workspace $a$, the load's centre of mass and the load's hanging point belong to line $a$ and their mutual distance changes as their positions change. The central axis of the load $b$ overlaps with the line $a$ during this type of load motion. However, when the hanging point leaves the trajectory of line $a$, the central axis of the load $b$ starts to rotate relative to the vertical axis $a$. The load rotates more if it is near the boundary positions of the system's workspace. By showing this fact, we conclude that the load rotates differently in comparison to the vertical axis $a$. It can be seen that the distance between the load carrier's hanging point I and load carrier's centre of mass T is so big near the boundary planes of the workspace that the starting presumption (from widely available literature) that these points overlap is completely unfounded. This result was discovered during many years of research and developing in the field of CPR systems and can significantly affect the dynamics of the response of these systems. With the results from this paper, the new space for research in fields of CPR system's kinematics and dynamics is open for the future analysis and development.

# References

1. Higuchi, T., Ming, A., Jiang-Yu, J.: Application of multi-dimensional wire crane in construction. In: 5th International Symposium on Robotics in Construction, Tokyo, pp. 661–668 (1988)
2. Gosselin, C., Grenier, M.: On the determination of the force distribution in overconstrained cable-driven parallel mechanisms. Meccanica **46**(1), 3–15 (2011). An International Journal of Theoretical and Applied Mechanics, Springer
3. Borgstrom, P.H, Borgstrom, N.P, Stealey, M.J, Jordan, B, Sukhatme, G, Batalin, M.A., Kaiser, W.J.: Discrete trajectory control algorithms for NIMS3D, an autonomous underconstrained three-dimensional cabled robot. In: Proceedings of the 2007 IEEE/RSJ International Conference on Intelligent Robots and Systems, San Diego, CA, USA (2007)
4. Merlet, J.P.: MARIONET a family of modular wire-driven parallel robots. In: Lenarcic, J., Stanisic, M.M. (eds.) Advances in Robot Kinematics: Motion in Man and Machine, pp. 53–61. Springer, Heidelberg (2010)
5. Miermeister, P., Pott, A., Verl, A.: Auto-calibration method for overconstrained cable-driven parallel robots. In: ROBOTIK 2012, 7th German Conference on Robotics, Munich, Germany (2012)
6. Duan, B.Y.: A new design project of the line feed structure for large spherical radio telescope and its nonlinear dynamic analysis. Mechatronics **9**, 53–64 (1998)
7. Su, X.Y., Duan, B.Y.: The application of the stewart platform in large spherical radio telescopes. J. Robot. Syst. **17**(7), 375–383 (2000). Wiley
8. Su, X.Y., Duan, B.Y.: The mathematical design and kinematics accuracy analysis of a fine tuning stable platform for the large spherical radio telescope. Mechatronics **10**, 819–834 (2000)
9. Filipovic, M., Djuric, A., Kevac, L.: The significance of adopted Lagrange principle of virtual work used for modeling aerial robots. Appl. Math. Model. **39**, 1804–1822 (2015)
10. Filipovic, M., Djuric, A., Kevac, L.: Contribution to the modeling of cable-suspended parallel robot hanged on the four points. In: IEEE/RSJ International Conference on Intelligent Robots and Systems, IROS 2012, Vilamoura, Portugal, pp. 3526–3531 (2012)
11. Filipovic, M., Djuric, A.: Mathematical model of the aerial robot base on its geometric relationship. FME Trans. Sci. J. **42**(2), 133–142 (2014). Faculty of Mechanical Engineering, Belgrade, Serbia
12. Filipovic, M., Djuric, A., Kevac, L.: The rigid S-type cable-suspended parallel robot design, modelling and analysis. Robotica 34(9), 1–13 (2014). Available on CJO 2014, doi:10.1017/S0263574714002677
13. Filipovic, M.: Comparative analysis of two types of cable-suspended parallel robots, RSCPR system and RFCPR system. In: Symposium INFOTEH-JAHORINA, Bosnia and Herzegovina, vol. 13, pp. 1057–1062 (2014)
14. Filipovic, M.: Relationship between external and internal forces for RSCPR and RFCPR systems. In: Symposium INFOTEH-JAHORINA, Bosnia and Herzegovina, vol. 13, pp. 1069–1074 (2014)
15. Filipovic, M., Djuric, A.: Cable-suspended CPR-D type parallel robot. J. Theoret. Appl. Mech. **54**(2), 645–657 (2016). doi:10.15632/jtam-pl.54.2.645. Warsaw

# Design, Modelling and Prototyping of a Mechanical Hand for Prosthetic Purposes

Vincenzo Niola, Cesare Rossi[✉], and Sergio Savino

University of Naples "Federico II", Via Claudio 21, 80125 Naples, Italy
cesare.rossi@unina.it

**Abstract.** In this paper the design, modelling and prototyping of a mechanical hand for prosthetic purposes are presented. In particular, the development of the project is presented, with the subsequent choices made to reach the prototyping step. In the last part of the paper the results of some tests are also shown, in order to verify the design choices.

**Keywords:** Mechanical hand · Prototyping · Mechanical prosthesis

## 1 Introduction

While technical progress has guaranteed the possibility of resorting to aids more and more efficient hand prostheses, the price of these devices represents the major limitation of their spread out [1–16]. The currently existing robotic hands provide good gripping capabilities, but many robotic hands are equipped with an actuation system that is placed completely within the structure of the hand and simultaneously governs the movement of the fingers and the thumb opposition. This aspect, combined with an actuation system based on traditional electric drives, considerably restricts the number of degrees of freedom, since it is not possible to have more than 1 or 2 actuators inside the hand. Few degrees of freedom cause many difficulties in "wrapping" the fingers around the object grasped during a generic gripping.

The main problem consists in obtaining an articulated movement of the fingers, capable to adapt to the generic form of the object and using a small number of actuators, that is able to operate the various degrees of freedom. The solution studied is to use underactuated mechanisms, with a number of actuators lower than the number of degrees of freedom.

In this paper we will be described the prototyping design of an underactuated hand prosthesis, based on differential mechanisms that uses mobile pulleys in cascade for the closure and rocker arms to actuate the antagonists tendons [17–23]. This is done in order to examine the possibility of realizing a hand prosthesis being economic, with a rather simple kinematic system and very light in terms of weight. The device is driven by a single inelastic tendon which allows an adjustment of the gripping force of an object directly by adjusting the pulling force by the only actuator. The paper describes the design of the prototype and the results of some experiments conducted on it in order to test its functionality and capabilities.

## 2   Design

The hand model includes five fingers, with a single motor by means of a pulley system in cascade, suitably dimensioned to convey movement to the phalanges. Each finger consists of three elements, representing respectively the distal, medial and proximal phalanges, joined by hinges, and activated by a single inelastic tendon. The grasp of an object of any shape is obtained by operating the main inelastic tendon, which, through the pulley system, distributes the force among the various fingers, and generates the
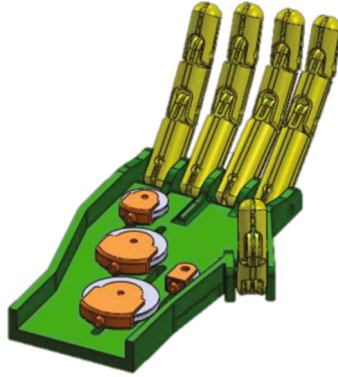


**Fig. 1.** The under-actuated self-adapting mechanical hand prostheses design

closure of each finger according to the resistance offered by the object to be grasped in the contact points.

The prototype has been designed for each component through the use of parametric CAD software, with which tests on mechanisms were carried out; possible interferences among the individual components have been studied, and dynamic simulations have been performed (Fig. 1).

The prototype in question was made by converting the CAD in binary format STL (Stereo Lithography interface format) born to the stereo lithography CAD software, to be reproduced by any 3D printer, thus greatly reducing costs.
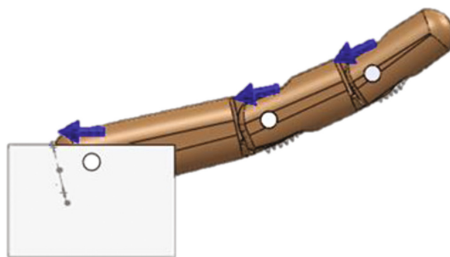


**Fig. 2.** Simulation model

**Table 1.** Finger parameters

| Phalanx | Mass (kg) | Length (m) - distance between previous and next hinge | Stiffness (N/m) |
|---------|-----------|-------------------------------------------------------|-----------------|
| Proximal | 0.01 | 0.045 | 15000 |
| Medial | 0.0055 | 0.030 | 5000 |
| Distal | 0.0030 | 0.025 | 1100 |

By means of parametric prototyping software, the behaviour of the single finger was studied. In particular, the action of the actuator tendon was obtained by applying forces with variable direction in the exit of the tendon guides, while the action of the antagonist tendon was obtained using elastic elements, Fig. 2. The rigidity values of the elastic elements were determined by means of a dynamic simulation of the model. The system response in the presence of the only force of gravity was studied by varying the values of stiffness of the springs. In this way the minimum values sufficient to guarantee the system to remain in its initial position, have been identified. These values are shown in Table 1.



a)                b)                c)
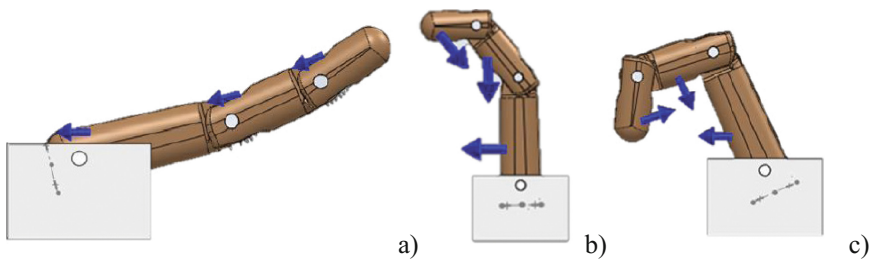
**Fig. 3.** Closing simulation

With a second group of simulations it was possible to identify the minimum value of the force of the actuator tendon to allow a complete closure of the finger in the absence of objects to be gripped. Simulating the presence of friction on each hinge, with a coefficient of dynamic friction equal to $\mu = 100$, a force applied to the tendon of 9 N is sufficient to the closure of the finger. In Fig. 3 some phases of the simulation are shown.

Table 1 shows the values of finger parameters.

The simulation clearly shows that the direction of the forces changes, depending on the configuration achieved by the finger.

The CAD model allowed the study of the movement of all five fingers during the grasping of various objects. So, before the hand prototyping, it was possible to study and analyse any interference among the components. In Figs. 4 and 5 two tests carried out to study and analyse the position of the phalanges during the grasp of two objects with different sizes and geometries are shown.

In particular, in Fig. 4 the object is represented by an element with a non-symmetrical geometric section, to test the grip on objects more complicated to grasp.

In Fig. 5, the object is a sphere, and it can be noted also in this case that the fingers of the hand are adapted to the object for grasping.

**Fig. 4.** Simulation of gripping a complex object
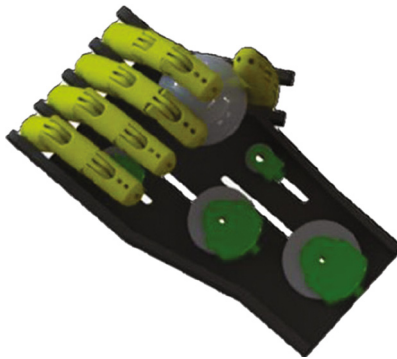


**Fig. 5.** Simulation of gripping a spherical object

## 3 Prototyping

With the three-dimensional CAD model of all the pieces, and by means of a 3D printer, the entire prototyping of the hand was made from plastic material (PLA).

The final position of the thumb has been chosen as a result of different simulations of the closing of the fingers in a CAD environment. An angle of the thumb of 25° with respect the palm central axis was considered as appropriate in order to achieve the closure of the thumb on the other fingers, resulting in greater effectiveness of the grip, since with this configuration the object is pushed towards the centre of the palm.

The finger is composed of three elements, representing the phalanges distal, medial and proximal, that are connected by means of hinges. The medial and distal phalanges lengths are constant for all the five fingers, while the proximal phalanx has a variable length and defines the overall length of the finger. Also for this component several changes during the design were made, also on the basis of the early experimental results. Figure 6 shows the evolution of the three phalanges from the first prototypes at the top, up to the final one at the bottom.
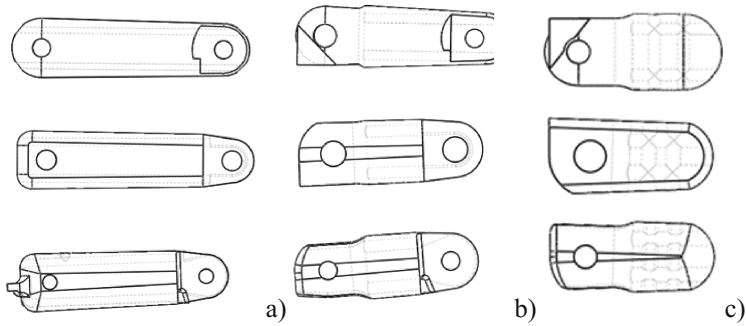
**Fig. 6.** Different prototypes of the phalanges: (a) proximal phalanx, (b) medial phalanx; (c) distal phalanx

The principal dimensions of the distal phalanx are length 22 mm and width 11 mm × 13 mm, as shown in Fig. 7a). In addition to the guides for the passage of the actuator tendon and extensor tendon, two transverse channels have been provided to allow the fixing of the ends of the tendons themselves.
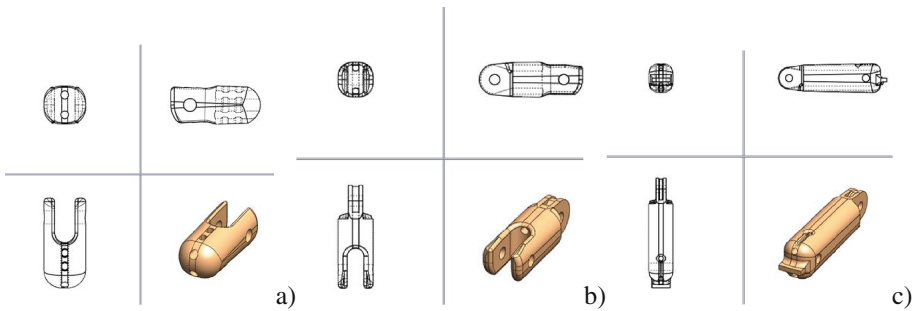


**Fig. 7.** (a) Distal phalanx; (b) Medial phalanx; (c) Proximal phalanx

The relative rotation between the medial phalanx, Fig. 7b), and the distal one can be at maximum of 78°, and the main dimensions of the medial phalanx are length 38 mm and width 13 mm × 13 mm, with a distance between the centres of the two hinges of 30 mm.

The proximal phalanx has different lengths depending on the finger to which it belongs, in particular 48 mm for thumb and little finger, 55 mm for ring finger and 59 for the index and middle. The proximal phalanx has a projection from the side of the palm to prevent the overextension of the finger, Fig. 7c).

In Fig. 8 three prototypes representative of the evolution of the finger are shown.

The differential mechanical system that permits the under-implementation of the fingers of the hand is very simple, Fig. 9, and is constituted by four pulleys suitably dimensioned (21,40 mm; 30,60 mm; 35,20 mm; 13 mm) which act in cascade. The first pulley (upper left) is connected to the tendons of the little finger and ring finger and
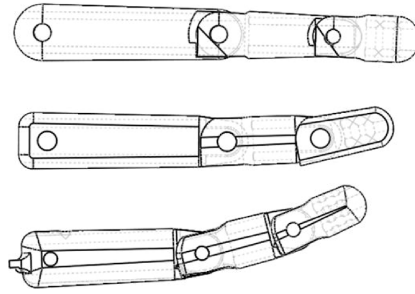
**Fig. 8.** Finger prototypes
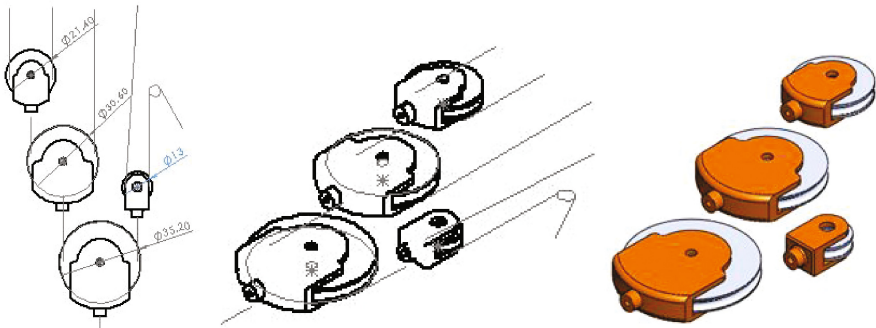


**Fig. 9.** Differential system for force distribution

is operated by a tendon which together with the tendon of the middle finger is wrapped up a second pulley. A third pulley is attached to thumb and index finger; finally, the second and the third pulley are connected to the main pulley on which acts the tendon traction. Figure 9 shows a plane image with the main dimensions and two isometric images of the differential system.

The final prototype is shown in Fig. 10.

The action of the extensor tendons, originally conceived with 5 elastic elements, one per finger, was opposed to the closing force exerted by the actuator tendon, causing an excessive increase of the traction force during the phases of closing of the hand. A differential system was introduced which uses the same scheme actuation, but based on rods and rocker arms in place of the pulleys; finally, only the main rod is connected to a single recall elastic element (Fig. 11). To automate the actuation of the mechanism, the prototype was equipped with a digital servo motor, driven and controlled by means of a programmable microcontroller, Fig. 12.
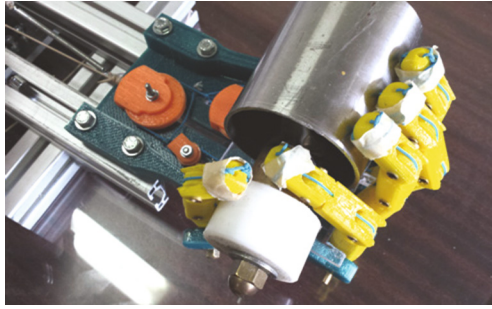
**Fig. 10.** Hand prosthesis prototype
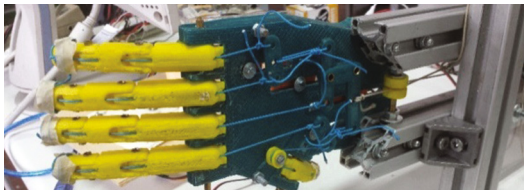


**Fig. 11.** Differential system applying the extensor action
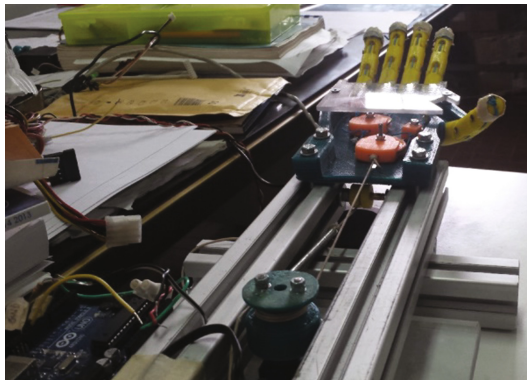


**Fig. 12.** The under-actuated, self-adapting mechanical hand prostheses actuated with digital servomotor and programmable microcontroller

## 4    Experimental Tests

Experimental tests were performed during the design and development of the prototype, and finally on the prototype to test its operation. In the following the results of the main tests carried on the finger are shown.

The first tests, carried out in the development phase of the prototype, were performed on a single finger, installed on a support in order to analyse its behaviour, see

**Fig. 13.** Test on a single finger

Fig. 13. In particular, the tests' main scope consisted in evaluating the pressure force with which the distal phalanx can operate.

Two types of phalanges with different diameters of the guide of the tendon have been realized: one of 2 mm and the other of 2,5 mm; the command tendon has been operated with 900 g, i.e. 9 N, and then the force exerted by the finger during the grasping phase was evaluated by means of a digital scale, positioned in such a way that the finger in fully closed position exerted a force on the scales with its distal phalanx, Fig. 13. The tests were carried out with and without the action of extension tendon; the results are shown in Table 1.

The results of tests carried out show that for an applied force of 9 N, the finger can apply with its last phalanx a force approximately equal to $1.54 \div 1.86$ N, about one-fifth of the traction force. A slight improvement is obtained in the prototype with largest guides where, probably, friction between the tendon and the conduit through which it flows is reduced.

To simulate the action of the extensor tendon a spring with an elasticity value of 15000 N/m was added, which brings the finger in the inactive configuration when the traction force is removed. In this case, as is clear from the data of Table 2, a further portion of traction force is lost due to the elastic element. In addition there are not substantial differences in the values found in the tests carried out on two fingers with different size guides, because the introduction of the action of extension tendon is dominant over friction phenomena.

**Table 2.** Results of tests on a single finger

| Tendon guide way diameter (mm) | 2 | 2,5 | 2 | 2,5 |
|---|---|---|---|---|
| Extension tendon | No | No | Yes | Yes |
| Traction tendon force (N) | 9 | 9 | 9 | 9 |
| Fingertip force (N) | 1,545 | 1,866 | 0,884 | 0,701 |

## 5    Conclusion

The design, the modelling and prototyping of a mechanical hand for prosthetic purposes were presented. This investigation allowed us to design a suitable device in order to correctly operate in a wide number of grasping tasks. The correct choice of a number of parameters such as the tendon guide position, the phalanx's length and the hinge position are essential in an underactuated mechanism. This result was achieved, first by a large number of CAD simulations and then by a number of prototypes; the latter were obtained in PLA by a 3D printer.

Some simulation examples of grasping rather complex objects with the last prototype are shown. Finally, some simulation examples were also presented on the grasping force on the fingertip obtained with a given actuator pull.

This work allowed us to obtain a satisfactory prototype in order to carry on a wide number of investigations on both the grasping and the control by using different human-prosthesis interfaces (e.g. EMG) and the trajectory planning algorithm [24, 25].

## References

1. Grioli, G., Catalano, M., Silvestri, E., Tono, S., Bicchi, A.: Adaptive synergies: an approach to the design of under-actuated robotic hands. IEEE/RSJ Int. Conf. Intell. Robots Syst., 7–12 (2012)
2. Roccella, S., Carrozza, M.C., Cappiello, G., Dario, P., Cabibihan, J.J., Zecca, M., Miwa, H., Itoh, K., Matsumoto, M., Takanishi, A.: Design, fabrication and preliminary results of a novel anthropomorphic hand for humanoid robotics: RCH- 1. In: Proceedings of 2004 IEEE/RSJ International Conference on Intelligent Robots and Systems, Sendai, Japan, 28 September–2 October (2004)
3. Roccella, S., Carrozza, M.C., Cappiello, G., Cabibihan, J.J., Laschi, C., Dario, P., Takanobu, H., Matsumoto, M., Miwa, H., Itoh, K., Takanishi, A.: Design and development of five-fingered hands for a humanoid emotion expression robot. Int. J. Humanoid Rob. **4**, 181–206 (2007)
4. Roccella, S., Cattin, E., Vitiello, N. Giovacchini, F., Chiri, A., Vecchi, F., Carrozza, M.C.: Design of a hand exoskeleton (handexos) for the rehabilitation of the hand. Gerontechnology **7**(2), 197, 207 (2008)
5. Cipriani, C., Controzzi, M., Carrozza, M.C.: The smart hand transradial prosthesis. J. Neuro-Eng. Rehabil. **8**, 29 (2011)
6. Gosselin, C., Pelletier, F., Laliberté, T.: An anthropomorphic underactuated robotic hand with 15 Dofs and a single actuator. In: Proceedings of 2008 IEEE International Conference on Robotics and Automation, Pasadena, CA, USA, 19–23 May 2008
7. Catalano, M.G., Grioli, G., Serio, A., Farnioli, E., Piazza, C., Bicchi, A.: Adaptive synergies for a humanoid robot hand. In: Proceedings of IEEE-RAS International Conference on Humanoid Robots, Osaka, Japan, October 2012
8. Bicchi, A.: Hands for dexterous manipulation and robust grasping: a difficult road toward simplicity. IEEE Trans. Robot. Autom. **16**(6), 652–662 (2000)
9. Lotti, F., Vasura, G.: Design aspects for advanced robot hands. In: Proceedings of IEEE/RSJ International Conference on Intelligent Robots and Systems, Lausanne, Switzerland, 30 September–4 October 2002

10. Brown, C.Y., Asada, H.H.: Inter-finger coordination and postural synergies in robot hands via mechanical implementation of principal components analysis. In: Proceedings of the 2007 IEEE/RSJ International Conference on Intelligent Robots and Systems, San Diego, CA, USA, 29 October–2 November 2007

11. Dechev, N., Cleghorn, W.L., Naumann, S.: Multiple finger, passive adaptive grasp prosthetic hand. Mech. Mach. Theory **36**, 1157–1173 (2001)

12. Baril, M., Laliberte, T., Gosselin, C., Routhier, F.: On the design of a mechanically programmable underactuated anthropomorphic prosthetic gripper. J. Mech. Des. **135**(12), 121008 (2013). doi:10.1115/1.4025493

13. Nelson, C.A., Dessauw, E., Saiter, J.M., Benzohra, M.: Design of a compliant underactuated robotic finger with coordinated stiffness. In: ASME 2013 International Design Engineering Technical Conferences and Computers and Information in Engineering Conference, p. V06BT07A017. American Society of Mechanical Engineers (2013)

14. Groenewegen, M.W., Aguirre, M.E., Herder, J.L.: Design of a partially compliant, three-phalanx underactuated prosthetic finger. In: ASME 2015 International Design Engineering Technical Conferences and Computers and Information in Engineering Conference, p. V05AT08A040. American Society of Mechanical Engineers (2015)

15. Townsend, W.: The barret hand grasper - programmable flexible part handling and assembly. Ind. Robot. Int. J. **27**(3), 181–188 (2000)

16. Hirose, S., Umetani, Y.: The development of soft gripper for versatile robot hand. Mech. Mach. Theory **13**, 351–359 (1978)

17. Rossi, C., Savino, S.: An underactuated multi-finger grasping device. Int. J. Adv. Robot. Syst. **11**(1), Article no. 20, 17 February 2014

18. Rossi, C., Savino, S., Niola, V., Troncone, S.: A study of a robotic hand with tendon driven fingers, robotica (2014). doi:10.1017/S0263574714001179, ISSN: 0263-5747

19. Penta, F., Rossi, C., Savino, S.: An underactuated finger for a robotic hand. Int. J. Mech. Control **15**(2), 63–68 (2014). ISSN: 1590-8844

20. Penta, P., Rossi, C., Savino, S.: Gripping analysis of an underactuated finger–advances in intelligent systems and computing. In: Proceedings of 24th International Workshop on Robotics in Alpe-Adria-Danube Region, Bucharest, Romania, 27–29 May 2015, pp. 71–78 (print version). doi:10.1007/978-3-319-21290-6, ISBN: 9783319212890

21. Niola, V., Penta, F., Rossi, C., Savino, S.: An underactuated mechanical hand: theoretical studies and prototyping. Int. J. Mech. Control **16**(1), 11–19 (2015). ISSN: 15908844

22. Carbone, G., Rossi, C., Savino, S.: Performance comparison between FEDERICA Hand and LARM Hand. Int. J. Adv. Robot. Syst. **12** (2015). doi:10.5772/60523, ISSN: 17298806

23. Niola, V., Rossi, C., Savino, S., Carbone, G., Gaspareto, A., Quaglia, G.: An underactuated mechanical hand prosthesis by IFToMM ITALY. In: Proceedings of 14th IFToMM World Congress, Taipei, Taiwan, 25–30 October 2015. doi:10.6567/IFToMM.14TH.WC.PS13.005

24. Niola, V., Rossi, C., Savino, S., Strano, S.: Robot trajectory planning by points and tangents. In: Proceedings of the 10th WSEAS International Conference on Robotics, Control and Manufacturing Technology, ROCOM 2010, Hangzhou, China, 11–13 April 2010, pp. 91–96 (2010). ISSN: 1790-5117, ISBN: 978-960-474-175-5

25. Rossi, C., Savino, S.: Robot trajectory planning by assigning positions and tangential velocities. Robot. Comput. Integr. Manuf. **29**(1), 139–156 (2013). doi:10.1016/j.rcim.2012.04.003. ISSN 0736-5845

# Multibody Model to Evaluate Quality Grasping of an Underactuated Mechanical Finger

Cesare Rossi[✉], Sergio Savino, and Francesco Timpone

University of Naples "Federico II", Via Claudio 21, 80125 Naples, Italy
cesare.rossi@unina.it

**Abstract.** A multibody model to analyse the gripping quality of an underactuated mechanical finger operated with tendon is described. To study the gripping ability of the finger a contact model that can simulate the interaction with the object to be taken has been developed. In the last section, some results related to the gripping of a spherical object, are described.

**Keywords:** Mechanical finger · Multibody model · Grasping analysis

## 1 Introduction

The gripping of the objects by a mechanical system is a key aspect in all the tasks in which the mechanical system must interact with the environment in which it operates. The goal of a correct grasp is to ensure that the object is constrained during the task, and it is not influenced by the presence of external disturbances. Many parameters can characterize a grasp, so, to evaluate the goodness of a grasp it is possible to introduce a "quality measure". A good review about the quality measures proposed in the literature is presented in [1, 2].

The research on dexterous robotic hands is especially attracted by underactuated hands, with a number of degrees of actuation minor than the number of degrees of freedom. In this sense, the application of bio-inspired principles allows developing approaches for the analysis of synergistic underactuated grasps [3, 4].

Simulation is one of the most important tools to analyse the behaviour of robotic system [5]. Several toolboxes have been presented for the modelling and control of robot systems [6–8], and some simulators have been developed for human and robot grasping evaluation, like GraspIt! [9], Opengrasp [10] and SynGrasp [11] which has been developed entirely in MATLAB.

In this paper, a preliminary version of a multibody model of an underactuated finger is presented. This model is based on the model and prototype of the underactuated finger and hand presented in [12–16]. The multibody model includes a contact model in order to study and analyse the grasping of the finger. The goal of building such a model is to get a tool for the study of the grasp of an underactuated hand that can also be used for prosthetic purposes [16].

## 2  Multibody Model of the Finger

The present paper concerns a multibody model of a single tendon, three phalanges finger that is used in a multi-finger grasping device. By means of this finger and a differential system, it is possible to use only one actuator to move all the fingers of a 5-finger hand. The input parameters of each phalanx (Fig. 1) are: length (L), width (W), thickness (T), peg-hole radius (R), and mass density.
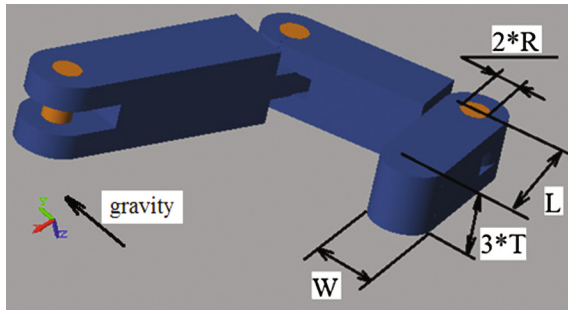


**Fig. 1.** Multibody finger model

The basis of the model consists of the "Body", "Rigid Transform" and "Revolute Joint" blocks. Each revolute joint has a subsystems "Hard stop" that allows to set up the excursion range of the joint, in particular each joint can rotate with 90°. The action which the tendon exerts on the phalanges is simulated by applying appropriate forces at points of entry and exit of the guides of the tendon itself, see Fig. 2.
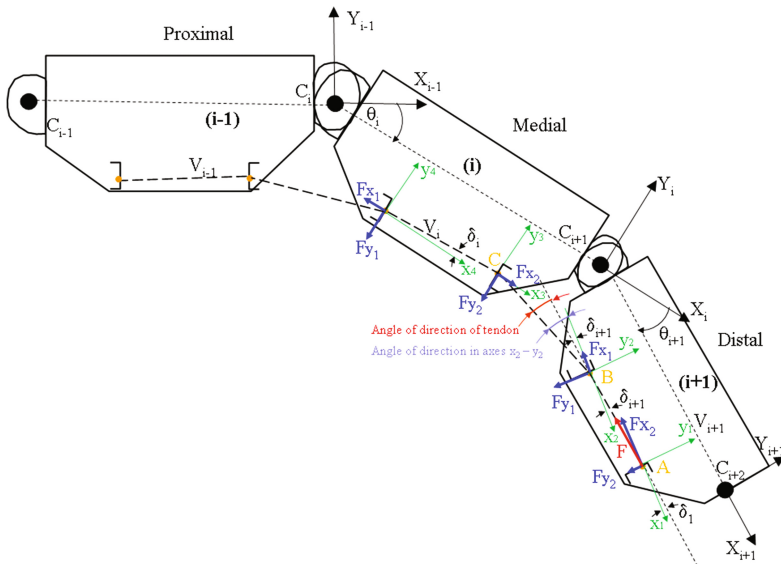


**Fig. 2.** Scheme of force of tendon acuated finger

In order to study the grasping of the finger the model of the finger has been simulated in a working environment in which a plane to simulate the presence of the palm and a spherical object were added, see Fig. 3.
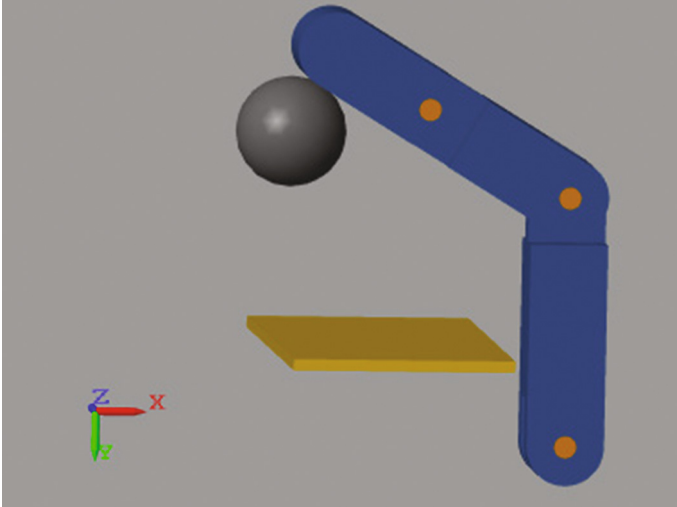


**Fig. 3.** The multibody finger model for grasping simulation.

The dimensional parameters of the finger are reported in Table 1.

**Table 1.** Dimensional parameters of the finger

| Phalanx | L(m) | W(m) | T(m) |
|---------|------|------|------|
| Proximal | $4.5 \times 10^{-2}$ | $1.4 \times 10^{-2}$ | $1.4/3 = 4.67 \times 10^{-3}$ |
| Medial | $3 \times 10^{-2}$ | $1.4 \times 10^{-2}$ | $4.67 \times 10^{-3}$ |
| Distal | $2 \times 10^{-2}$ | $1.4 \times 10^{-2}$ | $4.33 \times 10^{-3}$ |

## 3   Contact Model

The contact of the fingertip of each phalanx with the objects was simulated with elastic damping reaction and friction force between the bodies. In particular, to analyse the contact of the finger with the object, each phalanx of the finger has been covered with a plain "skin"; in this way the contact takes always place between a plane and a sphere. Figure 4 depicts the model with the plain skin.

The contact between two bodies was simulated with a force applied only along the direction of penetration of the two bodies. Figure 5 shows this force as $F_n$, and it acts on the plane and on the sphere in the opposite direction.

The friction force is also included in the contact model; it acts as a tangential force in the contact point on both bodies. In Fig. 5 the friction force is indicated as $F_t$.
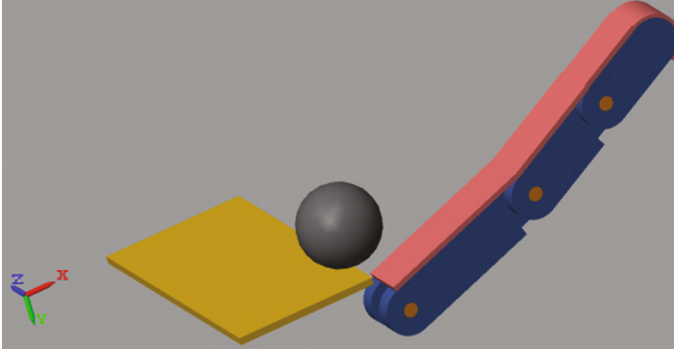
**Fig. 4.** The multibody finger model with plain "skin" to simulate the contact with the object
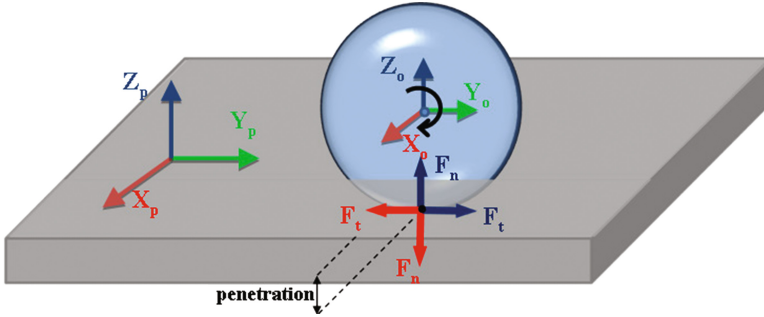


**Fig. 5.** Contact scheme with normal force $F_n$ and friction force $F_t$

The normal force $F_n$ acts by opposing the penetration of the two bodies and the damping is zero when the penetration decreases.

$$F_n = \begin{cases} k \cdot Z_{penetration} + b \cdot v_{penetration} & \forall Z_{penetration} > 0, v_{penetration} > 0 \\ k \cdot Z_{penetration} & \forall Z_{penetration} > 0, v_{penetration} < 0 \\ 0 & \forall Z_{penetration} < 0 \end{cases} \quad (1)$$

where $Z_{penetration}$ is the penetration between the two bodies, $v_{penetration}$ is the velocity of penetration, k is the contact stiffness and b is the contact damping.

The friction force $F_t$ is the product of the normal force and a coefficient of friction that is a function of the relative velocity at the contact point.

$$F_t = F_n \cdot \mu, \quad \mu = f(v_{CP}) \quad (2)$$

where $\mu$ is the coefficient of friction and $v_{CP}$ is the relative velocity at the contact point.

In particular the coefficient $\mu$ has the following expression (3).

$$\mu = f(v_{CP}) \begin{cases} v_{CP} \cdot \mu_s / v_{thr} & v_{CP} < v_{trh} \\ \mu_s - v_{CP} \dfrac{\mu_s - \mu_k}{0.5 \cdot v_{thr}} & v_{trh} \leq v_{CP} \leq 1.5 \cdot v_{trh} \\ \mu_k & v_{CP} > 1.5 \cdot v_{trh} \end{cases} \tag{3}$$

where $\mu_s$ is the static friction coefficient, $\mu_k$ is the kinetic friction coefficient and $v_{thr}$ is a velocity threshold above which it is necessary to use the kinetic friction coefficient.

## 4    Grasping Simulation

The next section gives some results obtained using the model described above. The simulations were done by securing the object to be grasped in the workspace and varying its position on a plane parallel to $X_p Z_p$ passing through the centreline of the finger, like shown in Fig. 6. In particular, the area in which the sphere's centre moves has a size of $4 \times 10^{-2}$ m along the $X_p$ axis and of $(4 - r_{obj}) \times 10^{-2}$ m along the $Z_p$ axis, where $r_{obj}$ is the radius of the sphere. Moving the centre of the sphere in this area, it is possible to verify the finger's different dynamical behaviours during grasping tasks.
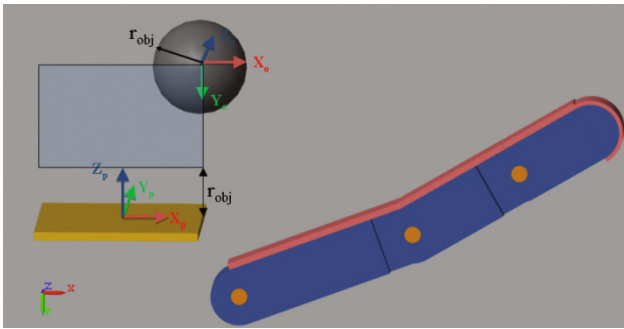


**Fig. 6.** Simulation scheme with the area in which the fixed object centre moves

The finger model is actuated with a constant tendon force that reaches its nominal values in 0.02 s. The positions of the ends of the tendon guides in each phalanx have been optimized in order to obtain a sequence of closing of the phalanges "proximal-medial-distal". In this way the gripping of the objects is advantaged.

The quality of the grasping is measured evaluating different parameters. In particular, the velocity of the object (sphere) respect to the phalanges, the velocity of the object respect to the palm, the contact of the object with the phalanges and the palm, are measured and are used to judge the quality of the grasp. The function, QG that describes the quality of grasping is expressed in (4):

$$QG = \begin{cases} 0.5 & \textit{if } v_{obj}distal \cong 0 \;\; v_{obj}medial \cong 0 \;\; v_{obj}proximal \cong 0 \\ 0.75 & \textit{if } v_{obj}palm \cong 0 \\ 1 & \textit{if there is contact with 2 surfaces} \\ 2 & \textit{if there is contact withat least 3 surfaces} \end{cases} \qquad (4)$$

where $v_{obj}palm$ is the velocity of the object with respect to the palm, $v_{obj}distal$ is the velocity of the object with respect to the distal phalanx, $v_{obj}medial$ is the velocity of the object with respect to the medial phalanx, and $v_{obj}proximal$ is the velocity of the object with respect to the proximal phalanx.

Obviously, QG can assume composite values if more conditions occur together.

Figure 7 shows a map of QG for an object with radius of $8 \times 10^{-3}$ m, i.e., the distance between distal phalanx and proximal phalanx when the finger is completely close. For this kind of simulation, with the object fixed in the working space, QG assumes always values equal or greater than 0.75.
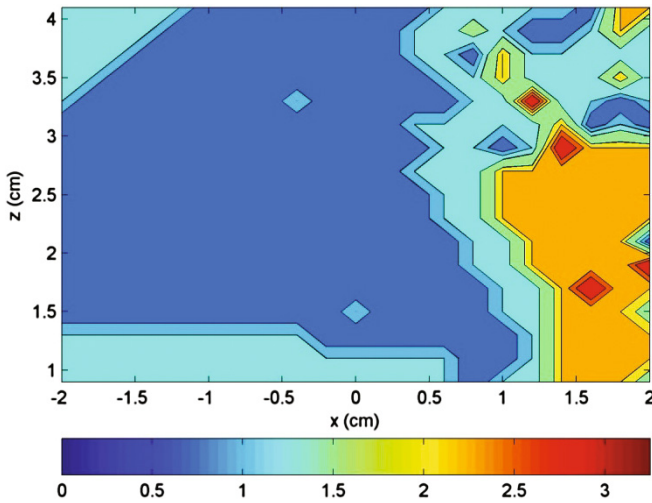


**Fig. 7.** QG map for an object with radius of $8 \times 10^{-3}$ m

Observing Fig. 7, it is clear that the best quality of grasping occurs when the object is near to the proximal phalanx. In this zone QG can be 3.25, which means that the phalanges have null relative velocity with respect to the object which is in contact with at least three surfaces including the phalanges and the palm.

However, near the proximal phalanx QG is 2.25, which means that the phalanges have null relative velocity with respect to the object which is in contact with two surfaces. In the other zones of the analysed area, the object is in contact with less than two surfaces.

When the object moves away from the proximal phalanx in direction –X, only the medial phalanx and distal phalanx can touch the object. When the centre of the sphere is placed with respect to the proximal phalanx at a greater distance of the effective

length of the medial and distal phalanges, the finger may not touch the object. This situation occurs in the upper left corner of Fig. 7.

QG assumes the value of 0.75 when the finger does not reach an equilibrium condition with respect to the object, whereas QG is 1.25 when the finger reaches equilibrium, but at most only one of its surfaces is in contact with the object.

In Figs. 8, 9 and 10 the radius of the sphere is increased to $1 \times 10^{-2}$ m, $1.15 \times 10^{-2}$ m and $1.5 \times 10^{-2}$ m respectively. When the radius of the sphere becomes $1.15 \times 10^{-2}$ m, the object has the same size as the distance between the medial phalanx and the palm, when the finger is completely closed.
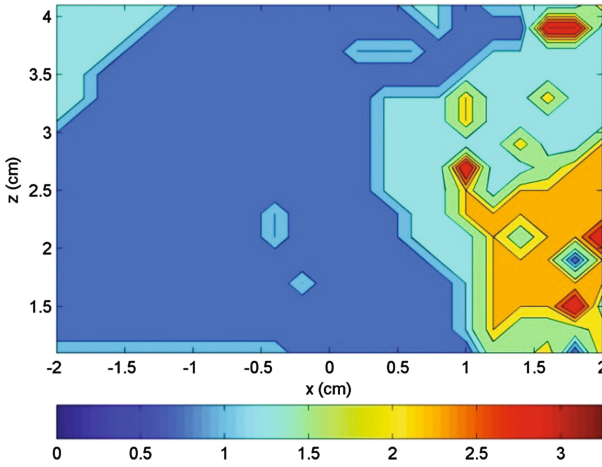


**Fig. 8.** QG map for an object with radius of $1.0 \times 10^{-2}$ m
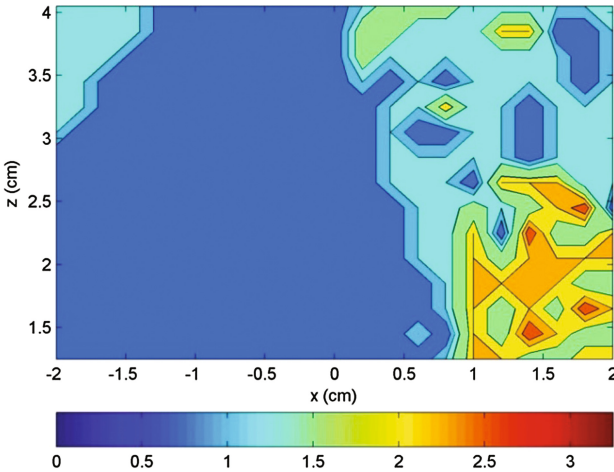


**Fig. 9.** QG map for an object with radius of $1.15 \times 10^{-2}$ m
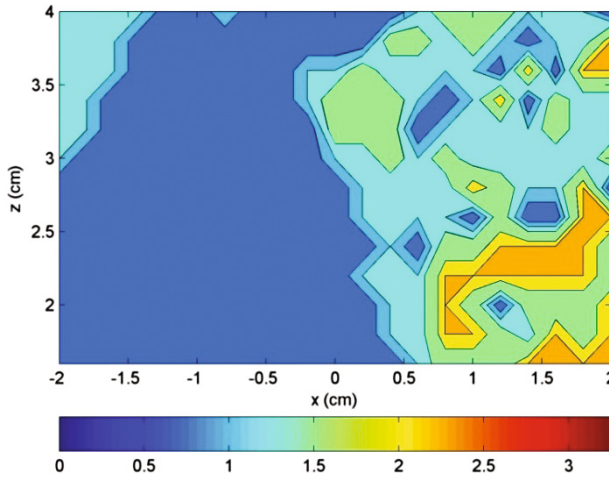
**Fig. 10.** QG map for an object with radius of $1.5 \times 10^{-2}$ m

If the radius of the sphere increases, the areas in which the finger is in contact with the object on three surfaces disappear, while the area in which the contact occurs on two surfaces decreases.

As can be seen in Fig. 10, in this condition the finger is not able to wrap around the object, so the maximum value of QG is 2.25 in small areas near the proximal phalanx and near the palm.

Figure 11 shows a map of QG for an object with the radius of $8 \times 10^{-3}$ m, when the traction force of the tendon is applied in a time interval of 0.12 s.
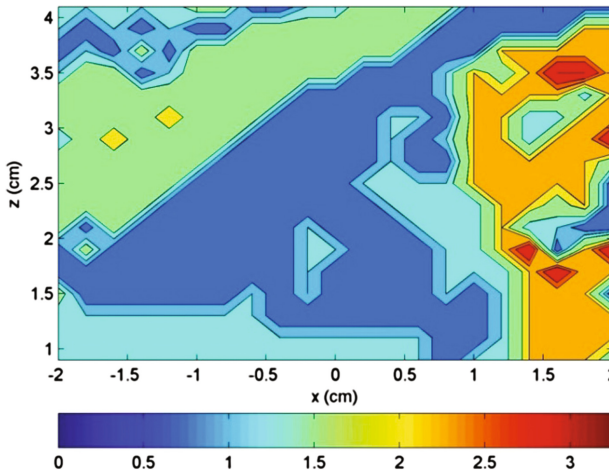


**Fig. 11.** QG map for an object of radius $8 \times 10^{-3}$ m and force application time of 0.12 s

It is possible to observe a different behaviour of the finger. In fact, applying the tendon force a longer time interval, the phalanges approach the object in a different way and the rebound phenomena do not occur when they touch the object itself. The effect of this different dynamical behaviour of the phalanges is an increase in the value of QG. In particular, the area in which QG is 2.25 near the palm and the proximal phalanx becomes greater, and in the area $x \in [-2, 0.5] \cup z \in [2, 4]$, QG assumes, at many points, the value 1.75. This last condition means that the object is in contact with two surfaces of the finger.

## 5    Conclusion

A multibody model of a tendon-driven finger has been developed; a contact model between surfaces has been added to it, in order to study the quality of the gripping performed by the finger. A quality index for gripping was considered when analysing the parameters of the model. Different gripping simulations were performed by moving the object in a working area of the finger, allowing the evaluation of maps for the QG index.

The developed model is a good tool to make more considerations on the gripping quality, by studying both the geometric parameters which influence the gripping and the dynamic parameters that affect the behaviour of the finger during a task. Regarding this last point, it was estimated that the way in which the tendon exerts the traction force is important (this can be observed in Figs. 7 and 11). This means that appropriate laws of motion assigned to the actuator which pulls the tendon can ensure a dynamic behaviour of the finger most suitable to the grip. Future tests, carried out using the model described, will allow evaluating the use of motion planning techniques already presented in previous studies [17, 18].

## References

1. Suárez, R., Roa, M.A., Cornellà, J.: Grasp quality measures. Technical University of Catalunya, Technical report IOCDT-P-2006-10 (2006)
2. Roa, M.A., Suárez, R.: Grasp quality measures: review and performance. Auton. Robots **38**(1), 65–88 (2015)
3. Gabiccini, M., Farnioli, E., Bicchi, A.: Grasp and manipulation analysis for synergistic underactuated hands under general loading conditions. In: International Conference of Robotics and Automation - ICRA 2012, Saint Paul, MN, USA, pp. 2836–2842 (2012)
4. Gabiccini, M., Farnioli, E., Bicchi, A.: Grasp analysis tools for synergistic underactuated robotic hands. Int. J. Robot. Res. **32**, 1553–1576 (2013)
5. Žlajpah, L.: Simulation in robotics. Math. Comput. Simul. **79**(4), 879–897 (2008). ISSN: 0378-4754
6. Chinello, F., Scheggi, S., Morbidi, F., Prattichizzo, D.: Kuka control toolbox. IEEE Robot. Autom. Mag. **18**(4), 69–79 (2011)
7. Corke, P.: A robotics toolbox for MATLAB. IEEE Robot. Autom. Mag. **3**(1), 24–32 (1996)

8. Mariottini, G., Prattichizzo, D.: EGT for multiple view geometry and visual servoing: robotics and vision with pinhole and panoramic cameras. IEEE Robot. Autom. Mag. **12**(4), 26–39 (2005)

9. Miller, A., Allen, P.: Graspit! a versatile simulator for robotic grasping. IEEE Robot. Autom. Mag. **11**(4), 110–122 (2004)

10. León, B., et al.: OpenGRASP: a toolkit for robot grasping simulation. In: Ando, N., Balakirsky, S., Hemker, T., Reggiani, M., Stryk, O. (eds.) SIMPAR 2010. LNCS (LNAI), vol. 6472, pp. 109–120. Springer, Heidelberg (2010). doi:10.1007/978-3-642-17319-6_13

11. Malvezzi, M., Gioioso, G., Salvietti, G., Prattichizzo, D., Bicchi, A.: SynGrasp: a MATLAB toolbox for grasp analysis of human and robotic hands. In: Proceedings of the IEEE International Conference on Robotics and Automation, Karlsruhe, Germany (2013)

12. Rossi, C., Savino, S.: Mechanical model of a single tendon finger. In: Proceedings of ICNAAM 2013: 11th International Conference of Numerical Analysis and Applied Mathematics, Rhodes, Greece, 21–27 September 2013

13. Rossi, C., Savino, S.: An underactuated multi-finger grasping device. Int. J. Adv. Robot. Syst. **11**(1) (2014). Article number 20

14. Penta, F., Rossi, C., Savino, S.: An underactuated finger for a robotic hand. Int. J. Mech. Control, **15**(2) (2014). ISSN: 1590-8844

15. Rossi, C., Savino, S., Niola, V., Troncone, S.: A study of a robotic hand with tendon driven fingers. Robotica (2015). ISSN: 0263–5747, doi:10.1017/S0263574714001179

16. Niola, V., Penta, F., Rossi, C., Savino, S.: An underactuated mechanical hand: theoretical studies and prototyping. Int. J. Mech. Control **16**(1), 11–19 (2015). ISSN: 15908844

17. Niola, V., Rossi, C., Savino, S., Strano, S.: Robot trajectory planning by points and tangents. In: Proceedings of the 10th WSEAS International Conference on Robotics, Control and Manufacturing Technology, ROCOM 2010, Hangzhou, China, pp. 91–96, 11–13 April 2010

18. Rossi, C., Savino, S.: Robot trajectory planning by assigning positions and tangential velocities. Robot. Comput. Integr. Manuf. **29**(1), 139–156 (2013). doi:10.1016/j.rcim.2012.04.003

# Robot Applications in Manufacturing and Services

# Multi-agent Solution for Automated Part Supply in Robotized Holonic Manufacturing

Silviu Răileanu[(✉)], Theodor Borangiu, and Octavian Morariu

Department of Automation and Industrial Informatics,
University Politehnica of Bucharest, Bucharest, Romania
{silviu.raileanu,theodor.borangiu}@cimr.pub.ro

**Abstract.** The paper describes a solution extending existing semi-heterarchical manufacturing control architectures with automated component supply of robotized workstations' local storages. Missing components are retrieved from a central feeding system by a visually guided SCARA robot and placed on pallets which are then carried by a twin-track conveyor towards the depleted storages. Workstation robots resupply then their local storages and acknowledge the current operation on the product to be resumed. The supply control at the central feeding station is based on the multi-agent technique; the information counterparts (the supply holons) of the component carriers (the supply pallets) generate simultaneously multiple requests to the central feeding robot (the supply station resource holon), compete to be granted immediate service, and cooperate to reach in common the best decision for the pallet feeding order that delays as little as possible production execution according to the current optimized batch planning and product scheduling.

**Keywords:** Multi-agent system · Robot-vision · Holonic manufacturing · Automated supply

## 1 Introduction

In today's ever changing economic environment manufacturing structures need to be agile in face of both external disturbances (order changes, adding new product types, a. o.) and internal ones (resource failures, stock depletions, a.o.). In this context the paper presents an extension to an existing control architecture [1] which automatically resupplies workstations that run out of components. In order to make the system operate in an optimized manner and also to avoid cell downtime the control architecture is a mix between a centralized and a decentralized, heterarchical solution so that a perturbation will be locally handled through negotiation for job continuity, and a priori computed, optimal scheduling will be only temporarily abandoned.

Nowadays there is a trend towards distributing the intelligence of control architectures [2] among composing entities so that perturbations consisting of resources break down and recovery will be properly handled for job continuity, and decisions will be taken closer to their implementation location. Paradigms of distributed intelligence such as: Product-driven automation, Intelligent product [3], Multi Agent control [4], Holonic Manufacturing System [5] have been developed in heterarchical

control topologies [6]. They permit dynamic reconfiguring of resource teams to provide rapid response to manufacturing changes, automated part re-supply at shop floor storage depletion, fault-tolerance to resource malfunction and adaptability to production variations. This shift from hierarchical to heterarchical control is also sustained by the latest IT developments which make it possible to add decisional capabilities to almost every entity of a manufacturing system (both resources and products).

The paper is structured as follows: Sect. 2 presents the multi-agent control model, Sect. 3 details the interactions between agents realizing the control part, Sect. 4 details the structure of the physical system and how the resupply process works and Sect. 5 presents the conclusions and future work.

## 2   Multi-agent Control System

The control structure of manufacturing cells is decentralized, meaning that each physical entity has an associated agent (information counterpart) responsible with the decision making process [7]. The physical resource (e.g., robot) with its informational counterpart form what is called a holon [9]. From a general point of view a manufacturing cell contains two basic holons [2, 8]: *resource holons* (RH) in charge with material transformation and transport and *order holons* (OH) in charge with the control of work in process (WIP). Additionally, some control architectures [10] incorporate the information necessary for product execution in an entity entitled product holon (PH) which is composed only of an information part storing the product's recipe. In the reported research we keep the order and resource holons extending them with a *supply holon* (SuH) and a *supply station holon* (SuSH), having as resource a robot.

The Supply Holon is an extension of the OH devoted to product execution control and is composed of the pallet on which necessary components are transported to the required station and an associated agent (supply agent) running on an Intelligent Embedded Device (IED) physically attached to the pallet. The supply agent is responsible with the decision making process, with the communication with the SuSH for components upload and with the RHs for unloading components at their local storages. The lifecycle of a SuH is defined by the sequence of the states through which it passes: waiting a supply order in front of the SuSH, loading components on the pallet and transporting components to the specified workstation (Fig. 1).
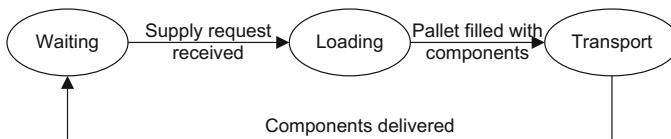


**Fig. 1.** SuH states diagram

To complete the previous stages the following information structure is defined:

- [string] Index: a unique identifier of the current SuH
- [string] State: the state of the current SuH; based on its state the first waiting SuH is chosen by a robotized workstation to refill its local storage

- [string] `Destination`: the workstation that the current SuH will refill with components of a given type
- [string] `Component_type`: the type of components the current SuH carries; each SuH will carry a single type of components
- [INT] `Number_of_components`: the number of components of a single type that the SuH will carry
- [string] `Component_localization_on_pallet`: a description of how components are located on the current pallet so that the destination workstation robot can automatically handle them.

The Supply Station Holon is composed of a set of resources (SCARA robot, vision, bulk feeders, dedicated buffers) for part handling and feeding, and one associated agent responsible with: (i) integration of the resources into the manufacturing cell, (ii) communication with the agent associated to the SuH and (iii) decision making. The operation of the SuSH is described by a cyclic behaviour represented by the following states: <u>waiting</u> (buffer full) – the SuSH waits for a supply command with the buffer of components full, <u>fill buffer</u> – the SuSH hasn't received any request from a SuH and visually sorts components into an available buffer, <u>fill pallet from buffer</u> – upon receiving a supply request the components are uploaded to the SuH from the ones available in the buffer, <u>fill pallet from part-feeding resource (PFR)</u> – if requested components are not available in the buffer they will be handled by the SCARA robot from the part-feeding resource (Fig. 2).
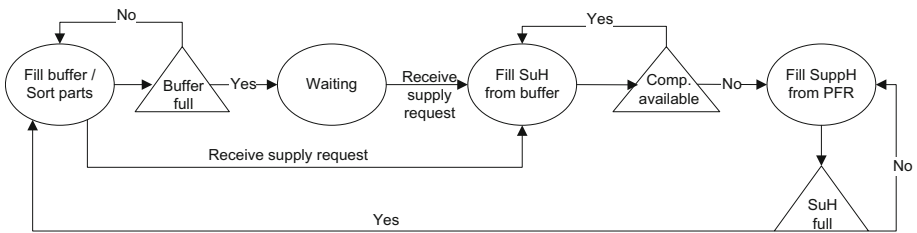


**Fig. 2.** Pallet filling procedure (SuSH state diagram)

The following information structure is defined for the SuSH:

- [string] `Index`: a unique identifier of the current SuSH,
- [string] `State`: the state of the current SuSH; based on its state the appropriate actions are taken in order to fulfil a supply demand (Fig. 2),
- [string] `SuH`: the SuH currently being served,
- set[string] `Components_type`: a set including the available part types
- set[INT] `MaxComponents`: the max. number of parts for each type,
- set[INT] `Components_number`: the current no. of components for each type,
- set[point] `PPpoints` – the set of points between which components are handled by the industrial robot.

Each holon is formed through an agentification process [7] by adding a software agent in charge with decision making and communication via a standard medium with the physical resources. These agents are seen as automation objects – abstraction of mechanical devices with encapsulated intelligence [11] allowing thus component reusability. The following agents compose the software model of the control system: order-, resource-, supply- and supply station- agents.

## 3   Dynamics of the Control Model

The start of the re-supply process is generated by a resource (robot, CNC machine) agent associated to a workstation where a type of component needed for product assembly is missing (Fig. 3). A signal is sent to the agents of the SuHs waiting for transporting components and the first SuH in the "waiting" state is chosen to realize the resupply process (or the SuH in the "waiting state" for the longest time). Based on the re-supply signal (component type and number of components) a negotiation takes place between the chosen supply agent and the supply station agent resulting in loading into the associated pallet the needed components.
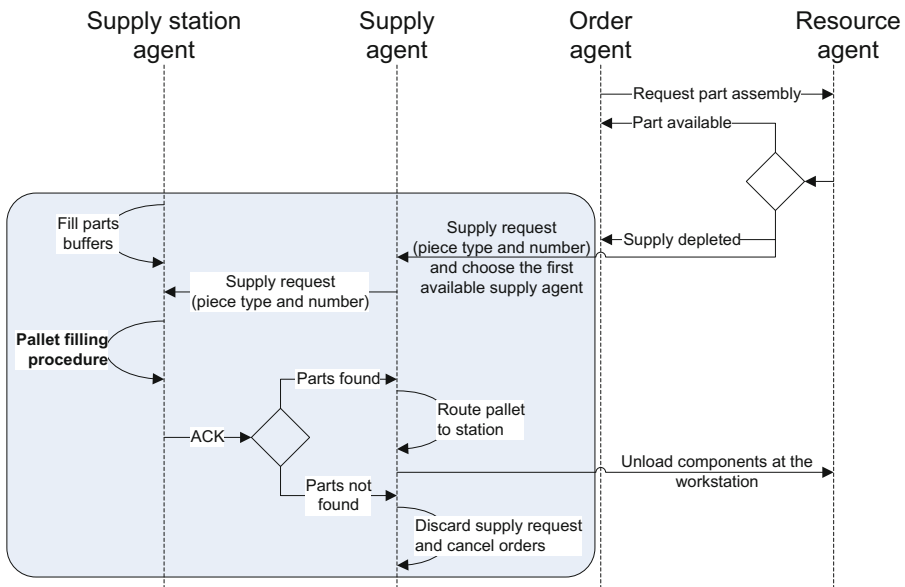


**Fig. 3.**  Re-supply process: "supply depleted" signal generated by a resource agent; supply agent requests components to supply station agent; parts are uploaded to the pallet associated to the supply agent and then sent to the resource which generated the initial signal

The pallet filling system described in Fig. 4 is implemented using a SCARA robot visually guided to pick components from a dual bulk feeding system (Adept's Any-Feeder). The robot handles components offered by the AnyFeeder and stores them in the intermediary ordered buffer in order to accelerate the process of pallet filling

(less time is needed to fill a pallet from the buffer rather than directly from the Any-Feeder). It takes the SCARA robot about 2 s to handle a component from the buffer to the pallet rather than approximately 8 s to make a request for a component and then handle it from the bulk feeder. When a request is received, if the necessary components are in the buffer the robot handles them; if the buffer does not contain enough components, the robot will look for the rest of them in the AnyFeeder, find them with vision (recognize, locate and pick them avoiding collision) and place them on the re-supply pallet. Timeouts are defined so that: (i) if not all requested parts are available in time, the re-supply command will be fulfilled only with the retrieved ones or (ii) if there are not requested parts in the bulk feeder, the re-supply command is discarded.
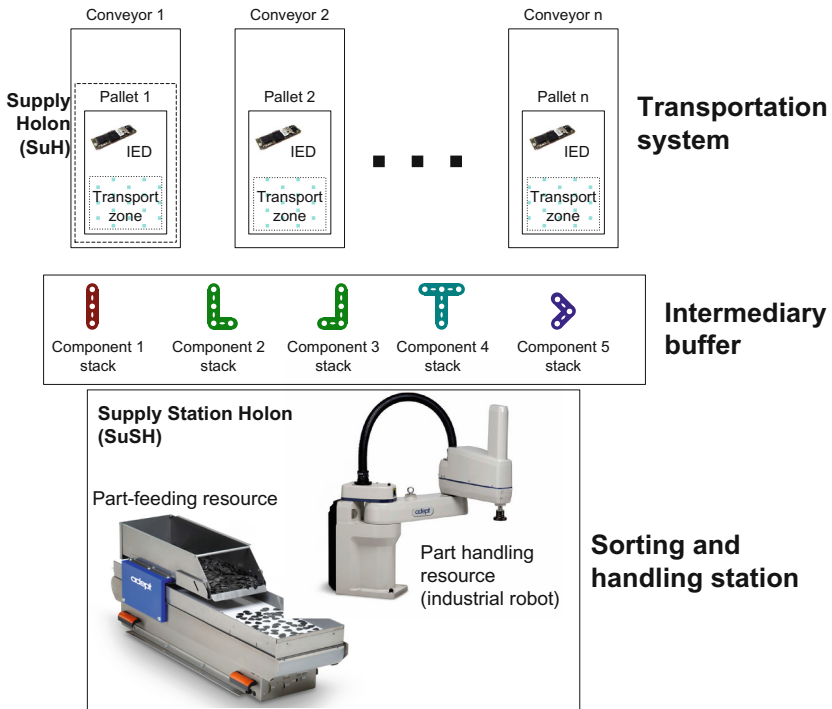


**Fig. 4.** Layout of the supply station

The technical characteristics of the holonic robot-vision supply system are:

– The pallet used to resupply a workstation has a capacity of 10 components, all the components being of the same type,
– The capacity of any local storage associated to a workstation for a certain component type is 10,
– The maximum distance travelled by the SCARA robot to retrieve a component from the AnyFeeder device and store it into the intermediary buffer is 740 mm = 600 mm (distance from pick to place) $+2*70$ mm (approach and depart distance),

- The average time for retrieving a component from the AnyFeeder device and storing it into the intermediary buffer is 8 s,
- The maximum distance travelled by the SCARA robot for handling a component from the intermediary buffer to the SuH: 340 mm = 200 mm (distance between pick and place) +2*70 mm (approach and depart distances),

The average time for handling a component from the buffer to the SuH is 2 s.

## 4   Multi-agent Implementation

The agents associated to the control system's holons (RH, SuSH, OH, SuH) are implemented in the Java Agent Development Framework (JADE) [4]. The framework implements multi-agent systems conforming to FIPA standards for intelligent agents [13]: language standardization for agent communication (FIPA-ACL and interaction protocols), and simple implementation of the decision process through a wide range of behaviours (simple, cyclic, one shoot, sequential).

The agents from Fig. 3 implemented in JADE and running on Java Virtual Machines (VM) are interfaces used to integrate products being assembled, manufacturing resources, supply resources and supply pallets into the control architecture (Fig. 5).
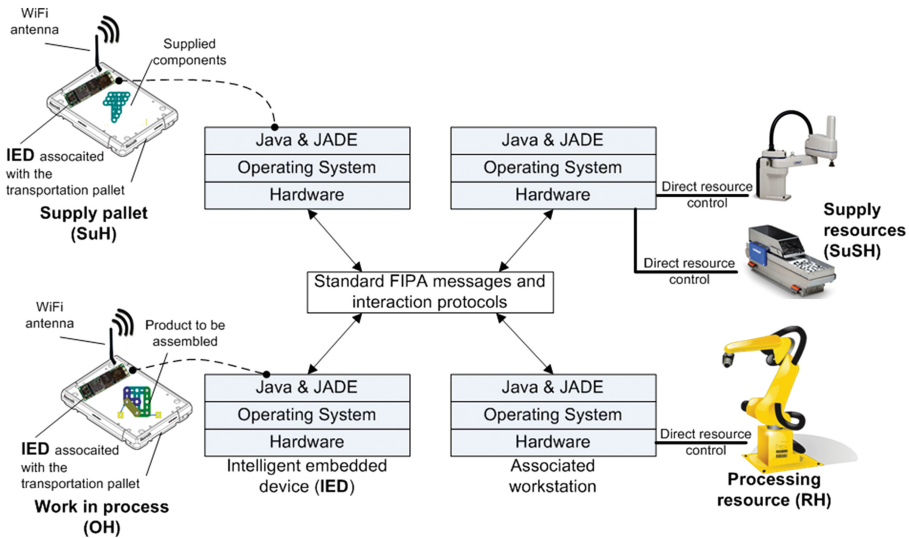


**Fig. 5.** Holons integration into supply control architecture using JADE multi-agent framework

According to [12] who realized a classification of intelligent devices used in manufacturing, the products being executed and the resources in the current architecture are: *Class 1 devices* (workstation (PC)-assisted shop floor device) for manufacturing and supply resources, and *Class 3 devices* (intelligent shop floor device) for products being executed and supply entities. Class 1 devices (Fig. 5 right) are integrated using the resource's associated workstation on which runs a JADE agent used to

communicate with the JADE platform containing all other agents representing the cell resources and products being executed. Class 3 devices (Fig. 5 the left) are directly integrated in the JADE platform using the IED physically associated to the product on which a JADE agent also runs, in a similar way as for Class 1.

The workstation resources, e.g., the robots performing operations on products, are monitored by the cell's PLC during batch execution; their status is displayed by the associated RH and may be: *available* – the resource can process products; *failed* – the resource is either isolated because its energy consumption exceeded the allocated amount or broken down; *depleted stock* – the local storage of the resource runs out components of the type needed for the product operation currently assigned to the resource. In this latter case, the workstation resource cannot be used in production during its re-supply, but it does respond to PLC status interrogations.

The cell's PLC acts as master over OH work in progress; it exchanges information in real time with the workstation RHs with the following timing:

- *Periodic interrogation*: polling of the resource's status by reading every 16 ms the specific data (available/failed) offered by the associated RH,
- *Ultimate interrogation*: once the pallet with product in current execution driven by the embedded OH arrives at the assigned workstation, just before taking the decision to authorize the execution of the scheduled operation the workstation's complete status is read from the RH (resource available/failed, storage contains needed parts/depleted, energy consumption in limits/exceeded, timeliness of previously executed operations, a.o.). The information obtained from this interrogation is used either to authorize starting the execution of the current operation or to activate a SuH and start executing the re-supply sequence.

In parallel with SuH execution, the OH getting no execution authorization in the workstation with depleted storage is delayed until the re-supply sequence is finished; the robot of this workstation is automatically involved in the last part of this sequence to refill the storage from the pallet with embedded SuH.

Meanwhile, the simultaneous execution of the other products already started is updated heterarchically, through OH cooperation, as follows: (i) any operation needing components which are missing and compulsory to be executed due to imposed operations precedence will be delayed; (ii) all other operations needing components which are missing but not compulsory to be executed will be rescheduled by a collective decision of their product-related OH, in such way to avoid collisions while pallets are travelling on the cell conveyor and to finish their execution in shortest time.

If, during the re-supply sequence, any products belonging to the category ii) above defined are finished and exit the cell, new pallets with embedded OH can be input in the system, but the scheduling of their execution will be updated as above.

## 5   Conclusions and Future Work

The paper presents a methodology for the integration of part re-supply functionality into an existing holonic manufacturing process. This functionality is based on adding to the production holarchy two specific holons: a Supply Holon embedded on supply

pallets (OH extensions), and a Supply Station Holon describing the part feeding processes, performed by a SCARA robot from a bulk feeder to the buffer (visually guided) and from the buffer to the SuH pallets. The integration is done through a heterarchical control system where agents are in charge of operating physical components. Future research aims at correlating the agentified supply process at shop floor level with the inventory management process at enterprise level in a SOA solution.

# References

1. Borangiu, T., Răileanu, S., Berger, T., Trentesaux, D.: Switching mode control strategy in manufacturing execution systems. Int. J. Prod. Res. **53**(7), 1950–1963 (2015). doi:10.1080/00207543.2014.935825. ISSN:0020-7543 (Print)
2. McFarlane, D., Sarma, S., Chirn, J.L., Ashton, K.: The intelligent product in manufacturing control and management. In: Proceedings of 15th IFAC World Congress, Barcelona (2002)
3. Meyer, G., Främling, K., Holmstrom, J.: Intelligent Products: A survey Computers in Industry. Elsevier, New York (2008)
4. Bellifemine, F., Carie, G., Greenwood, D.: Developing Multi-agent Systems with JADE. Wiley, Chichester (2007). ISBN 978-0-470-05747-6
5. Băbiceanu, R.F., Chen, F.F., Sturges, R.H.: Framework for control of automated material-handling systems using holonic manufacturing approach. Int. J. Prod. Res. **42**(17), 3551–3564 (2004)
6. Gouyon, D., David, M.: Implementing the concept of product-driven control using wireless sensor networks: some experiments and issues. In: 17th IFAC World Congress, IFAC Proceedings Volumes, vol. 41(2), pp. 5488–5493 (2008)
7. Raileanu, S., Borangiu, T., Radulescu, S.: Towards an ontology for distributed manufacturing control. In: Borangiu, T., Trentesaux, D., Thomas, A. (eds.) Service Orientation in Holonic and Multi-Agent Manufacturing and Robotics. SCI, vol. 544, pp. 97–109. Springer, Heidelberg (2014). doi:10.1007/978-3-319-04735-5_7
8. Borangiu, T., Gilbert, P., Ivănescu, N.A., Rosu, A.: An implementing framework for holonic manufacturing control with multiple robot-vision stations. J. Eng. Appl. Artif. Intell. **22**(4–5), 505–521 (2009)
9. Van Brussel, H., Wyns, J., Valckenaers, P., Bongaerts, L., Peeters, P.: Reference architecture for holonic manufacturing systems: PROSA. Comput. Indus. Spec. Issue IMS **37**(3), 255–274 (1998)
10. Valckenaers, P., Hadeli, K., Saint Germain, B., Verstraete, P., Van Brussel, H.: MAS coordination and control based on stigmergy. Comput. Indus. **58**(7), 621–629 (2007)
11. Obitko, M., Mařík, V.: Ontologies for multi-agent systems in manufacturing domain. In: DEXA Workshop, pp. 597–602 (2002)
12. Morariu, C., Morariu, O., Borangiu, T., Sallez, Y.: Formalized information representation for intelligent products in service-oriented manufacturing. In:11th IFAC Workshop on Intelligent Manufacturing Systems, Sao Paolo, Brazil, vol. 11, Part 1, pp. 318–323 (2013)
13. FIPA: consulted in March 2016. www.fipa.org/index.html

# Robot Programming with Flexible Geometric Relations

Karol Dobrovodský[✉] and Pavel Andris

Institute of Informatics, Slovak Academy of Sciences, Dúbravská cesta 9,
842 37 Bratislava, Slovakia
{utrrdobr,utrrandr}@savba.sk

**Abstract.** A programming system with robot language ROBOL is developed to control robotic workplaces. It is modular for various configurations of technical resources and many types of kinematic structures. This programming environment allows the user to control several effectors simultaneously. The system is "made-to-measure" for each specific workplace. Application programs are prepared through dialogue with the control system. In order to maximize the flexibility of geometric relations, the source text of procedures is in program files and position data in the separated data files.

**Keywords:** Robot · Programming · Technological positions · Flexible geometric relations

## 1 Introduction

Modern robots are performing tasks considered routine and dangerous at places ranging from automobile assembly to space shuttles in outer space. Before the robots enter the production process, engineers are using software that simulates the robots in real situations, to analyse safety and effectiveness. The programming environment is helping to animate robot activities and supports off-line programming. Animation of work cell activity is used to conduct feasibility studies on manufacturing processes while the product is still being designed. It is not necessary to take the work cell down in order to reprogram the robots. We just have to download the programs from the PC directly to the work cell. Engineers can also efficiently construct the entire robotic work cells to realistically evaluate safety scenarios. The technology enables the modelling of geometrically precise and accurately calibrated robots, robot end-effectors and safeguard devices within the robotic work cell.

The concrete implementation of the control system of a particular workplace is oriented either to the control of the real workplace (on-line) or to work on a PC offsite robot (off-line). In both cases, the system works in real time and therefore allows you to create and verify application programs beyond the robot workplace. The robot language ROBOL allows the user to program and directly perform all processes specific to the robotic workplace. The first steps toward ROBOL originate in (Andris et al. 1992, 1993a, 1993b; Dobrovodský and Janáč 1995 and Dobrovodský 1996).

## 2   Operational Activities

In ROBOL language, there is no difference between programming commands and commands intended for interpretation immediately upon insertion. Syntactic analysis of the command line begins immediately after insertion. If the command has no line number, then its interpretation will take place immediately. Otherwise, the command is inserted into the current program. This enables the user to have a dialogue with the control system. Furthermore, a set of operational commands is available that is not intended to enter the program.

The operational commands are used to communicate directly with the control system. The control system responds almost immediately and performs the requested operation or enters the desired mode. The system offers a core group of commands at the bottom of the screen; this core group consists of commands that serve for operational management, programming and debugging programs.

A separate group of commands includes ones that are used for manual control (guidance) of effectors using the buttons Grey + and Grey – and for simulation of the input signals by pressing Grey *. The system reacts immediately to pressing and releasing of these three buttons.

The process of the user's dialogue with the control system is effectively supported by the information continuously displayed on the screen. According to the nature of the current activity (program editing, verification, guidance, demonstration) the user has commands available for insight into the control system and various support and operational commands. Graphic display of selected objects depends on the observer's position and perspective. The observer's initial position is given by the reserved variable VIEW. The observer's distance and position can be changed operatively.

Operation of the control system is designed to allow the user to operate continuously and at the same time to prepare and test user programs step by step through dialogue. The control system works under Linux operating system and in formal terms it is an executable file ROBOL.EXE. During start up the program assumes the existence of AUTOEXEC.ROB file that contains positions of the effectors within the workplace. If this file is present, the corresponding program is activated and executed automatically.

The control system allows the user to guide effectors or the objects affixed to one of the effectors. The possibility of direct guidance of objects greatly simplifies programming by demonstration and supports the independence of programs from a particular type of kinematic structure. Guidance of the last link of the kinematic chain relative to the base is a special case of guidance of one object relative to another one.

## 3   Technological Positions

We separate the procedure and the numerical data needed for the control in user programs. The procedure of the operation is written in a program file. Relative positions of the tool with respect to the object of the operation are written in a data file. It is recommended to compose any position of the tool relative to the object from the two technological positions:

- The position relative to the tool.
- The position relative to the object.

We can put all technological positions with respect to the tool into the data file TOOL.DAT and all technological positions with respect to the object into the file OBJECT.DAT. Thus the quantitative point of the operation is involved in the two data files belonging to the tool and the object, respectively. The procedural part of the operation does not depend on this data and is written in the program file. From the geometrical point of view, motion statements of the procedure have the common goal to make identical technological positions from the file TOOL.DAT and the corresponding technological positions from the file OBJECT.DAT.

Typically, work objects differ from each other although they enter into the same technological operations. We have in mind even considerable differences like a small and a big box of the same shape. Each type of work object should be accompanied by its own data file characterizing its relative positions relative to the technological positions of objects coming into the consideration.

A partial goal of the assembly procedure is to make the corresponding technological positions of the two objects identical. For example, the partial goal is to make the technological position of the tool identical with the relevant technological position of the object. Of course, the same principle takes place for possible intermediate relative positions defined by intermediate technological positions.

For practical reasons, in most cases it is not possible to define the position of the object directly by specifying the coordinates of its location. In robotic applications, it is often easier and more convenient to define the object position relative to another object by demonstration.

## 4   Workplace Configuration

The initial location of objects in the workplace is defined in the file with the reserved name AUTOEXEC.ROB. In this file we place the information on the basic setup of effectors, work benches, storage, sensors and other objects whose positions are relatively constant. If the workplace contains only one effector, its base may be identified with the primary reference coordinate system of the workplace. Nevertheless, it is useful to configure the workplace by entering a constant position of the working table, pallets and storage components. For a number of effectors, the definition of their relative positions is inevitable.

The name of the effector (HAND, ARM, TB, and TG) serves precisely to mark its last link in the kinematic chain. The base of the effector has the name ending with the $ sign (HAND$, ARM$ TB$, TG$). Moreover, we have FTS (force-torque sensor) and CAM1, CAM2 (visual sensors) objects, etc. Other constants that can be defined in this file are constants of POINT type (i.e. sets of joint coordinates) for synchronizing positions (HAND$S, ARM$S, TB$S, TG$S) and the upper and lower limits of the joint coordinates (HAND$U, HAND$L, etc.). The previously mentioned reserved constants have always predefined values. If we insert new values of these constants in AUTO-EXEC.ROB, then these take precedence.

# 5   Programming

Application programs may be prepared in two ways, either by using an ordinary text editing program or through dialogue with the control system.

The first way assumes that we write the program's source text using an ordinary editor. One program is put in one file. ROBOL language does not distinguish between programs and sub-programs. The name of the file that contains programs in ROBOL must have extension .ROB. The names of data files must have.DAT extension.

When we are ready with the source text of the program or data, we can activate it in an already running control system by the LOAD command. During the activation a syntactic analysis is performed. In case of any errors we continue through the dialog with the control system. In this case, under the preparation of the application program we understand insertion, viewing, testing and correcting particular command lines, programming by demonstration and testing of just programmed segments. The user inserts numbered command lines (syntactic units) into the activated program. Syntactic analysis is performed immediately after inserting of each command line. The system can execute particular commands immediately after insertion. The control system is executing commands in real time, irrespective of whether it is "on-line" or "off-line" (i.e. real robot or graphical animation). This enables the user to discover most of the bugs out of the actual work with robots.

Programs prepared and pre-tested on a personal computer are transferred to the real robot workplace, where the final verification is completed. It should be noted that the preparation of the program with animation in advance is optional.

We can view the activated program line by line in the direction of increasing line numbers by pressing the Enter key or in the opposite direction by pressing the Esc key. The last viewed line is ready to be executed in the AUTO, TRACE or DEBUG mode. We can execute the whole program in the AUTO mode, line by line in the TRACE mode and step by step in the DEBUG mode. The mode may be changed at any time during the execution.

The program status is indicated by the following symbols in the command line prompt string:

> The program run suspended between commands.
* Ongoing performance of a non-positioning command.
+ Ongoing performance of a positioning command.
? Ongoing waiting to meet the conditions; simulation by pressing Grey *.
! Command execution suspended between system periods.
Continue (Go) or give up (Abort).

Changes in the program can be made only between commands. The connection of subroutine parameters is performed by name. Programming of the robot activity may be associated with the demonstration of the position or the tool path with respect to the object. Such programming is done in TEACH or TRACK mode, respectively.

## 6   Sample Example

During start-up of the control system the program with a reserved name AUTOEXEC. ROB is automatically executed. This program is appropriate to define basic setup of effectors and other objects of robotic workstation like sensors and cameras (Andris et al. 1996; Dobrovodský et al. 2005), see Fig. 1. Moreover, we can also define the synchronization and the relevant upper and lower limits for particular joint variables, Figs. 2 and 3.

```
   AUTOEXEC.ROB:
10   SYNCH
20   SET acc=7.000; vel=300.000
30   DRIVE hand (125.000,24.000,39.000,90.000,-90.000,
  -27.000)
40   LOAD  main.ROB
50   LOAD  grab.ROB
60   LOAD  put.ROB
70   LOAD  leave.ROB
80   LOAD  hand$.DAT
90   LOAD  hand$1.DAT
100  LOAD  hand$2.DAT
110  LOAD  hand$3.DAT
120  LOAD  hand$4.DAT
130  LOAD  hand$5.DAT
140  LOAD  hand$6.DAT
150  LOAD  hand.DAT
160  LOAD  table.DAT
170  LOAD  belt.DAT
180  LOAD  stand.DAT
190  LOAD  cam1.DAT
200  LOAD  cam2.DAT
210  LOAD  box1.DAT
220  LOAD  box2.DAT
230  FRAME hand$=base:\z,0.000
240  FRAME table=base:(1000.000,0.000,-700.000)\z,0.000
250  FRAME belt=base:(1000.000,1000.000,
  -600.000)\z,0.000
260  FRAME stand=table:(750.000,0.000,750.000)
270  FRAME cam1=stand:(700.000,0.000,650.000)\
  (1.000,0.000,0.000),180.000
280  FRAME cam2=hand:(-100.000,0.000,-200.000)\z,0.000
```

```
290 FRAME box1=belt:(-600.000,0.000,225.000)\x,0.000
300 FRAME box2=belt:(-400.000,0.000,100.000)\x,0.000
310 FRAME view1=base:(1000.000,-3300.000,100.000)\
  x,-90.000
320 FRAME view2=base:(1000.000,-1000.000,3000.000)\
  x,-160.000
330 DISPLAY hand; table; belt; stand; cam1; cam2; box1;
box2
340 FRAME view=view1
350 STOP
360 CALL  main
370 STOP
380 FROTATE table table :y,-5.000
390 STOP
400 CALL  main
410 STOP
420 FROTATE table table :y,10.000
430 STOP
440 CALL  main
450 STOP
```



**Fig. 1.** Work cell configuration

```
  MAIN.ROB:

10  FRAME view=view2
20  FRAME box1=cam1:(-150.000,-100.000,1175.000)\
   (-0.966,-0.259,0.000),180.000
30  FRAME box2=cam1:(350.000,0.000,1275.000)\


  (-0.866,0.500,0.000),180.000
40  STOP
50  FRAME view=view1
60  CALL  grab  hand; box1
70  CALL  put box1; belt
80  CALL  leave hand
90  FSHIFT  box1  belt :x,-400.000
100 CALL  grab  hand; box2
110 CALL  put box2; belt
120 CALL  leave hand
130 AFFIX box2  box1
140 FSHIFT  box2  belt :x,-200.000
150 PRINT "boxes on the belt"
160 PRINT "operation completed"
170 RETURN
```
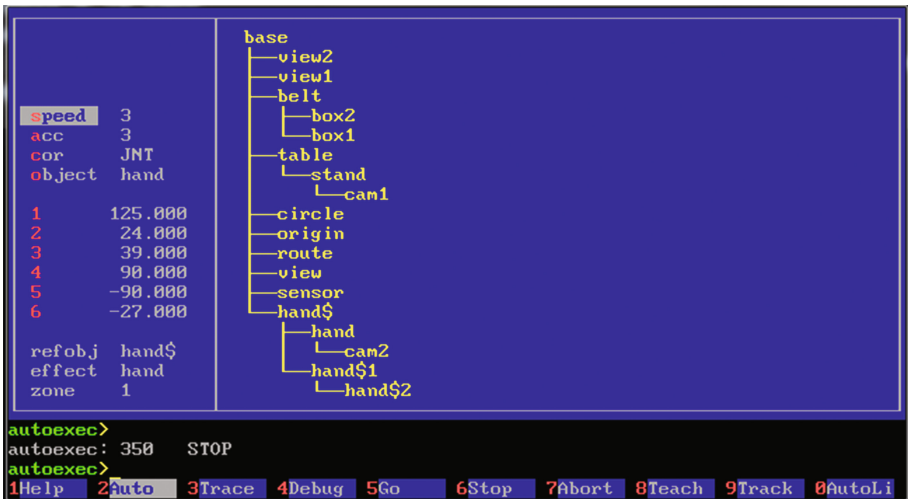


**Fig. 2.** Temporary world model tree

```
   PUT.ROB:
10   PARAM object;   palette
20   MOVE    object:4  palette:3; cor=jnt
30   MOVE    object:4  palette:2
40   AFFIX   palette object
50   RETURN

   GRAB.ROB:
10   PARAM tool; object
20   MOVE  tool:1  object:3; cor=jnt
30   MOVE  tool:1  object:2
40   AFFIX tool  object
50   MOVE  tool:1  object:3
60   RETURN

   LEAVE.ROB:
10   PARAM tool
20   SHIFT tool  tool:z,-100
30   RETURN
```
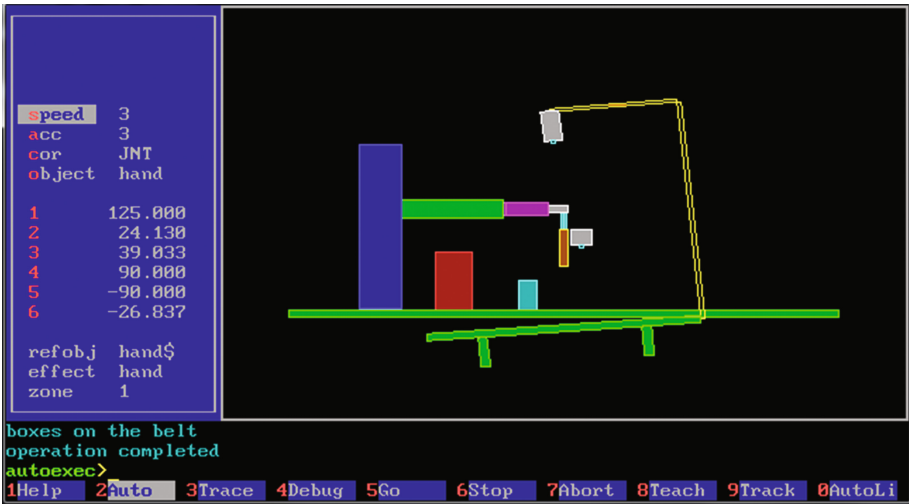


**Fig. 3.** Program is flexible with respect on any sub tree

```
   TABLE.DAT:

1  (0.00,0.00,0.00); green 1500.00,1500.00,50.00
2   (0.00,0.00,25.00)
3   (0.00,0.00,50.00)
4   (0.00,0.00,-25.00)
11  (450.00,450.00,-125.00); green 50.00,50.00,200.00
12  (450.00,-450.00,-125.00); green 50.00,50.00,200.00
13  (-450.00,450.00,-125.00); green 50.00,50.00,200.00
14  (-450.00,-450.00,-125.00); green 50.00,50.00,200.00




   STAND.DAT:

1 (10.00,0.00,0.00)\(0.00,0.00,0.00),0.00;           brown
  20.00,20.00,1500.00
2 (-350.00,0.00,760.00)\(0.00,0.00,0.00),0.00;       brown
  700.00,20.00,20.00




    BELT.DAT:

1   (0.00,0.00,0.00); green 3000.00,400.00,50.00
2   (0.00,0.00,25.00)
3 (0.00,0.00,50.00)
4   (0.00,0.00,-25.00)
```

## 7  Conclusion

The proposed methodology is simple, but very powerful. Having programmed elementary operations, we can add new tools and objects into the technology easily. A new gripper accompanied with its data file containing a set of technological positions requires no changes in procedures. The same is true for new objects appearing due to innovations. The user can immediately test the whole program or any desired part of it with new tools and objects by visualization and animation of the robot cell activity.

# References

Andris, P., Berka, I., Dobrovodský, K., Janáč, L., Kurdel, P.: Integrated programming system for robot cells control. In: Proceedings of the 1$^{st}$ International Meeting on Robotics in Alpe-Adria Region, Portorož, Slovenia, 21–23 June 1992, pp. 154–161 (1992)

Andris, P., Berka, I., Dobrovodský, K.: Transformations in robot world model. In: International Workshop: Software Engineering for Parallel Real-Time Systems, Smolenice, Slovakia, 1–3 March 1993, pp. 63–68 (1993a)

Andris, P., Dobrovodský, K., Kurdel, P.: Robot work cell configuration. In: Gabko, P., Kopacek, P., Voicu, M. (eds.) Proceedings of the Workshop Computer Science Topics for Control Engineering Education, Wien, Austria, 13–15 September 1993, pp. 95–100 (1993b)

Dobrovodský, K., Janáč, L.: Representation of a robot cell world model, In: Proceedings of 4$^{th}$ International Workshop on Robotics in Alpe-Adria Region, Portschach, Austria, pp. 163–165 (1995)

Dobrovodský, K.: On the analogy of robotic operations. In: Proceedings of the 5$^{th}$ International Workshop on Robotics in Alpe-Adria-Danube Region, Budapest, Hungary, 10–13 June 1996, pp. 459–461 (1996)

Andris, P., Berka, I., Dobrovodský, K., Janáč., Kurdel, P., Linek, V.: A robot control system for active vision. In: Proceedings of the 5$^{th}$ International Workshop on Robotics in Alpe-Adria-Danube Region, Budapest, Hungary, 10–13 June 1996, pp. 543–546 (1996)

Dobrovodský, K., Andris, P., Janáč, L., Kurdel, P., Lányiová, E., Pajorová, E.: A real-time linux implementation of a robot programming system. In: Proceedings of the 14$^{th}$ International Workshop on Robotics in Alpe-Adria-Danube Region, CD, Bucharest, Romania, 26–28 May 2005. ISBN 973-918-241-3, 136-141

# Improvement of a Robotic System for Spring End Treatment Through Plasma Cutting

Sergey Platov[(✉)] and Yuriy Turygin

Izhevsk Kalashnikov Engineering State Technical University, Izhevsk, Russia
serge.platov@gmail.com, turygin@istu.ru

**Abstract.** This article describes a method of increasing production rate of the Robotic System (RS) for spring end cutting by use of plasma cutter. A new upgraded part treatment process has been designed with the provision of upgraded structured pattern of the RS. Simulation models of the existing and upgraded RS have been designed and are included. A simulation experiment of the provided models in real time mode for a specified period of time in accordance with calendar events and even initial data has been carried out. As a result of analysis of data available from simulation, a 2.5x increase rate of production output has been obtained.

**Keywords:** Robotic system · Industrial robot · Plasma cutting

## 1  Introduction

Nowadays, considering the increase of production volumes at spring manufacturing enterprise, the production output is not sufficient provided by the existing equipment during the operations of part treatment. One of the bottlenecks is the technological operation of spring end treatment. Earlier work [1] examines solutions needed for treatment quality and production rate increase with Robotic System (RS). This article proposes an enhanced RS structure to provide double and even higher production volume as compared with an existing layout. Calculations and simulation modelling have been carried out for Spring 003, with diameter bars of 25 mm.

## 2  RS Improvement

The robotic system presented in Fig. 1 performs the treatment of spring ends made from spring steel bars with the maximum diameter of 50 mm.

In order to evaluate the timing required for one single spring treatment, the total time needed by the operations required to provide the treatment of the spring was considered, without actually including its complete execution sequence that includes additional operations, like loading/unloading, etc. In this case the total time of one spring treatment equals the sum of executed operations 01–03, 05, 07 and 09 shown in Fig. 2.

The treatment cycle includes the sequence of the completed operations, listed in Fig. 2.
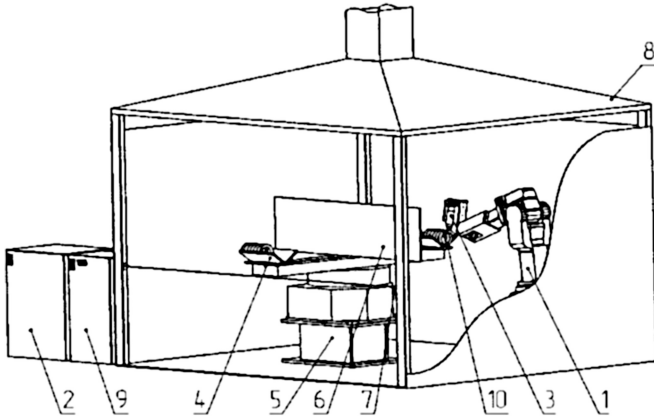
**Fig. 1.** Robotic system: 1-robot, 2-plasma cutting equipment, 3-cutter, 4-clamp, 5-index base, 6-protection shield, 7-laser shield, 8-ventilation supply, 9-robot control cabinet, 10-processed spring

| № | Parameter | Value | Unit |
|---|-----------|-------|------|
| 01 | Spring loading and positioning | 4,3 | sec |
| 02 | Displacement into the treatment zone | 5,3 | sec |
| 03 | Spring end finish | 19,2 | sec |
| 04 | Displacement from the treatment zone | 5,3 | sec |
| 05 | Spring rotation and position | 3,5 | sec |
| 06 | Displacement into the treatment zone | 5,3 | sec |
| 07 | Spring end finish | 19,2 | sec |
| 08 | Displacement from the treatment zone | 5,3 | sec |
| 09 | Spring unloading | 2,0 | sec |

**Fig. 2.** Spring treatment cycle with RS, $i$ – sequence number of the treated spring

*Improvement of the spring end treatment.* The presented operations may be divided into two categories: general and secondary. The first one includes the operations connected directly with spring end treatment – these are operations no. 03 and 07, as depicted in Fig. 2. The remaining operations are secondary operations. One of the methods to increase the production output consists in reducing the duration of the secondary operations or excluding it at all; in addition, the simultaneous distribution of operations is proposed, when the secondary operations are carried out in a compact sequence. To do so, the following solution was proposed:

- Exclude the working cycle the base rotation of the SR; install a second robot system. This will help to exclude the supplementary operations 02 and 06, as shown in Fig. 2.
- Using two robots instead of one allows carrying out the treatment of two spring ends simultaneously, i.e. permits to carry out two main operations 03 and 07 at the same time, refer to Fig. 2.

- Automating the installation process and defining the initial position of the springs by means of a measurement unit provides complete avoidance of extra operations 01, 05 and 09 as indicated in Fig. 2.
- Eliminating the transportation movements of the crate filled with material is proposed, with the installation of a conveyor in order to provide the displacement of springs from on operation step to the next one.

Based on the above proposed measures, a new spring end treatment cycle composed of the sequence of operations described in Fig. 3 was developed.

| № | Parameter | Value | Unit |
|---|---|---|---|
| 01 | Loading of the spring into the chute | 2,0 | sec |
| 02 | Conveyors displacement per 1 position | 5,5 | sec |
| 03 | Measurement of the springs parametrs | 4,8 | sec |
| 04 | Spring fixation by Robot 1 | 3,0 | sec |
| 05 | Spring treatment by Robot 1 | 14,0 | sec |
| 06 | Spring unfixation by Robot 1 | 3,0 | sec |
| 07 | Spring reloading | 3,0 | sec |
| 08 | Spring fixation by Robot 2 | 3,0 | sec |
| 09 | Spring treatment by Robot 2 | 14,0 | sec |
| 10 | Spring unfixation by Robot 2 | 3,0 | sec |
| 11 | Unloading of the spring from the chute | 2,0 | sec |

**Fig. 3.** New spring treatment cycle at RS, $i$ – sequence number of the treated spring

Operations 04–06 and 08–10 are the general operations. The remaining operations are secondary ones and can be carried out simultaneously. In accordance with the data provided in Fig. 3, the time of treatment for one spring equals 20 s. To carry out a new spring treatment cycle, an upgraded structural diagram of the robotic system was developed, as represented in Fig. 4.

Springs for treatment are loaded by means of the conveyor system. The movement of the spring is realized in a specified step that equals dimensionally the distance between the axes of the adjusting springs fixed on the conveyor chutes. The last position of the break point of the conveyor system 1 is the position of the spring grip which is done by Robot 1 prior to the following treatment. Next to the last position is the measurement position where the evaluation is carried out using a complex spatial geometry measurement unit (this is necessary for the calculation of the parameters of the treatment process with plasma cutting).

Robot 1 picks the spring from the conveyor loading system, performs the treatment of the first dead coil in the zone 1 and transfers the spring into the reloading area. Robot 2 picks the spring from the reloading zone from the opposite side, carries out the treatment of the second dead coil in the cutting zone 2, and moves the spring to the conveyor unloading system. Picking the spring and fastening it by the robot manipulators is done by means of 3-jaw self-centre grippers with pneumatic drive. The plasma
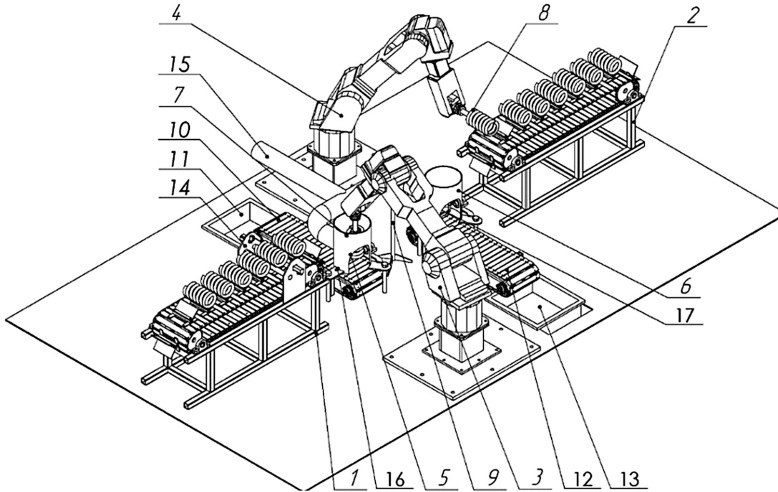
**Fig. 4.** Upgraded structural diagram of the robotic system for spring end treatment: 1-conveyor loading system; 2-conveyor unloading system; 3-robot 1; 4-robot 2; 5-treatment zone 1; 6-treatment zone 2; 7, 8-treated springs; 9-spring overloading zone; 10-scrap transportation system 1; 11-scrap chute 1; 12-scrap transportation system 2; 13-scrap chute 2; 14-measurement unit; 15-smoke exhaust system; 16, 17 – scale nozzles of cutting zones 1 and 2

cutting treatment is carried out in the real time mode controlled by the algorithms developed on the basis of some mathematical models [3]. The scrap transportation 1 and 2 provide displacement of the spring end cuts towards the scrap chutes, the scrap being formed in the process of spring dead coil treatment; then, the chutes are emptied automatically or manually.

## 3   Imitation Modeling of RS Operation

*Simulation modelling*. In order to evaluate the production output of the proposed upgraded robotic system and its increase, a simulation modelling of the robotic systems based on data presented in Figs. 2 and 3 was performed.

The development of the operation models of the robotic system was carried out using the software tool AnyLogic [4], with its capable of identifying complex features with the possibility to unify the system's dynamics through discrete event modelling in agent-based framework. The present software product allows developing the model with specified operation rules to define the external impact and the response reaction and to carry out simulation in real time mode in accordance with assigned operation timing. Figures 5 and 6 shows the simulation models of the current and upgraded robotic system respectively.

The simulation model is a graphical representation of cycle operations with specified time sequence and completion time defined by the connection lines and timing parameters. In order to carry out an objective estimation the simulation of the RS was
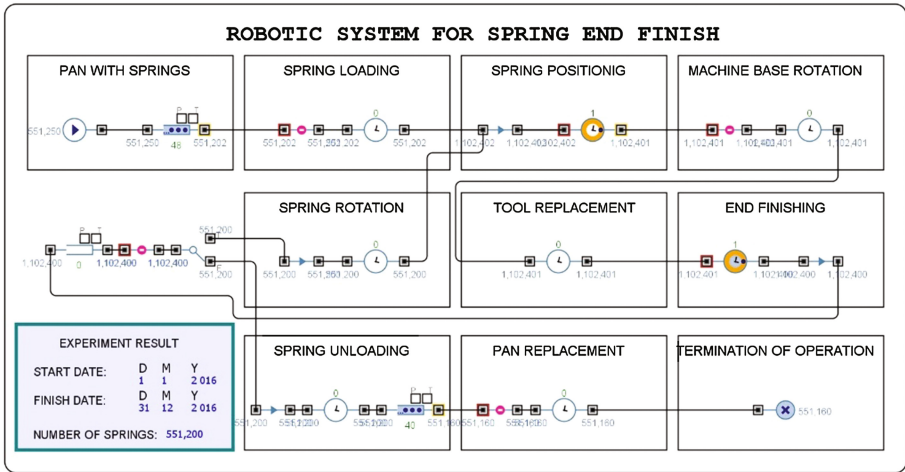
**Fig. 5.** Simulation model of the existing RS
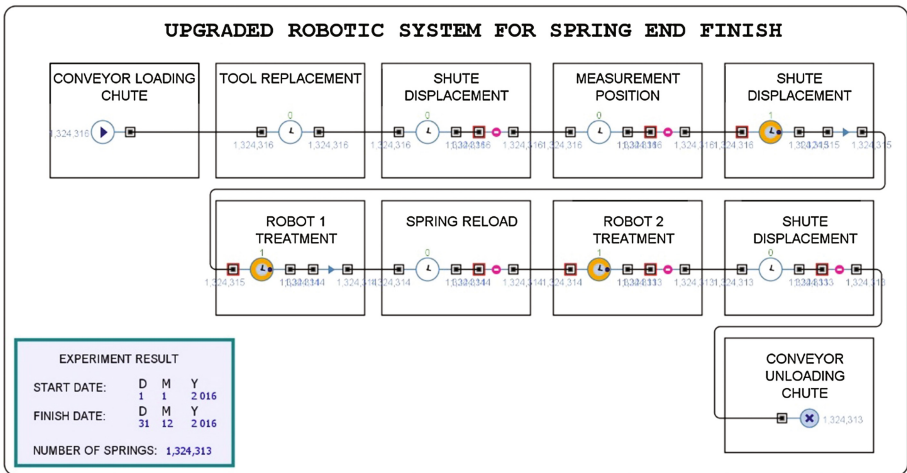


**Fig. 6.** Simulation model of the upgraded RS

realized on the basis of certain initial parameters. The correspondence with the real timing events is presented in Fig. 7.

The results of the simulation modelling are presented in Figs. 5 and 6, with the proven capability to describe the treatment of 551200 springs with the existing RS, whereas the upgraded dual RS allows the production of 1324313 springs in the same period of time and with the same initial parameters of operation durations for the entire operation cycle.
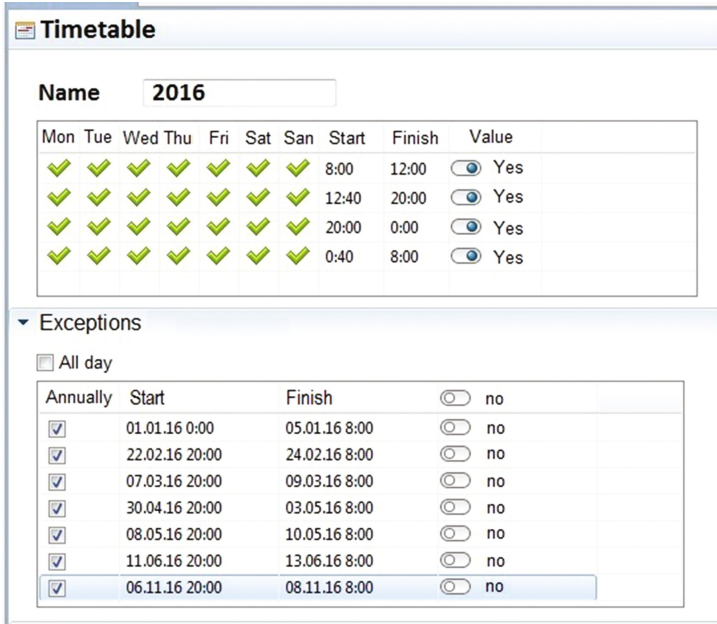
**Fig. 7.** "Timetable" element

## 4   Conclusions

The partition of the part treatment cycle into "useful" and "supplementary" operations, as well as their optimized distribution and simultaneous execution permit increasing the production rate of a single RS 2.4 times, which is confirmed by the results obtained from the data analysis done in the course of the simulation modelling of the existing and upgraded robotic systems. This solution considers the practical implementation too, with an estimated payback period of 1–2 years.

## References

1. Turygin, Y., Platov, S.: Issledovanie ossobennostej obrabotki torcov pruzhin goryachej navivki metodom plazmennoj rezki s ispolzovaniem robototehniceskogo kompleksa/Mehatronika, avtomatizaciya, upravlenie, No. 2, Moskva: OOO "Novie tehnologii", pp. 102–105 (2015). ISSN 1684-6427
2. Platov, S., Turygin, Y.: Railtruck robotic spring end process control system. In: 23rd International Conference on Robotics in Alpe-Adria-Danube Region, Proceedings volume, 3–5 September 2014, Smolenice, Slovakia. ISBN 978-80-227-4219-1
3. Platov, S., Turygin, Y.: Obrabotka tortsov pruzhin vagonnyih telezhek metodom plazmennoy rezki, Intellektualnyie sistemyi v proizvodstve. Izd-vo IzhGTU, pp. 96–100 (2013)
4. Mnogopodhodnoe immitacionnoe modelirovanie. www.anylogic.ru/overview

# Calibration of a Robotized Bending System

Carlo Ferraresi[1(✉)], Francesco Pescarmona[2], and Giuseppe Di Biase[1]

[1] Department of Mechanical and Aerospace Engineering,
Politecnico di Torino, Turin, Italy
{carlo.ferraresi,giuseppe.dibiase}@polito.it
[2] Amada Engineering Europe, Santena, Italy
francesco.pescarmona@amada-engineering.eu

**Abstract.** The paper describes a method to identify the mechanical inaccuracies which may be present in the swinging unit of a robotized bending system. The method allows calculating the corrections that must be provided to the control system to compensate the mechanical inaccuracies. Finally, the procedure has been applied to a real bending system and the results are presented.

**Keywords:** Robot calibration · Bending system · Inaccuracy compensation

## 1 Introduction

In automatic bending of sheet metal, the accuracy of the result may be compromised by possible mechanical defects present in the swinging unit. In order to overcome this problem, such defects should be identified and compensated.

An effective way to solve the problem is to exploit and apply the wide knowledge evolved in the robotic field as concerns manipulator calibration.

Numerous publications provide solutions for robot calibration [1, 2], mainly proposing closed loop methods which require a kinematic model of the structure and a metrological system to detect the full pose of the end effector [3, 4, 5, 6, 7]. Most of such applications are concerned with typical serial structures of industrial robots. Once pose inaccuracy is measured, by means of proper algorithms it is possible to calculate the values of the structural errors, whereupon a certain logic to compensate the inaccuracies must be individuated and implemented in the controller.

The aim of this work was to apply this knowledge to compensate the errors of the swinging unit of the bending system, which is actually a 2 DOF serial kinematic chain with intersecting joint axes. In order to take into account the mechanical inaccuracies of the structure, it was necessary to conceive a 'virtual' 3-link serial chain, where links represent all mechanical errors. Then an analytical method, based on a Denavit-Hartenberg model of the structure, was developed.

The whole procedure starts from the experimental measure of the swinging unit pose, performed by means of a specially conceived tool, and calculates, by means of a proper algorithm, all parameters of the model, representing the structural errors. Finally, the corrections that must be applied to the reference input of the system controller are calculated.

This procedure was then applied to a real robotized bending system, the Amada Lasbend-AJ®, which integrates four processes: laser cutting, forming, tapping and bending of sheet metal. The results of the analysis are presented.

## 2    Description of the Bending System

The Amada Lasbend-AJ® is composed of two sections: the first one is devoted to laser cutting of the sheet metal, and the second one is the actual bending system. The latter is shown in Fig. 1; it is made up of two controlled elements: a 3 DOF Gantry Cartesian robot which places a part cluster between punch and die for bending operation, and a swinging unit provided with two rotational degrees of freedom.
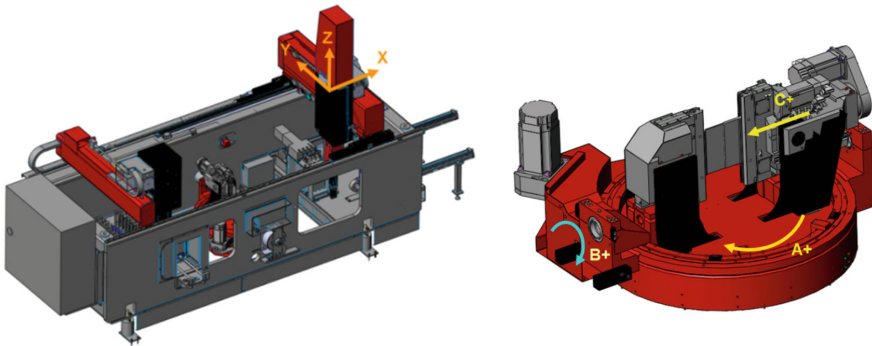


Fig. 1. (a) The whole bending system; (b) the swinging unit

The first degree of freedom of the swinging unit, A, is a rotation around an axis parallel to the bending line; the second one, B, is orthogonal to the first one and determines the direction of the bending line. A third movement is the displacement between punch and die, indicated as C in the figure.

Various inaccuracies of bends may be induced by several structural characteristics such as backlashes in drive line, dimensional inaccuracies, flexion of bending tools, etc. Therefore, respect of tolerance can be guaranteed by a calibration procedure able to evaluate and correct the deviation between the ideal structure and the real one.

To this aim, the 2 DOF structure of the swinging unit, provided with two concurrent axes, was transformed into a 3-link serial kinematic chain, whose links represent all mechanical errors of the unit.

Figure 2 shows the kinematic scheme of the swinging unit, including all errors due to mechanical inaccuracies. Frame 0 is the global reference frame, frame 3 is fixed to the end-effector, frame T is related to the bending tools, it is integral to frame 3 with offset $h$ along Z3 axis, axis Z1 is related to joint J2 (coordinate B), and axis Z2 is related to joint J3 (coordinate A). In an ideal condition, axes Z0, Z1 and Z2 should be concurrent and orthogonal, and axes ZT and Z3 aligned with Z2. Dash-dot lines represent the joints axes, the dashed segments ($a1$, $a2$ and $a3$) are the lengths of the 'links', segments $d1$, $d2$
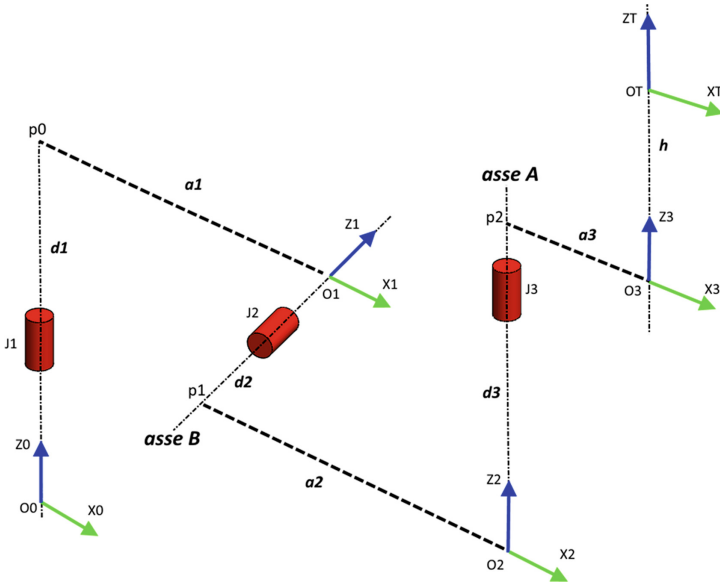
**Fig. 2.** Kinematic scheme of the swinging unit: A is the d.o.f. which actuates bending, B is the d.o.f. defining the bending line. The scheme includes all errors due to mechanical inaccuracies

and *d3* are the distances between links. A fictitious joint J1 is created to consider possible position and angular deviation of frame 1 from the global one.

The parameters of the real structure, including twist angles between joint axes, are reported in Table 1, according to the Denavit-Hartenberg (D-H) convention. Each parameter represents every possible inaccuracy in the structure of the swinging unit, except for joint coordinates (A, B) and nominal twist angles ($\pm$ 90°). From the parameters of Table 1, the relative pose matrices between consecutive links, and the general transformation matrix from frame T to global, are obtained:

$$^0\hat{A}_T = {}^0\hat{A}_1 \cdot {}^1\hat{A}_2 \cdot {}^2\hat{A}_T \tag{1}$$

**Table 1.** Real structure parameters in Denavit-Hartenberg convention

| Joint | Distance | Joint angle | Length | Twist |
|-------|----------|-------------|--------|-------|
| J1 | *d1* | $\theta1 = d\theta1$ | *a1* | $-90 + \alpha1$ |
| J2 | *d2* | $\theta2 = (B + d\theta2)$ | *a2* | $+90° + \alpha2$ |
| J3 | *d3* | $\theta3 = (A + d\theta3)$ | *a3* | $\alpha3$ |

## 3 Determination of Error Parameters

All parameters described in Table 1, i.e. the mechanical inaccuracies of the swinging unit, can be determined considering the system posed in a defined condition.

*Correction of B Axis.* The aim is to calculate the corrections that must be applied to the axis B during its positioning motion, in order to compensate the mechanical inaccuracies of the structure. The axis A is fixed in 0° position; also the initial position of axis B is set at 0°. In this condition, the joint angles only contain the errors $d\theta2$ and $d\theta3$. Approximating the trigonometric functions of $\theta1$ and $\theta3$, and taking $\cos(\theta2) = c2, \sin(\theta2) = s2, \cos(\theta3) = c3, \sin(\theta3) = s3$, the orientation matrix ${}^0A_T = {}^0A_3$ becomes:

$$
{}^0A_T = \begin{bmatrix} c2 & -c2\theta3 + (\alpha3 + \alpha2)s2 - \theta1 & s2 \\ \theta3 + \alpha1s2 + \theta1c2 & 1 & \theta1s2 - \alpha1c2 - \alpha3 - \alpha2 \\ -s2 & s2\theta3 + (\alpha3 + \alpha2)c2 + \alpha1 & c2 \end{bmatrix} \quad (2)
$$

In matrix ${}^0A_T$, the terms $A_{12}, A_{21}, A_{23}$ and $A_{32}$ can be considered much smaller than the other ones, thus the matrix represents the frames 3 and T rotated of angle $d\theta2$ about y axis of frame 0.

To evaluate the actual errors due to mechanical inaccuracies, a special instrumented tool was realized and used. The tool, installed in place of the actual bending tools, is composed of a sphere of radius $r$ placed on the top of a prism, whose surfaces were detected by a laser sensor placed at the end-effector of the Cartesian robot. The centre of the sphere was considered as the tool centre point TCP. Posing the bending unit in initial condition (A = B=0°), the measure of the prism surface provided the value of $d\theta2$, that is the required correction of B axis in zero-axis configuration.

The position of the TCP can be expressed in the global frame 0 by pre-multiplying the vector $[0\ 0\ h\ 1]^T$ by the pose matrix ${}^0\hat{A}_T$. It is influenced by all the mechanical inaccuracies of the bending unit. In order to evaluate only the influence of the angle $\theta2$ on the TCP position, all parameters can be considered small with respect to $\theta2$; this leads to the following expression for TCP position in the global frame:

$$
{}^0\hat{p}_T = \begin{bmatrix} (h + d3)\sin(\theta2) + (a3 + a2)\cos(\theta2) + a1 \\ d\theta1h\sin(\theta2) - \alpha1h\cos(\theta2) + (-\alpha3 - \alpha2)h + d2 \\ (-a3 - a2)\sin(\theta2) + (h + d3)\cos(\theta2) + d1 \\ 1 \end{bmatrix} \quad (3)
$$

By projecting this vector on the X0-Z0 plane of global frame, it is possible to get information about some error parameters, as depicted in Fig. 3. An angle $\gamma$, depending on error parameters $a2$, $a3$ and $d3$, is then generated:

$$
\gamma = \operatorname{atan}\left(\frac{a2 + a3}{h + d3}\right) \quad (4)
$$

in this plane, the coordinates of TCP are:

$$
\begin{aligned}
T_{X0} &= a1 + \sin(\theta2 + \gamma)\sqrt{(a2 + a3)^2 + (h + d3)^2} \\
T_{Z0} &= d1 + \cos(\theta2 + \gamma)\sqrt{(a2 + a3)^2 + (h + d3)^2}
\end{aligned} \quad (5)
$$
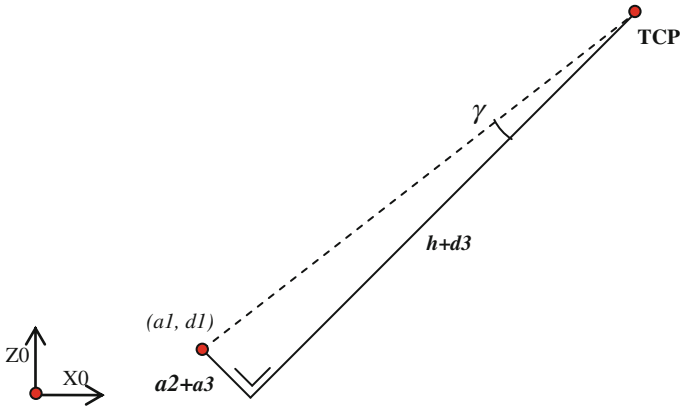
**Fig. 3.** Projection of TCP position in X0-Z0 plane, for a given value of θ2 angle

The evaluation of errors *a1* and *d1* (offset coordinates of B axis) is possible by experimental measurement of the TCP position on varying B. For each value of B, a couple of coordinates $x_i$ and $z_i$ of the tool sphere centre is determined, then offset errors *a1* and *d1* of B axis can be calculated by minimizing the function:

$$S = \sum \left[ (x_i - a1)^2 + (z_i - d1)^2 - r^2 \right]^2 \tag{6}$$

Putting in expression (3) the calculated values of *a1* and *d1*, the terms $(h + d3)$ and $(a3 + a2)$ can be evaluated and then the angle $\gamma$ is calculated.

From each sample it is then possible to extract a *nominal value* $B_i$ of the coordinate axis and an *actual value* $\theta 2_i$, calculated as:

$$\theta 2_i = \text{atan2} \left( \frac{x_i - a1}{z_i - d1} \right) - \gamma \tag{7}$$

Assuming that the main inaccuracies are due to backlash on the driveline and deformation in the unit structure, the actual value of θ2 angle can be approximated as a cubic function of joint coordinate B:

$$\theta 2 = d\theta 2 + c_1 B + c_3 B^3 \tag{8}$$

For each sample detected by the instrumented calibration tool, it is:

$$\frac{\theta 2_i - d\theta 2}{B_i} = c_1 + c_3 B_i^2 \tag{9}$$

Considering all samples, it is necessary to solve the following system in matrix form:

$$\boldsymbol{\theta} = \begin{bmatrix} 1\mathbf{B}^2 \end{bmatrix} \mathbf{c} \tag{10}$$

The vector $\mathbf{c} = [c_1\ c_3]^T$ is calculated from the pseudo-inverse of $[1\ \mathbf{B}^2]$.

*Correction of Axis A.* The corrections that must be applied to axis A can be calculated considering again the orientation matrix $^0A_T$, but expressed now for $\theta3 = 0$:

$$^0A_T = \begin{bmatrix} c2 & (\alpha3 + \alpha2)s2 - \theta1 & s2 \\ \alpha1 s2 + \theta1 c2 & 1 & \theta1 s2 - \alpha1 c2 - \alpha3 - \alpha2 \\ -s2 & (\alpha3 + \alpha2)c2 + \alpha1 & c2 \end{bmatrix} \tag{11}$$

With swinging unit in zero-axis condition, supposing axis B corrected as described above, only angular inaccuracies $d\theta1$, $d\theta3$, $\alpha1$, $\alpha2$, $\alpha3$ remain:

$$^0A_T = \begin{bmatrix} 1 & -d\theta3 - d\theta1 & 0 \\ d\theta3 + d\theta1 & 1 & -\alpha1 - \alpha3 - \alpha2 \\ 0 & \alpha1 + \alpha2 + \alpha3 & 1 \end{bmatrix} \tag{12}$$

By means of the instrumented tool it is possible to experimentally get the direction cosines of the matrix, thus being able to write three independent equations:

$$\begin{cases} -d\theta3 - d\theta1 = A_{12} \\ d\theta3 + d\theta1 = A_{21} \\ \alpha1 + \alpha2 + \alpha3 = A_{32} \end{cases} \tag{13}$$

Repeating the same procedure for $\theta3 = 90°$, we get:

$$^0A_T = \begin{bmatrix} d\theta1 - \alpha2 & \alpha3 & 1 \\ -1 & d\theta3 + \alpha1 & d\theta1 - \alpha2 \\ -d\theta3 - \alpha1 & -1 & \alpha3 \end{bmatrix} \tag{14}$$

Being able to write two more independent equations:

$$\begin{cases} \alpha3 = A_{33} \\ d\theta1 - \alpha2 = A_{11} \end{cases} \tag{15}$$

Solving the system (13) + (15), the angular errors $d\theta1$, $d\theta3$, $\alpha1$, $\alpha2$, $\alpha3$ are calculated.

## 4 Correcting the Reference Values to the Controller

All reference values to control axes A and B and the Cartesian manipulator can be corrected by using the 12 error parameters calculated as above.

In an ideal condition, all errors in Table 1 are equal to 0 and the positioning matrix of TCP and related frame T with respect to the global frame 0 is:

$$^0\hat{A}_{T(ideal)} = \begin{bmatrix} \cos(At)\cos(Bt) & -\sin(At)\cos(Bt) & \sin(Bt) & h\sin(Bt) \\ \sin(At) & \cos(At) & 0 & 0 \\ -\cos(At)\sin(Bt) & \sin(At)\sin(Bt) & \cos(Bt) & h\cos(Bt) \\ 0 & 0 & 0 & 1 \end{bmatrix} \quad (16)$$

where $At$ and $Bt$ are the correct reference values to impose to swinging unit axes.

Concerning axis B, it is possible to use Eq. (8), whose coefficients $d\theta2$, $c_1$ and $c_3$ have been previously determined. Given the desired values $Bt$ of joint coordinate, the reference values B can be calculated by solving the following cubic equation:

$$Bt = d\theta2 + c_1 B + c_3 B^3 \quad (17)$$

As regards the axis A, given the desired value $At$ of bending angle, the reference value A is calculated as:

$$A = At - d\theta3 \quad (18)$$

Finally, gaps $dx$, $dy$ and $dz$, to enter the Cartesian robot control in order to recover the offsets of the structure, can be calculated by subtracting the ideal pose matrix of the TCP from the real one:

$$[dx\,dy\,dz0]^T = {^0\hat{A}_T}(:,4) - {^0\hat{A}_{T(ideal)}}(:,4) \quad (19)$$

## 5 Experimental Procedure and Results

Figure 4 shows the tool used to evaluate the inaccuracies of the system. It is composed of a sphere placed on the top of a prism, whose surfaces are detected by a laser sensor (Panasonic HL-G108-A-C2) placed at the end-effector of the Cartesian robot. The prism is divided in two parts, installed in place of the actual bending tools.

In the procedure, the laser sensor measures the position of a given number of points located on the surface of the sphere and of the prism. The measure is repeated for a proper number of samples, to acquire a significant data base. In this way, the position of the sphere centre, considered as the TCP, and of the bending line located along the contact surfaces of the two parts of the prism, are detected. Applying the method described in Sect. 3, all error parameters of the bending system are evaluated.

The procedure has been applied to the Amada Lasbend-AJ® bending system. The Table 2 reports the resulting error parameters. In general, you may notice that parameters related to displacement errors are more relevant than those related to angular errors. The experiment highlights mechanical inaccuracies that require correction of the reference values inputted to the control system. As concerns the correction for axis B to compensate errors due to backlashes and compliance in the
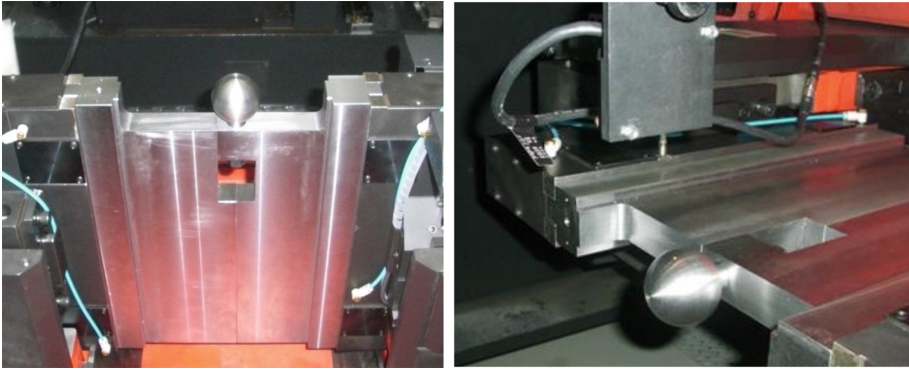
**Fig. 4.** The special tool used to evaluate the mechanical inaccuracies of the bending unit. The tool is installed on the swinging unit in place of the actual bending tools

**Table 2.** The parameters of mechanical inaccuracies of the tested bending system, evaluated by means of the calibration procedure

| | |
|---|---|
| *a1* | −1.41 mm |
| *dθ1* | −0.0008 rad (−0.0461°) |
| *d1* | 2.19 mm |
| *α1* | −0.0033 rad (−0.1885°) |
| *a2* | −0.26 mm |
| *dθ2* | 0.0005 rad (0.0277°) |
| *d2* | −0.61 mm |
| *α2* | −0.0010 rad (−0.0586°) |
| *a3* | 1.67 mm |
| *dθ3* | 0.0009 rad (0.0544°) |
| *d3* | −0.77 mm |
| *α3* | 0.0026 rad (−0.1503°) |

driveline, as expressed by Eq. (17), the experimental procedure allowed to determine the coefficients of the cubic polynomial:

$$Bt = -0.0049 + 0.9866 \cdot B + 0.0056 \cdot B^3 \tag{20}$$

## 6    Conclusion

The described procedure allows an easy determination of the main mechanical inaccuracies of the swinging unit, and is able to calculate all corrections necessary to compensate the reference values provided to the control system.

The application of the procedure to a robotized bending system highlighted error parameters that, if not corrected, may compromise the quality of the product.

The procedure can be easily integrated in the general control of the bending system, thus providing a fully automatic tool for identification and compensation of possible mechanical inaccuracies of the machine.

# References

1. Mooring, B.W., Roth, Z.S., Driels, M.R.: Fundamentals of Manipulator Calibration. Wiley, New York (1991)
2. Hollerbach, J.M., Wampler, C.W.: The calibration index and taxonomy for robot kinematic calibration methods. Int. J. Robot. Res. **15**, 573 (1996)
3. Judd, P.J., Knasinski, A.B.: A technique to calibrate industrial robots with experimental verification. IEEE Trans. Robot. Autom. **6**, 1 (1990)
4. Renders, J.M., Rossignol, E., Becquet, M., Hanus, R.: Kinematic calibration and geometrical parameter identification for robots. IEEE Trans. Robot. Autom. **7**(6), 721–732 (1991)
5. Nahvi, A., Hollerbach, J.M.: The noise amplification index for optimal pose selection in robot calibration. In: IEEE International Conference on Robotics and Automation, Minneapolis, USA (1996)
6. Conrad, K.L., Shiakolas, P.S., Yih, T.C.: Robotic calibration issues: accuracy, repeatability and calibration. In: 8th Mediterranean Conference on Control and Automation, Patras, Greece (2000)
7. Hoai-Nhan, N., Zhou, J., Kang, H.J.: A new full pose measurement method for robot calibration. Sensors **13**, 9132–9147 (2013)

# Requirements and Constraints for a Robotized Roll Hemming Solution

E. Esquivel[1,2(✉)], Giuseppe Carbone[2], Marco Ceccarelli[2], and J. Jáuregui[1]

[1] Universidad Autónoma de Querétaro, Santiago de Querétaro, Mexico
eesquivelg0687@gmail.com
[2] University of Cassino and South Latium, Cassino, Italy
ceccarelli@unicas.it

**Abstract.** The objective of this study is the design of a new roller hemming tool. For this purpose, main parameters affecting the final quality of the rolled hemmed part have been studied in order to identify and outline the key factors in roller design as well as in roller hemming process stages. A preliminary set of experiments has been carried out to study the pre-hemming force and springback relation in an aluminium sheet. Experiments showed the required forces in first pre-hemming stage and allowed to calculate a stiffness coefficient based on the springback deformation angle.

**Keywords:** Robotics · Roll hemming · Tool design · Modelling and testing

## 1 Introduction

Flanging and hemming are used as the last stage of stamping operations, mainly in the automotive industry. Hemming is used either to improve appearance (a smooth edge rather than a razor edge with burrs) or to attach one sheet metal part to another mainly in the case of automotive panels such as doors, hoods and deck lids [12]. In the place of traditional hemming tabletop, a roller is guided by a robot along the hemmed line and progressively bends the angle height along the part [11]. However, the low stiffness due to the open kinematic chain, may affect the performance in the roll hemming process as well as in many others roboforming and machining applications [2]. In 2011 Shuhui Li developed a finite element model considering flanging, pre-hemming and hemming for a flat surface-straight edge in aluminum alloy 6061T6, [11]. They worked out experiments to measure the roll in/out to compare them with simulation results. In 2012 Le Maoût proposed the identification of an anisotropic elastic-plastic mixed hardening material model [9], for a curved surface-curved edge part with a good representation of the wrinkles in experiments due to the pre-strain history of the material. In 2014 Drossel analyzed the quality of the final shape in roll hemming process according to different material sections, showing that the geometry affects final quality in hemmed sheet during robot's trajectory [8].

In 2011 Abele proposed two models in SimMechanics and ADAMS to predict the stiffness of an industrial robot, the simulated path deviation is compared to the process force [2]. In 2011, Meier reported theoretical and experimental investigations on the influence of superimposed pressure by considering roboforming applications [13], where an increase of 12.5% in draw angle was achieved. In 2013 Belchior, [4], brings a contribution to Meier's work, [13], proposing a robust and systematic notation for an elastic model of industrial open and closed manipulators that considers elasticity in links. However, the focused application is Single Point Incremental Forming. Comau (Consorzio MAcchine Utensili) [7], covers from closures and wheelarch to sunroofs production systems. A roller hemming tool consisting of a push-pull system, with a roller pack has a double spring system, with 2 load cells to measure the force. The dimensions of the tool are $305 \times 82 \times 186$ mm and can work with forces in range of $\pm 2200$ N. The hemming process can reach $50°$ in one step and completing in 2 steps with a speed up to 750 mm/s [7]. ABB Robotics designed a roller tool that uses a proportional valve to achieve stable force between the hemming bed and the roller [1]. Similarly, KUKA roller hemming tool consists in a system called HIGH Output Quality (HOQ) hemming [3]. The hemming can produce different types of flanges and can reduce the time of producing a flange by 50%. Based on the above mentioned literature described we propose to design a new roller hemming tool that can provide low cost and user friendly features. For this purpose we first study the main parameters of the roller hemming process.

## 2   Main Process Parameters

This study focuses on understanding the interaction between roller and sheet metal part during shaping the flange to $60°$ pre-hemming. It is important to consider the main parameters of the material, the tool and the robot. The material consists of an aluminium alloy usually 6061T6 [11], where the geometry at starting will affect the result of the process as based on the main parameters shown in Fig. 1(a). The flange length $l$ is the length at which the flange is bent at the beginning of the roller hemming process. The thickness $t$ plays an important role, too. This will increase the stiffness of material to be shaped by the roller. The initial bending angle, $\theta_s$, starts at $90°$, [10]. The flange radius is also an important parameter $R_f$. Other parameters to consider are the shape of the metal work-piece, since it could be a flat surface-straight edge, see Fig. 1(b), flat surface-convex edge, shown in Fig. 1(c), curved surface-straight edge and curved surface-convex edge. These involve different trajectories the robot. There are different defects produce while doing roll hemming process. Main defects are: roll in, roll out, recoil and warp. The roll in, shown in Fig. 2(a), and roll out, shown in Fig. 2(b), are the most widely addressed defects, roll in being the reference standard for hem quality. Recoil, shown in Fig. 2(c), and warp, shown in Fig. 2(d), are generated when the roller presses the part and an unusual deformation appears under the sheet; it could be a bubble or a gap. Wrinkles, appear as consequence of applied force, speed tool and material inconsistent deformation; these affects the part appearance, see Fig. 3(a).
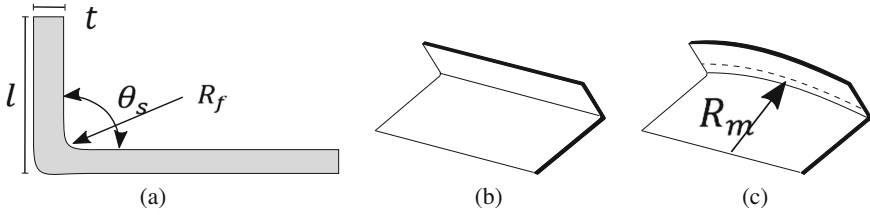
**Fig. 1.** (a) Shows main parameters at starting process. $l$: Flange angle, $t$: Thickness, $\theta_s$: Initial angle, $R_f$: Flange radius. (b) Shows a flat surface-straight edge part to be hemmed. (c) Shows a flat surface-convex edge part to be hemmed, with $R_m$: Material radius.
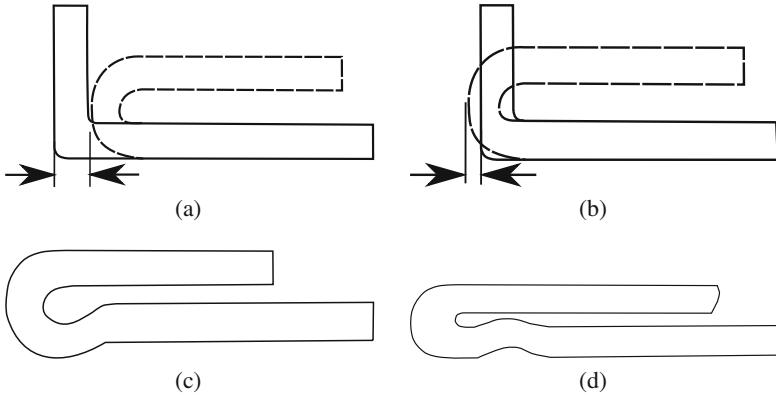


**Fig. 2.** (a) Roll in. (b) Roll out. (c) Recoil. (d) Warp.

The robot used during the process is key factor for shaping material, robot's stiffness, could bring higher force and less trajectory variation, stiffness is also a geometrical problem dependent on the robot configuration. Common robot types are 400 kg payload range RRR serial robots. A study of part hemmed quality according to different robot's stiffness is required, see Fig. 3(b), where position A and B corresponds to a higher and a lower robot's stiffness configuration, respectively. Drossel establishes in [8] a better quality corresponds to a higher robot's stiffness configuration. Different reaction forces are assumed to be present in the roller-part interaction, see Fig. 4: pressing reaction in robot hand direction $R_P$, advance reaction when robot moves $R_A$, define a $F_i$ force vector. $F_i$ varies along the robot's path, so $F_{i+1}$ differs from $F_i$. Wrinkles, a main defect, could be related to $F_i$. A hypothesis is presented, a wrinkles formation leads to a higher $F_i$ variation as shown in Fig. 5(a); otherwise, the absence of wrinkles leads to a lower $F_i$ variation as shown in Fig. 5(b). Force varies due to material deformation.
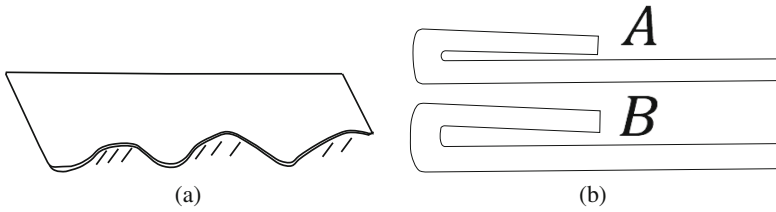
**Fig. 3.** (a) Wrinkles. (b) A: High robot stiffness, B: Low robot stiffness.
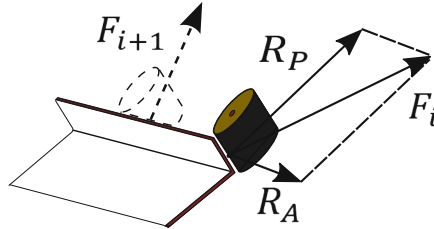


**Fig. 4.** Vector forces along robot path; $R_A$ is the reaction to advance, $R_P$ is the reaction to pressing, $F_{i-1}$ is the resultant vector.
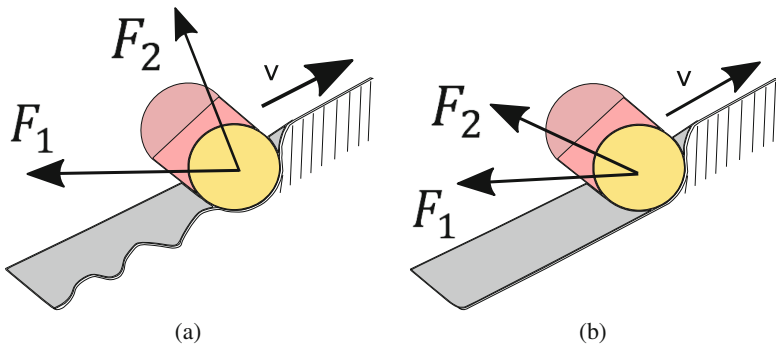


**Fig. 5.** Schemes force variation (contact forces may vary from $F_1$ to $F_2$). (a) With wrinkles. (b) Without wrinkles.

## 3 Preliminary Experiments

The objective of the experiments is to verify some of the main process parameters that can influence a roller hemming tool design. In particular, preliminary experiments have been carried out to determine the stiffness of hemmed part in $60°$ pre-hemming step. Force and angle are measured and related as shown by Budynas [5]. In Eq. 1, $F$ is the force applied, $d$ is the distance at force application, $k_t$ is the stiffness of the material and $\triangle\theta$ is the variation in angle.

$$Fd = K_t \triangle \theta \tag{1}$$

The initial parameters are: part size without bending of $100\,\mathrm{mm} \times 50\,\mathrm{mm}$, initial bending angle of $90°$, material type is aluminium, material thickness of $1\,\mathrm{mm}$, flange length of $50\,\mathrm{mm}$, position of the IMU (inclination sensor) at top flange and the sensor force used is a load cell S type. The workpiece deflects a determined angle $\theta_{max}$ when a flange centre force is applied [6], see Fig. 6.
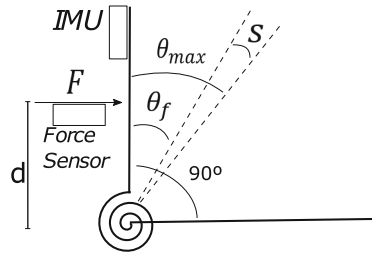


**Fig. 6.** Proposed model to correlate force with angle.

The procedure consists in applying a force deformation on material flange until certain angle, register the force and retrieve the applied force in order to register the springback. The force will be applied to move the aluminium sheet flange from $0°$ to $30°$ from the vertical initial position, approximately.

The procedure for a sample test is featured as follows.

1. Start test
2. Bending an aluminium sample sheet of $1\,\mathrm{mm}$ $90°$
3. Fixing the IMU sensor at the centre of the flange
4. Position the Force sensor at the centre of flange
5. Apply a force, bending the sample $30°$
6. Collect force and angle data
7. End test

The material used is aluminium of $1\,\mathrm{mm}$ thickness bended $90°$. The IMU is a sensor capable of measuring angle and acceleration in three axis; in this experiment the only used axis is X, according to the orientation of the position in the aluminium sheet. The Load Cell used was a S type for measuring the force, it required a Weathstone bridge connection based on the NI usb 6009 DAQ acquisition hardware; the calibration of the sensor was done by using different weights from 0 to $80\,\mathrm{N}$. The IMU sensor has been used to detect the inclination angle in combination with Arduino data acquisition board. The IMU was positioned and attached with adhesive at top of flange, as shown in Fig. 7(a). The force sensor is positioned at the centre of the flange to apply the force, Fig. 7(b). The graph Fig. 8(a), shows the force application vs time for the first test, the graph Fig. 8(b), shows the inclination angle vs time for the first test. The final results of the sheet bended are shown in Table 1.

The springback is the difference in angle between the maximum angle and the final angle. Considering the distance of force application $25\,\mathrm{mm}$ and the angles

(a)                                        (b)
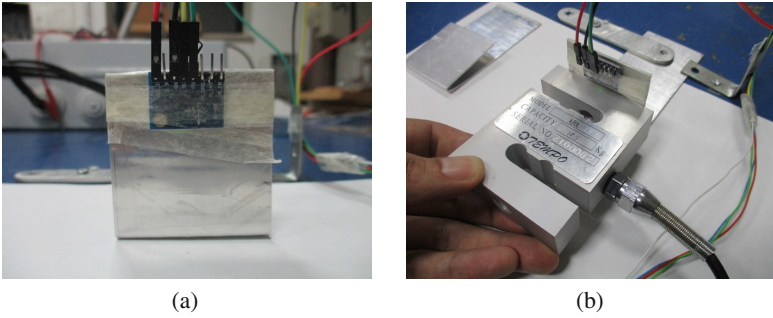
**Fig. 7.** (a) Positioning IMU. (b) Force application.



(a)                                        (b)
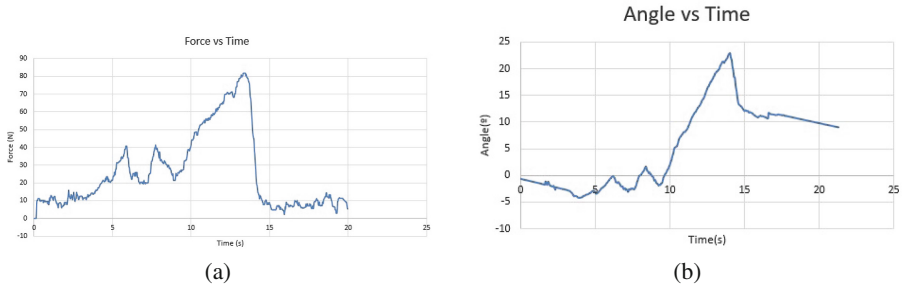
**Fig. 8.** (a) Force applied during pre-hemming step. (b) Angle measured during pre-hemming step.

**Table 1.** Experimental results.

| Run | $F_{max}(N)$ | $\theta_{max}(Deg)$ | $t(s)$ | $S(Deg)$ | $\theta_f(Deg)$ |
|-----|------------|------------------|--------|----------|----------------|
| 1 | 81.48 | 21.11 | 13.62 | 11.46 | 9.56 |
| 2 | 120.77 | 23.72 | 14.16 | 11.22 | 12.05 |
| 3 | 87.54 | 27.91 | 13.26 | 11.2 | 16.71 |
| 4 | 104.45 | 23.12 | 13.42 | 11.2 | 11.92 |

in radians, Eq. 2, shows an average stiffness coefficient for the material in the pre-hemming stage.

$$k_t = Fd/ \triangle \theta$$
$$k_t = 12.58 Nm/rad \tag{2}$$

## 4   First Design

Based on the outcomes of previous sections we propose a preliminary design for a low cost user friendly roller hemming tool. In particular, Fig. 9(a), shows a

first scheme of the proposed tool, while Fig. 9(b), shows key components in its design and Fig. 9(c), shows the complete tool design in a 3D CAD model. Main qualitative requirements are considered for tool design based on experimental test as follows:

1. The roller height must be equal to flange length
2. Tool must measure at last one force direction
3. Tool must handle different roller diameters (cylindrical)

Quantitative requirements have been defined as referring to existing commercial products as follows:

1. Hemming force range 0–1 KN (industry 0–2, 200 N)
2. Roller diameter Medium (40 mm) and Small (32 mm)
3. Roller height (10 mm)

A prototype constitution and preliminary test of the proposed tool are currently starting at LaRM (Laboratory of Robotics and Mechatronics).
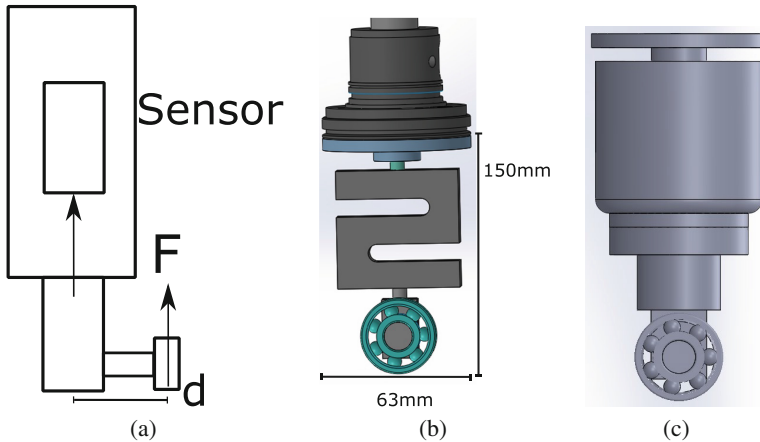


**Fig. 9.** Proposed tool design. (a) First scheme. (b) Preliminary design. (c) Preliminary design complete.

## 5 Conclusions

This paper gives an outline of main requirements for the design of a low cost user friendly roller hemming tool. In particular, main design parameters have been outlined also through preliminary experimental tests. A 3D CAD model is proposed, its constriction and testing is currently undergoing at LaRM in University of Cassino.

# References

1. ABB robotics: roller hemming head. Product Catalog, p. 2 (2012)
2. Abele, E., Bauer, J., Hemker, T., Laurischkat, R., Meier, H., Reese, S., von Stryk, O.: Comparison and validation of implementations of a flexible joint multibody dynamics system model for an industrial robot. CIRP J. Manufact. Sci. Technol. **4**, 38–43 (2011)
3. Automotive, K.S.: Full throttle for your production. Product Catalog, p. 9 (2012)
4. Belchior, J., Guillo, M., Courteille, E., Maurine, P., Leotoing, L., Guines, D.: Off-line compensation of the tool path deviations on robotic machining: application to incremental sheet forming. Robot. Comput. Integr. Manufact., 58–69 (2013). http://dx.doi.org/10.1016/j.rcim.2012.10.008
5. Budynas, R.G., Nisbeth, J.K.: Mechanical Engineering Design, vol. XXXIII, 9th edn. McGraw Hill, New York (2012)
6. Carbone, G.: Stiffness analysis and experimental validation of robotic systems. Front. Mech. Eng. **6**, 182–196 (2011). Higher Education
7. Comau, C.M.U.: RHevo roller hemming. Product Catalog, p. 2 (2014)
8. Drossel, W.G., Pfeifer, M., Findeisen, M., Rössinger, M., Eckert, A., Barth, D.: The influence of the robot's stiffness on roller hemming processes. In: ISR Robotik, pp. 531–538 (2014)
9. Le Maoût, N., Manach, P.Y., Thuillier, S.: Influence of prestrain on the numerical simulation of the roller hemming process. J. Mater. Process. Technol. **212**, 450–457 (2012)
10. Le Maoût, N., Thuillier, S., Manach, P.Y., Debois, D., Wadoux, J.: Numerical simulation of flat-surface roll hemming: influence of geometry and material models. In: International Conference on Deep Drawing Research Group Conference IDDRG, pp. 287–294, Porto (2006)
11. Li, S., Hu, X., Zhao, Y., Lin, Z., Xu, N.: Cyclic hardening behavior of roller hemming in the case of aluminum alloy sheets. Mater. Des., 2308–2316 (2011). http://dx.doi.org/10.1016/j.matdes.2010.09.017
12. Livatyali, H., Müderrisoglu, A., Ahmetoglu, M.A., Akgerman, N., Kinzel, G.L., Altan, T.: Improvement of hem quality by optimizing flanging and pre-hemming operations using computer aided die design. J. Mater. Process. Technol. **98**, 41–52 (2000)
13. Meier, H., Magnus, C., Smukala, V.: Impact of superimposed pressure on dieless incremental sheet metal forming with two moving tools. CIRP Ann. Manufact. Technol. **60**, 327–330 (2011)

# Weed Segmentation from Grayscale Tobacco Seedling Images

Petre Lameski[(✉)], Eftim Zdravevski, and Andrea Kulakov

Faculty of Computer Science and Engineering, University of Saints Cyril
and Methodius in Skopje, Skopje, Macedonia
{petre.lameski,eftim.zdravevski,andrea.kulakov}@finki.ukim.mk

**Abstract.** Manual weed extraction from young seedlings is a hard manual labour process. It has to be continuously performed to increase the yield per land unit of any agricultural product. Precise segmentation of plant images is an important step towards creating a camera sensor for weed detection. In this paper we present a machine learning approach for segmenting weed parts from images. A dataset has been generated using bumblebee camera under various light conditions and subsequently training and test patches were extracted. We have generated various texture-based descriptors and used different classification algorithms aiming at correctly recognizing weed patches. The results show that in a case when the images are grayscale, the light conditions are varying, and the distance of the camera to the weeds is not constant machine learning algorithms perform poorly.

**Keywords:** Weed control · Image processing · Machine learning · Precision agriculture

## 1 Introduction

According to [15] the agricultural production increasing trend is insufficient to reach the population demand in the future. One of the ways to increase the production is to increase the per land unit yield since the land units available for production are limited. Automation and introduction of Robots in Agriculture is not a new concept [3], and could help in the food production efficiency while at the same time, reducing the environmental impact of the food production in agriculture.

The interest about using autonomous robots in weed control has increased in recent years [16]. Weed control is a process of eliminating undesired plants from the plantations by using chemical compounds or removing them mechanically. It has been proven that precise appliance of chemical compounds decreases the amount of pesticides and makes the products healthier [11] by using special end effectors. Both mechanical and chemical weed control require precise localization of the plants that need to be eliminated. There are several existing approaches towards using machine learning and image processing for weed control.

In [12] the authors propose a robust technique for plant segmentation from land using normalized green index. NDVI index for images is used in [8] to segment land from plants and build their descriptors to classify different types of plants (both known and weed plants). There are existing datasets that contribute towards the automated weed detection from images. In [9] authors present Near infra red (NIR) and visible RED images from carrot plantation taken under controlled light. Authors use the NDVI index to segment green areas and use machine learning approach to classify weed and usable plants.

There are many machine learning approaches towards plant images classification including several competitions [7] where machine learning approaches have proven to give promising results towards plant recognition from images [5,18]. To precisely localize the weeds in images in order to be able to aid the control of a weeding robot, it is important to segment the image to weed and non-weed regions. In this paper we are using images from low resolution camera under various light conditions. The approach uses several texture patch features to classify patches as weed or not weed.

The problem assessed in this dataset is the problem of segmenting closely seeded plants in seedling plantations as they are traditionally seeded in the agricultural area of Prilep in Macedonia.

The main contribution of our work is the dataset and the initial results from the segmentation using several texture descriptors and feature selection processes to reduce the dimensionality. The goal of the presented work was to evaluate the possibility of using cheap cameras as sensors under variable light conditions and to train a classifier able to detect weed regions from those images.

## 2  Dataset and Algorithms

### 2.1  Dataset

The dataset is consisted of 66 randomly selected images taken under various light conditions and various heights from a cluttered tobacco seedling plantation. The dataset is then split to 45 train and 21 test images. The images are then labelled manually for their content: tobacco seedlings or land as one class and weed as another class.

From the images we extracted a total 160000 patches with size of $65 \times 65$ pixels that were used for training and from the test images 50000 patches used for testing. To obtain a balanced dataset we tuned the number of randomly selected patches to 80000 from each class for training, and 25000 from each class for testing.

The images used were converted to grayscale since we were interested in the texture characteristics for the segmentation process. The patches were labelled based on the central pixel. If the pixel belongs to a weed its label was marked as weed, else it was marked as non weed patch. Figure 1 shows an example of the images used for the dataset where the traditionally closely placed seedlings in the plantation can be observed.
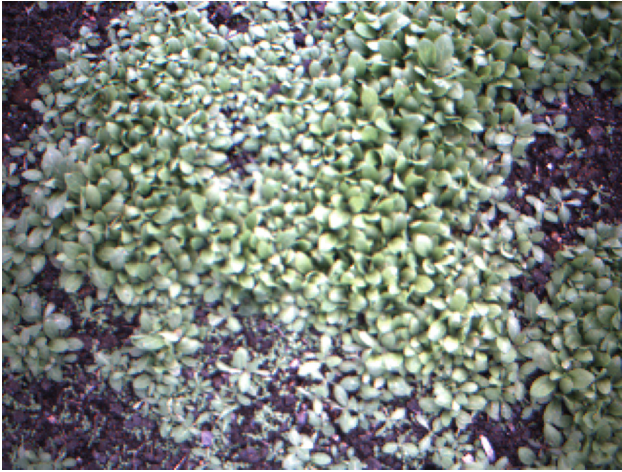
**Fig. 1.** Example image from the dataset containing tobacco seedlings

## 2.2  Texture Descriptors

To generate the classification data we used several patch descriptors.

First we generate an image of differences between each pixel from the patch and the central pixel and we generate a histogram of these differences. Then a Histogram of Oriented Gradients [4] (HOG) descriptor was calculated from the grayscale image and also on the difference image, and a HOG descriptor was calculated on the regular grayscale patch. The hog descriptor requires patches with size of $65 \times 65$, so we ignored the rightmost column and bottommost row from each patch when generating the HOG descriptor. For the HOG descriptor we used the OpenCV [2] implementation with the following parameters: windows size 64, block size 16, block stride 8, cell size 8 and number of bins 9. The descriptor is generated for the window so for each block a different histogram is generated. Then the blocks are moved with overlapping. The idea behind the descriptor is that objects can be recognized based on the local intensity gradients distributions without the knowledge of their exact location.

We also generate a Local binary pattern [13] (LBP) histogram. Local binary pattern takes N pixels in radius R around the central pixel and calculates whether the pixel has a smaller or larger value than the central pixel. If the value is larger the bit is set to 1 and otherwise it is set to 0. All the bits are then encoded in a single number. For the LBP descriptor we used the scikit-image implementation [17] with radius of 1 and 8 points. This gives an 8 bit number of different variations of ones and zeros that can be encoded in 256 different values.

The descriptors are chosen because of their good overall performance in texture classification. The total length of the descriptor used is 3784, 256 from the histogram of differences, 256 from the LBP histogram and 1636 each for the HOG descriptor on the grayscale and the HOG descriptor on the difference image.

### 2.3 Pre-processing and Classification

The length of the descriptor is reduced by using ensembles of trees. First it uses Random Forest (RF) for evaluating initial dataset score, but more importantly feature importance. It is used with the default parameters, as we have noticed that tuning them does not improve the performance dramatically (unlike SVMs for example). As a wrapper approach for evaluating feature subsets during the feature engineering and elimination loop, the framework uses Extremely Randomized Trees (ERT) [6], as they are significantly faster (over 50 %) than Random Forests (RF), especially when the number of features is larger. They also provide estimate for feature importance, however it is not as stable as the feature importance estimated by the Random Forests.

Because we are using different training and test datasets, we also want to avoid including features that easily over-fit to the training dataset. Therefore we use an approach based on the idea presented in [1]. For each feature we calculate two scores - one for its importance related to the target class and one for its ability to predict whether the patch comes from the train or the test set. Ideally the reduced dataset will have features that are good predictors of the target class, but bad predictors of the dataset. Using a grid search we discard some features and get optimal dataset. The implementation for Extremely Randomized Trees used is the Python implementation included in scikit-learn [14]. The algorithm creates an ensemble of classifiers from random subsets from the dataset and from the features.

## 3 Results and Conclusion

The results on the test set show that the best precision of 52.57 % and AUC ROC of 0.535 was obtained using the ERT with selected total of 845 features. It is important to note that similar performance was obtained with both ERT and RF when using only the top 6 features (52.41 % for RF and 52.39 % for ERT).

There are several observations that are important to note regarding the generated features. After the analysis of the importance of each feature, none of the features generated from the HOG or the LBP descriptor were in the top features. The most important feature characteristic found based on the dataset was the first value of the difference histogram that actually represents the number of pixels that have the same value as the other pixels in the patch and all of the top 10 features were based on the difference histogram from the patch.

Table 1 shows the top 2 classification schemes for both ERT and RF with the number of descriptor values selected and the resulting classification performance.

The results show that it is difficult to distinguish the weed patches from tobacco patches based on grayscale image patches using texture descriptors. The texture descriptors failed to emphasise the difference between the classes. One of the reasons for this difficulty could be the various light conditions in which the images were taken as it can be seen on two of the images in Fig. 2.

**Table 1.** Classification performance on the dataset

| Classifier | Number of features | Training time [s] | Accuracy % | AUC ROC |
|---|---|---|---|---|
| ERT | 845 | 117.96 | 52.57 | 0.5348 |
| RF | 459 | 83.59 | 52.47 | 0.5382 |
| RF | 6 | 0.97 | 52.42 | 0.5122 |
| ERT | 6 | 0.93 | 52.39 | 0.5106 |
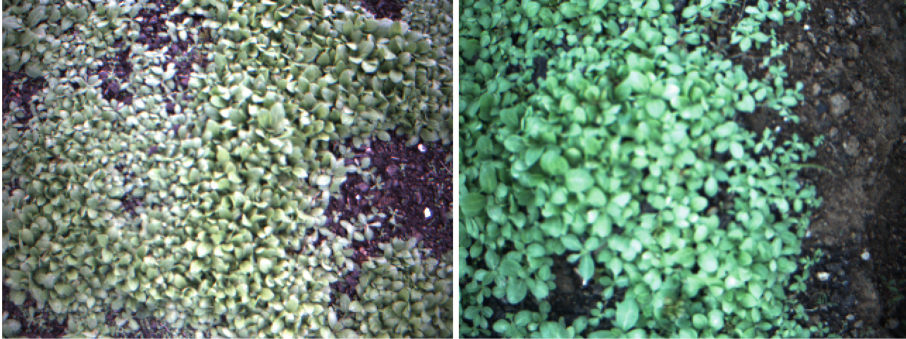


**Fig. 2.** Images taken under various light conditions and different heights

In order to improve the accuracy several things can be considered. The images could be acquired from a higher resolution camera in order to be able to distinguish the leafs better. On the current data even a human distinguishes with difficulty the weed areas on some images. The images can be taken using multispectral camera in order to obtain the best light frequencies that can be used to classify the different species of plants on the plantation. The NDVI index generated from the difference between NIR and visible light shows promising results so it could be used for generating new datasets using adequate cameras.

Another approach would be using deep learning to automatically generate the descriptors and perform the classification [10]. Considering other types of classifiers could improve or degrade the results by certain percentage but it will not improve the overall classification significantly, since during the preprocessing phase we consider only the features that give the highest information gain and are the best choice for the characterization of the classes. We are confident that images in different colour spectre should be considered for the task of weed detection.

It is important to note that any system that will used for weed detection and removal should be tuned to have as small as possible false positive rate since a false positive would identify a useful plant seedlings as weed. This must be done so that the detection system will be viable for usage on real agricultural plantations and on real commercial systems.

# References

1. Boull, M.: Tagging fireworkers activities from body sensors under distribution drift. In: 2015 Federated Conference on Computer Science and Information Systems (FedCSIS), pp. 389–396, September 2015
2. Bradski, G.: The opencv library. Dr. Dobb's Journal of Software Tools (2000)
3. Cosmin, P.: Adoption of artificial intelligence in agriculture. Bull. Univ. Agric. Sci. Vet. Med. Cluj-Napoca **68**(1), 1–10 (2011). Agriculture
4. Dalal, N., Triggs, B.: Histograms of oriented gradients for human detection. In: 2005 IEEE Computer Society Conference on Computer Vision and Pattern Recognition CVPR 2005, vol. 1, pp. 886–893. IEEE (2005)
5. Dimitrovski, I., Madjarov, G., Kocev, D., Lameski, P.: Maestra at lifeclef 2014 plant task: Plant identification using visual data. In: CLEF (Working Notes), pp. 705–714 (2014)
6. Geurts, P., Ernst, D., Wehenkel, L.: Extremely randomized trees. Mach. Learn. **63**(1), 3–42 (2006)
7. Goëau, H., Joly, A., Bonnet, P., Selmi, S., Molino, J.F., Barthélémy, D., Boujemaa, N.: Lifeclef plant identification task 2014. In: CLEF2014 Working Notes for CLEF 2014 Conference, Sheffield, UK, 15–18 September 2014, pp. 598–615. CEUR-WS (2014)
8. Haug, S., Michaels, A., Biber, P., Ostermann, J.: Plant classification system for crop/weed discrimination without segmentation. In: 2014 IEEE Winter Conference on Applications of Computer Vision (WACV), pp. 1142–1149, March 2014
9. Haug, S., Ostermann, J.: A Crop/weed field image dataset for the evaluation of computer vision based precision agriculture tasks. In: Agapito, L., Bronstein, M.M., Rother, C. (eds.) ECCV 2014. LNCS, vol. 8928, pp. 105–116. Springer, Heidelberg (2015). doi:10.1007/978-3-319-16220-1_8
10. Hung, C., Xu, Z., Sukkarieh, S.: Feature learning based approach for weed classification using high resolution aerial images from a digital camera mounted on a uav. Remote Sens. **6**(12), 12037–12054 (2014)
11. Jeon, H.Y., Tian, L.F.: Direct application end effector for a precise weed control robot. Biosyst. Eng. **104**(4), 458–464 (2009)
12. Jeon, H.Y., Tian, L.F., Zhu, H.: Robust crop and weed segmentation under uncontrolled outdoor illumination. Sensors **11**(6), 6270–6283 (2011)
13. Mäenpää, T.: The Local binary pattern approach to texture analysis: Extenxions and applications. Oulun yliopisto (2003)
14. Pedregosa, F., Varoquaux, G., Gramfort, A., Michel, V., Thirion, B., Grisel, O., Blondel, M., Prettenhofer, P., Weiss, R., Dubourg, V., Vanderplas, J., Passos, A., Cournapeau, D., Brucher, M., Perrot, M., Duchesnay, E.: Scikit-learn: machine learning in python. J. Mach. Learn. Res. **12**, 2825–2830 (2011)
15. Ray, D.K., Mueller, N.D., West, P.C., Foley, J.A.: Yield trends are insufficient to double global crop production by 2050. PloS one **8**(6), e66428 (2013)
16. Slaughter, D., Giles, D., Downey, D.: Autonomous robotic weed control systems: A review. Comput. Electron. Agric. **61**(1), 63–78 (2008)

17. van der Walt, S., Schönberger, J.L., Nunez-Iglesias, J., Boulogne, F., Warner, J.D., Yager, N., Gouillart, E., Yu, T.: The scikit-image contributors: scikit-image: image processing in Python. Peer J. 2, e453 (2014). http://dx.doi.org/10.7717/peerj.453
18. Yanikoglu, B., Tolga, Y., Tirkaz, C., FuenCaglartes, E.: Sabanci-okan system at lifeclef 2014 plant identification competition. In: Working Notes of CLEF 2014 Conference (2014)

# Human Energy Consumption During Harvesting of Saffron Flowers

Andrea Manuello Bertetto[1]([✉]), Mario Garau[1], Roberto Ricciu[2],
Luigi Lorrai[3], and Alberto Concu[3]

[1] Department of Mechanical, Chemical and Materials Engineering,
University of Cagliari, Cagliari, Italy
{andrea.manuello,mariogarau}@unica.it
[2] Department of Civil, Environment Engineering and Architecture,
University of Cagliari, Cagliari, Italy
ricciu@unica.it
[3] 2C Technologies Ltd., Academic Spin-off,
University of Cagliari, Cagliari, Italy
luigi.lorrai@gmail.com, aconcu44@gmail.com

**Abstract.** In this paper the oxygen uptake using a metabolic measurement system and energy cost of a human operator during the harvesting of saffron flowers are discussed. The measurement of energy cost was performed for a traditional harvesting handmade activity compared to a harvesting phase with a facilitator machine. In the paper the facilitator machine prototype is described and its mechanical performances are presented. The metabolic measurements layout and results are then discussed, the test protocols are declared and the measures outlined and discussed comparing the energy cost with and without facilitator machine. For the experimental evaluation of the energy consumption a significant number of measurement samples for a statistically reliable evaluation has been used. A quantity synoptic parameter has been proposed for the comparison of energy consumption with and without the facilitator machine.

**Keywords:** Harvesting device · Human energy expenditure · Facilitator machine · Human energy in agriculture

## 1 Introduction

Agriculture is the engine of sustainable development and energy is a major driver in this process. The agriculture contributes are very significantly to economic and social development in the vast majority of countries. The primary role of agriculture is to produce food and other primary goods for human consumption. The production and transformation steps require human energy linked to fatigue and with important consequences on the operator's health. This fact is a key factor for achieving sustainable development. The work in agriculture and its implications on health and productivity are linked to the mechanization in agriculture and the use, in particular, of the facilitator machines. In recent years the agriculture mechanization has increased a lot thanks to facilitator machines and operating machines. The facilitator machines are used in small

agricultural reality and give a great contribution to the development of crops now impractical on a large scale. Human energy and mechanization are highly influential on the health and agricultural productivity, in particular for small farms like those producing saffron spice. Crocus Sativus, commonly known as Saffron, is distributed primarily in the Mediterranean Region and South Western Asia.

The safranal (for odour), picrocrocin (for taste) and crocin (for pigment) components of this geophyte constituting the spice "saffron" are localized in the red stigmatic lobes of the flower [1, 2]. Saffron crocus grows up to 20–30 cm and bears up to four flowers, each with three vivid crimson stigmas in the flower goblet. The flowers harvesting phase is one of the most long and expensive phases. Saffron harvesting begins when flowers start opening, during mid or late October, and lasts for a few weeks. The high price of saffron, like the gold, is due to the difficulty of manually harvesting large numbers of stigmas at minute. In order to yield marketable amounts of saffron an exorbitant number of flowers need to be processed. Obtaining one kilogram of dry saffron spice requires the harvesting of some two hundred thousand flowers, and a field of about five thousand square meters, the equivalent of a half football area. The quantity of produced spice depends on the typical stigma size of each saffron plant. Another complication arises in the flowers' simultaneous and transient blooming. Since so many crocus flowers are needed to yield even derisory quantities of dry saffron, the harvesting can be a frenetic affair entailing continuous hours of intense labour. Once extracted the stigmas must be dried quickly, in order to avoid decomposition and loss of marketable lots. The Saffron harvesting phase, if automated, would not represent anymore the heaviest phase of production of the saffron spice.

The harvesting activity on fields is an action transferable to a robotic device. This action is often performed by human operators: thanks to the combination of the eyes, brain and hands it is possible to identify and collect delicate fruits. Some mechanical aids as collectors for example of asparagus, cherries and olives are used by harvesting machinery to make human work easier, faster and more secure. The collection of soft fruits is still mainly performed manually in order to avoid damaging the crop. In particular the harvesting phase of flowers is an action performed by hand.

The use of different techniques for picking delicate and soft objects, like fruits, is described in [3–5]. In [6] a hand is proposed for the automatic harvesting of asparagus in field. A soft hand with flexible fingers, pneumatically driven, for delicate fruit harvesting, capable of adapting to the object location and size, has been developed in [7]. The yield is very high in the case of flowers to produce spices like Saffron: the Saffron morphology imposes a particular attention to design harvesting devices treating objects having different geometries, sizes and masses [8, 9].

During saffron harvesting, the workers perform many repetitive activities and the recovery phases of the overdriven musculoskeletal apparatus are limited [10]. Those movements are usually performed with muscles of the hands, arms, legs, and back, assisted by the eyes that require torso movements. These physical factors like posture and movements are often associated with leg and back pains which imply the fatigue onset. Excessive strains increase physical tiredness, occupational illnesses and accidents and decrease work productivity. Repetitive arm, leg and torso movements contribute to the development of physical disorders [11].
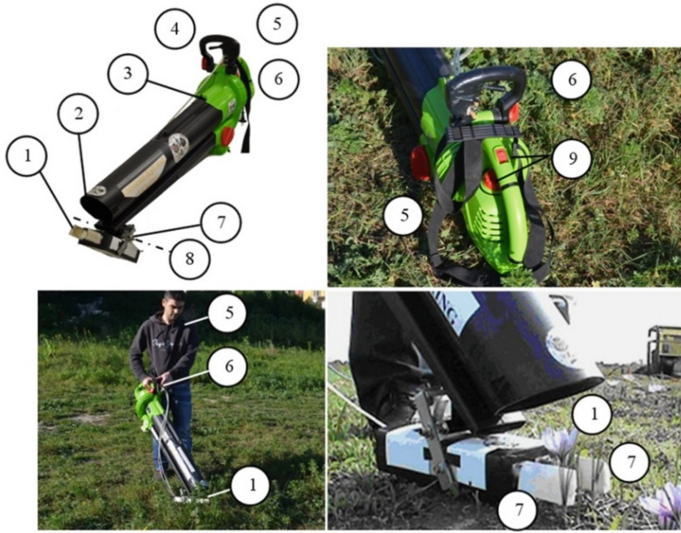
**Fig. 1.**  The harvesting prototype

It is necessary to identify and make known alternatives that increase labour productivity, modifying the conditions of work and reducing its hardness. This work is based on the analysis of the human energy expended during the harvesting phase of saffron flowers with and without a facilitator machine.

## 2   The Harvesting Prototype and the Characterizing Tests

The prototype is an integrated system for the detachment of the flower and its collection, wearable by a human operator on field. Two main tasks of the prototype mission are the detaching and the harvesting of flowers.

The prototype is shown in Fig. 1. The detaching gripper (1) exploits the strong difference in behaviour from the structural point of view of the stem of the flower and leaf, in order to avoid damage to the leaves which often surround the flower. A suction mouth (2) collects the cut flower by vacuuming and stores it in the high part of the system (3). The actuation of the detaching gripper is realized by compressed air controlled by a pneumatic valve, mounted in the prototype command group (4).

The operator wears the prototype by using a harness (5) and holds the handle (6) where there is the valve trigger control to start the detaching gripper motion. The hinge (7) links the body of the prototype to the detaching gripper (1) allowing a relative rotation around a horizontal axis (8). The suction flow regulation is controlled by the operator with knobs (9). In the detaching phase, the operator approaches the flower (10) stem positioning the detaching gripper at two fingers (7) to the flower side.

The detaching gripper is shown in Fig. 2. It consists of an aluminium alloy body (1) and a linear pneumatic actuator (2), acting on a translating crossbar (3) that pushes two cylindrical bodies (4). These bodies rot translate in two bushings (5); this rot
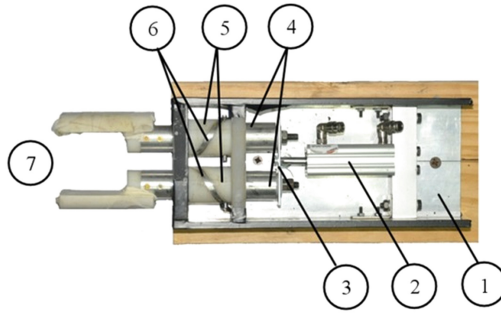
**Fig. 2.** The detaching gripper device

translating motion comes from a helical constraint: two pins, linked to the cylindrical bodies, slide in guides with helical shape (6). The fingers (7) are rigidly linked to cylindrical bodies, also the fingers motion is a rot translating helical motion parallel to the cylinder axis.

The dynamic motion equations of the system are described in [12] referring to [13, 14]. Showing the image in Fig. 2, the model was defined taking into account the helical constraint (3), the friction Coulomb's model in the helical guide and in the pneumatic actuator; also the moment transmitted by a plate type dry disk clutch is considered. The clutch is assembled between the translating crossbar (3) and the cylindrical bodies (4) allowing the cylindrical bodies to rotate with respect to the bar [15, 16]. The friction force of the cylinder is a function of the pressures in the cylinder chambers and of the piston velocity, for a given lubricating condition. This force was experimentally estimated [17–20].

The dynamic model results are compared with experimental measurements performed on the system. The gripper behaviour was investigated with an image analysis. By means of image analysis technique it is possible to detect the displacement and velocity of the gripper fingers without an invasive assembly of transducers.

In the graph of Fig. 3a the supply pressure in the posterior chamber is coming from experimental tests. These pressure values represent the input values for the model.

The supply pressure in the cylinder chambers was detected by pressure transducers. The transducer signals are processed by an acquisition board (Compact DAQ) National Instruments model NI 9219 with a resolution of 24 Bit and 100S/s/ch; the signal are then stored. The pressure transducers have a range of $\pm 1,46\ 106$ Pa with a sensitivity of 6,89 103 Pa/mV. In order to detect the system kinematics, a target was connected to the rod piston and its movement was followed on a uniform black background. Ten cycles of the piston were recorded at 1000 fps by means of a high speed camera (Redlake Motionpro Y3) with CMOS sensor and resolution of $1024 \times 1280$ pixels, equipped with a professional 50 mm lens. The outputs are the variables given in graphs of Fig. 3b and d where the cylinder stroke and the cylinder rod velocity are given in time. These rod position and velocity are able to represent bi-univocally the fingers' position and velocity because of the rod - fingers link represented by the transmission described in Fig. 2. The stroke and velocity trends coming from the model are compared with these
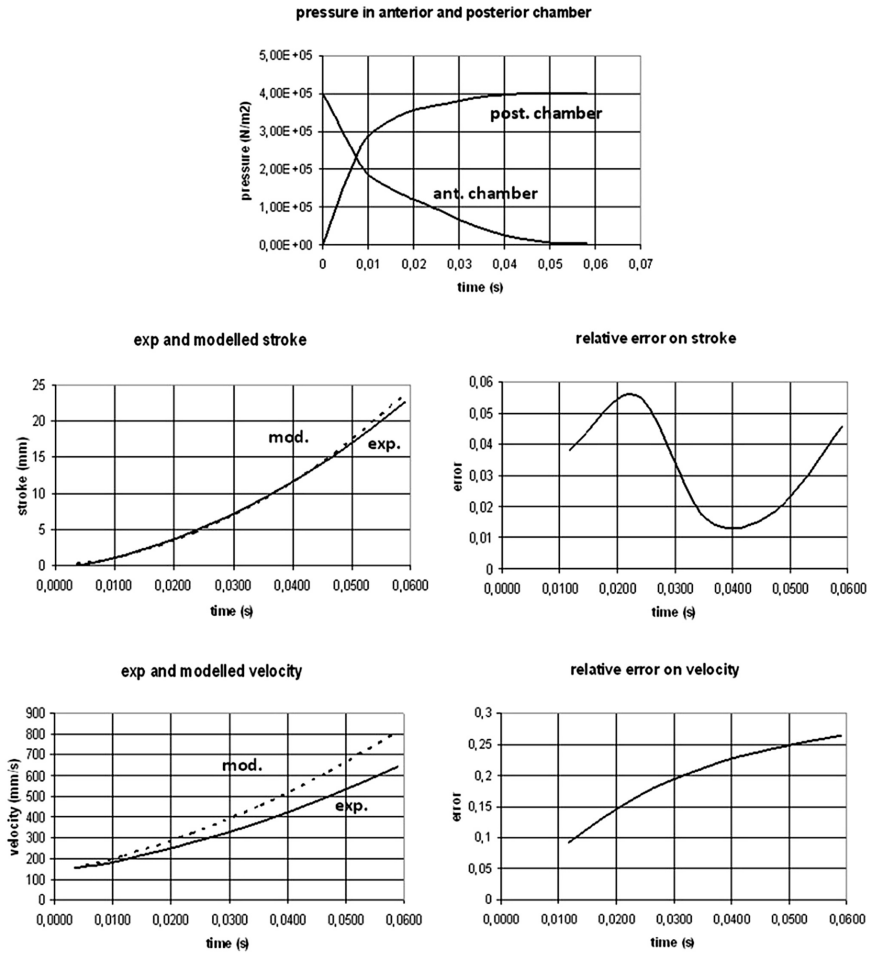
**Fig. 3.** The pressure trend in the cylinder chambers and the comparison between rod position and velocity coming from analytical model and experimental tests

strokes, less for the velocity. In Fig. 3c and d the error values are traced in time during the actuation of the fingers. It can be noted that the stroke error is defined as the difference between the computed measured experimentally. The results are in good agreement especially with the measured values, the error being less than 6%.

## 3  Human Energy Analysis

As a source of power, the human body operates typically like a heat engine with thermos physical regulators and overload controls. Chemical energy input in the form of food is converted into energy output some of which is useful for doing work. In this task the method used for measuring human energy is an indirect calorimetric technique.

The volume of oxygen one uses is usually expressed in litres (l) or millilitres (ml) remembering that one litre corresponds to $1 \times 10^{-3}$ m$^3$.

In general, humans need oxygen, which helps to metabolize the various nutrients in the body to produce energy. It is known that when oxygen combines with a gram of carbohydrate, fat, or protein, a certain amount of energy is released. If the oxygen consumption of an individual can be accurately measured, it can be a pretty good measure of energy expenditure. The amount of oxygen used can be equated to other forms of energy, such as work done in Joules (J) or heat produced in Calories (cal).

**Table 1.** Anthropometric data of examined tests (Average ± SD)

| Parameters | Males (n = 10) |
|---|---|
| Height (cm) | 173,6 ± 8,5 |
| Weight (kg) | 72,7 ± 10,4 |
| Years Old | 32,3 ± 7,3 |



**Fig. 4.** Harvesting test with and without the facilitator machine

## 3.1   Methods and Materials

In general people who work in the sector of manual harvesting frequently execute activities that are physically really onerous in terms of energy expenditure. Aerobic energy expenditure was measured to assess the physiological demand in saffron harvesting.

The tests procedure was done under laboratory conditions, with a lightweight portable oxygen analyser from the air exhalation (FitmatePro, COSMED, Italy). Ten healthy, not particularly skilled male subjects were tested while they simulated the saffron harvesting in a laboratory task (see Table 1). The experiment was divided in two sessions. In the first task (TA) subjects assumed typical harvesting posture, i.e. with the trunk tilted down and arms stretched out to touch the floor. They proceeded to pick up small spherical objects scattered on the floor, as if they were Saffron flowers,
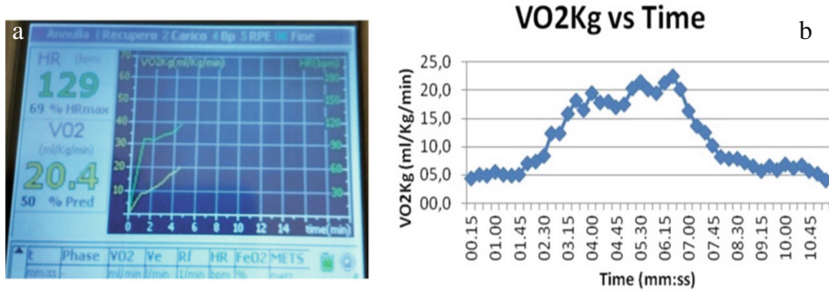
**Fig. 5.** Screen image of the device used to assess oxygen consumption expressed in (ml kg$^{-1}$ min$^{-1}$) vs. time in minutes (a). Typical trend of Oxygen Consumption (VO2) in one tested subject during saffron harvesting simulation test. The VO2 is given in (ml kg$^{-1}$ min$^{-1}$) vs. time in minutes (b).

with a rate of one every two seconds, and lasting 270 s with 30 s of pause in the middle (Fig. 4).

After a congruous recovery time (up to recover pre-test heart rate and oxygen consumption values), the subjects performed a second laboratory task (TB). This task also lasted 270 s with 30 s of pause in the middle. In this case they were standing and wearing the facilitator machine through special ergonomic straps. The rate was the same as the first session.

During sessions TA and TB subjects were connected, by a face mask, to the device for the oxygen consumption (VO2) assessment.

The metabolimeter released indications each 15 s (Fig. 5) as VO$_2$ per each kg of body mass and per each minute of work performed (ml kg$^{-1}$ min$^{-1}$). From indirect calorimetry [21] in a labourer, subjected to heavy work, each litre of oxygen consumption corresponds to an energy expenditure of about 20,9 kJ.

However, the mechanical efficiency of this energy conversion does not exceed 25% of the energy expenditure [22].

The left column in Fig. 5a indicates the numerical value (VO2, down) of oxygen consumption last lecture in (ml kg$^{-1}$ min$^{-1}$), just assessed after about 4 min from the test beginning (see also the yellow trace in the graph).

The device also consents to assess heart rate per minute with a green trace and its numerical value (HR, up). In the graph abscissa is indicated the time corresponding to the traces. Immediately after the end of TA and TB sessions, by means of the Borg Scale for perceived exertion [23], subjects were asked to define their level of discomfort due to performed exercise from a minimum value of 6 to a maximum value of 10. After tested all subject, from the collected VO2 measurements, those occurred within the first 150 s of assessment were discarded since it was considered that subjects spent this initial test time to reach a stabilization in the exercise induced oxygen consumption (Fig. 5b). The remaining 120 s, which corresponded to 8 VO2 assessments for every tested subject at each of the two tasks (80 VO2 values from each task), were utilized to compare VO2 between TA and TB sessions.
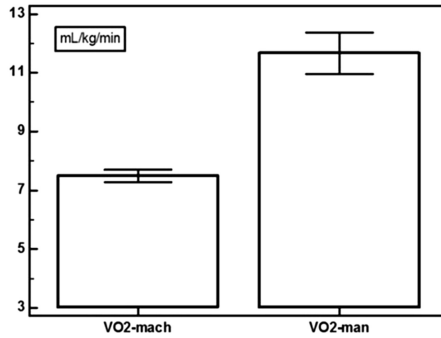
**Fig. 6.** Oxygen consumption VO2 during harvesting with the facilitator machine (on the left) and without (on the right) expressed in (ml kg$^{-1}$ min$^{-1}$)

Statistical differences in either groups, TA and TB, were analysed using student's t-test for paired observation. The probability P < 0.05 was considered statistically significant (MedCalc Statistical Software, Belgium).

In the graph of Fig. 5b the points represent VO2 assessment each 15 s from the test beginning. Up to 1:45 min the subject tested stayed at rest. After he starts the saffron simulation, harvesting continued for 6:15 min, after which he stopped and stayed at rest for the next 5 min up to 11:15 min. This timing procedure, previously described, allows to be sure that the subject recovered the rest metabolic condition before the test. It is evident that oxygen consumption ceases to increase after 4:15 min from the test beginning. The eight assessed points from 4:15 min to 6:15 min were considered as points in which oxygen consumption has reached a relative stability.

Figure 6 shows that the VO2 assessed using the facilitator machine (7,50 ± 0,11 ml kg$^{-1}$ min$^{-1}$) is 36,6% lower than VO2 assessed with manual harvesting (11,68 ± 0,35 ml kg$^{-1}$ min$^{-1}$). This mean difference was highly significant (P < 0,0001). Borg Scale test indicated that the perceived exertion during the manually simulated saffron harvesting reached a value of 8,35 ± 0,21 while, when using the facilitator machine, the value was 6,74 ± 0,08, or 19,2% lower (P < 0,0001). In order to highlight the device benefits, the following considerations can be extrapolated from the obtained data. The following consideration allows having an overall view of the advantages brought by the harvesting device, in terms of saved human energy.

Considering an average body mass of the tested subjects of 72,7 kg and an activity time of one minute, the VO2 of TA session was 860 ml min$^{-1}$ instead of 545 ml min$^{-1}$ of TB session. Therefore during session TB the subjects consumed 315 ml min$^{-1}$ of oxygen less than during the TA session, in other words the energy saving was about 37% with respect to the energy in session TA. The higher oxygen consumption in sessions TA was associated with the different posture assumed by the operator who, of course, recruited a great number of muscles. Based on the indirect calorimetric calculations, each intake of one ml of oxygen corresponds to an energy of 20,9 J. In addition, the muscle mechanical efficiency of the metabolic energy conversion into mechanical one does not exceed 25%. TA and TB sessions differ in oxygen consumption by 315 ml min$^{-1}$. So the oxygen consumption in TA session is about

60% higher than the oxygen spent in TB session: (VO2 TA-VO2 TB)/VO2 TB = 0,60. The energy difference is 6583,5 J. Taking into account an efficiency of 0,25, for the conversion of the metabolic energy into the mechanical one, the energy difference at output is 1645,9 J. This fact could be read in terms of equivalent different weight of harvested objects. During both session TA and TB tests, 30 flowers (objects) were harvested at a height of half a meter. This means that in session TA the equivalent object mass is about 30,54 kg, instead of 19,35 kg for the object mass harvested in session TB; in other words the advantage is of about 37% in terms of perceived mass of harvested objects.

## 4   Conclusions

The tests described in this paper show that the use of the described facilitator machine for harvesting saffron flowers allows a significant saving of human energy in respect to a manual harvesting activity. This saving, evaluated with tests using a statistically significant sample, is of about 40% compared to the energy expenditure required for the manual activity. In addition, the use of the facilitator machine allows operators not to be specialized and to obtain a constant quality of the product harvested, doing a harvesting activity not affected by fatigue and by the variable working conditions.

## References

1. Plessner, O., Negbi, M., Meira, Z., Basker, D.: Effects of temperature on the flowering of the saffron crocus (Crocus Sativus L.): induction of hysteranthy. Isr. J. Bot. **38**, 1–7 (1989)
2. Fernández, J.A.: Biotechnology and biomedicine of saffron. Recent Res. Dev. Plant Sci. **2**, 127–159 (2004)
3. Harrell, R.C., Adsit, P.D., Pool, T.A., Hoffman R.: The Florida robotic Grove-lab. In: Proceedings of ASAE Paper 88-1578, St. Joseph, Michigan USA (1988)
4. Sarig, Y., Edan, Y., Katz, N., Flash, T.: Some aspects of robotics for fruit picking. In: Proceedings of French-Israel Bi-National Symposium on Advanced Robotics, Theory and Practice, Tel-Aviv, Israel (1988)
5. D'Esnon, A.G., Rabatel, G., Pellenc, R., Journeau, A., Aldon, M.J.: "MAGALI": a self-propelled robot to pick apples. In: Proceedings of ASAE Paper 87-1037, St. Joseph, Michigan, USA (1987)
6. Ferraresi, C., Manuello Bertetto, A.: Self-adaptive three-fingered robot hand with tactile sensors. In: Proceedings of the Fourth International Symposium of Measurement and Control in Robotics, Slovakia, 12–16 June 1995, pp. 275–280 (1995)
7. Carello, M., Ferraresi, C., Visconte, C.: A new flexible pneumatic finger for a fruit-harvesting hand. In: Proceedings of 7th International Symposium on Fluid Control, Measurement and Visualization, Sorrento, Italy (2003)
8. Gambella, F., Paschino, F.: Manuello Bertetto, A., Ruggu, M.: Application of mechanical device and airflow systems in the harvest and separation of saffron flowers (Crocus Sativus L.). Trans. ASABE **56**(4), 1259–1265 (2013)
9. Gambella, F., Manuello Bertetto, A.: Perspectives in the mechanization of saffron (Crocus Sativus L.). Int. J. Mech Control **14**(2), 3–8 (2013)

10. Gilad, I.: A methodology for functional ergonomics in repetitive work. Int. J. Ind. Ergon. **15**, 91–101 (1995)
11. Lomond, K.V., Cotè, J.N.: Differences in posture-movement changes induced by repetitive arm motion in healthy and shoulder-injured individuals. Clin. Biomech. **26**, 123–129 (2011)
12. Manuello Bertetto, A., Ricciu, R., Badas, M.G.: A mechanical saffron flower harvesting system. Meccanica **49**(12), 2785–2796 (2014)
13. Capecchi, D., Drago, A.: On Lagrange's history of mechanics. Meccanica **40**, 19–33 (2005)
14. Ceccarelli, M.: Fundamentals of mechanics of robotic manipulation. Meccanica **41**, 233–236 (2006)
15. Liu, Y., Qin, D., Jiang, H., Liu, C., Zhang, Y.: Clutch torque formulation and calibration for dry dual clutch transmissions. Mech. Mach. Theory **46**, 218–227 (2011)
16. Galvagno, E., Velardocchia, M., Vigliani, A.: Dynamic and kinematic model of a dual clutch transmission. Mech. Mach. Theory **46**, 794–805 (2011)
17. Tran, X.B., Yanada, H.: Dynamic friction behaviors of pneumatic cylinders. Intell. Control Autom. **4**, 180–190 (2013)
18. Belforte, G., Mattiazzo, G., Mauro, S., Tokashiki, L.R.: Measurement of friction force in pneumatic cylinders. Tribotest J. **10**, 33–48 (2003)
19. Belforte, G., Manuello Bertetto, A., Mazza, L.: Test rig for friction force measurements in pneumatic components and seals. Proc. Inst. Mech. Eng. Part J, J. Eng. Tribol. **227**(1), 43–59 (2013)
20. Manuello Bertetto, A., Mazza, L.: Contact analysis and wear in two pneumatic reciprocating seals. Int. J. Mech Control **1**(1), 43–49 (2000)
21. Pinna, M., Roberto, S., Milia, R., Marongiu, E., Olla, S., Loi, A., Migliaccio, G.M., Padulo, J., Orlandi, C., Tocco, F., Concu, A., Crisafulli, A.: Effect of beetroot juice supplementation on aerobic response during swimming. Nutrients **6**(2), 605–615 (2014)
22. Laconi, P., Melis, F., Crisafulli, A., Sollai, R., Lai, C., Concu, A.: Field test for mechanical efficiency evaluation in matching volleyball players. Int. J. Sports Med. **19**(1), 52–55 (1998)
23. Reed, J.L., Pipe, A.L.: Practical approaches to prescribing physical activity and monitoring exercise intensity. In: Can. J. Cardiol., pii. S0828-282X(15)01695-5 (2015). doi:10.1016/j.cjca.2015.12.024

# Possibilities of Applying Robotic Systems and Smart Sensor Networks in Integrated Agricultural Apple Production

Jonel Subić[1(✉)], Miloš D. Jovanović[2], Željko Despotović[2], and Marko Jeločnik[1]

[1] Institute of Agricultural Economics, Belgrade, Serbia
{jonel_s,marko_j}@iep.bg.ac.rs
[2] Robotics Laboratory, Mihajlo Pupin Institute,
University of Belgrade, Belgrade, Serbia
{milos.jovanovic,zeljko.despotovic}@pupin.rs

**Abstract.** This paper presents an intelligent approach to integrated data collection and management system for irrigation and fertilisation of plants in agricultural production (specifically in apple plantations) applied to control and optimization of all parameters necessary for an adequate level of agricultural production. The approach tends to reduce investment costs, minimize power consumption and implement environmentally clean power production methods, as well as to apply proper treatment of chemical preparations in order to achieve economically viable integrated food production. Application of modern systems of complex sensor networks connected via mobile solar power generators as main node connection allows the collection of all data and parameters necessary for the continuity of integrated agricultural production. The mobile robotized solar power generator is also the executive device that manages complex hydraulic system for irrigation and fertilisation, treating the field with chemicals depending on available land, meteorological and environmental conditions.

**Keywords:** Sensor network · Mobile robotized solar power generator · Apple plantation

## 1 Introduction

Modern agricultural production is unimaginable without advanced technological solutions, information technology, robotics, mechanical engineering, etc. Due to the human population growth, one of the primary issues in upcoming future is a production of food in quantity that will satisfy this expansion. Even today the vast majority of mankind is starving, so the food production has already become an imperative. Also, considering the problems arising from global warming phenomena, expecting the additional reduction of arable land, expansion of desert areas unsuitable for agricultural production, and reduction of available amount of potable water in near future, there is a need for use of latest technological methods in agricultural production that will optimize the utilization of resources and capacities, reduce power consumption, in order to maximize agricultural production and increase the overall yields per unit area of

production. For this purpose it is necessary to constantly monitor certain parameters during the period of crops growth and development in order to apply requested pest protection, nutrition and irrigation activities, in line to soil and weather conditions, as well as to potentially protect the crops against unpredictable external conditions.

Therefore, application of advanced technologies in whole gets fully importance, both in order to optimize production and to reduce energy consumption, or protect and control the entire system. For this purpose, contemporary technological achievements play a key role. Application of advanced sensor networks for monitoring the field parameters is one of the basic principles in the process of data collection about the agricultural land condition. Modern agricultural production is primarily based on controlled land irrigation and controlled application of chemical and technical inputs for plant nutrition and protection. Controlled irrigation assumes optimal water consumption depending on the soil condition, stage of crop growth and development, as well as current weather conditions and short-term weather forecast for observed area [1]. Application of modern sensor networks in agriculture can lead to significant yield increases, parallel with monitoring of all parameters during the crop growth.

Proper timely response to the observed disturbances within the period of agriculture crops growth and development is one of the main technological achievements of smart sensor network greed using. This activity is primarily related to the crop irrigation depending on soil conditions, then to adequate pesticides treatment, proper crop nutrition and possible physical protection of crops and land from weather and other external factors. All these mentioned activities have to be done by use of appropriate work equipment (pumps, sprinklers, etc.) that require specific energy consumption. Supplying the energy at production area for automated action is a technical challenge, both in terms of automated action and of environmental protection of agricultural production. The use of mobile robotized solar power generator [2] as a source of environmentally clean energy for the processes of plants irrigation, fertilisation and chemical treatments presents an optimal approach to efficient production.

## 2  Agricultural Land Monitoring Using Smart Networks

The smart system of sensor networks is one of the latest technological achievements applied in order to increase the efficiency of agricultural production. The goal of sensor networks implementation at agricultural land is a collection of all needed data about the soil and air condition. There are several ways of implementation sensor networks in agriculture [1, 3, 4]. Two main methods of implementation are the wired and wireless installation of sensor networks. Wire installation requires adequate infrastructural preparation of agricultural land for the installation of sensor network nodes. The sensor network nodes are mutually interconnected by network cables (electrical or optical). This network is characterized by reliable communication, with small power consumption, high speed data exchange, simple fault detection within the structure of sensor networks and easy errors correction. Difficulties of these types of networks have infrastructural nature; network installation and removing requires additional time and work which greatly complicates the entire system.

On the other hand, wireless sensor networks are characterized by simple installation, which is a basic advantage for all modern sensor networks, making them potentially dominant in upcoming future. Also, wireless sensor networks are characterized by flexibility, simple installation, connectivity and upgrade. Caused by the absence of physical communication infrastructure, modification and diversification of wireless sensor networks is quite simple.

The proposed implementation of sensor networks uses the so-called ZigBee technology. The main characteristic of this type of sensor network is simple implementation and mutual interconnection, as well as inexpensive technology. ZigBee sensor networks are small power consumers with sufficient reliability of data transfer on small and medium distances (up to 40 m). Each sensor network node includes a microcontroller that manage the node, then realizes the communication with neighbouring nodes by ZigBee interface, or collects data from sensors installed within the node and transmits its and nearby data through the network.

Each node contains a system of sensors that allows measurement of relevant land parameters at given point. Figure 1 shows a scheme of the implemented ZigBee node with the appropriate sensor system. It can be seen that the node is equipped with three temperature sensors that measure air temperature at 30 cm above the ground, at the ground and at 10 cm under the ground. Also, there are three moisture sensors that measure air humidity at 30 cm above the ground, at soil surface and soil humidity at 10 cm under the ground. The node is equipped with a soil Ph sensor to measure current soil acidity. Rain gauge sensor measures rainfall in the point and a wind speed sensor set at 1 m above the ground measures speed and direction of the wind. Each node has an internal GPS receiver that allows determining the exact geographical position of the observed node. Each node has a thunder sensor, providing the information about the possible electrostatic charge in close surrounding, and a sensor for motion detection in order to reveal the presence of the unwanted animals or people within the area covered by the sensor network. This is particularly interesting in order to protect crops from hail, sudden storms and other damages.

The block scheme of the off-grid solar power system for supplying wireless node is given in Fig. 2. The system is composed of several important components: (1) solar panel with blocking diode, (2) solar charge controller, (3) battery pack (battery bank) with Li-ion battery (4) low voltage disconnect switch, (5) step-down DC/DC power converter, (6) equipment enclosure with mounting accessories.

The solar panel (1) uses light energy to generate electricity; it is integrated with a blocking diode (marked with D in Fig. 2). In order to obtain the smallest possible voltage drop at nominal current of solar panel, a Schottky diode is used. The blocking diode prevents discharging of the battery bank during the night. The solar panel is oriented toward south during the wireless sensor node installation in the field. Angle elevation of the panel can be manually adjusted to correct the angle, with four independent mechanical positions depending on the season. The solar charge controller (2) is connected between the solar panel (1) and the Li-ion battery pack (3). This controller is based on maximum power point tracking (MPPT) algorithm and it regulates the charge battery bank from a solar panel. Charge controllers are rated based on the amount of current they can process and they protect the battery from overcharging. A low voltage disconnect switch prevents damage of the battery due to excessive
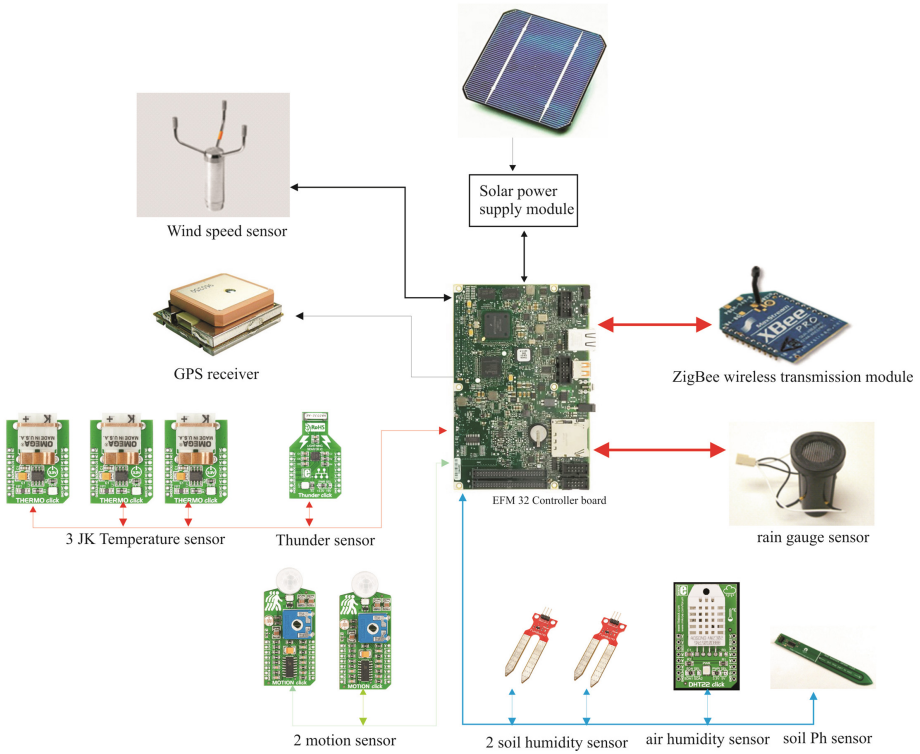
**Fig. 1.** Block diagram of one node of implemented ZigBee sensor network
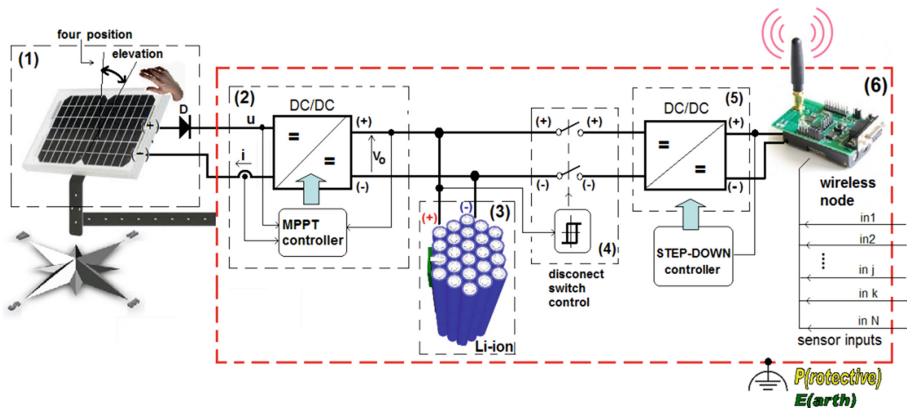


**Fig. 2.** Principal block scheme of solar power of wireless node

discharge. The switch is installed between the battery pack and load (sensor network node) and disconnects the battery pack if the battery voltage drops below 10.5 V. A very low" on "resistance type of switch with incorporated hysteresis function is used in this application; this switch is acting depending of battery status. The output power supply (5) which stabilizes the voltage for wireless node is a step-down DC/DC power converter. It provides a stable voltage of 5VDC in all operating regimes (from no-load to a full load of 1A). All solar equipment (excluding solar panel), and the wireless node with corresponding electronic modules are mounted in a hermetically sealed enclosure (6), which provides mechanical protection and protection against external influences (rain, snow, hail, etc.). The enclosure is grounded via the protective earth (PE) joint.

Solar power is optimized on the basis of input parameters such as: average annual, monthly and daily solar irradiances for requested location, required power consumption and autonomy. The wireless sensor node operates at exact time intervals. During the time interval the node is active and requires working power. In the majority of the time, the wireless node is in idle mode and consumes low current (50 µA). The interval time in which the node is active is programmable and has usually a value of 5 min. During active cycle, local node consumption is 80 mA average and working time is 30 s. The controller powers up the sensors one by one and reads their data in separate active cycles. When the sensor data is read and stored in local memory, the sensor is powered off to minimize current consumption. Periodically (each 30 min), the main node polls all nodes in the network requesting data transfer. The required autonomy for wireless node application is 48 h.

For average solar irradiance in the most unfavourable case (2.3 kWhW/m$^2$, for month December), time of autonomy of 48 h and average power consumption of 5 W, the solar power system is designed for supplying the wireless node (ZigBee). Table 1 gives the results of the calculations carried out.

**Table 1.** Design parameters of the solar power system of the wireless node

| Components | Rate |
|---|---|
| Solar panel | 18VDC (26VDC max), 10 W |
| Charge controller | 12VDC/6A |
| Li-ion battery pack | 12VDC/6Ah/77Wh (10.5 V, 14,5 V) |
| Low voltage disconnect | 10.5VDC–11.5VDC, with hysteresis control |
| Step-down DC/DC power converter | 10.5VDC…14VDC to 5VDC/1A |
| Enclosure | 300 × 200 × 100 mm, NEMA IP65 |

The detailed schematic diagram of the implemented sensor network greed based on ZigBee technology, together with described nodes is shown in Fig. 3. It can be seen that the network, because of the wireless ZigBee technology, is reconfigurable, easy extensible and dynamically organized. Each node communicates with up to 8 nearest nodes. In this way an easy transfer of information from each separate node to the main node it is realized, as well as effective network inspection of possible faults, identification of any malfunctioning node and its bypass within the system without loss of information. Figure 3 also shows that the main node is the mobile robotized solar
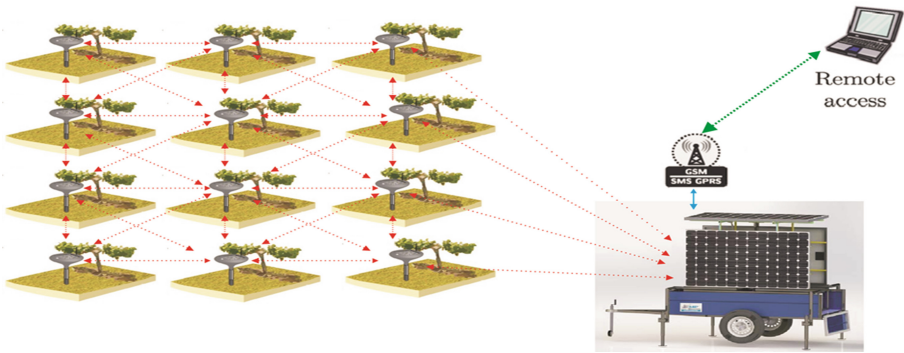
**Fig. 3.** Topology view of ZigBee sensor network

power generator [2]. It is a central place which through ZigBee communications collects and processes data, sends data via wireless GPRS communication to the supervisory system and takes automated actions depending on collected data and overall state of the sensor system.

Figure 4 presents a complex hydraulic drip irrigation system, acting also as system for dosing chemical compounds in fertilisation and plant protection (throughout the root zone). The hydraulic system includes several pipelines for drip irrigation and chemical treatments, a valve distributor (selecting of adequate pipeline for plant treatment), a water tank which is refilled with water by submerged pump in draw well, and a container with appropriate chemical preparations for plant nutrition or plant protection.
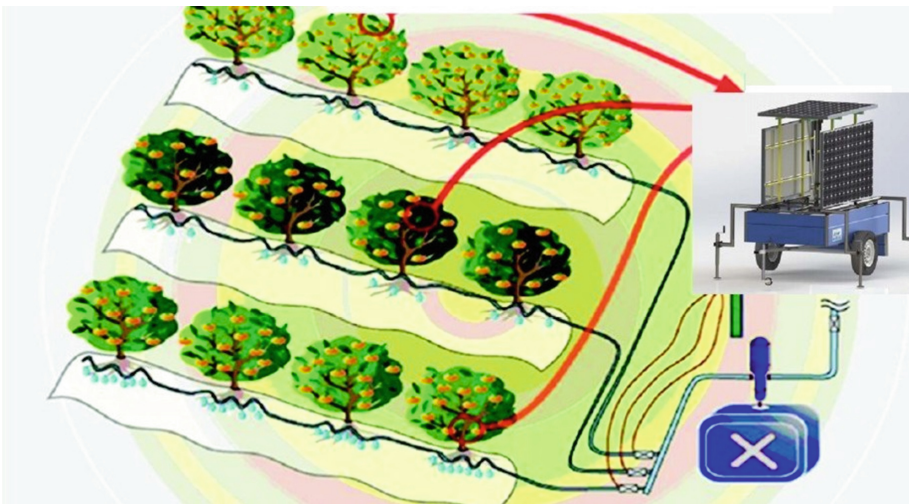


**Fig. 4.** Schematic view of the drip irrigation and chemical treatment system

As a major node of the ZigBee sensor system, a robotized solar electro generator receives the data from all nodes of the sensor network. Based on the received information, it creates a database with information about the condition at agricultural parcel, and then transmits data to the supervisory system at the higher level of hierarchy (SCADA system, operations center, etc.). Via GPRS network, the main node is in constant communication with the supervisory system from which it receives feedback information regarding the required actions. It is also connected to the national weather forecast system (via GPRS), collecting the data about expected short and medium term weather conditions. Considering all the necessary data from the sensor network nodes as well as weather forecast, the robotized solar electric generator can independently realize irrigation according to the request from the supervisory system. It can also realize actions of fertilisation and chemical protection. If within the area of sensor network a risk of storm or thunder is detected, the main node sends an alert signal to the supervisory centre, in order to realize certain land protection measures. A similar alarm signal is sent if the presence of animals or people is detected within the area protected by the system. The main node communicates with other nodes in the network in short time intervals, allowing efficient energy savings in the sensor network system. Simultaneously, there is timely accomplished data reading and data transfer trough the network. If some of nodes report a malfunction, or fail to respond to successive calling, the main node decides, based on the network state and structure, through which nodes the data will be routed. It also signals to the supervisory system possible failures in order to take appropriate repair action.

## 3   Apple Production

Republic of Serbia has on disposal optimal agro-climatic conditions for apple growing, but unfortunately previously described facilities are insufficiently used. After determination of apple growing system as adequate relation of growth form, planting density and genotypic characteristics of selected sort and rootstock, expectations in contemporary production are based on stable and high yields during the exploitation period of plantation, with a focus on highly intensive production [7]. Modern apple plantations in Serbia usually have planting density determined by row spacing of 3–3.7 m or in row spacing of 0.5–1.1 m (a good example is the technological approach offered by the South Tirol technology, which assumes a high planting density bundled with the installed elements of production infrastructure - irrigation and fertilisation system, meteorological station, anti-frost and anti-hail system, etc. - that initiates a high yields with high percentage of I class fruits) [6].

Besides that, proper choice and timeliness of maintenance activities in established apple plantations, primarily agro-technical measures (land maintenance, fertilization, chemical protection and irrigation) and promo-technical measures (pruning, branch distribution and fruits thinning guarantee for good tree growth and development, as well as achieving of satisfactory fruit yields. Only such types of plantations contribute to the rapid return of invested assets with minimization of human labour participation [5].

The focus in this paper is on irrigation and fertilisation of apple plantations. Apple trees nutrition is directly correlated to the production size and fruit quality, as well as to

the vegetative growth balance, resistance to diseases and pests, etc. It implies the constant presence of certain content and volume of macro and micro elements in soil, enabled by well-planned nutrition (through the basic and additional fertilization during the growing season).

After basic fertilization (dissipation or injection of certain amount of mineral fertilizer NPK, AN, KAN, etc.) several times during the growing season, according to identified needs of fruit trees for basic micro and macro mineral elements, the orchard has to be additionally fertilized (usually by fertilisation or foliar application of fertilizers) [8]. Good mobility and availability of nutrients within the zone of root system is often a problem in arid production conditions. Fertilisation (fertigation - adding of water soluble fertilizers) together with the use of irrigation (drip system) represents a good solution, along with the benefits of adequate dosage and timing of certain macro and micro nutrients application. Compared to conventional application, this method reduces the total amount of inputted nutrient with an efficiency increase of up to 40% [11]. Different formulations of NPK fertilisers are usually added (such as next preparations Ferticare, Green plant, Yara, Kristalon, etc.), as well as fertilisers in which specific micronutrients are dominant.

As the drought of certain intensity is very common during the summer period in Serbia, which can significantly reduce crops, irrigation in orchards is a highly desirable agro-technical measure. During each vegetation cycle apple trees need around 550–600 mm of easily accessible water. The greatest needs for bacteriological and chemically clean water are in the period from the end of flowering until the end of the intensive fruit growth (during the period July–August) [9]. At national level, the system of drip irrigation is highly recommended for the regions with pronounced level of evaporation and water scarcity. In this system, laterals (with droppers) in apple plantation are usually set at maximally 60 cm above the ground, where the depth (impact) of wetting is around 0.5 m or T-tape strips (dripping strips) are laid down. Besides the low water and energy consumption, this type of system allows hydration of just a limited zone around the plant, high labour automation, ease to determine the norms and timing of watering, low costs of system exploitation and maintenance, etc.

Economical apple production also considers timely protection against weeds, diseases and pests. On the other hand, it has to meet the expected fruit quality requirements, so the choice of pesticides is relying on their selectivity and toxicological impact of applied concentration on the environment. The sensitivity of apples requires a relatively large number of different treatments with pesticides during the production cycle. From the point of view of produced fruits safety, the implementation of integrated production system involves methods and measures that reduce the use of synthetic-chemical preparations and fertilisers in line with environmental, economic and toxicological principles, in other words with the accent on the protection of human health and nature resources [10].

## 4   Assessment of the Effects of Smart Sensor Networks Application for Integrated Apple Production

Within the assessment of the effects of smart sensor networks application for integrated apple production, an analysis of changes in contribution margin due to changes in value of total production, as well as changes in value of variable costs, was done. In particular, the level of increase of contribution margin under the conditions of rational use of irrigation systems (trickle irrigation) and fertigation (precisely planned dosage and time of macro and micro nutrients application) was analysed.

The calculation model in apple production is expressed through several tables: base-line (Table 2), contribution margin in conditions of irrigation and fertigation (Table 3), contribution margin in conditions of irrigation and fertigation with application of smart sensor networks (Table 4) and effect of irrigation and fertigation with the application of smart sensor networks (Table 5).

**Table 2.**  Baseline

| Production line: apple (plantation in full yielding) | Territory: Serbia – North (Vojvodina region) |
|---|---|
| Unit of production measure: 1 ha | Technological approach: integrated plantation (with drip irrigation) |
| Production year: 2015 | Sort: Gala and Braeburn |

**Table 3.** Contribution margin in integrated apple production (without application of smart sensor networks)

| Description | Quantity | Unit of measure | Price (EUR/kg) | Total (EUR/ha) |
|---|---|---|---|---|
| *Income* | | | | |
| I class (71%) | 50,430.59 | kg | 0.71 | 35,805.72 |
| II class (16%) | 11,364.64 | kg | 0.55 | 6,250.55 |
| Box (7%) | 4,972.03 | | 0.60 | 2,983.22 |
| For processing (6%) | 4,261.74 | kg | 0.09 | 383.56 |
| **Production value (VP)** | **71,029.00** | **kg** | **0.64** | **45,423.05** |
| *Variable costs* | | | | |
| Seedlings (change) | 39 | pcs | 3.79 | 147.79 |
| Fertilizers (mineral fert. 29%; fertigation 71%) | | | | 969.39 |
| Pesticides | | | | 2,039.35 |
| Packaging (carton box - 15 kg) | 4,736 | pcs | 0.30 | 1,420.77 |
| Costs of mechanisation | | | | 2,100.47 |
| Irrigation | | | | 114.20 |
| Engaged labour | | | | 2,275.71 |
| Costs of cooling and other variable costs | | | | 8,567.94 |
| **Variable costs (VT)** | | | | **17,635.62** |
| **Contribution margin: MP = VP – VT** | | | | **27,787.43** |

**Table 4.** Contribution margin in integrated apple production (with application of smart sensor networks)

| Description | Quantity | Unit of measure | Price (EUR/kg) | Total (EUR/ha) |
|---|---|---|---|---|
| *Income* | | | | |
| I class (77%) | 67,597.53 | kg | 0.71 | 47,994.25 |
| II class (12%) | 10,534.68 | kg | 0.55 | 5,794.07 |
| Box (6%) | 5,267.34 | | 0.60 | 3,160.40 |
| For processing (5%) | 4,389.45 | kg | 0.09 | 395.05 |
| **Production value (VP)** | **87,789.00** | **kg** | **0.65** | **57,343.77** |
| *Variable costs* | | | | |
| Seedlings (change) | 48 | pcs | 3.79 | 182.66 |
| Fertilizers (where: mineral 24%; fertigation 76%) | | | | 761.91 |
| Pesticides | | | | 2,520.55 |
| Packaging (carton box - 15 kg) | 5,853 | pcs | 0.30 | 1,756.02 |
| Costs of mechanisation | | | | 2,596.10 |
| Irrigation | | | | 95.24 |
| Engaged labour | | | | 2,812.69 |
| Costs of cooling and other variable costs | | | | 10,589.63 |
| **Variable costs (VT)** | | | | **21,314.79** |
| **Contribution margin: MP = VP − VT** | | | | **36,028.98** |

**Table 5.** Effects of irrigation and fertigation (with application of smart sensor networks)

| Description | Total (EUR/ha) | % |
|---|---|---|
| *Calculation of irrigation and fertigation* | | |
| $VP_0$ (Production value) | 45,423.05 | |
| $VT_0$ (Variable costs) | 17,635.62 | |
| **$MP_0$ [Contribution margin ($VP_0 − VT_0$)]** | **27,787.43** | |
| *Calculation of irrigation and fertigation (with application of smart sensor networks)* | | |
| $VP_1$ (Production value) | 57,343.77 | |
| $VT_1$ (Variable costs) | 21,314.79 | |
| **$MP_1$ [Contribution margin ($VP_1 − VT_1$)]** | **36,028.98** | |
| *Calculation of effects of irrigation and fertigation (with application of smart sensor networks)* | | |
| $VP_1 − VP_0 = VP_P$ (increase of production value) | 11,920.73 | 26.24 |
| $VT_1 − VT_0 = VT_P$ (increase of variable costs) | 3,679.17 | 20.86 |
| **$MP_1 − MP_0 = MP_P$ (increase of contribution margin)** | **8,241.56** | **29.66** |

In economic analysis, the contribution margin is an extremely important indicator that can be used for determination of optimal production structure (by use of linear programming), then for business risk determination, etc. Contribution margin is defined as the difference between the value of total production (main product value plus value of by-products and incentives) and the value of proportional variable costs.

Mathematically it can be represented by the formula below [12]:

MP = VP – VT, where: VP = (q x c) + p, with symbols meaning:

MP: contribution margin; VP: total production; VT: variable costs; q: products quantity; c: product price; p: incentives.

The result obtained by analytical calculation is also called Gross financial result, based on which the manager of an agricultural farm can easily determine how much assets, after variable costs covering, remain for fixed costs covering and profit gaining. In this case, calculations are made on the basis of production value and variable costs obtained on the area of 1 ha. In order to enable comparison of production indicators, variable costs and value of total production are expressed in official currency of the EU (EUR/ha).

Integrated apple production is an important element of agricultural production, and also an important factor of Serbian agribusiness competitiveness. The mentioned reasons are sufficient for use of analytical calculations based on variable costs, as well as for analysing smart sensor networks effects in application of irrigation and fertigation in integrated apple production. The research was carried out during the period 2015–2016 in the Vojvodina region, referring to results collected (and later processed) from selected agricultural holdings that apply different production technologies, have not a unique approach to input purchase and do not sell their products at the same market.

## 5   Conclusions and Future Work

Results achieved in integrated apple production, without or with the application of smart sensor networks for optimal use of systems for irrigation and fertigation, refer to following observations:

- In the structure of variable costs, costs of irrigation and fertigation (with the application of smart sensor networks) are close to the bottom (share of around 16.3%);
- In the structure of costs for irrigation and fertigation (with application of smart sensor networks), fertigation takes the largest allocations (share of about 85.88%), while the costs of irrigation are significantly lower (around 14.12%);
- Use of smart sensor network system for irrigation and fertigation increase:
  - yields for 23.60% (or 1.24 times higher yields);
  - production value for 26.24% (or for 1.26 times);
  - total variable costs for 20.86% (or for 1.21 times);
  - contribution margin for 29.66% (or for 1.30 times).

Considering the integrated concept of apple production, it can be said that the application of smart sensor networks for rational use of irrigation and fertigation has significant contribution to the growth of profitability and competitiveness of agricultural

holdings. Considering total costs, the implementation of mentioned measure also leaves enough space (after variable costs covering) for fixed costs covering and achieving of positive financial result. The application of smart sensor networks in irrigation and fertigation causes increase in total variable costs, but without larger impact on gross financial result, as the level of increase in yields caused significant growth of incomes and contribution margin. In the conditions of using smart sensor networks, there is enough space for payment of fuel costs and other variable costs arising from irrigation and fertigation system application, after all irrigation taxes are covered.

# References

1. Morais, R., Fernandes, M.A., Matos, S.G., Serodio, C., Ferreir, P.J.S.G., Reis, M.J.C.S.A.: ZigBee multi-powered wireless acquisition device for remote sensing applications in precision viticulture. Comput. Electron. Agric. **6**(2), 94–106 (2008)
2. Rodic, A., Despotovic, Z.V., Jovanovic, M.D., Popic, S., Stevanovic, I.: Mobile robotic solar generator MobiSunProEnergy™ - application in new energy tehnologies. In: 8th International Forum for Clean Energy Technologies, Energy Charter – Sustainable Development of Serbia, Novi Sad, 30 September–1 October 2014. http://www.ktt.uns.ac.rs/reec/FORUM%202014/dan%202/02.5DespotovicIMP.pdf
3. Fujita, A., Nakamura, M., Kameoka, T.: Soil moisture measurement support production of high-quality oranges for information and communication technology (ICT) application in production orchards (in Japanese). Agric. Inf. Res. (Jpn.) **20**(3), 86–94 (2011)
4. Togami, T., Yamamoto, K., Hashimoto, A., Watanabe, N., Takata, K., Nagai, H., Kameoka, T.: A wireless sensor network in a vineyard for smart viticultural management. In: Proceedings of SICE Annual Conference, pp. 2450–2454 (2011). http://www.zigbee.org/what-is-zigbee/
5. Bugarčić, S.: Podizanje voćnjaka, portal Zdrava Srbija (2013). http://www.zdravasrbija.com/lat/Zemlja/Vocarstvo/445-Podizanje-vocnjaka-.php. Accessed March 2016
6. IAE: Nezavisna studija izvodljivosti o ekonomskoj opravdanosti biznis plana podizanja zasada jabuke Apple World d.o.o., Study, Institute of Agricultural Economics, Belgrade, Serbia, p. 61 (2013)
7. Jeločnik, M., Ivanović, L., Subić, J.: Analiza pokrića varijabilnih troškova u proizvodnji jabuke. Škola biznisa **2**, 42–49 (2011)
8. Keserović, Z., Magazin, N., Injac, M., Totis, F., Milić, B., Dorić, M., Petrović, J.: Đubrenje voćnjaka, Faculty of Agriculture Novi Sad, Serbia, portal Agrovizija (2016). http://agrovizija.rs/teme/vocarstvo.php?id=1390062811. Accessed March 2016
9. Novković, S.: Potrebe jabuke za vodom, PSSS Kragujevac, portal of Agriculture extension service of Serbia (2012). www.psss.rs/e107_plugins/forum/forum_viewtopic.php?8333. Accessed March 2016
10. Obradović, A., Radivojević, D., Vajgand, D., Rekanović, E.: Priručnik za integralnu proizvodnju i zaštitu jabuke, Institute for Appliance of Science in Agriculture, Belgrade, Serbia, p. 194 (2013)

11. Soldo, T.: Navodnjavanje i fertirigacija plantažnih nasada, portal Agroklub (2015). www.agroklub.rs/vocarstvo/navodnjavanje-i-fertirigacija-plantaznih-nasada/16707/. Accessed March 2016
12. Subić, J., Ivanović, L., Jelocnik, M.: Uticaj podsticaja na pokriće varijabilnih troškova u proizvodnji ratarskih useva. Zbornik naučnih radova Instituta PKB Agroekonomik **16**(1–2), 251–264 (2010)

# Autonomous Systems, Humanoid and Walking Robots

# Model of the Human Arm Stiffness Exerted by Two Antagoniste Muscles

Daniele Borzelli[(⊠)], Stefano Pastorelli, and Laura Gastaldi

Department of Mechanical and Aerospace Engineering,
Politecnico di Torino, Turin, Italy
{daniele.borzelli,stefano.pastorelli,
laura.gastaldi}@polito.it

**Abstract.** Due to the increasing working age, in the last years more and more attention is turned to exoskeleton for industrial applications. Exoskeletons reduce fatigue and the effort that would cause injuries on the operator. Exoskeletons designed for industrial applications are mostly finalized to relieve the operator from a heavy load. However in industrial practice, worker fatigue is not only due to heavy load carrying, but also to the increase of the arm stiffening requested by some operations, like drilling, screwing or precision operations. This paper represents the first step for a new approach of exoskeleton stiffness control, whose input is given in real time directly by electromyographic signal from muscles. In this paper we attempt to study the stiffness of the elbow on which two muscles act as agonist-antagonist. The model used for the muscles is the one proposed by Hill.

**Keywords:** Hill muscle · Ergonomics · Stiffness control

## 1 Introduction

Exoskeletons are robotic devices that combine the high forces a robot may exert with the accurate and flexible control laws biologically implemented in the human. Since some manufacturing applications require complex gestures and dexterity that modern robotic technologies still cannot provide, exoskeletons are getting more and more attention from the manufacturing industry. On the other side some hand works, performed by human workers, have to be limited in time to avoid fatigue and, in the long run, injuries [16]. In this situation exoskeletons are a promising solution to increase the efficiency without reducing the accuracy of the operations. In the last years some groups started designing exoskeletons for industrial applications [1] while some studies were addressed to evaluate the positive effect of exoskeleton in industrial manufacturing [2, 17, 18].

The main goal requested to the industrial exoskeletons studied or developed so far, was to relieve the operator from a load, to reduce discomfort and fatigue. However the discomfort and the fatigue that occur during operations in which a particular accuracy is requested, like drilling, screwing, or engraving, are not due to the carrying of a load, but to arm stiffening, achieved by co-activating the muscles [3]. The development of an exoskeleton whose purpose is the increase of the operator's arm stiffness may reduce fatigue and discomfort.

Arm stiffness is calculated in literature as the ratio between the force exerted by the arm when an external displacement is applied, and the displacement itself. [4] Since muscles are the actuators that are responsible for the arm stiffness, the recording of their activation, obtained from the measurement of the electromyographic (EMG) signal, might lead to an estimation of the arm stiffness.

In recent studies EMG signals were used to control the stiffness of robotic devices [5] and of an exoskeleton of the knee for rehabilitation purpose [6]. However, none of the exoskeletons, whose stiffness could be controlled directly by biological signal recorded by the operator, has been developed for industrial use.

In this paper we study and evaluate the model of the elbow, activated by two antagonist muscles. This model may be implemented in future works such as to be a valid device for the development of the control law of an exoskeleton whose stiffness is calculated from the EMG signal acquired from the operator muscles.

## 2    Methods

### 2.1    Arm and Musculo-Tendon System Models

We use a simplified model of the human elbow composed of two links connected by a single degree of freedom (DoF), and two actuators, simulating the muscles Brachio-radialis (BRD, muscle (1) and Lateral head of the Triceps (TriLat, muscle (2) acting on the joint (Fig. 1A). The elbow was treated as an hinge joint, as commonly reported in literature [7] whose angle decreases with the extension and increases with the flexion of the elbow. The two actuators were approximated with wires, and could exert only pulling actions, as in previous studies [8]. The directions of the actions exerted by the two actuators were opposed.

The musculo-tendon systems are approximated on the basis of the model developed by Hill [9]. This approximation remains a commonplace in the computational literature and a valid method when the purpose of the study is the analysis of the feasible mechanical behaviour of the limb for which an analogue of musculo-tendons is requested. The Hill musculo-tendon model [9] is composed of different elements (Fig. 1B) that model the muscle and the tendon actions. The muscle segment (lp) is composed of an active element (A), that models the actin-myosin action, and a non-linear spring in parallel with A (parallel spring), that models the collagen tissue. The tendon segment (ls) is composed of a non-linear spring in series with A (serial spring).

The forces exerted by the active element ($F_A$) and by the parallel spring ($F_p$), in relation to the length of the muscle segment ($l_p$), and the force exerted by the serial spring ($F_s$) in relation to the length of the tendon ($l_s$), together with their coefficients, are derived from literature [10] (Fig. 1C–E):

$$F_A = m \cdot F_{MAX} \cdot \left[ -a \cdot \left( \frac{l_p}{l_{ceopt}} \right)^2 + 2a \cdot \frac{l_p}{l_{ceopt}} - a + 1 \right]$$
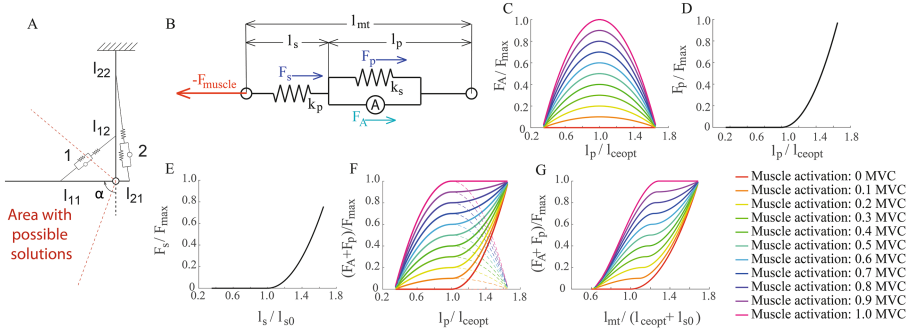
**Fig. 1.** Elbow model and musculo-tendon element characteristics. (A) Model of human elbow and range of elbow flexion in which solutions of equilibrium between torques exerted by the muscles exist. (B) Hill muscle model used in the study. (C) Force exerted by the active element of the muscle in relation to its length at different activations. (D) Force exerted by the parallel spring in relation to its length. (E) Force exerted by the serial spring in relation to its length. (F) Force exerted by the muscle segment in relation to its length at different activations of the active element. (G) Force exerted by the musculo-tendon system in relation to its length at different activations.

$$F_p = k_p \left[ \max\left( 0, \frac{l_p}{l_{ceopt}} - \frac{l_{p0}}{l_{ceopt}} \right) \right]^2$$

$$F_s = k_s [\max(0, l_s - l_{s0})]^2$$

where $a = 1/width^2$; $width$ is the width of the muscle and is equal to 0.66; $m$ is the muscle activation, measured as a fraction of the Maximum Voluntary Contraction (MVC); $l_{ceopt}$ is the optimal length at which the muscle exerts its maximal active force ($F_{MAX}$); $k_p$ is the stiffness of the muscle (chosen such that at $F_p = F_{MAX}$, $l_{cerel} = 1 + width$); $l_{p0} = l_{ceopt}$ is the muscle relaxation length, that indicates the maximum length of the muscle for which the parallel spring did not exerted any passive force; $k_s$ is the tendon stiffness (chosen such that at $F_{MAX}$, $l_s = 1.04 * l_{s0}$); $l_{s0}$ is the tendon slack length that indicates the maximum length of the tendon for which the serial spring does not exert any force. $F_{MAX}$, $l_{ceopt}$, and $l_{s0}$ are muscle specific and their values, for the muscles used in this study, were got from literature and reported in Table 1.

The couple of mono-articular antagonist muscles are chosen as in [11] and are the BRD, that acts as a flexor of the elbow, and the TriLat that acts as an extensor of the elbow. Anthropometrical information on the attachment of the muscles on the bones are got from literature and are reported in Table 1.

## 2.2    Equations for the Force Balancing

The equations that describe the equilibrium among the forces and torques, shared between the two muscles and their elements are:

**Table 1.** Anatomical parameters used in the study

| Muscle | lceopt (m) | lp0 (m) | ls0 (m) | Fmax (N) |
|---|---|---|---|---|
| 1: BRD | 0.0858 | 0.0858 | 0.0535 | 261.33 |
| 2: TriLat | 0.1138 | 0.1138 | 0.0980 | 624.3 |
| | $k_p$ (N/m) | $k_s$ (N/m) | Attach on Radius-Ulna (m) | Attach on Humerus (m) |
| 1: BRD | 600 | $163 \cdot 10^3$ | $l_{11}$: 0.1274 | $l_{12}$: 0.1004 |
| 2: TriLat | 1433 | $390 \cdot 10^3$ | $l_{21}$: 0.0219 | $l_{22}$: 0.1735 |

$$\begin{cases} F_{s1} = F_{p1} + F_{A1} \\ F_{s2} = F_{p2} + F_{A2} \\ m_{a_2}\left(F_{p2} + F_{A2}\right) = m_{a_1}\left(F_{p1} + F_{A1}\right) \end{cases}$$

where $F_{s1}$, $F_{p1}$, $F_{A1}$, and $m_{a_1}$ are respectively the forces exerted by the serial spring, by the parallel spring, by the active element and the moment arm of the muscle 1, and $F_{s2}$, $F_{p2}$, $F_{A2}$, and $m_{a_2}$ are respectively the forces exerted by the serial spring, by the parallel spring, by the active element and the moment arm of the muscle 2.

The force equations are coupled with geometrical equations:

$$\begin{cases} l_{mt1} = l_{p1} + l_{s1} \\ l_{mt2} = l_{p2} + l_{s2} \\ l_{mt1} = \sqrt{l_{11}^2 + l_{12}^2 - 2 \cdot l_{11} \cdot l_{12} \cdot \cos \alpha} \\ l_{mt2} = \sqrt{l_{21}^2 + l_{22}^2 - 2 \cdot l_{21} \cdot l_{22} \cdot \cos(\pi - \alpha)} \\ m_{a_1} = \dfrac{2}{l_{mt1}}\sqrt{\dfrac{P_1}{2}\left(\dfrac{P_1}{2} - l_{11}\right)\left(\dfrac{P_1}{2} - l_{12}\right)\left(\dfrac{P_1}{2} - l_{mut1}\right)} \\ m_{a_2} = \dfrac{2}{l_{mt2}}\sqrt{\dfrac{P_2}{2}\left(\dfrac{P_2}{2} - l_{21}\right)\left(\dfrac{P_2}{2} - l_{22}\right)\left(\dfrac{P_2}{2} - l_{mut2}\right)} \end{cases}$$

where $l_{muscle1}$, $m_{a_1}$, and $P_1$ are respectively the length, the arm moment of the muscle 1, and the perimeter of the triangle whose sides are $l_{11}$, $l_{12}$, and $l_{mt1}$. $l_{mt2}$, $m_{a_2}$, and $P_2$ are respectively the length and the arm moment of the muscle 1 and the perimeter of the triangle whose sides are $l_{21}$, $l_{22}$, and $l_{muscle2}$. $\alpha$ is the angle of the elbow defined such that $\alpha = 0 rad$ when the elbow is completely extended and $\alpha = \pi rad$ when the elbow is completely flexed (Fig. 1A). The arm moment has a complex expression that cannot simply be approximated with a sine or a cosine function and derives from the geometry of the muscle.

The system composed of geometric and force equations, together with the equations for the evaluation of the forces exerted by the muscle elements, is implemented in Matlab.

### 2.3    Stiffness Calculation

Once the arm configuration is set, a virtually infinite set of solutions can be obtained. The differences among these solutions depend on the level of co-activation of antagonist muscles. In this study we fix the activation of the muscle 1 and we consequently calculate, for each elbow angle, the activation of the muscle 2 solving the system of equation previously described.

The rotational stiffness of the musculo-tendon system $K_i$ was defined as the elbow angle-torque curve:

$$K_i = m_{a_i} \frac{\partial \left( F_{pi} + F_{Ai} \right)}{\partial \alpha}$$

The procedure for the calculation of the elbow stiffness is the one reported in [4]. A small deflection of 0.01° is applied to the elbow joint in both positive and negative directions and the activations of the muscles are maintained unchanged. A corresponding torque at the elbow is calculated. Since the deflection is small [12] the elbow angle-torque relation could be approximated to be linear around the unperturbed configuration. The stiffness of each muscle is then calculated as the slope of the line passing for the deflected points, in the elbow angle-torque relation. The rotational stiffness of the elbow is assumed to be the difference between the slopes of the elbow angle-torque curves of muscle 2 respect with muscle 1.

## 3    Analysis

### 3.1    Elbow Angle Boundaries

The range of the angles the elbow may assume, due to physiological boundaries, was reported in literature [13]. However other boundaries, due to the muscles force exertion characteristic, may be identified (Fig. 2). The physiological boundaries and the boundaries due to the muscles characteristic may not coincide. In Fig. 2 the upper value of the elbow flexion is fixed to 130° due to physiological boundary. However possible solutions for co-contraction could be obtained also for higher elbow flexion values. On the other side bibliography identified the lower boundary close to 0° while no possible intersection between the characteristics of the two muscles is possible below 20°. This discrepancy may be due to the approximation of the muscles with a string or to the action of other muscles acting on the same elbow joint, neglected in this model, whose activation would permit higher extensions.

It can be observed that intersections between two specific activations of muscles 1 and 2 are possible at most for one elbow flexion. In other words, the activations of the antagonist muscles univocally identify the elbow flexion if no torque is exerted by the elbow joint.

## 3.2    Antagonist Muscle Activation

In Fig. 2 the activation of muscle 2, that assures the equilibrium at the elbow, is represented at different elbow configurations and muscle 1 activations. Curves regarding low activation of muscle 1 are more sparse respect with curves regarding high activation of muscle 1. For this reason, the step among muscle 1 activation is fixed to be non-constant in Figs. 2 and 3. Any equilibrium is possible for angles lower than 85°, maintaining both muscles with no activation. Activating muscle 2 is always necessary for elbow flexion higher than 85° to compensate the force exerted by the passive element of muscle 1.
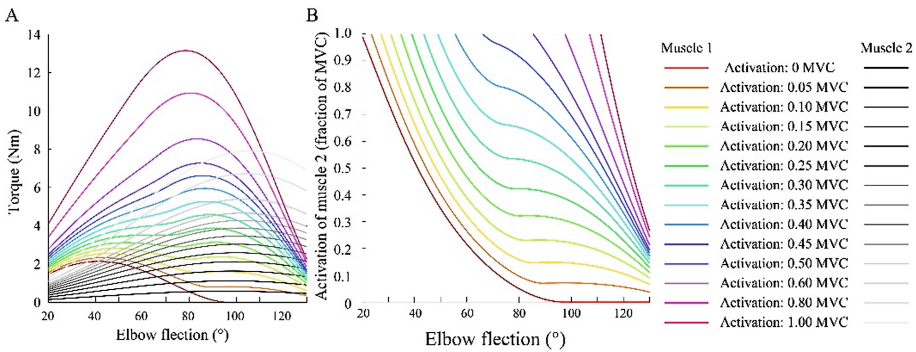


**Fig. 2.** Characteristics of the elbow torque and activation of muscle 2 necessary to balance the torque exerted by muscle 1. (A) Characteristics of the torque related to the elbow flexion, exerted by the two antagonistic muscles, at different levels of activation of muscle 1 (coloured) and 2 (gray scale). Muscle activations are not equally spaced. (B) Activation of muscle 2 necessary to balance the torque exerted by muscle 1, for different elbow flexion. Different levels of muscle 1 activation are reported with different colours. Muscle 1 activations are not equally spaced.

Not all possible elbow flexion and muscle 1 activations are feasible together. In particular higher activations of muscle 1 are balanced by muscle 2 only for higher values of elbow flexion. Lower activations of muscle 2 are balanced by muscle 1 only for lower values of elbow flexion. These boundaries defined a range of muscle activations in which the stiffening of the elbow, without exerting a torque, is possible.

## 3.3    Arm Stiffness

The stiffness of the two muscles is reported in Fig. 3A. While the stiffness of the muscle 2 is always non-negative, the stiffness of muscle 1 can assume negative values. This behaviour can be physiological and it is a consequence of the negative slope of the elbow flexion-torque relation.

The joint stiffness grows up with the muscle activation for each elbow angle (Fig. 3B). Two peaks can be found, due to the passive and active elements of muscle 1.

Since the balancing of the torque exerted by high activation of muscle 1 is possible only for some joint angles, the stiffness of higher muscle activations can be computed
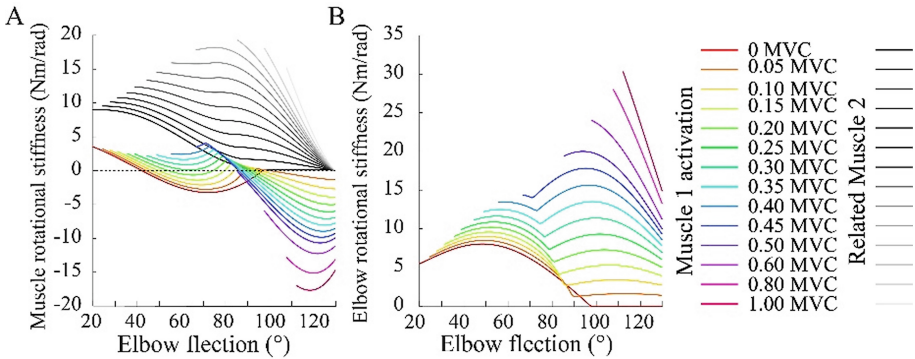
**Fig. 3.** Muscles and elbow stiffness in relation to elbow flexion. (A) Rotational stiffness of the muscles. The stiffness of muscle 1 is represented with a coloured scale, each muscle 1 activation is represented with a different colour. The stiffness of muscle 2 is represented with a gray scale, the muscle 2 activation, whose torque balanced the torque exerted by muscle 1, is represented with a different level of gray. (B) Stiffness of the elbow at different elbow flexion and muscle 1 activations are reported with different colours.

only for these angles. Since there exist some elbow flexion at which both muscles are not activated, a range of angles at which the stiffness is null can be found.

## 4   Discussion

The purpose of this study was the development of a model for the evaluation and the analysis of the elbow stiffness. This model can be successively implemented and used for the study of a control law of an exoskeleton, for industrial purpose, whose stiffness could be modulated on the basis of the operator arm's stiffness. The muscle model used in this study is a simple approximation of the real muscle, and more complex muscle models were developed [14]. However, since the purpose of this model is the study of the mechanical characteristics of the arm stiffness, and not the study of the properties of the muscle itself, we may assume that the approximations of the present model are acceptable in relation to its use [15].

On the other hand the model shows some limitations. No physiological values are obtained for elbow flexion lower than 20°, due to the approximation of the muscles shape with strings or to the reduction of the number of muscle to two. However, since the presented model could be used for developing industrial exoskeletons, in this field elbow flexion lower than 20° are rare and ergonomically deprecated. However, non-physiological behaviour may be due to the reduced number of muscles. The increasing of the number of muscles considered in the model may solve this kind of discrepancy. This would lead to the increasing of the redundancy of the system, so the same stiffness may be achieved by virtually infinite combinations of the muscle activations.

In future work we plan to add another joint, modelling the shoulder, and to increase the redundancy of the system, using a physiological law to choose the muscle activations.

# References

1. van der Vorm, J., Nugent, R., O'Sullivan, L.: Safety and risk management in designing for the lifecycle of an exoskeleton: a novel process developed in the robo-mate project. Procedia Manuf. **3**, 1410–1417 (2015)
2. Sylla, N., Bonnet, V., Colledani, F., Fraisse, P.: Ergonomic contribution of ABLE exoskeleton in automotive industry. Int. J. Ind. Ergon. **44**(4), 475–481 (2014)
3. Hogan, N.: Adaptive control of mechanical impedance by coactivation of antagonist muscles. IEEE Trans. Autom. Control **29**, 681–690 (1984)
4. Mussa-Ivaldi, F., Hogan, N., Bizzi, E.: Neural, mechanical, and geometric factors subserving arm posture in humans. J. Neurosci. **5**, 2732–2743 (1985)
5. Ajoudani, A., Tsagarakis, N., Bicchi, A.: Tele-impedance: teleoperation with impedance regulation using a body-machine interface. Int. J. Ind., Ergon (2012)
6. Karavas, N., Ajoudani, A.: Tele-impedance based stiffness and motion augmentation for a knee exoskeleton device. In: Proceedings International Conference on ICRA. IEEE (2013)
7. Marieb, E.N., Hoehn, K.: Human Anatomy & Physiology. Pearson Benjamin Cummings, San Francisco (2007)
8. Buhrmann, T., Di Paolo, E.A.: Spinal circuits can accommodate interaction torques during multijoint limb movements. Front. Comput. Neurosci. **8**, 144 (2014)
9. Hill, A.V.: The mechanics of active muscle. Proc. R. Soc. B Biol. Sci. **141**(902), 104–117 (1953)
10. Kistemaker, D.A., Wong, J.D., Gribble, P.L.: The central nervous system does not minimize energy cost in arm movements. J. Neurophysiol. **104**(6), 2985–2994 (2010)
11. Osu, R., Gomi, H.: Multijoint muscle regulation mechanisms examined by measured human arm stiffness and EMG signals. J. Neurophysiol. **81**, 1458–1468 (1999)
12. Hu, X., Murray, W., Perreault, E.: Muscle short-range stiffness can be used to estimate the endpoint stiffness of the human arm. J. Neurophysiol. **105**, 1633–1641 (2011)
13. Iannotti, J.P., Parker, R.D.: The Netter Collections of Medical Illustrations: Musculoskeletal System, part I - Upper Limb, vol. 6, 2nd edn. Saunders, Philadelphia (2013)
14. Lichtwark, G., Watson, J.: Intensity of activation and timing of deactivation modulate elastic energy storage and release in a pennate muscle and account for gait-specific initiation of limb. J. Neurophysiol. **212**, 2454–2463 (2009)
15. Inouye, J.M., Valero-Cuevas, F.J.: Muscle synergies heavily influence the neural control of arm endpoint stiffness and energy consumption. PLoS Comput. Biol. **12**(2), e1004737 (2016)
16. Belforte, G., Gastaldi, L., Sorli, M.: Active orthosis for rehabilitation and passive exercise. In: Proceedings of the IV International Conference on Simulations in Biomedicine, BIOMED, pp. 199–208 (1997)
17. Galetto, M., Gastaldi, L., Lisco, G., Mastrogiacomo, L., Pastorelli, S.: Accuracy evaluation of a new stereophotogrammetry-based functional method for joint kinematic analysis in biomechanics. Proc. Inst. Mech. Eng. Part H J. Eng. Med. **228**(11), 1183–1192 (2014)
18. Takeda, R., Lisco, G., Fujisawa, T., Gastaldi, L., Tohyama, H., Tadano, S.: Drift removal for improving the accuracy of gait parameters using wearable sensor systems. Sensors **14**, 23230–23247 (2014)

# Experimental Characterization
# of Human Walking on Stairs Applied
# to Humanoid Dynamics

Daniela Tarniţă[1]([⊠]), Ionuţ Geonea[1], Alin Petcu[1],
and Dănuţ-Nicolae Tarniţă[2]

[1] University of Craiova, Craiova, Romania
`tarnita.daniela@gmail.com`, `petcu.alin@gmail.com`,
`igeonea@yahoo.com`
[2] University of Medicine and Pharmacy, Craiova, Romania
`dan_tarnita@yahoo.com`

**Abstract.** The paper presents a comparison between an experimental study of flexion-extension movement in human leg joints and numerical simulations on a virtual mannequin computed in ADAMS virtual environment. Using Biometrics data acquisition system based on electrogoniometers, data were collected for each of three joints of right and left legs during experimental climbing and descending on stairs. The mean flexion-extension cycles for legs joints were obtained. This obtained experimental data series were introduced as input in the joints of the virtual mannequin and a walking simulation was performed in ADAMS environment software. The variation of joints forces and torques during walking obtained by virtual simulation could be used in future work in order to obtain stress and displacements maps in bones and joints by applying the finite element method.

**Keywords:** Walking on stairs · Kinematics · Electrogoniometers · Ground reaction forces · Force platforms · Virtual mannequin · ADAMS simulation

## 1 Introduction

In last years, several humanoid robots which are able to walk and perform human-like movements have been developed [1–5]. In papers [4, 5] the authors present a human-oriented approach to the study of the biped gait for a humanoid robot. Climbing and descending stairs is a daily activity of people. Compared to the normal gait this is a much more demanding activity [1] especially in people whose motor skills are reduced [2]. During the activity of ascending and descending stairs, the muscle moments at joints ankle, knee and hip are much higher compared to normal walking [3–5].

In gait analysis, the measurement of ground reaction forces (GRF) has a long tradition [6], but few studies have been conducted to determine the reaction forces for the ascent or descent of stairs. In papers [7–9] the authors have presented experiments on determining the variability of soil reaction forces by the coefficient of variation in healthy young subjects. The sizes and inclination of stairs varies by destination and use, so in [2] the authors presented the biomechanical analysis of movement during

climbing the stairs resulting at healthy young subjects. Force platforms with a system for measuring motion video were used by the authors in the paper [4] to identify normal operating parameters of the legs while climbing stairs. In climbing stairs GRF can reach values up to 1.4 body weight and 1.8 body weight at stairs descent [10, 11], contrary to normal walking when GRF values are 1.1-1.2 weight [12].

Biomechanical analysis of motor functions using force platforms and goniometer involved in ascent and descent of stairs helps improving knowledge of human loco-motion, being useful in gait rehabilitation or in the design of humanoid robots [2]. Already everyday human activities are taken over by robots; in the near future we expect a significant pickup of human activity and the gait of humanoid robots to be more natural, like-human. For this purpose modelling as close to the human is required [12]. Execution of certain movements such as ascent and descent of stairs can put problem to robots due to robust mechanical construction and shock of impact [13]. In order to be able to ascent or descent of stairs walking, robots require constant adapt-ability to environmental conditions and maintaining balance as humans [14, 15].

The objective of this study is to measure the variation of flexion-extension angles of the human leg joints and to obtain the ground reaction force variation while the subject performs ascent and descent walking on stairs. The obtained experimental data series will be introduced as input data in the lower limbs joints of a virtual mannequin and virtual ascent and descent of stairs simulation will be performed in ADAMS envi-ronment software. The variation of reaction forces and torque in every joint will be obtained and, for future work, they could be introduced as input data in a finite element analysis to obtain stress and displacements maps and study the joints behaviour.

## 2  Experimental Study

The experimental method which allows obtaining the kinematic parameters diagrams for the human knee joint uses a Biometrics Ltd data acquisition system [16]. Wearable sensing systems make it possible to analyse data outside the laboratory and capture information about the human gait during the person's everyday activities [17–23]. Using Biometrics electrogoniometers and force platforms the experimental measurements was performed for 5 trials of 12 consecutive ascending, respectively, descending stairs walking cycles of a healthy male subject having the following anthropometric data: age = 35years, body weight = 70 kg, height = 1.67 m, hip-knee length = 0.42 m, knee-ankle length = 0.39 m and ankle-little toe = 0.18 m. The 12 stairs are placed inside the laboratory building and have the following dimensions: height = 0.2 m, width = 0.25 m, length = 1.5 m. The experimental data were acquired for the right and left ankle joints, right and left knee joints and right and left hip joints. In the experiments 6 FP4 Biometrics force platforms, 3 for right leg and 3 for left leg, were used. For data acquisition an 8-channel DataLOG at a frequency of 500 Hz (MWX 8 Biometrics Ltd) was used; DataLOG was connected with each platform and the data were transferred to the computer in real time via Bluetooth communication. For measuring angles variation during trials, 6 flexible electrogoniometers connected with the second DataLOG were used. In Fig. 1 the data acquisition system mounted on the subject and the virtual mannequin model are shown.

**Fig. 1.** Subject with electro-goniometers and DataLog system
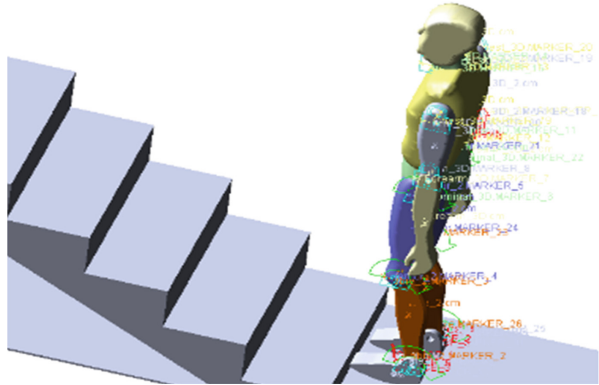


**Fig. 2.** Virtual mannequin model

## 3 Numerical Simulations

### 3.1 Dynamic Model of Mannequin Walking on Stairs

Multibody methods are used for human gait analysis when the investigation is directed on mechanical aspects, such as establishing joints reaction forces and torques [21, 24, 25]. To establish the joints reaction forces and torques, the inverse dynamics approach is used, considering as input data the angular variations of human leg joints.

In Fig. 3 the dynamic model of a virtual mannequin, in the hypothesis of ascending stairs, is presented. The virtual model, developed in Solid Works environment and composed of 13 rigid parts, follows the anthropometric data of human subject (Fig. 2). The mannequin legs are modelled of 3 parts: thigh, shank and foot. Each revolute joint, representing the hip, knee and ankle, is constrained by a motion law, established by experimental measurements. Experimentally motion laws of the human leg joints are introduced in ADAMS using spline functions based on Akima fitting method [26].
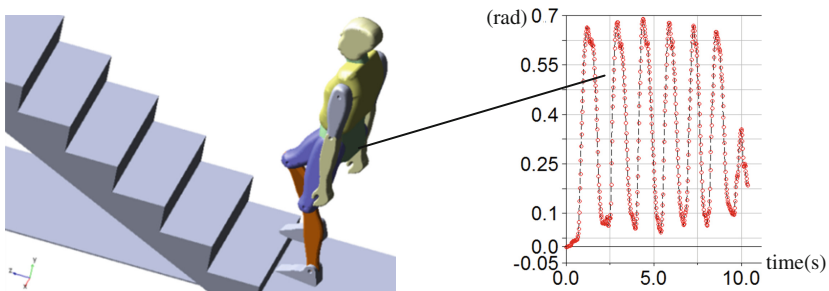


**Fig. 3.** Right hip angular motion is defined using a spline function

For this simulation approach, the ground reaction forces are defined introducing the experimental data in the contact model, as shown in Fig. 4. The dynamic simulation in ADAMS is performed using the WSTIFF solver and SI2 integrator.
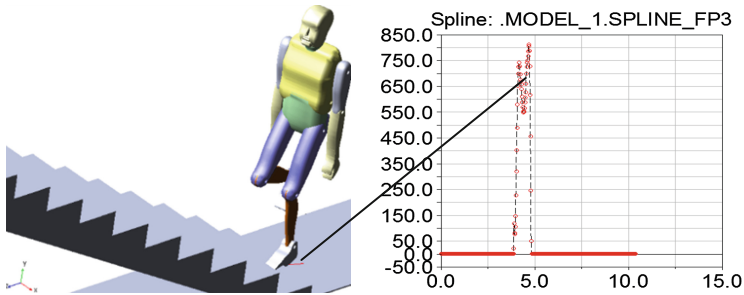


**Fig. 4.** Reaction ground forces [N] as function of time [s] introduced in the contact model

## 4    Results

The angular amplitudes of the six human flexion-extension joints during the gait performed on stairs were obtained from the report generated by the acquisition system as data files. The diagrams of Ground Reactions Forces (GRF) function of time [s] corresponding to the trial 1 are shown in Fig. 5. The corresponding diagrams of ankle, knee and hip flexion angles for right and left legs, functions of time [s] are shown in Fig. 6.
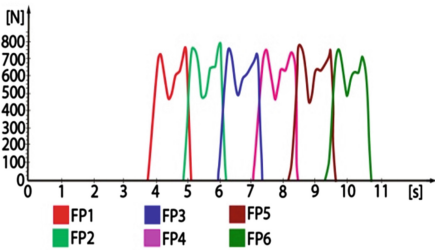


**Fig. 5.** The Ground Reactions Forces
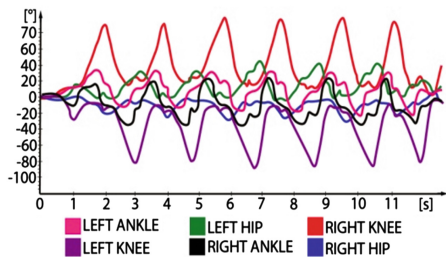


**Fig. 6.** The angles diagrams of legs joints

The medium GRF obtained from the platforms during five ascending on stairs trials, for left leg is presented in Fig. 7(a). The mean flexion-extension cycles for the left leg joints obtained from the collected data of five ascending stairs trials are also presented in Fig. 7(b)–(d).

Figure 8 presents comparative diagrams of medium GRF for climbing and descending stairs and for flexion-extension medium cycles of right leg joints. Similar diagrams are obtained for the left leg joints.
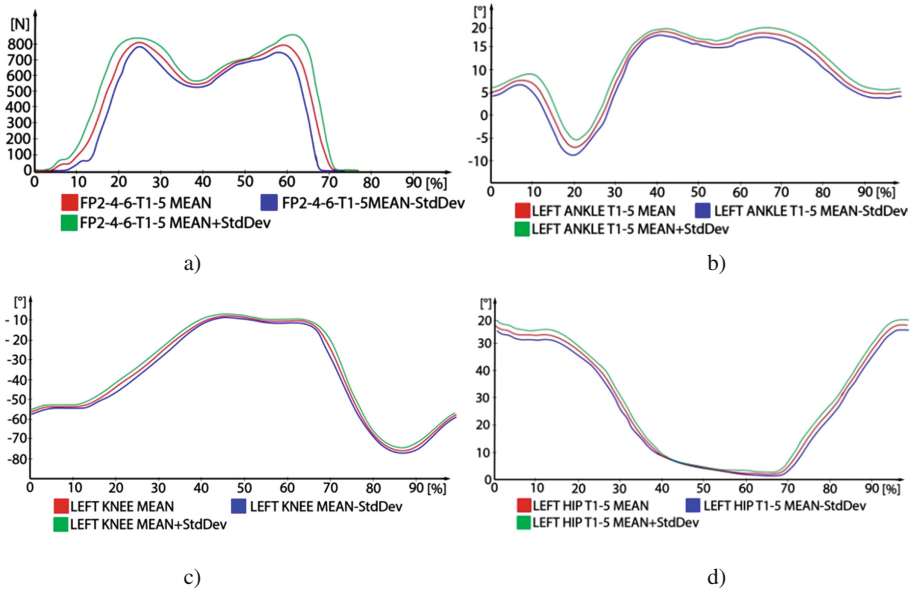
**Fig. 7.** (a) Mean GRF for left leg; (b) Flexion-extension medium cycle - left ankle; (c) Flexion-extension medium cycle - left knee; (d) Flexion-extension medium cycle - left hip
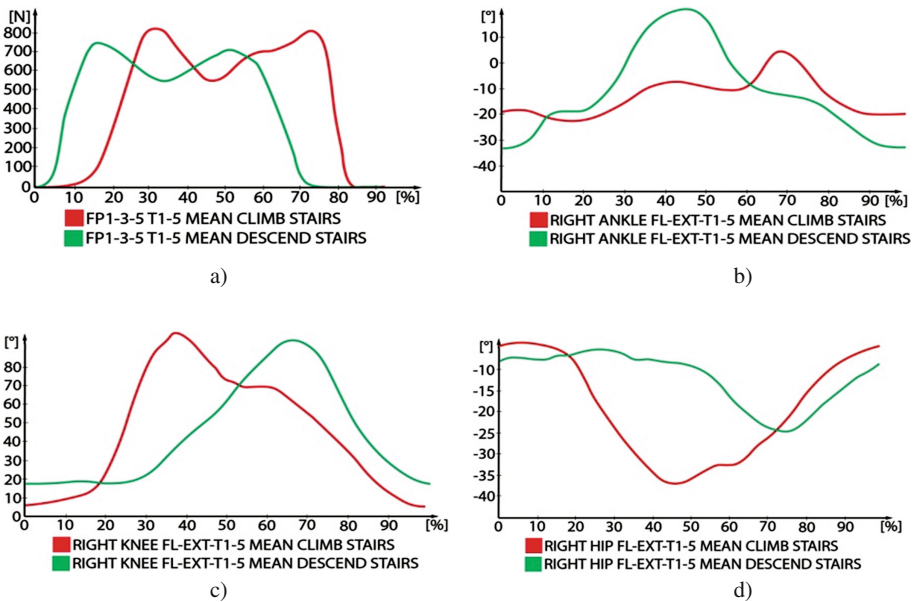


**Fig. 8.** (a) Medium GRF for climbing and descending stairs. Flexion extension medium cycles for: (b) right ankle; (c) right knee; (d) right hip

We can see in Figs. 5 and 7(a) that the GRF values vary during the time the foot is in contact with the floor. The maximum pressure occurs when the heel touches the floor and when the toes push off to take another step. During this time, GRF may reach up to 1.1–1.3 of the subject's body weight [N]. From Fig. 8(a) we can observe that the values of GRF are bigger on descending stairs than on ascending stairs. The results are similar with those obtained by other researchers in their papers [1, 4, 21, 24].

The second set of results is obtained by numerical simulations of mannequin walking on stairs, performed in ADAMS. The simulation results consist in legs joints reaction forces and torque. Vertical reaction forces for ankle and knee joints of mannequin, in the case of stair ascending, are presented in Figs. 9 and 10.
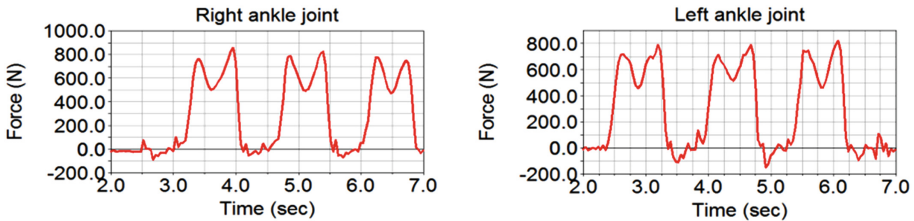


**Fig. 9.** Vertical reaction forces for the mannequin right and left ankle joint.
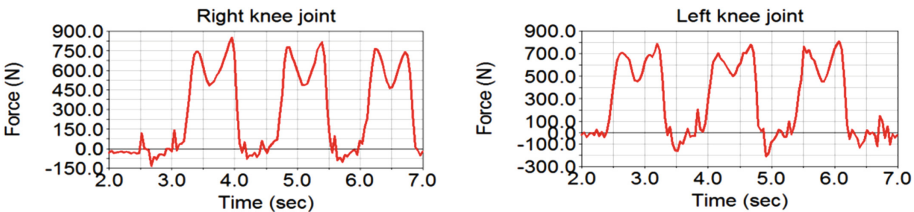


**Fig. 10.** Knee joint vertical reaction forces, computed in ADAMS simulation

The maximum value for the ankle joint vertical reaction force is 850 N, for the knee joint the maximum value reaches 800 N, and for the hip joint the value is 700 N, the smaller one. Also, the joint torques is computed in ADAMS simulation. In Figs. 11 and 12 the knee joint torque variation and the hip joint torque variation, as functions of time, in the case of mannequin ascending on stairs are shown.

The torque maximum values are the biggest for the ankle joint, with values comprised in the interval [730–850] Nm. For the hip joint, the maximum torque values decrease to [420–480] Nm, while for the knee joint, the maximum values are smaller, being contained in the interval [350–390] Nm. The results obtained in our paper are comparable with those obtained by other researchers in their studies [1, 2, 4, 21, 24]. The torque values obtained for the case of descending stairs are smaller than those obtained in the case of ascending stairs.
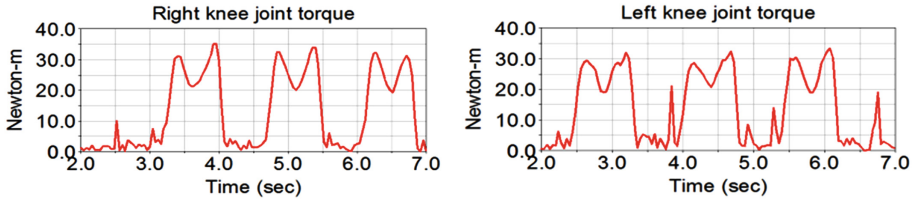
**Fig. 11.** Right and left knee joints torque variation.
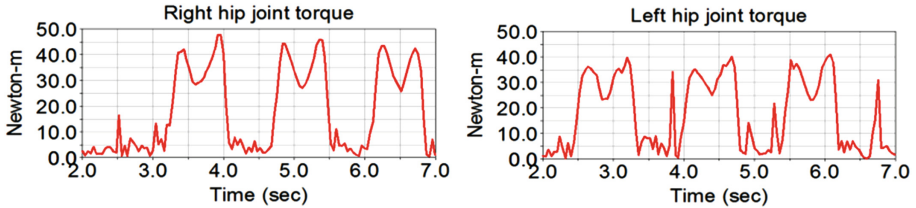


**Fig. 12.** Right and left hip joints torque variation.

Analyzing the variation of computed joints reaction forces and joints torque, we can conclude that their allure follows the variation of ground contact forces, established experimentally. This is feasible, because the ADAMS contact model is defined based on measured ground reaction forces. Computed forces and torques variations follow the same path as experimental ground forces, have peaks when the heel touches the ground and when the toes push off the ground to take another step.

## 5 Conclusions

The purpose of this research was to study the flexion-extension movements of the human lower limbs joints and the ground reaction forces developed during climbing and descending stairs. A Biometrics system was considered to collect and analyse the data files of flexion-extension angles for human ankle, knee and hip joints. Using SolidWorks software the virtual model of a mannequin was developed and transferred to ADAMS simulation environment.

To perform a dynamic simulation of mannequin ascending and descending stairs, a computational algorithm in ADAMS multibody dynamics software was developed. The results obtained in this paper are similar with the results obtained by other researchers. The main purpose of ADAMS dynamic simulation was to obtain the reaction forces in lower limb joints which are very useful for the study of joints and bones stresses and displacements using the Finite Element Method, in order to design and develop human-inspired robotic structures, or humanoid and walking robots.

# References

1. Stacoff, A., Diezi, C., Luder, G., Stussi, E., Kramers-de Quervain, I.A.: Ground reaction forces on stairs: effects of stair inclination and age. Gait Posture **21**(1), 24–38 (2005)
2. Riener, R., Rabuffetti, M., Frigo, C.: Stair ascent and descent at different inclinations. Gait Posture **15**(1), 32–44 (2002)
3. Nadeau, S., McFadyen, B.J., Malouin, F.: Frontal and sagittal plane analyses of the stair climbing task in healthy adults aged over 40 years: what are the challenges compared to level walking. Clin. Biomech. **18**, 950–959 (2003)
4. Protopapadaki, A., Drechsler, W.I., Cramp, M.C., Coutts, F.J., Scott, O.M.: Hip, knee, ankle kinematics and kinetics during stair ascent and descent in healthy young individuals. Clin. Biomech. **22**, 203–210 (2007)
5. Costigan, P.A., Deluzio, K.J., Wyss, U.P.: Knee and hip kinetics during normal stair climbing. Gait Posture **16**, 31–37 (2002)
6. Leitner, M., Schmid, S., Hilfiker, R., Radlinger, L.: Test–retest reliability of vertical ground reaction forces during stair climbing in the elderly population. Gait Posture **34**, 421–425 (2011)
7. Luder, G., Baumann, T., Jost, C., Schmid, S., Radlinger, L.: Variability of ground reaction forces in healthy subjects during stair climbing. Physioscience **3**, 181–187 (2007)
8. Suzuki, T., Bean, J.F., Fielding, R.A.: Muscle power of the ankle flexors predicts functional performance in community-dwelling older women. J. Am. Geriatr. Soc. **49**(9), 1161–1167 (2001)
9. Della, C.U., Bonato, P.: A novel design for an instrumented stairway. J. Biomech. **40**(3), 702–714 (2007)
10. Chao, E.Y., Laughman, R.K., Schneider, E., Stauffer, R.N.: Normative data of knee joint motion and ground reaction forces in adult level walking. J. Biomech. **16**, 219–233 (1983)
11. Christina, K.A., Cavanagh, P.R.: Ground reaction forces and frictional demands during stair descent: effects of age and illumination. Gait Posture **15**, 153–158 (2002)
12. Seungsuk, H., Youngjoon, H., Hernsoo, H.: Adaptive gait pattern generation of biped robot based on human's gait pattern analysis. In: World Academy of Science, Engineering and Technology (2007). Int. J. Electr. Comput. Energ. Electron. Commun. Eng. 1(10)
13. Katayon, R., Christophe, M., Moritz, M., Dorian, S., Andre, S., Von Oskar, S.: Concept and design of the biobiped1 robot for human-like walking and running. Int. J. Humanoid Rob. **8**(3), 439–458 (2011)
14. Qiang, H., Kazuhito, Y., Shuuji, K., Kenji, K., Hirohiko, A., Noriho, K., Kazuo, T.: Planning walking patterns for a biped robot. IEEE Trans. Robot. Autom. **17**(3), 280–289 (2001)
15. Tlalolini, D., Christine, C., Yannick, A.: Human-like walking: optimal motion of a bipedal robot with toe-rotation motion, transactions on mechatronics. Inst. Electr. Electron. Eng. **16**(2), 310–320 (2011)
16. http://www.biometricsltd.com/
17. Muro-de-la-Herran, A., Begonya, G.Z., Amaia, M.Z.: Gait analysis methods: an overview of wearable and non-wearable systems. Highlighting Clin. Appl. Sens. **14**, 3362–3394 (2014)
18. Tao, W., Liu, T., Zheng, R., Feng, H.: Gait analysis using wearable sensors. Sensors **12**, 2255–2283 (2012)
19. Tarnita, D., Marghitu, D.: Analysis of a hand arm system. Robot. Comput. Integr. Manuf. **29**(6), 493–501 (2013)

20. Tarnita, D., Catana, M., Tarnita, D.N.: Experimental measurement of flexion-extension movement in normal and osteoarthric knee. Rom. J. Morphol. Embryol. **54**(2), 309–313 (2013)
21. Patton, J.L.: Forward Dynamic Modeling of Human Locomotion, Ph.D. Thesis, Michigan State University (1993)
22. Van der Linden, M.L., Rowe, P.J., Nutton, R.W.: Between-day repeatability of knee kinematics during functional tasks recorded using flexible electrogoniometry. Gait Posture **28**, 292–296 (2008)
23. Tarnita, D.: Wearable sensors used for human gait analysis. Rom. J. Morphol. Embryol. **57** (2), 373–382 (2016)
24. Wojtyra, M.: Dynamical analysis of human walking. In: 15th European ADAMS users Conference, Warsaw, Poland (2000)
25. Chowdhury, S., Kumar, N.: Estimation of forces and moments of lower limb joints from kinematics data and inertial properties of the body by using inverse dynamics technique. J. Rehabil. Robot. **1**, 93–98 (2013)
26. MSC. ADAMS User Manual (2013)

# Path Planning for Formation Control of Autonomous Vehicles

Elias Xidias[1]([✉]), Claudio Paliotta[2], Nikos Aspragathos[3],
and Kristin Pettersen[2]

[1] Department of Product and Systems Design Engineering,
University of the Aegean, 84100 Ermoupolis, Syros, Greece
xidias@aegean.gr
[2] Department of Engineering Cybernetics,
Norwegian University of Science and Technology, NTNU,
NO-7491 Trondheim, Norway
{claudio.paliotta,kristin.y.pettersen}@itk.ntnu.no
[3] Department of Mechanical Engineering and Aeronautics,
University of Patras, 82200 Patras, Greece
asprag@mech.upatras.gr

**Abstract.** In this paper a two-stage approach is introduced for optimum path planning of a team of autonomous vehicles in an environment cluttered with obstacles. The vehicles are requested to move in formation from an initial point to a final point. The Bump-Surface concept is used for the representation of the environment while the formation of the vehicles is presented by a deformable Delaunay triangulation. The proposed approach is presented in detail and test cases with multiple vehicles are simulated to demonstrate the efficiency of the method.

**Keywords:** Path planning · Formation control · Autonomous vehicles

## 1 Introduction

Teams of autonomous vehicles are widely used in many applications, where the vehicles are requested to meet formations or other constraints to accomplish complex tasks such as transportation of large objects [1], localization and mapping [2], search and rescue missions [3]. This interest is motivated by the necessity of having more vehicles performing tasks which are more difficult to perform with only one vehicle, for instance surveillance missions [4]. Furthermore, the motion in formation is particularly important when spatially distributed tasks have to be accomplished, like for instance, source seeking missions [5].

In this paper we present an approach for the path planning problem for a multi-vehicle system. In particular, we consider a multi-vehicle system which consists of autonomous vehicles. The objective is to find an optimal path for each vehicle which connects an initial point with a final point while simultaneously the vehicles should be moving in a given formation.

The path planning problem for formations control of a team of autonomous vehicles has been investigated [6–8]. In [6], the authors presented a method based on rapidly exploring random trees (RRT) for path planning of formations with under-actuated vehicles. This method randomly samples the environment and chooses a free collision configuration for each vehicle. The authors revised the classical RRT to generate feasible paths for non-holonomic vehicles. Furthermore, they designed a priority strategy which makes the vehicles to move in a given formation. The work [7] describes a method based on Voronoi Fast Marching (VFM) for formations of fully actuated mobile robots. This method can be classified as a potential field method but avoids the drawbacks related to local minima. In [8] an abstract manifold A was defined which is the product of two manifolds G and S. The manifold G is a Lie Group, which captures information about the orientation and position of every vehicle, while S is a manifold, which captures information about the shape of the group of vehicles. The states in the two manifolds G and S are controlled independently.

In this paper we extend the method proposed in [9, 10] to multi-vehicle systems consisting of autonomous vehicles. The vehicles should be moving in a given formation. By using the proposed approach, it is possible to obtain simultaneously an optimum path for each vehicle. Each path is constructed considering both the environment constraints and the formation constraints.

The main contribution of this paper is the introduction of a method for the path planning of a flexible formation of $n$ autonomous vehicles in an environment cluttered with static obstacles. For the first time the formation relationship is represented by a deformable Delaunay triangulation, which has the ability to find a solution even when the vehicles are requested to move through narrow passages. Furthermore, the smoothness of the path is obtained by controlling the angles between the control-polygon segments, which define the system's path. A multiplicity of optimization criteria and constraints could be incorporated easily to the formulated optimization problem according to the mission requirements of the team of vehicles.

## 2 Basic Assumptions and the Two Stage Approach

It is assumed that a formation of autonomous vehicles should move in a 2D environment which is cluttered with known prohibited areas (obstacles-danger zones). A formal statement of the problem, the assumptions and the structure of the proposed method are given in this section.

### 2.1 The Path Planning Problem for a Formation of Autonomous Vehicles

Consider a team of $n \geq 3$ autonomous vehicles which should move from an initial to a goal location by keeping the desired formation in a 2D environment cluttered with known static obstacles. The basic assumptions are:

1. Each vehicle is represented by a point which is moving only forward.

2. Each vehicle is requested to move from an initial point $S_i$ to a goal point $G_i$ inside the desired formation, which should not split, while the length of the path should be minimal.
3. The path of each vehicle should be smooth.
4. The formation is modelled as a deformable polygon. The user defines both the minimum and maximum allowed formations of the polygon. The maximum formation is the desired one.

## 2.2    The Geometry and the Representation of the Formation

We assume that a team of autonomous vehicles is enclosed in a deformable convex polygon, while no splits are allowed. The vertices of the convex polygon are the "external" vehicles. Figure 1 shows a visual representation of a team of 15 point-vehicles.
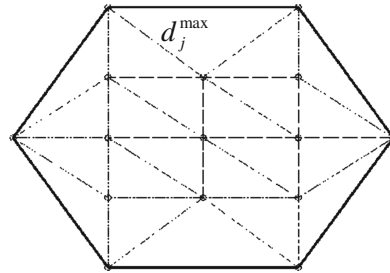


**Fig. 1.** A team of 15 vehicles (black points). The corresponding: Delaunay triangles (dash lines) and the convex hull (black bold line).

The convex polygon is used in order to exploit the fact that the centroid **R** always lies inside the polygon. Furthermore, by using convex polygon, we avoid to increase the problem's complexity which is happening when we use non-convex polygons.

The Delaunay triangulation [11] is used to facilitate the geometric relations between the vehicles within a geometry, where constraints could be defined easily. Generally, Delaunay triangulation is characterized by its simplicity and its "economy" in data storage. Furthermore, the Delaunay triangulation is independent of the order in which the points are processed. For a team of $n$ vehicles we have $2n - 2 - m$ triangles and $3n - 3 - m$ edges, where $m$ is the number of vehicles on the convex hull. The length of each edge $d_j, j = 3, \ldots, 3n - 3 - m$ is associated with the constraint $d_i^{min} \le d_i \le d_i^{max}$, where $d_i^{min}$ is the minimum safe distance and $d_i^{max}$ is the maximum, which is the desired distance between a pair of vehicles.

## 3   First Stage: The Sub-optimal Path for the Minimum Size Formation

In this stage, the minimum size formation is considered as a fixed shape and the shortest path is searched on the Bump-Surface. For the construction of the Bump-Surface representing a given 2D environment, a normalized workspace W is constructed by linearly mapping the initial environment to $[0, 1]^2$. The construction of the corresponding Bump-Surface $S$ is obtained by a straightforward extension of the Z-value algorithm [9].

It is assumed that the team has a reference point which lies at the centroid of the polygon representing the minimum size formation. The reference point traces a path $\mathbf{R}(s)$ in the normalized $\mathbf{W}$ which starts from the given start point and terminates at the desired goal point. In order to define $\mathbf{R}(s)$ we use a B-Spline curve [12] to represent the path of the fixed minimum size formation:

$$\mathbf{R}(s) = \sum_{h=0}^{Q-1} N_h^2(s)\mathbf{p}_h, \ 0 \leq s \leq 1 \tag{1}$$

where $Q$ is the number of control points $\mathbf{p}_h$, $N_h^2(s)$ are the B-Spline basis functions and 2 is the curve degree. The goal of the proposed global path planning strategy is the determination of the position of $(Q-2)$ control points $\mathbf{p}_h$ which define the requested path $\mathbf{R}(s)$.

### 3.1   Safe Optimum Motion of the Minimum Formation

A safe path $\mathbf{R}(s)$ is one that (i) does not collide with the obstacles and (ii) is smooth. Following the results from [10], the arc length of $\mathbf{R}(s)$ approximates the length $L$ of its image $\mathbf{S}(\mathbf{R}(s))$ on the Bump-Surface $S$ as long as $\mathbf{R}(s)$ lies onto the flat areas of $S$. Furthermore, in order to take into account the shape of the formation, a set of feature points $\mathbf{A}_i$ is selected on its boundary according to its shape and the requested accuracy [10].

Taking the above analysis into consideration, the path planning problem is formulated as an optimization problem which is described by,

$$\text{minimize } E_{comp} = \left\{ L, \sum_{i=1}^{m} \sum_{a=0}^{N_p} H_i^a, 1/\varphi_1, \ldots, 1/\varphi_{Q-2} \right\}, \ \text{subject to } \varphi_h \leq 180°, h$$
$$= 1, \ldots, Q-2 \tag{2}$$

where $N_p$ denotes the number of points taken on $\mathbf{R}(s)$ to discretize it, $\varphi_h$ is the $h$-th angle between the control-polygon segments $h$ and $h + 1$ $\mathbf{R}(s)$ and $H_i$ is the "flatness" of $\mathbf{A}_i(s)$ on $S$. $\mathbf{R}(s)$ follows the shape of the defining control polygon which is derived by connecting the control points $\mathbf{p}_k$[12].

Then, a Genetic Algorithm is adopted in order to search for a solution to the formulated optimization problem (Eq. (2). A floating point representation scheme is

selected since the coordinates of the control points and the angles of the control polygon are real numbers. A fitness assignment strategy based on Pareto-optimal solutions called GPSIFF [13] is implemented. The following three genetic operators were selected: *reproduction*: the proportional selection strategy is adopted, where chromosomes are selected to reproduce their structures in the next generation with a rate proportional to their fitness; *crossover*: the one-point crossover was adopted; *mutation*: a boundary mutation is used.

## 4   Stage 2: Determining the Smooth Path of Each Vehicle in the Deformable Formation

With the reference path $\mathbf{R}(s)$ derived by the first stage, the path of every vehicle is determined considering the location of the vehicles in the desired formation. Since the formation has to pass through areas where the minimum size formation is able to move safely, then in the second phase a deformable formation is considered.

A deformation cost function is formulated with an optimum cost at the desired formation. In this stage each vehicle has its own "independent" smooth path but along its path it has to respect the desired formation. In order to ensure that $n - m$ the vehicles do not cross the border of the convex hull, the following condition is taken into account. At every point $R(s_a), a = 1, \ldots, N_p$ of the path $\mathbf{R}(s)$ the location of the vehicle $\mathbf{R}^i, i = 1, \ldots, n - m$ is computed by the convex combination of the $m$ vehicles which define the convex hull. Therefore,

$$\mathbf{R}^i = \sum_{f=1}^{m} w_f^i \mathbf{R}_f, \ i = 1, \ldots, n - m \tag{3}$$

where the weight factors $w_f^i$ satisfy,

$$w_f^i \geq 0 \ \text{ and } \ \sum_{f=1}^{m} w_f^i = 1, \ i = 1, \ldots, n - m \tag{4}$$

The goal of the proposed path planning strategy is the determination of the $Q - 2$ control points $\mathbf{q}_k^i$, which define the requested path $\mathbf{R}^i(s)$ for the $i$-th vehicle given by the same equation as Eq. (1).

In order to take into account that the formation of the vehicles should adapt to the geometric characteristics of the environment while simultaneously trying to keep the desired shape, the following deformation function is proposed:

$$CD_j = e^{k_j}, j = 3, \ldots, 3n - 3 - m, \ and \ k_j = \begin{cases} \left| d_j - d_j^{\max} \right|, \ d_j \in [d_j^{\min}, d_j^{\max}] \\ a \ \text{very big value (defined by the user), otherwise} \end{cases}$$

$$\tag{5}$$

Equation (5) gives a penalizing function, which takes the optimum value when $d_i = d_i^{max}$ and the worst when $d_i \notin \left[d_i^{min}, d_i^{max}\right]$. The minimum size polygonal shape of the formation is obtained when $d_i = d_i^{min}$.

According to the above requirements the derived objective function is a vector which is represented by

$$\min E_{comp} = \left\{L^1, \ldots, L^n, CD_1, \ldots, CD_j\right\}, \ j = 3, \ldots, 3n - 3 - m, \ subject\ to \begin{cases} w_f^i \geq 0 \\ \sum_{f=1}^{m} w_f^i = 1, i = 1, \ldots, n - m \end{cases}$$

(6)

where $L^i$ is the path's length for the $i$-th vehicle which is computed in a similar way as in Stage 1. In the optimization problem defined by Eq. (6), the optimization variables are the control points which define the path $\mathbf{R}^i(s)$ of each vehicle and the weight factors $w_f^i$.

A Micro-GA is used to search for a sub-optimum path of each vehicle. The main characteristics of the developed Micro-GA are the following: a floating point representation scheme is selected for the chromosome syntax. Each chromosome represents a possible $\mathbf{R}^i(s)$ as a sequence of the unknown control points $\mathbf{q}_k^i$. A fitness assignment strategy based on Pareto-optimal solutions is implemented.

It should be noticed that the quality of the individual solution generated in the initial phase plays a critical role in determining the quality of the final optimal solution. Thus, the solution which is derived from Stage 1 (the control points which define the path $\mathbf{R}(s)$), is used as an initial solution in the Micro-GA (seeding) for each vehicle's path $\mathbf{R}^i(s)$. This helps the Micro-GA to converge in short time to the sub-optimal path for each vehicle. The same genetic operators as in Stage 1 are used except the mutation operator which is ignored. In most cases, a maximum number of iterations (generations) is defined in advance for the termination. However, it is difficult to determine beforehand the number of generations needed to find near-optimum solutions. Thus, an assessment of the quality level of the Genetic Algorithm is made on-line. The proposed algorithm terminates either when the maximum number of generations is achieved or when the same best chromosome appears for a maximum number of generations.

## 5 Simulations

The performance of the proposed method is investigated through a number of simulation experiments for a variety of formations moving in 2D environments. All simulations are implemented in Matlab. In all test cases, the grid size is set to $N_g = 100$. For the first stage, the control parameters of the GA are the following: population size = 250, maximum number of generations = 500, crossover rate = 0.75, boundary mutation rate = 0.004. For the Micro-GA we set: population size = 50, maximum number of generations = 30, crossover rate = 0.75. It is worth noting that the selection of the appropriate control settings is the result of extensive experimental efforts with various control schemes adopted following the indications of the literature.
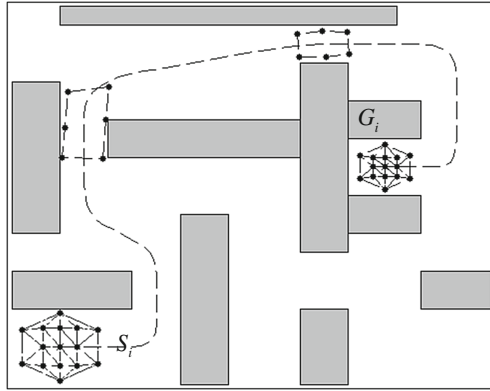
**Fig. 2.** The resulting solution path $\mathbf{R}(s)$, the initial and final convex hull with the corresponding Delaunay triangles and the trace of the convex hull in two different time instances
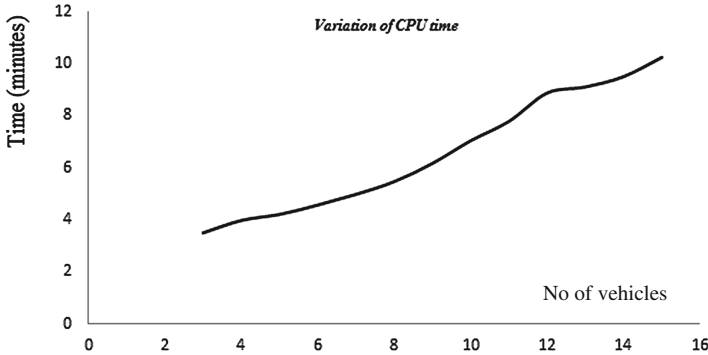


**Fig. 3.** A CPU time study

**Test Case:** we assume the environment of Fig. 2. Here, a team of 15 vehicles is requested to move in formation from the initial points $S_i$ to goal points $G_i$, $i = 1, \ldots, 15$. The convex hull is defined by six vehicles. A visual representation of both initial and final formations, the computed path $\mathbf{R}(s)$ and the corresponding Delaunay triangles are shown in Fig. 2. Each vehicle's path is defined by 8 control points. The computed solution takes about 10.24 min. Furthermore, Fig. 2 shows the formation of the convex hull while the team of vehicles is passing through narrow passages, where the formation is not just shrinked but it changed its shape autonomously to adapt to the environment.

Despite the fact that the problem under consideration is off-line, the computational time results with respect to the number of the vehicles and is of immense interest. The variation of CPU's time is indicative for the problem complexity. In these experiments the environment is the one shown in Fig. 2 and the number of control points is

constant, while the number of vehicles is changed from 3 to 15. Figure 3 shows that CPU time increases almost linearly with the increase in the number of vehicles.

## 6 Conclusion

A new approach for the path planning of a deformable formation of autonomous vehicles is proposed. The Delaunay triangulation is proved to be very convenient for the modelling of a deformable formation since the extreme formations (minimum and maximum allowed formations) are defined by the user and thus we can easily determine the limits of the distances between the vehicles. Furthermore, the smoothness of the path is obtained by controlling the angles between the control-polygon segments, which define the system's path.

In future work the proposed approach should be extended to semi-known 2D and 3D environments, and in addition to the motion planning the guidance and control of the vehicles should be considered.

## References

1. Wang, Y., Silva, C.: sequential q-learning with Kalman filtering for multirobot cooperative transportation. IEEE/ASME Trans. Mechatron. **15**(2), 261–268 (2010)
2. Chen, H., Sun, D., Yang, J., Chen, J.: SLAM based global localization for multi-robot formations in indoor environment. IEEE/ASME Trans. Mechatron. **15**(4), 561–574 (2010)
3. Tang, Z., Ozguner, U.: Motion planning for multi-target surveillance with mobile sensor agents. IEEE Trans. Robot. **21**(5), 898–908 (2005)
4. Saska, M., Chudoba, J., Precil, L., Thomas, J., Loianno, G., Tresnak, A., Vonasek, V., Kumar, V.: Autonomous deployment of swarms of micro-aerial vehicles in cooperative surveillance. In: 2014 International Conference on Unmanned Aircraft System, ICUAS 2014 - Conference Proceeding, pp. 584–595 (2014)
5. Han, J., Chen, Y.: Multiple UAV formations for cooperative source seeking and contour mapping of a radiative signal field. J. Intell. Robot. Syst. Theor. Appl. **74**, 323–332 (2014)
6. Liu, S., Sun, D., Zhu, C.: A dynamic priority based path planning for cooperation of multiple mobile robots in formation forming. Robot. Comput. Integr. Manuf. **30**(6), 589–596 (2014)
7. Garrido, S., Moreno, L., Lima, P.U.: Robot formation motion planning using Fast Marching. Rob. Auton. Syst. **59**, 675–683 (2011)
8. Belta, C., Kumar, V.: Motion generation for formations of robots: a geometric approach. In: Proceedings of IEEE International Conference on Robotics and Automation, ICRA 2011, (Cat. No. 01CH37164), vol. 2 (2001)
9. Azariadis, P.N., Aspragathos, N.A.: Obstacle representation by Bump-surfaces for optimal motion-planning. Robot. Auton. Syst. **51**(2–3), 129–150 (2005)
10. Xidias, E.K., Azariadis, P.N.: Mission design for a group of autonomous guided vehicles. Robot. Auton. Syst. **59**(1), 34–43 (2011)
11. Preparata, F.P., Shamos, M.I.: Computational Geometry. Springer, New York (1985)
12. Piegl, L., Tiller, W.: The NURBS Book. Springer, Berlin, Heidelberg (1997)
13. Chen, J.H., Ho, S.Y.: A novel approach to production planning of flexible manufacturing systems using an efficient multi-objective genetic algorithm. Int. J. Mach. Tools Manufact. **45**, 949–957 (2005)

# Developing a Climbing Maintenance Robot for Tower and Rotor Blade Service of Wind Turbines

Josef Schleupen[1(✉)], Heiko Engemann[1], Mohsen Bagheri[2],
Stephan Kallweit[1], and Peter Dahmann[2]

[1] Institute for Mobile Autonomous Systems and Cognitive Robotics
(MASKOR), University of Applied Sciences Aachen, Aachen, Germany
`{schleupen,engemann,kallweit}@fh-aachen.de`
[2] Faculty for Aerospace Engineering,
University of Applied Sciences Aachen, Aachen, Germany
`{bagheri,dahmann}@fh-aachen.de`

**Abstract.** Today, more than 275.000 wind turbines generate over 400 GW electrical power worldwide. So the demand for maintenance constantly raises. Since September 2014 the University of Applied Sciences Aachen and partners develop SMART (Scanning, Monitoring, Analyzing, Repair and Transportation), a maintenance platform for wind turbines. The research project is funded by the German federal ministry of economic affairs (BMWi), to support the upcoming industrial needs. While the reliability of the mechanical parts, like main bearing, generator, gears and main shaft increased during the recent years, the maintenance and improvement of rotor blades should be improved. A weatherproof cabin for rotor blade maintenance can extend the annual maintenance period from eight to twelve months, a major goal of the SMART development. In addition, a climbing mechanism for conical shaped, thin and slippery surfaces is generated and tested. SMART successfully completed the proof-of-concept milestone by demonstrating climbing in December 2015.

**Keywords:** Climbing · Robot · Rotor blade · Wind turbine · Maintenance · Service · Tracking · ADAMS · Chain drive · ROS · ar_track_alvar

## 1 Introduction

The wind market is growing rapidly. In China, the annual growth is about 45% [1]. The technology of generating electricity from wind power is still young. The amount of installed wind turbines raised the need for maintenance.

The reliability of mechanical parts, e.g. main bearing, generator, gears and main shaft evolved during the recent years, while the rotor blade maintenance needs to be improved [2]. The SMART demonstrator is a downscaled model (Fig. 1) for research and development. The main goal is the design of a fully functional prototype for a 2.5 MW wind turbine, including a weatherproof cabin. Current rotor blade maintenance is limited to convenient weather conditions: wind speed lower than twelve meter per second, low humidity, temperature above 10°C. These requirements currently limit
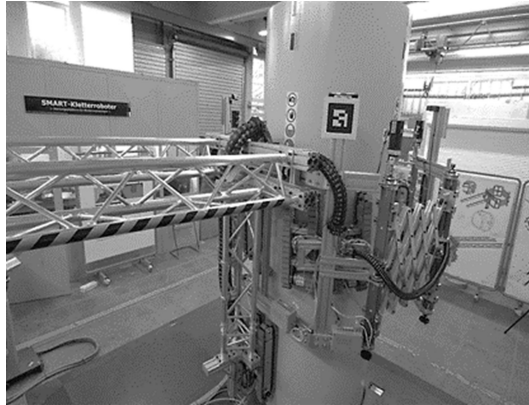
**Fig. 1.** SMART demonstrator, scale one to three

the maintenance period to the warmer period of the year. A weatherproof cabin for rotor blade maintenance extends the annual maintenance period from 8 to 12 months and from 3 to 24 h a day.

In addition, SMART can increase the quality of monitoring rotor blades: state of the art technologies for inspection, like ultrasonic- and terahertz-spectroscopy, X-ray and thermography, may be established to support the engineers and technicians. Rotor blade manufacturing procedures can be scaled down and integrated into the platform, in order to avoid expensive and inefficient dismounting of the rotor blades for full-inspection, repair and replacement. Further research and development is focusing the possibilities of cooperative or stand-alone robot systems for inspection and repair duties. Customization of the platform for special applications, e.g. RBE - rotor blade extensions (Energiekontor), fully autonomous inspection and turbine tower maintenance are part of the challenging development.

The following two subchapters intend to summarize general principles for the climbing robot design and associated research and development topics.

## 1.1   Kinematics of the Climbing Robot Motion

SMART is a novel mobile robot design. One application for this kind of robotic system is the monitoring and maintenance of the rotor blades and the tower of wind turbines. There are two possible solutions to climb a wind turbine – either by using ropes from the top or by climbing based on friction.

The robotic system SMART uses a frictional connection to the tower. Such mechanism can be split into two subsystems: the tensioning system and the climbing system. The role of a tensioning system is to provide the essential normal force for static friction between the tower surface of the wind turbine and the climbing system. The climbing system can either be intermittent or continuous.

The following approach introduces a continuously climbing system, based on a tracked vehicle design (Fig. 2). Parts of the tracked drives are: chain disk, harmonic
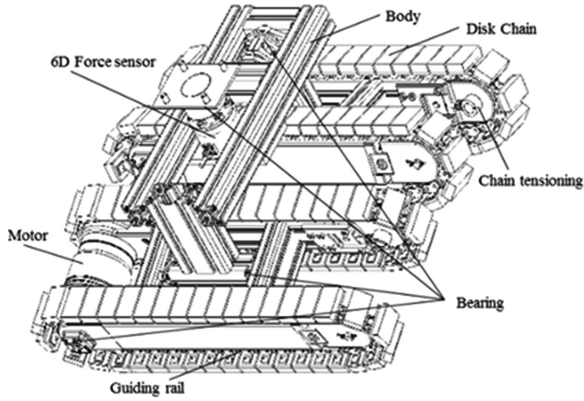
**Fig. 2.** Dual tracked drive of SMART robot
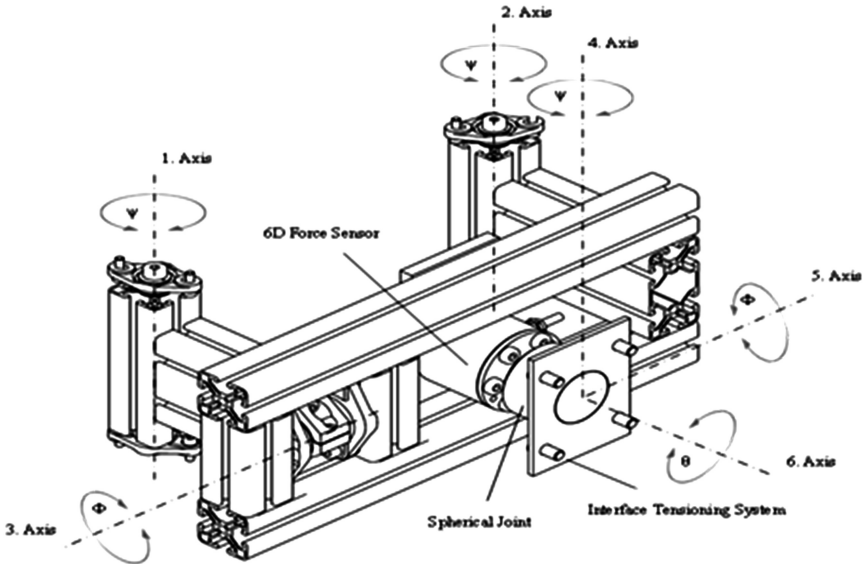


**Fig. 3.** Kinematic model of tracked drive chassis frame

drive motor, guiding rails, chain tensioning mechanism, body, bearings and a 6D force sensor.

Many wind turbine towers are conically shaped. Therefore a major requirement for the SMART robot is to continuously decrease the perimeter of the tensioning system, while climbing up. In addition, the attachment and suspension of the tracked drive must permit a pitch angle towards the tower axis around 5 to 15°. There are several other scenarios and circumstances that will require further degrees of freedom, e.g. skid-steering to climb horizontally.
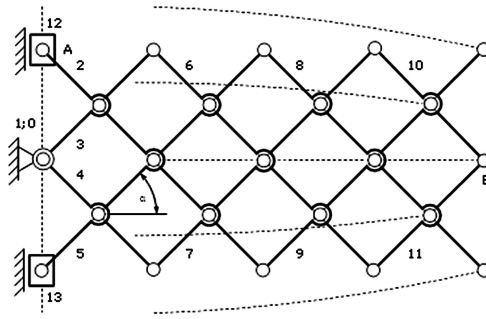
**Fig. 4.** Kinematic model of the tensioning system

In the following a kinematic model of the climbing robot will be explained, simulated and experimentally tested for scientific prove. Figure 3 illustrates the degrees of freedom of the current robot design that belong to the chassis frame of the tracks. Axis one and two are required to compensate different tower perimeters and to allow the tracks to contact the tower tangentially. Axis 3 is required for the relative pitching between two tracks during the steering process. The necessity will be underlined later with the virtual model in ADAMS ATV. Finally, the spherical ball joint (axis 4, 5, 6) is required to let the tracked drives move relative to the tensioning system. The interface to the tensioning system is mounted on top of a 6D force sensor to measure forces and torques induced by the robot movement. The kinematic model for the tensioning system, derived from the "Nurnberg Scissors" model, is displayed in 2D in Fig. 4.

The climbing robot consists of around 95 moving parts, 49 revolute joints, 6 screw joints, 5 spherical joints, 12 translational joints and 17 fixed joints.

## 1.2 System Dynamics of SMART Demonstrator

Similar to the experimental SMART demonstrator, shown in Fig. 1, a model is de-rived utilizing ADAMS (acronym of Automated Dynamic Analysis of Mechanical Systems). Current demands from use cases suggest that this device will have a mass of up to 5 tons, including payload and power supply. A strong commitment to composites could reduce the weight by 20%.

The virtual model (Fig. 5) possesses the same links, joints, masses and forces like the experimental model. The virtual model will be verified by the experimental demonstrator. The final goal of this process is to establish a valid virtual model to support upscaling into a one-to-one prototype. The prototype will be designed for a 2.5 MW wind turbine. More than 65% of the weight is distributed concentrically around the wind turbine tower axis as part of the power supply and the climbing mechanism. This will reduce the bending moment on the tower.

There are three different ways of power supply in the evaluation process: electric power cable to ground, on board generator, on board LiFePo4 batteries similar to electric cars. The most promising supply is based on batteries with a total weight of up

**Fig. 5.** Virtual SMART model (ADAMS ATV simulation)

to 400 kg in a worst-case scenario as part of the 5 tons total mass. The batteries and the BMS will be stored inside the tracked drives to support the weight distribution concept.

## 2   Model Based Kinematic and Dynamic Simulation

Essential for analysing the climbing process of SMART are static and dynamic loads (Fig. 6) in combination with a variety of different movements, so called scenarios. A standard scenario for a climbing robot is moving up and down. The movement path is described as a vertical path, parallel to the tower axis. Other scenarios consist of steering or rather horizontally climbing, described by a spiral path around the tower axis. Finally, steering on a conical shaped surface is analysed. The static forces shown in Fig. 6 are expected to change significantly during the steering processes. Subsequently to the dynamic simulation many results are shared with ANSYS Workbench, an FEM analysis tool, to optimize the design and the structure of the climbing robot.



**Fig. 6.** Static forces climbing robot SMART

**Table 1.** Steering towards left and right, "horizontally climbing"
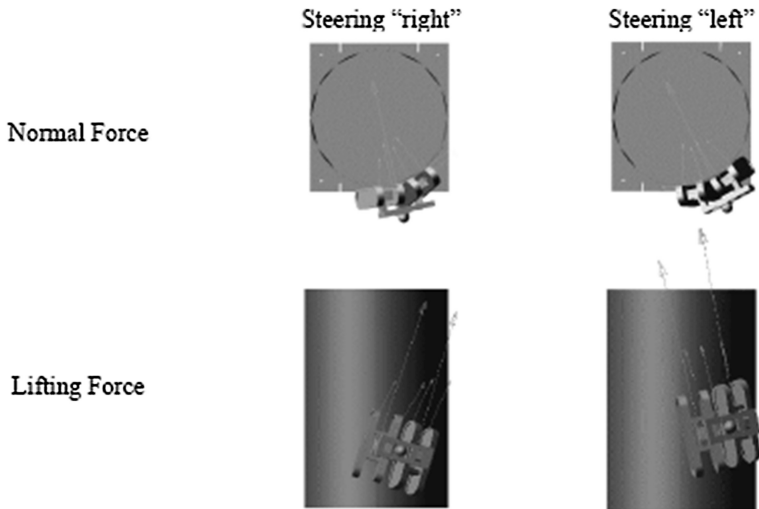


ADAMS Tracked Vehicle (ATV) supports the modelling of the climbing robot with a framework to simulate track drives. Table 1 illustrates two similar scenarios, steering towards right and left, regarding normal forces and lifting forces.

The ADAMS simulation shows that the forces are equally distributed between the tracks in both scenarios. The model offers the possibility to track all motions and forces of SMART virtually. To validate these results several sensors are integrated in the experimental demonstrator.

## 3 Experimental Analyses of SMART Demonstrator

A major goal of the experimental analyses is to validate the simulation and theoretical calculations of the climbing robot. The measurements are split into two parts: motion tracking and force acquisition.

### 3.1 Setting Up a 3D Vision System for Motion Tracking

The motion tracking is done by a 3D vision system. It is based on four high resolution cameras, which are used to detect specific landmarks attached to the SMART robot. The task of the tracking system is to identify the 6D pose of each individual landmark in relation to a fixed frame in space – the world frame. As a result the motion tracking system provides a punctual observation of the motion process of the SMART robot.

A Manta G609B camera offers Mono8 images with a resolution of $2752 \times 2206$ pixels at a maximum of 15 fps. The cameras are mounted around the SMART robot,
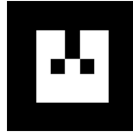
**Fig. 7.** Landmark for vision tracking [3]
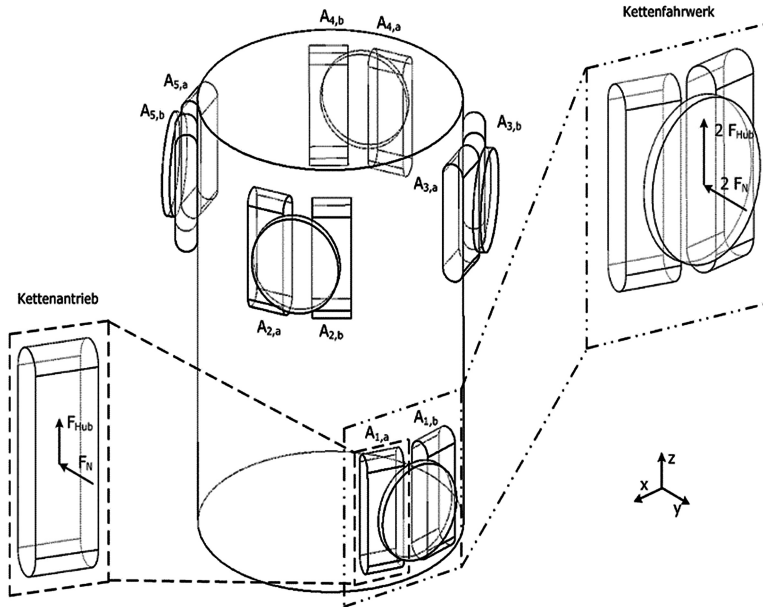


**Fig. 8.** System overview SMART robot

with individual distances to the robot greater than 3 m. Camera lenses with a focal length of 25 mm are used. As a result the ROI is covering the whole motion area of the robot. The identification of different landmarks is possible by a binary coding of the markers. Multiple landmarks are mounted at fixed positions of the SMART robot (Fig. 7).

The software ar_track_alvar of the Robot Operating System ROS includes an open source AR tag tracking library. It is used to determine the 6D poses of the landmarks in relation to the world frame of the camera. The software camera_calibration is used to provide the parameters of the camera system.

The determination of the 6D pose of a landmark with reference to the world frame depends on the 6D pose of the specific camera system in relation to the world frame. The software tf of the Robot Operating System is used to calculate these trans-formations. In addition, a gyroscope is added to each track drive to validate the tilt angles while steering.

## 3.2  Force Sensors

The SMART demonstrator consists of five similar drives distributed over the tower surface (Fig. 8). The z-axis of the coordinate frame is parallel to the tower axis and is pointing upwards. The Y-axis points in radial direction of the tower towards drive A1. In each drive, A1 to A5, a 6D force sensor, K6D68 10kN/500Nm from ME-Systems, is implemented to measure Fx, Fy, Fz, Rx, Ry and Rz. This customized sensor can measure loads of up to 20 kN in z direction. In the current design a ball joint is mounted on top of the 6D sensor. Therefore, the torques are currently not significant. In addition to the 6D force sensors 10 strain gauges are installed in the tensioning system to measure the stress during the climbing process. The feedback from the Harmonic Drive motors delivers absolute position, torque, acceleration and velocity. In fact, the multiturn absolute encoder feedback is not relevant at this point, because there is still slip between the drives and the tower surface.

The following test results display the current state of development. An advanced controller is currently established to reduce slip and unbalanced forces for the track drives.

## 4  Results

The data is generated during a standard climbing scenario test run. The SMART demonstrator climbs 0.6 m up and down in around 52 s.

All drives are controlled manually and started at the same time (Fig. 9). The real-time controller is disabled to show the effects of non-linear force distribution. The velocity profile characteristics are: 5% from 7.5 s to 22.5 s, 15% from 22.5 s to 42.5 s, 5% from 42.5 s to 55.0 s.

Figure 10 displays the forces Fx, Fy and Fz for all drives. In addition, a 1D force sensor is measuring the force between the tensioning system and the vertical connection to drive A1 (FzA1). This force reflects the share of the lifting-force that is generated by drive A4 and A5 on the other side of the tower. This force should be the
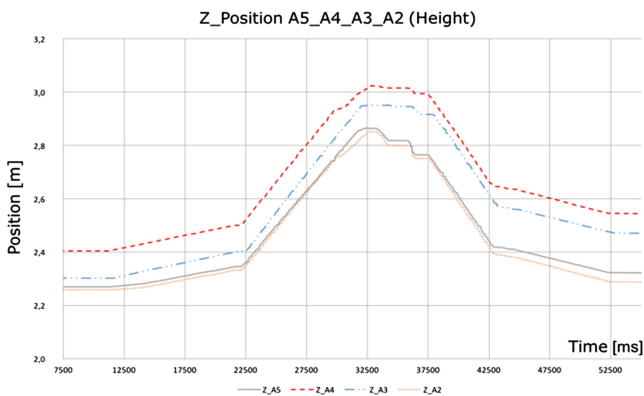


**Fig. 9.** Motion tracking of SMART demonstrator
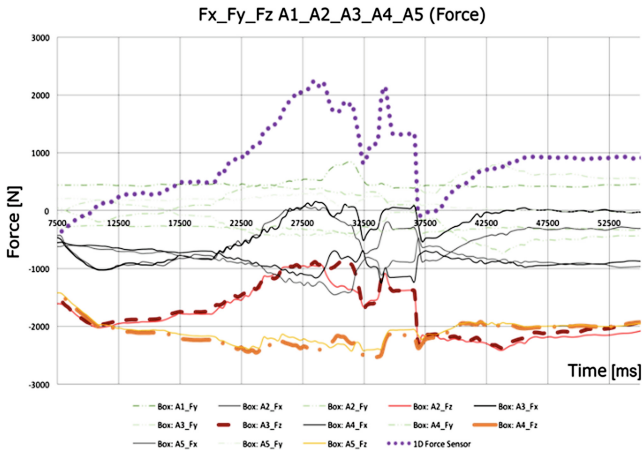
**Fig. 10.** Force measurements of SMART demonstrator

same for all drives climbing at the same speed. When all front drives A1, A2 and A3, are generate slip – the 1D forces FzAn raises. The critical point is reached at 27.5 s. The height difference of all drives need to be compensated thus resulting in a different force distribution.

## 5    Conclusion and Future Aspects

The SMART demonstrator concept is able to climb vertically based on friction between the tracked vehicle rubber parts and the tower surface. The results from the tracking system are similar to the movement in ADAMS ATV. Results from the force sensor – without the force feedback controller – differ significantly from the expected values generated by the dynamic simulation.

This specific test run shows the necessity for advanced model based control [4]. To generate an equally distributed force over all drives, each motor speed needs to be accurately controlled. The feedback loop actuator consists of the speed control of the motors from the tracked vehicles as well as the motors from the tensioning system.

Pressure sensors are currently implemented on top of the rubber-chain-parts of the tracked vehicle to validate the surface pressure between the tower and the tracked drives.

Subsequently it will be possible to investigate the steering process for further improvement of the SMART kinematics. The validation of the analytical model of the SMART by experimental data will allow the future upscaling of the robot system.

The SMART prototype is designed for wind turbines of up to 2.5 MW in the test phase. Therefore the maximum distance between the tower and the rotor blade is around 12 m. Current FEM analyses [5] and some tests on the 1:3 climbing robot demonstrator allowed lifting a 140 kg payload, corresponding to a payload of around 500 kg for the 1:1 prototype. The demonstrator presented in the paper is able to carry

the load at the end of the cabin arms and has not yet reached its limit. The cabin arms are based on a multiple triangle framework that supports guide rails for the cabin movement. Both cabin arms are connected to each other in order to compensate torque. The cabin structure is lightweight and made of composites. Therefore all forces generated by the rotor blade movement or coming from the working platform inside are guided directly into to cabin arms. The cabin structure will absorb the wind forces and its own weight.

# References

1. Global Wind Energy Council (GWEC): Global Wind Statistics 2015 (2015). http://www.gwec.net
2. Deutsche Windtechnik: On- and Offshore Services. http://www.deutsche-windtechnik.de
3. Quigley, M., Conley, K., Gerkey, B., Faust, J., Foote, T., Leibs, J., Wheeler, R., Ng, A.: ROS: an open-source robot operating system. In: ICRA Workshop on Open Source Software (2009)
4. Chitta, S., Sucan, I., Cousins, S.: MoveIt! IEEE Robot. Autom. Mag. **19**(1), 18–19 (2012)
5. Kallweit, S., Dahmann P., Bagheri, M., Schleupen, J., Engemann, H.: Entwicklung eines Kletterroboters zur Diagnose und Instandsetzung von Windenergieanlagen. In: 13th AALE Conference (2016)

# Optimized Leg Proportion to Enhance Rough Terrain Mobility of a Biomimetic Walking Robot

Florian Winter[1]([✉]), Stefan Landkammer[1], Rüdiger Hornfeck[1], Peter Heß[1], and Kristin Paetzold[2]

[1] Technische Hochschule Nürnberg, 3D-Visualisierungszentrum, Nuremberg, Germany
florian.winter@th-nuernberg.de
[2] Institut Für Technische Produktentwicklung, Universität der Bundeswehr München, Neubiberg, Germany

**Abstract.** A new approach on the optimization of leg proportions for a biomimetic walking robot is presented in this paper. The main focus is on optimizing robot leg proportions through evaluation of different parameters. These include the workspace volume, circular and spherical radius of movement and the angular variation at the leg endpoint with predefined workspaces of the joints in compliance to biological analogies. Therefore mathematical dependencies are considered separately and finally combined to one value indicating the performance level.

**Keywords:** Walking robot · Limb proportion · Optimization · Radius of movement · Rough terrain robotics

## 1 Introduction

Development of a walking robot for tasks in emergency situations or natural catastrophes demands a high all terrain capability and high energy efficiency. A joint optimized for this use case, which incorporates these features, was developed [1]. For this patented antagonistic hinge joint [2] a static mathematical model also exists [3]. The main advantage of this joint is its inherent variable stiffness. Compared to joints driven by electric motors, an improved energy efficiency is expected.

For maximum manoeuvrability on rough terrain, the legs must have sufficient degrees of freedom (DOF) and correspondingly proportioned limbs. Since the maximum angle of rotation of the bionic joint is specified, the optimization is carried out primarily by determining the limb proportions for one robot leg.

### 1.1 Biology

Due to biological investigations [4–7] analysing the biomechanical properties, the leg of the wandering spider Cupiennius is defined by 12 DOF and 7 leg limbs. For forward and backward leg movement, the wandering spider Cupiennius

has, according to Ehlers [8], 5 joints with angular ranges from 15° to 70°. To realize upward and downward movement, the spider has 7 joints with angular movements from 20° to 160°.

Biomechanical studies on the locomotion of spiders [8,9] and approaches on the kinematic behaviour [10,11] show that the locomotion is mainly realized by only four joints. Therefore, spider-inspired robots should be equipped with this number of joints. Three joints are used for up- and downward motion and one for the forward and backward movement.

## 1.2    Optimization of Robot Arms

In Fig. 1 an abstract model of a robot arm is shown in the cylindrical coordinate system. The $z$-axis value defines the height of the leg end point or describes a level on a specific height. The joint at the origin has two DOF, which are used for rotation around the z-axis ($\varphi$) and for adjusting the angle $\alpha_1$. The other two joints only have a rotational DOF for adjusting the angle $\alpha_2$ and $\alpha_3$. The axes of the joints $\alpha_1$, $\alpha_2$ and $\alpha_3$ are parallel and their relative positions are given by the length of the limbs $l_1, l_2$ and $l_3$.
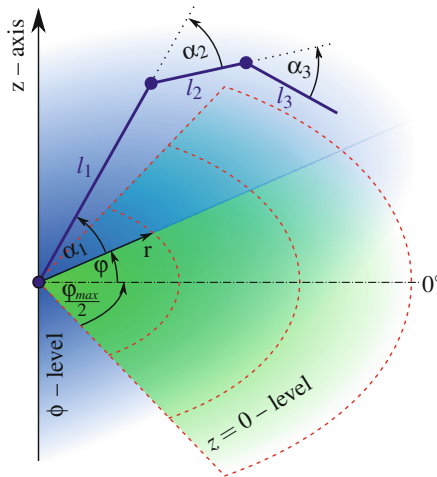


**Fig. 1.** Abstract model of the three limbs robot leg in a cylindrical coordinate system.

In 1985, Tsuneo Yoshikawa [12] researched optimization of robot arms. His paper discusses the manipulating ability of robotic mechanisms in positioning and orientating end-effectors and proposes a measure of manipulability.

A robotic arm with two links ($l_1, l_2$) and two rotary joints ($\alpha_1$, $\alpha_2$) is identified as the best robot working link constellation and the maximum manipulability index at the following constellation. The two links should have the same length ($l_1 = l_2$) and form an angle of $\alpha_2 = 90°$ in the initial position. The angle

$\alpha_1$ can take any value and does not affect the manipulability index. According to Yoshikawa this constellation can also be found in the human being. The human upper arm and forearm are about the same length and the included angle in working position usually is 90°.

This possibility of optimization was also used by Roennau [13] to optimize the walking robot Lauron. Thus, the optimum angle for a walking robot in regard to the manipulability index was found. However, this method of optimization does not consider limitations of the joint's angular range. Therefore, other means to optimize robot leg geometry for rough terrain deployment, using joints with given angular ranges and variable limb lengths, will be discussed in the next chapter.

## 2   Optimization Methods

To increase the efficiency of walking robots regarding functionality, lightweight design and energy consumption, it is necessary to optimize all components in regard to their requirements and limitations. In the following, mathematical approaches based on geometric dependencies of the spider leg design are presented for optimization of the robot locomotion.

In order to validate the results of this method for all robot sizes, proportions are considered instead of absolute measurements for one specific case. This is ensured by scaling the sum of all limb lengths for each investigated combination to the mathematical value of 1.

Because of the biomimetic joint drives, the actuators have a limited pivot angle. The operating range for the biomimetic joints ($\alpha_2$ and $\alpha_3$) amounts from 0° to 70°. The universal joint ($\varphi$ and $\alpha_1$) that connects the robot leg with the torso, is to be driven by two conventional electric motors with an angular range of −60° to 60°. By defining the angular ranges the robot can straighten the leg completely and thereby exploit the maximum range.

To optimize limb lengths, individual limb length variations are used in the following sections. It is analysed how the leg proportions affect properties such as the maximum volume, distribution of the working areas, moving circle or sphere radius and the remaining angular variation at the leg end point.

### 2.1   Volume Optimization

An obvious optimization is to maximize the volume of the leg workspace. The bigger the volume, the more endpoint positions can be reached by the robot leg from only one stance. Calculation of the volume $V$ can be simplified by definite integration using a cylindrical coordinate system.

$$V = \sum_{n=1}^{m} \int_{z_{\min}}^{z_{\max}} \int_{\varphi_{\min}}^{\varphi_{\max}} \int_{r_{\min}}^{r_{\max}} r_n(z)\, \mathrm{d}r\, \mathrm{d}\varphi\, \mathrm{d}z \qquad (1)$$
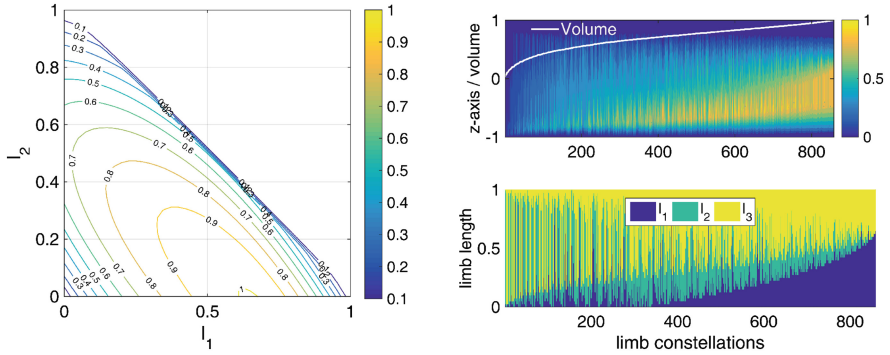
**Fig. 2.** Working volume of the robot leg with different leg lengths $l_3 = 1 - l_1 - l_2$ (*left*). Work surface as a function of height above the considered leg proportions (*right*).

In the left part of Fig. 2 the achievable volume of work is represented by contour lines. From the contour lines it can be seen that leg length proportions in the range of ($l_1 \approx 0.65$; $l_2 \approx 0$; $l_3 \approx 0.35$) provide the best results in terms of volume maximization. Striking here is the fact that the maximum is reached with a leg in which the axes of the joints $\alpha_2$ and $\alpha_3$ are superimposed. This means that two joints act as one joint with the combined angular range of both individual joints. This constellation is known as a two-limb robot leg with a double rotation angle maximum.

## 2.2    Area Optimization

To enable a fast movement of the mobile robot on ground level, the step size must be at maximum. Considering only the potential regardless of the direction, the surface at the appropriate height (in $z$-axis) may be used as a an optimization target. The area $A(z)$ can be calculated by a definite integral.

The right part of Fig. 2 shows the surface profile on the $z$-axis and the respective working volume. The sorting of the leg constellation is done here by ascending total volume. It is also apparent that the height ratios $z \in [-0.5, 0]$ have the largest areas and this therefore highlights the main application area for fast movement.

The disadvantage of this approach is the fact that the area in the tread surface assumes the form of one or two circular sectors in this leg kinematics. But as the desired leg movement doesn't necessarily utilize the entire room, this optimization can be further refined.

## 2.3    Circular Radius of Movement

The work area on a predefined height is a critical feature for a pick and place robot, but not for a walking one. Therefore a large but connected work area is particularly advantageous. This enables a good off-road capability. These two

parameters can be significantly compressed by a radius which describes a circle or a sphere. This radius depends on given proportions and leg joint angles only by the height of the leg end point.

If the walking robot is used for locomotion on a flat surface, the largest possible range of motion on this level would be desirable. If we define a circular area, it can be ensured that the movement doesn't depend on its direction, provided that the starting point of the movement is in the centre of the circle.

The dependence of the radius on the height $z$ of the leg's end point and the leg proportions are shown in Fig. 3 left. The absolute value of the radius refers to the total length of the three leg limbs and reaches a maximum of about 40%. Accordingly the leg end point can reach a circular area with a diameter of up to 80% of the total leg length in the height ranges from $z \in [-0.5, -0.3]$. This maximum value is achieved at the limb length proportions of $l_1 \approx 0.525$, $l_2 \approx 0$ and $l_3 \approx 0.475$.
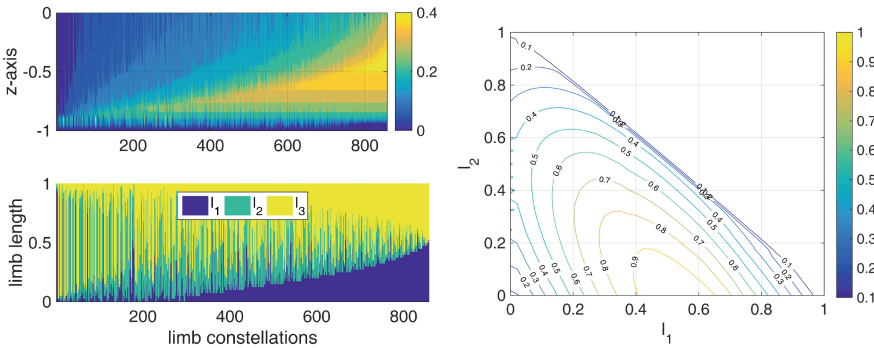


**Fig. 3.** Radii of the moving circle depending on the leg proportions and the height of the leg endpoint (*left*). Dependence of the normalized circle radii sum of the leg proportions (*right*).

The contour lines in Fig. 3 right represent the normalized sum $R_{\text{circle,sum}}$ of the individual radii. This summation is to embody the potential of the constellation. Geometrically, the sum of the areas defines a value which is proportional to the volume of a cylinder with varying diameter.

### 2.4 Spherical Radius of Movement

To optimize the geometry of a robot leg for use in rough-terrain appliances, the third dimension should be considered as well. In order to provide sufficient mobility, a spherical movement range can be defined which only depends on the height $z$ of the leg's endpoint. A larger radius results in an increased range of movement. Figure 4 shows the spherical radii of all leg proportions.

The right part of Fig. 4 shows the correlation of spherical radius and range of movement through summation of all individual radii. This has no geometrical
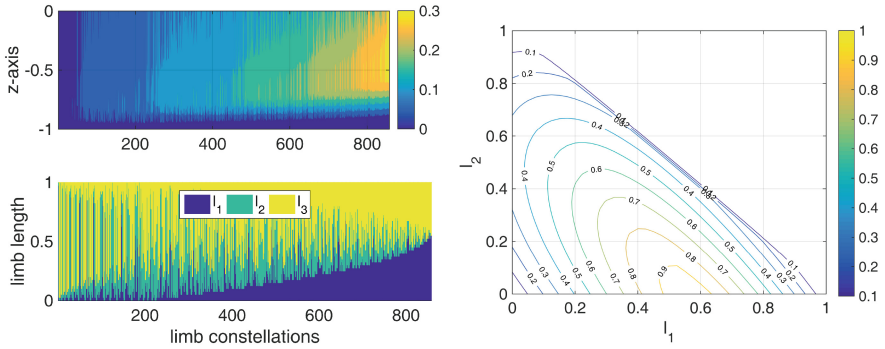
**Fig. 4.** Radii of the movement sphere relative to the leg proportions and the height of the leg endpoint (left). Dependence of the normalized sphere radii sum on the leg lengths $l_1$ and $l_2$ (right).

implications, but it provides an overview over different variants. The sum of the radii $R_{sphere,sum}(z, l_n, \alpha_n, \varphi)$ can be used as quality criterion whose amount does not provide an absolute statement and is therefore normalized. A greater range of movement is achieved through an increased radii sum.

$$R_{\text{sphere,sum}}(z, l, \alpha, \varphi) = \sum_{i=1}^{m} R_{\text{sphere}}(z_i, l, \alpha, \varphi); \text{ with } z = (z_1, z_2, \ldots, z_m) \quad (2)$$

### 2.5 Angular Variation at Leg Endpoint

If the robot legs are not only used for locomotion, but also to interact with the environment, the variation of the angle at the target point can be used as a optimization target. As shown in Fig. 5, the optimum shifts towards the shortest possible length for limb $l_3$ ($l_3 > 0$). The summation of all calculated variation
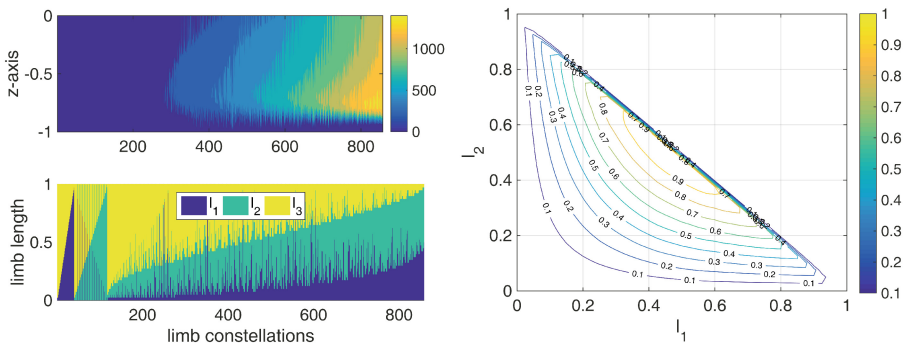


**Fig. 5.** Summarized angular variation per level depending on the leg proportions (*left*). Depending on the overall angular variation sum of the leg limb lengths (*right*)

angles will also produce one representative value. This normalized variation value $\zeta_{\text{variation}}$ is presented in the right side of Fig. 5.

## 2.6    Performance Level Optimization

The normalized representation of the relevant criteria in a three dimensional plot shows which proportions meet the individual requirements best. Request-specific representations can be generated by a weighting of the individual criteria. The performance level $P$ of these requirements will be depicted as a percentage.

$$P(l_1, l_2, l_3) = \begin{pmatrix} p_{\text{volume}} & p_{\text{circle}} & p_{\text{sphere}} & p_{\text{variation}} \end{pmatrix} \cdot \begin{pmatrix} V \\ R_{\text{circle,sum}} \\ R_{\text{sphere,sum}} \\ \zeta_{\text{variation}} \end{pmatrix} \tag{3}$$

For example, if the robot leg shall have a large working volume (priority $p_{\text{volume}} = 0.3$), a large sphere movement radius ($p_{\text{sphere}} = 0.5$) and an angular variation ($p_{\text{variation}} = 0.2$), the degree of performance $P$ for this request, as a function of the limb lengths, is presented graphically in Fig. 6.
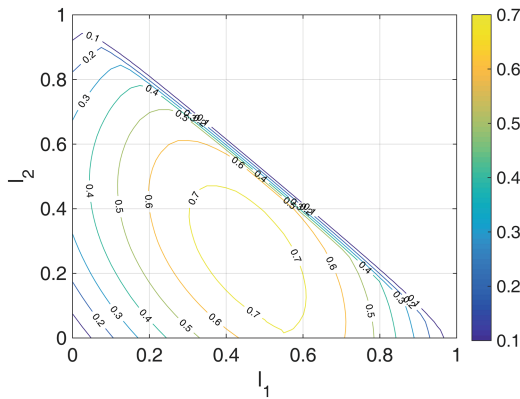


**Fig. 6.** Degree of performance of the requirements for a high volume, large sphere of movement radius and an angular variation.

## 3    Conclusion

In this study, a process to enhance rough terrain mobility of a biomimetic walking robot through optimization of its leg proportions is presented. The optimization of the workspace volume was analysed, with the result that the limb length $l_2$ should be minimal. For a walking robot only treading on a flat surface, the movement area in dependence of its height, could be a measure for the manoeuvrability. For a convenient and reliable programming of the robot's locomotion,

a circular area could provide a workspace which is independent of the moving direction and reduce the calculation workload. Thus, the optimization can be used to maximize the circular radius of a specific height. The circular radius is especially useful for flat surfaces, whereas the spherical radius can be used for more challenging terrain. For further optimization, a similar process, which additionally considers the angular variance between leg endpoint and target surface, could be devised.

The summation and normalization of all calculated values is used for comparison. Depending on the use case, corresponding weightings $p$ of the individual optimization strategies are reasonable. For the shown priority assignment in Fig. 6, the best leg limb length are around $l_1 \approx 0.45$, $l_2 \approx 0.25$ and $l_3 \approx 0.3$.

# References

1. Landkammer, S., Hornfeck, R.: A novel bio-inspired fluidic actuator for robotic applications. In: ICAST2014 - International Conference for Adaptive Structures and Technologies, The Hague (2014)
2. Landkammer, S., Hornfeck, R.: Drehantrieb, German patent application: 20.12.2013, Reference number: DE 10, R.: 114 660 A1. Technische Hochschule Nürnberg Georg Simon Ohm, Applicant (2013)
3. Landkammer, S., Schneider, D., Winter, F., Heß, P., Hornfeck, R.: Static modeling of a antagonistic pneumatic actuator for robotic applications. In: 12th ECMSM IEEE. Libèrec (2015)
4. Parry, A.: Spider Leg-muscles and the autotomy mechanism. Quartely J. Microscopical Sci. **98**, part 3, 331–340 (1957)
5. Schultz, J.: Evolution of locomotion in anarchida: the hydraulic pressure pump of the giant whipscorpion. J. Morphol. **210**, 13–31 (1991)
6. Foelix, R.F.: Biology of Spiders. Oxford University Press, New York (2011)
7. Sens, J.: Funktionelle Anatomie und Biomechanik der Laufbeine einer Vogelspinne (Grammostola spatulata F.O. Pickard-Cambridge). Universität des Saarlandes (2006)
8. Ehlers, M.: Untersuchungen über Formen aktiver Lokomotion bei Spinnen. Zoologische Jahrbücher, pp. 373–497 (1939)
9. Biancardi, C.M., Fabrica, C.G., Polero, P., Loss, J.F., Minetti, A.E.: Biomechanics of octopedal locomotion: kinematic and kinetic analysis of the spider grammostola mollicoma. J. Exp. Biol. **214**, 3433–3442 (2011)
10. Vidoni, R., Gasparetto, A.: Efficient force distribution and leg posture for a bio-inspired spider robot. Robot. Auton. Syst. **59**, 142–150 (2011)
11. Weihmann, T., Karner, M., Full, R.J., Blickhan, R.: Jumping kinematics in the wandering spider cupiennius salei. J. Comp. Physiol. **196**, 421–438 (2010)
12. Yoshikawa, T.: Manipulability of robotic mechanisms. Int. J. Robot. Res. **4**, 3–9 (1985)
13. Roennau, A., Heppner, G., Pfotzer, L., Dillmann, R.: LAURON V: optimized leg configuration for the design of a bio-inspired walking robot. In: 16th International Conference on Climbing and Walking Robots, p. 563–570 (2013)

# Orientation and Depth Control in Rippling Water for an Autonomous Underwater Robot

Roland Dóczi[1,2(✉)], Bence Takács[2], Balász Sütő[1,2],
Tamás Haidegger[2], Miklos Kozlovszky[1], and József K. Tar[2]

[1] BioTech Research Center, Obuda University, Budapest, Hungary
roland.doczi@irob.uni-obuda.hu,
suto.balazs@biotech.uni-obuda.hu,
kozlovszky.miklos@nik.uni-obuda.hu
[2] Antal Bejczy Center for Intelligent Robotics,
Obuda University, Budapest, Hungary
{bence.takacs,haidegger}@irob.uni-obuda.hu,
tar.jozsef@nik.uni-obuda.hu

**Abstract.** This paper describes an algorithmic solution for simple and efficient underwater orientation and depth control. Maintaining a position with an underwater robot is a difficult task. In the case of an Autonomous Underwater Vehicles (AUVs), not only the underwater conditions, but also the environmental effects off the surface need to be considered. There is a large number of algorithms have been designed by researchers based on computer vision, sensor fusion, etc. to estimate the location precisely, yet most of them are specific for the given hardware. Our solution employs a multi-sensor fusion based algorithm, where the data is taken from magnetic and pressure sensors. A PID controller was designed and implemented to ensure proper orientation keeping and depth control in rippling water. The solution has been tested in various environments, and successfully used during the marine challenges of the euRathlon 2015 competition.

**Keywords:** Autonomous underwater vehicle · AUV depth control · Response robotics · Underwater navigation

## 1 Introduction

One of the main challenges of (underwater) robotics is how an autonomous robot can adapt to the environment, identify and localize themself. For example, an underwater current or drift can easily relocate an AUV in the water. To design a solution for position keeping problems, one should reckon with not only the underwater conditions, but also the interactions above the water. Potentially useful sensory input includes any measurable data indicating the stream, the wind speed or drifts. With a proper sensor-fusion algorithm and adjoin process control, an AUV is able to keep its position and depth. Our aim was to design a controller that can stabilize a specific AUV, even under extreme conditions. There are numerous types of sensors, such as gyroscope,

camera, accelerometer, pressure sensor etc. that can be employed for underwater applications.

## 2  Control Problems

There are several ways to control an underwater vehicle [1]. During a field mission, an AUV would encounter interactions such as drifts, buoyancy forces or streams. Many of these are unknown, with non-linear [2] effects, so they cannot be included directly in the motion equations. However, these forces take effect on the AUV and influence its motion.

Magnetic sensors are susceptible to external magnetic fields, such as the one generated by the thrusters. Furthermore, these magnetic fields can interfere with the communication link between other electrical components. To avoid this, the electrical parts - which are able to disrupt the communication during a mission - must be insulated from other parts. AUVs are specifically crowded devices (regarding their interiors), so electronic measurement systems should be shielded and designed properly to keep the measurement error between known intervals and minimalize them as much as it possible.

Measurements, simulations or approximation methods should be used in order to add the unknown forces with non-linear effects to the motions equations. One of the most popular controller systems used by industry and academia is the historical PID controller, which can be adequate for this solution as well, where a proper depth and orientation keeping is presented with error minimization regarding the measurement errors of the sensors.

### 2.1  PID Control

The PID controller is a closed loop controller. It consists of three main elements: P (proportional), I (integral) and D (derivative). A PID controller deals with cumulated errors, which are derived from the difference of the system's measured output value from a predefined setpoint. It is a linear controller; however, the underwater systems are non-linear because of the non-linear effects that can influence them.

For example, the buoyancy effect is always acting back to the AUV, but on the other hand, there could be different kind of underwater streams which are not always linear. In order to design a linear controller for a non-linear system, a feedback linearization approach can be used. In this case, the input or the output of the controller system should be transformed to make it linear. A common approach to solve this is feedback linearization, or the use of adaptive process controllers.

All three PID parameters have a significant influence on the system. With a high P value, the control system will be fast, but on the other hand, an extremely high parameter selection will lead to instability or oscillation. With I term added, faster error elimination can be reached, but meanwhile, there will be larger overshoots. A larger D parameter will decrease the overshoot, otherwise slows the response of the system.

Both underwater depth and orientation keeping should be described as a linear system.

## 2.2    Adaptive Process Control

During an underwater mission in rippling water, an AUV can become under- or over actuated. If the parameters of a control system are configured well for one particular environment, they may not work properly in a different one. This means that if a depth control problem is solved in calm water, there is only a small chance that it will work in rippling water as well. Furthermore, the salinity of the freshwater and sea water is different, which can cause larger resistance and a different buoyancy effect to the AUV. In order to implement a controller which is able to deal with the rippling water, an adaptive process controller or a feedback linearization method can be a suitable approach. The adaptivity means that the P, I or D parameters are changing relatively to the error during runtime. In case of the depth keeping the mentioned value is the output of the pressure sensor, and as for the orientation keeping, that is the output of the compass sensor.

The adaptive process control is a good approach to control a non-linear system with a linear PID controller. It keeps changing the parameters of the controller relatively to a function. This function can be a much more complex method, such as a quadratic- or a cube root function, or a fuzzy system. A simple approach is to use a quadratic ramp function for adjusting the control parameters. The input of the process controller should be separated into smaller sections after the measuring, so a single value can represent a group of values. With a quadratic function a process controlling can be achieved, wherein the output will be larger if the system is far from the setpoint, otherwise it will be close to zero. This can minimalize the disturbing effect of the streams, which occurs randomly and may influence the position keeping of an AUV.

## 2.3    Underwater Position Keeping

Position keeping is a process which is used to enable an underwater vehicle to keep orientation (separated to roll, pitch, yaw) and depth, based on sensors and actuators. The position keeping can be separated into orientation and depth keeping. Both of them are supposed to be kept relative to a baseline. The base value can be the magnetic North (for orientation) and the output of the pressure sensor (for depth), or an initiated value which is set when the system starts, such as an Inertial Measurement Unit (IMU). When employing an IMU, the system must reckon with the inaccuracy of the measurement, because usually these values should be filtered.

A compass sensor should be used in order to solve the orientation keeping problem in one degree of freedom; furthermore, a gyroscope module is needed in order to compensate the error during the measurement. On the other hand, in the case of the depth keeping, a pressure sensor can be used, combined with another sensor, to increase its effectiveness. A variety of algorithms can be used to filter the acquired

signals for more precise measurement, such as an adaptive, median filter, extended Kalman filter [8].

## 3 AUV System Components

Nowadays, modularity is in the focus on robot control solutions. This means that the source code of a program is not only one large code or a state machine. In modular software, functions which deal with a different problem (for example, during data collecting, usually a filter must be applied that needs several functions) should formulate a different component. For example, measuring, controlling, or filtering functions should be in different software components.

### 3.1 Software

The Robot Operating System (ROS) [4] is a widely known, modular, open source framework, with a message passing interface. The main elements of the ROS are the nodes. A node is a program which communicates through a ROS master component with other nodes. The ROS master gives the parameter server, the naming and the registration services to the nodes. The nodes are able to communicate in two ways; through a topic or through a service. A topic is a broadcast message (open communication for nodes that are in same ROS network), the service is a point-to-point connection (secured communication for alarm, and secured data exchanging). A node needs to be subscribed for a topic in order to listen to its communications. If a node would like to publish to a topic, it should not be subscribed to it. For example if a node needs pressure sensor data, it should subscribe for a topic that provides this data by a publisher node. The publisher node releases the measured values and other parameters, such as a time stamp, ID etc., to the topic. With this solution, separated communication interfaces can be defined. However, there is no security solutions implemented for the publishing or subscribing process. This means that each node can subscribe or publish to a topic without any authentication or authorization process.

One of the key features of ROS is that it supports several programming languages (Java, C++, Python, LUA, etc.), and because of the message passing interface, different language codes can smoothly communicate with each other. There are available tools for testing, or visualizing measurement values, for example the rqt_plot for 2D data visualization, or the rViz for 3D visualization [7]. The ROS proved to be a proper framework to implement and test codes, furthermore, the available hardware uses ROS interface too.

### 3.2 Hardware

The hardware that was available for testing these functions was a Sparus II AUV [3] which was developed by the University of Girona, Center for Maritime Research (CMRE). It is a torpedo-shaped AUV, with a mass of 52 kg and a length of 160 cm. Because of its shape, it has proper hydrodynamic characteristic, and is ideal for distant,

underwater operations. There are 3 thrusters mounted on it: one of them is on the centre of gravitation of the hull (can be used for depth control), and two others at the end of the hull lengthwise (for movement). Because of its length and the two lengthwise thrusters, the Sparus II is not able to turn in one place, which could be a problem during operation in narrow places. To support the on-board computations, the Sparus II is equipped with an Intel i7 processor, 4 GB of RAM and 250 GB SSD storage, and is powered by a 1.5 kWh battery (providing up to 8 h autonomous navigation). Ubuntu 14.04 Trusty Tahr is installed on the device with ROS hydro distribution. There is another software element developed by the manufacturers and installed on the Sparus II; the COLA2 (Component Oriented Layer-based Architecture for Autonomy) framework, which is developed as a part of ROS provides implemented functions to get data from the built-on sensors and manipulate the actuators or configure them.

Due to the location of the thrusters, the Sparus II cannot be controlled in pitch and roll axes. The passive ballast is located at the bottom of the AUV, not far from the centre of gravity. This means that it is not allowed to control the roll direction. The manual balancing of the hull was needed before launching, so its effect on the pitch could be mitigated.

## 4  Structure of the Solution

To solve the orientation and depth keeping problem, built-in compass and pressure sensors were used. These sensors are validated by the manufacturer of the Sparus II AUV.

There are predefined COLA2-based topics in the ROS environment, where data from these sensors are published. The orientation and the depth keeping can be separated and behaving independently from each other and each can be handled as 1–1 degree of freedom (DOF).

To tune the P, I and D controller parameters properly, the Ziegler–Nichols method was used. This is a classical, empirical PID design method where the step response of the system is not necessary to be known. The steps are the following: convert the PID controller into a simple P controller by eliminating I and D parameters, or setting them to 0, then turn the Kc (P) parameter up until the response of the system is in a sustained periodic oscillation in the output. Store the Ku (gain) value, the Pu (period time of the oscillation). Then adjust I and D parameters as the Ziegler–Nichols tuning chart recommends (Table 1).

**Table 1.** Ziegler–Nichols tuning chart

| P | I | D |
|---|---|---|
| $K_u/1.7$ | $P_u/2$ | $P_u/8$ |

We tested this controller in a computer simulation environment, with satisfying outcome, as presented in Fig. 2.
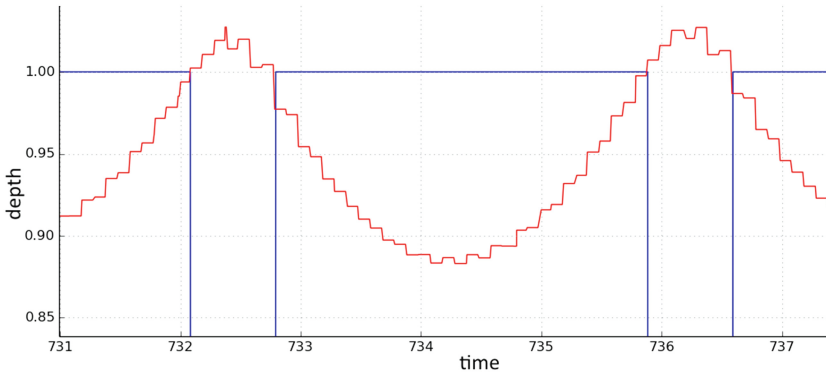
**Fig. 1.** Measuring the $K_u$ and $P_u$ values in the oscillated system. The red lines show the actual depth of the Sparus II AUV, and the blue represents the control value. The horizontal axis is the elapsed time in seconds, and the vertical axis is the actual depth in meters.

To solve for an adaptive controller, I and D parameters should be changed. By modifying I and D values, the controller can be fine-tuned. The windup can be a problem during tuning the control parameters. This issue occurs when the output of the control system cannot influence the controlled characteristic. This can happen when there is a large positive change in the setpoint. To avoid this, the setpoint should be increased along a ramp function, or the integral term should be disabled until the actual state of the system is not in a controllable region.

### 4.1   Orientation Keeping

To keep the orientation, the Sparus' built-in compass sensor combined with a PID controller was used. The input of the controller was the measured orientation value from the compass sensor, with regard to the magnetic North. The output of the control system should be a value between −1 and 1, because the COLA2 provides a topic where the control can be solved, and it accepts only a value between the aforementioned intervals. Depending on the lateral direction of the target regarding to the AUV, the thrusters can be controlled with opposite signs of the control system output. This means that if the setpoint is defined as −90°, so it is to the right from the hull, the output will be sent to the left thruster, and the negated value of the output will be the input of the right thruster.

### 4.2   Depth Keeping

In the case of depth keeping, the built-in pressure sensor and an adaptive PID controller were used. The input of the controller is the depth value, which is calculated from the pressure sensor and provided by the COLA2 framework through a ROS topic. The output of the control system is a value between −1 and 1 as it was mentioned in Sect. 4.1.

## 5    Experiments

The methods have been tested in four different test environments. Initial experiments were done in software simulation (provided by the ROS and COLA2), then the hardware was tested in a pool (of limited size), followed by a freshwater lake test, while the final testing was conducted on the two marine sections of the euRathlon 2015 competition (www.eurathlon.eu).

### 5.1    Simulator

The simulation environment [5] was the UWsim (Underwater Simulator) scenario, provided by the COLA2 framework, and developed for testing AUV solutions and implementations. In this environment the parameters of the controller can be reconfigured and tested before a field mission. The environment has adjustable hydrodynamic parameters. This means that for example, if an AUV has a movement speed and intends to do a 90° right turn, the AUV will drift during the turning process. The density, the drift or the stream of the water can all be configured before starting the simulator.

During the simulation, one of the built-in functions of ROS has been used to record measurement data for the offline process (rosbag). In Fig. 1, the adaptive PID control solution can be seen. In this case the setpoint of the control system is 1.0.
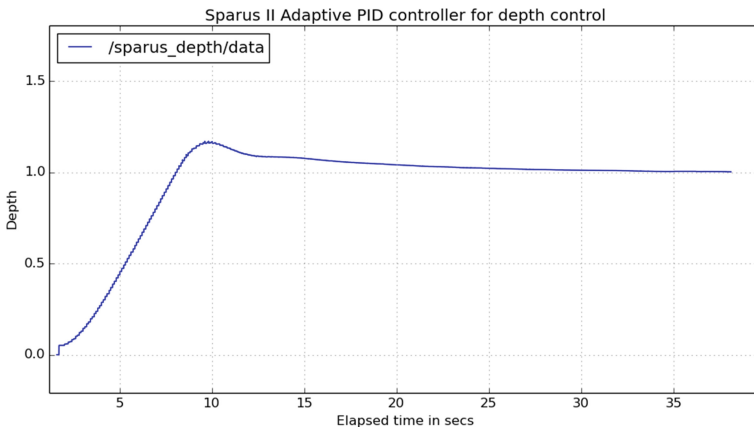


**Fig. 2.** The adaptive PID depth control solution plotted in UWSIM with rqt_plot, when the setpoint was 1 m depth. The vertical axis is depth in meters and the horizontal axis is time in seconds.

### 5.2    Test Scenario 1: Pool (Freshwater)

A pool with rigid walls has been set for testing experiments. It has dimensions of 4 × 2 × 2 m, so only the depth keeping could be tested. The pool was filled up with fresh water (Fig. 3).
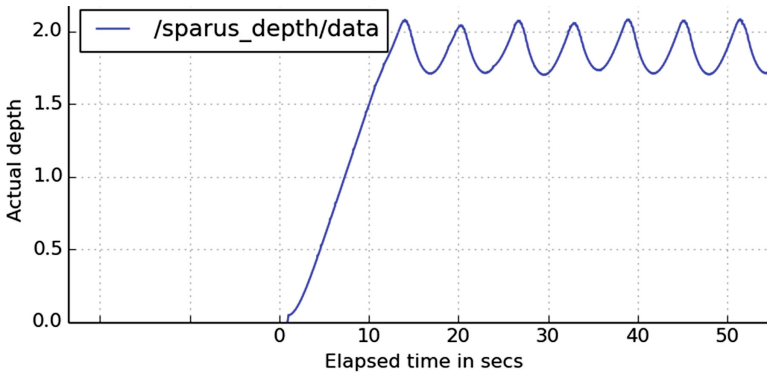
**Fig. 3.** The adaptive PID controller for depth control in a pool, plotted in UWSIM with rqt_plot. The vertical axis is depth in meters and the horizontal axis is time in seconds.

## 5.3  Test Scenario 2: Lake (Freshwater)

The first field tests were conducted at a fresh water lake. During these, the measured speed of the wind was 2–3 km/h which means that there were 5–10 cm waves, creating drifts at the surface of the water. The experiments with the depth keeping solution were similar to the pool tests.

## 5.4  Test Scenario 3: Seawater

The ultimate environment was at the marine section of the euRathlon 2015 robotic competition, which was organized in shallow sea water. The parameters of the controller had to be reconfigured because of the density of the sea, and it was accounted by the adaptive PID controller [6], as presented in Fig. 4.
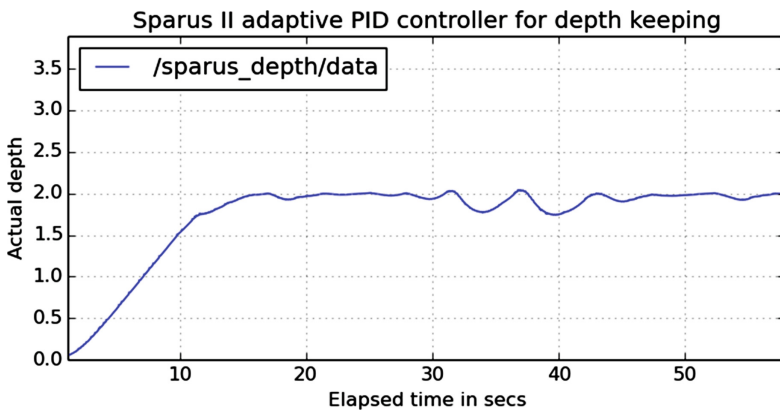


**Fig. 4.** Adaptive PID based depth control solution measured in euRathlon 2015, plotted in UWSIM with rqt_plot.

## 6   Conclusions

This paper described a practical and low-cost solution for the problem of orientation- and depth keeping of an autonomous underwater vehicle. With an adaptive PID controller, the orientation- and depth keeping problems could be solved in a cheap and efficient way, under limited conditions. These solutions do not provide robustness, and are only meant for limited experiments. During the euRathlon competition entered with a Sparus II (Fig. 5), we did not deal with the position keeping, because of the shape of the hull and the placement of the thrusters. The Sparus II is not able to turn in one place, so the Y direction (sideway) errors could not be corrected in a simple way.



**Fig. 5.** Participating teams at the euRathlon 2015 competition with their Sparus II AUV units

## References

1. Zhao, S., Yuh, J.: Experimental study on advanced underwater robot control. IEEE Trans. Rob. **21**(4), 695–703 (2005)

2. Santhakumar, M., Asokan, T.: Non-linear adaptive control system for an underactuated autonomous underwater vehicle using dynamic state feedback. Int. J. Recent Trend Eng. **2**, 384–389 (2009)
3. Carreras, M., et al.: Sparus II, design of a lightweight hovering AUV. In: Martech 5th International Workshop on Marine Technology, SARTI (2013)
4. Quigley, M., et al.: ROS: an open-source robot operating system. In: ICRA Workshop on Open Source Software, p. 5 (2009)
5. Prats, M., et al.: An open source tool for simulation and supervision of underwater intervention missions. In: IEEE/RSJ International Conference on Intelligent Robots and Systems (IROS), pp. 2577–2582. IEEE (2013)
6. Takacs, B., Doczi, R., Suto, B., Kallo, J., Varkonyi, T., Haidegger, T., Kozlovszky, M.: Extending AUV response robot capabilities to solve standardized test methods. Acta Polytech. Hung. **13**(1), 157–170 (2016)
7. Available tools in Robot Operating System. http://wiki.ros.org/Tools
8. Ahn, K.K., Dinh, Q.T.: Online tuning fuzzy PID controller using robust extended Kalman filter. J. Process Control **19**(6), 1011–1023 (2009)

# Vision-Guided Autonomous Forklift

Mohammad M. Aref$^{(\boxtimes)}$, Reza Ghabcheloo, Antti Kolu, and Jouni Mattila

Department of Intelligent Hydraulics and Automation,
Tampere University of Technology, 33101 Tampere, Finland
m.aref@ieee.org,
{reza.ghabcheloo,antti.kolu,jouni.mattil}@tut.fi

**Abstract.** This paper tackles the problem of integrating *Visual Servoing Control* (VSC) into the functionalities of an *Articulated-Frame-Steering* (AFS) hydraulic forklift. The controller is capable of breaking down high-level messages into piecewise commands for the different software modules of the vehicle. It also preserves seamless cooperation of the modules for a successful pallet-picking mission. The proposed architecture has been verified on a real machine. Videos of the test runs are available on YouTube.

**Keywords:** Mobile manipulation · Visual servoing · State machine

## 1 Introduction

Robotics has become an important aspect of logistics and automation in many application fields. Efficient material handling plays a significant role in the optimization of construction processes among others. The invention of containers and pallets has radically changed the way logistics is performed in all sectors, particularly in the construction business, both for buildings and infrastructures, e.g. roads. Automated Guided Vehicles (AGVs) are possibly among the best-selling robotic units, used mostly for warehouse management, such as the Kiva Systems of Amazon [1]. In indoor cases following the traditions of factory robots both palletizing systems and AGV localizations and navigation are rather accurate, and system operation relies on this certainty. However, in outdoor applications, e.g. in construction, the pallet-handling control system needs to be robust against both localization and control inaccuracies. Localization may be improved using more expensive equipment, though for a cost-conscious industry such as construction, this is not usually acceptable. Forklift trucks used for pallet handling in construction are built to move on uneven terrain, and they are made robust with simple components, which makes the accurate control of these machineries a real challenge. Notice that, contrary to typical logistics, the challenge is not only in navigation in semi-/un-structured and dynamic environments but also in the manipulation and coordination of the body and the boom. In a series of publications, we have proposed methodologies for vision-guided navigation that are robust against the uncertainties mentioned above [2–4]. In this paper, we present the details of the control system's architecture and report on the system integration of such a complex system.

For vision-based autonomous systems, errors in target detection and limitations of the mechanical system are both common sources of error [5]. A proper controller should overcome both obstacles, improving overall performance. In the literature, many studies focus on one of these issues over the other. A group of studies gives more weight to the pallet-detection problem. Pallet detection and the integration of a visual sensor in the control topology are the main focuses in [6], whereas [7] aims to correct data while approaching the pallet. Most previous work has employed at least two cameras, a monocular vision system with defined CAD models [8], or both a laser scanner and a camera [9]. In this paper, we introduce a modular architecture and a state machine that integrates a VSC [2] with preexisting path-following and manipulation controllers. This architecture can fill the gap between robot functionalities for test cases and real-world problems.

## 2   Software Modules

This section briefly describes the software modules of the vehicle for the components shown in Fig. 1a. Their interaction is shown in Fig. 2, which is categorized by the relevant environment of each software module. The design criteria for the architecture include reliability, availability, and maintainability. Our proposed solution is a modular approach, which allows one to benefit from team work and from the use of the existing advances made in the required and relevant functionalities. Therefore, the controllers are self-dependent and not necessarily flexible. The desired flexibility is achieved by controlling the interactions between the modules by a state machine, described in Sect. 3. The machine's control system is composed of primitive functionalities such as path planning, path-following control (body), manipulator control (boom), and pallet detection, which are all coordinated by stateflow machines. VSC then becomes a capability built on the coordination of these primitive functions by a stateflow machine, which is detailed in this paper. An important benefit of this architecture is modularity.

### 2.1   Control Modules

Pallet-picking problems can be defined as generating control commands that lead the fork frame to the pallet frame without any collisions. This clearly restricts



**(a)** Hardware architecture                    **(b)** Autonomous forklift
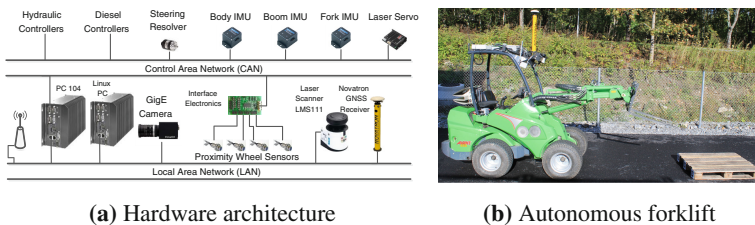
**Fig. 1.** Autonomous forklift and its hardware.
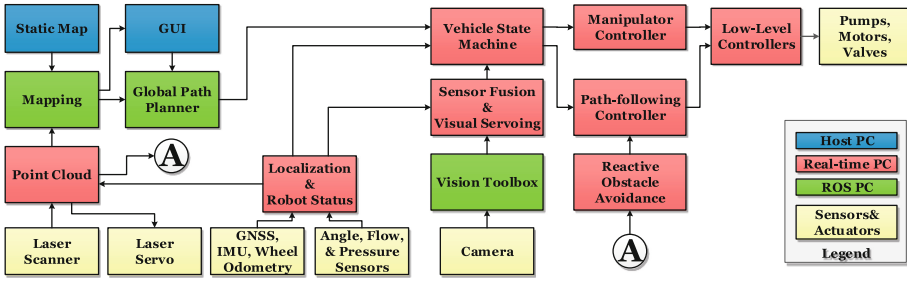
**Fig. 2.** Software modules of vehicle control

the final segment of the fork path to a line that is parallel to the pallet frame. Moreover, the machine has limited maneuverability (detailed in the next section); it requires a minimum of 3 m to reduce a 0.5 m lateral error to 5 cm, a value that prevent collision with the pallet.

**Path-Following Control:** The machine in this study is a hydraulically actuated (AFS) machine (with the steering mechanism of a wheel-loader). An AFS consists of two bodies, front and rear units, joined by a hinge, each with freedom in yaw motion. Normally, these units have freedom in pitch as well, to allow good ground contact over rough surfaces. In a commercial AFS machine, bending angles are limited to about 42 degrees on each side to ensure roll stability.

Given a desired 2D geometrical obstacle-free path (smooth Bézier curves, in this case) together with a desired velocity profile (trapezoidal, in this case), a path-following controller generates the linear and angular speed of the body frame attached to the middle of the front axle. A motion controller then generates the required commands for the valve controlling of the steering cylinder and for the drive power transmission controller (pump displacement and diesel RPM) to control the speed. More details are found in [10], where we showed AFS kinematics can be approximated by two attached unicycles, for which a nonlinear path-following controller is designed.

**Manipulator Control:** As shown in Fig. 1b, the forklift manipulator in this research has three *Degrees Of Freedom* (DOF) in a rotary–prismatic–rotary (RPR) configuration, in such a way that the height and reach of the fork and its pitch angle are controllable. All DOF are controlled by linear hydraulics actuators, which are driven by pressure-compensated proportional valves. In control terminology, that means an inner loop servo controller compensates for nonlinear dynamics and receives velocity control commands of the cylinders. In other words, we will control the manipulator at the kinematic level. Given the target pose in the body frame, a relevant Jacobian matrix is used to generate the valve speed commands. Notice that the roll angle of the end effector (fork) is not controllable, neither by the manipulator or the body DOF.

## 2.2   ROS Packages

Robot Operating System (ROS) is used by high-level control systems for mapping, path planning, obstacle avoidance, and marker detection. The core components of the high level control system are presented in Fig. 2.

**Mapping and Obstacle Detection:** The mapping system uses the calibration and localization error-tolerant segmented mapping method [11]. A tilting 2D laser scanner is installed in front of the forklift. The laser range measurements are transformed from the sensor frame into the global frame using the localization information. Each point in the point cloud is attached with a height variance value based on the localization's uncertainty at the time of the range measurement. The point clouds are gathered in the mapping module, and are processed once per tilting motion of the servo. The height of the terrain in each cell is calculated using the height of each point assigned to each cell. The Bayesian update is used to update the height, so the uncertainty of the measurement is considered. The maximum gradient for each cell is calculated, and the predefined threshold value is used to define the cell as free or occupied. A static obstacle map is combined with the map calculated based on the point cloud to avoid forbidden areas, such as roads, and areas with static obstacles, such as buildings and fences.

**Path Planning:** Path-planning algorithms are presented more closely in [12]. The first step of the algorithm is to compute a finite set of feasible motions connecting discrete robot states to construct a search graph offline. The motion primitives based on Bézier curves are generated by solving the constrained optimization problem. The path planning receives an obstacle map from the mapping system every time the map is updated. When a new goal is received, the current pose of the machine is considered to be the start state for the path-planning algorithm. $A^*$ search is then conducted through the graph of motion primitives, resulting in a list of feasible motions from the start to the goal. This list of Bézier curves are combined when feasible and are then further optimized by solving the constrained optimization problem. This leads to a smooth and feasible set of Bézier curves.

**Marker Detection:** The images are grabbed using `camera_aravis` and published as unrectified raw images into ROS. The calibration is performed using `camera_calibration` with a calibration plate that has a $12 \times 8$ grid of 6 cm square cells. The camera calibration file is saved into ROS so that it is found by the marker detection package. The camera used in our tests was a GimaGO GO423C GigE camera with a resolution of $1296 \times 966$ pixels. The camera's lens is a Kowa 1.4 lens with a focal length of 12 mm. Marker detection is implemented using `ar_track_alvar` that uses the Alvar marker-detection library for augmented reality. It uses unrectified images and uses the camera calibration to rectify the images. A bundle of three individual markers is placed on the front

side the pallet as shown in Fig. 1b. Alvar library recognizes them as a single marker. This brings better reliability, as one or even two of the markers may be occluded or unrecognizable in the camera image.

## 3    Vehicle State Machine (VSM)

As shown in Fig. 2, the messages from the planner, GUI, and any higher-level modules arrive to the VSM. This module distributes them as commands among the relevant control modules depending on their content and the robot's status. Some of these *message types* are: driving, manipulation, forced driving, forced manipulation, VSC, and placement. The VSM should handle and monitor the continuous functionality of the control modules as well as interruptions and delays.

For instance, on one hand, it should maintain smooth operation of the robot during the communication delays of the long-distance wireless network or package drop; therefore, the VSM uses a FIFO (First In, First Out) scheduling system as a buffering method. On the other hand, the vehicle should immediately react to forced message types as the first priority; therefore, forced message types should bypass the buffers and interrupt the current work.

In the following, a selected part of the VSM is described. It focuses on executing a sequence of driving and manipulation commands individually or as part of a VSC. The VSM runs at each minor sample time of the control system. It consists of three main steps: preprocessing, processing, and post-processing. The separation of phases not only simplifies the VSM's design process but provides synchronization of the actions before tasking the command of the control modules. The notation for the flags referred to in Figs. 3, 4 and 5 are as follows:

**X-Active:** allows the processing phase to turn on the corresponding controller.
**X-Done:** marks task accomplishment for local use.
**X-Release:** declares task accomplishment for the high-level modules. Turns off any busy signs for the corresponding control module.
**X-Wait:** pauses the command and prevents the release of the controller module.

### 3.1    Preprocessing

The preprocessing phase of the VSM picks the necessary control modules and updates the VSM's status according to the latest messages from the buffer. As a general rule, a block in the preprocessing phase:

1. can read inputs and flags,
2. can write internal flags, and
3. should not update any outputs.
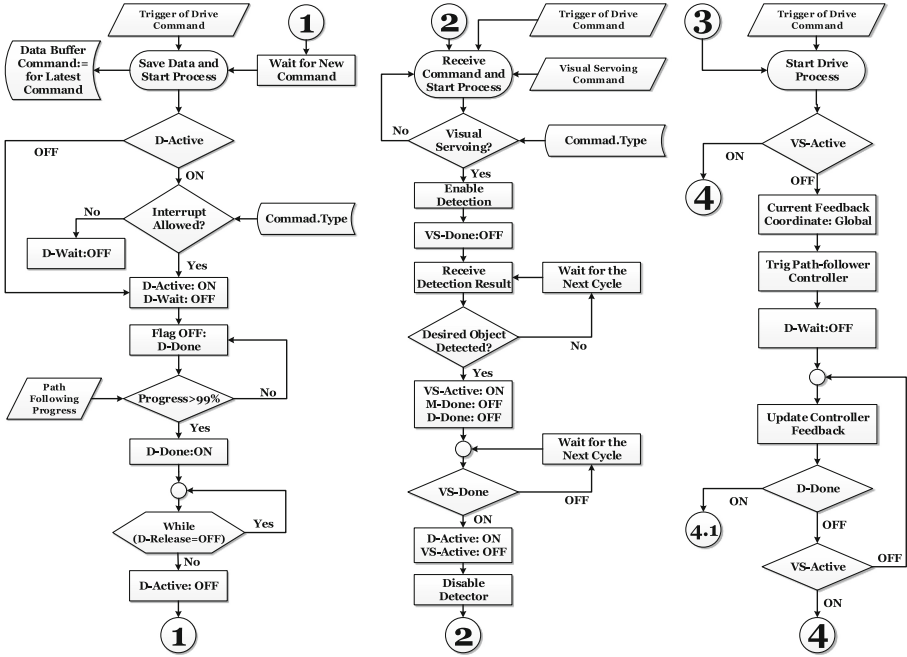
**Fig. 3.** Flowcharts of the state machines: (1), (2) Preprocessing, (3) Processing
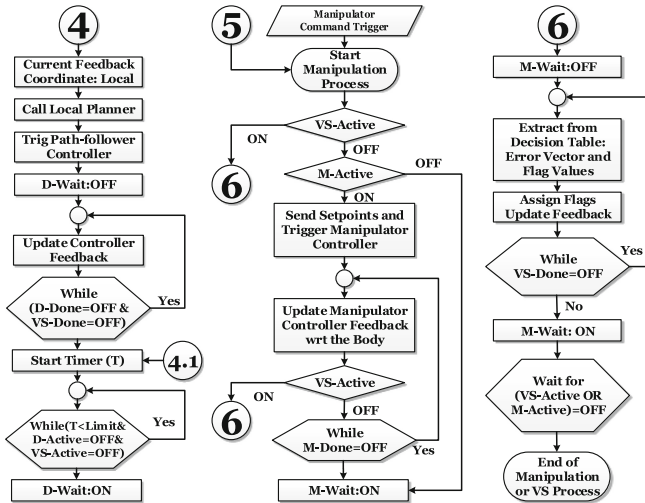


**Fig. 4.** Processing phase flowchart of state machine
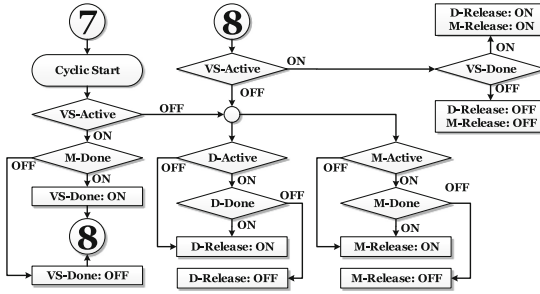
**Fig. 5.** Post-processing phase of state machine.

**Table 1.** Sample rules for decision making

| No. | VS Status Description | 1st Cond. | 2nd Cond. | $[e_x, e_z, e_\theta]$ | Flag |
|---|---|---|---|---|---|
| 1 | Global plan | $VS_{Active} = 1$ | ${}^Le_x \geq D_1$ | $\left[{}^Ge_x, {}^Ge_z, {}^Ge_\theta\right]$ | D-Wait:OFF |
| 2 | VS adjusts height | — | ${}^Le_x \leq D_1$ | $\left[\ 0,\ {}^Le_z, {}^Ge_\theta\right]$ | D-Wait:OFF |
| 3 | Acceptable height | ${}^Le_z > \epsilon_z$ | ${}^Le_x \leq D_2$ | $\left[\ 0,\ {}^Le_z, {}^Ge_\theta\right]$ | D-Wait:ON |
| ... | | | | | |

Based on these rules, we simplify the design of the VSM and avoid vicious circles. A sample preprocessing phase for the drive command is shown by the flowchart numbers 1 and 2 in Fig. 3. Column 1 manages flags relevant to the driving control. The drive message can also carry the VS command and an object ID. Therefore, the second column makes the decision about running VS-related modules. The VSM blocks for the manipulator are similar to those in column 1. However, the statement of accomplishment depends of the 2nd-norm of the controller error. Note that the loops similar to the "While" loop of flowchart 1 avoids resetting the internal flags without informing the high-level planner. X-Release flags are updated during the postprocessing phase Fig. 5.

### 3.2   Command Processing

This phase provides the necessary data and actions for the controller modules. Flowchart 3 in Fig. 3 and the flowcharts in Fig. 4 show the processing phase of the VSM. The blocks of this phase:

1. can read inputs and flags,
2. can write internal flags if they do not change the system status,
3. can update the outputs for the low-level modules, and
4. should not update the outputs for the high-level modules.

The VS task is based on the macro-micro controller proposed in [2].

### 3.3    Postprocessing

This phase updates the outputs based on the status of the controllers and the decisions made in the earlier phases of the VSM. The blocks in this phase:

1. should not read inputs,
2. should not write internal flags except those for task accomplishment, and
3. can update the outputs for the high-level modules based on the internal flags.

The postprocessing phase for driving and manipulation are shown in Fig. 5. Note that the X-Release flags in this phase are monitored by the high-level modules. Unlike the other phases, this phase is triggered by the system clock. Its blocks run sequentially at each sample time from the start to the last possible block.

## 4    Conclusions

The proposed method takes advantage of cooperative manipulation and path-following in different operational coordinates. The robot receives messages from a global planner and drives on the desired path. When the path contains a pallet as its end-point, the vehicle state machine (VMS) smoothly switches the modules to fit the visual-servoing architecture. In addition, VMS preserves all the functionalities of the modules to run tasks sequentially or to interrupt messages from the authorized high-level supervisory system. The architecture is implemented on an autonomous forklift made by the Department of Intelligent Hydraulics and Automation at the Tampere University of Technology, based on the Avant 635. The videos of the experimental evaluation are available on YouTube[1].

## References

1. Wurman, P.R., D'andrea, R., Barbehenn, M.T., Hoffman, A.E., Mountz, M.C.: Kiva transporting inventory items#3, uS Patent Ap. 14/095,751. http://www.freepatentsonline.com/y2014/0100690.html
2. Aref, M.M., Ghabcheloo, R., Mattila, J.: A macro-micro controller for pallet picking by an articulated-frame-steering hydraulic mobile machine. In: IEEE International Conference on Robotics and Automation (ICRA), Hong Kong, pp. 6816–6822 (2014)
3. Aref, M.M., Ghabcheloo, R., Mattila, J.: Real-time vision-based navigation for nonholonomic mobile robots. In: Accepted for IEEE International Conference on Automation Science and Engineering (CASE) (2016)

---

[1] https://www.youtube.com/channel/UCxemrk8NrIj-db6h06VBVLA.

4. Aref, M.M., Ghabcheloo, R., Kolu, A., Mattila, J.: A multistage controller with smooth switching for autonomous pallet picking. In: IEEE International Conference on Robotics and Automation (ICRA), Stockholm, Sweden (2016)
5. Yoder, J.D., West, J., Baumgartner, E., Perrollaz, M., Seelinger, M., Robinson, M.: Experiments comparing precision of stereo-vision approaches for control of an industrial manipulator. In: Desai, J.P., Dudek, G., Khatib, O., Kumar, V. (eds.) Experimental Robotics, pp. 245–256. Springer International Publishing, Switzerland (2013)
6. Holeva, L.F., Elston, E.R., Seelinger, M.J., Yoder, J.D.S.: Identifying and selecting objects that may correspond to pallets in an image scene, uS Patent 9,025,886, 5 May 2015
7. Ban, K., Warashina, F., Yamada, M., Namiki, Y.: Robot system comprising visual sensor, uS Patent 8,326,460, 4 December 2012
8. Byun, S., Kim, M.: Real-time positioning and orienting of pallets based on monocular vision. In: 20th IEEE International Conference on Tools with Artificial Intelligence, 2008, ICTAI 2008, vol. 2, pp. 505–508. IEEE (2008)
9. Baglivo, L., Biasi, N., Biral, F., Bellomo, N., Bertolazzi, E., Da Lio, M., De Cecco, M.: Autonomous pallet localization and picking for industrial forklifts: a robust range and look method. Meas. Sci. Technol. **22**, 085502 (2011)
10. Ghabcheloo, R., Hyvönen, M.: Modeling and motion control of an articulated-frame-steering hydraulic mobile machine. In: Proceedings of the 17th Mediterranean Conference on Control and Automation, Greece, June 2009
11. Kolu, A., Lauri, M., Hyvonen, M., Ghabcheloo, R., Huhtala, K.: A mapping method tolerant to calibration and localization errors based on tilting 2D laser scanner. In: European Control Conference (ECC), pp. 2348–2353. IEEE (2015)
12. Choi, J.W., Huhtala, K.: Constrained global path optimization for articulated steering vehicles. IEEE Trans. Veh. Technol. **65**(4), 1868–1879 (2015)

# Application-Driven Cloud-Based Control
# of Smart Multi-robot Store Scenario

Aleksandar Rodić[(✉)], Miloš Jovanović, Milica Vujović,
and Djordje Urukalo

Robotics Laboratory, Mihajlo Pupin Institute,
University of Belgrade, Belgrade, Serbia
{aleksandar.rodic,milos.jovanovic,milica.vujovic,
djordje.urukalo}@pupin.rs

**Abstract.** The paper concerns the structure and management of application-driven, cloud-based, smart, multi-robot scenario to be implemented in a typical megastore environment where people (consumers and staff) intertwine with goods flow and service robots operating in the store. Heterogeneous models of human actors, things and robots making a unique dynamic system were developed. The system operates as a distributed, wireless, robot-sensor network configured in the megastore's information structured environment. The smart store is modelled and simulated by several networked PC computers connected to the cloud architecture. The aim of cloud system configuration is to control collaborative strategies of multi-robotic system in the considered application – high automated megastore. Research results are verified by simulation experiments instead of configuring expensive real experimental system. Particular models of physical environment (megastore infrastructure), different-purpose service robots, consumers, staff and goods (things) together with wireless sensorial and communication system are developed and simulated in parallel on several cloud computers.

**Keywords:** Cloud robots · Application-driven scenario · Internet of Things · Wireless robot-sensor network · Ambient-distributed intelligence

## 1 Introduction

The progress of information and communication technologies, especially wireless communications and sensor technology, has opened a large space for use of robots in areas where it was previously not imaginable. As the invention of the personal computer (PC) and the Internet Technology launched mankind toward faster digitization, it is also expected for service robots, in the near future, to get involved in a new industrial revolution that will represent a radical technological step forward for mankind. In the future, robots will increasingly become partners of men in performing difficult and delicate or monotonous daily tasks. Despite the rapid progress in the development of robot technology, robots still have not reached the people with their capabilities primarily in their perceptual and cognitive abilities. Although today's robots are distinguished by an enviable degree of artificial intelligence, versatile perception and

decision-making in real-time, this area is still in development. If the design approach of service robots is based on "technological copy" of the human, then we are placed in front of the impossible requirements for robots, expecting them to simultaneously solve a lot of complex numerical tasks such as planning developments and navigation, avoiding obstacles, pattern recognition, sound recognition, planning, visual-motor actions and making a decision in the absence of complete info. Performing such complex tasks in parallel (simultaneously) requires extremely powerful computing resources. For this reason, there is an alternative solution that promotes the so-called distributed ambient intelligence approach as technologically feasible, progressive approach to solving the problem of the accumulation of tasks and solving management problems in the system with simple distribution of tasks among agents. Cloud robotics is an emerging concept as real alternative to the built-in (embedded) management robot system, which overcomes the above-mentioned technological constraints in implementation. For these reasons, the paper will consider a characteristic example of high automated megastore that allows wider application of service robots managed by cloud computing systems.

Today's megastores are complex, dynamic systems in which the "flow" of goods, capital, people (consumers and employees) and energy take place. Goods flow is monitored for a regular supply on shelves and in warehouse. The conventional way of doing jobs in megastore is by engaging human staff in performing various typical tasks such as handling goods, management of store business, delivery information and various services (e.g. cleaning, packing goods, payment, etc.). Economic effects of business organization in stores in a conventional manner significantly depend on the human factor. This paper also touches socio-economic aspects of implementing cloud robots in shopping centres and will put emphasis on technical feasibility and advantages of such novel application-driven approach to managing smart scenarios.

The large retail chains are trying to automate the process of goods traffic in order to minimize the influence of the human factor in the end results of operations. In the last decade, several initiatives have been launched that are aimed to define a new concept of operations and the organization of future commercial practices in large department stores. One of these initiatives is the "future store" [1].

The paper is organized in several sections. In the introductory section, there is a problem definition and the possibilities of solving the problem using cloud computing systems are suggested. Section 2 provides an overview of achievements in the field of robot-based cloud structures. In Sect. 3 the model of automated megastore with application-driven scenario based on cloud computing is presented. Section 4 discusses implementation aspects and presents some simulation results as concept verification. In Sect. 5, the conclusion and future work are considered.

## 2 State-of-the-Art

Cloud robotics is a field of robotics that attempts to invoke cloud technologies such as cloud computing, cloud storage, and other Internet technologies centred on the benefits of converged infrastructure and shared services for robotics [2]. When connected to the cloud, robots can benefit from the powerful computational, storage, and

communications resources of modern data centre in the cloud, which can process and share information from various robots or agent (other machines, smart objects, humans, etc.). Humans can also remotely delegate tasks to robots through networks. Cloud computing technologies enable robot systems to be endowed with powerful capability whilst reducing costs through cloud technologies. Thus, it is possible to build light-weight, low cost, smarter robots that have intelligent "brain" in the cloud. The "brain" consists of data centre, knowledge base, task planners, deep learning, information processing, environment models, communication support etc.

RoboEarth [3] was funded by the European Union's Seventh Framework Program for research, technological development projects, specifically to explore the field of cloud robotics. The goal of RoboEarth is to allow robotic systems to benefit from the experience of other robots, paving the way for rapid advances in machine cognition and behaviour, and ultimately, for more subtle and sophisticated human-machine interaction. RoboEarth offers a Cloud Robotics infrastructure. RoboEarth's World-Wide-Web style database stores knowledge generated by humans and robots in a machine-readable format. Data stored in the RoboEarth knowledge base include software components, maps for navigation (e.g., object locations, world models), task knowledge (e.g., action recipes, manipulation strategies), and object recognition models (e.g., images, object models). The RoboEarth Cloud Engine includes support for robots which require lots of computation for navigation [4].

Rapyuta [5] is an open source cloud robotics framework based on RoboEarth Engine developed by the robotics researcher at ETHZ. Within the framework, each robot connected to Rapyuta can have a secured computing environment (rectangular boxes) giving them the ability to move their heavy computation into the cloud. In addition, the computing environments are tightly interconnected with each other and have a high bandwidth connection to the RoboEarth knowledge repository [6].

KnowRob [7] is an extension of the RoboEarth project. It is a knowledge processing system that combines knowledge representation and reasoning methods with techniques for acquiring knowledge and for grounding them in a physical system. The KnowRob can serve as a common semantic framework for integrating information from different sources.

RoboBrain [8] is a large-scale computational system that learns from publicly available Internet resources, computer simulations, and real-life robot trials. It accumulates everything from robotics into a comprehensive and interconnected knowledge base. The goal is as direct as the project's name to create a centralized, always-online brain for robots [9].

MyRobots is a service for connecting robots and intelligent devices to the Internet [10]. It can be regarded as a social network for robots and smart objects (i.e. Facebook for robots). With socializing, collaborating and sharing, robots can benefit from those interactions too by sharing their sensor information giving insight on their perspective of their current state.

The COALAS [11] project aims to develop new technologies for handicapped people through social and technological innovation and through the users' social and psychological integrity. The objective is to produce a cognitive ambient assistive living system with Healthcare cluster in cloud with domestic service robots like humanoids and intelligent wheelchairs connected in the cloud.

ROS (Robot Operating System) provides an eco-system to support cloud robotics. ROS is a flexible and distributed framework for robot software development. It is a collection of tools, libraries, and conventions that aim to simplify the task of creating complex and robust robot behaviour across a wide variety of robotic platforms. A library for ROS that is a pure Java implementation, called RosJava, allows Android applications to be developed for robots. Since Android has a booming market and billion users, it would be significant in the field of cloud robotics [12].

## 3   Modelling of the Megastore

At the present level of technology, robots still remain in their physical and intellectual abilities behind humans, although they have certain advantages. Robots for example do not feel fatigue, they can quickly count, have a high degree of repeatability, execute human commands and their performance does not depend on the motivation and the current psycho-physical condition. Accordingly, it is anticipated that robots and people will continue to work together and collaborate as partners in different projects.

If we look at a typical example of megastore, as one of the possible scenarios of application of robots in the future, robots can perform the following tasks: (i) transport of goods from warehouses to retail display cases, (ii) free handling tasks of loading and filling the range of goods on the shelves of cabinets, (iii) monitor and control the consumption and supply of goods on sale, (iv) the maintenance of hygiene and removal of waste from containers, (v) advertising, marketing and consumer information, (vi) anti-fire protection, etc. In that work structure, employees in megastores would do more creative and responsible tasks that require specific human skills such as providing services to consumers, food processing, measurement and collection of goods. In Fig. 1a and b, a typical model of a megastore is shown, which will serve in this paper to demonstrate cloud-based management methodology in a multi-robot scenario in the automated trading centre.

The model shown in Fig. 1 has a corresponding input and output with the cash register; it follows display of goods distributed throughout the interior of the store, in several specialized departments - bakers, butchers, drugstore, cafe-restaurant and a warehouse. Showcases for goods are distributed by sectors that offer specific goods from certain categories: sweets, meat, milk and dairy products, baked goods, fruit and vegetables, household chemicals, etc. Cabinets are numbered in a sequence from S.1 to S.107 (Fig. 1a) as well as the associated shelves in the cabinet (e.g. from S37.1 to S37.12, Fig. 1b). In practice, cabinets and shelves would be systematically marked with the appropriate radio-frequency identification (RFID) markers that would contain the appropriate label in addition (previously described on the model) and basic information about the items for their easy identification and keeping records of transactions (inventory of goods). The goods on the shelves within the cabinet are marked with barcodes and have their strictly defined place on the shelf, which is recorded in a central database cloud system (see Fig. 2) so that each item can be relatively easy accessed knowing his exact position in sales (number of cabinets and shelves). Showcases in the store are separated by corridors. They are used by consumers, employees and robots as auxiliary equipment which makes the system dynamic
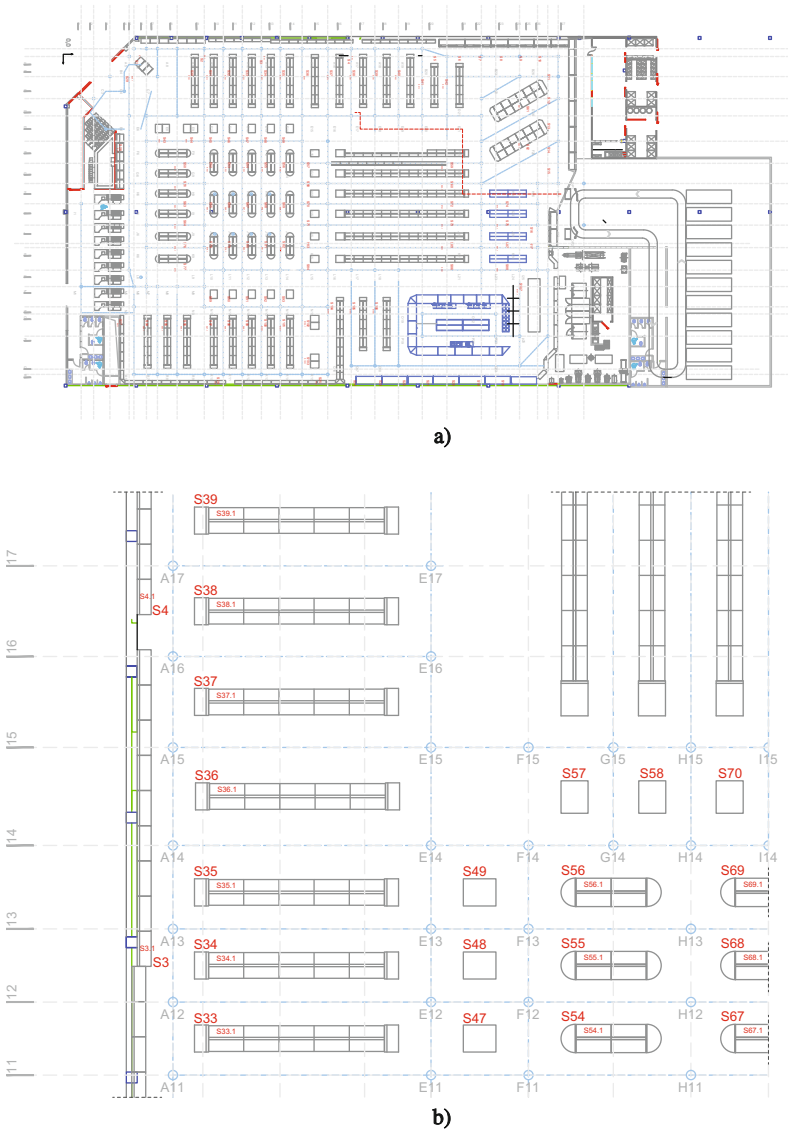
**Fig. 1.** Model of a megastore considered in the context of a cloud-robotic scenario. (a) Global view; (b) Particular sector zoom.

and complex for management and control as the situation in the shop is changing continuously.

Corridors intersect and their intersection areas are called "waypoints". Intersection points form a matrix of important points that determine the possible pathways of the robot in the store. The matrix of waypoints is arranged by rows named by alphabet letters from A to D and the columns numbered from 1 to 28. Thus, each intersection
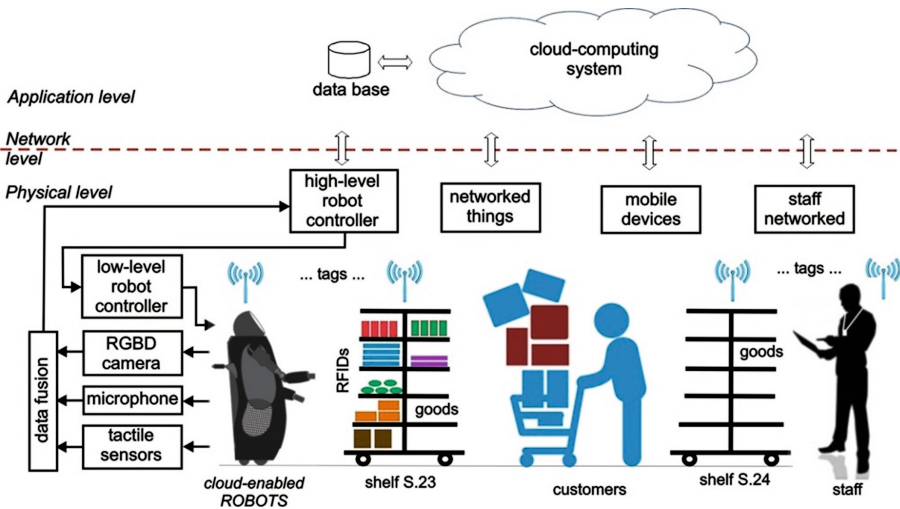
**Fig. 2.** Scheme of application-driven cloud-based control of multi robot store scenario

point is unambiguously defined and determined by its absolutes coordinates in the global coordinate system (Fig. 1).

In the given model of megastore robots fulfil their routine, monotonous and simple transportation and handling tasks instead of people 24 h a day. In accordance with the selected scenario models for the application of robots in the megastore, in the demonstration case considered in this study, several types of service robots are employed: (i) transport, (ii) handling, (iii) control, (iv) robot for hygiene and waste disposal and (v) the info-bot, a robot in charge of marketing and provision of service information to consumers. In order for this multi robot system to function reliably and be technically viable in the cloud computing system, it is necessary that a megastore is fully information structured, i.e. that there is a distributed sensor network and fast and reliable wireless communication between agents in the system. Cloud customers in the considered system are: people (employees/staff), service robots, furniture and things that are networked and important for the functioning of the cloud-system (see Fig. 2).

Any change in the cloud system is identified in the central computer, and information of the resulting changes is exchanged between clients interconnected and networked. In this way, it is possible to plan the accomplishing of various tasks globally, sequentially and in parallel (simultaneous) execution. Such an approach is, in literature, called spatial distributed intelligence. Each client of the system individually performs its assigned job and informs other clients, if it is of interest for their activities. The flow of information among clients is provided via wireless, high-speed network so that the information is available throughout the whole information area covered by cloud computing system. The cloud system architecture shown in Fig. 2 has the capacity to keep the records and traces the path of each item that is on the shelves of cabinets in the store.

Figure 3 shows a table of data for items that are stored in the database cloud computer. The table contains all the relevant information on the goods, starting from their identification code, the place in the showcases and on the shelves, manufacturers of items, expiry date, retail price, etc. By selling the items, they get deleted from the database as "available". At the request of an authorized person, it is possible at any time to issue a report on the state of the goods on sale, in the warehouse and from the list of sold items and how big the profits are. In this way, the flow of goods in megastore is followed from its input to output. Networking things in space is known in literature as Internet of Things, and it is increasingly being used in the future concepts of smart buildings in the corporate business.

|   | Goods | ID | Producer | Warehouse | Shelf | Image | Barcode | Produced | Valid until |
|---|-------|-----|---------|-----------|-------|-------|---------|----------|-------------|
| 1 | Crumpets | FB283 | "Bambi" doo. Požarevac | OP1 | S43.1 | I_FB283.jpg | B_FB283.jpg | 31.12.2015 | 31.12.2016. |
| 2* | Eggs | FE131 | "Agroživ" doo. Bačka | OP2 | S55.8 | I_FE131.jpg | B_FE131.jpg | 20.06.2016 | 20.07.2016. |
| 3 | Beef | FM1512 | "Carnex" doo. Vrbas | OP2 | S88.3 | I_FM1512.jpg | B_FM1512.jpg | 15.03.2016 | 15.09.2016 |
| 4 | Toothpaste | CH606 | Henkel GmbH | OP1 | S12.7 | I_CH606.jpg | B_CH606.jpg | 28.01.2016 | 28.01.2017 |
| 5 | Toilet paper | PG2422 | Paloma Co. | OP1 | S12.15 | I_PG2422.jpg | B_PG2422.jpg | 18.05.2016 | 18.05.2017 |
| ... | ... | ... | | | | | | | |

|   | Packaging | Net weight (gr) | Category | Net price (EUR) | Gross price (EUR) | In stock | In market | Sold | Turnover (EUR) |
|---|-----------|-----------------|----------|-----------------|-------------------|----------|-----------|------|----------------|
| 1 | 1 | 500 | sweets | 2.30 | 2.75 | 20,800 | 500 | 3670 | 10,092.50 |
| 2* | 10 | 60 | eggs-A | 3.50 | 4.20 | 37 | 2 | 512 | 2,150.40 |
| 3 | 1 | 500 | meet | 5.30 | 6.36 | 3,500 | 100 | 83 | 527.88 |
| 4 | 1 | 120 | hygiene | 1.35 | 2.05 | 13,000 | 230 | 517 | 1,059.85 |
| 5 | 6 | 200 | paper | 1.80 | 2.16 | 7,000 | 370 | 1200 | 2,592.00 |
| ... | ... | ... | | | | | | | |

**Fig. 3.** Goods items database

Employees of the store, according to the given scenario shown in Fig. 2, wear tags attached to the body belts (or around the neck) for their identification and networking in the cloud system. They also can send and/or receive tweet messages from the central computer via tablet or mobile device (paging device), and by that they get the necessary information concerning distant objects and devices for example at the other end of the store. Employees at the store are active clients of the cloud operating system, which is also designed to support the application for traffic of goods and services in the megastore.

Several service robots are engaged in the megastore to perform different tasks previously mentioned. Each robot has a corresponding tag that allows it to be located easier in the area. His current position and the destination of movement are being exchanged as data with the central computer. Indirectly through a wireless network, it does the same with other clients in the system, who are interested to know the position and movement of any client. It is necessary to optimize the cloud server and wireless communication network hardware for the purpose of regular information exchange in the system and for performing timely computations, searching the database and decision-making at the global level. This ensures the functioning of the system in real time without major delays and congestion in information flow. The robot is equipped with a WiFi modem and communicates wirelessly with cloud computer (Fig. 2). From

the computer network, robots receive coded commands and requirements in terms of their movement and assigned tasks. The robot sends back information on the state of execution of commands but also additional information about changes in the immediate environment. In this way, the robots represent mobile sensors distributed in computer structured space. In the case of some irregularities robots send messages to the cloud and these are forwarded to other clients over the network. In this way, the robot does not take the burden of sending the information to larger number of clients and information is sent to other system layers in the simplest and fastest way, which is the essence of application of cloud computing. Robots have the ability to send and receive other standardized commands and messages in the cloud system. Basic commands discussed in this paper are shown in Fig. 4.

| | Commands | Code | Data format (I/F/C) | Command entries |
|---|---|---|---|---|
| 1 | WAIT | COM00 | C4; I3; | where(G24); time(120); |
| 2 | GO | COM01 | C4; 16C4; F4.2; | where(OP1); path(E12,…,E15,H15,…,H26,OP1); speed(0.50); |
| 3 | TRACK | COM02 | C4; | leader(R01); |
| 4 | SLEEP | COM03 | C4; | where(J13); |
| 5 | MEET | COM04 | C4; 16C4; F4.2; | what(ID); path(E12,…,E15,H15,…,H26,OP1); speed(0.50); |
| 6 | GET | COM05 | C4; 16C4; F.4.2; C6; I3; | where(E12); path(OP1,H26,…,H15,E15,…,E12); speed(0.30); what(ID); quantity(50); |
| 7 | CHARGE | COM06 | C6; I4; C6; | what(ID); quantity(83); shelf(S34.12); |
| 8 | DISCHARGE | COM07 | C6; I4; C6; | what(ID); quantity(15); shelf(S34.12); |
| 9 | MONITOR | COM08 | 6C3; | shelf(S24, S25, S26, T24, T25, T26); |
| 10 | CLEAN | COM09 | 2F5.2; | site(35.20,58.50); |
| 11 | SHAREINF | COM10 | C3; C35; | where(H15); message('Action! Goods at discount!'); |
| 12 | CHANGE | COM11 | / | … robot interupt current command and wait for new one. |
| 13 | CHECKFUN | COM12 | 2C5; | test(FUN01; FUN05); |

**Fig. 4.** Table of standardized coded commands that cloud system sends to robot agents.

The commands shown in Fig. 4 refer to the completion of tasks of movement or handling operation that the cloud server sends to the individual robots. The movement commands are for example: wait (1), go to (2), follow (3), make break (4) intersect (5). The set of handling commands is: get (bring) (6), load (7), unloading (8) inspect (9), clean (10), exchange of information (11), change of command (12) and perform a functional system test (13). The cloud computer sends commands encoded in the form of message series (strings). Depending on the type of messages, they have different formats: character codes (C), integer (I) and decimal/floating point (F). Each message contains the identification code of commands, information about the destination (position), quantity, place in cabinet and on shelf, etc. Robots and cloud system use the same interpreter that allows messages to be understandable by both sides.

Reliable real-time indoor localization of staff people, robots and mobile objects is possible in the megastore by applying new technologies of KIO RTLS sensors [13]. KIO RTLS is a precise real-time localization system for determining the position of any object in 2D space with applications such as warehousing, occupational safety, sports etc. Ultra Wide Band (UWB) technology enables finding positions of objects through obstructions like concrete walls. KIO RTLS is suitable for tracking single or hundreds of objects with precision of 0.3 meters within the operation range of 20 meters. The communication channel enables to build applications with both connectivity and micro-positioning requirements.

Monitoring sales of goods (items) in the exhibition display cases is carried out using RFID sensors. The robots are equipped with the appropriate RFID that detects objects from a distance of couple meters. At the same time, to detect objects it is not necessary to directly approach the case as required by the barcode reader. RFID sensors have the same precision as UWB sensors and fully meet the purpose of carrying out an inventory of items on the shelves of megastore. In a situation where consumers accidentally mix goods on the shelves and the robot detects the irregularity, the robot will attempt to return the object to its proper place. In this case, the robot sends a request to the cloud server to send him a photo of the item (packaging) and additional information about the item, if necessary, to help visually locate it on the shelves, take it with gripper and place in the appropriate position in the display counter. If necessary, the robot can take "misplaced" goods to other display case sometimes away from this place. In the considered application, service robots which supervise goods are equipped with additional barcode readers in order to correctly select the case. Finally, the robot can use its cameras (vision) to more easily recognize the item by the package's colour or shape. Image processing is a demanding task for microprocessors and in such applications should be preferably avoided or applied in the case of necessity.

In order to move between the shelves along the corridors, the robot receives data on its trajectory from a cloud server. For this purpose, intersection points are used whose coordinates are stored in a central cloud database. Combining intersection points by the method of the shortest path or least congested path, the reference trajectory of the robot is computed. Thus, the robot is relieved from planning motion since the task is entrusted to the cloud computer. During its motion, at any time, the robot has the information about the absolute position in space as well as the position of the target point to be reached.

Between consecutive intersection points the robot maintains the direction and avoids fixed and moving obstacles using proximity sensors whose operating range is from 0.25 to 2.0 meters. With the help of proximity sensors the robot stops in case it encounters an obstacle, waiting for a moving object to pass or bypasses the barrier if it is stationary (e.g. cabinet). In the presence of moving obstacles, whether it is about employees or consumers in the megastore, the robot takes care of the security of other clients by stopping and waiting to create the conditions to continue the movement. If the wait lasts longer than 1–2 min the cloud server can send a command to the robot to change the route of motion by sending him information about an alternative "free" path.

The central cloud server keeps a record of the current congestion in corridors due to the accumulation of the number of consumers or merchandise and makes real-time changes in the strategy of the movement of the robot. This achieves a high efficiency operation of the system in the presence of obstacles and perturbations of various origins.

## 4   Simulation of Smart Store Scenario

One of the typical robot tasks is localization and path planning in presence of obstacles. These numerically demanding tasks can be dislocated from the robot controller to the cloud computer. Concerning the megastore scenario, one of the typical tasks that can be
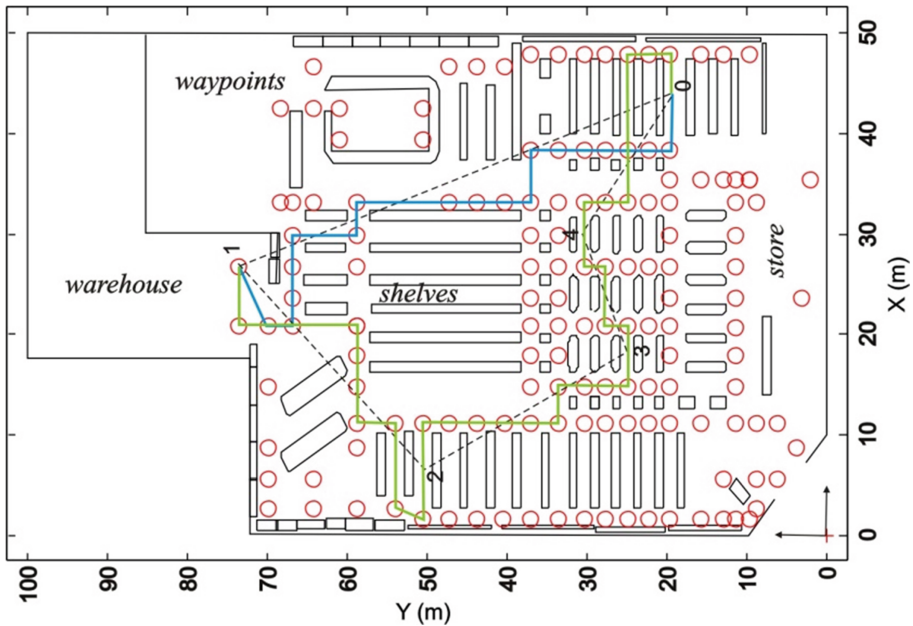
**Fig. 5.** Simulation of path planning task within a typical robotic megastore scenario

assigned to the robot is to send it to the warehouse to bring some goods in an a priori defined place, on the shortest path and in the shortest time. The digital map of the megastore is presented in Fig. 5 based on the plan shown in Fig. 1a. In the digital map, the shelves positions and waypoints are precisely determined by their coordinates.

Let us consider the scenario of one task. If the robot receives the command to move from point "0" to point "1" which is deployed in the warehouse, the cloud computer will calculate the shortest route which connects these two points. The calculated route is marked as blue solid line in Fig. 5. From the warehouse (point "1"), the robot is required to move goods to the appropriate shelves in the megastore. Their locations are marked with the points "2", "3" and "4". At the end, the robot should return to the starting position (point "0"). The cloud computer calculates the optimal route on the way 1-2-3-4-0. This route is represented by the green solid line in Fig. 5. During the motion along the desired route, the robot takes care about static and mobile obstacles in the megastore and reports the cloud computer about its current position, the position of obstacles and the strategy for their avoidance. In this way, reliable motion of the robot and transport of goods in the megastore are achieved. The same principle is used for realizing the collaborative behaviour of robots in known environments. Robot can share the maps of the environment with other agents.

# 5  Conclusion and Future Work

The paper presents a concept of multi-robot control for smart store scenarios using cloud robot structures. The proposed concept of smart scenario control is verified by simulation using several computers networked in a cloud structure. The reported research proved that the majority of robotic tasks accomplished in the smart store scenario are performed faster and more reliable if they are subordinated to the cloud control system. The results obtained in this work will be implemented in a real system that will be developed in an experimental pilot project demonstrating smart scenarios with several networked robots performing tasks in environments with obstacles.

# References

1. Metro future store. http://www.spychips.com/metro/overview.html. Accessed Mar 2016
2. Cloud robotics. https://en.wikipedia.org/wiki/Cloud_robotics. Accessed Mar 2016
3. Roboearth. http://roboearth.org/. Accessed 7 Dec 2014
4. Waibel, M., Tenorth, M., D'Andrea, R.: RoboEarth. IEEE Robot. Autom. Mag. **18**(2), 69–82 (2011). doi:10.1109/MRA.2011.941632
5. Rapyuta. http://rapyuta.org/welcome. Accessed 7 Dec 2014
6. Hunziker, D., D'Andrea, R., Gajamohan, M., Waibel, M.: Rapyuta: the RoboEarth cloud engine. In: 2013 IEEE International Conference on Robotics and Automation (ICRA), pp. 438–444, May 2013. DOI:10.1109/ICRA.2013.6630612
7. KnowRob. http://ias.in.tum.de/research/knowledge. Accessed 8 Dec 2015
8. RoboBrain Project. http://robobrain.me/#/. Accessed 7 Dec 2015
9. Robo Brain' mines the Internet to teach robots. http://www.news.cornell.edu/stories/-2014/08/robo-brain-mines-internet-teach-robots
10. MyRobots. http://www.myrobots.com/wiki/About. Accessed 9 Dec 2015
11. Hu, H., McDonald-Maier, K.D., Gu, D., Li, R.: COLAS project. http://coalas-project.eu/indexen.php?p=team. Accessed 7 Dec 2014
12. ROS java-Cloud Robotics. http://docs.rosjava.googlecode.com/hg/rosjava_core/html/index.html. Accessed 9 Dec 2014
13. KIO RTLS sensor, Eliko .(http://www.eliko.ee/products/kio-rtls/)

# Human-Robot Interaction and Collaboration

# Realisation of an Experimental Cooperative Workplace for Assembly Tasks

Marek Vagaš[(✉)], Jan Semjon, and Mikulas Hajduk

Faculty of Mechanical Engineering, Technical University of Kosice,
Kosice, Slovak Republic
{marek.vagas,jan.semjon,mikulas.hajduk}@tuke.sk

**Abstract.** In this paper, an innovative approach to human-robot cooperation is designed and applied to real cooperative workplace based on a practical assembly task. Therefore, the object of assembly which is actually produced was chosen, used and deployed in practice. Security of the cooperative workplace is resolved by an external device, i.e. a security 2D laser scanner from the company SICK. Simulation and technical feasibility of the solutions were analysed with the software package Tecnomatix produced by Siemens. Checking of the grip and sequence of assembly operations are ensured through human operator using the control panel with LEDs and acknowledgment buttons.

**Keywords:** Cooperation · MOTOMAN SDA10F robot · Assembly

## 1 Introduction

The continuous development and growing trend in robotics increasingly shift from individual, isolated deployment of industrial robots to group building of cooperative workplaces, of human-robot type. Typically, in an industrial field both a human and a robot operate separately from one another to avoid the collisions. Industrial robots can be deployed both in control applications and in tuning which reduces potential human error. The robot gets into hardly reachable places easier, achieves incomparable accuracy and speed, and relieves people from the repetitive work. On the other hand, the human operator is more flexible and more adaptable to new or adverse situations, and has incomparable higher sensorimotor skills which are also used in other sectors (such as surgery, orthopaedics, a.o.). Therefore, the continuous development and growing trend in robotics have been increasingly shifting from individual and isolated deployment of industrial robots towards group building of cooperative human-robot workplace, typically in SMEs [1].

The term human-robot cooperation means mutual cooperation employment which complements each other, for example during assembly, handling, palletizing and de-palletizing, surface treatment and various technological operations. The advantage of this cooperation is shortening innovation cycles and flexible responding to market demand which is difficult to predict or to specific requirements of customers. In such cases, the cooperation between humans and robots is an ideal choice. Robots can be used in control and debug applications, which reduces the possibility of human error.

The robot can access hard to reach places with high accuracy and speed and can relieve people from monotonous work [2]. Thus, humans can focus more on creative processes and perform more valuable tasks that a robot is able to do without changing tools. The robot is also flexible and easily adaptable to adverse situations. Typical for fully automated workplaces with robots (equipped with appropriate end effectors) is continuous operation and high productivity [3]. The robots are not subject to work fatigue, especially when these workplaces are used for simple assembly tasks. On the other hand, the human prove unmatched sensory-motor skills for complex operations, and can easily adapt to new processes, see Fig. 1; limitations occur however concerning the force and accuracy of tasks performed by humans. A cooperative workplace combines the advantages of manual labour with fully automated workplace that uses robots [4].
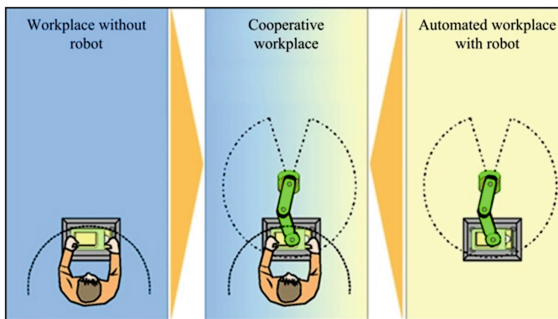


**Fig. 1.** Combinations of workplace: without robot, cooperative workplace and automated workplace with robot

## 2   Safety of Cooperative Workplace

Safety is a key issue to design human-robot collaboration, i.e. whenever a robot and a person share a common workplace. This is especially true with this new kind of collaborative cage free robots, many of which are designed to operate very close (shoulder to shoulder) with their human partners [5]. Currently there are various standardisation bodies that deal with safety in the context of human-robot collaboration. The most important are the Organization for Standardization (ISO) and the American National Standards Institute (ANSI). ISO 10218 is the most recent set of standards regarding safety in industrial robots environments (ISO 10218-1, 2011; ISO 10218-2, 2011). The European Union has adopted it immediately. Other safety norms, concerning the safe distance to be maintained between humans and robots are included in ISO 13855 (2010).

In addition, as the interaction between humans and robots is becoming an increasingly relevant argument inside the robotics community, a new ISO 15066 (2014) norm about this problematic is under development [6]. To avoid injury, it is necessary to find a mutual link between the behaviour of the robot and possible

**Fig. 2.** Location of 2D laser scanner on the work desk of robot within cooperative workplace

personal injury. It is usually necessary to ensure that the robot does not exceed the maximum safe zone, and thus it does not enter into contact with the human operator [7]. As the industrial robot SDA 10F itself has not directly integrated sensors of this type, we have used an external security device of 2D laser scanner type, see Fig. 2.

Using the small 2D laser scanner S300 mini connected to a computer, three safety zones (one is protective and two are warning) can be tracked, in programmable mode using the CDS software [8]. Various parameters setting, such as the shape of zone, the range of scanning zones, the response format, etc. can be configured by software. Figure 3 shows the design and drawing of 2D laser scanner safety zones with CDS software.
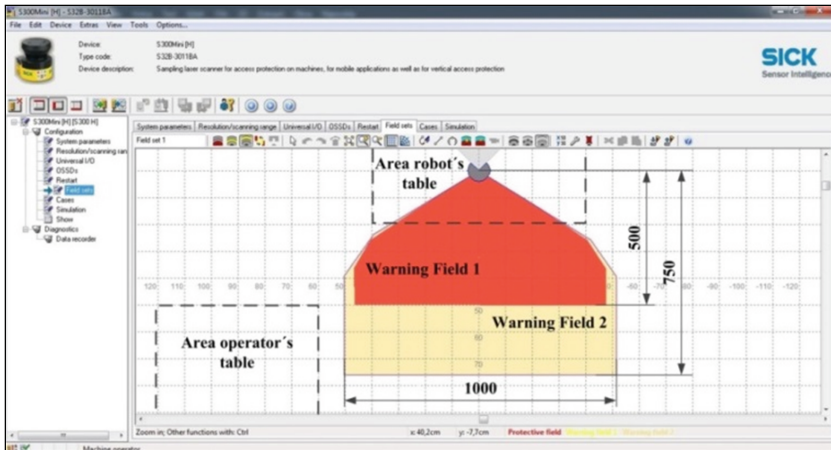


**Fig. 3.** Drawing of the proposed 2D laser scanner security zones

Workplace safety is based on the functions of the robot control system Speed Limit-speed restriction robot, which is represented by *warning field 2* connected to the FS100 standard I/O LIO-08R Circuit Board. The safety is also ensured by the function

Hold - suspension of the robot which represents the *warning field 1*. Based on type 3 laser scanner class, a direct reference was established to safety category 3 in EN 954-1 and safety integrity level (EN 62061) to category 2. Sick recommends the application of EN ISO 13849-1.

## 3   Experiments and Tests of Cooperative Workplace

Verification of the functionality of the cooperative workplace is a key aspect to validate solutions. One major goal is perform experiments that will be later executed in real application scenarios. In this context, the set up and modification of an assembly processes was realized through software simulation, which offered the possibility to test rapidly functionalities, planned changes or improvements of the cooperative assembly processes. Based on this simulation, the future layout and operating of the real cooperative assembly workplace can be validated. 3D Simulation can reflect the actual status and conditions on the running system and, after some improvements it can show the final layout of the cooperative workplace [9]. The cooperative workplace simulator was realized with the software package Tecnomatix produced by Siemens; it allows the verification of the workstations' design and the achievement of required safety during product execution (Fig. 4).

In addition to the detection and prevention of collisions, an ergonomic assessment procedure for evaluating the motion sequence of the human model regarding ergonomics is performed during simulation, see Fig. 5.

This evaluation methodology is based upon the observation of body postures, which are described by the combination of all joint positions of the human model. The joint coordinates and motion data are provided by human simulation and are used for evaluating the resulting load on the human.
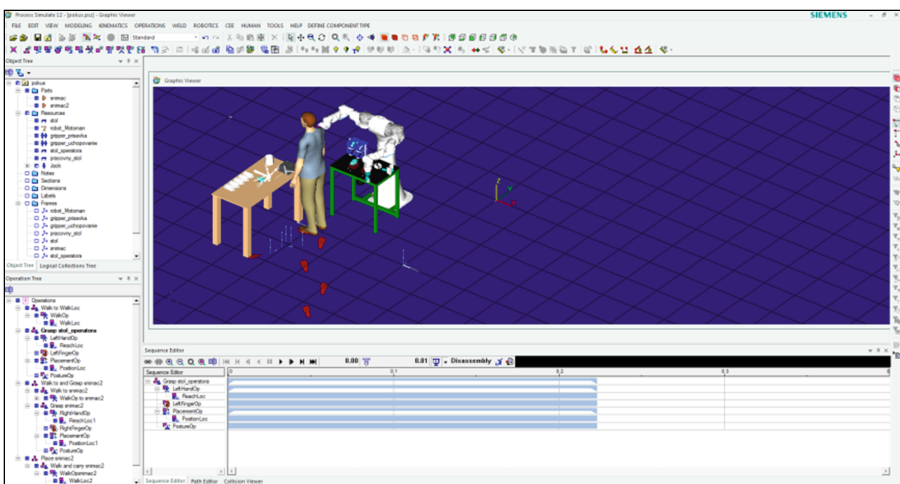


**Fig. 4.**  Simulation of designed assembly cooperative workplace at process simulate software
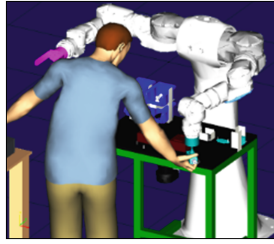
**Fig. 5.** Evaluating of ergonomics of human during grasping of an assembly object

The experiments have been executed in the Laboratory of robotic systems, Dept. of Robotics, TUKE, Slovakia. Some experiments were carried out with the safety 2D laser scanner, others were realised in the software simulation from Tecnomatix (Process Simulate) [10]. Two approaches were mainly taken into account: the safety with regards to persons entering the shared workspace at assembly time. The assembly consists of mounting two Telemecanique limit switches into a prepared package box. The safety laser scanner inspects the workplace surroundings several times during assembly. From the data configured, the CDS reports the frontier and size of the human access warning field within the protection zone, see Fig. 6.
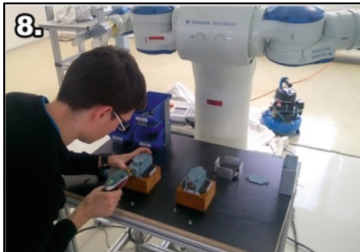
To demonstrate the implementation and usefulness of the proposed algorithm, the cooperative assembly sequence is illustrated in Table 1. A number of sequences were chosen based on the assembly cycle of the final product. The experimental case study is of particular importance, as it assesses the performance of the actual assembly cooperative processes and allows for comparison with other scenarios and theoretical approaches for the analysis of compliant assembly processes.

The assembly sequence is split into steps (or frames) that put in evidence the basic assembly processes performed by the robot and the human operator in the cooperative
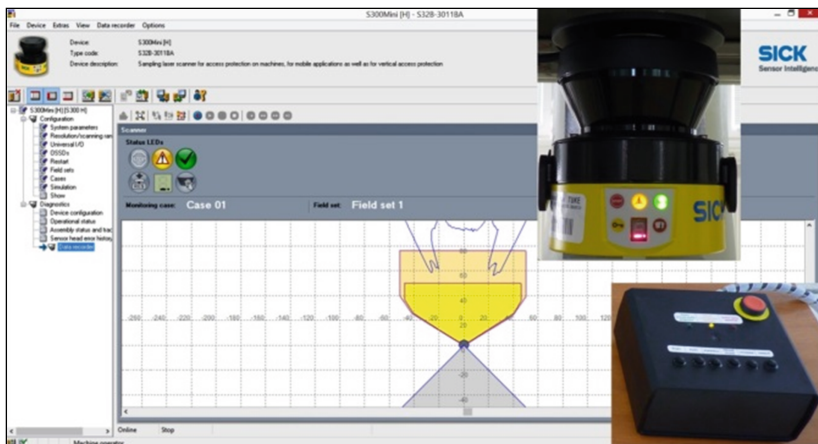


**Fig. 6.** Experiment for reading of warning field in case of human access into protection zone.

**Table 1.** Cooperative assembly sequence of one limit switch

| | |
|---|---|
| 1. In the first step the robot is situated in HOME position<br> | 2. After program start, left robot hand gives to human limit switch body, right hand gives stack with electric switch<br> |
| 3. Left hand takes base plate of switch and put it on working table. Right hand puts back simultaneously stack with electric switch<br> | 4. At human ack. (from operator panel), man take screws to fix electric switch on limit switch body<br> |
| 5. This step is characterized by placing two metal pads on the limit switch body<br> | 6. At human ack. (from operator panel), man takes screws to fix two metal pads on limit switch body<br> |
| 7. Left hand places limit switch body on base plate of limit switch, right hand gives to human steel roller plunger<br> | 8. Operator fixes by srews 2 pieces of steel roller plunger on limit switch body<br> |

| | |
|---|---|
| 9. Right hand of the robot gives to human stack with cable | 10. Left hand turns by 180 deg. limit switch body for screwing cable by human operator |
| 11. After human ack. for taking two cables, human screws them to limit switch body | 12. Finished product (limit switch) is presented by left hand to human operator |
| 13. Human operator takes finished products for packing | 14. Robot moves in HOME position, prepared for next cycle |
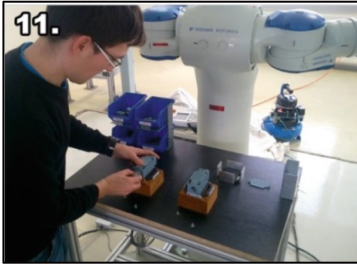
workplace. The assembly sequence starts in the home position of the dual-arm robot that waits for instructions from a human operator concerning the progress of the assembly process.

The operator stands in front of the dual-arm robot work desk and works on the assembly of the product too. The operator enters instructions via the control panel buttons and controls the execution and accuracy of the assembling process. The final step in this sequence is the return to the start position.

## 4  Conclusion

The goal of this work is to propose and experimentally verify the cooperation strategy and structure between the human operator and an industrial robot applied to an assembly process. The continuous development and growing trend in robotics increasingly shift from individual, isolated deployment of industrial robots to group building of cooperative workplaces, of human-robot type. The authors propose an innovative human-industrial robot cooperative workplace while solving the problems of mutual safety, growing cost for employees in manufacturing tasks and frequent changing of product types. The main aim is to find out an optimal way on how to ensure human security alongside an industrial robot. Moreover, some extensions and details of cooperation are provided. With this framework of cooperative workplace, the solution is sufficiently flexible to deal with various and complex assembly tasks.

The presented framework allows implementing cooperative workplace for a given industrial application, and to evaluate its efficacy with respect to other assembly technologies. Moreover, the concept of cooperative framework can be applied to production domains that are different from assembly. In the future, a complex 3D camera system will be implemented into the cooperative workplace to make a closer connection with the robot control system. This connection ensures better practical testing and implementation of assembly applications requiring object recognition by vision.

## References

1. Pires, J.N., Veiga, G., Araújo, R.: Programming-by-demonstration in the co-worker scenario for SMEs. Ind. Robot. Int. J. **36**(1), 73–83 (2009)
2. Consiglio, S., Seliger, G., Weinert, N.: Development of hybrid assembly workplaces. In: CIRP Ann. Manufact. Technol. **56**(1), 37–40 (2007)
3. Havlík, Š., Hricko, J.: The RCC mini-gripper for precise assembly. In: Modern Machinery Science Journal: 20th International Workshop on Robotics in Alpe-Adria-Danube Region, RAAD 2011, special edition, pp. 128–133 (2011). ISSN 1805-0646
4. Krüger, J., Lien, T.K.: CIRP annals - manufacturing technology **58**(2), 628–646 (2009)
5. Anandan. T.M.: The end of separation: man and robot as collaborative co-workers on the factory floor, Robotic Industries Association, 06 June 2013
6. Massa, D., Callegari, M., Cristalli, C.: Manual guidance for industrial robot programming. Ind. Robot. Int. J. **42**(5), 457–465 (2015)
7. Albu-Schäffer, A., Haddadin, S., Ott, Ch., Stemmer, A., Wimböck, T., Hirzinger, G.: The DLR lightweight robot: design and control concepts for robots in human environments. Ind. Robot. Int. J. **34**(5), 376–385 (2007)
8. https://www.mysick.com/eCat.aspx?go=FinderSearch&Cat=Row&At=Fa&Cult=English&FamilyID=282&Category=Produktfinder&Selections=59608,59491

9. Trebuňa, P., Popovič, R., Klos, S.: Methodology of the creation of human and robot operation in the tecnomatix process simulate. Procedia Eng. Model. Mech. Mech. Syst. **96**, 483–488 (2014). ISSN:1877-7058
10. Vince, T., Molnár, J.: Remote measurements of variable topology system. In: Proceedings of Annals of DAAAM, pp. 1179–1180. Rakúsko: DAAAM International Vienna, Viedeň (2001). ISBN:978-3-901509-83-4, ISSN:1726-9679

# Multi-level Human-Machine-Interaction Monitoring and System Reconfiguration

Achim Wagner[(✉)], Christian Bartolein, and Essameddin Badreddin

Automation Laboratory, Institute of Computer Engineering, Heidelberg University,
B6, 26, 68131 Mannheim, Germany
achim.wagner@ziti.uni-heidelberg.de

**Abstract.** A hierarchical approach for human-machine-interaction monitoring and system reconfiguration is proposed, which is grounded on local quality of interaction detection and mode-switching in real-time. For integrating the human behaviour in the closed-loop control structure, the overall technical system is decomposed recursively into nested behaviour levels and interfaced to the user on the corresponding level. In a gaze-based wheelchair control application, the local interaction with the user's gaze is assessed in order to estimate the intention for a specific action related to wheelchair control. Besides the level of interest directed to a goal object, the quality of estimation is forwarded to a reconfiguration component. Finally, the system is switched to the interaction mode, which provides maximum assistance under the given interaction constraints.

**Keywords:** Human-machine-interaction · Gaze-based wheelchair control · Interaction monitoring · System reconfiguration

## 1 Introduction

Safety-critical technical systems such as medical systems with physical human-machine-interaction need to be highly dependable. One fundamental property of such a dependable system is fault-tolerance. Diverse Active Fault Tolerant Control (AFTC) approaches and techniques are known from literature (see e.g. [7,8]). AFTC in general is based on fault detection, isolation, diagnosis and system recovery [7]. While Fault Detection and Isolation (FDI) units in general recognize symptoms for undesired system behaviour supervising controllers reconfigure the system and prevent fault propagation within the system by selecting a pre-computed control law or by synthesizing a new control law in real-time. The AFTC concept accepts a larger range of unknown faults and a graceful degradation of the overall system. In this paper, the concept of AFTC is applied to fault-tolerant human-machine-interaction.

---

C. Bartolein—Now with the John Deere European Technology Innovation Center, Kaiserslautern, Germany.

The proposed user monitoring and system reconfiguration approach is applied to multi-level control systems interacting with the human-in-the-loop. Such system candidates can be found e.g. in automotive, avionics, service robotics and rehabilitation. This work utilizes a computer-controlled wheelchair system, which provides assistance behaviour for velocity control, collision avoidance, position control, and navigation (Fig. 3) [3]. The system is structured according to a Recursive Nested Behaviour-based Control (RNBC) structure [1], which relies on a decomposition of overall system behaviour into behaviour levels. Monitoring and reconfiguration are embedded locally on the corresponding behaviour level [6]. Since the architecture is founded on a behavioural description of components and since it provides designated interfaces between the technical system and the user, it is very appealing for a human-technology-interaction [9].

The concept is demonstrated on specific behavioural levels within a gaze-based assistant wheelchair control application, while results from previous work related to gaze-based wheelchair control are taken into account [2–4]. Gaze-based control is used for supporting people with needs for special input devices such as sip-puff controls [4]. The direction of gaze is measured in the wheelchair reference frame by an eyetracking device (iViewX HED, Sensomotric Instruments GmbH) and magnetic head-tracking (Polhemus, FASTRAK). The setup of the wheelchair system is shown in Fig. 1. For more details about the system realization refer to [2].



**Fig. 1.** Wheelchair prototype with head-mounted eye tracking system and real-time control system providing multiple assistance behaviours [4].

## 2   Interaction and Control System

The interaction and control concept is applied to a gaze-based Assistance Wheel Chair (AWC) control solution and a human-machine-interaction on multiple behavioural levels (Fig. 2). The higher levels always operate on the next lower levels recursively. The behaviours are active simultaneously, while multiple reference inputs are fused and/or selected on the specific level for combining the reference signals. The original gaze-based interaction system provides three interaction levels, while two of the intention estimation levels are worked out in this example. In the lower level (motion estimation), the reference velocity is derived from the user's gaze direction relatively to the wheelchair coordinates utilizing a pattern recognition procedure [4]. The reference velocity and the quality of estimation is forwarded to the collision avoidance block, which subsequently adopts the velocity reference for controlling the velocity of the wheelchair. On the goal estimation level, the direction of gaze relative to a known object in floor coordinates is processed. For this purpose the duration of objects fixations and their distance to objects are assessed in real-time and the level of interest directed to goal objects is determined by weighting functions (see below). The resulting target pose is the reference input of the navigation level.
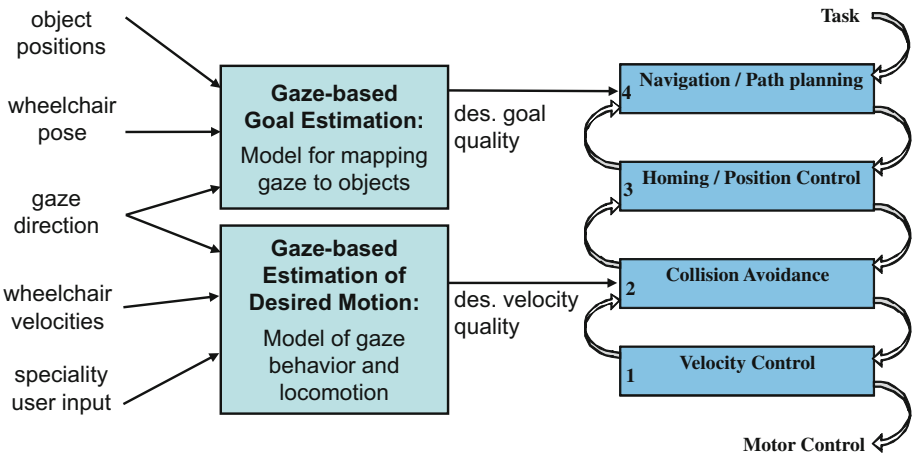


**Fig. 2.** User behaviour-modelling and intention estimation on three control levels with reference inputs and a related quality measure for each level (adapted from [4]).

Finally, the user is provided with most possible assistance and with the highest available interaction level, i.e. the navigation level if the goal estimation quality reaches a minimum value. In presence of faults or uncertain input signals on the upper levels, the system switches to lower level control, which is performed by a local reconfiguration mechanism on the corresponding level. Besides the gaze-based devices, additional inputs such as specialty control are utilized as fall-back device.

# 3   Monitoring of Human Gaze States

This paper focuses on gaze-based interaction monitoring on the two proposed wheelchair control levels and system reconfiguration on the velocity control level. Therefore the two interaction modes are described briefly based on previous work related to multi-level wheelchair control [2–4]. Furthermore, the basic interaction approaches were evaluated in a comprehensive study in indoor scenarios [5].

## 3.1   Motion Estimation

The human gaze-behaviour can be classified into motion-relevant gaze states and non-motion-relevant gaze states on the intended action of the user on possible external influences [3]. The gaze-states state detection is based on a Hidden Markov Model (HMM) approach, which is explained in detail in [3]. The models can be trained to the individual user's gaze behaviour, while a generalized data set is applied successfully. Motion relevant gaze states are combined with the continuous gaze data to control the velocity and the orientation of the wheelchair. Non-motion-relevant gaze states can be interpreted as faulty input, which must be handled by the velocity control system.

The overall structure is decomposed into a number of HMM-subsystems, where the input sequence $O_k = (\alpha_k, \Delta\alpha_k)$ of horizontal gaze directions is provided by the eye tracker component. The subsystem outputs are the probabilities $P(O|\lambda_m)$ for the observing sequence related to a state $\lambda_m$. Furthermore, the maximum likely observation sequence $m^{\max} = \arg\max_{1 \le m \le M} [P(O|\lambda_m)]$ is selected by the system. A measure for the level's confidence of gaze classification is the ratio $q_{ME}$ of probabilities between the selected and the next most likely state, which should be significantly higher than unity. The avarage of $q_{ME}$ over the evaluation time $t_e$ is a symptom indicating the quality of gaze classificaton, which can be used to switch the system configuration (see below).
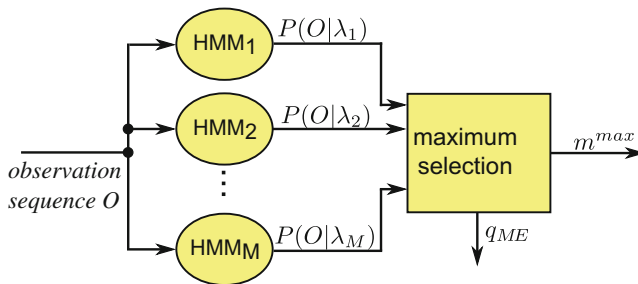


**Fig. 3.** Gaze state estimation using a number of Hidden Markov Models (HMM) (adapted from [4]).

## 3.2   Goal Estimation

On the goal estimation level the user-intended target position is retrieved by object related gaze behaviour [2,4]. The object related target position is forwarded to the navigation control level, where the desired path is planned and executed autonomously (see Fig. 2). The goal estimation signal flow is shown in Fig. 4.
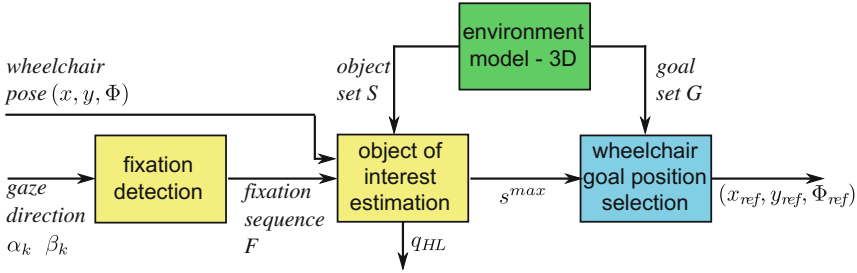


**Fig. 4.** Goal estimation: the object with maximum interest $s^{max}$ is estimated by a sequence of fixations $F$ and a set of objects $S$ in the environment; generation of a goal position $x_{ref}, y_{ref}, \Phi_{ref}$ and of a quality measure $q_{HL}$ (adapted from [4]).

The interest directed towards objects is derived from the time-dependent intensity of fixating of task-related objects. For a detailed description of the technical and psychological background see [2,3]. The goal estimation retrieves the object with the highest user interest based on sequences of fixations. While the fixations are given by the I-DT (dispersion-threshold identification) algorithm [10], the duration of fixations and their distance from the centre of all known objects in the field of view are processed by the interest level function:

$$I_p(k) = \begin{cases} I_p(k-1)\epsilon + \frac{f_r}{D_{\max}} A e^{-\frac{1}{2}\left(\frac{\delta_p^r}{\sigma + \frac{1}{2}\arctan\frac{s_p^{obj}}{d_p}}\right)^2} & \text{if new fixation } F_r, \\ \\ I_p(k-1)\epsilon & \text{else}, \end{cases} \tag{1}$$

for all objects $S_p \in S$, time step $k$, fixation duration $f_r$, and angular (central angle) distance $\delta_p^r$ for every detected fixation $F_r \in F$. $D_{max}$ is the maximum fixation duration and $\epsilon$ the fading time extinction factor. The normalization factor $A$ keeps the interest level in range $0 \leq I_p \leq 1$. If the highest interest level $p^{max} = \arg\max[1 \leq p \leq S_p, I_p(k)]$ exceeds the interest threshold the corresponding object is forwarded for goal position generation.

In addition, a request for high level control ("reqHLC") is triggered, which can be accepted by the user ("HLC") or rejected ("LLC") as indicated in Fig. 5(c). In order to find the appropriate threshold value, test drives with multiple users ($n = 21$) in a realistic indoor scenario have been carried out. During the

manual test drive using a joystick as input device, the object-directed gaze was recorded and processed subsequently. Based on the gaze data, the threshold value has been adjusted in a way that only objects, to which the user clearly showed interest by targeting them repetitively and for a longer fixation time, have been selected. This leads to a value $T_I = 0.5$, which can be further adjusted manually to individual gaze behaviour of the wheelchair driver. Finally, the resulting threshold is utilized for gaze-based wheelchair control on the goal estimation level. For an exemplary test drive goal estimation signals are plotted in Fig. 5.

The first diagram of Fig. 5(a) shows the interest level for all known objects together with the interest threshold. The objects with the highest interest and the goal objects are plotted in Fig. 5(b), which also indicates the goal objects proposed to the user once the interest threshold has been reached, while Fig. 5(c) shows the selected high level action (see above). As measure for the estimation confidence level, the quality signal $q_{HL}$ is derived from the ratio of the highest and the second highest interest level. The quality signal is used for behaviour selection in the reconfiguration component.
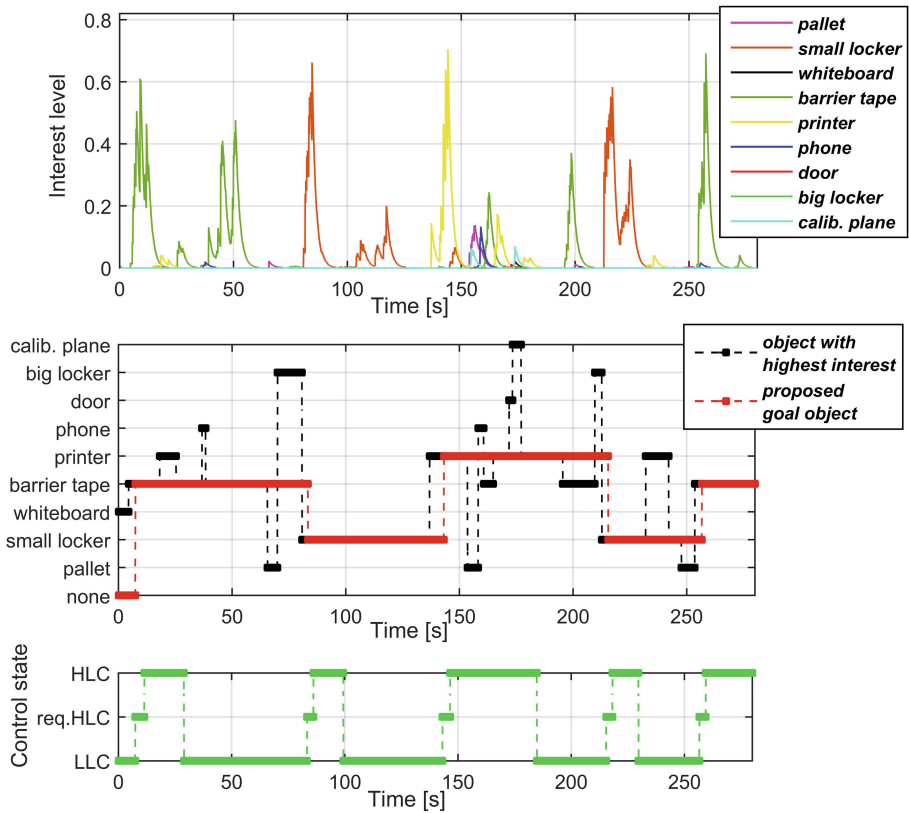


**Fig. 5.** Interest levels with threshold for a test drive (a), object with highest interest and proposed goal object (b), control state for goal acceptance (c) [2].

# 4 Gaze-Based System Reconfiguration

Gaze-based wheelchair control is demonstrated on two behaviour levels, i.e. the velocity control (collision avoidance if available) and navigation level. Utilizing the quality signals of the specific interaction level the system is reconfigured in order to reach the most dependable overall system behaviour taking into account environmental uncertainty and user's gaze behaviour. For that purpose, a low goal estimation quality on the higher navigation level is propagated through the intermediate levels reaching the velocity level (Fig. 6). The decision about the local configuration and the switching is carried out on the local level, i.e. the velocity control level. The block diagram contains the local controller "C", the reasoning component "R" and switching/fusion component "F". The "R" block receives the quality measures for input signals (gaze motion input $q_{ME}$, higher level input $q_{HL}$) and switches to the reference related to the highest available control level. Besides a pure switching, the concept includes also a sliding between modes and an adaptation of the control parameters in the "C" block. While the basic gaze-based wheelchair control behaviours were evaluated in former studies [5], the evaluation of the overall reconfiguration behaviour is still work in progress.
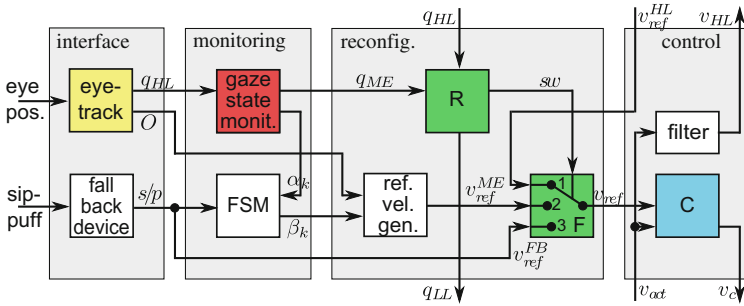


**Fig. 6.** Velocity control level of the wheelchair with interface, monitoring, reconfiguration and control blocks.

# 5 Conclusion

A general concept is proposed to use quality measures for all stages of human-machine-interaction, in order to provide a criterion for dependable system reconfiguration. In the application, human gaze behaviour provides features for controlling advanced semi-autonomous systems such as assistance wheelchairs on diverse behavioural control levels. This is demonstrated on two levels, i.e. the motion (velocity) control level (low level) and the navigation level (high level). In order to avoid dangerous situations the raw gaze direction signals are processed in order to retrieve the user's gaze state, which may be relevant or not for the

intended motion. On the higher behaviour level, the gaze directed to objects in the environment is captured as interest related to object-specific actions (autonomous driving to goal positions). We propose to generate quality measures for gaze processing on both levels providing a switching signal for system reconfiguration. Since this quality measures constitute dynamical signals, which depend on the available information about the environment (known objects available or not) and the user state, the signals are retrieved in real-time for dependable system reconfiguration. The reconfiguration takes place on the local level in order to ensure proper system function, if higher level behaviours are not available.

# References

1. Badreddin, E.: Recursive nested behavior control structure for mobile robots. In: Proceedings of the International Conference on Intelligent Autonomous Systems 2 (IAS.2), pp. 586–596. Amsterdam (1989)
2. Bartolein, C.: Design, implementation, and evaluation of a gaze-based wheelchair assistance system. Ph.D. thesis, University of Mannheim (2012)
3. Bartolein, C., Wagner, A., Jipp, M., Badreddin, E.: Multilevel intention estimation for wheelchair control. In: European Control Conference. Kos, Greece, 2–5 July 2007
4. Bartolein, C., Wagner, A., Jipp, M., Badreddin, E.: Easing wheelchair control by gaze-based estimation of intended motion. In: 17th IFAC World Congress (2008)
5. Jipp, M., Bartolein, C., Badreddin, E.: The impact of individual differences on human information acquisition behavior to enhance gaze-based wheelchair control. In: IEEE International Conference on Systems, Man and Cybernetics, SMC 2008, pp. 2591–2596 (2008)
6. Luo, Y., Wagner, A., Zouaghi, L.M., Badreddin, E.: An integrated monitor-diagnosis-reconfiguration scheme for (semi-) autonomous mobile systems. In: International Workshop on the Design of Dependable Critical Systems, Hamburg (2009)
7. Patton, R.J.: Fault-tolerant control: the 1997 situation. In: Proceedings of IFAC Symposum SAFEPROCESS 1997, Hull, UK, pp. 1033–1055 (1997)
8. Siewiorek, D.P., Swarz, R.S.: Reliable Computer Systems: Design and Evaluation, 3rd edn. A K Peters Ltd., Natick (1998)
9. Wagner, A., Jipp, M., Kandil, A.A., Eck, C., Badreddin, E.: Generic system architecture for dependable interactive systems: a flying robot example. In: 2010 IEEE International Conference on Systems Man and Cybernetics (SMC), pp. 2129–2136 (2010)
10. Widdel, H.: Operational problems in analysing eye movements. In: Gale, A.G., Johnson, F. (eds.) Theoretical and Applied Aspects of Eye Movement Research, pp. 21–29. Elsevier Science Publishers B.V, North-Holland (1984)

# Gaze-Based Human-SmartHome-Interaction by Augmented Reality Controls

Tim Cottin[✉], Eugen Nordheimer, Achim Wagner,
and Essameddin Badreddin

Institute of Computer Engineering, Automation Laboratory,
University of Heidelberg, Heidelberg, Germany
{tim.cottin,eugen.nordheimer,achim.wagner,
badreddin}@ziti.uni-heidelberg.de

**Abstract.** The use of eye tracking systems enables people with motor disabilities to interact with computers and thus with their environment. Combined with an optical see-through head-mounted display (OST-HMD) it allows the interaction with virtual objects which are attached to real objects respectively actions which can be performed in the SmartHome environment. This means a user can trigger actions of real SmartHome actuators by gazing on the virtual objects in the OST-HMD. In this paper we propose a mobile system which is a combination of a low cost commercial eye tracker and a commercial OST-HMD. The system is intended for a SmartHome application. For this purpose we proof our concept by controlling a LED strip light using gaze-based augmented reality controls. We show a calibration procedure of the OST-HMD and evaluate the influence of the OST-HMD to the accuracy of the eye tracking.

**Keywords:** User interfaces · Gaze based SmartHome control · Optical feedback system · Eye-tracking · Augmented reality controls

## 1 Introduction

People who suffer from motor disabilities, e.g. locked-in-syndrome or amyotrophic lateral sclerosis, cannot use conventional computer input devices. With the use of eye-tracking systems these people are able to generate input commands through their eye movement, which enables them to interact with their environment. For example communication systems can be built up by displaying a virtual keyboard on a monitor. The user selects letters by gazing on them to formulate words and phrases. Such systems depend on the use of monitors which are placed in front of the user. The disadvantage of using conventional computer monitors is that the user's sight is impaired. This problem can be solved by the use of optical see-through head-mounted displays (OST-HMD). Furthermore, OST-HMDs allow the superposition of real objects with virtual objects to generate an augmented reality (AR). In addition, by combining an

eye-tracking system with an OST-HMD AR system, the user is able to interact with SmartHome actuators in the environment by means of gaze on virtual ones representing actions the SmartHome actuator can perform.

There are three main areas of relevant works regarding our research. The first is eye tracking in human-computer-interfaces. The use of eye tracking systems to interact with a computer is the focus of many researchers. In [8] Majaranta and Bulling give a good overview of the recent development in this field.

The second area is the integration of eye tracking systems and HMDs. Toyama et al. present in [13] a wearable integration of an eye-tracker and a see-through head-mounted display. The system tracks the users gaze position during document reading. The OST-HMD provides additional information about specific key words the user is gazing on. The user can interact with the display by gazing on elements shown in the display. The elements are triggered after a gazing dwell time of 2 s. In [12] Sonntag and Toyama present a similar system; they use gaze data and object recognition to register objects for location awareness. The OST-HMD provides navigation instructions. In [9] Nilsson et al. use a video ST-HMD with an integrated eye tracking system; they use marker tracking to highlight virtual information about corresponding real objects. The system is used for instructional applications and allows the user to respond to instructions or questions by gazing on virtual elements. Recently, commercial systems combining eye tracking and HMDs became available [7,10,11].

The last area is the interaction with the environment respectively home appliances using AR. An early work in this area is described in [4]. The user's field of view is determined by a head tracking sensor. Informations and control options of home appliances in the user's field of view are highlighted in a OST-HMD. The user needs to press a mouse button to trigger control options. In [14] Ullah et al. propose a system for elderly or physically disabled people to remote control home appliances using a smartphone. The system tracks QR codes with the smartphone for home appliances recognition. Control options and informations about the recognized home appliances is shown on the smartphone and can be selected using the touchscreen of the smartphone. A similar system is described in [5]. To the best of our knowledge no system exists which combines eye tracking and OST-HMD AR in a home automation application.

This paper presents a new interface for Human-SmartHome-Interaction. The first prototype was realized during a student project of Cottin [1]. The enhanced and embedded version is a first result of the AICASys Project [3]. We present a prototype system consisting of a wearable eye tracker and an AR OST-HMD. The system enables the user to trigger "on-off" actions of real objects in a domestic environment by gazing at dedicated virtual elements which are attached to the real object. Furthermore the OST-HMD gives visual feedback of the available actions of an object and simultaneously displays the measured gaze position in display coordinates. The proposed system consists of commercial hard- and software components which can be easily integrated, are lightweight and allow a mobile setup. For the proof of our concept we used the system to control a LED strip light as an example of a SmartHome application.
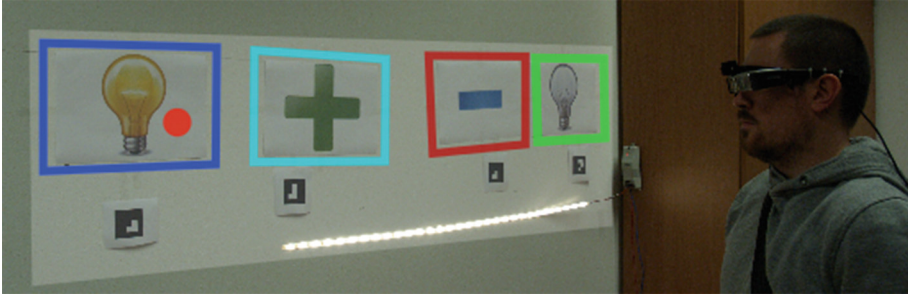
**Fig. 1.** User wearing the system. The augmented reality controls of the actions are depicted as frames around the real object in the OST-HMD. Additionally the Point of Gaze is displayed in the OST-HMD.

Figure 1 shows a user wearing the system. The user sees augmented reality controls represented as frames and the computed Point of Gaze (PoG) in the OST-HMD. By gazing on the virtual controls the user can control the LED strip light.

## 2   Implementation Details

At the time of this study there were no commercial systems available which combined an eye tracker and an OST-HMD. Therefore we built up the system with separate eye tracker and OST-HMD and integrated them by ourselves. The *Pupil Pro* eye tracking system [10] is an affordable wearable eye tracker and allows the integration with an OST-HMD because of the open physical design.
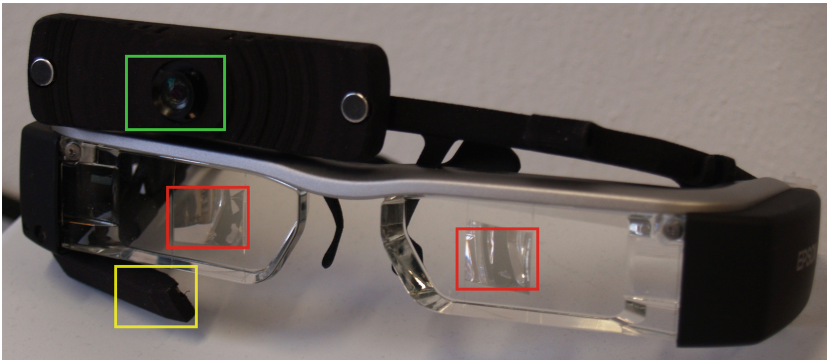


**Fig. 2.** Integrated Pupil Pro eye tracker with the Epson Moverio BT-200. Green frame: scene camera. Yellow frame: eye camera. Red frames: optical see-through display

For the OST-HMD we chose the *Epson Moverio BT-200* [2], which is a binocular OST-HMD and can be physically integrated with the *Pupil Pro* eye

tracker. Figure 2 shows the physically combined systems. We chose an *ODROID XU3 Lite* single board computer as processing unit for the eye tracker. It is a creditcard sized computer to allow a mobile setup. The home automation application is a LED strip light controlled by a FS20 DC-LED-dimmer. The LED-dimmer can be controlled with a FS20 remote control, connected to the *ODROID XU3 Lite.* With the dimmer one can perform on, off and dimming actions. Figure 3 depicts a block diagram showing the main components of the system. Additionally the information flow with the user and the environment is given.
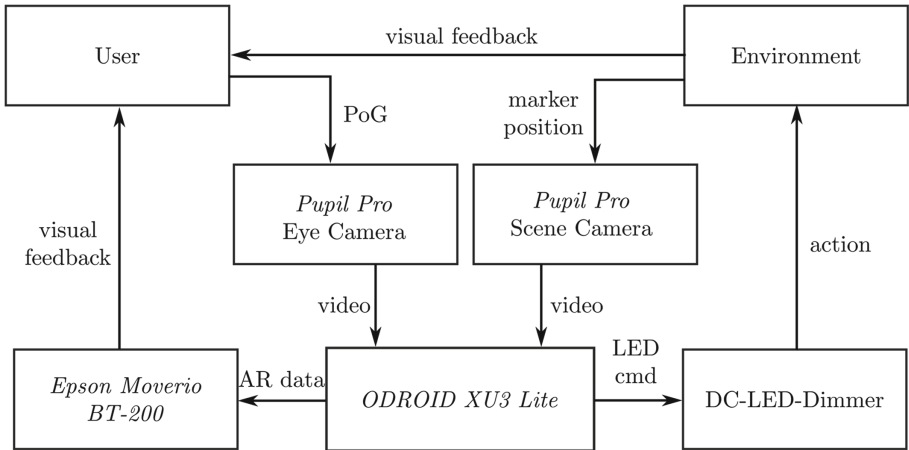


**Fig. 3.** The systems components and information flow

The software of the *Pupil Pro* eye tracking system is used to calculate the gaze position of the user. The user's pupil respectively its centre is detected by illuminating the eye with an IR LED, finding the dark pupil region in the eye camera image and approximating it with an ellipse [6]. The gaze position in scene camera coordinates is a function of the pupil position in the eye camera image and the function parameters are determined by point correspondence calibration [6].

Furthermore, the *Pupil Pro* software provides a fiducial marker tracking in the scene camera image. To each marker a so called surface can be attached. This surface is a virtual object and can be placed arbitrarily relative to its marker. In our system we use these surfaces and connect them with control inputs of our DC-LED-dimmer. By calculating the PoG relative to a surface we can determine if the user is gazing on it. With this mechanism the user can trigger actions by gazing on the surfaces with a dwell time. We have 4 different surfaces for the 4 actions: LED on, LED off, LED dimm lower, LED dimm higher. The surfaces are displayed in the OST-HMD if the corresponding marker is detected in the scene camera image and the surface overlaps the display (see Fig. 1). The user

is provided with visual feedback of triggered actions in the OST-HMD and by the LED strip light itself.

Figure 4 shows the geometrical relationships between the coordinates of the scene camera $\{S\}$, the display $\{D\}$, the eye camera $\{E\}$, the marker and a surface $\{Su\}$ from the users view.
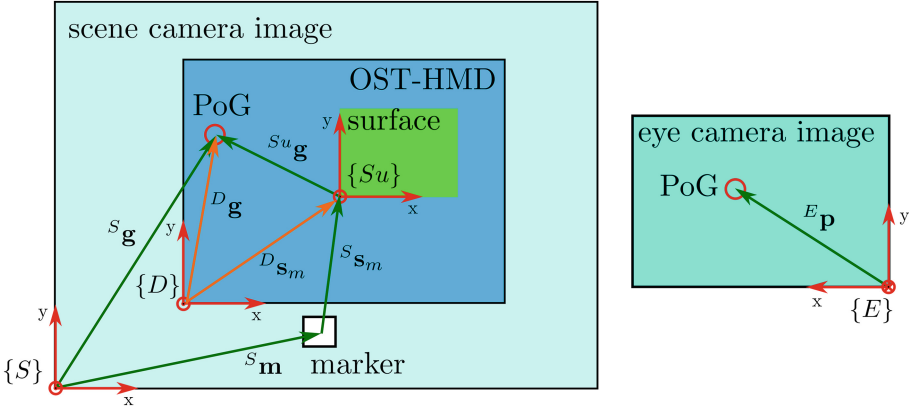


**Fig. 4.** Geometrical relationships between the scene camera $\{S\}$, display $\{D\}$, eye camera $\{E\}$, marker and surface $\{Su\}$ from the user's view [1]. The green vectors are calculated by the Pupil Pro software. The orange vectors are required.

The green vectors are known and provided by the *Pupil Pro* software. This are the pupil position in the eye camera image $^E\mathbf{p}$, the PoG $^S\mathbf{g}$, the marker position in scene camera coordinates $^S\mathbf{m}$, the surface relative to the marker $^S\mathbf{s}_m$ and the PoG in surface coordinates $^{Su}\mathbf{g}$.

## 3    Referencing the OST-HMD in the Scene Camera

To display the PoG and the surface in the OST-HMD the vectors $^D\mathbf{g}$ and $^D\mathbf{s}_m$ are required (see Fig. 4). For this purpose the transformation from scene camera coordinates to OST-HMD coordinates need to be calibrated. The display is physically attached to the frame of the *Pupil Pro* eye tracker. Thus the position of the OST-HMD relative to the scene camera coordinate system is constant and the calibration needs to be done only once. We use a simple point correspondence calibration procedure. The user has to sit in front of a computer monitor where 5 reference markers are shown. In the OST-HMD there are 5 markers shown which have to be aligned by the user with the ones on the monitor. Figure 5A shows a user during the calibration process. In B the detected markers in the scene camera image $^S\mathbf{m}_{1,\dots,5}$ (orange markers) and the markers shown in the display $^D\mathbf{m}_{1,\dots,5}$ (green markers) are depicted.

The transformation is given by

$$^D\mathbf{m} = \mathbf{T} \begin{bmatrix} ^S\mathbf{m} \\ 1 \end{bmatrix} \tag{1}$$

**A**

**B**
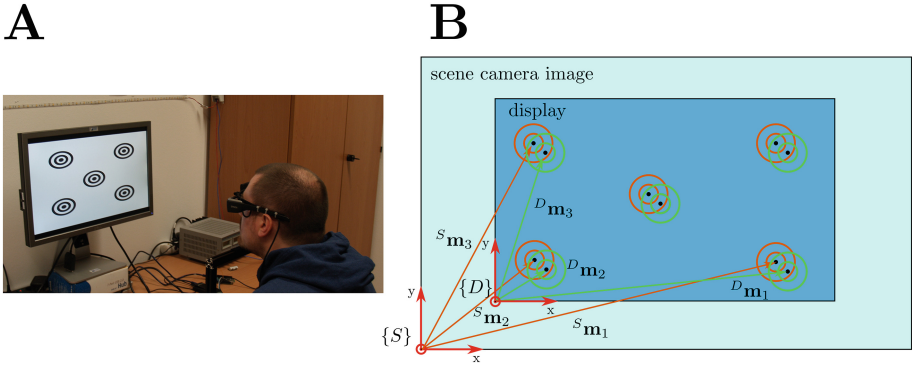


**Fig. 5. A**: user during the calibration procedure. **B**: scene camera image and display with the corresponding markers. [1]

with $\mathbf{T}$ the $3 \times 4$ transformation matrix. Combining the known points in this equation yields

$$\begin{bmatrix} ^{D}\mathbf{m}_1 \ \dots \ ^{D}\mathbf{m}_5 \end{bmatrix} = {}^{D}\mathbf{M} = \mathbf{T} \begin{bmatrix} ^{S}\mathbf{m}_1 \ \dots \ ^{S}\mathbf{m}_5 \\ 1 \ \dots \ 1 \end{bmatrix} = \mathbf{T}\,{}^{S}\mathbf{M} \tag{2}$$

This can be solved by computing the pseudo inverse $^{S}\mathbf{M}^{+}$ of $^{S}\mathbf{M}$. Now $\mathbf{T}$ can be determined

$$\mathbf{T} = {}^{D}\mathbf{M}\,{}^{S}\mathbf{M}^{+} \tag{3}$$

## 4 Experiments and Results

To evaluate the system we performed two experiments. The first one is an accuracy test for the eye tracker with real markers. The user sits in front of a computer monitor at a distance of $50\,\mathrm{cm}$. After the calibration the user is asked to gaze on random markers shown on the computer screen. The second experiment is an accuracy test using virtual markers which superimpose real markers shown on the monitor. In this experiment the OST-HMD is covered so that the user does not see the real marker. 5 users performed the experiments.

The angular error between the calculated gaze point and the detected point on the screen can be used as a measure for the accuracy of an eye tracking system. The calculation of the accuracy is taken from the *Pupil Pro* software. The mean angular accuracy $\bar{\alpha}$ of $n$ samples of PoG respectively $^{S}\mathbf{g}_{1,\dots,n}$ to the marker positions $^{S}\mathbf{m}_{1,\dots,n}$ is given by

$$\bar{\alpha} = \frac{d_{fov}}{n\sqrt{w^2 + h^2}} \sum_{i=1}^{n} \left\| {}^{S}\mathbf{g}_i - {}^{S}\mathbf{m}_i \right\| \tag{4}$$

where $d_{fov}$ is the diagonal field of view of the scene camera, $w$ and $h$ the pixel width and the pixel height of the scene camera.
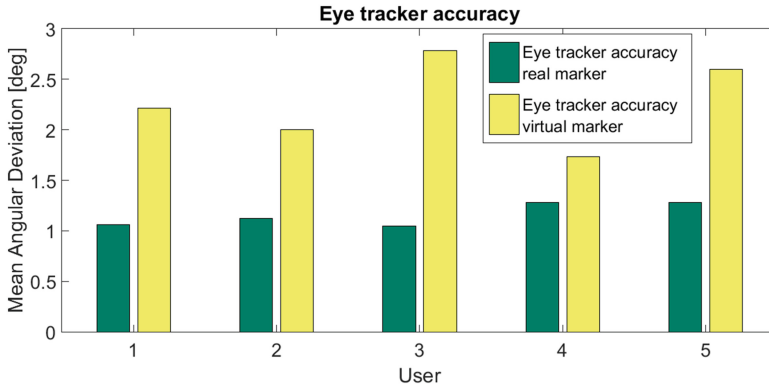
**Fig. 6.** Bar plot of the accuracy test results.

Figure 6 shows the results of the experiments. The angular accuracy of the eye tracker itself during the first experiments (green) is for all users about 1°. The second experiments (yellow) shows the influence of the OST-HMD calibration. It varies widely for the individual users which shows the disadvantage of user intervention during the calibration procedure.

## 5    Conclusion

Our hardware setup shows that the combination of an eye tracker and an OST-HMD is possible with commercial and low cost components. We trigger the actions by evaluating the gaze point relative to the surfaces and use a dwell time to infere the users intend. The usage of the OST-HMD in this application brings an important advantage. The surfaces are virtual objects and can be positioned arbitrarily relative to the interactive objects which are used as augmented controls. Because they are displayed in the OST-HMD the user must not necessarily know the position of the surfaces in his environment.

The calibration procedure of the display needs to be done only once. But it is unfavourable because it is time consuming and requires a highly focused user to align the markers in the display with the ones shown on the monitor manually. We see this as the main drawback of the proposed system. Future works need to tackle this problem and propose a calibration procedure which does not need user intervention.

Another goal for future works is the use of a object recognition algorithm based on natural features like SIFT instead of using markers. Furthermore to encounter the Midas Touch problem there has to be a focus on alternative trigger mechanisms by user gaze.

# References

1. Cottin, T.: Aufbau und Implementierung eines tragbaren, blickbasierten Steuerungssystems zur Interaktion mit der Umgebung (2014)
2. Epson: Epson moverio bt-200. http://www.epson.de/de/de/viewcon/corporatesite/products/mainunits/overview/12411
3. German Ministery of Education, Research: AICASys. http://www.mtidw.de/ueberblick-bekanntmachungen/ALS/aicasys
4. Hammond, J.C., Sharkey, P.M., Foster, G.T.: Integrating augmented reality with home systems. In: Proceedings of the 1st International Conference on Disability, Virtual Reality and Associated Technologies (ECDVRAT), pp. 57–66 (1996)
5. Heun, V.M.J.: Smarter objects: Programming physical objects with AR technology (2013)
6. Kassner, M., Patera, W., Bulling, A.: Pupil: An Open Source Platform for Pervasive Eye Tracking and Mobile Gaze-based Interaction. ArXiv e-prints, April 2014
7. Lusovu: Lusovu eyespeak. http://www.myeyespeak.com/
8. Majaranta, P., Bulling, A.: Eye tracking and eye-based human-computer interaction. In: Fairclough, S.H., Gilleade, K. (eds.) Advances in Physiological Computing. Human–Computer Interaction Series, pp. 39–65. Springer, London (2014)
9. Nilsson, S., Gustafsson, T., Carleberg, P.: Hands free interaction with virtual information in a real environment: Eye gaze as an interaction tool in an augmented reality system. PsychNology J. **7**(2), 175–196 (2009)
10. Pupil Labs: Pupil labs eye-tracking systems. https://pupil-labs.com/
11. SMI: Smi eye tracking upgrade for ar glasses. http://www.smivision.com/augmented-reality-eyetracking-glasses/
12. Sonntag, D., Toyama, T.: Vision-based location-awareness in augmented reality applications. In: 3rd International Workshop on Location Awareness for Mixed and Dual Reality (LAMDa 2013), pp. 5–8 (2013)
13. Toyama, T., Dengel, A., Suzuki, W., Kise, K.: Wearable reading assist system: Augmented reality document combining document retrieval and eye tracking. In: 12th International Conference on Document Analysis and Recognition (ICDAR), pp. 30–34, August 2013
14. Ullah, A.M., Islam, M.R., Aktar, S.F., Hossain, S.K.A.: Remote-touch: Augmented reality based marker tracking for smart home control. In: 15th International Conference on Computer and Information Technology (ICCIT), pp. 473–477, December 2012

# Toward an Active Protection for Robot Arms

Annalisa Bianchi[(✉)] and Marco Ceccarelli

LARM: Laboratory of Robotics and Mechatronics – DICEM,
University of Cassino and South Latium,
Via Di Biasio 43, 03043 Cassino, FR, Italy
{bianchi,ceccarelli}@unicas.it

**Abstract.** This paper describes the main requirements and key issues that are related with the design of active protections for robotic arms. A literature overview is reported to give insight on the existing solutions and challenges. Then, a novel design concept is proposed and a 3D CAD design is reported and described in order to show the feasibility and practical usefulness of a novel active protection for robot arms that is expected to provide improvements also in the interaction between human beings and robots.

**Keywords:** Service robots · Active protections · Protection design

## 1 Introduction

In the last decades, the use of robot has significantly increased in industrial environments. Recently, robots are attracting more and more interest for their possible use in service tasks for humans at their homes, offices, hospitals, as described, for example in [4, 16]. In particular, they are becoming a useful aid in dangerous or boring tasks even in non-industrial frames. Recent applications also propose significant human robot interactions for the daily aid and assistance to elderly and/or disabled people, [5, 14]. Nevertheless, two main issues still prevent a wide use of robots in non-structured human-populated environments, namely Safety and Reliability. These two main issues have been addressed in a large number of papers. The recent ISO standard, EN-ISO-13482-2014: Robots and robotic devices, Safety requirements for personal care robots, [7] has been developed in recognition of the particular hazards that are presented by newly emerging robots and robotic devices for novel applications in non-industrial environments. Unlike previous standards, EN-ISO-13482 focuses its attention to the safety requirements for a barrier-free human-robot interaction of personal care robots in non-medical applications.

In the available literature, several solutions, methodologies, and devices have been proposed for increasing safety and reliability of a robot. The existing approaches can be classified as either being "passive" or "active". The passive solutions aim at achieving an increase of safety and reliability by using soft materials, [12] or soft covers or similar means that can passively absorb or reduce the effects of impacts or other undesired collisions of a robot with the environment or with a human being.

The active solutions use tactile sensors [13], vision, or any other means to detect or even predict a potential impact or collision in order to take a specific active action of prevention or impact reduction.

In this paper the problem of safe operation of a robot interacting with human operators is analysed by looking at a protection that can prevent direct collision or reduce the impact between a robot structure and a human user. Additionally, if an impact occurs the proposed solution is able to transfer and/or transform a significant part of the impact energy to minimize its effects.

The proposed system includes a protective flexible cover, which is combined with mechanisms that are capable of transferring the impact energy to springs and dampers. An impact on the protective cover produces a deformation and the activation of the underlying mechanisms which are able to absorb the impact energy and also to return part of the accumulated energy at a later time. This energy may be accumulated to help the robot in its successive movements. For example, a humanoid robot that falls can use the stored impact energy to for returning to the upright position.

## 2   The Analysed Problem

Traditionally, safety in industrial applications is guaranteed mostly by using physical barriers between robots and operators [7], but this approach is no more suitable in many novel applications requiring direct and extensive human-robot interaction. Accordingly, robot design should be reconsidered to take into account the key issues given by safety constraints. In particular, the close cooperation among robots and humans deems to identify any possible technical solution not only to prevent accidental collisions, Fig. 1, but also to minimize their consequences. Great importance is given to the impact of a robot with human body or parts of it. Studies on biomechanics can provide useful information on the hazards and consequences of an impact of a robot part on a human body. In particular, the highest risk for the human life is given by impacts involving the human head. Accordingly, some authors propose different strategies to study the biomechanics of the head injury through different observation approaches, [6]. Head injury criterion (HIC) is also one of the key aspects to assess the safety of cars through crash tests. Similarly, indices can be formulated to link the amount of head injury with the level of safety of a robot such as, for example in [2].



a)                                                      b)
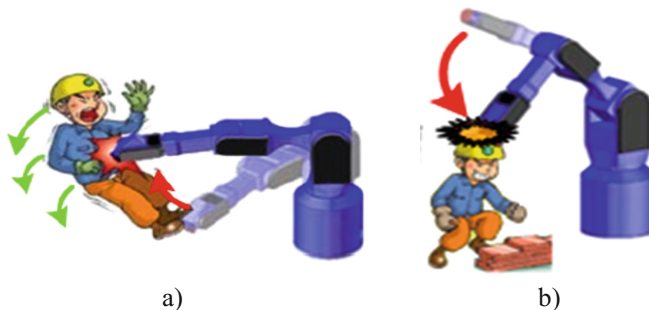
**Fig. 1.** Examples of risk situations during robot operation

## 3  Existing Protections: Characteristics and Drawbacks

One can identify two main approaches to increase safety, namely passive and active. Passive safety consists of solutions that can reduce/minimize the occurrence of an impact as well as reduce/minimize the damage caused by a possible impact. On the contrary, active safety consists of solutions that can detect/predict the occurrence of an impact and can take active actions to avoid or reduce its occurrence and effect.

All methodologies to increase the passive safety in the interaction of humans with robots are essentially designed to amend the robot structure and/or the robot operation so as to decrease the probability of impact occurrence. Robots designed by following the above passive safety criterion are characterized by lightweight, low inertia, flexible structures that can minimize the damage caused by a possible impact on a human being, [9]. Attention is often paid in smoothing out the rough edges, [8]. Very common is also the use of covers made by lightweight, soft, visco-elastic materials as proposed. Additionally, passive safety can be also achieved by focusing the attention at the robot actuators for reducing the inertia and the weight of all the movable parts of a manipulator, for example, through a Distributed Macro-Mini actuation DM, [9]. This technique consists of a different distribution of the robot actuators. Near the base of the robot are placed all the heavier parts, such as engines, then to transmit the motion to the joints cables and pulleys are used appropriately, [15]. Another technique aimed at improving the intrinsic safety for robotic manipulators consists in the use of so-called actuators with variable impedance or VIA (Variable Impedance Actuator) [18]. These devices are able to vary the mechanical impedance, i.e. the relationship between the torques applied to a point and the relative motion, depending on the work phase. The practical effect will be to have high speed machining phases modified such as to reduce the stiffness and the damping of the manipulator, and thus to minimize damage caused by a possible impact. At low speed, however, the change of the impedance will cause an increase of stiffness and damping, in order to obtain a better response in acceleration of the link and a lower oscillation during braking. An example of robot with solutions for passive safety is WENDY, Fig. 2, (Waseda ENgineering Designed sYmbiont) developed at Sugano Lab. Waseda University in 1998.
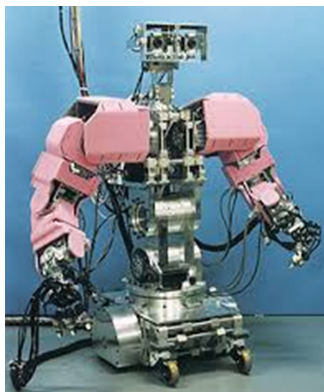


**Fig. 2.**  Wendy robot

In particular, robot designers have proposed the combination of high joint compliance and a soft cover for achieving shock absorption in potential human robot interactions, [11]. Active safety is the development of particular control strategies by integrating dedicated sensor(s) that take advantage of the constant monitoring of the surrounding environment to predict and avoid potentially risky situations. There are two types of sensors usually used in control algorithms for safety purposes, namely sensors that have the function to reconstruct the geometry of the environment surrounding the robot (cameras, laser scanners, proximity sensors, radars, infrared) or sensors that can directly detect a collision such as force sensors, pressure sensors, strain gauges.

Recently, several robots have been proposed with active safety features. For example, in 2013 KUKA has produced the robot "LBR iiwa 14 R820" (LBR stands for lightweight robot and "iiwa" stands for industrial intelligent work assistant), [10]. A prototype of this robot is shown in Fig. 3(a). LBR iiwa 14 R820 weighs only 29.90 kg. It has an exterior design without corners, sharp or pointed edges. This robot is equipped with integrated sensors at each joint that run built-in-high-performance collision detection algorithms.



a)                                    b)                                    c)
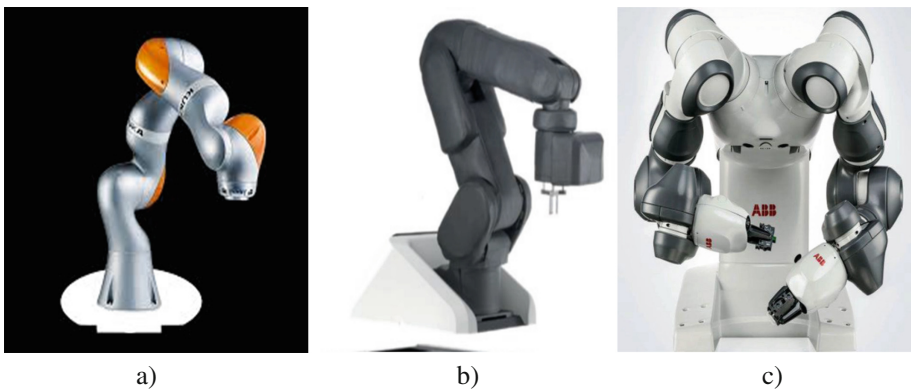
**Fig. 3.** Examples of safe-designed robot: (a) KUKA LBR iiwa 14 R820; (b) APAS assistant; (c) YUMI

Similarly, in 2013 BOSCH has launched in the market the collaborative robots APAS assistant, [3], Fig. 3(b). This manipulator arm has an outer cover that has been defined as "sensor skin", which reacts immediately when someone approaches. Accordingly, the control loop can stop the robot as soon a contact with the soft skin is detected. The robot will stay in standby state until humans are detected to move away from the danger zone that is set to be approximately 50 mm from the robotic arm.

Also ABB has designed a robot with two collaborative safe arms called "YUMI" weighting only 38 kg, Fig. 3(c). These robotic arms have a lightweight magnesium structure wrapped in a padded plastic cover. If the robot encounters an unexpected obstacle such as when colliding with an operator the control system stops the robot in few milliseconds, [1].

# 4 Design of an Active Protection

In this paper, the problem for safe operation of a robot interacting with human operators is considered by looking at a protection that can prevent direct collision between a robot structure and a human user. Additionally, if an impact occurs the proposed solution should be able to transfer and/or transform a significant part of the impact energy to minimize its effects. The proposed concept has been developed starting from the design of helmets that are used, for example, in sports such as football, baseball, cycling, ice hockey, mountain climbing, boxing, Fig. 4. All helmets attempt to protect the user's head by absorbing mechanical energy and protecting against penetration. Practical concerns also dictate helmet design: a bicycling helmet should be aerodynamic in shape and well ventilated, while a rock climbing helmet must be lightweight and small so that it does not interfere with climbing. In particular a motorbike helmet is composed of an outer cap and an inner cap, and the external shell does not absorb energy, but has the function to redistribute it over its entire surface in such a way as to eliminate the stress concentration at localized points. The inner shell has the aim to deform during impacts, thus absorbing the kinetic energy that would otherwise discharge on the head of the wearer of the helmet, and is usually moulded in foamed polymers. Additional useful inspiration for a proper active protection has come from the observation of nature in terms of biomimetism of the armadillo or woodlouse as shown, for example, in Fig. 5.



a)                    b)                    c)                    d)

**Fig. 4.** Examples of protective in: (a) cycling; (b) industrial; (c) motorbike; (d) football



a)                              b)
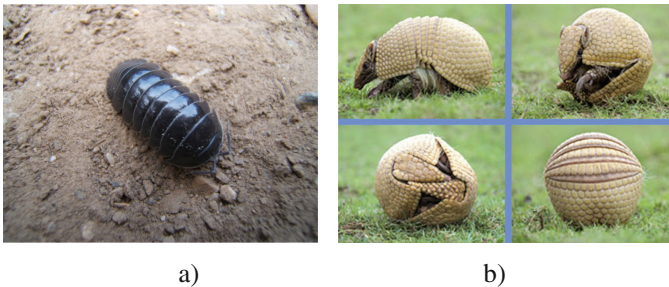
**Fig. 5.** Examples of external animal covers: (a) woodlouse (Armadillidium Vulgare) [17], (b) armadillo (six-banded armadillo)

The woodlouses (Armadillidium Vulgare) use their exterior to protect themselves by forming a sphere that does not offer footholds to an aggressor, [17]. Additionally, the cover is made of sliding elements that allow large movement and adjustment of the cover shape to specific impacts or movements. Based on the above inspiration it is proposed to combine a pliable protective cover with mechanisms capable of transferring the impact energy to dissipation into elastic and damping systems. As detailed in the conceptual diagram in Fig. 6, a possible impact on the protective cover produces a deformation and a handling of the underlying mechanism that is connected to appropriate springs and dampers.
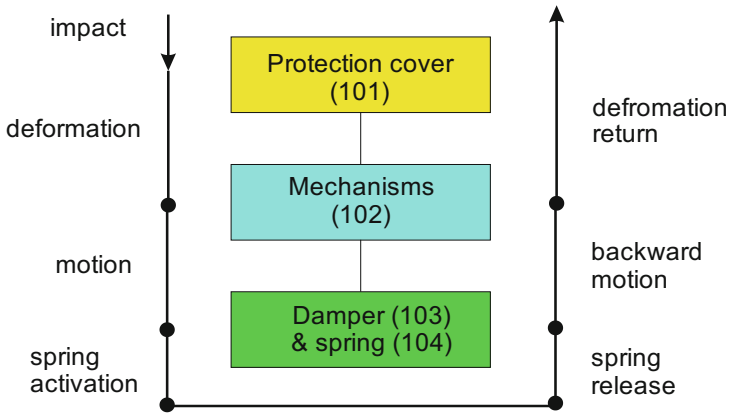


**Fig. 6.** A conceptual design scheme for robot protection

Thus an active protection for the robot is designed as in Fig. 7, constituted by a deformable protective cover of appropriate shape and dimensions, and two articulated mechanisms installed in the protective structure. Each articulated mechanism is composed of rigid rods, a spring and a damper. The main advantage of this active protection consists in its light structure based on a protective covering and two articulated mechanisms with springs and dampers that determine an operation easily adaptable to the dimensions of the joints and of the robot parts to be protected. In addition, the active protection structure lends itself to a realization with lightweight materials and in various levels of easy construction and simple operation. Its use in industrial and service robotics applications includes humanoid robots.

Figure 7 shows a 3D CAD model of the proposed robot arm protection. Its main components are a soft protection cover that directly interacts with a human in the event of an impact. It can be equipped with force/pressure sensors. The protection cover is connected with a mechanism that, in this example, is a slider - crank mechanism. This mechanism is connected to a spring/damper that stores/dissipates the energy of an impact. A mechanical trigger keeps the spring/damper in the compressed configuration until the human is close to the robot arm. Then, the release of the mechanical trigger brings the mechanism to its original configuration. Part of the stored energy could eventually be used by energy harvesters to transform mechanical energy into electrical energy to be even used as robot auxiliary power source.
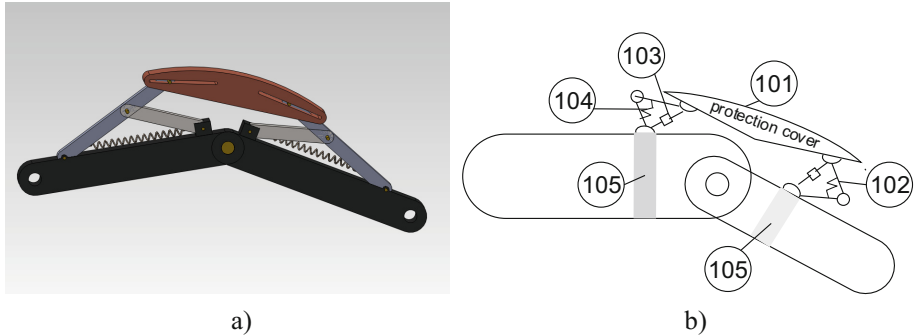
**Fig. 7.** Proposed concept for active protection: (a) 3D CAD model showing a mechanism solution with two slider-crank mechanisms; (b) conceptual scheme of the system and active protection operation: (100) active protection, (101) protective cover, (102) articulated mechanisms, (103) dampers, (104) springs

## 5   Conclusions

This paper describes the main issues that are related to the safety of robotic systems. In particular, the existing passive safety solutions aim to reduce/minimize the occurrence of an impact as well as to reduce/minimize the damage caused by a possible impact. Active safety solutions aim to detect/predict the occurrence of an impact and can take active actions to avoid or reduce its occurrence. This paper provides a preliminary design of a novel solution that aims to transfer and/or transform a significant part of the energy of an impact to minimize its effects as well as to prevent direct collision between a robot structure and a human user. A novel design concept is proposed and a 3D CAD design is reported in order to show the feasibility of the proposed novel active protection for robot arms that is expected to provide improvements also in the interaction between human beings and robots.

## References

1. ABB. http://www.abb-conversations.com/2015/04/introducing-yumi-the-worlds-first-truly-collaborative-robot/. Accessed Feb 2016
2. Alén, C.C., Carbone, G., Ceccarelli, M., Echávarri, J., Muñoz, J.L.: Experimental tests in human–robot collision evaluation and characterization of a new safety index for robot operation. Mech. Mach. Theory **80**, 184–199 (2014)
3. Bosch. http://www.bosch-apas.com/en/apas/produkte/assistant/assistant_product_detail/produktdetails_1.html. Accessed Feb 2016
4. Ceccarelli, M.: Problems and issues for service robots in new applications. Int. J. Social Robot. **3**(3), 299–312 (2011)
5. Ceccarelli, M.: Problems and experiences on cable-based service robots for physiotherapy applications. In: Pisla, D., Bleuler, H., Rodic, A., Vaida, C., Pisla, A. (eds.) New Trends in Medical and Service Robots. MMS, vol. 16, pp. 27–42. Springer, Cham (2013)

6. Echávarri, J., Ceccarelli, M., Carbone, G., Alén, C., Muñoz, A., Díaz, A., Munoz-Guijosa, J. M.: Towards a safety index for assessing head injury potential in service robotics. Adv. Robot. **27**, 831–844 (2013)
7. EN ISO 2014 13482, Robots and robotic devices. Safety requirements for personal care robots (2014)
8. Greenemeier, L.: What should a robot look like? October 2013. http://www.scientific american.com/article/what-should-a-robot-look-like/. Accessed 23 Mar 2015
9. Khatib, O., Roth, B., Zinn, M., Salisbury, J.K.: A new actuation approach for human-friendly robot design. In: International Symposium on Experimental Robotics (2002)
10. KUKA. http://www.kuka-robotics.com. Accessed Feb 2016
11. Morato, T., Iwata, H., Sugano, S.: Development of human symbiotic robot: WENDY. In: Proceedings of the 1999 IEEE International Conference on Robotics & Automation, Detroit, Michigan, May 1999, pp. 3183–3188 (1999)
12. Mukai, T., Hirano, S., Yoshida, M., Nakashima, H., Guo, S., Hayakawa, Y.: Whole-body contact manipulation using tactile information for the nursing-care assistant robot RIBA. In: 2011 IEEE/RSJ International Conference on Intelligent Robots and Systems, 25–30 September 2011, San Francisco, CA, USA, pp. 2445–2451 (2011)
13. Nagakubo, A., Alirezaei, H., Kuniyoshi, Y.: A deformable and deformation sensitive tactile distribution sensor. In: Proceedings of the 2007 IEEE International Conference on Robotics and Biomimetics, Sanya, pp. 1301–1308 (2007)
14. Schiavi, R., Bicchi, A., Flacco, F.: Integration of active and passive compliance control for safe human-robot coexistence. In: 2009 IEEE International Conference on Robotics and Automation, Japan, pp. 259–264 (2009)
15. Yoshikai, T., Hayashi, M., Ishizaka, Y., Fukushima, H., Kadowaki, A., Sagisaka, T., Kobayashi, K., Kumagai, I., Inaba, M.: Development of robots with soft sensor flesh for achieving close interaction behavior. Adv. Artif. Intell. **1**, Article ID 157642 (2012)
16. Siciliano, B., Khatib, O.: Springer Handbook of Robotics. Springer, Berlin (2008)
17. http://animaldiversity.org/accounts/Armadillidium_vulgare/. Accessed Mar 2016
18. Rizzini, S.L., Bicchi, A., Tonietti, G.: Compliant design for intrinsic safety: general issues and preliminary design. In: IEEE International Symposium Intelligent Robots and Systems, Hawaii, vol. 4, pp. 1864–1869 (2001)

# Recognizing Hand Gestures Using Local Features: A Comparison Study

Zuhair Zafar[1(✉)], Karsten Berns[1], and Aleksandar Rodić[2]

[1] RRLAB, Department of Computer Science, University of Kaiserslautern,
67663 Kaiserlsautern, Germany
{zafar,berns}@cs.uni-kl.de
[2] Mihailo Pupin Institute, University of Belgrade, 11060 Belgrade, Serbia
aleksandar.rodic@pupin.rs
http://rrlab.cs.uni-kl.de

**Abstract.** Interest point approaches that extract local features from images are commonly used in human action recognition field. In this paper, a comparison study is performed in which different interest point approaches are used. Each approach is discussed with its advantages and drawbacks. Common keypoint extractors like scale invariant features transform (SIFT), speeded up robust features (SURF), etc. are used in context to human hand gestures recognition. In human-robot interaction, efficiency is important in any recognition task along with recognition rate. Hence in this work, performance of 8 different versions of keypoints are evaluated in terms of recognition rates along with their robustness and efficiency with respect to time. SIFT features show best recognition results while SURF and maximally stable extremal regions features (MSER) show better efficiency.

**Keywords:** Keypoints · Human-robot interaction · Local features · Hand gestures · Depth sensor

## 1 Introduction

Hands are the most important part of human body. The major purpose of hands is to perform daily life activities. However, they are not only limited to help us in performing different tasks but also, they are used to express different states and behaviours of humans. Research demonstrates that the movements we make with our hands when we talk constitute a kind of second language, adding information that is absent from our words. After facial expressions, hand gestures play an important part in expressing the inner state of humans.

Human-robot interaction is one of the most emerging topics studied recently. The objective is to develop robots that can not only help humans but also understand their needs, their emotions their actions and their surroundings. For this, robots must have a system that can recognize humans and their actions. Not only the system should be reliable, but it should be robust and efficient too. As already discussed the importance of hand gestures in different domains

of life, there is need to develop a robotic system that can recognize different hand gestures reliably and efficiently.

Numerous hand gesture applications have been reported so far in the literature. In [1], hand gestures are used to control the VLC player in real time using principle component analysis and k-nearest neighbour algorithm. Another classical appearance-based approach for hand tracking is used in [2]. They used a eigen tracker to be able to detect two hands. Colour and motion cues are used for initialization. The eigen space is updated on-line to incorporate new viewpoints. Neural network is used to handle illumination variations. In [3], hand positions are localized by detecting skin colored blobs in the images using Bayesian classifier. Then, hand pose is estimated by detecting the fingers. In [4], hand positions are detected in the image using Camshift. A scale and rotation invariant hand descriptor is obtained by computing a contour. After locating the hand position, a semicircle detector is used to detect the finger tips. Using particle filtering and k-means algorithm, the finger positions are computed. Jain [5] implemented a vision based hand gesture pose estimation application for mobile devices. Pavlovic et al. [6] stated in their work that the gestures of users must be explained logically for developing a good human computer interaction based system. Another hand gesture recognition method based on input-output Hidden Markov Models of tracking skin color blobs was proposed by Marcel et al. [7]. The sign language tutoring tool studied by Aran et al. [8] oriented their research designed towards teaching the fundamental of the sign language in interactive way.

Microsoft Kinect SDK and OpenNI (NiTe Middleware library), both provide human joints and skeletal information. Since the body and hand tracking are reliable, researchers focus more on classification of hand gestures instead of localization of hands. NiTe Middleware library provides 3-D position of the hand which can be used to segment the hand. In this domain of study, we present a system that recognizes automatically different hand gestures in real-time. We present different interest point approaches and show their effectiveness and robustness during human robot interaction. We discuss the advantages and disadvantages of each interest point approach and based on reliability and efficiency, we select the best one out of them. This paper is organized as follows: Sect. 2 describes different interest point detection approaches in detail. Classification of hand gestures are discussed in Sect. 3. We evaluate our methodology in Sect. 4 and in the end, we conclude the paper in Sect. 5

## 2   Hand Gesture Recognition Using Interest Points

The proposed work is presented in the context of human-robot interaction. Using depth data, which is independent of illumination variation, hands position can be determined easily. The challenge in registering the hand is to extract it irrespective of the scale. If the hand is near to the sensor, the hand region would be greater and if it is far from the sensor, then the hand region would be smaller. In order to segment the hand region, there exists different strategies. The most

suitable and efficient way of hand segmentation is to use the depth value of the hand image. In our study, we use depth value to construct a square window size [15]. Using empirical studies, a linear relationship in between depth of hand and window size is generated as expressed in 1,

$$d = 100 - \frac{z - 500}{15}. \tag{1}$$

In the above formulation, $d$ is the side of square window and $z$ is the depth value of the hand. $d$ would be bigger if the depth of the hand, $z$, is lower. This formulation is valid for $640 \times 480$ resolution. For $320 \times 240$ resolution, the side of the window will be half. As can be seen from 1, if the depth value of hand is increased, the window size decreases. Since the NiTe library provides hand positions accurately in the depth range of 500 to 2000 mm, the system detects and segment the hands in this region. After 2000 mm distance, hand window becomes too small and recognition of hand gesture is impossible. Hand window is segmented from the colour image which is further processed for hand gesture recognition.

The next step after segmentation and preprocessing is to extract features. In this work, we use interest point features to recognize hand gestures. Interest point features are types of local features which exploits the pattern locally. These local features are then translated in a specific way to extract global features. In the following section, detection of different local features and computing of descriptors are explained.

### 2.1   SIFT Features

Scale invariant feature transform (SIFT) features are local features based on the appearance of the object at specific interest points. SIFT is presented by Lowe [9]. The algorithm extracts keypoints (interest points) by convolving the image with Gaussian filters at different scales. The difference of Gaussian (DoG) is computed between consecutive Gaussian blurred images and keypoints are then identified as local maxima or minima of the DoG. In order to process these keypoints, a descriptor is needed to encode all the information of the keypoint. A set of orientation histograms are computed in $4 \times 4$ pixel neighborhoods with 8 bins. This orientation information stored in the descriptor makes SIFT descriptor rotation invariant to an extent. There are 16 histograms, each with 8 bins, hence the descriptor size becomes 128.

SIFT features are rotation invariant up to affine transformation of $50°$ and are illumination invariant. The features extracted are unique and capture the most amount of variance as compared to other features. SIFT features are also scale invariant up to 2.5 m and outperform other local features apart from SURF. The main disadvantage of these features is that SIFT descriptors are high dimensional and therefore, they can make the system computationally intensive.

## 2.2   SURF Features

Speeded up robust features (SURF) perform much faster as compared to SIFT features and slightly more robust than SIFT. SURF is presented by Bay et al. [10]. In SURF, box shaped filters are used as an approximation of Gaussian smoothing. Integral image is used for filtering the original image with box shaped filters of different sizes. In order to determine interest points, a blob detector based on Hessian matrix is used. For scale and location of keypoints, the SURF algorithm depends on the determinant of Hessian matrix. For orientation assignment, SURF uses wavelet responses in horizontal and vertical direction for a neighbourhood of size 6s. For description of features, SURF uses Haar wavelet responses in horizontal and vertical direction in an integral image. A neighbourhood of size $20s \times 20s$ is considered around the interest point where s is the size. This neighborhood is further divided in $4 \times 4$ subregions. For each subregion, horizontal and vertical wavelets responses are taken and a 64-dimensional vector is formed.

SURF features are local features and, like SIFT features, also are scale and rotation invariant. The most important advantage of using these features is the smaller computational cost in contrast to SIFT. The reason lies in the descriptor dimensionality which is 64 as compared to the SIFT descriptor of 128 dimensions. However, a short descriptor may be more robust against appearance variations, but may not offer sufficient discrimination and thus give too many false positives.

## 2.3   Dense Features

Features that are sampled densely of the same scale and orientations are known as dense features [11]. In this type of feature detection, more features are computed at each location and scale in an image. This provides all possible information at every location in the image. Since dense features are detected at each location of an image, SIFT or SURF descriptor must also be computed at each location. This process makes the system computationally more intensive. In cases where time is not important, dense SIFT can report better results than normal SIFT.

## 2.4   FAST Features

Features from accelerated segment test (FAST) is a corner detection method, which can be used to compute interest points and then use them for tracking, classification or recognition tasks. The FAST corner detector [12] uses a circle of 16 pixels to validate whether the point $p$ is a corner. Each pixel in the circle is labelled from 1 to 16. If all the pixels or $N$ pixels in the circle are brighter than the pixel or darker than the pixel with some threshold then $p$ is classified as a keypoint. These keypoints are then describe by using SIFT/SURF descriptors. The dimensionality remains 128 in case of SIFT and 64 in case of SURF, but to some extent these features are scale invariant.

The advantage of FAST corner detector is its computational efficiency. As the name suggests, it is faster than many other well-known feature extraction methods, such as difference of Gaussian (DoG) used by SIFT, SUSAN and Harris. FAST corner detector is very suitable for real-time video processing applications because of high-speed performance. However, the main disadvantage lies in computing keypoints. There is a trade off in selecting $n$ number of pixels. The number of keypoints detected should not be too many and on the other hand if it is too low then it may affect the recognition rate.

### 2.5   MSER Features

Maximally stable extremal regions (MSER) are used as blob detection method in an image. MSER is based on the idea of taking regions which stay nearly the same through a wide range of thresholds. The algorithm [13] such that initially all the pixels below a given threshold are white and pixels above or equal to the threshold are black. All those white spots are then merged together, till all the image is white. The set of all the connected components in the image is basically formed by the extremal regions of an image. Additionally, elliptical frames are attached to MSERs by fitting ellipses to the regions. These elliptical regions are used as feature points of the image. To describe the feature points, SIFT/SURF descriptor are used.

The biggest benefit of MSER features is that they are invariant to affine transformation of image intensities. The extracted regions are stable and can still report stable regions even the image is skewed. However, the approach is sensitive to illumination changes or shadows and motion blur. Despite this, MSER performs well for small regions and shows good repeatability and is computationally lighter than other region detectors.

## 3   Classification

Before classification, the extracted local features generated by different keypoints algorithms are represented globally by using bag-of-features approach (BoF) and k mean clustering [15]. This step represents local features into global features for whole image without affecting the characteristics of local features.

In our study, we use support vector machines (SVM) for classification tasks. SVM is a supervised learning algorithm that is able to perform classification and regression [14]. For training and testing phases, a database, containing 6 subjects with different ethnicities, is generated. The database is recorded by using ASUS Xtion sensor. Only segmented hand regions are stored. In total of 10 different static gestures are recorded, and 150 frames are taken for each gesture of a subject. Figure 1 shows the segmented images from the database.

We use one-vs-all SVM approach for our multi-class problem. The feature vector, which we have created using the bag-of-features approach with labels on training images, are fed into the multi-class support vector machines in order to obtain the model. This model is further used in the testing stage for hand
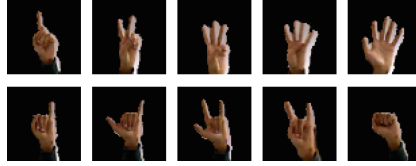
**Fig. 1.** Hand segmented images of number gestures (1–10).

gesture recognition. In this domain of study, SVM with RBF kernel is used for training purpose.

## 4   Experimentation and Evaluation

Since this work is in context of Human-Robot interaction, a humanoid robot, Robothespian, is used in the study. It is also equipped with intelligent hands with 8 degrees of freedom. The whole arm has 14 DoF. The robot also has a speech synthesis module, through which it can speak in English and in German language. A RGB-D sensor is installed on the chest of the robot in addition with a HD camera, which is attached on the head of the robot. The robot can also move his head 45° and the torso to 20° each side.

Table 1 shows the performance of hand gestures using different interest point approaches. Recognition rates for different hand gestures have been reported. We recognize number of gestures as shown in Fig. 1. From Table 1, it can be seen that SIFT features report better results as any other type of features. MSER-SURF performs better than MSER-SIFT. In MSER-SIFT, the gesture *two* and *three* are confused with each other. The same phenomena happened in MSER-SURF as well. The recognition rate of gesture *three* is 65%, which shows that the blob detected for this gesture is not accurate enough. In FAST-SURF and FAST-SIFT, gesture *one* and *six* are interchangeably recognized, resulting in low recognition rate for both these gestures. The reason is easier to understand as in both these gestures, there is only one finger open (index finger for *one* and little finger for *six* gesture). On the other hand, FAST-SIFT recognizes gesture *eight* rarely as compared to all the other kinds of interest point approaches which also reduces the overall recognition rate.

Dense SIFT also reports good results; however, because of too many keypoints, recognition rate is affected. Generally, dense SURF failed badly as the SVM classifier is unable to generate hyperplane, which results in poor classification results. The major reason is that the extracted keypoints are randomly distributed and even the SURF descriptor does not describe them efficiently, resulting in poor classification.

Another more critical aspect in human-robot interaction is the efficiency and robustness of the implemented approach. Table 2 shows the average processing time for a frame for each interest point approach and also average frames per second information.

**Table 1.** Recognition rates in percentage (%) of number gestures using different approaches with SIFT(I) or SURF(U) descriptors on 150 images for each gesture.

| Gestures | SIFT | SURF | Dense(I) | Dense(U) | FAST(I) | FAST(U) | MSER(I) | MSER(U) |
|---|---|---|---|---|---|---|---|---|
| One | 90 | 93.3 | 96 | 0 | 86 | 74 | 88.6 | 92 |
| Two | 98.6 | 97.3 | 96.6 | 0 | 92 | 91.3 | 60 | 94.6 |
| Three | 92 | 84 | 73.3 | 0 | 88.6 | 92.6 | 69.3 | 64.6 |
| Four | 88.6 | 86 | 86 | 0 | 77.3 | 92.6 | 86.6 | 96 |
| Five | 98 | 96 | 98 | 100 | 98.6 | 94.6 | 86.6 | 92.6 |
| Six | 94.6 | 97.3 | 95.3 | 0 | 48 | 72 | 98.6 | 98.6 |
| Seven | 98.6 | 99.3 | 99.3 | 0 | 98 | 96.6 | 97.3 | 99.3 |
| Eight | 97.3 | 96.6 | 99.3 | 0 | 56 | 91.3 | 89.3 | 88 |
| Nine | 97.3 | 96.6 | 75.3 | 0 | 90 | 90.6 | 95.3 | 98 |
| Ten | 91.3 | 89.1 | 91.3 | 0 | 86.9 | 89.1 | 91.3 | 86.9 |
| Avg. | **94.8%** | 93.7% | 91% | 10% | 82% | 88.5% | 86.1% | 91.2% |

**Table 2.** Table shows average processing time in millisecond for a frame and average frames processed per second for each interest point approach.

| | SIFT | SURF | Dense(I) | Dense(U) | FAST(I) | FAST(U) | MSER(I) | MSER(U) |
|---|---|---|---|---|---|---|---|---|
| Avg. time | 77 ms | 64 ms | 83 ms | 89 ms | 58.7 ms | 111 ms | 65.5 ms | 61.6 ms |
| Frames/sec | 13 | 15.6 | 12 | 11.2 | 17 | 9 | 15.3 | 16.2 |

From Table 2, it can be seen that generally, SIFT features take more time as compared to SURF features. Dense SIFT performs above 90% recognition rate; however, it takes more time to process single frame, which constitutes 12 frames per second as compared to 13 frames per second. On the other hand, MSER interest point are one of the efficient features. However, the recognition rate for MSER features is not so high. FAST-SIFT reports most efficiency in terms of frames processed but again, the recognition rate is average especially for *six* and *eight* gestures. Approaches, with processing over 12 frames per second, can be regarded as real time. In our case, SIFT features report better recognition rates and satisfactory processing time and can be selected over other approaches.

## 5   Conclusion

Interest point features are commonly used in the human action recognition field. In this work, we study different interest point approaches and discuss their advantages and drawbacks. SIFT, SURF, MSER-SIFT, MSER-SURF, FAST-SIFT, FAST-SURF, Dense SIFT and Dense SURF features are used in human hand gesture recognition. Efficient hand segmentation using OpenNI and NiTe library can be done by using a linear relationship between the window size and depth. We classified each approach using feature vectors generated by bag-of-features method. The multi-class SVM classification algorithm is used for

classification. After experimentation, SIFT features report best recognition rate and SURF follows just behind it. MSER, FAST and SURF tend to perform more efficiently as compared to SIFT with respect to time. In future work, we propose to use SIFT features in recognizing dynamic hand gestures along with hidden Markov model.

# References

1. Rautaray, S.S., Agrawal, A.: A novel human computer interface based on hand gesture recognition using computer vision techniques. In: Proceedings of ACM IITM 2010, pp. 292–296 (2010)
2. Barhate, K.A., Patwardhan, K.S., Roy, S.D., Chaudhuri, S., Chaudhury, S.: Robust shape based two hand tracker. In: 2004 International Conference on Image Processing, ICIP 2004, pp. 1017–1020 (2004)
3. Argyros, A.A., Lourakis, M.I.A.: Tracking multiple colored blobs with a moving camera. In: IEEE Computer Society Conference on Computer Vision and Pattern Recognition, CVPR 2005, p. 1178 (2005)
4. Wang, X., Zhang, X., Dai, G.: Tracking of deformable human hand in real time as continuous input for gesture-based interaction. In: Proceedings of the 12th International Conference on Intelligent User Interfaces, pp. 235–242 (2007)
5. Jain, G.: Vision-based hand gesture pose estimation for mobile devices. University of Toronto (2009)
6. Pavlovic, V., Sharma, R., Huang, T.S.: Visual interpretation of hand gestures for human-computer interaction: a review. IEEE Trans. Pattern Anal. Mach. Intell. (PAMI) **7**(19), 677–695 (1997)
7. Marcel, S., Bernier, O., Viallet, J.E., Collobert, D.: Hand gesture recognition using input-output hidden markov models. In: Proceedings of the FG'2000 Conference on Automatic Face and Gesture Recognition (2000)
8. Aran, O., Ari, I., Benoit, F., Campr, A., Carrillo, A.H., Fanard, F., Akarun, L., Caplier, A., Rombaut, M., Sankuru, B.: Sign language tutoring tool. In: eNTER-FACE 2006, The Summer Workshop on Multimodal Interfaces, Croatia (2006)
9. Lowe, D.G.: Object recognition from local scale-invariant features. In: Proceedings of the International Conference on Computer Vision, pp. 1150–1157 (1999)
10. Funayama, R., Yanagihara, H., Gool, L.V., Tuytelaars, T., Bay, H.: Robust interest point detector and descriptor. Published 24 September 2009 (2009)
11. Veksler, O.: Dense features for semi-dense stereo correspondence. IJCV **47**(1–3), 247–260 (2002)
12. Rosten, E., Drummond, T.: Fusing points and lines for high performance tracking. In: IEEE International Conference on Computer Vision, vol. 2, pp. 1508–1511 (2005)
13. Matas, J., Chum, O., Urban, M., Pajdla, T.: Robust wide baseline stereo from maximally stable extremal regions. In: Proceedings of British Machine Vision Conference, pp. 384–396 (2002)
14. Cortes, C., Vapnik, V.: Support-vector networks. Mach. Learn. **20**(3), 273 (1995)
15. Zafar, Z., Berns, K.: Recognizing hand gestures for human-robot interaction. In: Proceedings of the 9th International Conference on Advances in Computer-Human Interactions (ACHI), pp. 333–338 (2016)

# Cognitive Robots and Emotional Intelligence

# Effect of Sequence Order on Autonomous Robotic Database Expansion

Tadej Petrič[(✉)] and Andrej Gams

Department for Automation, Biocybernetics and Robotics (ABR),
Jožef Stefan Institute, (JSI), Jadranska c. 39, Ljubljana, Slovenia
{tadej.petric,andrej.gams}@ijs.si

**Abstract.** Generating trajectories autonomously through generalization requires an extensive database of motion, which is usually time-consuming and difficult to obtain. Recently approaches for autonomous database expansion for the generation of compliant and accurate motion were proposed, all showing that autonomous generation of the database of motion can be significantly speed up. However, no extensive analysis was performed to show what would be the optimal sequence of learning. In this paper we analyze different strategies to further speed up the learning process of autonomous database expansion for compliant movement primitives (CMPs). An extensive analysis was performed for finding an optimal learning sequence in a simulated environment for a peg-in-hole task with a Kuka LWR-4 robot. The obtained results were then confirmed on a real Kuka LWR-4 robot set up performing a peg-in-hole task.

**Keywords:** Compliant movement primitives · Autonomous learning · Internal dynamic models

## 1 Introduction

For autonomous generation of new Compliant Movement Primitives, statistical generalization is a successful tool which can synthesize a similar motion trajectory from a set of recorded movements as shown by [4]. However, two main challenges vastly reduce the applicability of generalization. Firstly, the database has to be provided in advance, and secondly, the generalization only works within the training space. To extend the applicability of the generalization, Petric et al. [8] proposed an algorithm for autonomous expansion of the database, where the robot uses an iterative learning approach to optimize its behaviour for new task conditions. The newly generated, optimized trajectories can then either increase the density of the database within the training space, or expand it beyond its current limits to provide a greater area of applicability.

Learning movement trajectories for database expansion is a time consuming and difficult process, which vastly depends on the chosen learning approach. For example, explorative methods, i.e., reinforcement learning, might take a long time, because a high number of repetitions are needed [7]. Supervised methods,

such as iterative learning control, are on the other hand faster, but need a reference to optimize [2]. However, even these might take too long time to expand the database which will be suitable for statistical methods to generate an accurate trajectory for the given task. In this paper we show how to considerably accelerate the learning by giving a better initial estimate that originates from at the time available database. By using initial estimates and iterative learning to obtain accurate movement trajectories for new entries into the database, the generalization results are getting better and better with every new entry.

The need for fast generation of new and at the same time accurate trajectories comes from the need to operate in unstructured environments, where the robot needs to be compliant in case of undesired contact with objects. Accurate dynamical models of the robot and the task allow such behaviour [1], but they are difficult to obtain, so methods of learning task-specific models have been proposed. One such method is with the use of *Compliant Movement Primitives* (CMP) [4], which encodes both the kinematic trajectory as well as the corresponding joint torques for the given task. The kinematic trajectory takes the form of a *Dynamic Movement Primitive* (DMP) [5], keeping all modulation and adaptation properties. The dynamic trajectory, i. e., the joint torques, are encoded as *Torque Primitives* (TPs), a set of weighted radial-basis type kernel functions. CMPs have been shown to allow statistical generalization based on given task-parameters, but their learning has so far remained constrained to recording the torques of an execution with a stiff robot which is potentially dangerous for autonomous database expansion. A more appropriate method for autonomous database expansion was recently proposed by [8], where from a given desired kinematic behaviour, the torques are learned iteratively through several repetitions until the error of compliant tracking is reduced below a predefined threshold. Here a good initial approximation reduces the number of needed iterations for learning CMPs. In this paper we analyze how the sequence of learning influences the speed of autonomous database expansion.

This paper is organized as follows: in the next Section we briefly describe autonomously learning of CMPs. In Sect. 3 we describe the process of autonomously expanding a database of motions for statistical generalization. Results of experimental evaluation on a Kuka LWR-4 robot arm learning to perform a peg-in-hole task are presented in Sect. 4 followed by a short conclusion.

## 2   Compliant Movement Primitives

Compliant Movement Primitives (CMPs) $h(t)$ are defined as a combination of kinematic trajectories encoded as DMPs and corresponding task-specific dynamics encoded in TPs

$$\boldsymbol{h}(t) = [\ddot{\boldsymbol{x}}_d(t), \dot{\boldsymbol{x}}_d(t), \boldsymbol{x}_d(t), \ \boldsymbol{\tau}_f(t)]. \tag{1}$$

Here $\ddot{\boldsymbol{x}}_d(t), \dot{\boldsymbol{x}}_d(t), \boldsymbol{x}_d(t)$ are the desired task-space acceleration, velocity and position trajectories, respectively, encoded in the DMPs. The $\boldsymbol{\tau}_f$ are the corresponding task-specific joint torques encoded in TPs. To obtain the CMPs a

two stage process is used. First, the kinematic motion trajectories are obtained either by human demonstration, or are predefined and encoded as DMPs [5,9]. Then, the corresponding torques are obtained using recursive regression based on error learning and encoded as TPs [3,4,8].

**Motion Trajectories:** First a short recap of the DMPs [5] for encoding the motion is given. Within this framework the trajectories can be given in either joint or task space. The movement trajectory for each DOF is described by the following system of differential equations

$$\dot{z} = \Omega \left( \alpha_z \left( \beta_z \left( g - y \right) - z \right) + f(s) \right), \tag{2}$$
$$\dot{y} = \Omega z. \tag{3}$$

where the linear part ensures that $y$ converges to the desired goal configuration $g$ once the nonlinear part $f(\phi)$ becomes zero. The nonlinear part $f(\phi)$ is defined as a linear combination of radial basis function $\Psi_i(\phi)$, defined as

$$\boldsymbol{F}(\phi) = \frac{\sum_{i=1}^{N} w_i \Psi_i(\phi)}{\sum_{i=1}^{N} \Psi_i(\phi)}, \tag{4}$$
$$\Psi_i(\phi) = \exp(h(cos(\phi - c_i) - 1)), \tag{5}$$

where, $N$ is the number of kernel functions (kernels), weighted with $\mathbf{w}$, which defines the actual shape of the encoded trajectory. The variable $h$ defines the widths, and $c_i$ defines the centres of the kernels, respectively. The phase variable $\phi$ has explicit time dependency and it is updated with

$$\dot{\phi} = \Omega = \begin{cases} \frac{1}{T}, & \text{if } \phi \leq 1 \\ 0, & \text{otherwise} \end{cases} \tag{6}$$

where $T$ defines the total duration of motion. To encode the DMPs, the weight vector $\mathbf{w}$ needs to be learned, for example, with incremental locally weighted regression, where the target data for fitting is

$$f_t = \frac{1}{\Omega^2} \ddot{p}_d - \alpha_z \left( \beta_z \left( g - p_d \right) - \frac{1}{\Omega} \dot{p}_d \right), \tag{7}$$

Given the target $f_t$, $w_i$ is updated for each time-step $j$ with

$$w_{i,j+1} = w_{i,j} + \Psi_i P_{i,j+1} e_j, \tag{8}$$
$$P_{i,j+1} = \frac{1}{\lambda} \left( P_{i,j} - \frac{P_{i,j}^2}{\frac{\lambda}{\Psi_i} + P_{i,j}} \right), \tag{9}$$
$$e_j = f_{t,j} - w_{i,j}. \tag{10}$$

Here $P_i$ is the inverse covariance. The regression starts with $w_i = 0$ and $P_i = 1$. $\lambda$ is the forgetting factor set to $\lambda < 1$, typically at $\lambda = 0.99$.

**Joint Torque Trajectories:** The Torque Primitives are learned recursively by executing the encoded DMP motion with low-gain impedance control using the following control law

$$\boldsymbol{\tau}_u = \mathbf{J}^T(\mathbf{K}_p\boldsymbol{e} + \mathbf{K}_d\dot{\boldsymbol{e}} + \mathbf{K}_i\ddot{\boldsymbol{e}}) + \mathbf{N}\mathbf{K}_n\dot{\boldsymbol{q}} + \boldsymbol{\tau}_f(s), \tag{11}$$

where, $\mathbf{J}^T$ is the Jacobian transpose, $\mathbf{N}$ is the null-space matrix, $\boldsymbol{e}$, $\dot{\boldsymbol{e}}$ and $\ddot{\boldsymbol{e}}$ are the differences between desired and actual position $\boldsymbol{x}$, velocity $\dot{\boldsymbol{x}}$ and acceleration $\ddot{\boldsymbol{x}}$, respectively and $\mathbf{K}_p$, $\mathbf{K}_d$, $\mathbf{K}_i$ and $\mathbf{K}_n$ are the constant gain matrices selected such that the robot behaves compliantly, i.e., set to match the low impedance control requirements. $\boldsymbol{\tau}_f(s)$ is a vector of feedforward torque trajectories $\boldsymbol{\tau}_f(\phi) = [\tau_{f,1}(\phi), \tau_{f,2}(\phi), ..., \tau_{f,j}(\phi), ..., \tau_{f,M}(\phi)]^T$, where M is the number of DOF. For one DOF, $\tau_{f,j}(\phi)$ is given by

$$\tau_{f,j}(\phi) = \frac{\sum_{i=1}^{N} \psi_i(\phi)w_{i,j}}{\sum_{i=1}^{N} \psi_i(\phi)}, \tag{12}$$

where the phase $\phi$ is common with the DMPs. Unlike the DMPs, the TPs are not time invariant, and they can not be stopped because torque usually does not scale linearly. Therefore, an execution time must be provided in advance, i.e. set by parameter $T$ for point-to-point movement. Note that for each movement variation, including movement speed, a new TP has to be obtained. A library of motion can be built by storing TPs. Furthermore, statistical generalization or graph search can be used to generate new TPs, which were previously not explicitly learned. For details see [3,4]. However, in cases when the desired movement is not covered by the database, the approaches from [3,4] will not work. To expand the database, a method that can autonomously learn new CMPs has to be used as in [8]. The proposed method recursively updates the weights $w_{i,j}$ of TPs. The recursive regression method is given by

$$w_{i,j}(t+1) = w_{i,j}(t) + \psi_i P_{i,j}(t+1)\epsilon_j(t), \tag{13}$$

$$P_{i,j}(t+1) = \frac{1}{\lambda}\left(P_{i,j}(t) - \frac{P_{i,j}^2(t)}{\frac{\lambda}{\psi_i} P_{i,j}(t)}\right), \tag{14}$$

where $P_{i,j}$ is the covariance. The initial parameters are set to $P_i = 1$, $w_i = 0$, $\lambda = 0.995$. The TPs update criteria is defined similarly as in [6], where the joint torques are learned based on proprioceptive errors in Cartesian space. By using the following definition, the error of the motion is defined with

$$\boldsymbol{\epsilon}(t) = \mathbf{J}^T(\alpha_t(\boldsymbol{x}_d(t) - \boldsymbol{x}(t)) + \beta_t(\dot{\boldsymbol{x}}_d(t) - \dot{\boldsymbol{x}}(t))). \tag{15}$$

Parameters $\alpha_t$ and $\beta_t$ define the update rate, and $(.)_d$ marks desired values. Note that the error vector is defined as $\boldsymbol{\epsilon} = [\epsilon_1, \epsilon_2, ..., \epsilon_j, ..., \epsilon_M]$, where $M$ is the number of DOFs. Each DOF is updated separately with (13) and (14). The learning process repeats while the desired error metric is above the desired threshold. Once the required accuracy of motion is met, the CMP can be added to the database. By using formulation (15), the TPs will converge towards joint torques that match the motion behaviour encoded in DMPs.

## 3   Database Expansion

Iterative learning of CMPs simplifies the execution of dynamical tasks while ensuring accurate and compliant execution of the motion. Because torques are usually not linearly scalable, TPs have to be learned for each variation of the task, including different payloads, goals, and even speeds. To avoid new learning for each task variation, Petric et al. [8] proposed using statistical generalization based on a given query point for initial TPs approximation. In case the executed generalized TPs satisfy the given criteria, for example the tracking accuracy, they can be immediately added to the database of motion. If not, the recursive regression method can be applied, using the generalized TPs as initial approximation. This vastly reduces the number of needed iterations for learning and building motion databases.

A common criterion for adding CMPs into a database is the sum of task space error defined in (15), which implies that the robot is accurately tracking the desired task-space trajectory encoded in DMPs. The database is given with $\boldsymbol{H}_x^{\mathrm{TP}}$ and the following error metric is defined by

$$e_p = \sum_{j=1}^{I} ||\boldsymbol{e}(j)||. \tag{16}$$

Here $\boldsymbol{e}(j)$ is the vector of absolute difference between the actual task space position $\boldsymbol{x}$, and the desired position encoded in the DMPs $\boldsymbol{x}_d$. $I$ is the number of steps for one movement execution (iteration). The database $\boldsymbol{H}_x^{\mathrm{TP}}$ for a given set of M examples is given by

$$\boldsymbol{H}_x^{\mathrm{TP}} = \{\boldsymbol{w}_{\tau k}, \boldsymbol{c}_k\}, \ k = 1, 2, ..., M, \tag{17}$$

where a TP, defined by weights $\boldsymbol{w}_\tau$ is used together with associated DMPs to execute a task, defined by the query point $\boldsymbol{c}$. Note that the task is executed in a compliant manner using low feedback gains. By using Gaussian process regression (GPR) for statistical regression as in [3,4]

$$\boldsymbol{F}_{\boldsymbol{H}_x^{\mathrm{TP}}} : \boldsymbol{c} \longmapsto [\boldsymbol{w}_q, \boldsymbol{w}_\tau], \tag{18}$$

we can compute the initial TP parameters for the given query $\boldsymbol{c}$. Note that generalization can also be used with DMPs, see [10]. The learning process of TPs repeats as long as the $e_p > e_c$, where $e_c$ is a given desired criteria. Once this criteria is met, the TP is added into the database of motion $\boldsymbol{H}_x^{\mathrm{TP}}$. With this approach, the database of CMPs can be autonomously expanded.

## 4   Effect of Sequence Order on Database Expansion

To investigate the performance in case of a possible collision while using CMPs, the peg-in-hole task was chosen. The peg insertion also requires that a certain degree of force is applied for successful completion of the task.
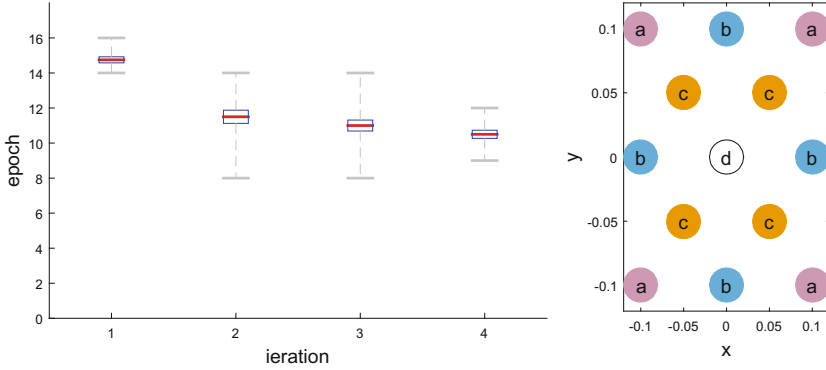
**Fig. 1.** Left plot shows the required average epochs needed for successful learning of CMPs for different hole locations. Here all possible permutations for groups a, b and c were analyzed, i. e. 12 for each group. The right plot shows the exact locations of holes and their groups.

The task for the robot was to move from an initial position, and insert the peg in one out of 13 possible hole locations. For this task we assume that the desired motion is known and encoded in DMPs, meaning that if the robot would accurately track this trajectory, then peg insertion would be successful. However, due to the limitation of high gain feedback control, which implies high forces when in contact, this type of control can't be used. Therefore this task is most suitable for studying the performance of the approach using CMPs which can gradually learn the corresponding torques for performing the task while being compliant. To study the ability of learning and gradually building a database of motion a 13 different positions for possible insertion of the peg were selected, all on the same plane. The exact locations of the holes can be seen in the right plot in Fig. 1. To analyze the effect of different learning sequence we used the MuJoCo dynamical simulator and a dynamic model of the Kuka LWR-4 robot. In the right plot on Fig. 1 we show the analysis of an average epochs needed for permutation of holes in groups a, b and c. We can see that for all three groups and all their permutations the standard deviations were small, which indicates that the building database of CMPs is independent on the chosen sequence.

To further analyze how important is the chosen sequence for the process of building of the database of CMPs, we analyzed the learning and gradually building the database by permutating the groups a, b, c, d. In Fig. 2, we can see that, using the previous experience significantly reduces the required learning epochs for obtaining the database of CMPs. Note that on average 13 epochs are needed for each hole location if there is no previous experience. On the contrary if previous experience exists and is used, i. e. the CMPs that were previously acquired, the learning and building of the database of CMPs is significantly accelerated. In this example, all possible permutations were analysed and the mean, STD, max and min values are reported in Fig. 2, where we can see that
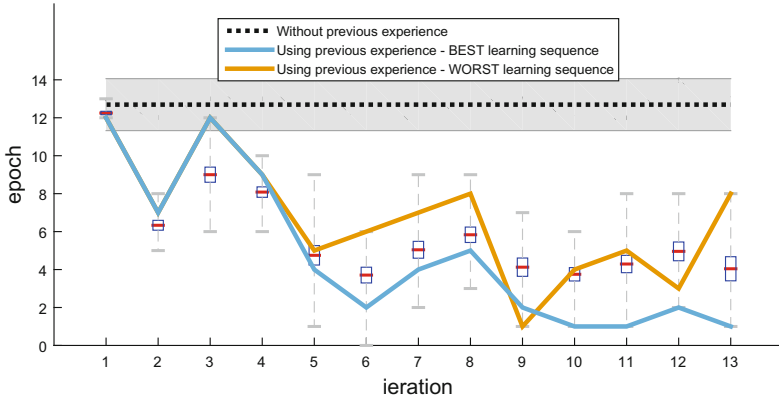
**Fig. 2.** The plot shows the required average epochs needed for successful learning of CMPs for different hole locations. Here all possible permutation of groups a, b c and d were analyzed and compared to the case if no previous experience was used for generating initial CMPs.
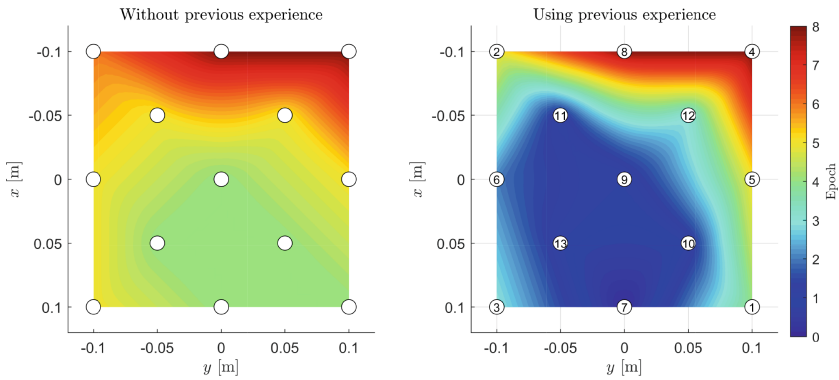


**Fig. 3.** Comparison between learning of TPs for the peg-in-hole task without previous experience and by gradually building the database using previous experience. The plots shows the epochs needed to successfully learn the skill for each location of the hole, respectively.

the worst and best learning sequences are close together. This one again indicates that building the database of CMPs is independent on the chosen sequence.

Finally, we evaluated the learning sequence on a real Kuka LWR robot. In Fig. 3 we show the performance of the CMPs approach while gradually building the database of motion. Note that here we assumed that at the beginning the database is empty. This sequence was chosen because it shows at the beginning, for cases from 1 to 4, that the proposed approach is able to successfully expand the database autonomously. In the following cases, from 5 to 14, it shows that the learning is significantly improved compared to learning without using any

database. Note that based on simulations the performance of the approach is not dependent on the chosen sequence.

## 5   Conclusion

The presented methods of autonomous expansion of TPs learning for the CMPs have shown applicability in unconstrained space or in contact with the environment. The methods expand the level of applicability of the CMP to real world scenarios. The results have shown that the database expansion is autonomous, fast and applicable with different constraints, such as contact with the environment. We also show that the method is also invariant with the sequence of learning.

## References

1. Albu-Schaffer, A., Eiberger, O., Grebenstein, M., Haddadin, S., Ott, C., Wimbock, T., Wolf, S., Hirzinger, G.: Soft robotics. IEEE Robot. Autom. Mag. **15**(3), 20–30 (2008)
2. Bristow, D.A., Tharayil, M., Alleyne, A.G.: A survey of iterative learning control. IEEE Control Syst. **26**(3), 96–114 (2006)
3. Denisa, M., Petrič, T., Asfour, T., Ude, A.: Synthesizing compliant reaching movements by searching a database of example trajectories. In: International Conference on Humanoid Robots, pp. 540–546 (2013)
4. Deniša, M., Gams, A., Ude, A., Petrič, T.: Learning compliant movement primitives through demonstration and statistical generalization. IEEE/ASME Trans. Mechatron. **21**(5), 2581–2594 (2016)
5. Ijspeert, A.J., Nakanishi, J., Hoffmann, H., Pastor, P., Schaal, S.: Dynamical movement primitives: learning attractor models for motor behaviors. Neural Comput. **25**(2), 328–373 (2013)
6. Kawato, M.: Feedback-errror-learning neural network for supervised motor learning. In: Eckmiller, R. (ed.) Advanced Neural Computers, pp. 365–372. Elsevier, North-Holland (1990)
7. Kober, J., Wilhelm, A., Oztop, E., Peters, J.: Reinforcement learning to adjust parametrized motor primitives to new situations. Auton. Robots **33**(4), 361–379 (2012)
8. Petrič, T., Colasanto, L., Gams, A., Ude, A., Ijspeert, A.: Bio-inspired learning and database expansion of compliant movement primitives. In: IEEE-RAS 15th International Conference on Humanoid Robots (Humanoids), pp. 346–351, November 2015
9. Schaal, S., Mohajerian, P., Ijspeert, A.: Dynamics systems vs. optimal control-a unifying view. Prog. Brain Res. **165**, 425–445 (2007)
10. Ude, A., Gams, A., Asfour, T., Morimoto, J.: Task-specific generalization of discrete and periodic dynamic movement primitives. IEEE Trans. Robot. **26**(5), 800–815 (2010)

# Action Unit Based Facial Expression Recognition Using Deep Learning

Salah Al-Darraji[1(✉)], Karsten Berns[1], and Aleksandar Rodić[2]

[1] Robotics Research Lab, Department of Computer Science,
University of Kaiserslautern, Kaiserslautern, Germany
{saleh,berns}@cs.uni-kl.de
[2] Robotics Laboratory, Mihailo Pupin Institute,
University of Belgrade, Belgrade, Serbia
aleksandar.rodic@pupin.rs

**Abstract.** Social interactive robot needs the same behaviours and capabilities as human to be able to work in human daily life. Humans usually use different types of verbal and nonverbal cues in their communication. Facial expressions are good examples of nonverbal cues used in inter-human interaction. This paper presents a facial expression recognition approach using deep learning. The approach is based on the analysis of subtle changes in facial features of human face. The detected facial features, action units, are mapped to two psychological measurements, arousal and valence using support vector regression. Facial expression is then recognized by using these two values. The proposed approach has shown a recognition rate of more than 90%.

**Keywords:** Humanoid robots · Facial expression recognition · Human-robot interaction · Deep learning

## 1 Introduction

Facial expressions of humans play an important role in inter-human interaction. Usually, humans express more feelings through facial gestures than any other body movements. The emotional state of humans can also be reflected on the face through facial expressions. Psychologists addressed diverse communicative functions for facial expressions such as giving feedback, opening and closing communication channels, and complementing verbal cues.

The facial action coding system (FACS) is the most widely used expression coding system in the behavioural sciences developed by Ekman and Friesen [1].

The basic element in this coding system is Action Unit (AU). Each action unit is related to the contraction of one or more facial muscles. FACS consists of 44 AUs which can occur in combinations as well. There are 12 AUs for upper face and 18 AUs for lower case. When more than one action unit are active together then a combination of action units occurs. More than 7000 combinations have been observed which can describe more complex facial actions. Action unit combinations can be either *additive* or *nonadditive*. Additive combination means

that the characteristics appearance of each AU in the combination is clearly recognizable and virtually unchanged. In nonadditive combinations, the characteristics appearance of all AU involved in the combination is changed and cannot be recognized separately.

The facial expression recognition approaches based on AUs differ in either the feature extraction techniques or the classification technique, or both. Valstar and Pantic [9], for example, detect only 15 action units that are relevant to the six basic emotions. They use facial feature points detector based on Gabor wavelets and GentleBoost classifiers to localize 20 fiducial facial points in the first frame and then tracked in all subsequent frames. Then the calculated features are given to 15 SVMs that are trained using features that describe the spatio-temporal relationships between the tracked points.

Tong et al. [8] focus on the temporal evolution and the semantic relationships among action units. They use Dynamic Bayesian Network (DBN) to model the relationships among different AUs. They use a set of multi-scale and multi-orientation Gabor wavelets to calculate wavelet features for each pixel. Then AdaBoost classifier combines the wavelet features to produce a measurement score for each AU. The drawback of this work is the high complexity and therefore, cannot be used in real time systems.

Khademi et al. [2] recognize single AUs and AU combinations using both geometric and appearance features. To detect the geometrical features, they place manually a point grid on the first frame and register this grid automatically with the face. They use optical flow tracker to track these points in the successive frames and calculate the displacement with respect to the first frame. They extract the appearance facial features by using a set of Gabor wavelets and then use a mixture of HMMs and neural networks to recognize subtle changes in AUs. Although this method is robust, the major drawback is the requirement to manually annotate the first frame.

This paper proposes an action unit based facial expression recognition using Convolutional Neural Network (CNN). Using 23 deep classifiers, the most relevant facial action units and combinations are detected. To reduce the dimensionality, two Support Vector Machines for Regression (SVRs) are used to map these action unit activations to only two values, arousal and valence. These values of arousal and valence are then used to determine the facial expression according to psychological studies. A genetic algorithm is used to select the proper parameters set for the CNN.

The rest of the paper is organized as follows: Sect. 2 explains the proposed approach. Section 3 discusses experiments and result. Finally, Sect. 4 provides the conclusion.

## 2   Facial Expression Recognition

Most of the existing facial expression analysis approaches focus on recognizing a small set of prototypic facial expressions, i.e. happiness, sadness, fear, anger, surprise, and disgust. In inter-personal interaction, many nonverbal cues that

occur due to subtle changes in the facial features can not be regarded as one of these prototypic expressions. In order to detect and interpret the small changes in the facial features, recognition of facial features (AUs) is needed.

### 2.1 Action Units Analysis

In this work, we use deep neural network, specifically convolutional neural network (CNN), to recognize each of the related action units and combinations. CNN consists of multiple different types of layers that are connected to each other. Each layer can be either convolution layer, pooling layer, or fully connected layer.

The convolutional layer applies a set of learnable filters to the input image. Using more than one convolutional layer enables to extract features on different levels. For $m \times m$ filter $w$, the output unit $x_{ij}^l$ of the convolutional layer $l$ is calculated by using Eq. (1).

$$x_{ij}^l = \sum_{a=0}^{m-1} \sum_{b=0}^{m-1} w_{ab} y_{(i+a)(j+b)}^{l-1}.$$

(1)

After calculating the convolution, nonlinearity is applied to calculate $y_{ij}^l$ using the activation function. In this paper, we have used hyperbolic tangent ($tanh$) function in all layers.

Usually, after each convolution layer a pooling layer is used for down-sampling the input image nonlinearly. We have used max pooling, in which a $k \times k$ region is reduced to a single value, which is the maximum value in that region. For an input layer of $N \times N$, the output of max pooling layer is $\frac{N}{k} \times \frac{N}{k}$.

After a set of pairs convolution and pooling layers, the high level reasoning is done by one or more fully connected layer. The fully connected layers represent a multilayer perceptron, which works as classifier. No spatial information exists after the fully connected layers and it can be represented as one dimensional layer.

Figure 1 depicts the architecture of the convolutional neural network that is used to recognize facial action units. The architecture comprises 6 layers (excluding input layers). It receives a human face as a $32 \times 32$ gray image and outputs the confidences of two classes *active* and *not active*. It uses two convolutional layers each one with its own sub-sampling layer (max-pooling).

In the learning phase, the mean squared error (MSE) is used as a loss function. The optimization function used in this work is the Levenberg-Marquardt gradient descent, which combines the advantages of the steepest descent method with the Gauss-Neuton method by adaptively varying the parameter updates between the two methods.

### 2.2 Arousal-Valence Estimation

Recognizing action units as basic components is very important to recognize various nonverbal cues such as facial expressions and some other nonverbal cues.
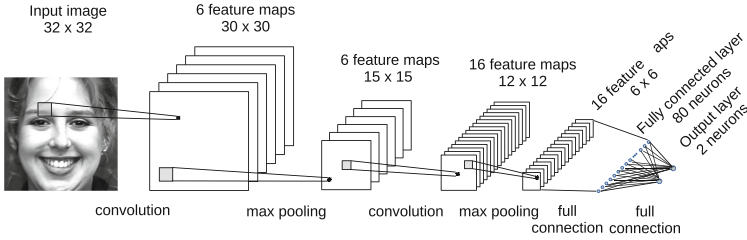
**Fig. 1.** Architecture of deep neural network for action unit recognition. It contains two convolutional layers each with its maximum sampling layer and two fully connected layers with 80 and 2 neurons respectively.

Paltoglou [5] mapped a subset of emotions to a 2D Cartesian coordinate system according to the circumplex model of Russell [6]. In this mapping, emotion states are represented as points where $x$-axis is *valence* and $y$-axis is *arousal*. Using this representation in computer vision systems enables to detect emotions with their corresponding intensity. It also enables to detect different emotions and is not restricted to some prototypic ones.

The challenge of using the arousal-valence representation is calculating these two values. In this work, the values are calculated using AU values of human face. Two SVRs, specifically $\epsilon$-SVRs, are used to calculate arousal and valence values. The input of these two SVRs are the 20 action unit values in addition to 3 action unit combinations: 1+4, 1+2+4, and 4+5. The aim of $\epsilon$-SVR is to find a function $f(x)$ that has at most $\epsilon$ deviation from the targets $y_i$ for all training data and is as *flat* as possible [7].

On a general scale and not limited to the prototypic ones, activation of AUs of human face is used to recognize the facial expression. Suppose, $U$ is a set of $n$ action unit activations that are involved in facial expressions, where

$$U = \{u_1, u_2, \ldots, u_n\}, \quad with \quad u_i \in [0,1], n > 0. \tag{2}$$

$P$ is a set of deep learners (CNNs) that detects the activation of all AUs $u_i$ of an input image $x$.

$$P = \{p_1, p_2, \ldots, p_n\}. \tag{3}$$

$$u_i = p_i(x) \quad where \quad x \in \mathbb{R} \times \mathbb{R}. \tag{4}$$

Suppose, $A$ and $V$ are two SVRs to calculate the *arousal* and *valence* respectively. Then $a$ and $v$ are the arousal and valence values of input image $x$.

$$a = A(u_1, u_2, \ldots, u_n), \qquad v = V(u_1, u_2, \ldots, u_n). \tag{5}$$

The function $f$ that calculates the facial expression is defined as follows:

$$f(a, v) = \arg\min_{i \in E} \left( \sqrt{(a - a_i')^2 + (v - v_i')^2} \right). \tag{6}$$

Where $E$ are all facial expressions, $a_i'$ and $v_i'$ are arousal and valence of expression $E_i$. Figure 2 shows the facial expression recognition process. The training process of deep learners and SVRs are discussed in Sect. 3.
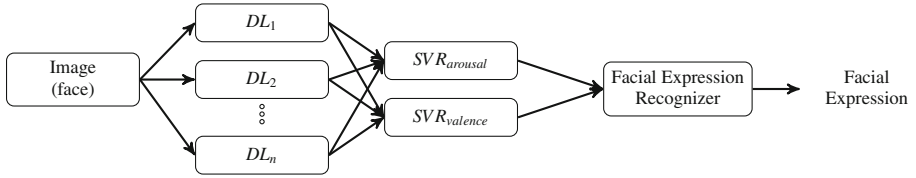
**Fig. 2.** Facial expression recognition process. $DL_i$ refers to the deep learner for action unit $i$. $SVR_{arousal}$ and $SVR_{valence}$ are the SVRs for arousal and valence respectively.

## 3 Experiments

### 3.1 Datasets

To evaluate the performance of the proposed facial expression recognition approach, two faces datasets are used: CK+ (Cohn-Kanade plus) [4] and RaFD (Radboud Faces Database) [3]. CK+ provides 593 sequences of frontal faces in still images from 123 subjects each with action units annotation. In our study, CK+ dataset is used to train the AU classifiers. For each action unit, a deep learner has been trained to classify two classes: *active* and *not active*. The deep learners output the confidence value of active $c_a$ and not active $c_n$ classes, where $c_a, c_n \in [0, 1]$. The activation value of each action unit refers to how much this AU is active, which can be calculated as follows:

$$activation = c_a \cdot (1 - c_n). \tag{7}$$

RaFD (Radboud Faces Database) is a high quality faces dataset that contains images of 67 subjects displaying 8 facial expressions (neutral, anger, disgust, fear, happiness, sadness, surprise, and contempt). It also provides additional validation data such as agreement percentage, intensity rating, clarity, genuineness, and valence rating for each image. It doesn't provide arousal value of images. In order to calculate arousal value of each image, the standard arousal of the corresponding facial expressions can be weighted using the intensity rating as described by [5].

### 3.2 Parameters Optimization for CNNs

Many parameters play an essential role in the design of any deep neural network. The number of layers, number of neurons in each layer, activation function, and cost function are examples of these parameters. Setting these parameters affects the learning process and the performance of the network. In this work, a Genetic Algorithm (GA) based optimization approach is used to set all network parameters.

Genetic algorithm is a heuristic search algorithm that mimics the process of natural selection. GA repeatedly modifies a population of individual solutions (chromosomes). At each step, GA selects parent chromosomes from the current

population to produce the children for the next generation. The optimization problem in the current work is a maximization of the recognition rate of facial action units. The main ingredients of GA are as follows:

**Chromosome:** In genetic algorithms, chromosome is a set of genes, which codes the independent variables as a solution of the given problem. In this optimization problem, a chromosome is a set of parameters that represents the structure of the network (classifier) such as *number of layers*, *kernel size*, *pooling size*, *activation function*, and so on. The size of chromosome is variable and depends on the number of convolutional and fully connected layers.

**Selection:** This process allows for better individual to contribute to the next generation. The goodness of an individual depends on its fitness. This can be determined by a fitness function, which is the recognition rate in this work.

**Crossover:** This process combines two individuals as parents to form children for the next generation. In this work, one point is randomly chosen, the values after this point are exchange to produce two children. Because of the different size of each chromosome, only the genes of one chromosome that have corresponding genes in the other one are exchanged.

**Mutation:** This means random change in the value of one or more genes with very low probability. It can maintain diversity within population and inhibit premature convergence.

All the above GA operations have been applied on a population of 50 chromosomes to obtain an optimum solution for the facial action units recognition. After 100 generations, the fittest chromosome is the network configuration that has been shown in Fig. 1.

**Table 1.** Action units recognition rates. The average is weighted i.e. depending on the number of positive examples.

| AUs | Samples | RR (%) | AUs | Samples | RR (%) | AUs | Samples | RR (%) |
|-----|---------|--------|-----|---------|--------|-----|---------|--------|
| 1 | 88 | 94.32 | 11 | 39 | 84.62 | 24 | 65 | 80.77 |
| 2 | 90 | 94.44 | 12 | 126 | 96.03 | 25 | 317 | 93.38 |
| 4 | 103 | 91.26 | 15 | 93 | 89.78 | 26 | 50 | 80.00 |
| 5 | 86 | 92.44 | 16 | 24 | 81.25 | 27 | 80 | 100.00 |
| 6 | 92 | 96.20 | 17 | 172 | 88.37 | 1+4 | 67 | 85.07 |
| 7 | 144 | 89.58 | 20 | 73 | 92.47 | 1+2+4 | 21 | 71.43 |
| 9 | 71 | 95.07 | 22 | 14 | 89.29 | 4+5 | 25 | 74.00 |
| 10 | 40 | 92.50 | 23 | 65 | 85.38 | | | |
| **Average** | | **90.85** | | | | | | |

## 3.3 Evaluation Results

To evaluate the recognition of action units, 23 classifiers have been trained to recognize two classes for each action units: *active* and *not active*. We have used leave-one-subject-out cross-validation to maximize the training and testing data. The overall recognition accuracy is more than 90%. Table 1 shows the recognition rate of action units.

In the same way, leave-one-subject-out cross-validation configuration is used to evaluate the two SVRs. The root mean square for the *arousal* and *valence* are 0.21 and 0.16, respectively. Figure 3 shows arousal values (a) and the valence values (b) of all examples categorized by the facial expression.
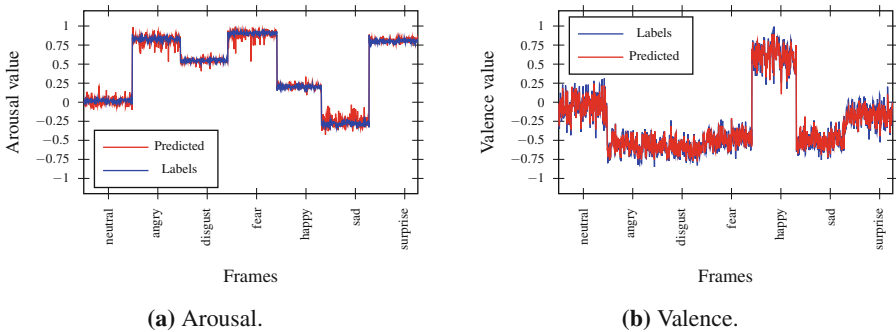


(a) Arousal.  (b) Valence.

**Fig. 3.** Arousal and valence regression.

The performance of the whole facial expression recognition using the proposed approach is given in Table 2. It is obvious from this table that *angry* and *fear* are overlapped because they are near to each other on the arousal-valence map. An average recognition rate of 90.3% is achieved using this approach.

**Table 2.** Confusion matrix of facial expression recognition.

| Detected as ⇒ | Neutral | Angry | Disgust | Fear | Happy | Sad | Surprise |
|---|---|---|---|---|---|---|---|
| Neutral | **95.2** | 0.0 | 0.0 | 4.8 | 0.0 | 0.0 | 0.0 |
| Angry | 0.0 | **81.0** | 9.5 | 4.8 | 0.0 | 4.8 | 0.0 |
| Disgust | 0.0 | 0.0 | **95.2** | 4.8 | 0.0 | 0.0 | 0.0 |
| Fear | 0.0 | 9.5 | 0.0 | **81.0** | 0.0 | 0.0 | 9.5 |
| Happy | 0.0 | 0.0 | 0.0 | 0.0 | **94.1** | 0.0 | 5.9 |
| Sad | 4.8 | 0.0 | 4.8 | 0.0 | 0.0 | **90.5** | 0.0 |
| Surprise | 0.0 | 0.0 | 0.0 | 4.8 | 0.0 | 0.0 | **95.2** |

## 4   Conclusion

In this paper, we have presented a facial recognition approach based on AUs. The most relevant 23 AUs and combination have been used in this work. This approach uses deep learning in action unit analysis. For each of these action units and combinations, a two-classes classifier has been trained. Two SVRs have been used to calculate the values of arousal and valence of the human depending on the activation values of these action units and combinations. The facial expression is recognized by finding the minimum Euclidean distance from the detected point (arousal and valence) and the basic emotions. The recognition rate of both AUs and facial expression is more than 90%.

## References

1. Ekman, P., Friesen, W., Hager, J.: Facial Action Coding System. Consulting Psychologist Press Inc., Palo Alto (1978)
2. Khademi, M., Manzuri-Shalmani, M.T., Kiapour, M.H., Kiaei, A.A.: Recognizing combinations of facial action units with different intensity using a mixture of hidden markov models and neural network. In: Gayar, N., Kittler, J., Roli, F. (eds.) MCS 2010. LNCS, vol. 5997, pp. 304–313. Springer, Heidelberg (2010). doi:10.1007/978-3-642-12127-2_31
3. Langner, O., Dotsch, R., Bijlstra, G., Wigboldus, D.H.J., Hawk, S.T., van Knippenberg, A.: Presentation and validation of the radboud faces database. Cogn. Emot. **24**(8), 1377–1388 (2010)
4. Lucey, P., Cohn, J.F., Kanade, T., Saragih, J., Ambadar, Z., Matthews, I.: The extended cohn-kanade dataset (CK+): a complete dataset for action unit and emotion-specified expression. In: IEEE Computer Society Conference on Computer Vision and Pattern Recognition Workshops (CVPRW), pp. 94–101 (2010)
5. Paltoglou, G., Thelwall, M.: Seeing stars of valence and arousal in blog posts. IEEE Trans. Affect. Comput. **4**(1), 116–123 (2013)
6. Russell, J.: The circumplex model of affect. J. Pers. Soc. Psychol. **39**, 1161–1178 (1980)
7. Smola, A.J., Schölkopf, B.: A tutorial on support vector regression. Stat. Comput. **14**(3), 199–222 (2004)
8. Tong, Y., Liao, W., Ji, Q.: Facial action unit recognition by exploiting their dynamic and semantic relationships. IEEE Trans. Pattern Anal. Mach. Intell. **29**(10), 1683–1699 (2007)
9. Valstar, M., Pantic, M.: Fully automatic facial action unit detection and temporal analysis. In: Computer Vision and Pattern Recognition Workshop (CVPRW), p. 149 (2006)

# Fast Setup and Adaptation of Industrial Assembly Tasks with Force-Based Exception Strategies

Aljaž Kramberger[1]([✉]), Casper Schou[2], Dimitrios Chrysostomou[2], Andrej Gams[1], Ole Madsen[2], and Aleš Ude[1]

[1] Humanoid and Cognitive Robotics Lab, Department of Automatics, Biocybernetics and Robotics, Jožef Stefan Institute, Ljubljana, Slovenia
`aljaz.kramberger@ijs.si`
[2] Robotics and Automation Group, Department of Mechanical and Manufacturing Engineering, Aalborg University, Aalborg, Denmark
`dimi@m-tech.aau.dk`

**Abstract.** In this paper we present a method for fast setup and adaptation of desired movement for industrial assembly tasks. Our method is based on adaption of desired movements acquired by Programming by Demonstration (PbD) and fast setup methods such as the Skill Based System (SBS) that are capable to quickly learn sequential skills to perform assembly. The major novelty of the proposed method is the integration of fast setup methods with force based adaptation skills and exception strategies for fast and efficient task execution. To improve the execution of the skill, the learned movements are online adapted according to forces and torques arising during the execution, effectively eliminating the environmental uncertainties. Results show that this approach can be arbitrarily applied to different robotics platforms. We performed tests on the 7-axis Kuka LWR-4 and on the 6- axis UR-5 Universal robot.

**Keywords:** Assembly · Skills · Learning by demonstration

## 1  Introduction

Robotization in small and medium enterprises is often not economically viable because of small-lot and high customized production that represents a trend in today's modern industry. Recently, novel methods of robotic control and programming paradigms have made it possible for fast and un-demanding setup of assembly processes for customized production. One of the main enablers of this transition is robotics and specifically robotic systems that can cope with uncertainty and interact with humans, handle a variety of different tasks, and are able to be reprogrammed fast by non-experts when a new task in the factory arises.

In this paper we investigate a classical robotic assembly problem: the peg-in-hole (PiH) skill. While the fine adaptation process itself has been studied in previous research [4,7] including our own [1], we focus on flexible and on-the-fly

adaption and execution of PiH skills in classical industrial assembly processes. For a successful PiH execution both desired position trajectories and force/torque profiles are required. Position control, when executing tasks in contact with the environment, is insufficient because even small errors in the desired trajectory can cause significant deviations from the desired forces and torques [1]. The major novelty of the proposed method is to show that PiH skills with adaptation and in combination with force based exception strategies can be used to sufficiently accomplish industrial use case assembly tasks.

The backbone of our method is Programming by Demonstration (PbD) in combination with fast setup strategies. Traditionally, programming of industrial robots requires expert programming knowledge and is not flexible to frequent changes. Recent works on intuitive, on-the-fly programming of robots [6,8] and learning by demonstration [3], e.g., through kinesthetic guiding [9] of robotic arms, provide the necessary framework for reconfigurability and knowledge transfer. In a typical learning by demonstration setup, position and orientation trajectories are recorded. Widely accepted approach in PbD is to encode the trajectories with dynamic movement primitives (DMP) [5]. This framework enables efficient modulation of trajectories while they are being executed, both spatially and temporarily, because they are not explicitly time dependent.

In some scenarios unexpected challenges can occur; therefore special methods have to be applied to successfully perform the desired tasks. In the work of Abu-Dakka et al. [2] stochastic force based search strategies are presented to enhance and overcome the gripping and pose estimation uncertainties in industrial tasks. The main focus of this paper lies on integrating exception strategies to resolve situations where the robot fails to accomplish the task outright. The purpose of exception strategies is mainly to locate the hole and perform the PiH with force control, if the PiH adaptation method is insufficient to conclude the action. We also briefly explain how PiH execution with force-torque adaptation is solved and incorporated in the assembly method. This paper is organized as follows. In the next section we describe the problem formulation. Separate segments of the proposed method are explained in detail in Sect. 3. Experimental evaluation follows in Sect. 4, with conclusions given in Sect. 5.
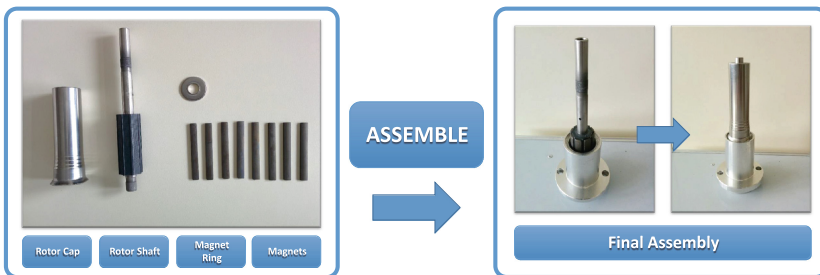


**Fig. 1.** Assembly parts (left), final assembled rotor (right).

## 2   Problem Formulation

The challenge presented in this work is to assemble a real industrial part, specifically a rotor for a water pump, that is comprised of: 8 magnets, a rotor shaft, a magnet ring and a rotor cap (Fig. 1). To assemble the rotor, next operations are needed:

– Pick and Place,
– Peg in Hole (PiH),
– Force based exception strategies.

The assembly task represents different challenges in terms of tight tolerances when assembling the object into subassemblies and unpredictable friction coefficients. To overcome the challenges an online adaptation algorithm has to be used to ensure reliability and maintain a high success rate of the assembly process. The entire assembly sequence consists of 11 steps:

– Pick the magnet ring from the feeder and place in to the assembly holder.
– Pick the rotor shaft from a fixture and assemble it with the magnet ring in the assembly holder.
– Pick the 8 magnets from the feeder and assemble them with the rotor shaft.
– Pick the rotor cap from the holder and put it on the rotor shaft.

Most of the operations can be accomplished with pick and place and Peg in Hole skills, that will be explained in the following section. Some of the assembly operations are more specific, therefore special force based strategies have to be applied. In this work we will mainly focus and evaluate the assembly procedure of the rotor cap and rotor shaft with specialized exception strategies to ensure a successful and rigid assembly operation.

## 3   Method Description

### 3.1   Teaching the Example Movements

Robot task trajectories can be recorded in several ways. In this work, we focus on recording trajectories with kinesthetic guiding. The example movement trajectories are recorded in Cartesian coordinates together with the appropriate end effector forces and torques. Note that some robots, like KUKA LWR-4 robot, use joint torques to estimate the end effector forces and torques, therefore the measured forces can be corrupted by the human demonstrator. Therefore to obtain the actual forces and torques acting on the robot tool, the recorded movement has to be replayed in exactly the same configuration of the work place.

Different robots like UR-5, also provide the capability of active gravity compensation and consequently enable kinesthetic teaching. The differences are evidential in the structure of the manipulator, meaning that the UR-5 does not provide torque sensors in the joints, therefore a force/torque sensor is mounted at the wrist of the manipulator to record the tool forces and torques. In the

recording phase, the operator physically grabs the robot arm and guides it along the desired trajectory, and thus receives the same force feedback from the environment as the robot. Consequently, the initial trajectories are more optimal and it is not necessary to refine them afterwards.

In this case the following data is recorded: Cartesian space positions and orientations (represented as quaternions), their first and second derivatives (linear/angular velocities and accelerations) and the end effector forces and torques measured in the tool centre point of the robot.

### 3.2    Fast Setup Using Robot Skills

In order to accomplish fast setup and easy programming of the desired assembly task we use the concept of "robot skills" [6,8]. In our system, skills are defined as abstractions of the functionalities of the combined hardware, encapsulating task related abilities. Therefore, the ability to pick up a rotor shaft from the fixture is represented by a *"pick"* skill and the ability to place the rotor cap on the platform is represented by a *"place"* skill, respectively.

The skill, as an entity, represents a generic and reusable module that can be parameterized for the task in hand. These parameters can be related to the hardware capabilities of the platform or to the task–related objects. A set of these parameters, such as the velocity of the robot manipulator and the potential typed of objects to identify, can be specified offline via a Graphical User Interface (GUI). Another set, such as the Cartesian position and required trajectories, can intuitively be specified online through kinesthetic guiding with the robot. Hence, a non-expert operator is able to quickly combine several robot skills into a sequence, define their parameters and create a robot task.

A tool, called Skill Based System (SBS), has been developed [8] to assist the operator during the phases of specification, parametrisation and execution of skill–based tasks. SBS acts as a robot operating tool enabling fast programming and easy combination of robot skills for the assembly task. Thus, a non-expert operator can instruct the robot to *"pick up"* a rotor shaft from a fixture, *"place into"* a platform by performing a *"peg–in–hole"* operation using previously taught, force–related trajectories.

### 3.3    Adaptation of the Desired Movement

While executing the demonstrated trajectories, the actual forces and torques can differ from the demonstrated ones. If the discrepancies increase during the execution of the demonstrated movement, the robot could jam and the execution would fail. Therefore, the demonstrated trajectories have to be properly adapted during the execution. As proposed in the work of Abu-Dakka et al. [1], an error feedback calculated from the actual and demonstrated forces and torques can be used to modify the robot movement, consequently reducing the discrepancies between the desired and actual forces and torques.

The proposed movement adaptation algorithm uses the DMP phase stopping mechanism described in [1,10], to slow down the robot movement and prevent it

from jamming. The slowing down of the robot motion allows the force feedback mechanism to adapt the motion and reduce the force/torque discrepancies. This means, however, that the task is executed slower than expected. The method presented in the work of Abu-Dakka et al. [1] utilizes online feedback error to learn a feedforward term. Applying the feedforward term in the control algorithm reduces the need for slowing down the movement e.g. phase stopping and consequently increases the speed of the execution.

### 3.4   Force Based Exception Strategies

A number of the assembly operations can not be accomplished with the previously explained adaptation methods, due to technicalities of the assembly objects. Therefore, exception strategies have to be applied to perform the assembly, in particular the assembly of the rotor shaft and the rotor cap. In this case force based search strategies are applied to ensure a successful assembly. The exception strategy is comprised of two steps:

**Approaching Step:** Move the robot tool down in global $Z$-coordinate using implicit force-torque control to detect the upper edge of the rotor shaft and make contact.

**Verification Step:** Due to the limited precision of grasping and other environmental factors, we never know whether the robot is at the required starting position above the rotor shaft and if the hole of the rotor cap is aligned with the rotor shaft to perform a successful placement. Therefore, the first step should be verification of the required starting pose. Because we cannot completely rely on the robot position, we use force-sensing instead.

Verification is executed in following steps, where we pre-assume that the workpiece i.e. rotor shaft, lies in the X-Y plane:

1. Perform linear motion in the global $X$ and $Y$ coordinates starting from the current contact point with the displacement of dx, dy and dx, -dy that correspond to the radius of the rotor cap hole while maintaining the contact between the rotor shaft and the rotor cap,
2. Determine the minimum in global $Z$ coordinate when the shaft falls into the hole and the desired contact force declines,
3. Perform hybrid force-torque control to determine the contact between the rotor and the rotor cap lower edge and conclude the action.

In some cases the global minimum in $Z$ coordinate that corresponds to penetrating the hole, might not be detected. In this case, we have to continue with the next procedure, which is stochastic hole-search:

$$\begin{bmatrix} x_{new} \\ y_{new} \end{bmatrix} = \begin{bmatrix} x_{start} \\ y_{start} \end{bmatrix} + \begin{bmatrix} \epsilon_x \\ \epsilon_y \end{bmatrix} \tag{1}$$

$$\epsilon_x = r * \cos(rand * 2\pi) \ \epsilon_y = r * \sin(rand * 2\pi) \tag{2}$$

**Searching Phase:** Using stochastic search algorithm to detect the hole. The algorithm calculates small random increments $\epsilon$ in $X$ and $Y$ coordinates to move the tool of the robot from the start position (position of the first contact) $x_{start}$ and $y_{start}$ to the new calculated position $x_{new}$ and $y_{new}$ (1), while maintaining the contact force. The displacement values $\epsilon$ (2) are random from a circle with a specific radius $r$, in our case 13 mm. After every search move is executed the robot moves back to the start position. If during the search movement the global minimum in $Z$ is determined and the desired contact force declines, the search phase is concluded and verification step 4 is performed to conclude the placement action.

## 4   Experimental Evaluation

The proposed methods were tested on two different robot platforms:

– Kuka LWR-4 (Fig. 2, left) with 7 DOFs, equipped with an RH-707 two finger gripper. This robot has a torque sensor in every joint, therefore no external force/torque sensor is needed. The measured joint torques are transformed to Cartesian forces and torques in real time using the robot dynamics model.
– Universal Robot arm – type UR-5 – (Fig. 2, right) with 6 DOFs, equipped with ATI (Gamma SI-130-10) force/torque sensor located at the wrist of the robot and a SCHUNK WSG50 two finger gripper. This robot is driven by a high gain non-compliant controller. The UR5 robot features active gravity compensation and free movement in teaching mode, thereby enabling kinesthetic guiding.

In both cases robot control was implemented in Matlab. For the KUKA robot we used the FRI interface to communicate with the robot controller. On the second platform ROS-Matlab interface was used to communicate with the ROS Industrial driver of the UR-5 robot. On both systems specialized gripper fingers were used to perform the grasping of all assembly objects (Fig. 1). Grasping plays
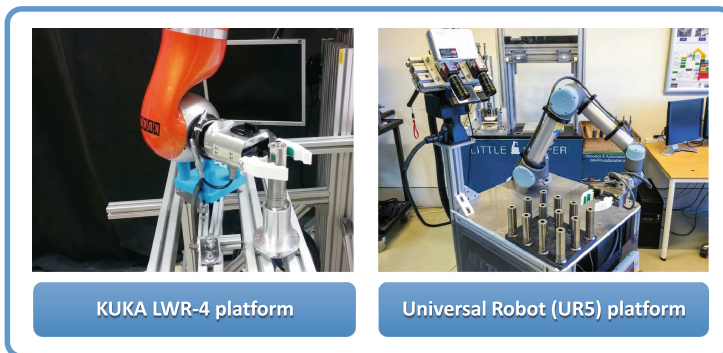


**Fig. 2.** Experimental platforms used to test the assembly methods.
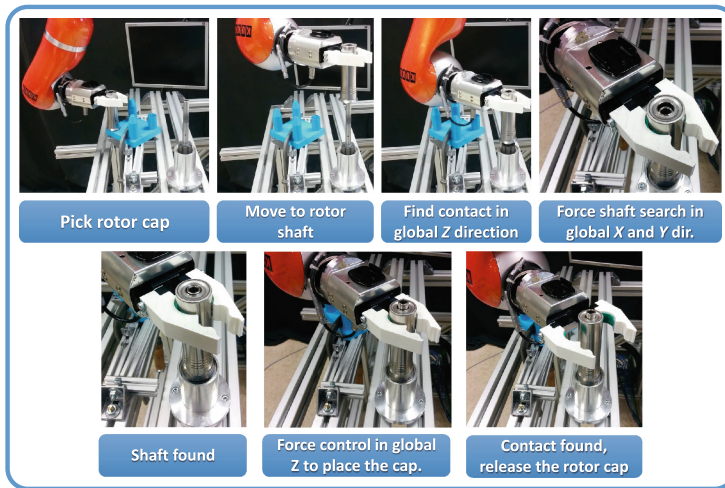
**Fig. 3.** Presentation of the assembly sequence for force based rotor cap assembly.
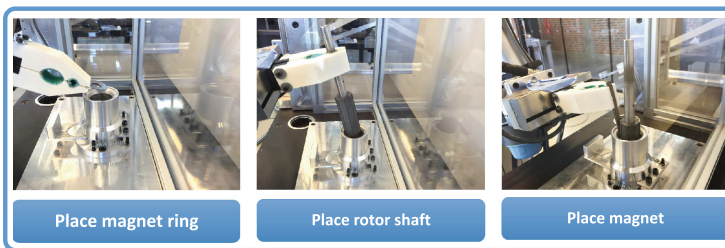


**Fig. 4.** PiH related assembly steps, to assemble magnet ring, rotor shaft, magnets with UR5 robot.

an important role, because unstable grasping can lead to slipping of the object and consequently the actual forces and torques that act on the manipulated object cannot be measured accurately.

In the first step the objects were picked from the fixtures and brought to the assembly fixture. The necessary knowledge to perform the specific manipulation action was taught via kinesthetic guiding and skill based system (SBS). In the second step the assembly of the objects was carried out. Most of the assemblies could be performed with the PiH skill using the adaptation algorithm. In this manner all objects i.e. magnet ring, rotor shaft and magnets were assembled as shown in Fig. 4.

The only exception was the rotor cap. For this operation the previously presented force based exception strategy was used. As a first action the rotor cap was picked from the fixture and placed just above the rotor shaft. The problem of placing the rotor cap on the shaft is presented as an "inverted peg in hole"

problem, therefore, the shaft has to be located initially by the rotor cap hole and secondly the "put on" action is carried out. The entire sequence can be seen in Fig. 3. In this manner several experiments were performed to test the reliability of the proposed approach. The experiments were performed on two different platforms, where the KUKA robot is not completely stiff due to the physical capabilities of the robot itself. It proved to be a virtue rather than a drawback in this case, yielding better results compared to the UR5 robot that does not provide that capability.



| Platform | Succ. Experiments with Except. Strat. | Succ. Pick and Place Experiments | Success rate of Except. Str. Exper. % |
|----------|----------------------------------------|-----------------------------------|----------------------------------------|
| KUKA | 19 | 12 | 95 |
| UR5 | 18 | 13 | 90 |
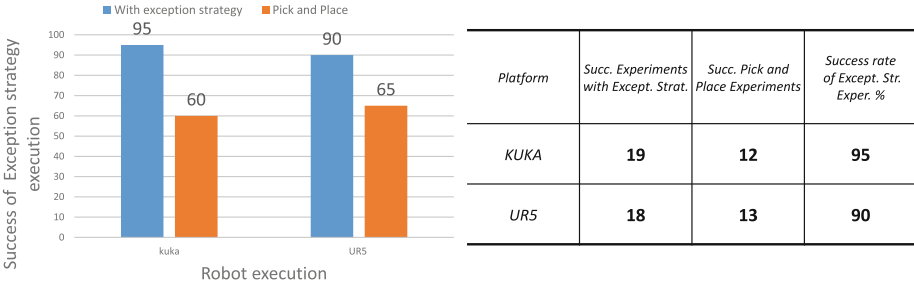
**Fig. 5.** Reliability of the proposed exception strategy, tested on assembling the rotor shaft and the rotor cap.

Two different experiments were performed on each platform. Figure 5 shows the experimental evaluation of the proposed method. Results compared to a simple pick and place operation, where the hole of the rotor cap was placed 4 mm above the rotor shaft and released, proved to be less reliable compared to the proposed exception strategy, where high success rate of execution was evident.

## 5   Conclusion

In this work we have shown that simple industrial tasks such as pick and place operations can be combined with more advance tasks such as Peg in Hole actions. Even further, we proved that the PiH action can be augmented with a force-based adaptation method to compensate for uncertainties present in the environment. We tested our method on two different robotic platforms: the LWR-4 robot, which is impedance controlled, and the UR-5 robot, which is admittance controlled. Despite of different controllers the proposed setup was successfully applied on both platforms. Experimental results show the robustness and fast adaptation capability of the proposed algorithm. In our future work we will investigate other methods to enhance the performance and speed of the assembly process so that the method could be used in real-world, industrial, small batch scenario with fast setup capabilities.

# References

1. Abu-Dakka, F.J., Nemec, B., Jørgensen, J.A., Savarimuthu, T.R., Krüger, N., Ude, A.: Adaptation of manipulation skills in physical contact with the environment to reference force profiles. Auton. Robots **39**, 199–217 (2015)

2. Abu-Dakka, F.J., Nemec, B., Kramberger, A., Buch, A.G., Krüger, N., Ude, A.: Solving peg-in-hole tasks by human demonstration and exception strategies. Ind. Robot: Int. J. **41**, 575–584 (2014)

3. Argall, B.D., Chernova, S., Veloso, M., Browning, B.: A survey of robot learning from demonstration. Robot. Auton. Syst. **57**, 469–483 (2009)

4. Dillmann, R.: Teaching and learning of robot tasks via observation of human performance. Robot. Auton. Syst. **47**, 109–116 (2004)

5. Ijspeert, A.J., Nakanishi, J., Hoffmann, H., Pastor, P., Schaal, S.: Dynamical movement primitives: learning attractor models for motor behaviors. Neural Comput. **25**, 328–373 (2013)

6. Pedersen, M.R., Nalpantidis, L., Skovgaard, R.A., Schou, C., Bøgh, S., Krüger, V., Madsen, O.: Robot skills for manufacturing: from concept to industrial deployment. Robot. Comput.-Integr. Manuf. **37**, 282–291 (2015)

7. Rozo, L., Jiménez, P., Torras, C.: A robot learning from demonstration framework to perform force-based manipulation tasks. Intel. Serv. Robot. **6**, 33–51 (2013)

8. Schou, C., Damgaard, J., Bøgh, S., Madsen, O.: Human-robot interface for instructing industrial tasks using kinesthetic teaching. In: 44th International Symposium on Robotics (ISR), pp. 1–6, October 2013

9. Steil, J.J., Emmerich, C., Swadzba, A., Grünberg, R., Nordmann, A., Wrede, S.: Kinesthetic teaching using assisted gravity compensation for model-free trajectory generation in confined spaces. In: Röhrbein, F., Veiga, G., Natale, C. (eds.) Gearing Up and Accelerating Cross-fertilization between Academic and Industrial Robotics Research in Europe: Technology Transfer Experiments from the ECHORD Project. STAR, vol. 94, pp. 107–127. Springer, Heidelberg (2014). doi:10.1007/978-3-319-03838-4_6

10. Ude, A., Nemec, B., Petrič, T., Morimoto, J.: Orientation in cartesian space dynamic movement primitives. In: IEEE International Conference on Robotics and Automation (ICRA), Hong Kong, pp. 2997–3004 (2014)

# Movement Recognition and Cooperative Task Synthesis Through Hierarchical Database Search

Miha Deniša[(✉)] and Aleš Ude

Humanoid and Cognitive Robotics Lab, Department of Automatics,
Biocybernetics and Robotics, Jožef Stefan Institute, Ljubljana, Slovenia
`miha.denisa@ijs.si`

**Abstract.** An approach for movement recognition and cooperative task synthesis is presented. It is based on a two-part hierarchical database, one consisting of human motion and the second on cooperative robot movements. While the motion recognition is done through hierarchical search on the primary part of the database, the secondary part is used for determining the most probable path for cooperative movement synthesis. Dynamic movement primitives are used to encode the path into a smooth and continuous movement. Initial evaluation, done in simulation, shows the validity of the proposed approach.

**Keywords:** Programming by demonstration · Motion recognition · Hierarchical database · Cooperative movement

## 1 Introduction

A successful transfer of robots from industry halls into home environments still remains one of the main goals of modern robotics. Robot manipulators, working in industry halls, constantly repeat the same programmed motions in a controlled and stable environment. In contrast, a robot used in an unstructured home environment has to constantly adapt to varying surroundings. These changing conditions make programming a robot by hand unsuitable. Programming by demonstration (PbD) [1,4,10] is a widely used approach for gaining new sensorimotor knowledge through human demonstration. Human movement can be observed using a magnetic or optical marker-based system [8,13]. Vision systems based on stereo cameras [7] and RGB-D sensors [12] have also been used to track a human while performing a task. Kinaesthetic guiding, where a human physically guides the robot, can also be applied [5,9].

Another vital aspect of autonomy in home environments is human robot collaboration. For a successful collaboration a robot must first recognize human intentions, i.e. motions, and secondly, it must synthesize and execute an appropriate cooperative movement. While there are several approaches to human robot collaboration, the work most related to our proposed approach, was done by Yamane et al. [14,15]. Similarly to our work, they used a binary tree database to

recognize human movement and then synthesized an appropriate robot reaching movement.

The approach proposed in this paper is based on an extended hierarchical database of demonstrated cooperative movements. A similar, more basic database was previously used in order to synthesize new, never directly demonstrated movements from a set of example trajectories [3]. It was later extended in order to generate new compliant movements, where the basic part of the database encoded kinematic trajectories and the secondary part stored corresponding torques [2].

The rest of the paper is structured as follows. Section 2 focuses on hierarchical database construction, its extension and transition graph implementation. Motion recognition is presented in Sect. 3 and cooperative task synthesis is explained in Sect. 4. Towards the end initial evaluation of the approach and final remarks are given.

## 2 Hierarchical Database

Before constructing the database, a set of example demonstrated cooperative movements is captured, where each example consists of a human movement and a corresponding robot movement. While human movement is used to build the basic part of the database, robot movements are stored in the secondary part. A simple example of a database can be seen in Fig. 1.
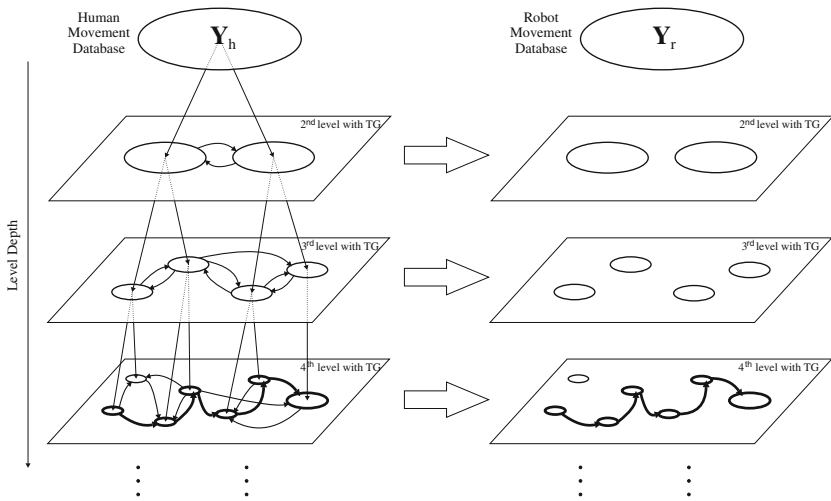


**Fig. 1.** A simple representation of an example hierarchical database. While the basic part of the database, seen on the left, encodes human movements and is used for construction and motion recognition, the secondary part, seen on the right, stores corresponding robot movements.

The construction of the basic part starts with concatenating all example human trajectories into a single sample human motion matrix,

$$\mathbf{Y}_h = [\mathbf{y}_1^h, \mathbf{y}_2^h, \ldots, \mathbf{y}_{n_f}^h], \tag{1}$$

where $h$ denotes *human*, $\mathbf{y}$ denotes state vectors sampled at a given discrete time interval and $n_f$ is the sum of all state vectors in all example human trajectories used in the example set. Each state vector can, for example, be defined as a position $p$ and velocity $\dot{p}$ of a single human marker in Cartesian space,

$$\mathbf{y}_i^h = [p_i^x, \dot{p}_i^x, p_i^y, \dot{p}_i^y, p_i^z, \dot{p}_i^z], \tag{2}$$

at a given sample time $t_i$. It can also store multiple markers or human joint angles.

Once all the human demonstrations are stored in a sample motion matrix, it is utilized to build the binary tree like database. The sample matrix $\mathbf{Y}_h$ represents the root node, which is divided into 2 child nodes, represented in the second level of the database. A clustering algorithm is used on the associated state vectors which divides them into two clusters containing similar state vectors. While a variety of clustering algorithms can be used, the k-means algorithm proved most suitable for our approach. The clustering is then repeated on both child nodes in order to gain the nodes at the next level. The process is repeated until all the nodes meet the *stop split* criterion. The criterion is based on the variability of state vectors associated with a node. To ensure all the data is represented at each level every branch is extended to the last level by copying the leaf nodes.

As all the data is clustered, the original sequence of state vectors in the example trajectories is lost. That is substituted through transition graphs build at each level of the hierarchical database (see Fig. 1). These weighted directed graphs represent the transitions probabilities between nodes at each level. The weight denotes the transition probability from node $v_k$ to node $v_l$ and is estimated as

$$\phi_{kl} = \frac{m_{kl}}{n_{v_k}}, \tag{3}$$

where $m_{kl}$ denotes the number of state vectors clustered in node $v_k$ which, based on the sample trajectories, have a successor in node $v_l$. The number of state vectors clustered in node $v_k$ is denoted by $n_{v_k}$. The time component is also lost in the process of clustering. It is explained later in the paper how time duration for each node is estimated.

After the basic database containing human example movements is constructed, the secondary database is built. For the purpose of synthesizing cooperative movements, additional transition graphs for robot movements are built on each level. Thus every node on each level of the basic database has a counterpart, i.e. an associated node, in the robot database. They are associated based on original example movements. That means that each node in the secondary database encodes robot state vectors recorded at same sample times as their counterparts in the human node. Again, see Fig. 1 for a simple representation of a database.

# 3   Movement Recognition

Human movement recognition is done by using the basic part of the database. It is traversed with a sequence of state vectors corresponding to the current captured part of human movement

$$\{\mathbf{y}_1^r, \mathbf{y}_2^r, \ldots, \mathbf{y}_{n_s}^r\}, \tag{4}$$

where $r$ denotes *robot* and $n_s$ the number of captured samples used for recognition, i.e., the size of the sliding window. The size of the sliding window is a compromise between the speed of recognition and the confidence of the result. Recognition is done by moving down through the levels of the basic database. At each level multiple steps are done:

1. Considered nodes $v_c$ are determined at the current level. These nodes are children of all nodes that were below the cut-off range at the previous layer. For the first level of the recognition, usually the 3rd level, all the nodes are considered.
2. The matrix of considered nodes $P$ is built. Each row has same length as the sliding window $n_s$ and contains a permutation of considered nodes $v_c$. The matrix $P$ includes all possible permutations.
3. Calculate the recognition criterion for each permutation

$$C = \sum_{i=1}^{n_s} d(\mathbf{y}_i^r, v_i) + \sum_{i=1}^{n_s-1} \tau(v_i, v_{i+1}), \tag{5}$$

where $d(\mathbf{y}_i^r, v_i)$ denotes a distance between the current captured human positions and state vectors corresponding to a considered node. The second term presents transition probability between considered nodes.
4. Determine which nodes have the recognition criterion above the cut-off range. Only their children will be considered at the next level. The range is an compromise between the speed of recognition and the confidence of the result.

Upon reaching the last level, the permutation of nodes with the highest recognition criterion value is considered as the most probable sequence of nodes $\{v_1, v_2, \ldots, v_{n_s}\}$. From this sequence the most probable path in the human database is determined by simply continuing through the transition graph following the highest probabilities.

# 4   Cooperative Task Synthesis

Through movement recognition the most probable human path is found. By looking at corresponding robot data in the secondary database, the most probable robot path, i.e. sequence of nodes, can be gained. This step is indicated in Fig. 1

with bold lines. As already mentioned, the time component is lost while constructing the database. In order to enhance the sequence of robot state vectors with time stamps, a duration of a single node is defined as

$$t_v = \frac{n_v}{m_v} \Delta t, \tag{6}$$

where $n_v$ denotes the number of state vectors associated with node $v$ and $m_v$ denotes the number of example movements passing through node $v$. The sampling frequency is defined as $1/\Delta t$. By combining node durations $t_v$ and means of state vectors associated with nodes $\overline{\mathbf{y}}^r$, the most probable robot movement can be written as a sequence

$$\{(\overline{\mathbf{y}}_1^r, T_1), (\overline{\mathbf{y}}_2^r, T_2), \dots, (\overline{\mathbf{y}}_{n_r}^r, T_{n_r})\}, \tag{7}$$

where $n_r$ is the number of nodes on the most probable robot path and time stamps are defined as

$$T_i = \begin{cases} 0 & \text{if } i = 1, \\ \frac{t_{v_{i-1}} + t_{v_i}}{2} & \text{if } i > 1. \end{cases} \tag{8}$$

Each dimension of the most probable sequence is encoded as a Dynamic Movement Primitive (DMP). DMPs encode trajectories through a non-linear system of differential equations and a linear combination of radial basis functions. We omit further details on DMPs and refer the reader to [6,11]. As the
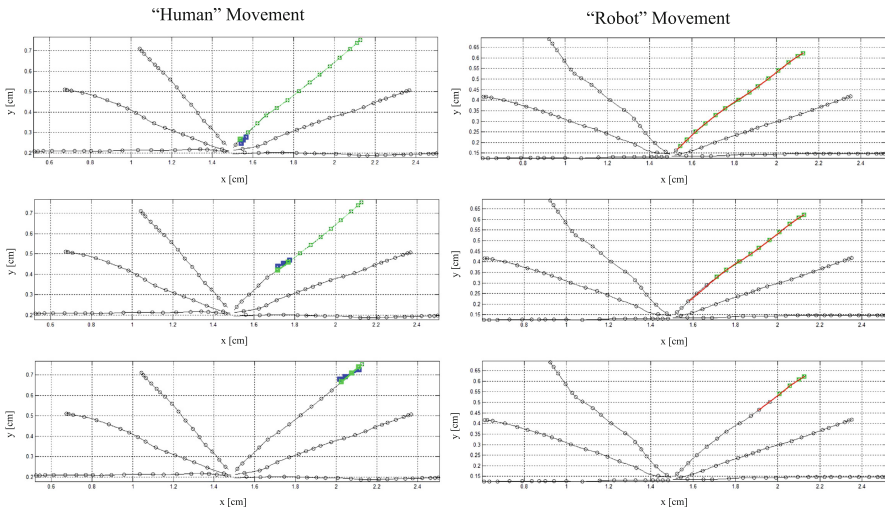


**Fig. 2.** Example recognition and movement synthesis. While left figures show *human* movements, corresponding *robot* movements are shown in right figures. Blue lines denote current observed *human* motion, i.e. the sliding window. Green colour represent most probable paths. Red lines denote synthesised *robot* cooperative movements. If we follow figures from top to bottom, we can observe the progress of recognition and synthesis at example times. Smooth and continuous *robot* trajectories can be observed.

recognition and robot movement synthesis is done on-line, during execution of the robot movement, the change in the most probable robot path can cause abrupt variations in positions. This is also mitigated through DMPs. A smooth and continuous transition can be achieved by setting the DMPs start values to the current robots position.

## 5   Evaluation

Initial evaluation of the proposed approach was done in simulation on a simple dataset. Two different sets of six two-dimensional trajectories were demonstrated by a human; one set representing the human movement, while the other set was a substitute for robot cooperative movement.

Example sets can be seen in Figs. 2 and 3. While the *human* and *robot* trajectories are similar, that is not necessary for the proposed approach. Similar sets were demonstrated in order to faster evaluate recognition. A hierarchical database was built as described. It had 12 levels and 108 nodes in each part at the last level. Motion recognition was done while a human movement was captured with a sliding window of length $n_s = 3$. The frequency of recognition and movement synthesis was at 5 Hz.
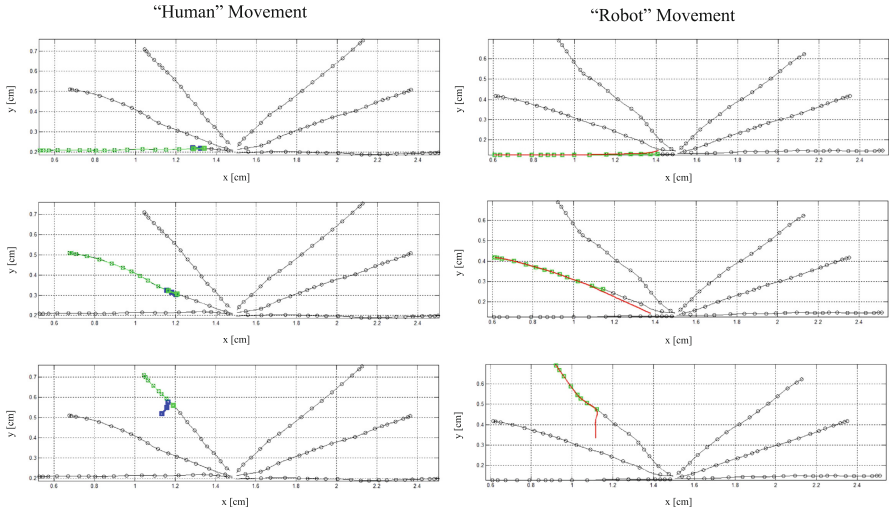


**Fig. 3.** Example recognition and movement synthesis. While left figures show *human* movements, corresponding *robot* movements are shown in right figures. Blue lines denote current observed *human* motion, i.e. the sliding window. Green colour represent most probable paths. Red lines denote synthesised *robot* cooperative movements. If we follow figures from top to bottom, we can observe the progress of recognition and synthesis at example times. Even though the human was switching between several demonstrated trajectories, a smooth and continuous *robot* trajectory was generated throughout the execution.

The first example of recognition and synthesis is presented in Fig. 2. It shows results while a human was trying to follow a single demonstrated trajectory. We can observe smooth and continuous synthesised trajectories. The second example, presented in Fig. 3 shows results of recognition and synthesis while a human is switching between several demonstrated trajectories. Even though there are large and discrete jumps in the most probable *robot* path, a smooth and continuous *robot* trajectory is synthesised.

## 6    Conclusion

The paper presents a hierarchical database search for human motion recognition and cooperative movement synthesis. While a part of the database encodes a set of demonstrated human motions, the secondary part encodes corresponding demonstrated robot movement. Human motion recognition is done by a hierarchical search through the primary part of the database. After the most probable human path is determined, the secondary part is used to produce the most probable cooperative movement. DMPs are used to interpolate the sequence and ensure smooth and continuous transition.

While the initial results show the validity of the approach, additional evaluation is planned. The approach needs to be validated on additional databases and compared to current state of the art. Future work also includes evaluation on a real robot using a larger database and synthesising new, never directly demonstrated movements. While the frequency of recognition is adequate, it will need to maintain at larger and deeper databases.

## References

1. Breazeal, C., Scassellati, B.: Robots that imitate humans. Trends Cogn. Sci. **6**, 481–487 (2002)
2. Deniša, M., Petrič, T., Asfour, T., Ude, A.: Synthesizing compliant reaching movements by searching a database of example trajectories. In: Proceedings of IEEE International Conference on Humanoid Robots, pp. 540–543, Atlanta, GA, USA (2013)
3. Deniša, M., Ude, A.: Synthesis of new dynamic movement primitives through search in a hierarchical database of example movements. Int. J. Adv. Robot Syst. **12**, 1–14 (2015)
4. Dillmann, R.: Teaching and learning of robot tasks via observation of human performance. Robot. Auton. Syst. **47**, 109–116 (2004)
5. Hersch, M., Guenter, F., Calinon, S., Billard, A.: Dynamical system modulation for robot learning via kinesthetic demonstrations. IEEE Trans. Robot. **24**, 1463–1467 (2008)
6. Ijspeert, A.J., Nakanishi, J., Hoffmann, H., Pastor, P., Schaal, S.: Dynamical movement primitives: learning attractor models for motor behaviors. Neural Comput. **25**, 328–373 (2013)
7. Moeslund, T.B., Hilton, A., Krüger, V.: A survey of advances in vision-based human motion capture and analysis. Comput. Vis. Image Und. **104**, 90–126 (2006)

8. Pollard, N.S., Hodgins, J.K., Riley, M.J., Atkeson, C.G.: Adapting human motion for the control of a humanoid robot. In: Proceedings of IEEE International Conference on Robotics and Automation (ICRA), pp. 1390–1397, Washington, DC, USA (2002)
9. Rozo, L., Calinon, S., Caldwell, D., Jiménez Schlegl, P., Torras, C.: Learning collaborative impedance-based robot behaviors. In: Proceedings of AAAI Conference on Artificial Intelligence, pp. 1422–1428, Bellevue, WA, USA (2013)
10. Schaal, S.: Is imitation learning the route to humanoid robots? Trends Cogn. Sci. **3**, 233–242 (1999)
11. Schaal, S., Mohajerian, P., Ijspeert, A.: Dynamics systems vs. optimal control-a unifying view. Prog. Brain Res. **165**, 425–445 (2007)
12. Shotton, J., Sharp, T., Kipman, A., Fitzgibbon, A., Finocchio, M., Blake, A., Cook, M., Moore, R.: Real-time human pose recognition in parts from single depth images. Commun. ACM **56**, 116–124 (2013)
13. Ude, A., Atkeson, C.G., Riley, M.: Programming full-body movements for humanoid robots by observation. Robot. Auton. Syst. **47**, 93–108 (2004)
14. Yamane, K., Revfi, M., Asfour, T.: Synthesizing object receiving motions of humanoid robots with human motion database. In: Proceedings of IEEE International Conference on Robotics and Automation (ICRA), pp. 1629–1636, Karlsruhe, Germany (2013)
15. Yamane, K., Yamaguchi, Y., Nakamura, Y.: Human motion database with a binary tree and node transition graphs. Auton. Robot **30**, 87–98 (2011)

# Embodiment of Human Personality with EI-Robots by Mapping Behaviour Traits from Live-Model

Aleksandar Rodić[1(✉)], Djordje Urukalo[1], Milica Vujović[1],
Sofija Spasojević[1], Marija Tomić[1], Karsten Berns[2], Salah Al-Darraji[2],
and Zuhair Zafar[2]

[1] Robotics Laboratory, Mihajlo Pupin Institute,
University of Belgrade, Belgrade, Serbia
{aleksandar.rodic,djordje.urukalo,milica.vujovic,
sofija.spasojevic,marija.tomic}@pupin.rs
[2] Robotics Research Laboratory, Department of Computer Science,
University of Kaiserslautern, Kaiserslautern, Germany
{berns,saleh,zafar}@cs.uni-kl.de

**Abstract.** The paper deals with the problems of the development of personality and temperament at robots based on the emotional cognitive mapping models from people as biological models. The investigations were based on the use of on-line tests to determine the profile of the human personality and the type of temperament as important factors that determine the character of the behaviour. A young professional actor is involved as a model of human personality - an actor with the ability of transformation of affective states depending on the different life situations. In order to develop cognitive affective personality model, different measurements with the actor are performed. His movements, facial expressions and voice effects as a reaction to the current situation (scenario) have been acquired. Measurement data are processed and an appropriate analysis, generalisation of knowledge and data fusion is performed in order to synthesize cognitive affective model of personality. A method for the implementation (mapping) of the obtained models from the biological systems to a humanoid robot is presented. Robothespian will be used for experimental verification of the obtained results.

**Keywords:** Personality traits · Human temperament · Emotional intelligence · Cognitive affective model · Social robots

## 1 Introduction

The new generation of personal robots, as a form of service robots for the support to humans (human-centric or human-oriented robots), is expected to have a cognitive behaviour similar to their biological model - the man. This means that the new generation of robots should have the individual personality and temperament as factors of the cognitive emotional behaviour, so-called emotional intelligence. Individual traits of people, such as the personality type and temperament, and also the external factors of

influence such as socioeconomic factors and living conditions determine the degree of so-called emotional intelligence.

Emotional intelligence (EI) is the ability to identify (perceive), assess (understand), use and control the emotions of oneself, of others, and in groups [1]. Emotionally intelligent robots with a strong personality traits show a greater ability of socialization and integration into the human community. In this way, service robots are becoming more desirable and better accepted by the users, due to the easier interaction with the social environment and a greater degree of mutual understanding.

Under the notion "personality" a special complex, integrated and relatively stable set of psychological traits of an individual that determines one's character and consistent behaviour is commonly assumed [2]. Personality does not change and is stable over lifetime. It is acquired from the birth date (as a consequence of the genetic code of an individual). Similarly, under human temperament a characteristic way of emotional reactions is assumed. Promptness, intensity, duration and type of reaction will depend on one's temperament [3]. Personality traits are expressed by our specific affective and social behaviour in different situations and social environments. In the theory of psychology, different personality traits are recognized by humans, such as [4]: introverted or extroverted, sensing or intuitive, feeling or thinking, perceiving or judging, etc. By combining these fore mentioned 4 dichotomies, 16 different personality types are known as presented in [5]. Also, 4 different human temperaments are known in practice [3]: sanguine, choleric, melancholic and phlegmatic. The goal of the research in this paper is to develop a cognitive affective model of human psychological behaviour that includes different personality types and human temperaments, that will be implemented with the humanoid robot Robothespian [6] in order to verify the methodology allowing robots to feel and behave socially as humans.

The paper is organized in several sections. In the opening section research objectives are set and the basic terms that will be used in the paper are defined. The second section provides an overview of the results of previous research in the area. The third section presents the emotional cognitive model of human behaviour which is the basis of the research presented in this paper. The fourth section deals with the measurements obtained from the professional actor's movements and facial expressions, in order to improve the accuracy of the mathematical model of the human emotional intelligence. The implementation of EI-controller for the humanoid robot Robothespian along with the conclusions and future directions of research are described in Sect. 5.

## 2 State of the Art

The idea about building personality with robots exists from earlier times, but recently it seems to become feasible. In 2015, Google owns a new patent outlining a concept of the robot that changes personalities based on circumstance and a wide variety of user information [7]. The system stores useful data in the cloud where it can be accessed by other robots. In one example of the patent, the robot goes so far as to assemble an entire personality on request. The robot in this patent can also modify its personality by inferring the user's mood through methods like correlating the current weather to previous moods. What is probably the most interesting in Google's patent, the robot

may even use one's diction and sentence structures from email, texts, or phone calls to estimate emotional state and respond accordingly.

Robots that change their personalities based on collected information would certainly be neat. But as far as it is known, the patent only covers the general idea, as opposed to a specific implementation that Google has developed. The patent doesn't protect a brilliant technical solution or large investment, but just an idea that will be realized in the future. Instead, it covers the mere concept of combining existing platforms and data to imbue robots with changeable personalities. This research paper should complement in a certain way the patent shortcomings having no ambition to reduce the importance of the Google shiny ideas.

There are "emotional" robots on the market now, but their capabilities are superficial [8]. These robots don't feel, but they can detect human emotions and respond accordingly. Aldebaran Robotics' Nao, a 2-foot-tall robot equipped with touch sensors, four microphones, and two cameras, can "learn" by downloading new behaviours from an Aldebaran's app store, as well as by recognizing faces, make eye contact, and respond to the users. The robot has been implemented in the classroom, particularly for children who are nonverbal, overstimulated, and/or autistic. Autistic children have difficulty discerning others' emotional states, and Nao helps them practice identifying expressions without feeling shy or uncomfortable. In fact, research indicates that computers are even better than humans at reading expressions, which means it will be increasingly difficult for humans to lie to robots.

Last year, Aldebaran released Pepper, the "first humanoid robot designed to live with humans." Pepper can identify a user's emotional state and then adapt by trying, for instance, to cheer up a user it identifies as sad. Pepper can also mirror a user's emotional state, which is something all humans do beginning from infancy. Mirroring works in both directions with robots - they reflect one's emotions, even though one knows they're robots and instinctively mirror theirs. Studies also indicate that when robots mirror our emotions, we're more likely to feel a bond with them; we're also more likely to assist them with tasks. Robots don't actually feel emotions yet, but they can appear as though they do.

Mammals' brains can produce basic emotions, such as desire, fear, and affection. But these emotions aren't volitional and don't require thought. Complex emotions are different [9]. Take jealousy, for example. To feel jealous, one has to desire something, recognize that someone else has that thing, and then feel negatively toward that person because of it. In this paper, we try not only to make a robot to perceive the emotions of others, but also to produce emotions that represent the reaction to the context – physical and social environment.

## 3   Modelling of Cognitive Affective Behaviour

Human psychological (affective and social) behaviour depends on several dominant factors. Some of them are acquired by birth (genetic factor), some are generated during the lifetime by the influence of the exterior factors (e.g. family and school education, companions, socioeconomic conditions, religion, etc.) and some of them are generated by the temporary interior factors (physical and psychological). Human-like affective

reactions are based on three dominant excitation signals as information carriers [10]: (i) the "trigger" of behaviour (that arouses different psychological reactions); (ii) the "profiler" (that shapes event-driven emotional state (ES) to fit the personality profile of the individual); (iii) the behaviour "booster" or behaviour "inhibitor" (that increases or decreases the expressiveness of the individual affective manifestations). The high-level block diagram of the cognitive emotional model is shown in Fig. 1. Details regarding the modelling of human affective behaviour are given in [9, 10].
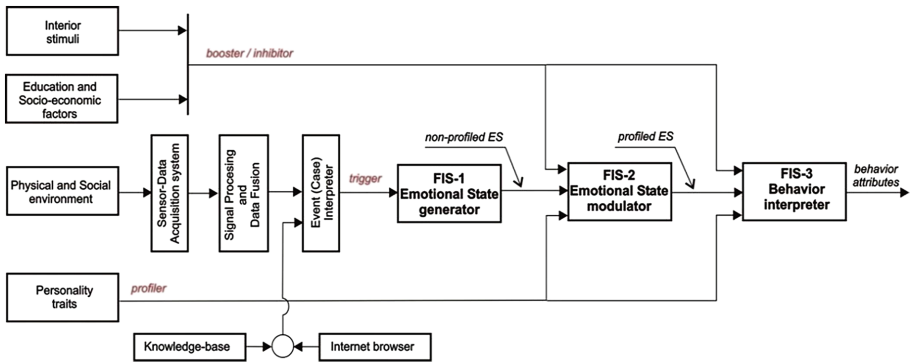


**Fig. 1.** Block-scheme of a three-stage human affective behaviour model

Fuzzy blocks in the knowledge-based model shown in Fig. 1 are designed to have appropriate membership function parameters (type of function, the focus of the figure, inflection points, etc.), adjusted based on the data taken from a group of subjects. Specifically, a group of 237 subjects of different age, gender and education [10] was asked to anonymously fill out online questionnaires on the Internet for determining the personality type [11] and temperament [12]. Based on the theoretical model of the human affective behaviour shown in Fig. 1 and on the basis of generalized knowledge taken from a database of subjects (whose personality type and temperament are numerically quantified [10]), an empirical model suitable for simulation on the computer was synthesized. In order to improve the accuracy of the model and enable the synthesis of EI controller, suitable for implementation on a humanoid robot Robothespian, the methodology shown in Fig. 2 is used. Membership functions FIS-1, FIS-2 and FIS-3 are additionally set using the results of measurements from a man as a biological model. For this purpose, a professional young actor performed different affective behaviours (hate, fury happiness, surprise, sadness, etc.) as a result of different situations (scenarios). The actor was asked to act out the same scenario in two different ways - very affective (temperamentally) and phlegmatically, respecting the main features of the famous personality types described in the introduction section.

As described above, by combining the knowledge of the characteristics of different personality types and temperaments (obtained from questionnaires and stored in the database) and the direct measurements of affective reactions of a living model – the actor, the final adjustment of cognitive affective model of human behaviour is performed. This model represents the algorithmic basis for the design of EI controller for a robot as shown in Fig. 2.
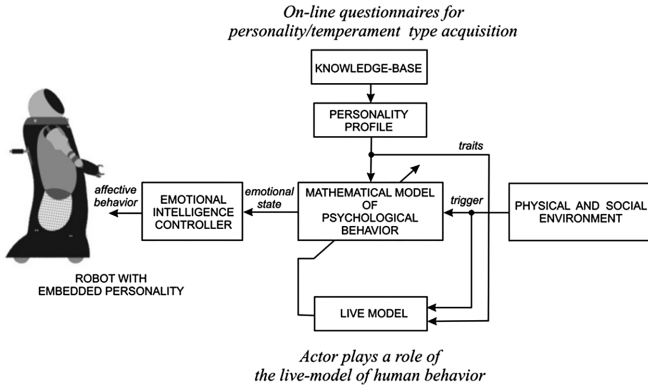
**Fig. 2.** Block-scheme of building robot emotional intelligence controller based on the personality traits acquired from biological model – human examinees

## 4 Measurement of Affective Actions

In the work with the actor the following measurements were acquired: (i) detection of the head and body gestures as a result of different affective states caused by the corresponding situations or events, performed by one Kinect sensor (RGBD camera); (ii) upper-body movements detection using Xsens motion capture system based on the use of inertial measurement units (3-axis accelerometer + 3-axis gyro sensor); (iii) facial expressions recorded with a camera (video and audio data). In this paper, the audio data are not processed and it will be the topic of future research.

The gestures acquired from the human actor as live-model of effective behaviour contain information about specific personality traits characteristic for an individual and for a particular situation. The actor has been asked to imitate (reproduce) two types of behaviour – very expressive and temperamental, and gentle and smooth in order to verify the methodology applied in the paper. The actor used the same trigger event/situation to demonstrate his different personality traits and temperaments.

### 4.1 Measurement of Body Gestures by Kinect Sensor

We want to investigate upper-body movement expressions during the performance of certain emotional scenarios. Consequently, we have acquired large-range movements of a subject in addition to the facial recordings. We assume that torso and hand movements are more involved when showing emotions such as happiness and surprise, while in the case of sadness the body stays more or less static. This will be confirmed later in our experiments through the analysis of the subject motion during particular scenario performing.

There are many available techniques used nowadays for motion tracking. Marker-based motion capture systems [13] are widely used for movement acquisition. Such systems are very expensive, but can deliver accurate measurements. Other possibilities include the attachment of the different sensors to the subject's body, like the

inertial sensor system we used [14]. More recently, low-cost marker-free based systems such as the Kinect and Xtion [15] become quite popular as a suitable alternative to complex and expensive motion capture systems. In addition to the inertial sensor system, we have used Kinect device for large-range movement acquisition. Kinect provides a satisfactory accuracy for indoor mapping applications [16], assessment of the postural control [17] and gesture and pose recognition.

Kinect is the new generation device developed by Microsoft, which consists of a standard RGB camera and a 3D depth sensor (infrared sensor + infrared projector). It operates in a range of approximately 0.6 m to 4 m and can achieve up to 30 frames per second. Kinect has a built-in algorithm for human skeleton detection and tracking. Namely, the 3D coordinates of the characteristic skeleton joints are collected for every frame during the motion performance. The acquired Kinect data from our experiments consist of RGB and depth video sequences and 3D positions of the fifteen skeleton joints (Fig. 3).



a)                                    b)                                    c)
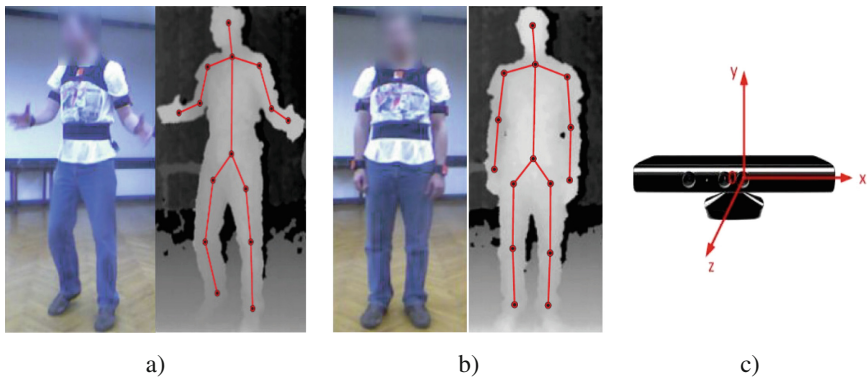
**Fig. 3.** (a–b) RGB streams (left) and depth streams with detected skeleton and collected joints (right) and (c) Kinect device with axis orientations

We want to explore the connection between the particular emotional states (angry, excited and sad) for choleric/phlegmatic or emotional/rational personality type and activity of the upper-body movements. Consequently, we have analysed the behaviour of the head, torso, elbow and hand joints during the performance of the angry, excited and sad emotional scenario. The evolution of the selected joints along X and Y direction (Fig. 3-c) for these scenarios is shown in Fig. 4. Joint trajectories are presented from the 5th second onwards since we omit the calibration phase at the beginning of the sequence in order to synchronize the signals obtained from Kinect and inertial sensors. The Kinect device is calibrated by performing a certain body posture. The joint trajectories in Fig. 4 clearly illustrate the larger activity of the upper-body movements during the angry and excited scenario in comparison to the sad scenario. Raw signals of joint trajectories are filtered with Butterworth low-pass filters with a cut off frequency of 3 Hz due to the measurement noise.
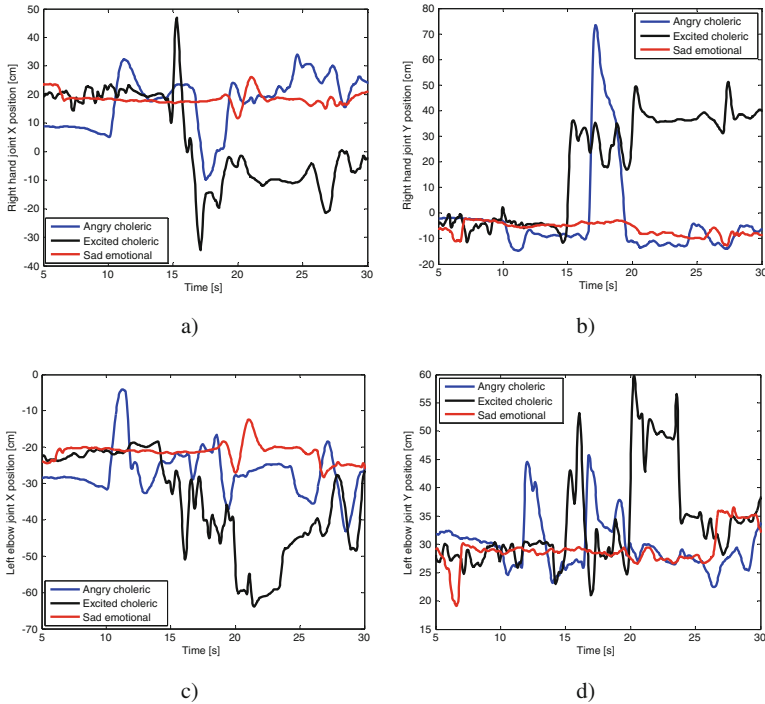
**Fig. 4.** Evolution of the right-hand joint (a–b) and left elbow (c–d) along X (a–c) and Y (b–d) direction

## 4.2 Measurement of Body Gestures by Xsens Capture-Motion System

Motion tracking of one human upper body is realized with seven XSENS IMU sensors [14]. The sensors are mounted on wrists, biceps, shoulder blades and lower-back. Each IMU sensor has five physical sensors: accelerometer, magnetometer, gyroscope, pressure sensor and thermometer. Besides raw sensor data, the sensor fusion scheme calculates free accelerations and velocity increments in three axes (x, y, z), as well as quaternions increments and quaternions. Quaternions have been used for the determination of angle values of the joints and body posture, because of their robustness relative to Euler angles (Gimbal lock).

Euler angles, presented in Fig. 5 are calculated from the rough measurement data taken from the IMU sensors and processed additionally to be implemented in the life sized humanoid robot RoboThespian designed for human interaction in a public environment.

Figure 5 shows the angular joint positions and body posture (torso) for the two human behaviours: thrilled choleric (red) and phlegmatic choleric (blue). Joint angular velocities and accelerations for the same human behaviours are calculated by derivations by taking into account the refresh rate of the capturing system.
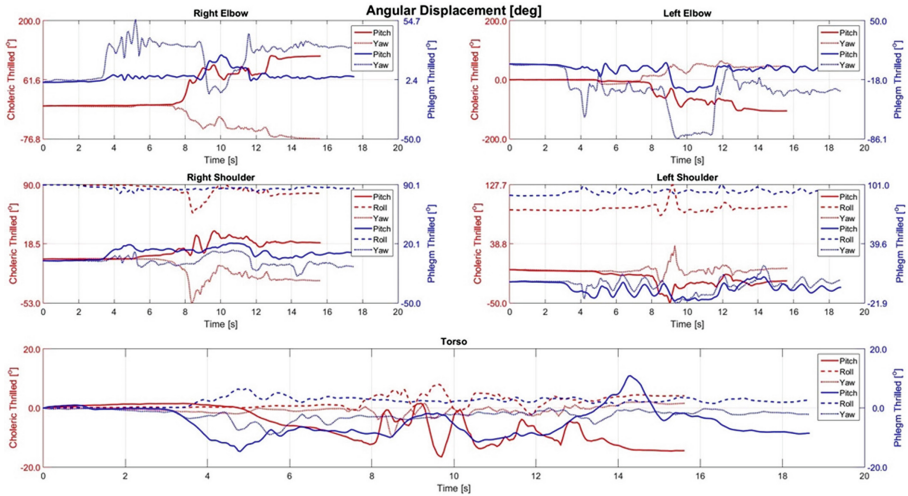
**Fig. 5.** The angular positions of joints for choleric and phlegm thrilled human behaviours

### 4.3   Face Mime Data Acquisition

The research presented in this paper examines the expressed emotions and the ways of detecting them. The aim is to create a basis for further work where the robot will be given the ability to recognize emotions and based on that, it will be able to make certain decisions. This direction of the research in robotics has applications in situations where robots interact with people and where it is essential to create a mutual reaction between robot and human.

During the described research, the actor's task was to display different emotional states through different temperaments, based on the given scenario (Fig. 6). The emotions that are portrayed were: happiness, sadness, anger, surprise, fear, disgust, etc. Personalities have assigned temperaments (phlegmatic and choleric or emotional and rational personality) in order to collect as much data for analysis as possible. The results are classified and prepared for further research using emotion recognition software.

The basis for emotion recognition is software based on the Facial Action Coding System (FACS). This is a system that classifies human facial movements and puts them in the category of emotional states. The system is based on the teachings of Professor



**Fig. 6.** The actor performing various emotional states

Carl-Herman Hjortsjö, and it is defined in more detail and developed by Professor Paul Ekman [18] the 80's. FACS is formed and developed after studies of the anatomy of the human face where the face changes were tracked during expression of different emotions. Facial muscles are grouped into so-called action units (Fig. 7). Based on the geometry of the face, for every action unit the category is defined that includes all the changes of muscles and their combinations that can occur with the human face. After categorizing each of the action units and observing all of them that make one person's face, the conclusions about the expressed emotion can be derived. The process of detection and analysis is automated using a computer which processes photos and based on that generates the results of the emotional state of the photographed person. This method is widely used in psychology and sociology, as well as in other disciplines dealing with technology that interacts with human.

| Upper Face Action Units | | | | | |
|---|---|---|---|---|---|
| *AU41 | *AU42 | *AU43 | AU44 | AU45 | AU46 |
| Lip Droop | Slit | Eyes Closed | Squint | Blink | Wink |
| Lower Face Action Units | | | | | |
| AU9 | AU10 | AU11 | AU12 | AU13 | AU14 |
| Nose Wrinkler | Upper Lip Raiser | Nasolabial Deepener | Lip Corner Puller | Cheek Puffer | Dimpler |

Fig. 7. The action units

To analyse the face of the actor who participated in the above experiment, the software developed by Microsoft was used. As part of the Cognitive Services, Microsoft has developed software for facial recognition, which has created an application that deals with recognizing emotions. The demo version of Emotion API [19] was used in this paper for analysis of the results. From the videos recorded during the actor's performance, when he imitated certain emotional states through different types of personalities, images were generated. The principle of the software is based on an analysis of uploaded photos with face recognition and FACS system where it generates the percentages of each of the emotions displayed on the face (Fig. 8). This method of analysis is acceptable for this phase of work and "happiness" and "surprise" are selected emotions to show the principle of operation. The displayed images show that the software recognizes the emotional states that the actor performed, based on the detected face movement; other emotions that are present are also shown. The idea is that, in the future this principle can be used in the interaction between human and robot. It will be based on the emotional state of the human which will determine the behaviour or actions of the robot.
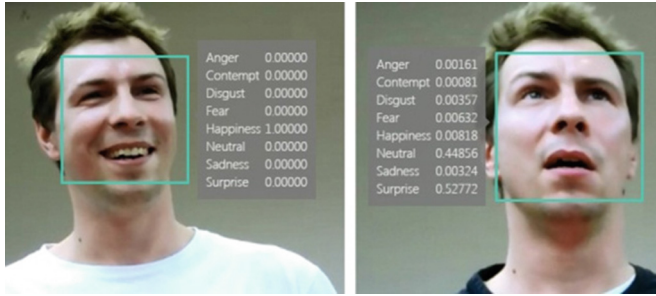
**Fig. 8.** Face emotion analysis
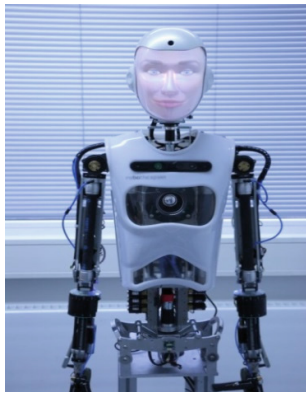


**Fig. 9.** Humanoid RoboThespian – testbed system for testing robot cognitive EI capabilities (TU Kaiserslautern)

## 5   Conclusions and Future Work

The model shown in Figs. 1 and 2, improved by taking into account the results of measurements on a live-model will be implemented on a humanoid RoboThespian (Fig. 9) for testing and verification of algorithms mapping the human personality and temperament on the machine. The developed model will be implemented as a part of the robot controller of emotional intelligence in situations of interaction with people.

# References

1. Emotional Intelligence (EI). https://en.wikipedia.org/wiki/Emotional_intelligence. Accessed Mar 2016
2. Personality psychology. http://en.wikipedia.org/wiki/Personality_psychology. Accessed Mar 2016
3. Temperament types. http://en.wikipedia.org/wiki/Four-temperaments. Accessed Mar 2016
4. Myers-Briggs, I., Myers, P.: Gifts Differing: Understanding Personality Type. Davies-Black Publishing, Mountain View (1995)
5. MBTI. http://en.wikipedia.org/wiki/Myers-Briggs-Type-Indicator. Accessed Mar 2016
6. RoboThespian. https://www.engineeredarts.co.uk/robothespian/. Accessed Mar 2016
7. Darling, K.: Why Google's robot personality patent is not good for robotics. IEEE Spectr. Autom. Robot., Robotics Software, online article, 8 April 2015
8. Renstrom, J.: Artificial intelligence, real emotion? Ex Machina asks whether machines can have feelings-or at least fake it, Future Tense project, Slate, Arizona State University and New America, on-line article, 9 April 2015
9. Rodić, A., Jovanović, M.: How to make robots feel and social as humans. In: The 6th IARIA International Conference on Advanced Cognitive Technologies and Applications (COGNITIVE 2014), Venice, Italy, 25–29 May, pp. 133–139 (2014). ISSN: 2308-4197, ISBN: 978-1-61208-340-7
10. Rodić, A., Jovanović, M., Stevanović, I., Karan, B., Potkonjak, V.: Building technology platform aimed to development service robots with embedded personality and enhanced communication with social environment. Digit. Commun. Netw. **1**, 112–124 (2015). doi:10.1016/j.dcan.2015.03.002. Elsevier, ISSN: 2352-8648
11. On-line personality test. http://www.16personalities.com/free-personality-test. Assessed Mar 2016
12. On-line temperament test. http://neoxenos.org/wp-content/blogs.dir/1/files/temperaments/temperament_test.htm. Accessed Marc 2016
13. Zhou, H., Hu, H.: Human motion tracking for rehabilitation – a survey. Biomed. Signal Process. Control **3**(1), 1–18 (2008)
14. Inertial sensors. https://www.xsens.com/. Accessed Mar 2016
15. Gonzalez-Jorge, H., Riveiro, B., Vazquez-Fernandez, E., et al.: Metrological evaluation of Microsoft Kinect and Asus Xtion sensors. Measurement **46**(6), 1800–1806 (2013)
16. Khoshelham, K., Elberink, S.: Accuracy and resolution of Kinect depth data for indoor mapping applications. Sensors **12**(2), 1437–1454 (2012)
17. Clark, R., Pu, Y., Fortina, K., et al.: Validity of the Microsoft Kinect for assessment of postural control. Gait Posture **36**(3), 372–377 (2012)
18. Matsumoto, D., Ekman, P.: Facial expression analysis. Scholarpedia **3**(5), 4237 (2008). Accessed Mar 2016
19. Microsoft Cognitive Services. Microsoft.com. Accessed Mar 2016

# Signal Processing Robotics Using Signals Generated by a Human Head: From Pioneering Works to EEG-Based Emulation of Digital Circuits

Stevo Bozinovski[✉]

South Carolina State University, Orangeburg, USA
sbozinovski@scsu.edu

**Abstract.** This plenary keynote paper describes some pioneering steps in robot evolution, regarding human-robot communication using signals generated by a human head: speech, EEG, and EOG signals. The work was done in 1980's Yugoslavia. Some of the experiments were significantly ahead of time: the 1988 robot control with human EEG was the only such experiment carried out in the $20^{th}$ century; in the $21^{st}$ century this research area is increasingly popular. The paper also presents a current research in a new direction in signal processing robotics, the EEG emulation of digital circuits for robot control.

**Keywords:** Robot evolution · Signal processing · Speech processing for robot control · EEG controlled robots – EOG controlled robots · EEG emulated digital circuits for robot control

## 1 Introduction

Human-robot interaction explores various ways of communication between humans and robots. This work is devoted to Signal Processing Robotics, which assumes a human-robot communication where an active signal generation from the human side is needed and active signal recognition from the robot side as well. It focuses on signals generated by a human head: speech, EEG, and EOG signals (Fig. 1).

Figure 1 shows a human wearing some kind of hat and/or glasses and/or a microphone, who generates signals which are processed by a co-robot.

This paper points out to some pioneering results in 1980's as well as some current results regarding EEG emulation of digital control circuits for robot control.

The paper has seven chapters. After this introduction, the research context in which this work was carried out is described, the collaboration on robotics in Yugoslavia in 1980's. The next three chapters describe the work on Signal Processing Robotics related to speech (1986), EEG (1988), and EOG (1989). The sixth chapter describes a current direction in EEG based control, the EEG emulation of digital circuits for robot control. The last is a discussion chapter.
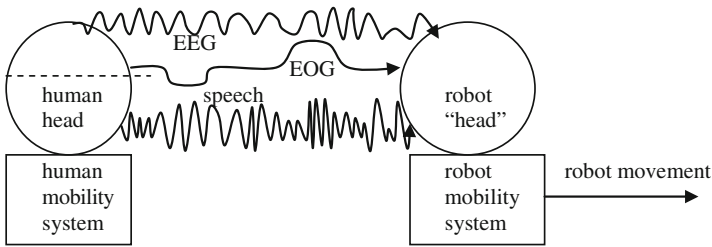
**Fig. 1.** Signal processing robotics: Actively generated signals from a human head

## 2   Robotics Collaboration in 1980's Yugoslavia

The 1980's Yugoslavia had several centres where robotics was pursued, with leading centre being Institute Mihajlo Pupin in Belgrade, under the leadership of Dr. Miomir Vukobratovic. The Belgrade School of Robotics [1] has established itself in the robotics research with early works on the robot walking problem [2–7], especially with the 1969 pioneering result on zero moment point [8]. Yugoslavia was a federation of 6 states: Bosnia and Herzegovina, Croatia, Macedonia, Montenegro, Serbia, and Slovenia. In 1980's the federal government encouraged collaboration between states in the area of advanced technologies and many meetings were held for preparing applications for federal grants. This enabled researchers in robotics to have coordination and understanding of what each research centre was doing. In addition to such collaboration, professor Vukobratovic was organizing symposia and visits to research centres in Moscow and Leningrad. The author of this paper had a privilege to be part of the Yugoslav delegation visiting these research centres. The friendship among Yugoslav researchers developed in these years lasts till today.

Working among other centres, the centre in Skopje had a direction toward using vehicle robots. The first vehicle robot was built 1982 from a toy car, and in 1983 it was controlled by a multitasking software system [9]. In 1984 the scientific foundation of the state of Macedonia approved a project named Adaptive Industrial Robots (AIR), and in 1988 a continuation project named Adaptive Intelligent Industrial Robots (AIIR). In addition to industry applications, the research directions pursued were signal processing robotics and flexible manufacturing systems (FMS) [10]. The results of the project were reported on Yugoslav symposia related to ETAN society, to IEEE societies, and at bilateral symposia in Soviet Union. In the bilateral symposia the Yugoslav robotic delegation presented its state of the art research. In such a context we presented in 1986 our work on genetics and flexible manufacturing systems [11, 12] and in 1989 our work on EEG and EOG head bio signals for robot control, published later in a Russian journal [13].

## 3   1986: Speech Signal Processing for Robot Control

Although automatic speech synthesis and understanding has been of interest for science and technology since 1930's [14], explicit addressing of speech recognition of isolated words was done in 1950's [15]. In robotics, the first control of a robot using speech commands was demonstrated in 1973 [16] on the humanoid robot Wabot-1 (Waseda robot 1). The next robot named Wabot-2 was built in 1984 as a keyboard music playing robot [17]. However the description given in the literature of both Wabot-1 and Wabot-2 did not cover the speech signal processing, because it was not the most important focus of the Wabot project. The first description of speech processing for robot control was given in a report from the AIR project in 1986. The vehicle robot used was named Adriel-2 (Adaptive Robot of Institute of Electronics). The description of the speech recognition system given in this paper is based on the 1989 report [18] which in turn is based on the project AIR Technical Report done in 1986 [19]. We were interested in Signal Processing Robotics, so for us the actual signal processing was an important part to be described.

### 3.1   Background Information: Human Speech Signals

Human speech has a distinct frequency spectrum, resembling an attenuating sine wave. The local maxima on the spectrum are named formants. The first formant is around 500 Hz. In the frequency range of a human speech, 0–4 kHz, there are up to 5 formants. There are variations of placement of formants in a frequency spectrum due to individual differences of speakers. Analysis of a human speech is usually performed on a time-frequency chart named spectrogram. The spectrogram actually converts a 1D time signal into a 2D time-frequency image, where gray image intensity corresponds to the power of a time-frequency coordinate.

### 3.2   System Setup and Hardware Used

The system diagram of our 1986 speech-to-robot interface is shown in Fig. 2. The speech-to-computer interface consisted of a microphone, the signal of which was further amplified by a custom made amplifier. The computer-to-robot interface consisted of power amplifiers needed to drive robot motors, and was custom built in our lab.

The robot Adriel-2-1 used in the experimental work was built in 1984 for demonstration of the gradient following experiments similar to the experiments done by Grey Walter [20], but in a Flexible Manufacturing Systems (FMS) scenario. It was able to avoid obstacles while navigating toward a light source (light bulb). As external sensors it contained two light sensors and two tactile sensors.

The available computer was IBM Series/1 process computer with a module for process control named S4982 Sensor Unit, with 16 analog inputs and 2 analog outputs. The speed of conversion (sampling rate) of its A/D converter was 1500 conversions/s (1500 Hz, sampling time 1/1500 Hz = 0.667 ms). It was not able to process the full spectral range of a human speech (4 kHz), for which the sampling theorem requires
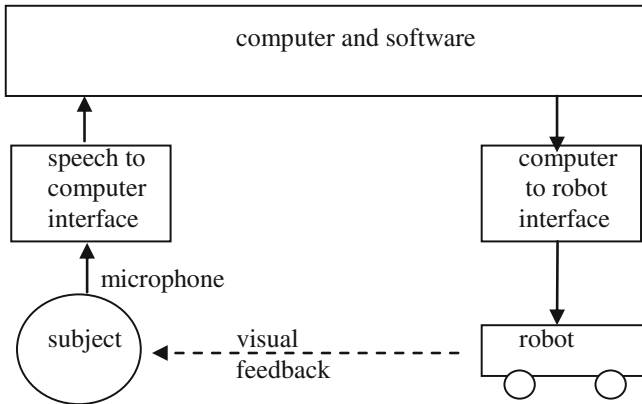
**Fig. 2.** A system diagram of the 1986 speech-to-robot interface

8 kHz sampling frequency (0.125 ms sampling time). This hardware limitation posed a challenge: develop a speech recognition system based only on the first formant, which for a given speaker can be found in the frequency range between 200 and 800 Hz.

### 3.3    Speech Signal Segmentation

We used a sound-string representation of a spoken word by which a word in time domain is divided into time elements named word segments. In our case each word contains 40 segments. Each word segment has fixed time duration of 10.67 s, and contains 16 time samples taken 2/3 of a second apart. There are 640 samples per word with the total sampling duration of 426.88 ms, which means that, because of equipment limitations, we take a fixed length sample of 426.88 ms per word. The beginning of a word was recognized automatically, but we did not used recognition of the end of the word. If the word is longer that the 426.88 ms sample it is truncated; if it is shorter it is filled with noise of 800 Hz maximal frequency limited by the input low pass filter.

### 3.4    Word Spectrogram, Feature Vector, and Robot Command Recognition

On the basis of segment duration, the resolution achieved along the frequency axis is $\Delta f = 1/\tau seg = 93.72$ Hz. Because the number of samples per segment was Nseg = 16, the maximal frequency in the obtained spectrum is fmax = (Nseg/2) $\Delta f = 749.76$ Hz. So we obtain 8 frequency bands each of width 93.72 Hz.

The first formant in the $i$-th band is denoted $F1_i$. Since the spectrum frequency components are multiples of $\Delta f$, for the value of the first formant we take the order number of the maximal Fourier coefficient $C_{ik}$, i.e. $F1_i = k \mid k = \max \{C_{ik}\}(0 \leq k \leq 7)$. Figure 3 shows the signal processing in frequency domain.

$$\begin{pmatrix} C_{0,0} & C_{0,1} & C_{0,2} & \cdots & C_{0,39} \\ C_{1,0} & C_{1,1} & C_{1,2} & & C_{1,39} \\ & & & & \\ C_{7,0} & C_{7,1} & C_{7,2} & & C_{7,39} \end{pmatrix}$$

Max

$k_0 \qquad k_1 \qquad k_2 \qquad\qquad k_7$

$C_{k,0} = \max_{i=0,7}\{C_{i,0}\}$ $\qquad\qquad\qquad C_{k,7} = \max_{i=0,7}\{C_{i,7}\}$

$F1_0 \qquad F1_1 \qquad F1_2 \qquad\qquad F1_{39}$
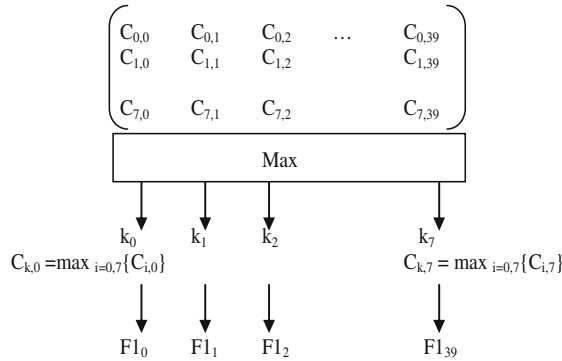
**Fig. 3.** Signal processing in frequency domain and obtaining feature vector of a word

Once the first formant is found in the spectrum of all the 40 segments, the formant function is determined, F1(iτseg), i = 0, 1, …, 39, which is defined in intervals τseg = 10.67 ms and whose amplitudes are integer numbers from 0 to 7. That way we obtain word patterns of the robot as a 40 dimensional feature vector.

We used 5 word commands in Macedonian language which correspond to commands "start to go", "left" "right", "back" and "stop".

The learning and pattern recognition algorithm is the following:

In the learning process create a vocabulary of 10 versions of the i-th command (i = 1,2,…,5). The command i is represented by the $10 \times 40$ matrix $Y_i = Y_{i,k,j}$ with k = (1,..,10) word versions and j = (1,..,40) signal features.

In the recognition process, when unknown spoken command **x** appears, then for i, compute all distances between features of **x** and of stored versions in $Y_i$:

$$d_{ik} = d(\vec{x}, \bar{y}_{ik}) = \sum_{j=1}^{40} (x_j - y_{ikj})^2$$

Then order distances in increasing order and change indexes to obtain

$$d_{i1} \leq d_{i2} \leq \ldots \leq d_{i10}$$

Then compute distance between command **x** and words $Y_i$ as

$$D_i = d_{i1}^2 + \delta \sum_{k=2}^{5} d_{ik}^2$$

where δ is discount factor (in our experiments δ = 0.01), which discounts the sum of the next 4 distances after $d_{i1}$, the minimal one. Let D is the set D = $\{D_1, D_2, D_3, D_4, D_5\}$. Let indmin(.) is index of the minimal value. So, if i = indmin(D) then **x** is recognized as $Y_i$.

To determine decision threshold, compute next greater minimum distance between **x** and D. Let R1 = $D_i$ = min(D) and let R2 = min{D-$D_i$}. Then R2 > R1. With (empirically determined) decision threshold $\varepsilon$ = 1.4 the decision rule of the algorithm is:

If (R2/R1 > $\varepsilon$ AND i = indmin(D)) then **x** is the command i, otherwise undecided. Unclassified command means the robot is not moving and will move on the next recognized command.

### 3.5    Experiments with Speech Control of a Robot

Among various types of experiments performed [18] containing 3, 4, and 5 spoken words, here we describe experiments with robot guidance avoiding obstacles in which 4 commands in Macedonian language were used, equivalent to "start to go", "left", "right", and "goback". In some experiments the "stop" command is not used because the reaction time is 3 s and recognition of the command "stop" might not finish on time. So the control of the motor forward-backward M1 is pulsed, with pulses of duration 2 s. The robot moves 2 s and then waits for another command, so a separate spoken command "stop" is not needed. Actually, in case of unrecognized command the robot executes the command "stop". This requires repeating the same command several times, which is only practical in environments rich with obstacles. For experimental work we used the room of the Series/1 computer lab, at the Mechanical Engineering Department. The robot was moving on the ground and several boxes were placed such that the subject controlling the robot using speech commands should give various types of commands in order to pass the planned trajectory. Note that the commands "left" and "right" move the wheels left and right and at the time the robot is not moving forward/backward. So the command on motor left/right is separate from the motor forward backward. The performance was 85% correct recognition, 5% incorrect recognition, and 10% unclassified. Usually incorrect recognition was from the command corresponding to "goback".

## 4    1988: Step in Robot Evolution: Robots Gain Capability of Recognizing Human EEG Messages

In 1988 robotics evolution acquired a new human-robot communication capability, recognition of some features of the electromagnetic energy emanated by a human brain. In that year, the movement of a vehicle robot was controlled by human EEG signals [13, 21–23]. In addition of adding a step in robot evolution, this was a challenge of possibility of solving the problem of psychokinesis, i.e., movement of a physical object with a human's brain power. The engineering solution we implemented was using EEG, which is a manifestation of processes inside a human brain. Let us note that moving robots (or other physical objects) by electromagnetic energy emanated from a human brain is not necessary about reading human thoughts. It is rather self-tuning or tuning a human brain to some mental states which can be translated into EEG features and then recognized by a robot.

## 4.1    Background Information: Human EEG Signals

EEG (electroencephalogram) signals are electrical signals which can be recorded by electrodes mounted on a human scalp. There are also invasive recordings, with electrodes inside the brain, which with humans are used only in medical needs. In the frequency domain, the EEG signals have range between 0 and 70 Hz, frequencies above that are assumed noise. Some frequency bands have special meanings and applications, for example the 8–13 Hz band named also alpha band (or in time domain, alpha rhythm), or in cases when it is measured from sensorimotor area it is also named mu rhythm. EEG reacts to external events such as sound and visual signals with components named EEG event related potentials. The robot evolution toward "understanding" EEG signals started [21] with recognizing changes of the intensity of EEG alpha rhythm, i.e. the contingent alpha variation (C$\alpha$V).

## 4.2    Methods: System Setup and Hardware Used

The EEG based setup used in 1988 was essentially the same as the speech based setup of robot control in 1986, described above. EEG sensors were used instead of microphones, and the EEG-to-computer interface was a biopotential amplifier.

A rack-based biopotential amplifier was designed and ordered for the Adaptive Industrial Robots project. It was custom made by the company Laboratorij Medicinske Elektronike (LME) from Zagreb, Yugoslavia in 1986. After our order of a rack-based system, the company started marketing it as a product named Poly Subcomplet. The maximal amplification was 10 $\mu$V/V and the maximal time constant was 10 s. For interfacing the biopotential amplifier with the computer we used a 14-bit A/D converter ADDA14 purchased in Munich, Germany.

The computer used was a PC/XT. The signal processing software extracted features from the EEG and then performed pattern recognition. The pattern recognition required a learning process, in which the computer learned some specific template parameters of a subject, using which the EEG-based commands were recognized.

The robot used was purchased at the Akihabara market in Tokyo, Japan, in 1984. It was a state-of-the-art vehicle robot named Elehobby Line Tracer II of the series Movit robots [24]. It carried own batteries, and had local intelligence to follow a black line drawn on a floor. In our lab the robot had an FMS outfit and played a role of a FMS shuttle robot moving along a closed line drawn on the Robot Polygon.

Robot Polygon was built as a two-floor facility inside our laboratory. Robots (both vehicles and arms) were placed on the first floor which looked like a white ping pong table, while on the second floor, above a human height, a support equipment was placed consisting of computer-to-robot interfaces. Each robot had both power and control lines coming from above, so they do not interfered with the robots movement. The Robot Polygon was the principal part of the Laboratory for Intelligent Machines, Bioinformation Systems, and Systems Software, (LIMBISS) of the Electrical Engineering Department, University Cyril and Methodius.

### 4.3    Pattern Classification: The Calibration (Learning) Method

A subject can generate increased amplitude of alpha rhythm for example, by closing eyes and relaxing. The relaxation state of the brain is manifested in increase of the energy (amplitude) in the alpha band. A process of calibration of a classifier is needed for a robot to recognize the change of alpha rhythm amplitude. The calibration of the classifier follows the following procedure:

In a 10 s calibration (machine learning) procedure, the subject opens and closes her/his eyes. Since our sampling frequency was 100 Hz, we acquired 1000 samples where from the template parameters will be learned. The biggest problem was what parameters to be learned, since they should be fast computable. It needed a procedure that reads EEG sample, computes the parameters, compares them to learned baseline parameters, and sends command to the robot, all that in less than 10 ms on a PC/XT in the year 1988.

The learned parameters were chosen to be both changes of EEG amplitude and changes of time intervals between EEG amplitudes. They are fast computable since it needs comparison only with the previous sample to obtain the changes. So the learning process scans the 1000 EEG samples and looks for local extremes, hills and valleys of the signal, the points where gradient changes the sign. For each hill, its amplitude is determined relative to the previous valley from where the hill started to rise. Also for each hill the width of the hill is determined as time distance between the bottom of the hill and the top of the hill. More details are given in [25].

### 4.4    Pattern Classification: Probability Distributions and Decision Threshold

Both obtained amplitude differences and time differences are counted and placed in corresponding probability density distributions. So each subject was represented by a pair of distributions, EEG amplitude difference $p(A)$ and EEG time difference $p(T)$. Due to mental states of relaxation (closed eyes) and attention (open eyes) the distributions have corresponding shift. The distributions overlap, so there are possibilities of false positive and false negative decisions. Decision thresholds should be determined empirically for each parameter. Let $\theta_{\Delta TO}$ be the threshold for eyes open and $\theta_{\Delta TC}$ be the threshold for eyes closed for a particular subject obtained during the calibration process. Between each EEG sample we obtain two values $\Delta T$ and $\Delta A$, and the areas of distributions

$$\Delta T < \theta_{\Delta TO} \text{ and } \Delta T > \theta_{\Delta TC}, \text{ as well as } \Delta A < \theta_{\Delta AO} \text{ and } \Delta A > \theta_{\Delta AC},$$

where a minimum number of false decisions are made. The decision could be made on the basis of amplitude distribution only, but we included time distribution for improved accuracy. We also used confirmation sequence of three samples in a row, meaning that in each sample its amplitude difference and time difference should be greater than $\theta \Delta A$ respectively. So the simplest computation was

if $(\Delta A(t) > \theta_{\Delta AC})$ for three consecutive times
then (mental state = relaxation) do (robot = resume movement)

### 4.5    Demonstration Experiments

The demonstration task consisted of a shuttle robot following a closed trajectory on a "factory" floor. The trajectory contains "stations" where the robot should stop. The task of a human operator is to stop the robot at a particular "station" and after a pause, to resume the robot movement. The initial behaviour of the robot is "move along the line". The subject observes the distance from a "station" S and closes the eyes and relaxes so that the robot moves toward S. Ideally, the subject opens the eyes before S is reached and stops the robot at S.

Six subjects were involved in the experiments. The needed training and examination time for a subject was in average 30 min. After that a subject was able to stop and move the robot with 70% accuracy. Two subjects were engaged in the task to follow the movement of the robot along the trajectory and stop it at particular points (stations) along the trajectory, and both were able to complete the task.

Let us note our 1988 work on human EEG based robot control was the only such work reported in the 20th century. In the 21st century there are many robots controlled by EEG and the research in this area is progressing.

## 5    1989: Step in Robot Evolution: Robots Gain Capability of Recognizing Human EOG Signals

In 1989 the project AIIR made a next step in controlling robots using signals generated by a human head. The signals generated by moving human eyes, electrooculogram (EOG), were used to control the movement of a vehicle robot. The robot used for this task was the Adriel-1 robot, the first robot built in our lab, even before the project AIR was approved. However inside AIR projects this robot obtained its FMS outfit. Adriel-1 robot had both body sensors and inside sensors. Body sensors were whiskers placed in front left side and back. Internal sensors were wheel sensors and timer sensor. It was a "wheels and whiskers" type robot, the classification used by Margaret Boden [26] in the description of robots built by Grey Walter [20]. The robot commands for Adriel 1 were: MoveForward (MoveBackward) for a timer value, MoveLeft (Move-Right) for angle step, and Stop.

The robot Adriel-1 was built in 1982 to solve the problem finding a goal ("orb", or exit) in a simple labyrinth, using wall following method. The "orb" was recognized by a voltage value sensed by front whiskers. Besides being the first robot driven by EOG signals in robotic evolution, to the best of our knowledge it was the first robot driven by parallel programming (multithreading) software [9]. The programming was done in Event Driven Language (EDL) of the Event Driven Executive (EDX) multitasking operating system of the IBM Series/1 computer.

The EOG setup is very similar to the EEG setup. Usually four EOG electrodes are needed for determining the gaze, direction where eyes are pointing; one pair is for horizontal movement and the other is for vertical movement. We used three electrodes: one in the middle between the eyes and two below both eyes. The eyes movements used were: up (robot move forward), down (move backward), left (move left), right

(move right), and wink several times (robot stop). The experiments with this robot were simple trajectories with moving left and right.

## 6  EEG Emulation of Digital Circuits for Robot Control

This chapter describes a state of the art work in robot control, the EEG emulation of digital circuits for robot control. The description here is part of a recent, more detailed report [27].

Control circuits for robot control contain standard elementary control devices, e.g. [28, 29]. For example, the most frequently used elementary control device is a control switch. Among other examples of elementary control devices are flip-flops (state determiners) and demultiplexers (serial to parallel converters). The idea of this research is to emulate some robot control devices in processes generating EEG signals.

### 6.1  EEG Emulated Switch and Control of a Robot

A switch is a necessary element of any control and usually activates or stops some activity, possibly after some other activity. The process of pattern recognition usually implements a switch announcing the event that a pattern has been recognized and appropriate action should be taken. Some kind of EEG switch was inherently used in control of objects since the challenge of brain-computer interface (BCI) which was made by [30]. All the three following experimental BCI works [21, 31, 32] controlled an object using EEG; however an EEG emulated switch was first time explicitly shown in the control of a robot in an application [21, 22]. An increased alpha activity activates an EEG emulated switch which controls stop/resume movements of a shuttle robot along a closed line.

### 6.2  EEG Emulated Flip-Flop

The EEG emulated flip-flop was first used in a work on CNV controlled buzzer [33, 34]. The open-loop CNV paradigm was proposed in [35] and the challenge of CNV based BCI was stated in [30] The closed loop paradigm remains state Q (expectancy present) after CNV is established, but then disables the S2 signal of the paradigm. That makes CNV to degrade and a new state is now established, noQ, meaning expectation state absent. Then S2 stimulus is activated again, and so on, the brain with its expectation state emulates a flip-flop which is shown manifested by its CNV potential. The CNV flip flop was used to control two robotic arms to cooperatively solve the Tower of Hanoi problem [36].

### 6.3  EEG Emulated Demultiplexer

The EEG emulated demultiplexer is a control device which is able to extract two or more commands from a single EEG channel. This allows the use of inexpensive applications in which several robot behaviours are controlled by a single EEG channel. An EEG epoch in a trial is divided into information frames. In other words, the EEG sentence is parsed into EEG words. Each word contains information for demultiplexer

decoders. The address decoder will activate an output command channel, and the command decoder will send command through the opened output channel. The proof of the concept was given by controlling two motors of a robot arm to move to a target area avoiding an obstacle along the way [27]. The current experiments in this direction are carried out in both the laboratories of Robotics and Embodied Intelligence Center of South Carolina State University.

### 6.4 EEG Emulated Modem

The dominant view in BCI since its onset [30] is that EEG in its nature is a random signal. BCI approaches usually compute EEG amplitude as a variance of a random signal. Our work [21] points out that EEG can be viewed as a broadband carrier of messages. A carrier frequency band (e.g. alpha band) carries a message modulated in its amplitude. So the idea is that human robot-interaction using EEG can be viewed as a modulator-demodulator (modem) system in which a human wants to send a message m (t) and it modulates the carrier EEGband(t) for example alpha band. So the message sent is m(t)EEGband(t). The robot receives that message and demodulates the signal obtaining the message m(t) and carries a command encoded in that message.

## 7 Discussion: Signal Processing Robotics and Robot Evolution

The discussion can be summarized based on Fig. 1 shown in the Introduction section. It is a modification of the figure shown in a book on robotics [37] where Signal Processing Robotics was introduced as a separate chapter.

Among many directions in robotic evolution, humanoid robots (both legged and R2D2 type) are a research area of significant interest, which can be traced back in history, but it seems the first designed humanoid robot was Wabot 1 [16]. It should be noted that in robot evolution one important part is the evolution of biped robots, which happened before Wabot 1. In biped robot evolution Vukobratovic and his team from Mihajlo Pupin Institute has a very important role influencing the subsequent research on biped and humanoid robots, including the work of Kato and his team [38]. Kato and his group added speech communication feature to the 1973 robot Wabot-1 (walking humanoid) and the 1984 robot Wabot-2 (keyboard playing humanoid) [17, 39]. In addition to the direction of humanoid robots, other types of robots - vehicle robots are of current interest, including self-driving cars [40], automatic guided vehicles (AGVs), and Mars rovers, among others. Although this evolution started back in history too, the first vehicle robot was designed by Grey Walter in 1950 [20]. Such robots were used as an approach to psychology named synthetic psychology, in the book indeed named "Vehicles" [41].

Working with vehicle robots, we achieved some pioneering results in robotics, such as multitasking software architecture for robot control in 1983, description of signal processing for robot control using speech commands in 1986, EEG control of a robot in 1988, and EOG control of a robot in 1989. This paper described the part of Signal Processing Robotics as applied to speech, EEG, and EOG commands for a robot.

Additional work, which started in 1985 [42] was done in relation between flexible manufacturing systems and genetic engineering. The collaboration in 1980's Yugoslavia was an important factor in the effort and presentation of the pioneering results described in this paper.

# References

1. Vukobratović, M.: Belgrade school of robotics. Facta Universitates **2**(10), 1349–1376 (2000)
2. Vukobratovic, M., Juricic, D.: Contribution to the synthesis of biped gait. In: Proceedings of IFAC Symposium on Technical and Biological Problem of Control, Erevan, USSR (1968)
3. Vukobratovic, M., Juricic, D.: Contribution to the synthesis of biped gait. IEEE Trans. Bio-Med. Eng. **16**(1), 1–6 (1969)
4. Vukobratovic, M., Stepanenko, Y.: On the stability of anthropomorphic systems. Math. Biosci. **15**, 1–37 (1972)
5. Vukobratovic, M., Stepanenko, Y.: Mathematical models of general anthropomorphic systems. Math. Biosci. **17**, 191–242 (1973)
6. Vukobratovic, M.: How to control the artificial anthropomorphic systems. IEEE Trans. Syst. Man Cybern. **SMC-3**, 497–507 (1973)
7. Vukobratovic., M., Hristic, D.: Locomotive robots and anthropomorphic mechanisms: realization of artificial walk (in Serbian). Institute Mihajlo Pupin, Belgrade, Yugoslavia (1975)
8. Vukobratovic, M., Borovac, B.: Zero-moment point - thirty five years of its life. Int. J. Humanoid Rob. **1**(1), 157–173 (2004)
9. Bozinovski, S., Sestakov, M.: Multitasking operating systems and application in robot control (in Macedonian). In: Proceedings of Symposium on the Informatics in Macedonia, State Association for Scientific Work, Skopje, Yugoslavia, pp. 195–199 (1983)
10. Bozinovski, S., Koco, I., Hristofi, A.: A model of a multirobot supervising control system in a flexible manufacturing system (in Macedonian). In: Proceedings of Symposium on JUROB, Opatija, Yugoslavia (1985)
11. Bozinovski, S.: Flexible manufacturing systems: a biocybernetics approach. In: Popov, E., Vukobratovic, M. (eds.) The 3rd Soviet-Yugoslav Symposium on Robotics and Flexible Manufacturing Systems, Moscow, USSR, pp. 192–197 (1986)
12. Bozinovski, S.: Flexible manufacturing systems: a biocybernetics approach (in Russian). Problemyi Mashinostroeniya i Avtomatizacii **16**, 31–34 (1987)
13. Bozinovski, S., Sestakov, M., Stojanov, G.: A learning system for mobile robot control using human head bio signals (in Russian). Problemyi Mashinostroeniya i Avtomatizacii **6**, 32–35 (1991)
14. Dudley, H., Riesz, R., Watkins, S.: A synthetic speaker. J. Franklin Inst. **227**, 739–764 (1939)
15. Davis, K., Bidulph, R., Balashek, S.: Automatic recognition of spoken digits. J. Acoust. Soc. Am. **24**(6), 637–642 (1952)

16. Kato, I., Ohteru, S., Kobayashi, H., Shirai, K., Uchiyama, A.: Information-power machine with senses and limbs. In: Proceedings of CISM-IFToMM Symposium on Theory and Practice of Robots and Manipulators, Udine, Italy, pp. 12–24 (1973)

17. Sugano, S., Kato, I.: WABOT-2: autonomous robot with dexterous finger-arm — finger-arm coordination control in keyboard performance. In: Proceedings of IEEE International Conference on Robotics and Automation, vol. 4, pp. 90–97 (1987)

18. Grujovski, G., Bozinovski, S.: Realization of a system for speech control of a mobile robot (in Macedonian). In: Proceedings of the 6th Yugoslav Symposium on Applied Robotics and Flexible Automation, Novi Sad, Yugoslavia, pp. 227–235 (1989)

19. Grujovski, G.: Realization of a system for recognition of isolated words and control of a mobile robot with speech commands (in Macedonian). Technical report, Project Adaptive Industrial Robots, based on Grujovski's Diploma Thesis, mentor S. Bozinovski, Electrical Engineering Faculty, University Cyril and Methodius, Skopje, Yugoslavia (1986)

20. Walter, W.G.: An imitation of life. Sci. Am. **182**, 42–45 (1950)

21. Bozinovski, S., Sestakov, M., Bozinovska, L.: Using EEG alpha rhythm to control a mobile robot. In: Harrism, G., Walker, C. (eds.) Proceedings of 10th Annual Conference of the IEEE Engineering in Medicine and Biology Society, New Orleans, LA, vol. 10, pp. 1515–1516, track 17, Biorobotics (1988)

22. Bozinovski, S., Sestakov, M., Stojanov, G., Bozinovska, L.: Bioelectric mobile robot control (in Macedonian). In: Proceedings of 6th Yugoslav Symposium on Applied Robotics and Flexible Automation, Novi Sad, Yugoslavia, pp. 237–242 (1989)

23. Bozinovski, S.: Mobile robot trajectory control: from fixed rails to direct bioelectric control. In: Kaynak, O. (ed.) Proceedings of IEEE International Workshop on Intelligent Motion Control, Istanbul, Turkey, vol. 2, pp. 463–467 (1990)

24. Onosko, T.: Enter the movits; high-tech toys. Creative Comput. **10**(12), 119 (1984)

25. Bozinovski, S., Bozinovska, L.: Kinesis of physical objects controlled by signals emanating from a human brain: an engineering and computer science approach, since 1988 (keynote paper). In: Proceedings of Conference IcETRAN, Vrnjacka Banja, Serbia, p. KP 1.5.1-8 (2014)

26. Boden, M.: Grey Walter's anticipatory tortoises. Rutheford J. **2** (2007)

27. Bozinovski, S., Bozinovski, A.: Mental states, EEG manifestations, and mentally emulated digital circuits for brain-robot interaction. IEEE Trans. Auton. Ment. Dev. **7**(1), 39–51 (2015)

28. Braga, N.: Robotics, Mechatronics, and Artificial Intelligence. Newnes, Boston (2002)

29. Xie, M.: Fundamentals of Robotics. World Scientific, River Edge (2003)

30. Vidal, J.: Toward direct brain-computer communication. Ann. Rev. Biophys. Bioeng. **2**, 157–180 (1973)

31. Vidal, J.: Real-time detection of brain events in EEG. Proc. IEEE **65**, 633–641 (1977)

32. Farwell, L., Donchin, E.: Talking off the top of your head: a mental prosthesis utilizing event-related brain potentials. Electroencephalogr. Clin. Neurophysiol. **70**, 510–523 (1988)

33. Bozinovska, L., Bozinovski, S., Stojanov, G., Sestakov, M.: Introduction of biofeedback in the CNV paradigm (in Serbian). In: Proceedings of Conference on ETAN, Novi Sad, Yugoslavia, pp. XII. 93–98 (1989)

34. Bozinovska, L., Bozinovski, S., Stojanov, G.: Electroexpectogram: experimental design and algorithms. In: Proceedings of IEEE International Biomedical Engineering Days, Istanbul, Turkey, pp. 58–60 (1992)

35. Walter, G., Cooper, R., Aldridge, V., McCallum, W.: Contingent negative variation: an electric sign of sensory-motor association and expectancy in the human brain. Nature **203**, 380–384 (1964)

36. Bozinovski, A., Tonkovic, S., Isgum, V., Bozinovska, L.: Robot control using anticipatory brain potentials. Automatika **52**(1), 20–30 (2011)
37. Bozinovski, S.: Robotics and Intelligent Manufacturing Systems (in Macedonian). Gocmar Press, Skopje (1997). Reviewer M. Vukobratovic
38. Li, Q., Takanishi, A., Kato, I.: Learning control of compensative trunk motion for biped walking robot based on ZMP stability criterion. In: Proceedings of IEEE/RSJ International Conference on Intelligent Robots and Systems, Raleigh, NC, pp. 597–603 (1992)
39. Matsusaka, Y.: History and current researches on building a human interface for humanoid robots. In: Wachsmuth, I., Knoblich, G. (eds.). LNCS (LNAI), vol. 4930, pp. 109–124. Springer, Heidelberg (2008). doi:10.1007/978-3-540-79037-2_6
40. Rodić, A., Vukobratović, M.: Contribution to the integrated control synthesis of road vehicles. IEEE Trans. Control Syst. Technol. **7**(1), 64–78 (1999)
41. Braitenberg, V.: Vehicles: Experiments in Synthetic Psychology. The MIT Press, Cambridge (1986)
42. Bozinovski, S.: Guest Editor's Introduction: Special Issue on Biological and Non-Biological Beings. Automatika **25**, 128 (1985)

# Medical, Human-Assistive Robots and Prosthetic Design

# Analysis of the Static Stability for an Electric Stair-Climbing Wheelchair

Giuseppe Quaglia[(✉)], Walter Franco, and Matteo Nisi

Department of Mechanical and Aerospace Engineering,
Politecnico di Torino, Turin, Italy
{giuseppe.quaglia, walter.franco,
matteo.nisi}@polito.it

**Abstract.** In this paper, an electric stair-climbing wheelchair is presented. The proposed solution is based on a smart hybrid leg-wheel locomotion system. This idea has been developed through several wheelchair concepts presented in the first part of the paper, pointing out the main advantages and disadvantages for each solution. In the second part, an optimization procedure regarding the geometry of the latest wheelchair architecture is presented. The aim is to maximize the wheelchair performances in terms of safety and comfort for the user. In particular, the geometric parameters of the wheelchair structure have been analysed in order to assess which configuration guarantees an acceptable static stability of the wheelchair during stair climbing motion. Moreover, considering the goal of maximizing the comfort for the user, the oscillation introduced on the wheelchair seat by the locomotion system has been studied and solutions able to reduce them are proposed.

**Keywords:** Stair-climbing wheelchair · Leg-wheel locomotion · Static stability · Mobile robot

## 1 Introduction

A significant number of persons worldwide use a wheelchair for daily mobility. There are around 1.2 million wheelchair users in the UK (roughly 2% of UK population) [1] and about 3.3 million people in the U.S.A. (1.4% of U.S.A. population) [2]. Moreover, the number of person with a reduced mobility constantly grows up also because the population aging. It has been calculated that with the current trend, the percentage of people with more than 60 years will reach the 22% of global population in 2050 while it was 10% in 2000 [3]. This aspect is more relevant in western countries where the percentage will reach the 36% in 2050 while in 2000 it was 18% [3]. It is evident that providing a complete accessibility to private and public buildings will be an important challenge for the future. Despite this, the required adaptations often cannot be done due to technical or economic issues. In these cases, people with a reduced mobility can be provided with devices able to climb obstacles and architectural barriers. With this purpose, some interesting solutions have been designed and sometimes they have brought to commercial products.

Obstacle climbing is a challenge shared with different engineering fields. For example, in mobile robotics, it could be an important feature for robots that move autonomously in an unknown and unstructured environment. In [4] a collection of possible locomotion system for obstacle climbing robot is presented. Different climbing mechanisms can be adopted: tracked, legged, wheeled or hybrid solutions are the most effective. The same architectures can be found in stair climbing wheelchairs. In [5] a pure leg locomotion is proposed. This solution is interesting from a stair climbing point of view but has high control requirements. In [6, 7] architectures with reconfigurable tracks are proposed. Tracked locomotion has an optimum behaviour on uneven terrains but has low efficiency compared to other solutions especially on flat ground. A pure wheeled locomotion is in general not suitable for high step climbing but thanks to its high efficiency and manoeuvrability is often used in hybrid architectures. For example, [8, 9] propose hybrid leg-wheel wheelchairs that move on wheel or on leg depending on the presence or absence of obstacles. Moreover, another solution in which each wheel is coupled with an articulated mechanism is showed in [10, 11]. Finally, in [12, 13] leg-wheel solutions based on double or triple wheels cluster locomotion units are proposed.

## 2 Evolution of Wheelchair.q Project

Authors also worked on this topic, designing and having designed four versions of *Wheelchair.q,* a novel stair-climbing wheelchair with the aim of improving the performances of the solutions presented in the introduction. In particular, the wheelchair: should be used in a completely autonomous way; must be similar in dimensions, weight and autonomy with respect to a traditional electric wheelchair; should have a simple structure with few actuators and sensors and should be simple to use without the necessity of complex controllers. The original idea that has been maintained in all the versions is the use of a triple-wheel locomotion unit: a hybrid wheel-leg solution with obstacle climbing ability. This solution has been firstly implemented in the *Epi.q* mobile robot family and has been described in several works such as [14, 15]. The locomotion unit has a triangular shaped frame with the wheels on the corners and an internal epicyclical mechanism. The structure has two degrees of freedom: the solar gear rotation and the planet carrier revolution. In the mobile robot applications, this feature has been used to develop a smart architecture able to climb obstacles in an autonomous way. The planet carrier revolution starts when the friction force between wheels and obstacle blocks the front wheels. The behaviour of the locomotion unit is indeed determined by dynamic conditions.

The first and second wheelchair concepts are presented in [16, 17] and shown in Fig. 1. In both cases, four triple wheel locomotion units are used. The front units are idle while the rear units are connected each one with a motor as in the *Epi.q* mobile robots. The principal advantage of this solution is the simplicity: only two motors are required to manage the wheelchair movements both on flat ground and on stairs and no sensors are required to trigger the step climbing sequence. The main disadvantages are related to oscillation during step climbing motion and with the controllability of the descent phase. The centre of the locomotion unit moves on an approximately cycloid trajectory during each step climbing as represented in Fig. 2. Depending on the stair
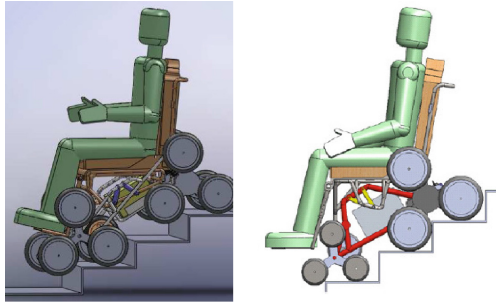
**Fig. 1.**  Wheelchair.q01 and Wheelchair.q02
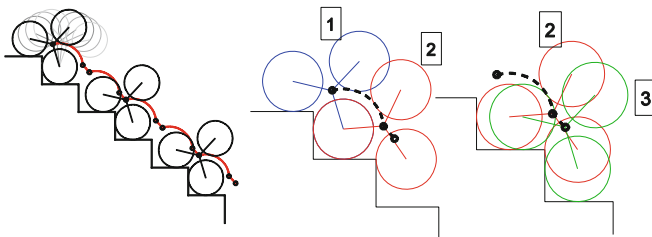


**Fig. 2.**  Representation of the trajectory of the locomotion unit centre during stair climbing

dimension, front and rear locomotion units could have asynchronous rotations and thus generate a continuous oscillation on the wheelchair that could be uncomfortable.

To solve this first issue, in the first two proposed wheelchairs a mechanism that actively controls the seat orientation has been introduced in order to keep the seat horizontally. This solution allows the wheelchair oscillation to be compensated, but it increases the complexity and the energy consumption. The other problem involves the controllability of the locomotion unit. As stated previously, the locomotion unit has two degrees of freedom and they can be controlled with only one motor during stair ascent thanks to dynamic effects. During stair descent, instead, the two degrees of freedom cannot be controlled by one motor and the wheelchair moves with repeated falls from one step to the lower. This behaviour can be accepted for robotics applications while it is not suitable for a wheelchair for comfort and safety reasons. The first and second architectures differ for the dimension of the front locomotion units and for the performances of the seat orientation mechanism that has been optimized in the second version.

In [18, 19] a third and a fourth wheelchair design are described and they are represented in Fig. 3. The principal innovation introduced is the replacement of the front locomotion units with an idle track. This solution reduces the seat oscillation amplitude by coupling the locomotion unit that generates a periodic oscillation during each step climbing with an element that moves on a more linear trajectory. The result is a smoothed movement for the seat that does not require an active mechanism to control orientation. The second achievement is the improvement of the wheelchair

controllability by introducing a third motor that controls the rotation of both planet carriers. This actuation architecture enables a complete control of the locomotion units both in ascent and descent phases even if the automatic climbing feature is lost. The difference between the third and fourth solutions is due to the implementation of a different reconfiguration mechanism that manages the relative position between track and locomotion unit.
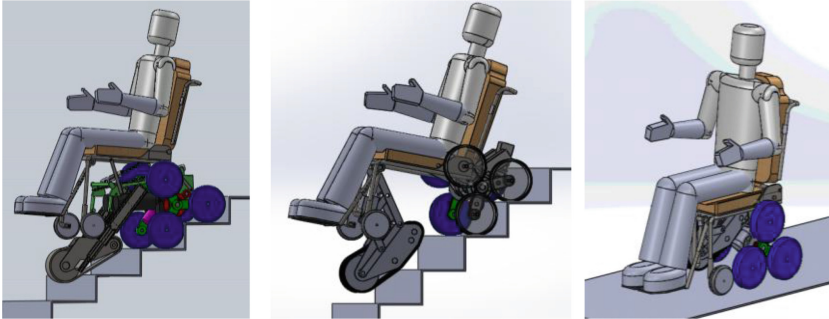


**Fig. 3.** Wheelchair.q03 and Wheelchair.q04 (in stair climbing and flat ground configurations)

The main characteristic of the latest versions of *Wheelchair.q* is the hybrid architecture. The wheelchair performances mainly depend on the interaction between the track and the locomotion unit and, thus, their relative position should be optimized. The aim of this paper is to analyse deeper the influence of the track position and its shape over the wheelchair behaviour in terms of oscillation and static stability.

## 3   Methodology

The track is the front foothold for the wheelchair. Its principal aim is to avoid the wheelchair overturning. The position and the shape of the track are important for static stability issues. If the load of vehicle and user is mainly on the locomotion unit, the track acts essentially as a not-overturning system. In Fig. 4 two different configurations of the wheelchair during stair climbing motion are represented. The reaction force on the track ($N_{CA}$) is perpendicular to the contact surface. Its horizontal component is directed down stair and it contrasts the wheelchair up stair motion. In order to have static stability, the relation in Eq. (1) must be verified:

$$T_{CP} < f_{CP} \cdot N_{CP} \tag{1}$$

where $f_{CP}$ is the friction coefficient between wheel and ground. According to this, the first configuration of Fig. 4 is stable while in the second the horizontal force on locomotion unit wheel ($T_{CP}$) is higher than the vertical force ($N_{CP}$) and thus the static stability cannot be guaranteed with a friction coefficient lower than 1 as in the wheel-ground contact. In general, the more the load on the track is higher the more the
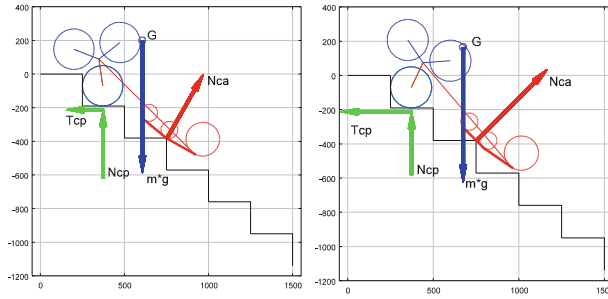
**Fig. 4.** Wheelchair in a stable and unstable configuration on stair

wheelchair stability is reduced. In order to have a stable configuration for any position of the step climbing sequence, an optimization process has been done. An optimal track shape and an optimal relative position between track and locomotion unit must be identified.

A single step climbing has been considered because in steady-state condition each step climbing sequence is equal to the others. The planet carrier motor manages the locomotion unit rotation with respect to wheelchair frame ($\theta_P$ in Fig. 5a). A step climbing sequence occurs with a $\Delta\theta_P = 120°$ and for each position (i.e. for each value of $\theta_P$) the contact configuration has been calculated by imposing geometrical conditions through the schemes of Fig. 5a. In particular, the orientation of the wheelchair frame with respect to the horizontal plane ($\varphi$) must be taken into account.
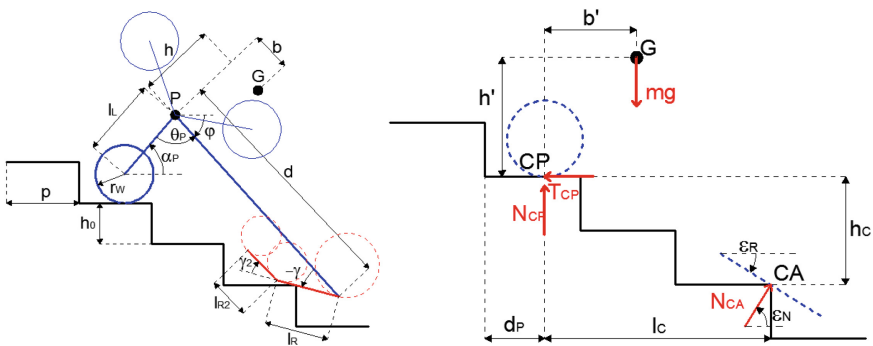


**Fig. 5.** Schematic representation (a) and free body diagram (b) of the wheelchair on stair

Once the contact configuration has been found, the free body diagram of Fig. 5b can be solved and the reaction forces $T_{CP}(\theta_P)$ and $N_{CP}(\theta_P)$ can be calculated with the hypothesis of no friction between track and stair. From these values it is possible to calculate the friction coefficient between wheel and stair necessary to guarantee the wheelchair stability. In order to assess the optimal wheelchair structure, three parameters have been analyzed: d and $\gamma$ that describe the relative position between the track

and the locomotion unit and $\gamma_2$ that affects the track shape as can be observed in Fig. 5a. Actually, also $l_R$ and $l_{R2}$ influence the track shape. In particular high values of these parameters are advisable; however, in order to save space these values have been fixed to 200 mm and 166 mm respectively. The optimization analysis has been conducted by testing several wheelchair configurations (i.e. several combinations of parameters) on different stair typologies and evaluating the performances of the wheelchair for each configuration.

Two quantities have been considered in the optimization process:

- the minimum friction coefficient ($f_{CP}$) necessary to guarantee the static stability for each configuration of the step climbing sequence (i.e. for each value of $\theta_P$);
- the wheelchair oscillation that occurs during a step climbing sequence ($\Delta\varphi$).

Both quantities are defined in Eqs. (2) and (3).

$$f_{CP} = f_{CP}(d, \gamma, \gamma_2) = max_{\theta_P}\left(\frac{T_{CP}(\theta_P)}{N_{CP}(\theta_P)}\right) \tag{2}$$

$$\Delta\varphi = \Delta\varphi(d, \gamma, \gamma_2) = max_{\theta_P}(\varphi(\theta_P)) - min_{\theta_P}(\varphi(\theta_P)) \tag{3}$$

The optimal structure is the one in which both values are smaller. Different results are obtained by considering different stairs. According to UNI10804 - gen1999 three reference stairs dimensions can be identified and they are summarized in Fig. 6.



|  | $h_0$ [mm] | P [mm] | $\alpha_s$ | e [mm] |
|---|---|---|---|---|
| Low slope | 145 | 350 | 22.5° | 378.8 |
| Medium slope | 170 | 300 | 29.5° | 344.8 |
| High slope | 190 | 250 | 37° | 314 |
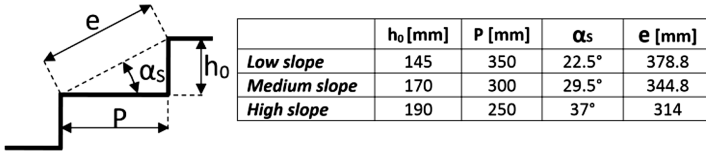
**Fig. 6.** Reference stairs dimensions

For each stair, an objective function ($f_{Stair}$) has be defined as in Eq. (4). The two quantities ($f_{CP}$ and $\Delta\varphi$) have been converted to dimensionless values dividing by their maximum value and have been taken into account with the same weight. Thus, for each stair, the objective function is a dimensionless number between 0 and 2.

$$f_{Stair} = \frac{f_{CP}(d, \gamma, \gamma_2)}{max_{(d,\gamma,\gamma_2)}(f_{CP})} + \frac{\Delta\varphi(d, \gamma, \gamma_2)}{max_{(d,\gamma,\gamma_2)}(\Delta\varphi)} \tag{4}$$

The results obtained for each stair have been collected in a global objective function ($f$) described by Eq. (5). The function can assume values from 0 to 1. The optimal solution will be the one with the lower value.

$$f = \frac{f_{Low\ Slope} + f_{Medium\ Slope} + f_{High\ Slope}}{6} \tag{5}$$

# 4   Results

In this section, the results obtained with the optimization analysis are presented. The three parameters d, $\gamma$ and $\gamma_2$ have been varied between the following discrete values:
    d = [700, 800, 900] mm $\gamma$ = [−10, −5, 0, 5, 10, 15] ° $\gamma_2$ = [−10, −5, 0, 5, 10, 15] °
    For each possible triads of values, the objective function (f) has been calculated and the results are shown in Fig. 7. Some triads of values (for example d = 700 mm, $\gamma$ = −10° and $\gamma_2$ = −5°) have been discarded because the specific structure generates a discontinuous wheelchair movement. This means that during the step climbing sequence the track loses the contact with the stair and falls on the lower step. From the data presented in Fig. 7 it is evident that the better performances can be obtained with a higher value for parameter d and a negative value for angle $\gamma$. As regard the track shape it can be observed that an optimal solution is obtained with $\gamma_2$ = 0°. The optimal values for d, $\gamma$ and $\gamma_2$ are collected in Table 1. Moreover, the values of $\Delta\varphi$ and $f_{CP}$ for the optimal configuration in the three reference stairs are presented.
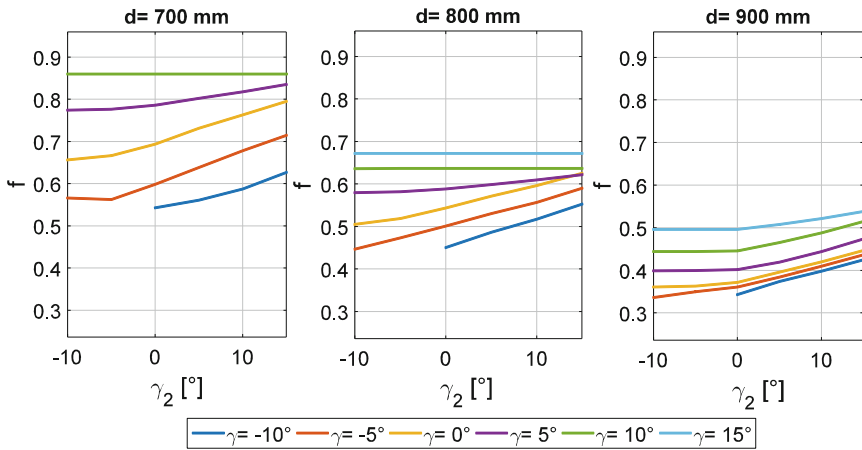


**Fig. 7.**  Trend of the objective function for different values of d, $\gamma$ and $\gamma_2$

**Table 1.**  Optimal values for d, $\gamma$ and $\gamma_2$

|  | d [mm] | $\gamma$ [°] | | $\gamma_2$ [°] |
|---|---|---|---|---|
| Optimum value | 900 | −10 | | 0 |
| Stair | $\Delta\varphi$ [°] | | $f_{CP}$ | |
| 145 × 350 | 4.85 | | 0.22 | |
| 170 × 300 | 5.46 | | 0.34 | |
| 190 × 250 | 5.68 | | 0.47 | |

## 5    Conclusion

In this paper, an optimization process on the last version of *Wheelchair.q* has been proposed. The purpose of this work has been the improvement of the wheelchair performances with respect to previous versions. In particular, the reduction of seat oscillation and the improvement of the static stability have been the main focuses. Acceptable oscillation amplitude has been obtained by choosing proper values for the geometrical dimensions of the wheelchair structure. The static stability has been guaranteed in any configuration of the step climbing sequence. Future works will regard the development of anew wheelchair architecture able to overcome some intrinsic limits of the actual version. Moreover, a multibody model will be developed to understand deeply the wheelchair behaviour during stair climbing motion.

## References

1. Papworth Trust, Disability in the United Kingdom 2014: Facts and Figures (2014)
2. U.S Census Bureau, Americans with Disabilities: 2005 (2008)
3. Lutz, W., Sanderson, W., Scherbov, S.: The coming acceleration of global population ageing. Nature **451**(7179), 716–719 (2008)
4. Bruzzone, L., Quaglia, G.: Review article: locomotion systems for ground mobile robots in unstructured environments. Mech. Sci. **3**, 49–62 (2012)
5. Sugahara, Y., et al.: Walking up and down stairs carrying a human by a biped locomotor with parallel mechanism. In: Proceeding of International Conference on Intelligent Robots and Systems (IROS 2005), Edmonton, Alberta, Canada, pp. 1489–1494 (2005)
6. Kritman, L., Trachtenberg, L.: U.S. Patent No. 7,316,405. Washington, DC (2008)
7. Yu, S., Wang, T., et al.: A tip-over and slippage stability criterion for stair-climbing of a wheelchair robot with variable geometry single tracked mechanism. In: Proceeding of International Conference on Information and Automation (ICIA), Shenyang, China (2012)
8. Yuan, J., Hirose, S.: Research on leg-wheel hybrid stair-climbing robot, zero carrier. In: Proceedings of International Conference on Robotics and Biomimetics ROBIO, Shenyang, China, pp. 654–659 (2004)
9. Lawn, M.J., Ishimatsu, T.: Modeling of a stair-climbing wheelchair mechanism with high single-step capability. Neural Syst. Rehabil. Eng. **11**(3), 323–332 (2003)
10. Gonzalez, A., Morales, R., et al.: Improving the mechanical design of new staircase wheelchair. Ind. Robot Int. J. **34**(2), 110–115 (2007)
11. Gonzalez, A., Ottaviano, E., Ceccarelli, M.: On the kinematic functionality of a four-bar based mechanism for guiding wheels in climbing steps and obstacles. Mech. Mach. Theory **44**(8), 1507–1523 (2009)
12. Sugahara, Y., Yonezawa, N., Kosuge, K.: A novel stair-climbing wheelchair with transformable wheeled four-bar linkages. In: Proceedings of International Conference on Intelligent Robots and Systems (IROS), Taipei, Taiwan, pp. 3333–3339 (2010)
13. Kenneth, R.C.: Battery powered stair-climbing wheelchair, U.S. Patent No. 6484829, 26 November 2002
14. Quaglia, G., et al.: The Epi. q-1 hybrid mobile robot. Int. J. Robot. Res. **29**(1), 81–91 (2009)
15. Quaglia, G., Bruzzone, L., et al.: A modular approach for a family of ground mobile robots. Int. J. Adv. Rob. Syst. **10**, 296 (2013)

16. Quaglia, G., Franco, W., Oderio, R.: Wheelchair.q, a mechanical concept for a stair climbing wheelchair. In: Proceeding of International Conference on Robotics and Biomimetics (ROBIO), Guilin, China, pp. 800–805 (2009)
17. Quaglia, G., Franco, W., Oderio, R.: Wheelchair.q, a motorized wheelchair with stair climbing ability. Mech. Mach. Theory **46**(11), 1601–1609 (2011)
18. Quaglia, G., Franco, W., Nisi, M.: Design of a reconfiguration mechanism for an electric stair-climbing wheelchair. In: Proceeding of the International Mechanical Engineering Congress & Exposition (IMECE), Montreal, Quebec, Canada (2014)
19. Quaglia, G., Franco, W., Nisi, M.: Evolution of Wheelchair.q, a stair-climbing wheelchair. In: Proceedings of 14th World Congress Mechanism & Machine Science, Taipei, Taiwan (2015)

# Motion Control Algorithm for Exoskeleton Push Recovery in the Frontal Plane

Sergey Jatsun[✉], Sergei Savin, and Andrey Yatsun

Southwest State University, Kursk, Russia
teormeh@inbox.ru, savin@swsu.ru, ayatsun@ya.ru

**Abstract.** In this paper a full body assistive exoskeleton is considered. A mathematical model for the case of the frontal plane motion is given. The paper focuses on the question of push recovery, considering two different cases: when the exoskeleton is pushed as a result of an interaction with another moving object and the case when the exoskeleton stands on a platform that rapidly changes its speed. A push recovery algorithm is proposed that allows the exoskeleton to regain vertical balance by taking one step. The algorithm was tested via numerical simulation; the results are shown and analysed in the paper. The results of the simulation demonstrated the similarity of the exoskeleton motion to that of a human.

**Keywords:** Assistive exoskeleton · Push recovery algorithm · Control system design · Mathematical modelling

## 1 Introduction

In recent years, the use of exoskeletons has seen rise, as they are finding applications in medicine, rehabilitation, industry and in the military. Use of exoskeletons to enhance human capabilities presents a possibility to improve life style for certain categories of disabled people, allowing them to walk instead of using a wheel chair. At the same time this application of exoskeletons presents new challenges, because it increases the need for high safety standards for these machines [1, 2].

In the literature on the exoskeleton control, questions such as stability of walking [3–6] and sit-to-stand motion [7–9] have been studied. One of the main approaches is to use concepts such as zero-moment point (ZMP) control, formulated by M. Vukobratović, which allows an exoskeleton to remain vertically balanced while moving [10–12]. At the same time there aren't enough studies on the preserving vertical balance of the exoskeleton that has been pushed. In the biped robotics literature this is known as push recovery, and there have been studies done on the matter [13–17]. Pratt et al. presented the concept of Capture Point, defined as a point on the supporting surface where the robot can step to in order to bring itself to a stop [13]. Stephens et al. described three types of control strategies to prevent fall due to disturbances [14], which include the centre of pressure balancing strategy, centroid moment point balancing strategy and stepping.

We observe that recovery from a push in the frontal plane can present additional challenges as compared with the case when the motion takes place in the sagittal plane.

One of the reasons for this difference is the smaller number of joints that are capable of motion in the frontal plane, which in turn restricts the possible motions of the exoskeleton. In this paper we study two cases of recovery from an abrupt change of velocity of the mechanism's links. In the first case there is a force that acts on the mechanism for a short period of time. This case represents a situation when the exoskeleton user is pushed as a result of an interaction with another moving object, for example, a human. In the second case the exoskeleton stands on a platform that rapidly gains velocity for a short period of time. This case represents a situation when the exoskeleton user stands in a vehicle that quickly accelerates. Both cases are likely to be experienced in everyday life by exoskeleton users, therefore extensive study that can allow us to develop appropriate safety measures is necessary.

## 2  Mathematical Model

In this paper we consider a full body assistive exoskeleton. The exoskeleton is a multibody system, assembled from 13 links. Each leg has three links (foot, shin and thigh) and each arm has three links too (shoulder, forearm and hand). The limbs are connected to the exoskeleton's trunk. Every connection between two links is done via a rotational joint.

We will consider the case when the patient stands on straight legs, with at least one foot remaining still on the supporting surface. This means that the mechanism is put into a singular position, and the shin and the thigh of each leg are instantaneously moving as one. We will also restrict arms to be moving only in the shoulder joints. These assumptions allow us to model both legs and arms as single links moving in the frontal plane of the exoskeleton. Figure 1 shows a diagram of the mechanism.

In Fig. 1 points $O_i$ are joints, each equipped with a motor that produces torque $M_i$, $C_i$ are the centres of mass of the links, and $\varphi_i$ are the absolute angles that define the
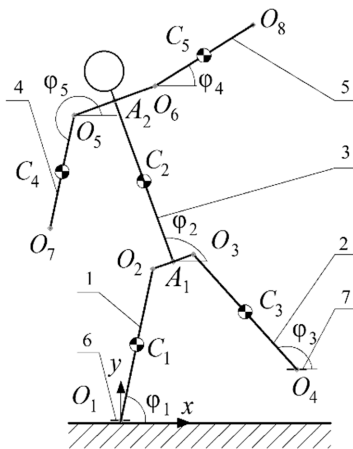


**Fig. 1.** Diagram of the full-body exoskeleton; 1–7 are the first-seventh links of the exoskeleton

orientation of the links relative to the horizontal plane. The links have masses $m_i$. The geometry of the robot is given by the following relations: $O_1O_2 = O_3O_4 = l_1$, $O_2A_1 = A_1O_3 = l_2$, $A_1A_1 = l_3$, $A_2O_5 = A_2O_6 = l_4$, $O_5O_7 = O_6O_8 = l_5$.

The forward kinematics of the mechanism is given by the following formulas:

$$\vec{r}_{O2} = \mathbf{T}(\varphi_1)\begin{bmatrix} l_1 \\ 0 \end{bmatrix}, \ \vec{r}_{A1} = \vec{r}_{O2} + \mathbf{T}(\varphi_2)\begin{bmatrix} 0 \\ -l_2 \end{bmatrix}, \tag{1}$$

$$\vec{r}_{O3} = \vec{r}_{O2} + \mathbf{T}(\varphi_2)\begin{bmatrix} 0 \\ -2l_2 \end{bmatrix}, \ \vec{r}_{O4} = \vec{r}_{O3} + \mathbf{T}(\varphi_3)\begin{bmatrix} -l_1 \\ 0 \end{bmatrix}, \tag{2}$$

$$\vec{r}_{A2} = \vec{r}_{A1} + \mathbf{T}(\varphi_2)\begin{bmatrix} l_3 \\ 0 \end{bmatrix}, \ \vec{r}_{O5} = \vec{r}_{A2} + \mathbf{T}(\varphi_2)\begin{bmatrix} l_4 \\ 0 \end{bmatrix}, \tag{3}$$

$$\vec{r}_{O6} = \vec{r}_{A2} + \mathbf{T}(\varphi_2)\begin{bmatrix} -l_4 \\ 0 \end{bmatrix}, \ \vec{r}_{O7} = \vec{r}_{O5} + \mathbf{T}(\varphi_4)\begin{bmatrix} l_5 \\ 0 \end{bmatrix}, \ \vec{r}_{O8} = \vec{r}_{O8}6 + \mathbf{T}(\varphi_5)\begin{bmatrix} l_5 \\ 0 \end{bmatrix} \tag{4}$$

where $\mathbf{T}(\varphi_i) \in SO(2)$ denotes a rotation matrix. We can find the position of the centre of mass of each link in the following way:

$$\vec{r}_{C1} = \lambda_1\vec{r}_{O2}, \ \vec{r}_{C2} = \lambda_2(\vec{r}_{A1} + \vec{r}_{A2}), \ \vec{r}_{C3} = \lambda_3(\vec{r}_{O3} + \vec{r}_{O4}), \tag{5}$$

$$\vec{r}_{C4} = \lambda_4(\vec{r}_{O5} + \vec{r}_{O7}), \ \vec{r}_{C5} = \lambda_5(\vec{r}_{O6} + \vec{r}_{O8}). \tag{6}$$

where $\lambda_i$ are coefficients that determine the position of the centre of mass of each link. The coefficients used in the simulation are obtained from [18]. Using Eqs. (1)–(6) we can find location of the centre of mass $\vec{r}_C$.

In the case when the point $O_1$ remains stationary we can introduce a vector of generalized coordinates $\vec{q} = [\varphi_1 \quad \varphi_2 \quad \varphi_3 \quad \varphi_4 \quad \varphi_5]^{\mathrm{T}}$. We can write the equations of the dynamics of the mechanism in vector form:

$$\mathbf{A}(\vec{q})\ddot{\vec{q}} + \vec{C}\left(\vec{q}, \dot{\vec{q}}\right) + \vec{G}(\vec{q}) + \vec{\Phi}(\vec{q}) = \mathbf{B}\vec{M} \tag{7}$$

where $\vec{C}\left(\vec{q}, \dot{\vec{q}}\right)$ is a vector of generalized forces of inertia, $\mathbf{A}(\vec{q})$ is a joint space inertia matrix, $\vec{G}(\vec{q})$ is a vector of generalized gravitational forces, $\vec{\Phi}(\vec{q})$ is a vector of generalized dissipative forces, $\mathbf{B}$ is a matrix connecting the torques of the motors with generalized forces they generate, $\vec{M} = [M_1 \quad M_2 \quad M_3 \quad M_4 \quad M_5]^{\mathrm{T}}$.

This vector equation of dynamics can be used for simulation of the robot's motion. We will consider the case when $\vec{M}$ is generated by a feedback controller.

## 3  Two Stage Push Recovery Control Strategy

In this paper we propose a control algorithm for push recovery that is being executed in two stages. The first stage, which lasts $t_1$ s, begins when the exoskeleton has been pushed to the side, its centre of mass obtaining nonzero velocity. During this stage point $O_4$ leaves the supporting surface and the exoskeleton performs a step to the side to recover its balance. At the beginning of this stage the control system estimates the trajectory of the centre of mass for the duration of the stage. Using this information the foot placement algorithm calculates the desired position of the point $O_4$ by the end of the stage, and finds a trajectory that would guide the point $O_4$ to that position. The control system also attempts to move the exoskeleton in such way as to minimize the change in the velocity of the centre of mass. This is done to ensure that reaction forces acting on the system are minimal during the first stage of the motion.

The second stage of motion, which lasts $t_2$ seconds, begins when point $O_4$ regains contact with the supporting surface. During the second stage the control system slows the centre of mass to a halt and then moves it towards the middle of the support polygon. The point $O_4$ remains stationary at all times during this stage.

Thus, the control system generates the desired trajectories for two vectors, $\vec{r}_{O4}$ and $\vec{r}_C$. The desired trajectory $\vec{r}_C^* = [x_C^* \quad y_C^*]^\mathrm{T}$ for the centre of mass is given by the following formulas:

$$x_C^* = \begin{cases} x_C(0) + \dot{x}_C(0) \cdot t & if \quad t \le t_1 \\ \sum\limits_{p=0}^{5} \left(c_{1,p} \cdot t^p\right) & if \quad t > t_1 \end{cases}, \quad y_C^* = \begin{cases} y_C(0) + \dot{y}_C(0) \cdot t & if \quad t \le t_1 \\ \sum\limits_{p=0}^{5} \left(c_{2,p} \cdot t^p\right) & if \quad t > t_1 \end{cases} \quad (8)$$

where $x_C(0), y_C(0)$ denote the position of the centre of mass of the moment of the push, $\dot{x}_C(0), \dot{y}_C(0)$ - the velocity it acquired from the push, $c_{1,p}$ and $c_{2,p}$ are polynomial coefficients.

The desired trajectory $\vec{r}_{O4}^* = [x_{O4}^* \quad y_{O4}^*]^\mathrm{T}$ for the point $O_4$ is given by the following formulas:

$$x_{O4}^* = \begin{cases} \sum\limits_{p=0}^{5} \left(c_{3,p} \cdot t^p\right) & if \quad t \le t_1 \\ x_s & if \quad t > t_1 \end{cases}, \quad y_{O4}^* = \begin{cases} \sum\limits_{p=0}^{5} \left(c_{4,p} \cdot t^p\right) & if \quad t \le t_1 \\ 0 & if \quad t > t_1 \end{cases} \quad (9)$$

where $c_{3,p}$ and $c_{4,p}$ are polynomial coefficients, $x_s$ is the foot placement position (also known as the capture point, see [16]), determined by the formula:

$$x_s = x_C(0) + \mu \dot{x}_C(0) t_1 \quad (10)$$

where $\mu > 1$ is the safety margin coefficient. This choice for foot placement position is motivated by the requirement to have the centre of mass within the control polygon during the second stage of the motion. The bigger the safety margin coefficient the further away from the boundary of the support polygon the centre of mass will end up.

The coefficients $c_{3,p}$ and $c_{4,p}$ are chosen such that the point $O_4$ will have zero velocity and acceleration at the beginning and the end of its motion.

## 4   Control System Design

To control the motion of the exoskeleton we use an adaptive feedback controller. A diagram of the control system is presented in Fig. 2.
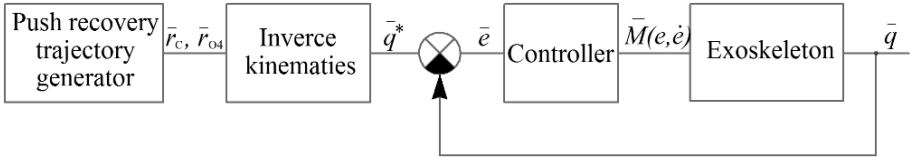


**Fig. 2.**  Diagram of the control system

The following notations are used in Fig. 2: $\vec{q}^*$ is the desired value of the vector of generalised coordinates obtained by solving the inverse kinematics problem, $\vec{e}$ is the control error vector: $\vec{e} = \vec{q}^* - \vec{q}$ and $\dot{\vec{e}} = \dot{\vec{q}}^* - \dot{\vec{q}}$ is its first derivative.

The regulator's action is described by the following equation:

$$\vec{M} = \mathbf{B}^{-1}\mathbf{A}\left(\mathbf{K}_p\vec{e} + \mathbf{K}_d\dot{\vec{e}}\right) \tag{11}$$

where $\mathbf{K}_p$, $\mathbf{K}_d$ are diagonal gain matrices with constant elements (regulator gains) $k_i$ This regulator type was studied, for example, in paper [19] where it was applied to control a lower limb exoskeleton.

## 5   Numerical Simulation

In this chapter we will first consider the case when the exoskeleton is recovering vertical balance after a platform the exoskeleton stands on has rapidly changed its velocity. We will consider a special case when instantaneous velocity changes are inducing in each link of the exoskeleton some nonzero velocities relative to the supporting surface.

Figure 3 illustrates the motion of the exoskeleton as it recovers vertical balance using the control algorithm proposed in the Sect. 3.

We can see that in the first part of the motion the torso leans to the right, allowing the centre of mass to move without changing its velocity, while the exoskeleton performs a step. After the exoskeleton takes the step, it begins to recover vertical balance, allowing the torso to take an upright position. At the end of the motion, the centre of mass is above the centre of the support polygon.
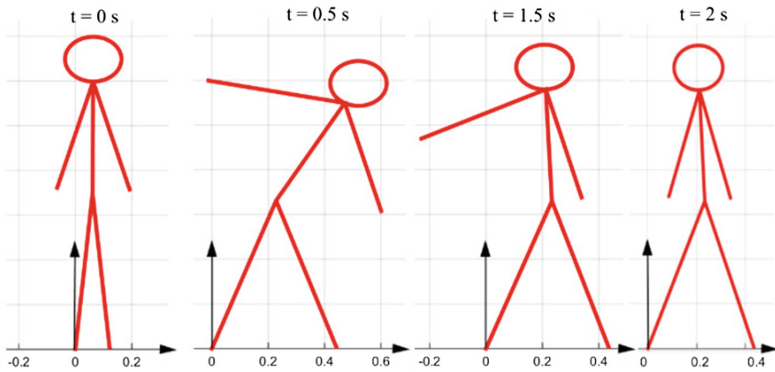
**Fig. 3.** Motion of the exoskeleton during push recovery

In Fig. 4 the time functions of the generalized coordinates are shown for the case when at time $t = 0$ the centre of mass of the exoskeleton here moves with a velocity of 0.5 m/s to the right relative to the ground.
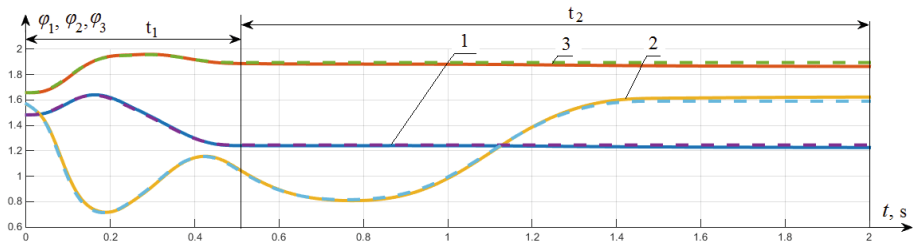


**Fig. 4.** Time functions of the joint angles $1 - \varphi_1$, $2 - \varphi_2$, $3 - \varphi_3$; dashed lines represent the graphs for the desired values of these angles

Analysing the graphs in Fig. 4 one can see that the control system is capable of moving the mechanism along the desired trajectory with high accuracy. We observe that during the second stage of the motion, while the torso returns to the vertical position, both legs demonstrate minimal motion, which is similar to the push recovery behaviour of a human.

Let us consider the case when the exoskeleton is pushed by a force that was applied to the centre of mass on its torso link for a short period of time. In Fig. 5 the graphs for $\varphi_1(t)$, $\varphi_2(t)$ and $\varphi_3(t)$ are shown for the case when a force of 250 N is applied in the horizontal direction during the first 0.1 s of the motion of the exoskeleton.

We can see that in this case the joint angles demonstrate a more oscillatory behaviour during the first stage of the motion, while the second stage is similar to the previously considered case. This shows that the algorithm can work for both types of balance recovery.
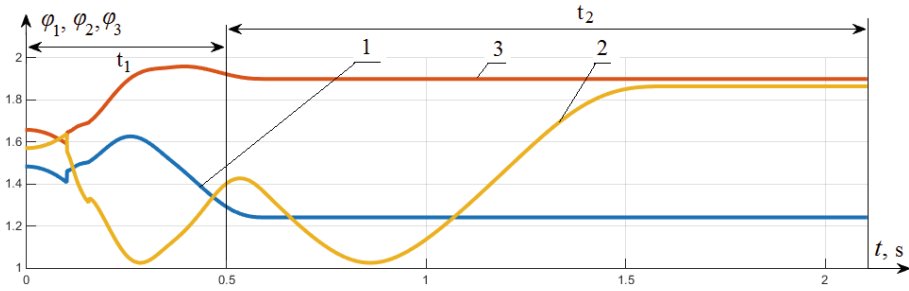
**Fig. 5.** Time functions of the joint angles $1 - \varphi_1$, $2 - \varphi_2$, $3 - \varphi_3$

## 6  Conclusions

In this paper we have presented a model of an exoskeleton moving in a frontal plane. The model allows simulating the exoskeleton's motion during push recovery. A two-stage push recovery algorithm was proposed, which allows the exoskeleton to recover from a situation when its links abruptly gain velocity relative to the supporting surface by taking one step. A control system design that realises the proposed algorithm was shown and simulation was carried out. The simulation showed that the motion of the exoskeleton that uses the proposed algorithm resembles the behaviour of a human in a similar situation.

Future work on this project includes a comparative experimental study of human push recovery behaviours with and without an exoskeleton, using the motion measuring exoskeleton system "Exomeasurer" developed in the Southwest State University.

## References

1. Miranda-Linares, D., Alrezage, G., Tokhi, M.O.: Control of lower limb exoskeleton for elderly assistance on basic mobility tasks. In: 19th International Conference on System Theory, Control and Computing (ICSTCC), pp. 441–446, October 2015
2. O'Sullivan, L., Power, V., Virk, G., Masud, N., Haider, U., Christensen, S., Bai, S., Cuypers, L., D'Havé, M., Vonck, K.: End user needs elicitation for a full-boy exoskeleton to assist the elderly. Procedia Manuf. **3**, 1403–1409 (2015)
3. Low, K.H., Liu, X., Goh, C.H., Yu, H.: Locomotive control of a wearable lower exoskeleton for walking enhancement. J. Vib. Control **12**(12), 1311–1336 (2006)
4. Barbareschi, G., Richards, R., Thornton, M., Carlson, T., Holloway, C.: Statically vs. dynamically balanced gait: analysis of a robotic exoskeleton compared with a human. In: 37th Annual International Conference of the IEEE Engineering in Medicine and Biology Society (EMBC), August 2015, pp. 6728–6731. IEEE (2015)
5. Anam, K., Adel, A.A.-J.: Active exoskeleton control systems: state of the art. Procedia Eng. **41**, 988–994 (2012)

6. Contreras-Vidal, J.L., Grossman, R.G.: NeuroRex: a clinical neural interface roadmap for EEG-based brain machine interfaces to a lower body robotic exoskeleton. In: 35th Annual International Conference of the IEEE Engineering in Medicine and Biology Society (EMBC), July 2013, pp. 1579–1582. IEEE (2013)
7. Jatsun, S., Savin, S., Yatsun, A., Malchikov, A.: Study of controlled motion of exoskeleton moving from sitting to standing position. In: Borangiu, T. (ed.) Advances in Robot Design and Intelligent Control, pp. 165–172. Springer International Publishing, Switzerland (2016)
8. Jatsun, S., Savin, S., Yatsun, A., Turlapov, R.: Adaptive control system for exoskeleton performing sit-to-stand motion. In: 10th International Symposium Mechatronics and Its Applications (ISMA), December 2015, pp. 1–6. IEEE (2015)
9. Jatsun, S.F., Vorochaeva, L., Yatsun, A.S., Savin, S.I.: The modelling of the standing-up process of the anthropomorphic mechanism. In: Proceedings of the International Conference on CLAWAR, pp. 175–182 (2015)
10. Vukobratović, M., Borovac, B.: Zero-moment point—thirty five years of its life. Int. J. Humanoid Rob. **1**(01), 157–173 (2004)
11. Mitobe, K., Capi, G., Nasu, Y.: Control of walking robots based on manipulation of the zero moment point. Robotica **18**(06), 651–657 (2000)
12. Choi, Y., You, B.J., Oh, S.R.: On the stability of indirect ZMP controller for biped robot systems. In: Proceedings, IEEE/RSJ International Conference on Intelligent Robots and Systems (IROS 2004), June 2004, vol. 2, pp. 1966–1971. IEEE (2004)
13. Pratt, J., Carff, J., Drakunov, S., Goswami, A.: Capture point: a step toward humanoid push recovery. In: 6th IEEE-RAS International Conference on Humanoid Robots, December 2007, pp. 200–207. IEEE (2007)
14. Stephens, B.: Humanoid push recovery. In: 7th IEEE-RAS International Conference on Humanoid Robots, November 2007, pp. 589–595. IEEE (2007)
15. Stephens, B.J., Atkeson, C.G.: Push recovery by stepping for humanoid robots with force controlled joints. In: 10th IEEE-RAS International Conference Humanoid Robots (Humanoids), December 2010, pp. 52–59. IEEE (2010)
16. Rebula, J., Canas, F., Pratt, J., Goswami, A.: Learning capture points for humanoid push recovery. In: 7th IEEE-RAS International Conference on Humanoid Robots, November 2007, pp. 65–72. IEEE (2007)
17. Yun, S.K., Goswami, A.: Momentum-based reactive stepping controller on level and non-level ground for humanoid robot push recovery. In: IEEE/RSJ International Conference on Intelligent Robots and Systems (IROS), September 2011, pp. 3943–3950. IEEE (2011)
18. Plagenhoef, S.F., Gaynor, E., Thomas, A.: Anatomical data for analyzing human motion. Res. Q. Exerc. Sport **54**(2), 169–178 (1983)
19. Jatsun, S., Savin, S., Yatsun, A.: Parameter optimization for exoskeleton control system using sobol sequences. In: Proceedings of 21st CISM-IFToMM Symposium on Robot Design (2016) (In publishing)

# Mechanical Design of a Prosthetic Human Arm and its Dynamic Simulation

José Alfredo Leal-Naranjo[1(✉)], Marco Ceccarelli[2],
and Christopher René Torres-San Miguel[1]

[1] Instituto Politécnico Nacional, SEPI ESIME Zacatenco,
Ciudad de México, México
lealnaranjo@gmail.com, ctorress@ipn.mx
[2] LARM: Laboratory of Robotics and Mechatronics,
DiCEM-University of Cassino and South Latium Cassino (FR), Cassino, Italy
ceccarelli@unicas.it

**Abstract.** In this paper the mechanical design of a prosthetic human arm with 7 DOFs that includes the shoulder, elbow and wrist is presented. The objective of this design is to have an anthropomorphic, functional and low cost prosthesis. A set of dynamic simulations were performed to determine the feasibility of the mechanism as well as the torque required to perform the activities. The results show that the design could be a good solution due to the physical characteristics and the kinematic of the system.

**Keywords:** Biomechanics · Upper limb · Prosthetic arm · Prosthetic design

## 1 Introduction

The aim on this work is to present the design of a low-cost functional prosthetic upper limb. Losing the human arm affects the life of a person due to the reduced capability to perform many daily life activities. Shoulder disarticulation is one of the cases with the minor incidences, and for this reason people in this condition do not have many available options [1].

The movement of the human arm is complex and its reproduction is usually achieved artificially with few degrees of freedom (DOF) [2]. Rejection of prosthetic arm is dependent of the amputation level; the most proximal the amputation is, the bigger the rejection rate is [3]. The main reasons of prosthesis abandonment include technical limitations of the device, discomfort, appearance and lack of user training [4]. Nowadays many commercial solutions exist for people with upper limb amputation but they have less degree of freedom than required. Some other systems are not practical for real life and others are not affordable for most of the population.

In [5] a prosthetic shoulder is presented with two actuated DOFs and one passive DOF for the humeral rotation. The first joint is a revolute joint and the second is an inverted slider mechanism. This module was tested with commercial upper limb prosthesis. The MPL [6] is the result of a 6 years program that was sponsored by the Advance Research Projects Agency of USA. It allows patients with different amputation levels to use it. The upper arm is composed by the shoulder with two actuators, a

humeral rotator, elbow and the battery. Its main features are 26° of freedom (including the hand), 17 motors, and a total mass of 4.8 kg with battery and a payload of 155 N with the static wrist. A low-cost prosthetic arm was reported in [7]. This arm includes the shoulder but is limited only to a planar movement. It is made of plastic and the total weight is 1.5 kg. The DEKA Arm [8] is another prosthetic arm, product of a project of DARPA. It is the 3$^{rd}$ generation after 2 years of research. This prosthesis weighs 4.45 kg and has 3 configurations, one for transradial amputation, another for transhumeral and the 3$^{rd}$ one for shoulder disarticulation. The prosthesis includes 10 powered DOFs that are distributed in 6 for the arm and 4 for the hand. This prosthesis can be controlled with different signals like switches, myoelectric signals, and even with targeted re-innervation. He et al. [2] designed the IIR prosthetic limb of 4.45 kg, which consists of a fully actuated arm with 7 DOFs and an underactuated hand with 15 DOFs. It uses differential gear mechanisms at shoulder and wrist in order to minimize the size of the joints and to share the load with two small motors.

The objective of this paper is to present a light prosthetic arm for people with shoulder disarticulation that is able to mimic as much as possible the kinematics of a person during a selected activities of daily living.

## 2   The Human Arm and its Characteristics

The upper limb is composed by the shoulder complex, the arm, the elbow, the forearm, the wrist and the hand, Fig. 1a. Its main bones are the clavicle, scapula, humerus, radius, ulna and the bones of the hand, Fig. 1b. They are connected by different articulations that allow a great mobility to the upper limb. It is one of the most complex and important part of the human body due to its high dexterity.
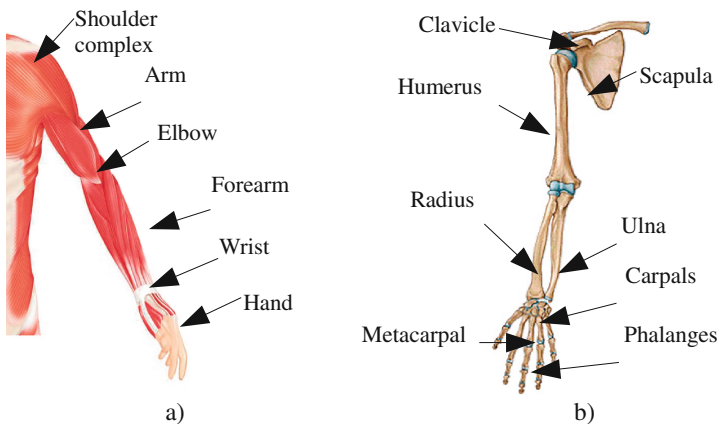


**Fig. 1.**   Anatomy of upper limb: (a) body segments with muscles; (b) main bones

The shoulder is composed by the sternoclavicular joint (sternum and clavicle union), acromioclavicular joint (scapula and clavicle union), glenohumeral joint (humerus and scapula union) and the scapulotoracic joint (union of the scapula with the

thorax through muscles of the back). The shoulder is capable of translations and rotations over a very wide range. The movements of the glenohumeral joint are the abduction-adduction of the humerus, flexion-extension and internal-external rotation [9]. The elbow joint is composed by two articulations and allows flexion and extension of the forearm. These articulations act in conjunction with the joints present in the forearm and make possible the pronation and supination of the hand. The radiocarpal joint (wrist) is a biaxial joint that is composed of the distal end of the radius and the carpal bones. The active movements of the wrist are flexion-extension, adduction (ulnar deviation)-abduction (radial deviation). These two movements are performed around oblique axes [10]. The hand is the most complex part of the upper limb and presents 22 DOFs distributed in the fingers to perform many gestures and grasps. All the above-mentioned articulations give to the arm a mobility whose range of motions is summarized as in Table 1.

**Table 1.** Range of motion of human arm [10]

| Articulation | Movement | Range of motion [°] |
|---|---|---|
| Shoulder | Extension - Flexion | 50–180 |
| | Abduction- Adduction | 180–30 |
| | Internal – external rotation | 100–80 |
| Elbow | Extension-Flexion | 0–145 |
| | Pronation- Supination | 85–90 |
| Wrist | Flexion -Extension | 85–85 |
| | Adduction- Abduction | 45–15 |

Due to the high complexity of the joints in the upper limb, in general the structure of the arm is simplified for prosthetic designs. The shoulder joint is modelled as a socket and ball joint to represent the movements of the flexion-extension, abduction-adduction and internal-external rotation [9]. The elbow is described as a cardan joint, despite in reality the flexion-extension and pronation-supination axes are not perpendicular [11]. In order to represent the two axes of movement of the wrist joint a cardan joint is again considered. Therefore, the kinematic model of human arm can be identified as an anthropomorphic 7-revolute joint serial arm.

## 3   Conceptual Design and CAD Solution

The design of a prosthetic device must be capable to reproduce as close as possible the human motion. The lack of dexterity of the prosthetic arm yields to compensatory movements [4] that could cause injuries in the long term. Although there are many prosthetic arms already available, there are still issues that need to be solved.

The design of an upper limb prosthesis involves the selection of appropriates actuators and mechanisms that will move the device. The anthropomorphic shape limits the size of the actuators whose high power density is crucial to allow the prosthesis to exert the required torques and forces during the activities. The control system in
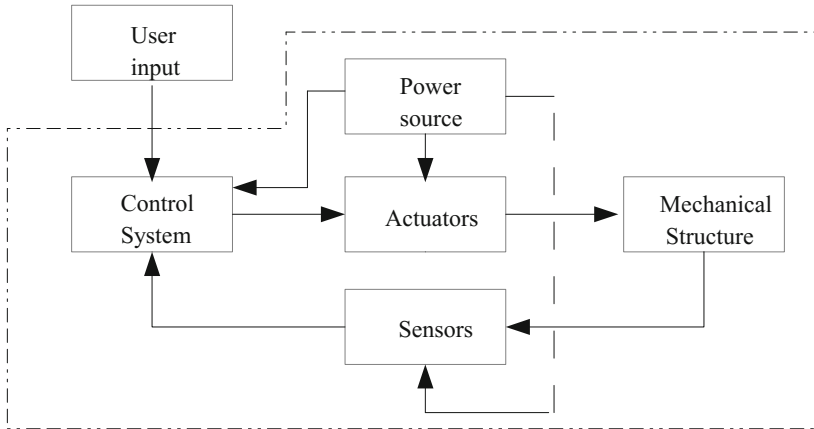
**Fig. 2.** A block diagram describing a system design for a prosthetic arm

conjunction with the sensors makes possible to the user to operate in a proper way the prosthetic device. A block diagram in Fig. 2 shows how the different components of the prosthetic arm can work together.

The shoulder of the prosthetic arm can be designed as a spherical parallel manipulator like the one that was conceived by Gosselin for other purposes [12]. This manipulator is formed by three identical arms. Each arm is made by three revolute join arranged in such a way that every axis of rotation converges to the same centre of rotation, Fig. 3. This arrangement gives to the manipulator 3 rotational degrees of freedom. These DOFs permit the motions of shoulder abduction- adduction, flexion-extension and inter-external rotation.
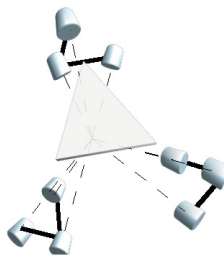


**Fig. 3.** Kinematic diagram of the 3 DOFs manipulator conceived by Gosselin

The flexion-extension elbow motion is achieved by means of a four bar mechanism. This makes possible to host the actuating motor in a location near the shoulder. Placing the weight closer to the shoulder reduces the rotational inertia. Furthermore, the four bar linkage can be set in a configuration in which the motor delivers higher torque in the position where it is most necessary.

The wrist is formed by the spherical manipulator that allows the forearm pronation-supination, ulnar-radial deviation and wrist flexion extension movements.

The proposed mechanism is assembled to form an anthropomorphic prosthetic arm, Fig. 4a. The shoulder contains the 3DOF spherical manipulator with its actuators. The end effector of the manipulator is rigidly attached to the forearm structure by means of a link. The motor that actuates the elbow is fixed at the base of the forearm, Fig. 4b. The spherical mechanism allows the three movements that the shoulder requires and the 3 motors share the load with small motors. Hence the prosthetic arm can be designed with anthropometric shape and volume. The focus of this work is on the design of the upper limb without the hand but for simulation purposes a mass of 500 gr to represent the load of the hand is included. The overall weight of the design, including the hand is 1,250 gr. Inside of the structure of the prosthesis there is enough room to allocate the power supply and control system.



a)                                    b)
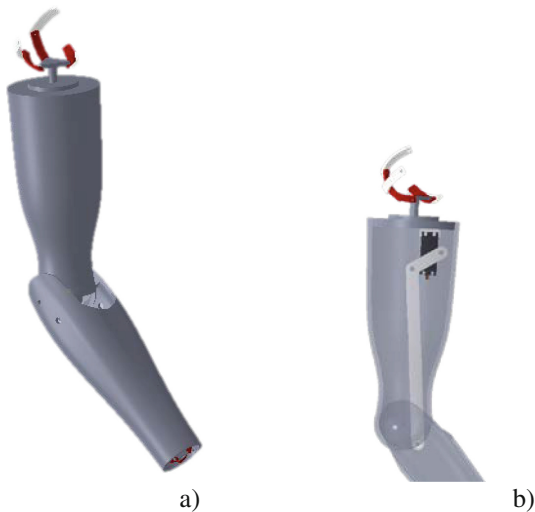
**Fig. 4.** Prosthetic arm (a) CAD model; (b) View of the mechanism actuating the elbow

## 4   Motion Simulation and Results

The proposed designed was modelled in Solid Works ®. A dynamic simulation was performed to evaluate the behaviour of the device when following three different trajectories. The output torques were obtained in order to design the actuation system. In all the simulations, a load of 10 N was applied in the hand to represent the payload that the prosthesis must be able to move.

The first task simulated was the flexion motion of the shoulder, Fig. 5a. The amplitude of the movement was planned of 90° starting with the arm totally vertical. The duration of the motion was 2 s with a sinusoidal velocity. The second simulation motion
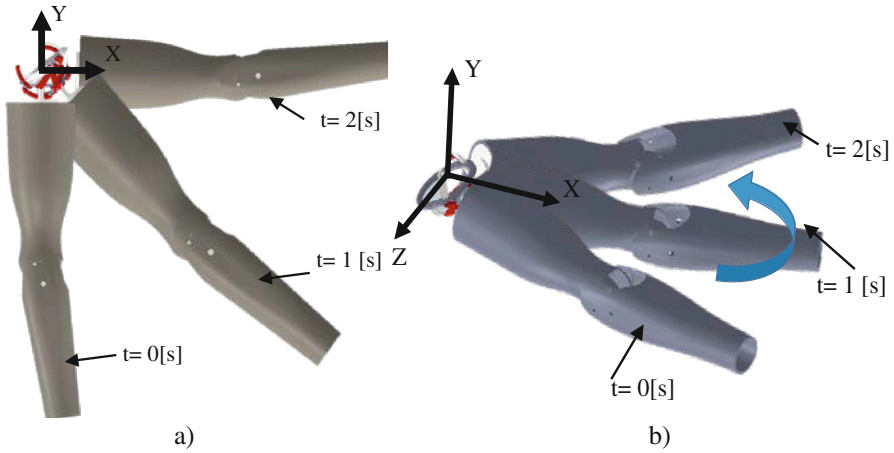
**Fig. 5.** Position of the prosthesis at different moments of the simulation: (a) first simulation; (b) second simulation

was an abduction movement with the prosthetic positioned in the horizontal plane, Fig. 5b. The amplitude of the movement was of 70° with duration of 2 s. The last simulation consisted in a flexion of the elbow from 0° up to 100° of with duration of 3 s.

The results show for the first and second simulations that when the prosthesis follows the desired trajectories, the three motors perform smooth movements, Fig. 6a and c. In Fig. 6b shows the torques to perform the prescribed movement of the test. The maximum torque occurs in a different moment than the maximum velocity. It can be seen that the maximum torques for the motor 1 and 3 take place at the end of the movement while motor 2 produces its largest torque at t = 1.4 s. But the maximum torque is 6 Nm. For the second test the main part of the movement is due to one motor, Fig. 6c. The largest torques occur at the very beginning of the test for motors 1 and 2. Motor 3 has a sudden increase at the final stage of the movement, reaching its maximum value at the end of the action. The maximum torque is 15 Nm. For the elbow flexion the motor performs a smooth sinusoidal movement, Fig. 6e, with a limited torque variation with respect to the maximum torque of 6.2 Nm occurring at the middle of the motion.
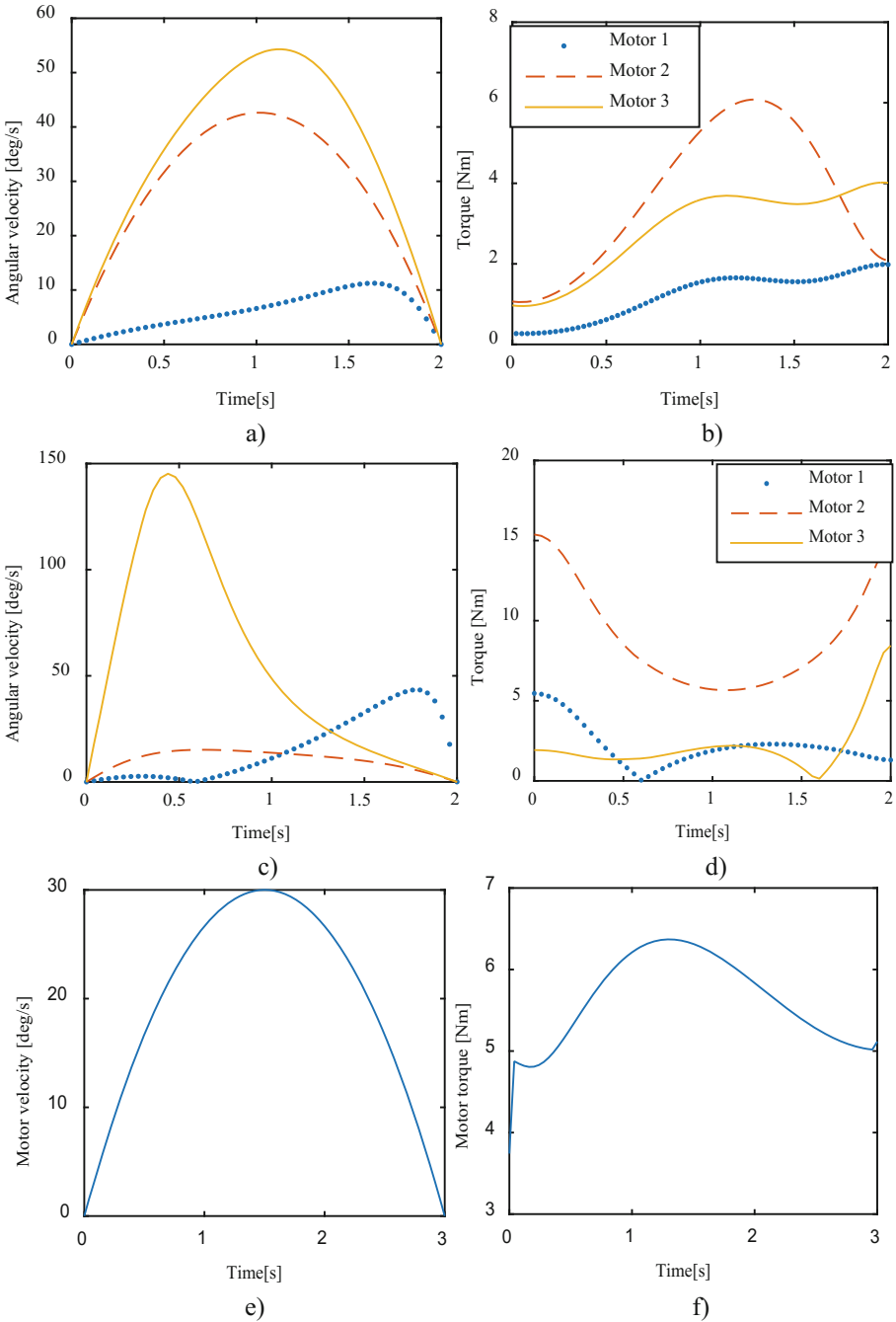
**Fig. 6.** Results from the simulations: (a) angular velocity from simulation 1; (b) motor torque from simulation 1; (c) angular velocity from simulation 2; (d) motor torque from simulation 2; (e) angular velocity from simulation 3; (f) motor torque from simulation 3

## 5   Conclusions

In this work the design of a 7 DOFs prosthetic arm is presented with an anthropo-morphic shape. The simulations show that typical motions are performed with a minimum of 15 Nm for the torque of motors. The actuators' torque is highly dependent of the configuration of the designed mechanisms that can be properly sized for more efficient operation. It is worth to mention that during the simulations the mechanisms did not reach any singular configuration. The simulation results show the feasibility of the operation with a mechanical design with light human-like structure.

## References

1. Dillingham, T., Pezzin, L., MacKenzie, E.: Limb amputation and limb deficiency: epidemiology and recent trends in the United States. South. Med. J. **95**(8), 875–883 (2002)
2. McFarland, L., Hubbard, S., Heinemann, A., Jones, M., Esquenazi, A.: Unilateral upper-limb loss: satisfaction and prosthetic device use in veterans and service members from Vietnam and OIF/OEF conflicts. J. Rehabil. Res. Dev. **47**, 299–316 (2010)
3. He, L., Xiong, C., Zhang, K.: Mechatronic design of an upper limb prosthesis with a hand. In: Zhang, X., Liu, H., Chen, Z., Wang, N. (eds.) ICIRA 2014. LNCS (LNAI), vol. 8917, pp. 56–66. Springer, Heidelberg (2014). doi:10.1007/978-3-319-13966-1_6
4. Metzger, A., Dromerick, A., Holley, R., Lum, P.: Characterization of compensatory trunk movements during prosthetic upper limb reaching tasks. Arch. Phys. Med. Rehabil. **93**(11), 2029–2034 (2012)
5. Troncossi, M., Borghi, C., Chiossi, M., Davalli, A., Parenti-Castelli, V.: Development of a prosthesis shoulder mechanism for upper limb amputees: application of an original design methodology to optimize functionality and wearability. Med. Biol. Eng. Compu. **47**, 523–531 (2009)
6. Johannes, M., Bigelow, J., Burck, J., Harshbarger, S., Kozlowski, M., Van Doren, T.: An overview of the developmental process for the modular prosthetic limb. Johns Hopkins APL Tech. Dig. **30**(3), 207–216 (2011)
7. Mohd, M., Jamil, M.: Biomechatronics design of a novel artificial arm. In: Biomedical Engineering International Conference (2013)
8. Resnik, L., Klinger, S., Etter, K.: The DEKA arm: Its features, functionality, and evolution during the veterans affairs study to optimize the DEKA arm. Prosthet. Orthot. Int. **38**(6), 1–13 (2013)
9. Luinge, H., Veltink, P., Baten, C.: Ambulatory measurement of arm orientation. J. Biomech. **40**(1), 78–85 (2007)

10. Kapandji, I.: The Physiology of the Joints Volume I: Editorial Medica Panamericana, Madrid (2006). (in spanish)
11. Kecskemethy, A., Weinberg, A.: An improved elasto-kinematic model of the human forearm for biofidelic medical diagnosis. Multibody Sys. Dyn. **14**, 1–21 (2005)
12. Gosselin, C.: Kinematic analysis optimization and programming of parallel robotic manipulators. Montreal (1988)

# Effects of Passive Ankle Exoskeleton on Human Energy Expenditure: Pilot Evaluation

Miha Dežman[✉], Tadej Debevec, Jan Babič, and Andrej Gams

Humanoid and Cognitive Robotics Lab, Department of Automatics,
Biocybernetics and Robotics, Jožef Stefan Institute, Ljubljana, Slovenia
`miha.dezman@ijs.si`

**Abstract.** Exoskeletons can be utilized for rehabilitation purposes as well as for assistance and augmentation of motion of patients with disabilities, workers, elderly and even healthy people. Compared to powered solutions, unpowered passive exoskeletons have been shown to have significantly higher chances of end user acceptance, because of simpler design, no complex electronics and potentially lower cost. In this paper we present the results of a flat walking test using an unpowered passive ankle exoskeleton. Important exoskeleton aspects such as ergonomics, comfort, and robust design are outlined and areas for improvement are highlighted. The paper also presents the results of the evaluation of the exoskeleton device in a pilot study, where its physiological effects are assessed for four participants via measurements of oxygen consumption and EMG muscle activity during five 10-min walking sessions under different conditions. Results show that significant metabolic cost reduction can only be achieved with a proper mechanism spring selection.

**Keywords:** Passive exoskeleton · Passive orthosis · Metabolic cost · Efficient walking · Energy cost reduction

## 1 Introduction

Exoskeleton technology has been, since its beginnings roughly 50 years ago [1], witnessing intense development [2]. Recent advances in actuators, sensors, materials, batteries and computer processors further intensified the development of wearable technology [3]. Furthermore, the increasing longevity and declining birth rate in post-industrial societies will in the future affect health spending, retirement policies, use of long-term care services, work-flow policies, and income [4]. This has led to an increase in the research of exoskeletons.

An important part of everyday human activities is walking, that apart from providing individual social independence also has significant effects on human near-term and long-term health [5]. Consequently, a considerable amount of exoskeleton development is now focused on the augmentation of lower extremities to assist walking. One of the aims of lower extremities exoskeleton research is the reduction of metabolic expenditure, which can be achieved in different ways.

Ferris et al. [6] have shown that muscle effort reduction of the hip and in the ankle can be achieved by providing assistance to the human hip only. Gams et al. [7] showed that statistically significant decrease in metabolic cost can be observed when using a robotic knee exoskeleton during periodic squats, if a proper control method is applied. Periodic squatting was used to roughly approximate human walking over a rough terrain. In a study by Galle et al. [8] it was shown that the metabolic reduction gets better with practice, because of neuro motor adaptation. Humans adapt other muscles on other joints, apart from the one that is actuated with the use of an exoskeleton, which then significantly reduces muscular activity in all leg muscles.

Jimenez-Fabian et al. [9] and Gams et al. [7] have shown that besides the exoskeleton design, the chosen control strategy can have a big impact on the end resulting metabolic reduction. Proportional myoelectric control shows some distinctive advantages over other types of control [10]. To accommodate uncertain dynamics of the human-robot system, iterative learning can prove to be very effective in learning of control of cyclic tasks [11]. The chosen control strategy can also have an effect on the human adaptation to the exoskeletons [12].

Another way to achieve metabolic reduction is with the use of passive solutions that do not use motors, batteries or controllers. These solutions can prove to be superior in some aspects to actuated solutions, because their weight, complexity and price make them simpler, more affordable and perhaps easier to introduce into everyday lives. Sawicki et al. [13] outlined the importance of tendons in human walking that enhance the efficiency of the ankle joint work, by storing and releasing elastic energy in the Achilles tendon during each step.

Collins et al. [14] presented an unpowered exoskeleton that achieved metabolic reduction of human walking with a completely passive device. The exoskeleton they presented used a spring between the insole and the frame around the calf. The spring is attached to a mechanical clutch, which allows the spring to store energy at some parts of the gait, release it at an appropriate time, and not hinder the motion while the leg is in the swing phase.

In this paper we present our implementation of such an unpowered exoskeleton. The goal of our research was to: (1) get insight into the workings of the unpowered exoskeleton; (2) confirm whether the exoskeleton reduces metabolic cost as intended; and (3) narrow the range of the appropriate spring stiffness that can achieve the reduction of metabolic cost. The exoskeleton presented here uses the same principle as the original, [14]. We replicated the exoskeleton and performed tests in order learn more about the concept and to find ways to improve the current design. We used different materials and introduced some minor changes in the design to make production cheaper and assembling more convenient. A small study was performed to test the exoskeleton and to see if a reduction in metabolic cost of walking can be observed.

## 2 Exoskeleton Design and Mechanics

We designed a prototype passive ankle exoskeleton based on the work of Collins et al. [14]. Our goal was to achieve a working prototype in as little iterations as possible. With this in mind, we incorporated some changes and used different materials to make

the production faster, cheaper and more convenient. The working principle, however, stayed the same as in the original work.

The exoskeleton comprises an insole part, a simple hinge joint, a stainless steel frame, an attachment strap, a mechanical clutch and a linear tension spring, as shown in Fig. 1. The frame of the exoskeleton is connected to the insole with a simple hinge joint. The user attaches it to the leg with a strap.
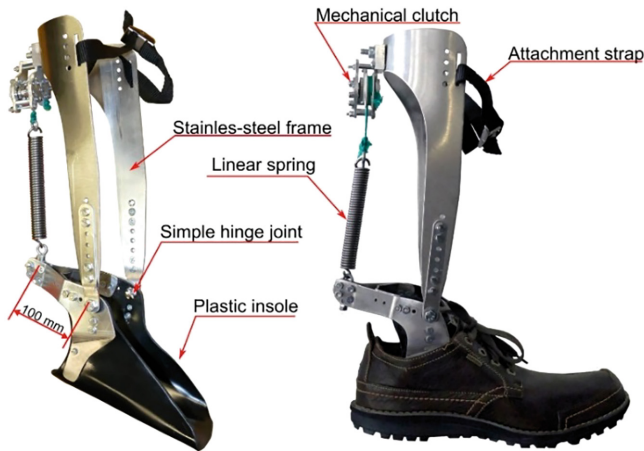


**Fig. 1.** Our prototype version of the unpowered passive ankle exoskeleton

A separate mirrored exoskeleton was made for the other leg. Plastic material was used to construct the insole part using a heat-forming process and reinforced with a stainless steel insole frame. The insole shape was designed to be comfortable and to still fit into an average adult male shoe. Thus, the users could use their own shoes.

Stainless steel, which is rigid and light enough, was used to construct the leg frame. A material with a larger strength/weight ratio could also be used. Due to the relatively high strength/weight ratio and accessibility of this material, we performed no weight/ strength optimization. The exoskeleton presented in this paper weights 0.8 kg. We believe, however, that the weight could be significantly reduced in next design iteration.

The mechanical clutch design (Fig. 2) is largely based on the original [14], with some modifications to make the production and assembly more convenient. Its components were manufactured out of aluminium, stainless steel and plastic, using laser-cutting process and 3D-addition technologies. The working principle of the clutch stayed the same as in the original.

Throughout the construction process we found out that the following aspects of exoskeleton design have to be taken into consideration. To maximize the effectiveness, commercial value and potential user acceptance, the exoskeleton should be as simple as possible. The possibility to use own shoes and donning the exoskeleton over clothes makes an impression that the exoskeleton is very simple and easy to use. The exoskeleton should be easy to don-on or don-off. Ergonomic design is an important factor of comfort and safety. The exoskeleton should not impede on the user, which

means that its kinematic obstruction should be minimal. Consequently the exoskeleton should have an appropriate size, movement range and enough kinematic degrees of freedom. It should also have minimal weight and minimal inertia, whereas it should still be sturdy enough for the intended task.
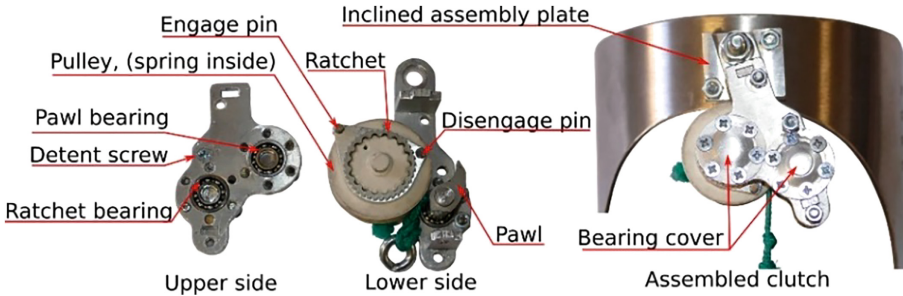


**Fig. 2.** Our mechanical clutch assembly

In the current design of the passive exoskeleton we found out that the pawl engaging and disengaging is an important factor of proper operation. During the gait phase, locking of the pawl relies only on gravity. Because the pawl is very small, the force of gravity is not very large. As a result, the working of the clutch is not very robust. Simply the friction in the pawl bearing can be large enough to prevent the pawl from engaging correctly. To accommodate this, we designed the shaft to only loosely fit the bearing. This makes the use of a rolling bearing unnecessary.

To magnify the effect of gravity on the movement of the pawl, we added an inclined assembly plate that keeps the mechanical clutch at a certain angle to the exoskeleton frame. This increased the reliability of the clutch. Using a different design approach, the usage of this plate could be prevented. The size of the ratchet teeth is an open issue. The one in our prototype should have larger teeth. This would prevent unwanted disengagement of the pawl during the walk, which proves to be problematic, since the disengagement of the clutch affects the kinematics of the walk. The user, relying on the pawl to engage, can stumble because he does not expect the sudden release of exoskeleton assistance.

Another issue is timing, which is determined by the positions of the engage pin and disengage pin, and depends also on the length of the rope. The problem is that the exchange of the spring with a spring of different stiffness can compromise the timing if the spring does not have an appropriate length, keeping in mind that springs of different characteristics normally have a different length, if the outer diameter of the spring and the thickness of the wire are the same.

The original exoskeleton from [14] had a system that could adjust the length of the rope with a screw. This is not very practical, especially if the exchange needs to be very fast. The use of a rope is also problematic since it is hard to tie it at a specific length.

## 3   Metabolic Cost Study Design

A randomized cross-over study was employed in order to evaluate the efficiency of the passive ankle exoskeleton. Four healthy males volunteered to participate in the study. They were informed about the procedures beforehand and gave a free informed consent. The baselines of participant characteristics are outlined in Table 1. The participants were asked to perform five 10-min series of walks on a horizontal treadmill at a constant speed of 4 km/h. Between the walking sessions, the subjects rested for at least 15-min, sitting on a chair.

**Table 1.**  Baseline participant characteristics

| Characteristic | Mean | Standard deviation |
|---|---|---|
| Age (years) | 30 | 7 |
| Weight (kg) | 76 | 5 |
| Height (cm) | 178 | 3 |
| Body Mass Index (kg/m$^2$) | 24 | 1 |

The five series consisted of a referential exoskeleton free walk; a walk with a springless exoskeleton; and three walks with the exoskeleton on both legs, but with spring of different characteristics (5 N/mm, 12 N/mm and 20 N/mm). The order of sessions was randomized for each participant.

To evaluate the exoskeleton operation and its effect on the user, we measured the *average oxygen consumption* ($VO_2$) of each user using a portable metabolic cart (K4b$^2$, Cosmed Italy). The whole measurement system is presented in Fig. 3(a). To assess the overall muscle effort during walking, we also measured the EMG activity of the Soleus muscle on the right calf of each participant. The signals were rectified and integrated for a time of 7-min, out of a 10-min walking session, to exclude the starting and ending discrepancies, and normalized to the normal walking value, as shown in Eq. (1).
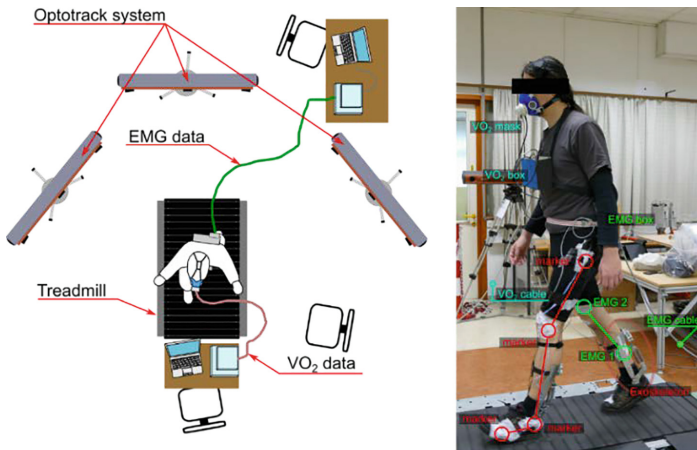


**Fig. 3.**  (a) Measurement system; (b) Participant during the test

$$E_{ki} = \int_{1.5min}^{8.5min} |U_{ki}(t)|dt / \int_{1.5min}^{8.5min} |U_{kn}(t)|dt \cdot 100\%, \quad (1)$$

where $E_{ki}$ is the integrated EMG response. $U_{kn}(t)$ is the EMG voltage with respect to time, where $n$ denotes normal walking session for a specific participant $k$ and $i$ denotes the walking session for five different boundary conditions. The EMG signals were recorded using the surface electrodes and the DataLog (Biometrics Ltd.) data acquisition device. The oxygen consumption and EMG activity were then compared between groups of participants and different boundary conditions using average value (2) and sample standard deviation (3) for four participants:

$$\bar{E}_i = \frac{1}{4} \sum_{k=1}^{4} E_{ki}, \quad (2)$$

$$S_{Ei} = \sqrt{\frac{1}{3}\left((E_{ki}) - \bar{E}_i\right)^2}, \quad (3)$$

where again the $k$ represents a participant and $i$ the chosen boundary condition.

## 4    Results

Figures 4 and 5 show the graph of measured $VO_2$ response and EMG activity of muscles depending on the boundary conditions. The measurement is divided into the average values for the first pair, then for the second pair and then for all four participants.

For participants 1 and 2, as shown in the Fig. 4, a decrease of average metabolic cost ($-10\%$) can be observed compared to normal walking, when using the exoskeleton with a spring of stiffness 5 N/mm. The decrease of average metabolic cost using
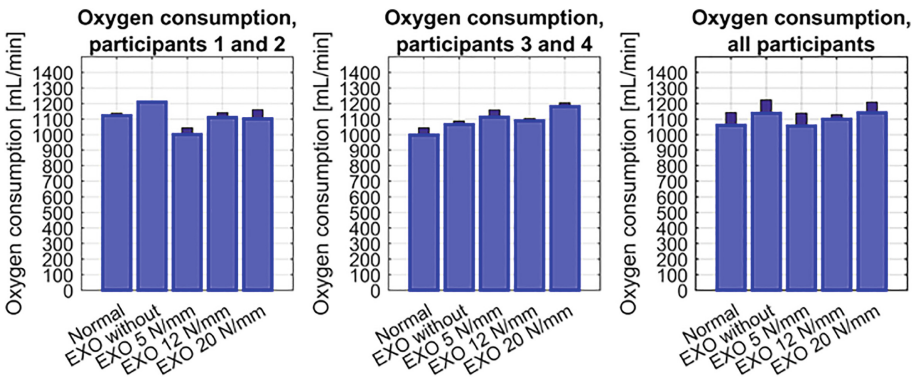


**Fig. 4.** Average Oxygen consumption and sample standard deviation for the first and second pair, and all of participants
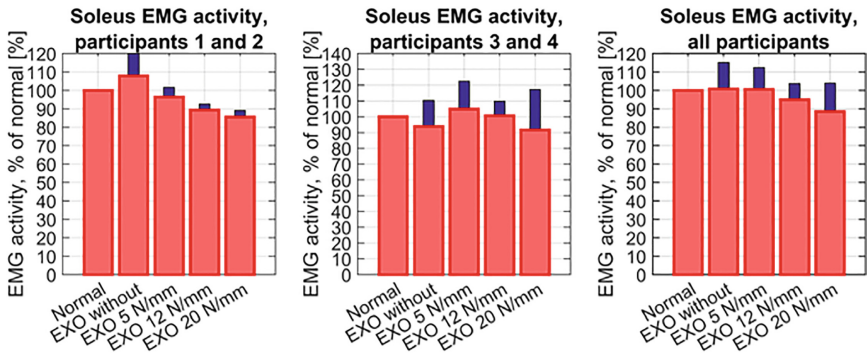
**Fig. 5.** Average Soleus muscle EMG activity and sample standard deviation for first and second pair and all of participants

springs of other stiffness can also be observed, but is not as apparent. The range of appropriate spring stiffness can thus be narrowed to an area lower than 12 N/mm and near 5 N/mm. The exoskeleton without the spring produced some load or constriction on the user, since the metabolic cost has risen significantly (+8%), compared to normal walking. The main cause could lie in the added weight (0.8 kg) or in the introduced kinematic constraints.

For participant 3 and 4, as seen in Fig. 4, the mechanism shows less promising results. With the usage of the exoskeleton, the average metabolic cost has risen in every series. The main reason for a change in results between the first pair and the second pair could be the wrong timing setup. Between the second and third participant the rope on one of the exoskeletons snapped because of wear and was then exchanged. The clutch timing was then probably compromised. This points at the importance of the timing of the engaging and disengaging of the mechanical clutch.

The average metabolic cost for all participants is shown in the last graph in Fig. 4. A decrease of metabolic cost can be seen when walking with the exoskeleton with the 5 N/mm spring. However, the reduction is not great compared to normal walking.

The exoskeleton effect on the Soleus muscle was approximated by measuring its EMG activity. The results are shown in Fig. 5; unexpectedly, the results do not directly coincide with the average oxygen consumption. For participants 1 and 2, as shown in the first graph of Fig. 5, the use of the exoskeleton increases the metabolic cost, which is expected. The Soleus EMG activity is smallest when stiffness is 20 N/mm, and not 5 N/mm, as in the measurement of the average oxygen consumption. This indicates that some other muscles are the source for the metabolic reduction, and not the measured Soleus muscle. Results for participants 3 and 4, shown in the second graph in Fig. 5 are different. This supports the assertion that the exoskeleton effect did change because of compromised clutch timing. Some decrease of EMG activity indicates that the effect is postponed to springs of greater stiffness. The third graph, showing the average for all the participants, shows the decrease of Soleus muscle activity.

## 5   Conclusion

The collected data shows that the exoskeleton can reduce the metabolic cost of walking, if the clutch timing is correct and if appropriate spring stiffness is chosen.

The exoskeleton ergonomic design seems to be important, since it can influence the metabolic cost reduction greatly. An important aspect is also the introduced kinematic constraints that can increase the metabolic load on the user. Therefore, special attention is needed in the light-weight exoskeleton design and weight/strength optimization. The clutch mechanism has some weak points that reduce the overall robustness of the clutch operation. When designing the clutch, focus at these areas is recommended. Based on the results, the appropriate spring stiffness seems to be smaller than 12 N/mm and near 5 N/mm. The pilot study confirmed the potential of the unpowered ankle exoskeleton for reducing the energy cost of walking.

## References

1. Vukobratovic, M.K.: When were active exoskeletons actually born? Int. J. Humanoid Rob. **4**(3), 459–486 (2007)
2. Ferris, D.P.: The exoskeletons are here. J. Neuroeng. Rehabil. 6(1), 17–19 (2009)
3. Viteckova, S., Kutilek, P., Jirina, M.: Wearable lower limb robotics: A review. Biocybernetics Biomed. Eng. **33**(2), 96–105 (2013)
4. Gray, A.: Population ageing and health care expenditure. Ageing Horiz. **2**, 15–20 (2005)
5. Morris, J.N., Hardman, A.E.: Walking to health. Sports Med. **23**(5), 306–332 (1997)
6. Ferris, D.P., Sawicki, G.S., Domingo, A.: Powered lower limb orthoses for gait rehabilitation. Top. Spinal Cord Inj. Rehabil. **11**(2), 34 (2005)
7. Gams, A., Petric, T., Debevec, T., Babic, J.: Effects of robotic knee exoskeleton on human energy expenditure. IEEE Trans. Biomed. Eng. **60**(6), 1636–1644 (2013)
8. Galle, S., Malcolm, P., Derave, W., De Clercq, D.: Adaptation to walking with an exoskeleton that assists ankle extension. Gait Posture **38**(3), 495–499 (2013)
9. Jimenez-Fabian, R., Verlinden, O.: Review of control algorithms for robotic ankle systems in lower-limb orthoses, prostheses, and exoskeletons. Med. Eng. Phys. **34**(4), 397–408 (2012)
10. Ferris, D.P., Lewis, C.L.: Robotic lower limb exoskeletons using proportional myoelectric control. In: Annual International Conference of the IEEE Engineering in Medicine and Biology Society, pp. 2119–2124. IEEE (2009)
11. Zhang, J., Cheah, C.C., Collins, S.H.: Experimental comparison of torque control methods on an ankle exoskeleton during human walking. In: IEEE International Conference on Robotics and Automation (ICRA), pp. 5584–5589. IEEE (2015)
12. Cain, S.M., Gordon, K.E., Ferris, D.P.: Locomotor adaptation to a powered ankle-foot orthosis depends on control method. J. Neuroengineering Rehabil. **4**(1), 1 (2007)
13. Sawicki, G.S., Lewis, C.L., Ferris, D.: It pays to have a spring in your step. Exerc. Sport Sci. Rev. **37**(3), 130 (2009)
14. Collins, S.H., Wiggin, M.B., Sawicki, G.S.: Reducing the energy cost of human walking using an unpowered exoskeleton. Nature **522**(7555), 212–215 (2015)

# Prospects of Robotics Development
# for Restorative Medicine

Maksim Arkhipov[1](✉), Aleksey Leskov[2], Vadim Golovin[1],
Yuriy Gercik[2], and Liudmila Kocherevskaya[3]

[1] Moscow Polytechnic University, Moscow, Russia
medicalrobot@mail.ru
[2] Bauman Moscow State Technical University, Moscow, Russia
[3] The Russian Presidential Academy of National Economy and Public
Administration, Moscow, Russia

**Abstract.** In this paper the automation of massage as one of the most effective restorative medicine techniques is considered. The aim is to increase the working ability of people. The implementation of robotics in preventive restorative medicine is the first phase of automation. The general problems of robotics are connected with the features of non-invasive interaction of the robot with viscous-elastic soft tissues. The method of most natural training by demonstration of the necessary trajectory, taking into account the deforming of soft tissues and then the reproduction of recorded data, is proposed. The method of force points training with program input of assigned forces is a special case of spatial training by demonstration with manual input of assigned forces. Some biomechatronic modules for the realization of training by demonstration and reproduction of recorded data are proposed. For experimental investigations the method of imitation of patient's mobility while breathing is considered. The research results open perspectives on several projects of robotic systems. The robotic systems performing more fine massage techniques for injured people with consequences of cerebral palsy and stroke will be further developed. The reasons of the lack of demand and prospects of development of robotics for restorative medicine are also analysed.

**Keywords:** Prospect · Robotics · Restorative medicine · Human - machine system · Massage · Surgery · Demonstration training · Compliant control · Biomechatronic module

## 1 Introduction

Among many directions for restorative medicine (balneotherapy, hirudotherapy, electrical stimulation, ozone therapy and others) the methods associated with mechanical action on the human body, including various massage techniques occupy a certain place as a non-drug method [8].

Many nations of the world created for centuries a culture of healing, where movement and mechanical impact had the leading role. In Eastern physical culture the alternation of loading and unloading, concentration and relaxation, active and passive recreation are of particular importance. For the modern man there is particularly

relevant physical culture, which is characterized not only by active intentional movements, but also by passive ones including a variety of massage, post isometric relaxation and other relaxation and mobilization techniques. The new techniques of combined application of massage, for example, with melotherapy, thermotherapy, aromatherapy and active movements can be effective [9].

Fatigue as a result of physical and mental efforts is one of the reasons for the declining of working ability that is studied in the labour hygiene. Physical fatigue is accompanied by a number of objective characteristics, expressed in muscle compaction, muscle pain, difficulty of movements and others.

Massage is an effective and widely accessible means to recover someone's working ability after physical fatigue and it is also a reliable means of occupational diseases prevention. Massage of tired muscles not only restores an initial muscular working ability but also increases it. Manual therapy and massage are necessary for a much wider range of people. Often there are people for whom the labour activity is exposed by hypodynamy. They are conference participants, administrators, lecturers and students, PC users, workers on the conveyor, truck drivers. Manual therapy and massage are necessary for physically overloaded people - athletes, astronauts, pilots and military men [14]. Apparatus as masseur assistants appeared and massage chairs and robots are the most developed means for this scope.

## 2   Robots in Preventive Medicine

The implementation phase of robotics in preventive medicine is most simple and safe technically. It is necessary to solve a number of problems before solving the problem of finer controlled mechanical effects for athletes, injured patients and the effects of cerebral palsy and stroke.

Academician N. Pirogov said that "the future belongs to preventive medicine. This science, going hand in hand with medical science, will bring undoubted benefit to humanity". Nobel Prize winner Pavlov I. emphasized a special role of preventive medicine. He said that "preventive medicine reaches the social purposes only in case of transition from pathology medicine to medicine of health of the healthy".

The Russian scientist N.V. Zabludovsky wrote in his dissertation "Materials to a question on massage action on healthy" in 1882 about the necessity of applying massage apparatus for healthy people: "Is it possible to take advantage of mechanical improvements to design machines that would replace manual actions, or even machine action would be more preferable than manual action? It would be necessary to invent the machine in which the force could be defined in numbers during each moment and deal with numbers instead of the masseur's work, depending on subjective muscular feeling", [8].

Currently, there are mobile robots and robot chairs to perform the mechanical impacts on the patient, but manipulative robots performing movements similar to the doctor's hand are the most effective.

Considering the above, the concept of development and implementation of adaptive and intelligent manipulation robots to improve the health of people and to improve their working ability on a large scale is very important.

## 3    Methods of Robotics for Restorative Medicine

In terms of mechanics, massage task is the deforming of soft tissues (ST). Also, at massage the blood and lymph vessels are deformed causing a draining effect, although the main massage effect is a reflex one. There are studies of the properties of ST [11] related to the diagnosis of tumours and research [12] related to the development of copying surgical manipulators. However, the problems of tumour recognition of and surgical manipulations on the ST differ from the tasks of controlled non-invasive ST deforming.

The developed framework of force interaction theory and control in contact problems suppose the interactions, mainly with solid bodies of non-biological nature, whereas the control objects of systems in massage are biological ST, having a number of features as the viscous-elastic bodies with non-linear characteristics and different properties [2].

The need for taking into account the interaction of the robot with ST leads to the idea of robot training trajectories, which reflect the assigned movement $X_0$ and force $F_0$, moreover in the most natural form of training - showing the necessary movement [6]. The training system is of man-machine type, in which the forces are not given programmatically by knowledge base, but by the sensitive masseur's hand. This is not a video screening but the reproduction of the masseur's force induced sensations by the robot. The scheme of performance of robotic massage modes is shown in Fig. 1. The first control phase is training by demonstration.
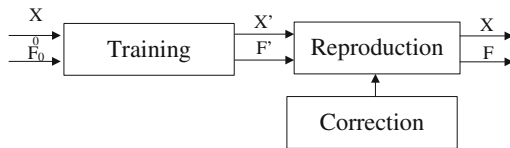


**Fig. 1.** The scheme of performance of robotic massage modes

The method of training by demonstration, considering ST deforming is significantly different from the well-known non-contact method of training of continuous geometric trajectories [10], such as they are used in spray painting or from the non-contact method of training of selected nodes from manual panel. The functional scheme of the robot trained by demonstration [6] is shown in Fig. 2. The purpose of the control is that a real force of interaction of the operator-masseur tool with ST should be developed by the operator on the handle to which the instrument is attached, in other words $F \rightarrow F_0$.

Since the operator-masseur deforms the ST not directly hand but using a tool, a definite training of the masseur to feel the ST through the instrument is necessary.
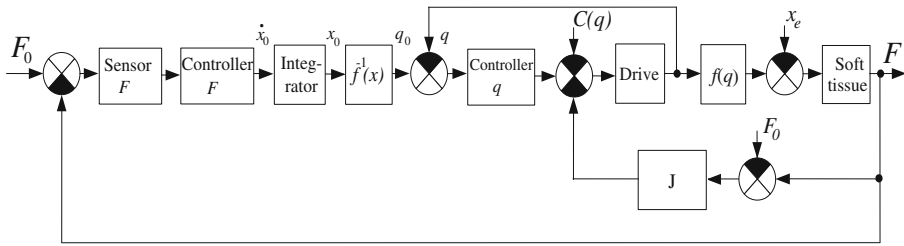
**Fig. 2.** Scheme of system of training by demonstration in view of ST deforming

The system of training force points, containing only one force component $F_z$, measured by one-component force sensor along the tool axis robot, directed perpendicular to the surface of the ST is a special case of the spatial training by demonstration system [5].

Indeed, $\{A_i;\ F_z\} = \{(x, y, z, o, a, t, F_z)^T\}$ is a set of force points and Fz is the programmed force. In the case of training by demonstration the continuous trajectory consists of force points, including six force components measured by a 6-component force sensor.

$\{A_i;\ F\} = \{(x, y, z, o, a, t, F_x, F_y, F_z, M_x, M_y, M_z)^T\}$ is a set of force points trained by demonstration and F is assigned manually. So, we have $A^{F_z} \subset A^F$.

Most experimental studies have been performed [2] with the robot, equipped with a system for training force points. The results of these studies relate to a certain degree to systems of trained manual demonstration.

The second control phase is the reproduction of recorded values of displacements and forces by the robot. The simplest system is positional reproduction which tracks the trained interpolated trajectory (Fig. 3). The assigned force $F_0$ is transferred by trained force points or trained by demonstration of the continuous trajectory $X = f(X_0, F_0)$ [3]. Real forces are not measured, because positional robot drives have high stiffness.
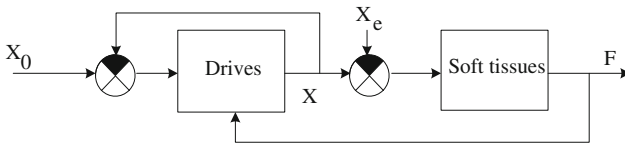


**Fig. 3.** Scheme of stiff position robot interacting with ST

If the robot software provides the calculation of robot displacements after polling the force sensor [2], then at limited time constant of drives only slow speed robot displacements at a small step that is necessary to ensure the accuracy are possible (see Fig. 4). Parallel position/force control supposes independent control of the robot movements along the assigned trajectory X0 and assigned forces F0 [13]. This control is necessary to support the assigned force at small ST movements, e.g., at patient breathing.
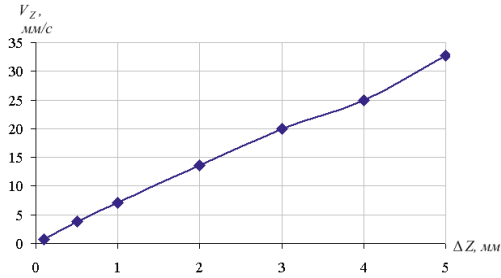
**Fig. 4.** The dependence of robot displacement speed on the step

The proposed apparatus operates according to the parallel position/force control principle, and therefore some drives, e.g., the six drives of angular robot track trained positional trajectory, and a separate one, e.g. the $7^{th}$ force linear drive fixed on the flange, track the evolution of force $F_{0z}$ along the tool axis (Fig. 4).

The movement of robot, providing the necessary deforming of the ST, is composed of the positional displacement drive $x_1$ and the displacement of the force module $x_2$ (Fig. 5).
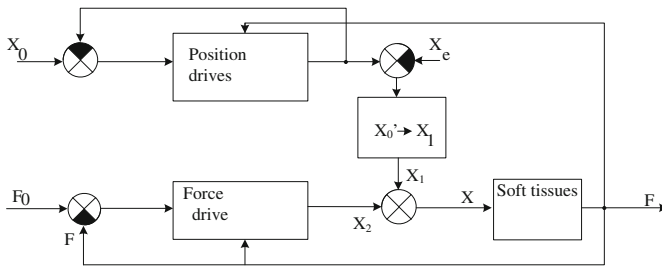


**Fig. 5.** Scheme of the system of parallel position/force control

## 4   Features of Robotic Systems for Restorative Medicine as Man - Machine Systems

A basic feature of the medical man-machine systems is the interaction of the robot and the operator with the human patient [5]. This characteristic allows us to create a combined control system for the simultaneous operation of the robot and the operator – masseur, and to create a system in which the robot as a massage chair is controlled by the patient only.

To implement the robotic system using the commercially available robots, the biomechatronic modules are used [4]. These modules offer the following functions: measurement of forces for position/force control systems, protection against overload, compliance control, measurement of muscle tone for biotechnical systems and tool change. Figure 6 shows the biomechatronic robot module with spring compensator and one-component force sensor [8].

**Fig. 6.** Biomechatronic module with one-component force induction sensor

Most of the experimental work has been carried out with the participation of a modernized robot RM-01, equipped with a one-component force sensor, enabling training of nodal force points [8]. To take into account the mobility of the patient from his breath [15], a new method that uses two interacting robots has been developed (Fig. 7). The first robot performs a positional function $z_0'(t) \approx A\sin 2\pi f$. The second robot provides an assigned force with force errors $\varepsilon_F (f) = (F-F_0)/F_0$.
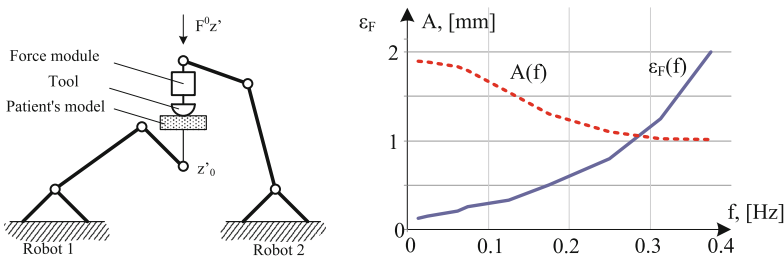


**Fig. 7.** Imitation of patient's breathing

The research allow to offer three project variants of robotic systems for the restorative medicine: with a one-component force sensor and positional reproduction; with a six-component force sensor, training by demonstration and positional reproduction; with a six-component force sensor, training by demonstration and force reproduction.

Priority of universal medical robots for the restorative medicine development belongs to Russia [14]. The development in the field of the restorative medicine robots can be taken into account because of proven achievements of robotics in surgery, where invasive actions such as transects and punctures are performed with the highest accuracy.

## 5 Development of Integrated Research and Industrial Structures for the Implementation and Production of Massage Robotics

The creation of medical devices and robotic systems, in particular for the restorative medicine and rehabilitation, is of considerable interest for practical medicine, as well as for developers, medical industry enterprises and higher technical educational institutions [7].

What reasons slow down the development of massage robotic systems? Are they technical, medical, organizational or economic? Currently there are no commercially available robots with 6-component force sensors, which are mounted on the end robot link. One of the explanations for the delay in development of massage robotics systems in comparison with surgical robotics and systems performing limb movements in the joints can be a prophylactic focus of the massage robotics in a promising future.

It is possible to combine the efforts of science, business and government in the realization of the priority directions of technological development of the economy in the form of integrated scientific and industrial structures, for example, the "Bio-Medical and Technical Cluster" [1]. It can be a significant contribution to solving the implementation task in the production of new innovative developments in the field of medical, in particular, massage robotics.

These developments allow enhancing the capabilities of all participants to expand international cooperation, commercialization, reducing costs and improving the efficiency of spending in all stages of the development and implementation of innovative robotic medical devices.

## 6 Conclusion

Currently the significant research results allow the development of robotics for preventive restorative medicine according to the principles of training by demonstration and reproduction of the training trajectory. Future investigations will be oriented toward the development of robots performing more fine massage techniques for the injured people, with consequences of cerebral palsy and stroke.

Combining the efforts of designers, producers of medical equipment and medical health institutions into integrated research and production structures in the form of clusters will allow extending the field of application of massage robotics, both on inpatient, health resort and outpatient phases of preventive medicine and rehabilitation.

# References

1. Gertsik, Y.: Organizational-economic stability and competitiveness of medical industry companies in integrated cluster. Russ. Econ. Internet J. **3**, 1–23 (2015)
2. Golovin, V., Arkhipov, M., Zhuravlev, V.: Force training for position/force control of massage robots. In: Rodić, A., Pisla, D., Bleuler, H. (eds.). MMS, vol. 20, pp. 95–107. Springer, Heidelberg (2014). doi:10.1007/978-3-319-05431-5_7
3. Golovin, V., Arkhipov, M., Zhuravlev, V.: Position/force control of medical robot interacting with dynamic biological soft tissue. In: Ceccarelli, M., Glazunov, V.A. (eds.). MMS, vol. 22, pp. 303–310. Springer, Heidelberg (2014). doi:10.1007/978-3-319-07058-2_34
4. Golovin, V., Arkhipov, M., Pavlovski, V.: Features of projection of robotic systems for restorative medicine. Mechatron. Autom. Control **16**, 664–671 (2015). № 10
5. Golovin, V., Arkhipov, M., Legotin, S., Kocherevskaya, L.: Expansion of ergonomics function in medical robotics. In: New Trends in Medical and Service Robots, Proceedings of 3rd International Workshop on Medical and Service Robots, pp. 207–218. Springer (2015)
6. Leskov, A., Golovin, V., Arkhipov, M., Kocherevskaya, L.: Training of robot to assigned geometric and force trajectories. In: Wenger, P., Chevallereau, C., Pisla, D., Bleuler, H., Rodić, A. (eds.). MMS, vol. 39, pp. 75–84. Springer, Heidelberg (2016). doi:10.1007/978-3-319-30674-2_6
7. Razumov, A., Gavrusin, S., Gercik, Y., Makarova, M., Gercik, G.: Biomechanical and clinical aspects of medical robotic systems. REMEDIUM. J. Russ. Market Med. Med. Equip. № 11, 46–49 (2015)
8. Golovin, V., Zhuravlev, V., Arkhipov, M.: Robotics in Restorative Medicine. LAP LAMBERT Academic Publishing, GmbH & Co. KG, Saarbrücken (2012)
9. Eremushkin, M.: Massage from classics to exotics. Complete encyclopaedia of systems, species, techniques and methods. Eksmo (2012)
10. Leskov, A., Yushenko, A.: Modeling and analysis of robotic systems. Mechanical Engineering, Moscow (1992)
11. Sadovnichi, V., Goryacheva, I., et al.: Application of Mechanics Methods of Contact Interaction in the Diagnosis of Pathological States of Soft Biological Tissues. MSU, Moscow (2009)
12. Tavakoli, M., Patel, R., Moallem, M., Aziminejad, A.: Haptics for Teleoperated Surgical Robotic Systems. Monograph Series in the World Scientific Publishing under the title "New frontiers in robotics". WSPC, Singapore (2003)
13. Vukobratovic, M., Surdilovic, D., Ecalo, Y., Kabic, D.: Dynamics and Robust Control of Robot — Environment Interaction. Monograph Series in the World Scientific Publishing under the title "New frontiers in robotics". WSPC (2009)
14. Golovin, V., Samorukov, A.: Massage method and device for its implementation, Russian patent, № 2145833 (1998)
15. Breathing Physiology. http://medvuz.com/noz/ch10.php

# A Method for Adjusting Moment Input on an Exoskeleton Robot with Fixed Linear Actuators

Huseyin Emre Ozgur[1(✉)] and Mehmet Ilteris Sarigecili[2]

[1] Department of Mechanical Engineering,
Adana Science and Technology University, Adana, Turkey
`huseyinemre@yandex.com`
[2] Department of Mechanical Engineering, Cukurova University, Adana, Turkey
`msarigecili@cu.edu.tr`

**Abstract.** Patients who lose walking ability get rehabilitation services that consist of repeated movements of the lower limbs such that the patients can regain their ability to move. Unfortunately, the change in the number of patients and need for gait rehabilitation is inversely proportional with the number of physiotherapists. There are many robotic rehabilitation systems available which are generally expensive. There is a direct need for an inexpensive rehabilitation robot that can be afforded (or can be reached) by the majority of people. As a solution to this problem, a pneumatically actuated, 4° of freedom exoskeleton robot for the movement of a patient in sagittal plane and which can be used together with a body weight support system has been developed. The novelty of the proposed approach lies in how pneumatic linear actuation is used to adjust the torque required to move a limb for a particular patient. The proposed system has also a simpler control technique than other available complicated and more advanced systems.

**Keywords:** Exoskeleton · Rehabilitation robotic · Pneumatic actuation · Lower gait

## 1 Introduction

There is a significant increase in the number of spinal cord injury (SCI) and stroke patients [1–3] as well as undesired burden of the patients leading to the need of occupying at least one person for daily activities for each patient. There are several rehabilitation methods such as Bobath, Brunstrom, Functional Electrical Stimulation (FES) and Task Oriented Training [4]. From these methods, task oriented training has drawn attention because therapists let the patient mimic daily life activities like walking, standing, sitting, etc.; hence, it is more easily accepted by the patients. Unfortunately, the training (e.g., for walking) requires high coordination and effort of multiple therapists. With the increase in the number of patients, it is hard to fulfil properly the rehabilitation needs of each patient. Robotic rehabilitation systems offer a solution. Repetitive movements of the rehabilitation can be applied competently. Additionally, in order to analyse the response of the patient to the therapy and to improve the applied

rehabilitation method, sensory data can be obtained by usage of robotic systems. Also several studies (e.g., Schwartz et al. [5] and Tong et al. [6]) have presented gait rehabilitation trial results in favour of robotic gait rehabilitation systems. According to the authors' opinions; robotic gait rehabilitation systems would be used more frequently in future. Unfortunately, robotic systems are quite costly. Cheaper robotic gait training systems with satisfactory solutions have been searched for making robotic rehabilitation systems reachable by mid to low income categories. As a result, general characteristics of the system point to a pneumatically actuated lower gait exoskeleton system.

## 2　Previous Studies

In literature, the lower extremity rehabilitation robots can be divided into two groups: (1) end effector (foot plate based) approach and (2) exoskeleton approach [7, 8]. The main problem with end effector based lower gait rehabilitation systems is that they may cause risk of abnormal positioning of joints for patients with weak balance and muscle control [9]. In the literature, Gait Trainer GT I and HapticWalker are examples of end effector based systems. Gait Trainer GT I developed by Werner et al. [10] is a body weight support (BWS) gait rehabilitation system. The system consists of a crank based end effector foot plate system, a BWS system and a control unit. They noted that the developed system needed less crew and had performance levels same as in the conventional lower gait rehabilitation methods. HapticWalker [11, 12] is developed as programmable foot plate based robotic gait rehabilitation system. The most predominant feature of HapticWalker is that it can mimic not only walking in horizontal plane but also it allows using the patient's experience climbing up and down stairs.

　　The exoskeleton based rehabilitation robots have a lower risk of featuring unplanned abnormal gait structure because the links are directly connected to each limb of the patient. However, the exoskeleton-based robots generally work in sagittal plane and do not allow pelvic motion. Driven Gait Orthosis developed by Colombo et al. [13] is a BWS, treadmill-based exoskeleton rehabilitation system which uses electromechanical actuators with precision ball screws, position and impedance as control method. The system allows motions of the patients in the sagittal plane and prohibits the pelvic motions of the patients. The system has been commercialized later as Lokomat. Lopes [14] is another significant example for lower gait exoskeleton system which can be used in treadmill-based lower gait rehabilitation. In Lopes, electro-mechanical actuation with Bowden cable system has been used so that the system can be placed correctly in an anatomical position. For the system's control the impedance control method has been used. Belforte et al. [15] have presented Pneumatic active gait orthosis which can be used for assisting paraleptic patients in terms of locomotion. The most interesting approach of the proposed system is that pneumatic cylinders are connected to a chain and sprocket system in order to produce required torque input on a linkage. Koceska et al. [16] have also developed a BWS, treadmill-based pneumatically actuated robotic rehabilitation system with fuzzy control system.

　　The main problem with exoskeleton based lower limb rehabilitation systems, restriction of pelvic motion, has been studied by Aeyagi et al. [17] and they have developed POGO and PAM. Both of them are actuated pneumatically; however the

pneumatic actuators are directly connected to the joints of a limb such as ankle, knee and hip, instead of assembling the cylinders parallel to the limbs. The main purpose of the method is directly controlling position of each joint such that a natural gait pattern is obtained. For achieving the desired results, they have used a non-rigid structure. Unfortunately, due to the characteristics of their end-effector like approach, risks of abnormal gait in weak patients are increased. In order to prevent abnormal gait, they developed a control algorithm which let patient to follow a natural gait pattern.

## 3 Materials and Methods

In this study, a pneumatically actuated, treadmill and exoskeleton based, lower limb gait rehabilitation system which uses BWS is considered. BWS helps stabilizing the weak patient in air hence balancing of the patient will not be a problem. Also, the movement of the limbs will require a simple mechanism. In a natural gait, significant movements occur not only in sagittal plane but also in coronal and transverse plane. For a complete gait recovery, the rehabilitation system should have at least some kind of guiding system which allows pelvic motion as well. However, only the motion in sagittal plane is considered and pelvic motion is neglected to make the study simple.

Pneumatically actuated systems generally have cylinders assembled almost parallel to the limbs. Extension or retraction of the cylinders results in a moment for moving the limb. The input moment requirement depends on the weight of the patient. In the conventional systems, the cylinders have fixed connection points. Hence, different moment inputs are obtained by either changing the cylinders or changing the supplied air pressure. In this study, a moment adjuster mechanism is presented for using the same pneumatic cylinder for patients with varying weights. The proposed method has several connection points for a pneumatic cylinder both in the hip and femur sections. For obtaining predefined levels (e.g. 100%, 80%, 70%, etc.) of effective moment values, the connection point of one end of a cylinder can be changed in the hip section as well as in the femur section, or both of the connection points of a cylinder can be changed to obtain a marginal change.

Even though the interaction forces in the mechanism are not static, forces are assumed as static by considering that patients cannot move and the system should move very slowly during a therapy session. Hence, a relationship can be defined between input cylinder forces and output moments based on static equilibrium conditions.

### 3.1 Setup of Mechanism

The mechanism consists of a hip, a femur and a tibia section with two pneumatic cylinders for each limb. Hence, it has two degrees of freedom (DOF) for each limb and overall 4 DOF with two limbs. The simplified model of the system is shown in Fig. 1 and the conceptual model of the overall system is shown in Fig. 2. Three different connection points on either the hip or the femur sections can be chosen arbitrarily based on the output moment and input pneumatic force values. The positions of the connection points on the hip section are identified at 0.4 m (H1), 0.45 m (H2) and 0.5 m
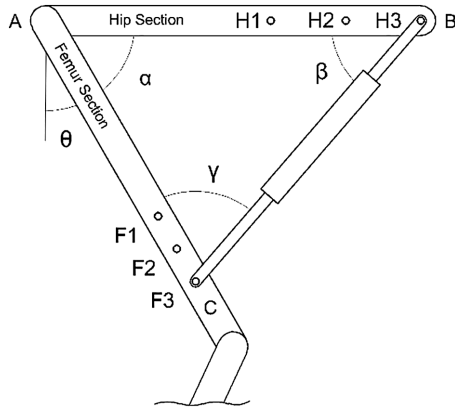
**Fig. 1.** Representation of the test mechanism setup that has been used
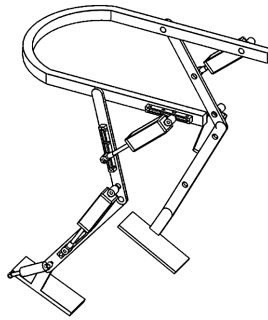


**Fig. 2.** Representation of the proposed exoskeleton robotic system [18]

(H3) from point A. Similarly, the positions of the connection points on the femur section are identified at 0.3 m (F1), 0.35 m (F2) and 0.4 m (F3) from point A.

A double acting, 25 mm bore diameter, ISO 6432 pneumatic cylinder has been used. The air pressure for the pneumatic actuator is 4 bars. The force at the tip of the piston rod can be calculated from Eq. (1) where $F_c$ is the force output of the cylinder, $P_c$ is the supplied air pressure to cylinder, $d_c$ is the diameter of cylinder bore, and $d_p$ is the diameter of piston.

$$F_c = \begin{cases} F_c = \frac{P_c \cdot \pi d_c^2}{4} & \text{for extension stroke} \\ F_c = \frac{P_c \pi (d_c^2 - d_p^2)}{4} & \text{for retraction stroke} \end{cases} \tag{1}$$

For the proposed system; $P_c$ = 4 bar, $d_c$ = 0.025 m, $d_p$ = 0.005 m have been selected. By using Eq. (1), $F_c$ can be calculated as 196 N (extension) and 188 N (retraction).

### 3.2    Test Process and Calculations

The input moment requirement of the designed system can be assessed based on the conditions when the system mimics natural gait cycle. A gait cycle is a periodic motion which starts with heel strike and ends with the same heel strike. In Observational Gait Analysis Handbook [19], it is presented how angle $\theta$ (Fig. 1) changes during a gait cycle. In the designed system, the complementary angle of $\theta$ (i.e., angle $\alpha$) in Fig. 1 is measured by a potentiometer. Hence, the relationship between the angle $\alpha$ and the extended piston length can be defined by cosine theorem as shown in Eq. (2). In this equation, AB is the distance from point A to the connection point (H1, H2 or H3) of the cylinder on the hip section; AC is the distance from point A to the connection point (F1, F2 or F3) of the other end of the cylinder on the femur section, and BC is the final length of the extended cylinder. Since AB and AC are constant, the extended cylinder length can be calculated directly for a particular gait posture position defined by angle $\theta$.

$$CB^2 = AB^2 + AC^2 - 2 . AB . AC . \cos(\alpha) \tag{2}$$

The input moment requirement created by piston force with respect to point A can be calculated from Eq. (3), if the cosine theorem applied to length AB by solving Eq. (2) with respect to AB for $\gamma$, Eq. (4) has been obtained:

$$M_{eff} = F_c \times \sin(\gamma) \times AC \tag{3}$$

The angle $\gamma$ can be calculated by the cosine theorem as shown in Eq. (4):

$$\gamma = \cos^{-1}\left(\frac{AC^2 + CB^2 - AB^2}{2 . AC . CB}\right) \tag{4}$$

The set of Eqs. (1)–(4) is used for calculating the moment input requirements for complete gait cycle. As a result, it is found out that the maximum moment input requirement occurs for posture position at angle $\theta$ is 30°. Hence, the next calculations are based on angle $\gamma = 60°$.

In the first application, the cylinder connection point to the femur is kept fixed and only the connection point on the hip section is changed. Different combinations of cylinder connection points are shown in Table 1. For each row, "Point 1", column represents the connection point of the cylinder on the hip section whereas "Point 2" column represents the connection point on the femur section. Final lengths and angles are also represented in the last three row of the Table 1. Predefined values have been given in regular font and obtained values have been shown in italic font.

In the first application, the user can obtain different effective moments on the linkage by just changing the position of the cylinder connection point on the hip section. This will alter the angle between the cylinder natural axis and linkage natural axis. Different angles will produce different normal forces which will produce different effective torque values on the linkage without altering force arm. In the second application, the user can obtain different effective moments by changing the connection

**Table 1.** The test mechanism setup (obtained values have been shown in italic font)

| Force input | | 196 N | | | | |
|---|---|---|---|---|---|---|
| Point 1 | Point 2 | AB(m) | AC(m) | α(°) | CB(m) | γ(°) |
| H3 | F1 | 0.5 | 0.3 | 60 | *0.436* | *83.413* |
| H2 | F1 | 0.45 | 0.3 | 60 | *0.397* | *79.107* |
| H1 | F1 | 0.4 | 0.3 | 60 | *0.361* | *73.898* |
| H3 | F2 | 0.5 | 0.35 | 60 | *0.444* | *76.996* |
| H2 | F2 | 0.45 | 0.35 | 60 | *0.409* | *72.216* |
| H1 | F2 | 0.40 | 0.35 | 60 | *0.377* | *66.587* |
| H3 | F3 | 0.5 | 0.4 | 60 | *0.458* | *70.893* |
| H2 | F3 | 0.45 | 0.4 | 60 | *0.427* | *65.818* |
| H1 | F3 | 0.4 | 0.4 | 60 | *0.4* | *60* |

points of the cylinder both on the hip and the femur sections. The combinations of the connection points, resulting lengths and angles are all shown in Table 1.

## 4 Results

The geometrical parameters are calculated by using Eqs. (2) and (4) as listed in Table 1. The effective moments have been calculated by using Eq. (3) for each position listed in Table 1 and the results are tabulated in Table 2. From the last row of the Table 2, it is seen that active input moment of 67.9 Nm to 74.08 Nm can be obtained by using first application whereas it is clear that an active moment of 56.493 Nm to 74.08 Nm can be obtained by using second application.

**Table 2.** The effective torque results by using various test mechanisms

| | H1 | H2 | H3 |
|---|---|---|---|
| F1 | 56.493 Nm | 57.741 Nm | 58.412 Nm |
| F2 | 62.952 Nm | 65.322 Nm | 66.841 Nm |
| F3 | 67.896 Nm | 71.52 Nm | 74.081 Nm |

## 5 Conclusion and Future Studies

There is an increase of stroke, SCI, hemiplegia patients and required therapy. In order to reduce the disease burden and improve conditions of the patient, gait rehabilitations have been conducted. There are several methods like robotic gait rehabilitation systems. Conventional methods are heavily labour based and in future, in the authors' opinion, therapists will not be able to answer the need completely. Robotic systems with/without FES show predominant results. Unfortunately robotic systems are costly and cannot achieve wide usage. For widening their usage, costs should be decreased. Hence, after careful analysis of readily available systems, lower gait robotic system with pneumatic actuation has been chosen as starting point. Pneumatic actuation is a

clean, non-hazardous, easily achievable, readily available technology. Unfortunately, systems with pneumatic actuation cannot answer the need of different moment input which changes from patient to patient and the level of the therapy. In order to overcome this problem, the proposed method has been found as a solution. By using different connection points for cylinder connections, different effective moments can be achieved without changing the cylinder or supplied air pressure, by altering the force arm on linkage. The results showed that this method can be applied in order to produce different effective moments on exoskeleton linkage without using multiple cylinders and without changing them. This inexpensive mechanism can reduce the cost of the exoskeleton system.

For future studies, the force and speed control of the system should be developed in addition to the position control. It is also possible to optimize the position of the connection points. In this study, in order to show how the method works, locations of connection points on hip and femur section have been selected by experience. To improve effectiveness, position of connection points on hip and femur can be optimized by using optimization methods. Also, due to usage of pneumatic cylinder with long stroke length, pneumatic actuation system should be investigated in both mechanical strength aspect and in service life aspect.

# References

1. Bill and Melinda Gates Foundation: Global, regional, and national incidence, prevalence, and years lived with disability for 301 acute and chronic diseases and injuries in 188 countries, 1990 – 2013 : a systematic analysis for the Global Burden of Disease Study 2013 (2015)
2. Feigin, V.L., Forouzanfar, M.H., Krishnamurthi, R., Mensah, G.A., Connor, M., Bennett, D., Moran, A.E., Sacco, R.L., Anderson, L., Truelsen, T., O'Donnell, M., Venketasubramanian, N., Barker-Collo, S., Lawes, C.M.M., Wang, W., Shinohara, Y., Witt, E., Ezzati, M., Naghavi, M., Murray, C.: Global and regional burden of stroke during 1990–2010: findings from the global burden of disease study 2010. Lancet **383**(9913), 245–255 (2014)
3. Feigin, V.L., Forouzanfar, M.H., Krishnamurthi, R., Mensah, G.: Global burden of stroke: an underestimate – authors' reply. Lancet **383**(9924), 1205–1206 (2014)
4. Belda-Lois, J.-M., Mena-del Horno, S., Bermejo-Bosch, I., Moreno, J.C., Pons, J.L., Farina, D., Iosa, M., Molinari, M., Tamburella, F., Ramos, A., Caria, A., Solis-Escalante, T., Brunner, C., Rea, M.: Rehabilitation of gait after stroke: a review towards a top-down approach. J. Neuroeng. Rehabil. **8**(1), 66 (2011)
5. Schwartz, I., Sajin, A., Fisher, I., Neeb, M., Shochina, M., Katz-Leurer, M., Meiner, Z.: The effectiveness of locomotor therapy using robotic-assisted gait training in subacute stroke patients: a randomized controlled trial. PM R **1**(6), 516–523 (2009)
6. Tong, R.K., Ng, M.F., Li, L.S.: Effectiveness of gait training using an electromechanical gait trainer, with and without functional electric stimulation, in subacute stroke: a randomized controlled trial. Arch. Phys. Med. Rehabil. **87**, 1298–1304 (2006)

7. Sale, P., Franceschini, M., Waldner, A., Hesse, S.: Use of the robot assisted gait therapy in rehabilitation of patients with stroke and spinal cord injury. Eur. J. Phys. Rehabil. Med. **48** (1), 111–121 (2012)
8. Meng, W., Liu, Q., Zhou, Z., Ai, Q., Sheng, B., (Shane) Xie, S.: Recent development of mechanisms and control strategies for robot-assisted lower limb rehabilitation. Mechatronics **31**, 132–145 (2015)
9. Mehrholz, J., Pohl, M.: Electromechanical-assisted gait training after stroke: a systematic review comparing end-effector and exoskeleton devices. J. Rehabil. Med. **44**(3), 193–199 (2012)
10. Werner, C., von Frankenberg, S., Treig, T., Konrad, M., Hesse, S.: Treadmill training with partial body weight support and an electromechanical gait trainer for restoration of gait in subacute stroke patients: a randomized crossover study. Stroke **33**(12), 2895–2901 (2002)
11. Schmidt, H.: HapticWalker - a novel haptic device for walking simulation. In: Proceedings of EuroHaptics 2004, pp. 60–67 (2004)
12. Schmidt, H., Werner, C., Bernhardt, R., Hesse, S., Krüger, J.: Gait rehabilitation machines based on programmable footplates. J. Neuroeng. Rehabil. **4**, 2 (2007)
13. Colombo, G., Wirz, M., Dietz, V.: Driven gait orthosis for improvement of locomotor training in paraplegic patients. Spinal Cord **39**(5), 252–255 (2001)
14. Veneman, J.F., Kruidhof, R., Hekman, E.E.G., Ekkelenkamp, R., Van Asseldonk, E.H.F., van der Kooij, H.: Design and evaluation of the LOPES exoskeleton robot for interactive gait rehabilitation. IEEE Trans. Neural Syst. Rehabil. Eng. **15**(3), 379–386 (2007)
15. Belforte, G., Gastaldi, L., Sorli, M.: Pneumatic active gait orthosis. Mechatronics **11**(3), 301–323 (2001)
16. Koceska, N., Koceski, S., Zobel, P.: Gait training using pneumatically actuated robot system. In: Advances in Robot Navigation. InTech (2011)
17. Aoyagi, D., Ichinose, W.E., Harkema, S.J., Reinkensmeyer, D.J., Bobrow, J.E.: A robot and control algorithm that can synchronously assist in naturalistic motion during body-weight-supported gait training following neurologic injury. IEEE Trans. Neural Syst. Rehabil. Eng. **15**(1), 387–400 (2007)
18. Ozgur, H.E., Sarigecili, M.I.: Agirlik Destekli Yurume Bandi Tabanli Robotik Tedavi Sistemlerinde Yeni Bir Yaklasim, in 1. Endustriyel Otomasyon Kongre ve Sergisi, pp. 163–169 (2015) (in Turkish)
19. Perry, J.: Observational Gait Analysis Handbook, Pathokinesiology Service and The Physical Therapy Department of Rancho Los Amigos Medical Center (1989)

# Planning of Needle Insertion
# for Robotic-Assisted Prostate Biopsy
# in Augmented Reality Using RGB-D Camera

Florin Gîrbacia[2(✉)], Răzvan Boboc[2], Bogdan Gherman[1],
Teodora Gîrbacia[2], and Doina Pîsla[1]

[1] CESTER, Technical University of Cluj-Napoca,
400114 Cluj-Napoca, Romania
`{Bogdan.Gherman,Doina.Pisla}@mep.utcluj.ro`
[2] Transilvania University of Braşov, 29 Eroilor Blvd., 500036 Braşov, Romania
`{Garbacia,Razvan.Boboc,Teodora.Girbacia}@unitbv.ro`

**Abstract.** Augmented Reality (AR) technologies are increasingly used in many areas. There is a vast research activity within the field of AR in medical applications. In this paper, an AR system using RGB-D camera is proposed to facilitate trajectory planning for a prostate biopsy robot. The advantage of the developed AR environment consists in the possibility to generate needle trajectories using a 3D virtual model of a specific patient directly in the robot workspace. It was shown from a test case that the generated biopsy needle trajectory reaches successfully the target area.

**Keywords:** Augmented reality · Robotic–assisted prostate biopsy · Depth sensing

## 1 Introduction

Nowadays, cancer constitutes a severe problem affecting more and more people. In 2012, there were about 14.1 million new cancer cases; 8.2 million cancer deaths occurred worldwide [16]. Lung cancer was the most frequently diagnosed cancer, followed by prostate cancer for men worldwide. The prostate cancer is the third cause of male cancer mortality in the EU, with 72600 deaths predicted for year 2015 [10]. Prostate biopsy is still an essential procedure for the diagnosis of prostate cancer [21]. In order to determine if the cancer is present in the body, a procedure to acquire a piece of tissue from the considered sick organ is performed, commonly known as biopsy [5]. For prostate biopsy the most used methods at this moment are the trans-rectal and transperineal biopsy [14]. Although most urologists perform transrectal prostate biopsies, some prefer transperineal biopsies considering the reduced risk of infection while performing the procedure [8].

The biopsy needle can be manually guided, but this method has a low level of precision. Robotic assisted procedures can be seen as important tools [1, 15] that offer increased precision for a better diagnostic yield.

In recent years, AR has been increasingly used in a variety of research areas, one of them being medicine. AR systems provide additional virtual information to the user, mixing the virtual and actual reality for a better perception [3]. In the last years many researchers have worked on developing AR-based systems for image guidance in minimally invasive surgery [2, 6, 11, 13]. In medical robotics systems Wen et al. [20] proposed an AR cooperative surgical robot system for percutaneous treatment, which can be guided by hand gestures. Volonté et al. [18] developed a stereoscopic augmented reality for da Vinci robotic biliary surgery. The authors noted that the collocation of 3D volume images on the robot console improves the focus of the surgeon and the control on the procedure. The advantages of AR navigation combined with robot-assisted surgery in craniomaxillofacial surgery are investigated in [9]. The results have shown that AR allows precision and automation in operational procedures. In [5] an AR system used for training the urologist to insert the biopsy needle using a robot is presented. However, in these researches the AR was used just to display additional information collocated with real environment.

The limitation of classic marker based AR system is the restriction of collision detection between the virtual and real objects from the environment. Also when the markers are not visible, the interaction is not achievable. Due to recent advances in depth-sensing technologies (RGB-D) the 3D information (both depth and colour information) regarding dynamic environments can be obtained using the same device. RGB-D devices have already been used for medical applications. In [19] is presented the first research regarding the precision of 3D/2D calibration and registration between RGB-D sensor and a mobile C-arm fluoroscope, and its application in medical AR. The authors noted that accurate calibration between the RGB-D sensor and a C-arm can be achieved. The use of RGB-D sensors in robotics has increased in recent years, being used mostly for mapping and recognition tasks [12].

This paper proposes a new method of planning biopsy needle trajectories based on AR technologies and RGB-D Microsoft Kinect camera, using as case study a serial robot. RGB-D devices are very popular due to their low costs and in addition to the video augmentation they provide depth information for each pixel. The proposed AR system is capable to perform collision detection between real biopsy needle guided by the robot and the virtual model of the patient in a dynamically 3D scene obtained from the RGB-D camera.

## 2   Materials and Methods

### 2.1   The Hardware and Software Architecture of the AR Robotic Biopsy System

A diagram of the developed system is shown in Fig. 1. It consists of the following subsystems:

- *The depth camera*: The Microsoft Kinect V1 RGB-D camera was used to collect depth information with the resolution of $640 \times 480$ pixels from the real environment and sends it to a PC. The image generation rate was around 30 frames per second (fps). The Kinect sensor was positioned at 150 cm above the ground, and at
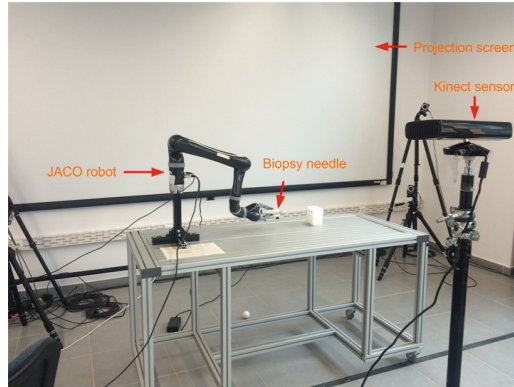
**Fig. 1.** The hardware architecture of the developed AR environment

130 cm from the robot. The positioning of the Kinect sensor depends on the robot workspace.

- *PC running the AR environment:* The Kinect camera is connected to a PC running an AR environment developed by the authors using C++ programming language based on Microsoft Kinect SDK 1.8. The AR images are projected on a front screen [4], which can be eventually replaced by a desktop monitor display.
- *Robot used for biopsy procedure:* In a previous study, the design and simulation of an innovative robot called BIO-PROS-1 was proposed [17]. Because the physical experimental prototype is not available yet, a serial six degrees of freedom Kinova JACO robot (www.kinovarobotics.com) was proposed to be used as case study. The robot is equipped with a 3-finger based gripper that can be used to grasp the biopsy gun.

The process flow of the developed AR environment is shown in Fig. 2. A method was developed for the continuous identification of the location of the biopsy needle tip on the Kinect-captured depth images. The depth images stream consists of live continuous x, y, z point clouds obtained using the Kinect Fusion algorithm [7]. The point clouds are filtered in order to remove all duplicated points. Then each component point from the point clouds is represented as a small dot in one image. The users of the AR systems are able to see the virtual objects and the real world coexisting in the same space (collocated). Because the real robot is used to generate biopsy needle trajectories using an anatomical 3D virtual model, the need of their registration emerges.

The reconstructed 3D virtual model of a specific patient is registered on the position of the patient body obtained from the point cloud. In this study, the registration is performed based on two sets of data: the 3D pelvis model reconstructed from the preoperative MRI data of a specific patient and the data referring to the actual patient's surface (skin) acquired as a point cloud from the RGB-D sensor. The target points inside the prostate are configured in the reconstruction process and represented as spheres. The user can adjust the visual parameters of the virtual patient to enable the visualization of the target points. In order to register the 3D virtual model with the patient body in the depth camera coordinates, a matching method is used to align the
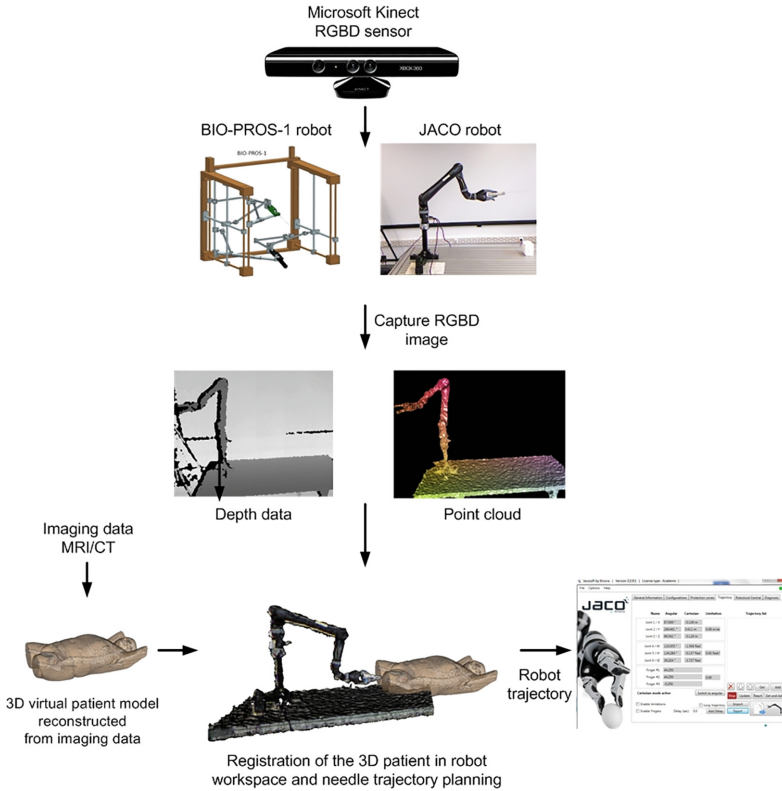
**Fig. 2.** Process flow of robotic-assisted prostate biopsy in augmented reality using RGB-D

points from both datasets. The user can modify the scale, position and orientation of the anatomical 3D virtual model relative to the actual patient data. After the registration process is finished, the user can proceed to plan the needle trajectories. This process requires the identification of collision detection between the tip of the biopsy needle and the target areas specified by the physician. Conventional collision detection algorithms cannot be used for point clouds.

Instead, for the efficient calculation of the collision detection between the needle tip and target areas the following algorithm is used:

- First, the number of points $N$ from the point cloud that are situated inside a bounding sphere $S_b(x_s, y_s, z_s, r)$ with the diameter $D_{thresh}$ corresponding to the patient virtual model dimensions (Fig. 3) is computed. For example these can be the points that are closest to the pelvis area. To determine if a point $P(x, y, z)$ is inside the sphere $S_b(x_s, y_s, z_s, r_b)$, the following formula is applied:

$$(x - x_s)^2 + (y - y_s)^2 + (z - z_s)^2 \; < \; r_b^2 \tag{1}$$
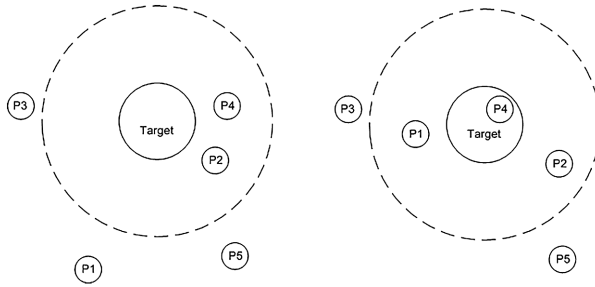
**Fig. 3.** Illustration of the point cloud around the target for two test cases. In the first test case the points P5, P3 and P1 are outside the bounding threshold sphere and not used for the calculation. P4 is the closest to the target area, but is not reaching it. In the second case P4 is inside the target area and P2, P1are situated inside the threshold bounding sphere.

The $r_b^2$ parameter is pre calculated to improve computational efficiency by avoiding square root calculations.

- If $N > 0$, the points $P_i$ are stored in an array.
- For each point $P_i$ the distance to the prostate target area specified by a sphere $S_t$ with diameter $D_t$ is calculated in order to determine if the point is situated inside the target sphere. If a point $P_i$ is detected inside of a target area, the robot coordinates are stored and a message is displayed to the user.

## 3 Test Case

In the conducted experiment, the task was to plan the biopsy needle trajectory using the Jaco robot as a test case in order to allow positioning of the biopsy needle tip inside of target area specified on a phantom (Fig. 5). The virtual model of the phantom object
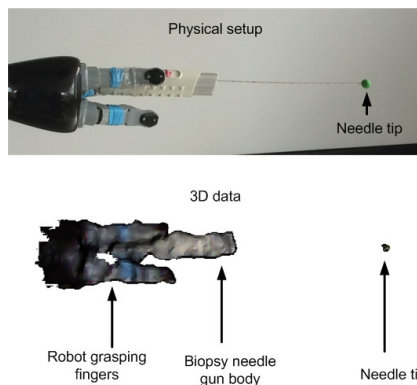


**Fig. 4.** Identification of the biopsy needle tip in the point cloud
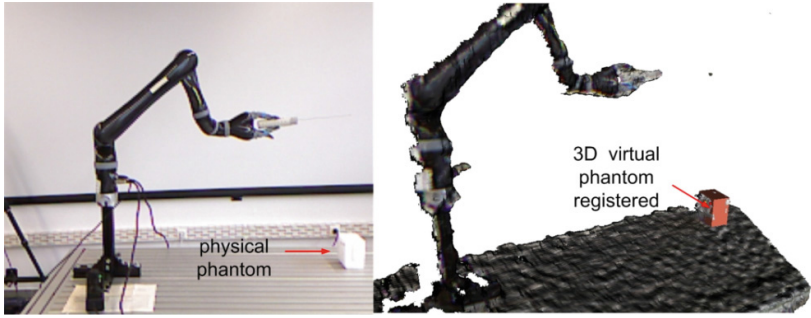
**Fig. 5.** The test case setup and alignment of the virtual object in the real robot workspace
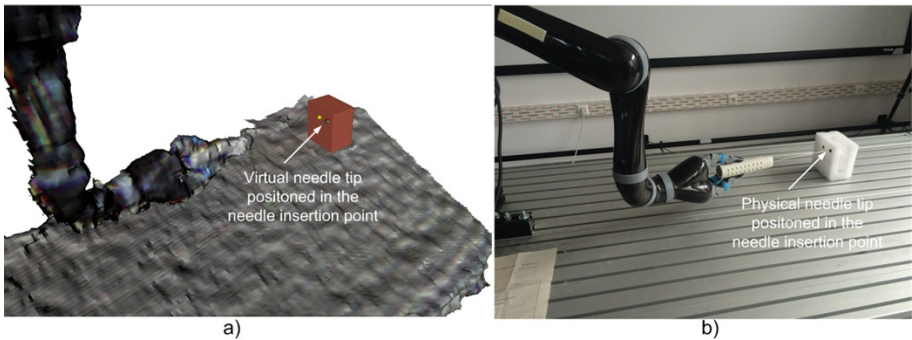


**Fig. 6.** The needle tip positioned at the target and the physical setup

was modelled in SolidWorks CAD software and exported as a STL model. The target area was displayed as a sphere shape.

Figure 5 displays the AR registration result on the physical phantom. Due to the low resolution of the Kinect sensor (640 × 480), the biopsy needle point clouds where not detected. In order to acquire the necessary data for the biopsy needle a sphere with a diameter of 8 mm was attached to the needle tip (Fig. 4). With the improvement of the RGB-D sensor resolution, this problem is avoided. The robot configurations were recorded using Jacosoft.

One can observe in Fig. 6 the robotic-assisted biopsy needle planning for the target area. The needle tip reaches successfully the target area in the AR environment (Fig. 6a) as well as in the physical environment (Fig. 6b).

## 4   Conclusions

This paper demonstrates the planning of needle insertion for robotic-assisted prostate biopsy using a RGB-D camera connected to an AR environment developed by the authors. In this collocated environment the user can create and save robot guided

needle trajectories, based on a 3D virtual model of a specific patient directly available in the robot workspace. It was shown from a phantom test case that a trajectory of the biopsy needle reaching the target area can be successfully generated. The developed AR environment has the potential of a promising tool for training and simulation of robotic biopsy needle guidance. Using this tool for practical robotics assisted biopsy requires a number of extensions. The precision of reaching the target area is influenced mainly by the registration of 3D virtual model for a specific patient on the position of the patient's body. Further work is focused on better automatic aligning of the two point clouds with Sampled Consensus-Initial Alignment and ICP Iterative Closest Point algorithms and thoroughly analyzing the precision of needle positioning. Another improvement will be the usage of RGB-D sensor with enhanced resolution of the depth image (for example the Kinect V2 has the resolution $1920 \times 1080$ @30 frames).

# References

1. Buchs, N.C., Pugin, F., Volonté, F., Morel, P.: Learning tools and simulation in robotic surgery: state of the art. World J. Surg. **37**(12), 2812–2819 (2013)
2. Bernhardt, S., Nicolau, S.A., Agnus, V., Soler, L., Doignon, C., Marescaux, J.: Automatic localization of endoscope in intraoperative CT image: a simple approach to augmented reality guidance in laparoscopic surgery. Med. Image Anal. **30**, 130–143 (2016)
3. Chen, X., Xu, L., Wang, Y., Wang, H., Wang, F., Zeng, X., Wang, Q., Egger, J.: Development of a surgical navigation system based on augmented reality using an optical see-through head-mounted display. J. Biomed. Inform. **55**, 124–131 (2015)
4. Fiorentino, M., Uva, A.E., Gattullo, M., Debernardis, S., Monno, G.: Augmented reality on large screen for interactive maintenance instructions. Comput. Ind. **65**(2), 270–278 (2014)
5. Gîrbacia, T., Gîrbacia, F., Duguleana, M., Butilă, E.: Augmented reality system for training robotic prostate biopsy needle guidance. In: The 10th International Conference on Virtual Learning, pp. 254–258 (2015)
6. Hallet, J., Soler, L., Diana, M., Mutter, D., Baumert, T.F., Habersetzer, F., Marescaux, J., Pessaux, P.: Trans-thoracic minimally invasive liver resection guided by augmented reality. J. Am. Coll. Surg. **220**, 55–60 (2015)
7. Izadi, S., Kim, D., Hilliges, O., Molyneaux, D., Newcombe, R., Kohli, P., Shotton, J., Hodges, S., Freeman, D., Davison, A., Fitzgibbon, A.: KinectFusion: real-time 3D reconstruction and interaction using a moving depth camera. In: Proceedings of the 24th Annual ACM Symposium on User Interface Software and Technology, pp. 559–568. ACM (2011)
8. Kaye, D.R., Stoianovici, D., Han, M.: Robotic ultrasound and needle guidance for prostate cancer management: review of the contemporary literature. Curr. Opin. Urol. **24**, 75–80 (2014)
9. Lin, L., Shi, Y., Tan, A., Bogari, M., Zhu, M., et al.: Mandibular angle split osteotomy based on a novel augmented reality navigation using specialized robot-assisted arms—a feasibility study. J. Cranio-Maxillofacial Surg. **44**, 215–223 (2016)

10. Malvezzi, M., Bertuccio, P., Rosso, T., Rota, M., Levi, F., La Vecchia, C., Negri, E.: European cancer mortality predictions for the year 2015: does lung cancer have the highest death rate in EU women? Ann. Oncol. **26**(4), 779–786 (2015)
11. Marescaux, J., Diana, M.: Next step in minimally invasive surgery: hybrid image-guided surgery. J. Pediatr. Surg. **50**, 30–36 (2015)
12. Morell-Gimenez, V., Saval-Calvo, M., Azorin-Lopez, J., Garcia-Rodriguez, J., Cazorla, M., Orts-Escolano, S., Fuster-Guillo, A.: A comparative study of registration methods for RGB-D video of static scenes. Sensors **14**, 8547–8576 (2014)
13. Nicolau, S., Soler, L., Mutter, D., Marescaux, J.: Augmented reality in laparoscopic surgical oncology. Surg. Oncol. **20**, 189–201 (2011)
14. Pîslă, D., Gherman, B., Gîrbacia, F., Vaida, C., Butnariu, S., Gîrbacia, T., Plitea, N.: Optimal planning of needle insertion for robotic-assisted prostate biopsy. In: Borangiu, T. (ed.) Advances in Robot Design and Intelligent Control. AISC, vol. 371, pp. 339–346. Springer, Heidelberg (2016). doi:10.1007/978-3-319-21290-6_34
15. Tilak, G., Tuncali, K., Song, S.-E., Tokuda, J., Olubiyi, O., et al.: 3T MR-guided in-bore transperineal prostate biopsy: a comparison of robotic and manual needle-guidance templates. J. Magn. Reson. Imaging **42**, 63–71 (2015)
16. Torre, L.A., Bray, F., Siegel, R.L., Ferlay, J., Lortet-Tieulent, J., Jemal, A.: Global cancer statistics, 2012. CA Cancer J. Clin. **65**, 87–108 (2015)
17. Vaida, C., Pisla, D., Tucan, P., Plitea, N., Gherman, B.: Robot paralel pentru biopsia transperineală a prostatei. Patent pending: 00761/26.10.2015 (2015)
18. Volonté, F., Buchs, N.C., Pugin, F., Spaltenstein, J., Jung, M., Ratib, O., Morel, P.: Stereoscopic augmented reality for da Vincii™ robotic biliary surgery. Int. J. Surg. Case Rep. **4**(4), 365–367 (2013)
19. Wang, X., Habert, S., Ma, M., Huang, C.H., Fallavollita, P., Navab, N.: RGB-D/C-arm calibration and application in medical augmented reality. In: Proceedings of the 2015 IEEE International Symposium on Mixed and Augmented Reality, pp. 100–103. IEEE Computer Society (2015)
20. Wen, R., Tay, W.-L., Nguyen, B.P., Chng, C.-B., Chui, C.-K.: Hand gesture guided robot-assisted surgery based on a direct augmented reality interface. Comput. Methods Programs Biomed. **116**, 68–80 (2014)
21. Yacoub, J.H., Verma, S., Moulton, J.S., Eggener, S., Oto, A.: Imaging-guided prostate biopsy: conventional and emerging techniques. RadioGraphics **32**, 819–837 (2012)

# Development of a Conceptual Model for Wrist/Forearm Rehabilitation Robot with Two Degrees of Freedom

Mustafa Dagdelen[(✉)] and Mehmet Ilteris Sarigecili

Department of Mechanical Engineering, Cukurova University, Adana, Turkey
{mdagdelen,msarigecili}@cu.edu.tr

**Abstract.** People who lose their upper limb functions (i.e., movement of their hand and arm) after a stroke or an injury need to follow rehabilitation practices which are defined by a physiotherapist. These exercises are repetitive in nature and robotic systems are well suited for such applications. Hence, there are many rehabilitation robots developed so far and some of them are already in commercial use. In this study, a pneumatically actuated, lightweight, singular free, two degrees of freedom wrist rehabilitation robot is proposed. The developed conceptual models are evaluated for the defined arm/ wrist rehabilitation purposes by comparing them with other available upper limb rehabilitation robots. The proposed robots have serial mechanisms. The main difference between the selected robot designs with other solutions is that actuators do not affect force/ torque requirements of other actuators such as in electrically actuated systems. It also uses a simpler control technique.

**Keywords:** Wrist rehabilitation · Robot · Pneumatics · Upper limb · Stroke · Injury

## 1 Introduction

Stroke and spinal cord injury cause people to lose their ability to use their upper and lower limbs. Disabilities occurred from one of these events can be rehabilitated by tedious, long term, repetitive, laborious physical therapy in rehabilitation. The physical rehabilitation is a process which consists of repeated movement of affected limbs of the body in a predefined manner. This rehabilitation is performed by physiotherapist. Since a rehabilitation service is laborious and exhaustive, a physiotherapist cannot offer the same level of performance for each patient during a day. However, robotic systems are not affected by the type of patient and offer the same level of service for each patient because repeated automated tasks are well suited for robotic systems. Another advantage offered by robotic systems is that the sensory data can be recorded in order to analyse and investigate better rehabilitation therapies. Rehabilitation robots available in literature can be classified into two main categories as upper extremity and lower extremity rehabilitation robots. The first one is used for upper limbs such as shoulder, elbow and wrist whereas the second one is used for lower limbs of the body as hip, knee or ankle. Only upper limb rehabilitation robots are focused in this paper.

The available upper limb rehabilitation robots can be firstly classified as grounded and ungrounded robots. Ungrounded devices are worn by the patient and they are mobile robots. DULEX-II [1] is an example of ungrounded, exoskeleton based upper limb rehabilitation robot. This kind of robots can provide more naturalistic movements. Unfortunately, because of their mechanical structure, torques that can be applied to body joints from the robots are generally low and supplied torques are not enough sometimes for the movement of the limb. The grounded robots transfer the weight of the robot directly to ground not affecting the applied force/torque to the joint of a limb and not stressing the patient. They can be classified as end effector based or exoskeleton based devices. The end effector based robots contact a subject's limb only at its most distal part, e.g. wrist of the device. The forces are transmitted to the body limbs only at a single point called end-effector or interface. On the other hand, exoskeleton based robots imitate the skeletal structure of the limb. Most of the wrist rehabilitation robots, e.g., Wrist Gimbal [2], RiceWrist [3], RiceWrist-S [4] and SUE [5], are of this type.

Actuators of robots are the main elements that drive the links of robots. Hydraulic, pneumatic and electrical systems are commonly used actuating systems. Hydraulic systems produce high forces but they are too heavy. There are few available hydraulically actuated upper limb robots, i.e., Sarcos Master Arm, [6] described in the literature. Electrical actuators, on the other hand, are used widely by wrist rehabilitation robots both in commercial and academic works such as Wrist Gimbal, RiceWrist and RiceWrist-S. The main reason for the popularity of electrical actuators is their easy control and availability; however, the main disadvantage is that they have too high impedance. The final actuator type – pneumatic, has lower impedance than an electric actuator and weighs less than this latter one [7]. The pneumatically actuated upper limb rehabilitation robots reported in the literature are SUE and DULEX-II. Another important criterion in rehabilitation robots is whether the robot has a serial or parallel mechanism. In parallel mechanisms, the end-effector can be moved by more than one actuator working in closed mechanical structure, whereas in serial mechanisms the end-effector is connected to the base with links in series; only one side is jointed to the other links and the other side is not in contact with the ground [8].

In rehabilitation robots, transmission of power from actuators is an important criterion to be considered. The transmission systems can be classsified as cable drive, gear drive and direct drive. Cable drives are suitable for haptic devices. The second type – the gear transmission allows simple designs with easy control of the system. The gear drives are easier to manufacture and cheaper than the cable drive systems. W-EXOS [9] uses gear drive transmission. Finally, the direct drive transmission does not have any component between the actuator and the output link; hence, it can provide easier control and high output torque/power. Rehabilitation robots are also distinguished based on the robot's active degrees of freedom (DOF) which determine the level of difficulty in the control system's design. In the literature, SUE and DULEX-II have been reported as 2-DOF robot; W-EXOS, Wrist Gimbal, RiceWrist-S have been reported as 3-DOF robot, and, lastly RiceWrist has been reported as 4-DOF.

The limits and the range of motion in joints for the rehabilitation robots are vital since they have to be compatible with human's normal upper limb movement

**Table 1.** Range of Motions (ROM) of wrist and forearm [10]

| Range of motion of forearm and wrist | |
| --- | --- |
| Movement | Range of Motion($^o$) |
| Wrist Extension | $70^o$ |
| Wrist Flexion | $75^o$ |
| Wrist Radial Deviation | $20^o$ |
| Wrist Ulnar Deviation | $35^o$ |
| Forearm Supination | $85^o$ |
| Forearm Pronation | $70^o$ |
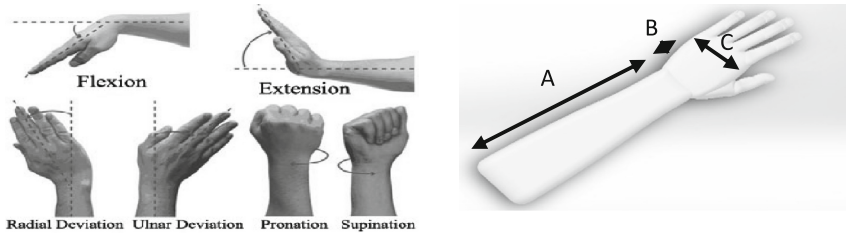


**Fig. 1.** Wrist and forearm motions and human hand average sizes [12]

characteristics. The types of motion with respect to the neutral position of the wrist (i.e., handshake position) are defined in [10] as listed in Table 1 (Fig. 1).

It is reported that rehabilitation efforts of distal limbs such as wrist and forearm have a positive direct effect on the rehabilitation of other limbs [11]. Hence, the design of a rehabilitation robot for wrist flexion/extension, radial/ulnar deviation and forearm pronation/supination is considered in this study. The designed robot is called CUWRIST indicating the Cukurova University WRIST rehabilitation robot. It is a grounded, pneumatically actuated, exoskeleton based and serial type mechanism as combination of gear and direct transmission. The wrist forces are transmitted by rack and pinion gear mesh, and forearm forces are actuated through direct drive. The main requirement for CUWRIST's design is that a normal hand should fit inside the robot's handling fixture; hence, the hand dimensions are important. In [12], the dimensions of a normal hand for a medium aged person are reported as follows: value "A" is the length from elbow to wrist and can be in the range from 240 mm to 280 mm, value "B" is the length from wrist to palm and can take values between 50 mm and 80 mm, and value "C" is the wrist width and can take values between 90 mm and 100 mm.

## 2   Conceptual Design of CUWRIST

Three conceptual designs were developed based on the requirements formulated in the previous section for the CUWRIST rehabilitation robot, the corresponding structures being pneumatically actuated. The power is transmitted either by direct drive or by gear drive. The materials used are mainly polymers and very little amount of metals are used

for stiffness and rigidity requirements. Eccentricity "e" between the centre of the forearm and the centre of the gear is zero in our designs. If this condition is not satisfied, the centre of the human wrist will perform simultaneously rotational and translational motions instead of pure rotation. However the motions of the wrist occur at four different axes i.e. the flexion axis is different from the extension axis. Likewise, the radial deviation axis is different from the ulnar deviation axis [13].

The first design is shown in Fig. 2. It has 2-DOF as wrist flexion/extension and wrist radial/ulnar deviation. It has one linear pneumatic actuator and one rotary pneumatic actuator. The power is transmitted to the end effector via gears. The main advantage of this conceptual design is that it is very simple and easy to control. However, unfortunately the centre of the wrist cannot make pure rotation because of the eccentricity. Also, this design does not provide forearm pronation/supination activity.
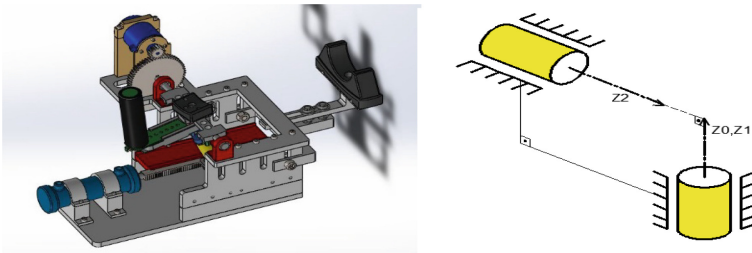


**Fig. 2.** Conceptual design-1 and its kinematic configuration

The disadvantages existing in this first version of design open the perspective for the second design which is shown in Fig. 3. It has 3-DOF for wrist flexion/extension, wrist radial/ulnar deviation and forearm supination/pronation. It has two linear pneumatic actuators and one rotary pneumatic actuator. Even though this conceptual design provides forearm pronation supination activity, there are two different eccentricities found in the forearm and wrist actuation mechanism. The main advantage of the second conceptual design is that actuators are grounded and hence the loads on the actuators are reduced. This leads to smaller actuators and lightweight structure.
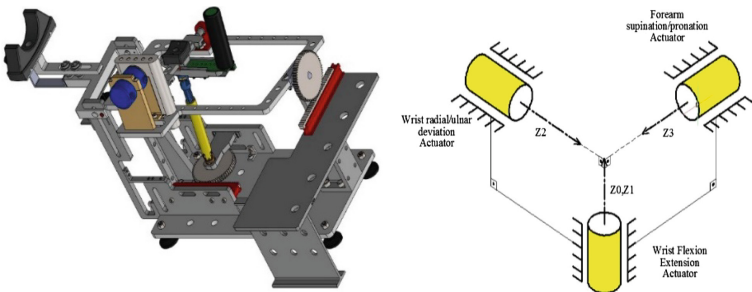


**Fig. 3.** Conceptual design-2 and its kinematic configuration

The final conceptual design in Fig. 4 is developed by eliminating the eccentricity problem. This design has 2-DOF; however it can provide all three motion activities separately in the wrist and forearm rehabilitations. It has one linear and one rotary pneumatic actuator. The forearm movement is achieved by the rotary actuator and there is no auxiliary transmission component in between the rotary actuator and hand holding fixture. This design provides direct driving and small size actuators. As a result, the design becomes smaller, lightweight and economic. The linear pneumatic actuator provides the wrist movements. Power from the linear pneumatic actuator is transmitted via a rack and pinion gear mesh and a driveshaft. In this conceptual design, the rotation axes for the wrist and forearm coincide with the mechanism's axes of rotation. The design provides also adjustable link lengths (Fig. 5) relative to the different limb (i.e., hand & forearm) sizes of patients. The adjustable lengths are the distance between wrist and elbow (i.e., "d1" in Fig. 5), the distance between palm and wrist ("d2" in Fig. 5), and the vertical elbow height which is denoted by "h" in Fig. 5. The ranges of motion for d1, d2 and h are 40 mm, 70 mm and 45 mm respectively.
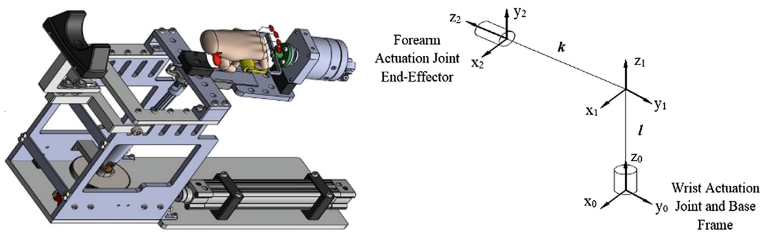


**Fig. 4.** Conceptual design-3 and its kinematic configuration
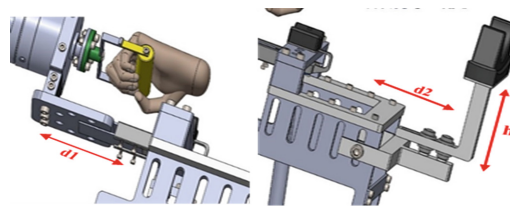


**Fig. 5.** The adjustable distances

## 3  The Kinematics of CUWRIST

Kinematics in robotics is obtained using the Denavit-Hartenberg notation. This notation refers to four parameters defining the spatial relationships of successive links of a robot; they consist of two translational ($a$, $d$) and two rotational ($\alpha$, $\theta$) parameters. Further details can be found in [14]. The kinematics of CUWRIST will be also expressed with Denavit-Hartenberg notations. In Fig. 4, $z0$ is defined as the axis of global frame at the intersection of the upper part of the driveshaft and the rotating part of the mechanism;

z1 represents the rotation axis of the wrist, and z2 represents the rotation axis of forearm. All three axes intersect at a single point. In this mechanism, the rotation about z2 axis and the forearm's position determine whether wrist flexion/extension activity or wrist radial/ulnar deviation activity is performed.

The Denavit-Hartenberg parameters for CUWRIST are represented in Table 2. In this table, i-1 is the link number, $a_{i-1}$ is the distance of the common normal between two successive z-axes, $\alpha_{i-1}$ is the angle of rotation of the preceding z axis about x axis, $d_i$ is the distance from the preceding x axis to the common normal along the z axis. Finally, θ1 is the rotation about z1 axis whereas θ2 is the rotation angle about z2 axis.

**Table 2.** Denavit-Hartenberg notation of CUWRIST

| i-1 | $a_{i-1}$ | $\alpha_{i-1}$ | $d_i$ | $\theta_i$ |
|---|---|---|---|---|
| 1 | 0 | 0 | $k$ | $\theta_1$ |
| 2 | 0 | $\pi/2$ | $l$ | $\theta_2$ |

The position of a point defined according to the forearm frame can be represented according to the ground frame as shown in matrix form in Eq. (1). In this equation, "c" represents cosine function and "s" represents the sine function.

$$
{}^0T_2 = \begin{vmatrix}
c\theta1 * c\theta2 & -c\theta1 * s\theta2 & s\theta1 & k * s\theta1 \\
s\theta1 * c\theta2 & -s\theta1 * s\theta2 & -c\theta1 & -k * c\theta1 \\
s\theta2 & c\theta2 & 0 & l \\
0 & 0 & 0 & 1
\end{vmatrix} \tag{1}
$$

## 4   The Actuators and Control Algorithm of CUWRIST

In the design of rehabilitation robotics, the range of motion (ROM) for joints and the torque applied to the joints are two main criteria. For CUWRIST design, one linear and one rotary pneumatic actuator are selected for the desired output motions. These actuators are selected based on the stroke length, piston diameter, and the force or torque producing capacity of 3–6 bar air pressure range, which is the nominal working pressure in pneumatic systems. The selected actuators are shown in Table 3 on the last column. The torques are calculated at 4 bar working pressure.

Control systems of available upper limb rehabilitation robots reported in literature are very complex due to their complex mechanical design, actuation and transmission types. Considering that the rehabilitation activities are generally performed very slowly and motions are performed between predetermined minimum and maximum levels, the control technique for CUWRIST is selected as simple On-Off control. For CUWRIST control, a microcontroller Arduino Mega R3 is used. The actuators are turned on or off by solenoid valves based on the signals sent by the microcontroller.

**Table 3.** Joint's actuators and their properties

| Part | Torque(Nm) | ROM($^o$) | Actuator |
|------|-----------|-----------|----------|
| Wrist Flexion/Extension | 9.42 | 106$^o$ | PLF25 $\times$ 250[a] |
| Radial/Ulnar deviation | 9.42 | 106$^o$ | PLF25 $\times$ 250[a] |
| Supination/Pronation | 14 | 180$^o$ | MCRD-80 $\times$ 270[b] |

[a]PLF25 $\times$ 250 is a rodless pneumatic cylinder of 25 mm piston diameter and 250 mm stroke
[b]MCRD-80 $\times$ 270 is a semi rotary pneumatic actuator having 270$^o$ rotating capacity

## 5 Results

In this study, three conceptual designs developed for the wrist has been reported. Each one was evaluated based on their degree of freedom, range of motions, torques applied to the joints and singularity situations. In the developed designs, the second model (Fig. 3) has singularity in the wrist flexion/extension when the forearm position reaches a certain value. The first model (Fig. 2) has no singularities; however it has eccentricity between the wrist's centre of rotation and the actuator's centre of rotation. It also does not have the capability of forearm pronation/supination. Finally, the third developed model (Fig. 4) was named CUWRIST. This design satisfies 73 % of wrist flexion/extension range of motion, 100 % of wrist radial/ulnar deviation and 100 % of forearm pronation/supination. Hence, CUWRIST's range of motions cover all three wrist and forearm rehabilitation activities achieved by only two pneumatic actuator.

## 6 Discussion and Conclusion

The rehabilitation robots gain importance as patients expect better from the technological developments. In our study, the wrist rehabilitation activities are performed with only two actuators. The actuators are carried directly by the base of the robot. Hence, the selected actuators are the smallest possible and do not need to carry any useless load. The designed robot has a very simple On-Off control due to the nature of rehabilitation activities which are done slowly, between predetermined levels. Since we are in the prototype manufacturing period, a prototype of the design will be manufactured soon and tested physically. The current design requires programing the microcontroller in computer for the predetermined wrist activity levels and to upload it to the microcontroller. It is required to develop a computer user interface so that wrist flexion/extension limits, wrist radial/ulnar deviation limits and forearm pronation/supination limits can be entered directly for each patient.

**Disclaimer.** Certain software products are identified in this paper; they were used only for demonstration purpose. This doesn't imply any approval or endorsement by Çukurova University, nor does it imply that these products are necessarily the best for the purpose.

# References

1. Bae, J., Moon, I.: Design and control of an exoskeleton device for active wrist rehabilitation. In: International Conference on Control, Automation and Systems, Jeju Island, Korea, pp. 1577–1580, 17–21 October 2012
2. Martinez, J.A., Ng, P., Lu, S., Campagna, M.S., Celik, O.: Design of wrist gimbal: a forearm and wrist exoskeleton for stroke rehabilitation. In: IEEE International Conference on Rehabilitation Robotics, Seattle, Washington, USA, 24–26 June 2013
3. Gupta, A., O'Malley, M.K., Patoglu, V., Burgar, C.: Design, control and performance of ricewrist: a force feedback wrist exoskeleton for rehabilitation and training. Int. J. Robot. Res. **27**(2), 233–251 (2008). doi:10.1177/0278364907084261
4. Pehlivan, A.U., Lee, S., O'Malley, M.K.: Mechanical design of ricewrist-s: a forearm-wrist exoskeleton for stroke and spinal cord injury rehabilitation. In: The 4th IEEE RAS/EMBS International Conference on Biomedical Robotics and Biomechatronics, Rome, Italy, 24–27 June (2012)
5. Allington, J., Spencer, S.J., Klein, J., Buell, M., Reinkensmeyer, D.J., Bobrow, J.: Supinator extender (SUE): a pneumatically actuated robot for forearm/wrist rehabilitation after stroke. In: 33rd Annual International Conference of the IEEE EMBS, pp. 1579–1582, Boston, Massachusetts, USA, August 30–September 3 2011
6. Mistry, M., Mohajerian, P., Schaal, S.: An exoskeleton robot for human arm movement study. In: Proceedings of IEEE/RSJ International Conference on Intelligent Robots and Systems, pp. 4071–4076, Alberto, Canada (2005)
7. Maciejasz, P.: A survey on robotic devices for upper limb rehabilitation. J. Neuro Eng. Rehabil. **11**(3), 1 (2014)
8. Tsai, L.W.: Robot Analysis: The Mechanics of Serial and Parallel Manipulators. Wiley, New York (1999)
9. Gopura, R.A.R.C., Kiguchi, K.: A human forearm and wrist motion assist exoskeleton robot with EMG-based fuzzy-neuro control. In: Proceedings of 2nd Biennial IEEE/RAS-EMBS International Conference on Biomedical Robotics and Biomechatronics, pp. 551–555, Scottsdale, USA, 19–22 October 2008
10. http://www.eatonhand.com/nor/nor002.htm
11. Krebs, H.I., Volpe, B.T., Williams, D., Celestino, J., Charles, S.K., Lynch, D., Hogan, N.: Robot-aided neurorehabilitation: a robot for wrist rehabilitation. IEEE Trans. Neural Syst. Rehabil. Eng. **15**(3), 327–335 (2007)
12. https://grabcad.com/library?page=1&per_page=100&time=all_time&sort=recent&query=human%20hand
13. Lo, H.S., Xie, S.Q.: Exoskeleton robots for upper limb rehabilitation: state of the art and future prospects. Med. Eng. Phys. **34**, 261–268 (2012)
14. Craig, J.J.: Introduction to Robotics: Mechanics and Control. Pearson Education International, USA (2005)

# Influence of an Assistive Hip Orthosis on Gait

Jeremy Olivier$^{(\boxtimes)}$, Amalric Ortlieb, Mohamed Bouri, and Hannes Bleuler

Robotic Systems Laboratory (LSRO), EPFL, Lausanne, Switzerland
{jeremy.olivier,amalric.ortlieb,mohamed.bouri,hannes.bleuler}@epfl.ch

**Abstract.** Powered orthoses are leading to an imminent change in the field of assistance. The major challenges faced by the technology concern the management of the interaction between the user and the wearable device and the coordination between the user intention and the actuated motion. In the present study, we used the HiBSO (Hip Ball-Screw Orthosis) to investigate the contribution of an assistance to the hip flexion/extension motion during walking. Four healthy subjects wearing the HiBSO performed a controlled walking at 3.6 km/h on a treadmill. Three conditions were evaluated: free walking (without orthosis), a transparent mode (orthosis providing no assistance) and an assistive mode (orthosis assisting 10% of walking torque). Kinematics tracking and heart rate recording have been used for the assessment of the assistance. The observations exhibited a clear influence of the assistance on the hip flexion velocity during the swing phase. The ranges of motion of the hip and the knee tend to increase in the assistive mode whereas the ankle range of motion is reduced. Thus the assistance of the hip has a global influence on all the joints. The heart rate acquisitions demonstrated a higher energy expenditure while wearing the orthosis in both transparent and assistive mode.

**Keywords:** Hip orthosis · Walk assistance · Lower limb coordination

## 1 Introduction

In 2012, the US National Health Interview Survey reported that 7% of the adult population is in the incapacity or has important difficulties to walk a distance of 400 m (one quarter of a mile) [1]. This percentage represents approximately 17 million people. Powered orthoses are a promising technology to address this issue. The development of such solutions face different challenges for instance: the wearability, the dynamical performances and the assistance strategy. Only few devices have been deployed for large and medium sized clinical studies (e.g. ReWalk, Ekso, Cyberdyne HAL). It appears that wearability and dynamical performances have met a relatively acceptable level (even though some challenges remain). Control strategies, however, are still considered as one major issue and will be investigated further in this study.

From the wide spectrum of developed powered suits, three main categories of control strategies can be defined as following: mobilization, performance augmentation and partial assistance. The first strategy consists in providing complete support to users who cannot control their legs e.g. spinal cord injury (SCI)

patients. The performance augmentation strategies are meant to enable exoskeleton users to perform heavy duty comfortably (e.g. carrying heavy loads or tools). The typical approach is to support the extra load through the exoskeleton while allowing the user to move freely. Model based or force rejection at interaction between the user and the exoskeleton are commonly implemented for this type of application [2]. Eventually, assistive strategies are usually designed to support a motion initiated by the user. Therefore the synchronization between the user and the device motions is crucial. Potential users are people with gait disorders (e.g. frail elderly or people suffering from muscular dystrophy) who need assistance to improve their walking capacities. Several solutions exist for this online task identification. The information can be measured from biological signals (e.g. electromyography (EMG)) or from position, force or IMU sensors.

This study focuses on assistive strategies and an analysis of the influence of partial support (hip flexion/extension) is conducted. Gait kinematics and heart rate are evaluated for different conditions where the subjects are asked to walk on a treadmill. Three different conditions are compared (i.e. free walking, orthosis in transparent mode and in assistance mode). The results are discussed by studying the impact of the assistance compared with free walking and to the transparent mode condition.

## 2   Material and Method

This section describes the protocol of the experiment, the measurement material, the used orthotic device and its control architecture.

### 2.1   Method

The experimental protocol consists in four walking sessions on treadmill at a controlled velocity of 3.6 km/h (1 m/s). Each session lasts 10 min in order to enable the subjects to accommodate to the different conditions and to stabilize their heart bit rate. The participants are equipped with seven markers on the lower limbs so as to collect their gait kinematics (for details about the motion capture system see [5]) and a chest belt to record the heart rate. In two sessions, they are also wearing the Hip Ball Screw Orthosis (HiBSO – see next subsection) for the transparent and the assistance mode conditions. First and last sessions are performed in Free Walking (FW), i.e. the subjects are not wearing any apparatus but the sensors. The first session is used as a baseline to which the last one can be compared so as to detect any modification of the natural gait due to fatigue for instance. The second session is performed with the orthosis in Transparent Mode (TM), no assistance is provided but the undesired effects of the orthosis are actively compensated for (see "Control modes" section). For the third session, the participants are assisted with 10% of their natural estimated walking torques (see Assistance Mode (AM) in "Control modes" section).

4 healthy adult subjects took part in this study. Their main characteristics are listed in Table 1.

**Table 1.** Characteristics of the participants.

| Subject | Gender | Age (years) | Height (cm) | Weight (kg) |
|---------|--------|-------------|-------------|-------------|
| S1 | Male | 22 | 175 | 74 |
| S2 | Male | 31 | 175 | 72 |
| S3 | Male | 26 | 185 | 78 |
| S4 | Male | 26 | 202 | 100 |

## 2.2   HiBSO

The orthotic device used in this study is the HiBSO [4] (see Fig. 1). Assistive torque can be provided at the hips in flexion and extension with nominal torques up to $17\ N \cdot m$. This corresponds to 30% of the torque developed at the hip level for a person weighing 70 kg. The other movements are unconstrained. The complete device represents an extra mass of 7.4 kg on the user. Note that the power source, the power electronics and the controller are remotely located.



Trunk interface

Motor with ball-screw transmission

Thigh interfaces
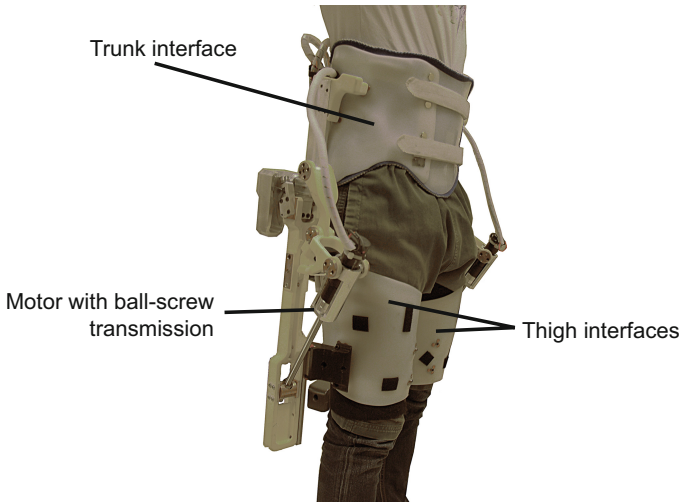
**Fig. 1.** The HiBSO device used to assist the hip flexion/extension during walking.

## 3   Control Modes

The two different control modes implemented on the orthosis are described hereafter.

## 3.1    Transparent Mode

The transparent mode describes a state where the device is theoretically not felt by the user. This corresponds to a compensation of the undesired effects of the orthosis such as the friction in the transmission, the inertia of the device and the gravity. The complete model used for the implementation of this control mode can be found in [4].

## 3.2    Assistance Mode

The selected assistive strategy is based on adaptive oscillators which have proven their effectiveness to synchronize a controller with an observed non-steady cyclic pattern [7]. The controller implemented on the HiBSO is similar to the one proposed by Lenzi et al. [3]. The assistance mode is implemented on top of the transparent mode so as to reduce the orthosis dynamical effects. The complete control scheme is presented in Fig. 2.
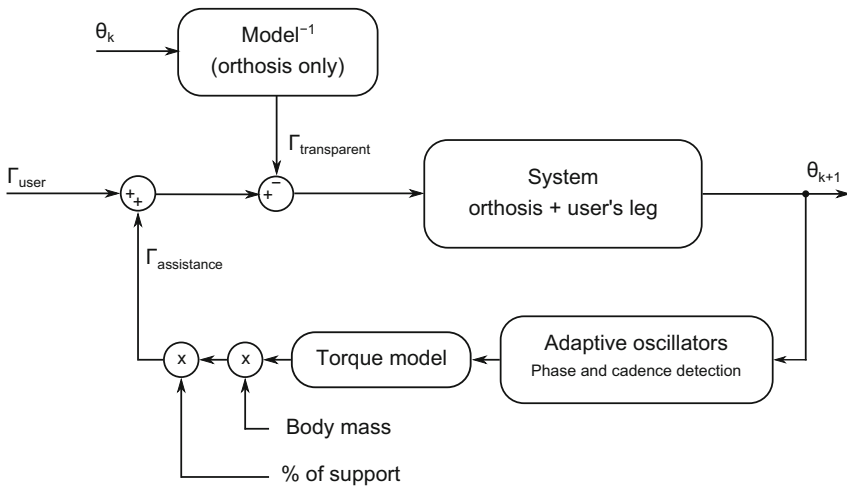


**Fig. 2.** Control scheme of the force assistive strategy based on adaptive oscillators and active compensation.

The assistance is based on a torque model that is extrapolated from typical torque profiles [8] (see Fig. 3). The proposed torque model is defined as a function of the cadence (number of steps per minute) and the gait stride phase. These two variables can be robustly determined using the adaptive oscillators approach applied to the joint kinematics. The torque model is approximated by the product of a $24^{th}$ order Fourier series (depending on the gait phase) and a

quadratic polynomial function (depending on the cadence):

$$\Gamma_{assistance}(stride, cadence) = (A + B \cdot cadence + C \cdot cadence^2) \cdot$$

$$\left( a_0 + \sum_{i=1}^{24} a_i \cdot cos(i \ \omega \ stride) + b_i \cdot sin(i \ \omega \ stride) \right) \tag{1}$$

where $A$, $B$, $C$, $a_i$, $b_i$ are the fitting variables. *stride* corresponds to the gait phase. The choice for the Fourier series model comes from the cyclic nature of the signal and guarantees the continuity between each cycles.
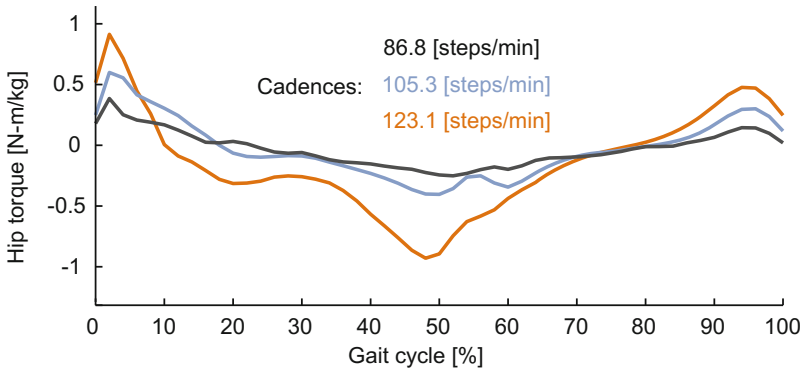


**Fig. 3.** Hip torque model for the flexion/extension during level walking adapted from [8]

The gait phase (or the stride percentage) evolution is given by the estimator. Nevertheless, a stride event is required to identify the beginning of the stride. In [3], the heel strike is detected by means of a foot switch. In this study, another approach involving no extra sensors has been implemented and demonstrated its robustness and repeatability over the different trials. It consists in detecting the global minimum of the position (hip full extension) which usually appears at approximately 54% of the gait cycle (note that this requires an individual tuning).

As it is illustrated on Fig. 2, the assistance can be easily tuned for subjects of different body mass or for different percentage of assistance by modifying the relative coefficient. In order to avoid to create a sudden change in the gait of the user as the assistance mode is turned on, the percentage of assistance is smoothly increased over a couple of seconds from 0% to the final assistance percentage. Three security conditions are also implemented to automatically turn off the assistance in case of unexpected event or gait interruption. First, the gait cadence has to stay between boundary values of 80 and 130 steps per minute. Secondly, the absolute cycle offset between the left and right leg should not be over 10% and finally, the range of motion over one cycle should not be smaller than 30° which would imply that the motion is not walking. If any of these conditions is not respected, the assistance is instantly turned to the transparent mode so that the user can walk freely.

## 4   Results

The kinematics of the lower limbs and the heart rate recording of the 4 participants in the three different conditions are presented hereafter.
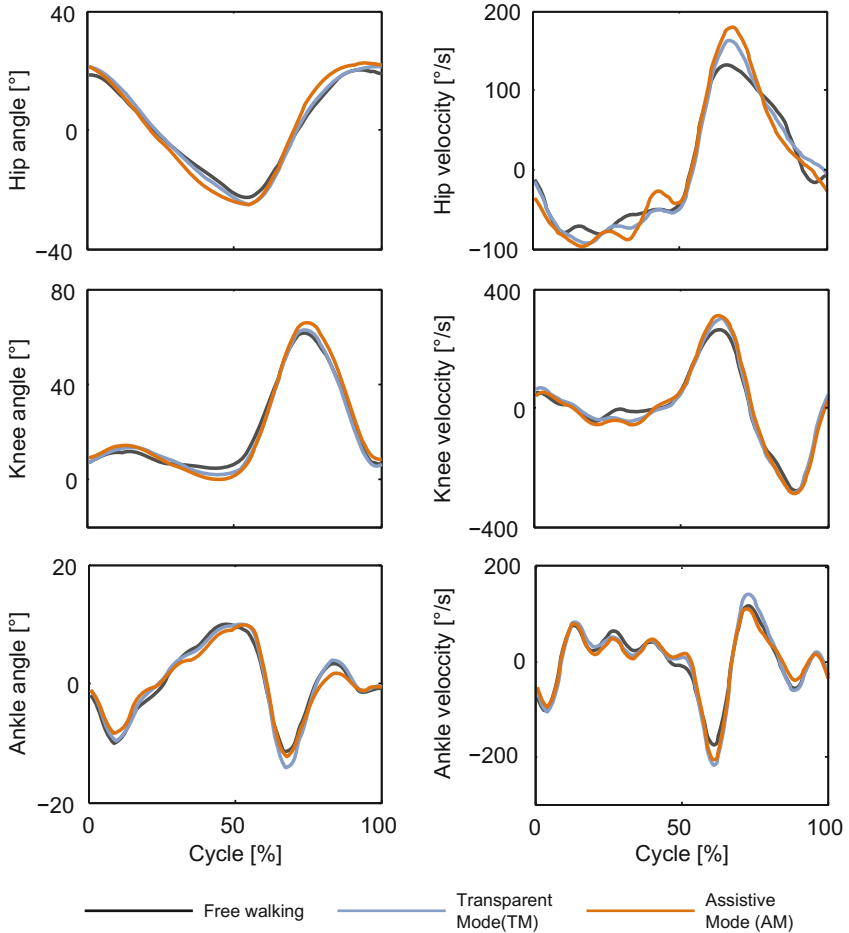
### 4.1   Kinematics

During each session and in the different experimental conditions, the lower limbs kinematics were recorded during a minimum of 1 min. Average curves are thus generated for each subjects. These curves are then combined with the curves of the other participants so as to get inter-subject averaged trajectories. Figure 4 illustrates the lower limb joints trajectories for the 3 experimental conditions.

The range of motion (RoM) for both the hip and the knee is increased of about 7% in transparent mode (TM) and about 12% in assistance mode (AM) compared to free walking (FW). For the ankle however TM and AM show opposite tendencies, with a bigger RoM in TM and a smaller one in AM. The peak amplitudes of velocity follow the same tendency i.e. large RoM are present when high velocity peaks are recorded and conversely. The most important velocity differences are recorded for the hip during the early swing phase and for the ankle during all the swing phase. All these observations have been found to be similar among all the subjects with the exception of the knee RoM which decreased for one of the participants in TM.

Other parameters of the gait have been compared between the different conditions but no global tendencies could be observed. Among the evaluated parameters stand the cadence and the step height which varies quite importantly in function of the participant. The cadence differences comparing AM and FW can vary between $-8\%$ to $+10\%$ and even more for the step height with a minimum of $-27\%$ and a maximum of $+32\%$. These observations comfort the hypothesis that several adaptation strategies may be adopted from the participants.

### 4.2   Heart Rate

The heart rate recorded over the sessions of 10 min enables to estimate the impact of the different condition on the metabolic expenditure. The results were averaged for the four participants. Individual tendencies have also been investigated but results show similar tendencies. The FW was performed twice i.e. in the first and in the last sessions to detect if fatigue occurred. The results of the 4 sessions are presented on Fig. 5 and the statistically significance is marked by one or two stars denoting respectively a 5% or 1% significance. The first observation is that the heart rate between the first FW and the second FW are very similar with a difference of less than 2 bpm for the mean values and no statistically significant difference. The difference of heart rate comparing the FW with any of the TM or AM (about $+8.5$ bpm) is important. This statement is statistically supported by the Student's t-test with p-values inferior than 1% for the TM and 5% for the AM, both compared to the FW. The comparison of the TM with the AM did not denote any significant reduction in the metabolic cost.

**Fig. 4.** Hip, knee and ankle angular position and velocity for the three conditions of free walking, transparent mode and assistance mode.

## 5   Discussion

The recorded kinematic data demonstrate that the effect of a partial device goes beyond the joint it assists. Indeed the knee is the joint on which the device has the most influence in terms of RoM. The passive influence induces an augmentation which is further increased by the assistance controller. This can be explained by the fact that the acceleration of the hip flexion is higher during the swing phase, both in TM and AM. As the knee has a relatively low stiffness during this phase [6], the motion of the thigh relatively to the shank is larger and the knee flexion is increased. Logically the subjects who increased the most their hip acceleration also had the largest increase in knee flexion. The fact that the acceleration is larger during the swing phase in AM is not surprising as this
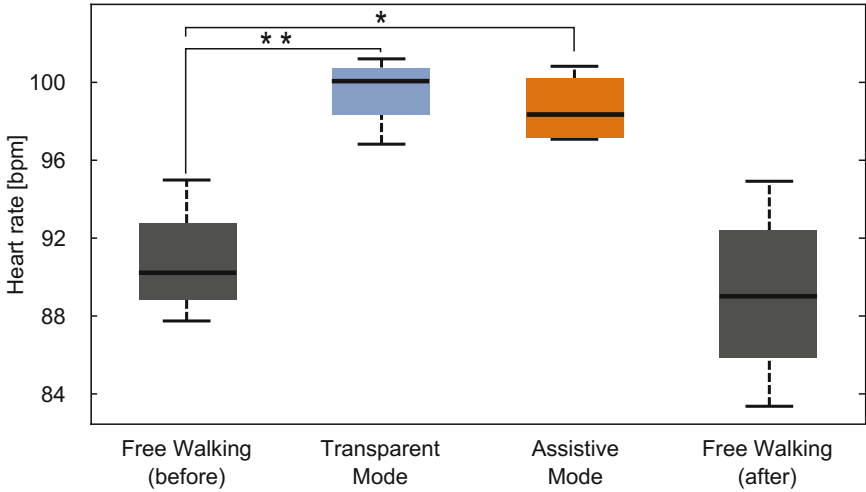
**Fig. 5.** Average heart rate of the four participants during the sessions in different walking conditions.

movement is aided by the orthosis. However, the hip acceleration is also larger in TM during that phase, which implies that some subjects tend to generate an even greater torque at this joint than what would be required to compensate the added load. This overcompensation may indicate that these subjects aim to adopt a safe behaviour where their hips are stiffened in order to reject the perturbations induced by the device. The velocity increase is smaller during the stance phase. This is probably due to the fact that the articulations are stiffer in stance and therefore less kinematic changes can be observed.

The kinematics of the ankle is also influenced by the device. In that case, the controller seems to play a major role as the TM and AM conditions have opposite effects on ankle velocity and acceleration when compared with FW. Even though this measurement does not represent a sufficient evidence on its own, it suggests that the ankle may benefit from this type of support. A study on the joints torques would then be required to confirm a possible reduction on the required ankle effort.

Attempts to reproduce the EMG measurements performed by Lenzi et al. [3] were also performed in order to manifest the differences in muscles activations (which are in direct link with joints torque and stiffness). Surface EMG signals of the Hamstrings (Semitendinosus), Quadriceps (Rectus Femoris), Gastrocnemius and Tibialis Anterior muscles were thus measured on several subjects during the study. This was done using a DataLINK system (Biometrics Ltd, United Kingdom). However, these measurements were unusable due to the low reliability of the surface EMG signal in amplitude. Indeed, the same condition exhibited drastically different amplitudes when measured at different points in time. A comparison between the different conditions would therefore be chancy and

inaccurate. Moreover, external parameters (e.g. placing the orthosis cuffs on top of the EMG electrodes attached to the thighs for two conditions only) may have an influence on the signal and compromises its correct interpretation.

The heart rate measurements indicate that the subjects have to spend more energy to walk with the HiBSO than in the FW condition. This was also the case when assistance was provided. No significant influence of the assistance could be established in terms of metabolic cost even though one of the subject had a lower heart rate while being provided with assistance. This measurement being relatively uncertain, no conclusion can be made here. It may however be hypothesized that 10% of assistance with a device that adds an important extra load on the wearer is not enough to assist gait properly. Two improvements are therefore required. First, the actuation needs to provide a larger proportion of the torque or another assistance strategy is required. Second, the negative influence of the device needs to be addressed properly. The kinematics, the weight of the device and its interface with the body have to be considered carefully. The actuation is also extremely important especially if not all its dynamic effects can be compensated perfectly.

## 6   Conclusion

In order to design an effective assistive strategy, a good understanding of biomechanics and human motor control is crucial. In this study a notable effect of the assistance could be observed in particular at the ankle joint even though the assistance was provided at the hip level. This reorganization of the joint activity could then possibly be exploited to assist people with reduced vigor at the ankle. However, the results of the study also highlight the difficulty of effectively assist an activity such as walking so as to reduce the metabolic demand. Indeed, even though the implemented controller provides a percentage of the required torque at the desired time (i.e. in coordination with the articulation movements), no positive impact on this metric could be observed unequivocally. In that context joint stiffness adjustments induced to reject the perturbations caused by the orthosis certainly plays a major role. Improved transparency of the device could then facilitate the overall device acceptance and that of the assistive strategy in particular.

# References

1. Blackwell, D.L., Lucas, J.W., Clarke, T.C.: Summary health statistics for us adults: national health interview survey, 2012. Vital Health Stat. **10**, 1–161 (2014). Data from the National Health Survey
2. Kazerooni, H., Racine, J.L., Huang, L., Steger, R.: On the control of the berkeley lower extremity exoskeleton (bleex). In: Proceedings of the 2005 IEEE International Conference on Robotics and Automation, ICRA 2005, pp. 4353–4360. IEEE (2005)
3. Lenzi, T., Carrozza, M.: Powered hip exoskeletons can reduce the user's hip and ankle muscle activations during walking. IEEE Trans. Neural Syst. Rehabil. Eng. **21**, 938–948 (2013)
4. Olivier, J., Ortlieb, A., Bouri, M., Clavel, R., Bleuler, H.: A ball-screw driven motorized hip orthosis. Trans. Control Mech. Syst. Jul 2014. http://tsest.org/index.php/TCMS/article/view/255
5. Ortlieb, A.L., Olivier, J., Bouri, M., Bleuler, H.: Evaluation of an active optical system for lower limb motion tracking. In: International Symposium: 3-D Analysis of Human Movement, No. EPFL-POSTER-198727 (2014)
6. Pfeifer, S., Riener, R., Vallery, H.: Knee stiffness estimation in physiological gait. In: 2014 36th Annual International Conference of the IEEE Engineering in Medicine and Biology Society, pp. 1607–1610, September 2014. http://ieeexplore.ieee.org/lpdocs/epic03/wrapper.htm?arnumber=6943912
7. Ronsse, R., Lenzi, T., Vitiello, N., Koopman, B., van Asseldonk, E., De Rossi, S.M.M., van den Kieboom, J., van der Kooij, H., Carrozza, M.C., Ijspeert, A.J.: Oscillator-based assistance of cyclical movements: model-based and model-free approaches. Med. Biol. Eng. Comput. **49**, 1173–1185 (2011)
8. Winter, D.: Biomechanics and motor control of human gait: normal, elderly and pathological. University of Waterloo Press, February 1991. http://trid.trb.org/view.aspx?id=770965

# Robots in Construction and Arts

# Why Does Architecture Need to Move?
# The Role of Integrated Technical Systems
# in Architecture

Djordje Stojanovic[1(✉)], Marko Milos[2], and Milica Vujovic[3]

[1] Faculty of Architecture, University of Belgrade,
Kralja Aleksandra 73, Belgrade, Serbia
`ds@arh.bg.ac.rs`
[2] Faculty of Mechanical Engineering, University of Belgrade,
Kraljice Marije 16, Belgrade, Serbia
`mmilos@mas.bg.ac.rs`
[3] Mihajlo Pupin Institute, University of Belgrade,
Volgina 15, 11060 Belgrade, Serbia
`milica.vujovic@pupin.rs`

**Abstract.** The emerging interdisciplinary field of mechatronics and integrated technical systems is becoming increasingly important to architecture. Technology comprised of sensors, controllers and actuators allows architects to reconsider the relationship between buildings and their environment, as well as between buildings and their users. The architectural education is finding itself on an uncharted territory while trying to introduce interdisciplinary collaboration into its own curricula. This paper will present outcomes of the research seminar conducted at University of Belgrade, Faculty of Architecture focused on the role of mechatronics and integrated technical systems in architecture. The discussion will focus on the notion of spatial adaptability and three possible reasons why architectural elements should move: efficiency, aesthetics and functionality.

**Keywords:** Mechatronics · Adaptive architecture · Built environment · Integrated technical systems

## 1 Introduction

A graphic representation in "The architectural relevance of cybernetics", Pask [1] points out at certain coupling of the inhabitant and house and suggests that architecture is the product of their interaction. This came as a stark contrast to the prevailing understating of architecture at the time, still very much based on Corbusier's hypothesis that "a house is a machine for living", Khan [2]. Rather than mere analogy, Pask's idea [1] is based on the transposition of the know-how from one discipline to another. What he suggests is that knowledge originating in one field may open up an entirely new paradigm in another discipline. To further comprehend this idea, we need firstly to understand what is meant by the term "cybernetics" and what its basic philosophy is. According to Khan's clarification [2], "Cybernetics is only applicable when the system being analysed is involved in a closed signal loop; that is, where action by

the system causes some change in its environment and that change is fed to the system via information (feedback) that enables the system to change its behaviour. This circular-causal relationship is necessary and sufficient for a cybernetic perspective."

Secondly, we would need to ponder why such principles could excite architects and what could be their relevance for the built environment. While architecture is still most commonly perceived as inert, and while buildings are wrongly understood as permanent due to their extensive lifecycles, architectural researchers are very keen to explore changing aspects and moving segments of the built environment.

One such line of research is named "Adaptive Architecture", implying a conceptual framework concerned with buildings that are specifically designed to adapt to their environment, to their inhabitants, to objects within them whether this is automatically or through human intervention, Schnädelbach, [3]. Along this line of research, adaptability of buildings is driven by different criteria and often measured against the needed investment and reliability of the proposed solutions. Therefore, we need to conclude with the question how to do this and which are the actual means to transform built environment.

The complex physical interactions are already made possible by the creative fusion of embedded computation (intelligence) with a physical, tangible counterpart (kinetics) as noted and illustrated in the book "Interactive Architecture" by Fox and Kemp, [4]. This is prompting architecture to look outside its own boundaries and seek collaboration with other fields end explore the use novel technologies. The emerging interdisciplinary field of mechatronics and integrated technical systems is specifically important for this reason. In the present time, technology comprised of sensors, controllers and actuators allows architects to reconsider the relationship between buildings and their environment, as well as between buildings and their users.

## 2    Mechatronics in Architecture

The principles of mechatronics within the realm of architecture are identical to those of any other mechatronic system applied in other areas such as robotics. The key concept of mechatronics illustrated in the diagram (Fig. 1) is defined by the three basic elements (input, controller and output). For the purpose of any project, this scheme is normally developed into a much more complex one, depending on the input data, ways of its mapping and measurement, method of its processing and the very way the action is executed in the end, or the means by which the movement or change of the designed system is delivered.

In Architecture, the scheme could represent a system that responds to the stimulants coming from the environment or users and is able to perform the movement of building parts and thus allow for spatial change in real time. The input is generated by different
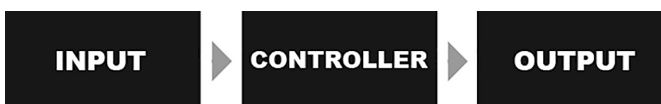


**Fig. 1.** The key concept of mechatronics

sensors which collect data from the environment. The output is created by actuators, which could be either motors used to produce certain movement, or screens if the objective is to display certain graphic information. More detailed description of plausible mechatronic systems applied in architecture will be given through an overview of student work. The presented proposals remain at the conceptual level but demonstrate clear understanding how such ideas could be realized as architectural objects.

## 3   Understanding Potentials of Adaptive Structures

This paper deals with three possible reasons why architectural elements move.

The first category of motion recognized by this study is a movement created in order to achieve more *efficient use of space*. According to this scenario, integral parts of a building, such as facades, walls etc. will move with the ultimate goal to help achieve more efficient use of energy needed for buildings, such as for heating, ventilating, cooling etc. Savings of energy in this way are obtained indirectly. For instance, the use of movable shutters could help to control the illumination of buildings interior and thus reduce the consumption of energy needed for heating and cooling. In the same way it is also possible to control the brightness of the interior space and reduce electricity consumption for lighting. A similar principle is applicable for the outdoor conditions where brightness can vary depending on various conditions. Such spatial transformation, based on movable architectural elements is just an example of the adaptability in architecture becoming a factor that contributes to a more efficient use of indoor or outdoor space.

The second category of the movement, relevant to this study, is concerned with *aesthetics characteristics of space*. The aesthetic contribution to the built environment aims primarily to provide visual comfort, which may encourage better use of space. Regardless of the type of use, changing environment could provide a range of spatial characteristics suitable to individual preferences.

The third aspect deals with the *functionality of space* and it is based on tangible enhancements which mechatronic systems could bring. As indoor or outdoor conditions change throughout the time, it is only reasonable to expect from architecture to look for ways to respond to such changes in pursuing functional characteristics of space.

This paper is focused on architectural education and will present outcomes of the research seminar conducted at University of Belgrade, Faculty of Architecture with participation of 32 students and two teachers. One of the main goals of the seminar was to help students understand the notion of spatial adaptability. Students were introduced to the basics of Integrated Technical Systems, an interdisciplinary field combining aspects of mechatronics, robotics, automatic control and digital fabrication, and ways of their application in architectural research and practice. The seminar was delivered in two segments. During the first part, students have analysed series of architectural precedents whereby Integrated Technical Systems have played an important role within the overall design intent. During the latter part of the semester students were guided to apply newly acquired understanding of Integrated Technical Systems within an architectural project to redesign a small public space in the city. Students were asked to conceptualize architectural proposals based on the measurable information gathered from the surrounding environment (e.g., temperature, humidity, atmospheric pollution,

rainfall, intensity of pedestrian and vehicular flows) and their immediate manifestation, i.e. translating the built environment (e.g. facade, lighting, furniture, paving) to achieve the architectural objectives.

Three student projects resulting as outcomes of the research seminar are selected and will be presented in the following chapters to offer the basis for discussion and consideration of benefits created through the use of Integrated Technical Systems in architecture. These beneficiary reasons are: efficiency, aesthetics and functionality.

## 3.1   Adaptive Lighting System

The project is based on an adjustable lighting system on the recreational track with the aim to make more efficient use of electric energy. The track is located in the forest and thus in the evening lighting the whole track would require a large consumption of electricity. Presented solution introduces adaptive system which activates lights if users are present. The lighting sources are connected to a group of infrared sensors detecting people passing along the route. Sensors supply information to the microcontroller, which then activates lamps and more importantly, regulates the intensity of each light depending on its distance from the user (Fig. 2).
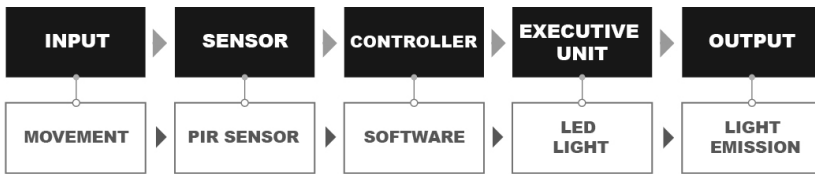


Fig. 2.  Adaptive lighting system

While running or walking down the recreational track, users affect a larger number of lamps in the following way: the lamp that is nearest to the user is the one illuminated the most, while the adjacent lamps are illuminated less, proportionally their distance from the user. The proposed algorithm, suggests that motion detection by any sensor affects seven lamps at the time, each casting gradually less light according to the distance (Fig. 3). The resulting energy savings could be considerable while the safety of the users along the route is not compromised. In addition, the choreography of sequentially diming lights triggered simultaneously by different users along the trail could provide for recognizable visual feature of the entire recreational track.
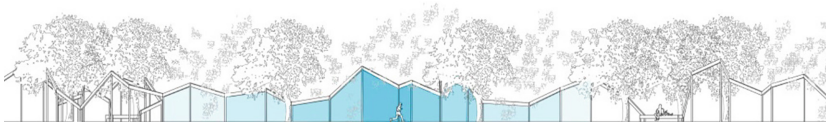


Fig. 3.  Choreography of variable lighting triggered by users

## 3.2 Transformable Shading Structure

The basic intent was to create a canopy above the promenade that reacts to the intensity of the sun light. If the brightness is too strong, the canopy will close to create shaded space (Fig. 4). The intensity of light is monitored in seven cycles each day and the proposed structure partially opens or closes accordingly. The geometry of the canopy is defined by the number of adjoining triangular facets, each inclined at a certain angle to allow for drainage. Each facet is divided into three smaller movable triangular panels and bordered by the twin "U" profile. Each of the inner movable panels consists of seven pairs of metal stripes (total of 14). Depending on the intensity of the sun light, they pull in or out of the "U" profile. If the intensity of the sun light is high, the canopy will close to creating shading, and if it is low the canopy will open to allow the light to reach the promenade (Fig. 5).



**Fig. 4.** Transformable shading structure



**Fig. 5.** Variable geometry of the canopy created with servomotors

A number of lux meters are positioned on the upper side of the structure in order to measure the intensity of the sunlight. In addition, several more sensors are mounted onto the underside of the canopy to measure reflected light.

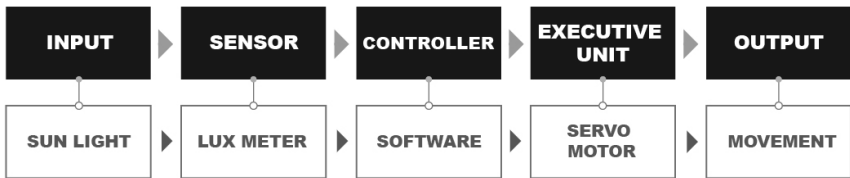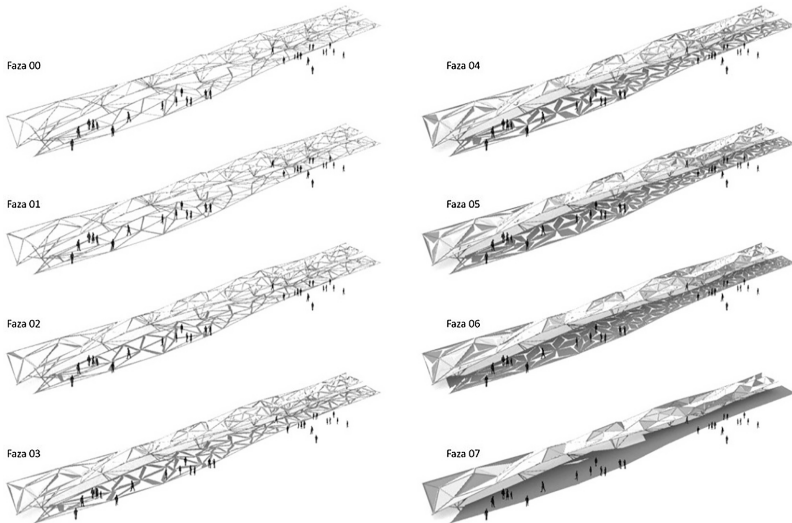The microcontroller processes the data acquired by the sensors and an algorithm is employed to define the output data which regulates the movement of the triangular panels, using servo motors. The axis of the servo motor is located at the point where the edges of the metal strips meet, causing them to rotate. In this way, the triangular panels open to let the light in or close to provide shading. As result, the space below the canopy maintains optimum lighting conditions. Once the panels readjust, a controller performs another check if conditions remain in the optimal range.

## 3.3  Touch Floor Tube

The paving of square fields and a tunnel of LED tubes together constitute a proposal for the installation in the public space. The focus is on the interaction between the user and spatial installation. The user sets the system in motion by stepping on the fields. Each field represents an individual activation unit, but it also activates two adjacent fields, in front of it and behind it. When activated, the field triggers the switch so that the LED tubes form a lighting tunnel above that field. The architectural intent is to establish direct connection between human movement and the way the space is lit (Fig. 6).
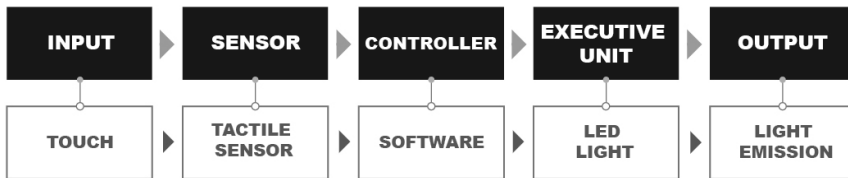


**Fig. 6.** Touch floor tube principle

A similar technology is used at another scale, the one of touch-screens of mobile phones.

The proposed system works on the principle of resistive touch screen. The first layer is ITO (Indium Tin Oxide). Its main role is to provide protection for the technology that is placed under it but without compromising the conductivity. Electrode fibber is used as sensor that reacts to touch. In this case, the electrode fibber is placed over the entire surface of the field so that the whole area remains sensitive to the touch. The data detected by sensors is forwarded to the controller and processed to generate a signal which is in turn sent to the actuator, or in this case to the switch activating the light. The result of motion detection across the distinct fields of the pavement is the brightness of the tunnel like structure, made of transparent plastic tubes which contain LED stripes (Fig. 7).

The main objective of this proposal is to introduce additional content in an open space and make passage through this space more interesting. In addition, this installation, seen from a certain distance presents a subtle play of light, which is the direct consequence of the way the area is used.
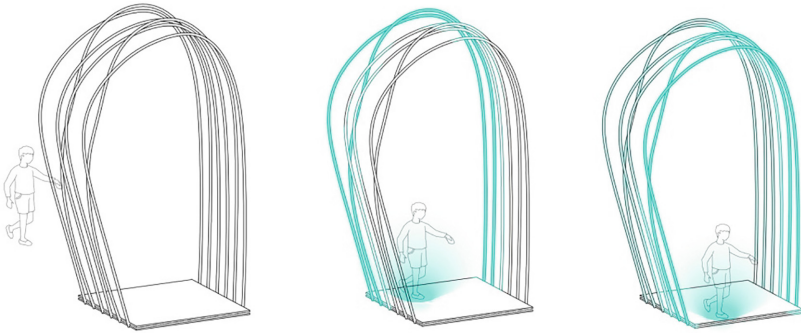
**Fig. 7.** Detected motion changes the brightness of the tunnel like structure

## 4    Conclusion

The presented case studies are conceptual solutions focused on the adaptive potentials of architecture. The inclusion of mechatronics and technical systems as an integral element of the architectural project provides for better of efficiency, aesthetics and functionality of space. The aim of the seminar was to inform future architects and expand their knowledge of the role of integrated technical systems in their discipline. With the knowledge of new technologies and possibilities, architectural solutions can thrive in a new direction.

## References

1. Fox, M., Kemp, M.: Interactive Architecture. Princeton Architectural Press, New York (2009)
2. Khan, O.: A communications primer revisited. In: Ayers, P. (ed.) Persistent Modelling, pp. 51–61. Routledge, London (2012)
3. Schnädelbach, H.: Adaptive Architecture: A Conceptual Framework (2010). http://www.cs.nott.ac.uk/~hms/pdfs/Schnadelbach_AdaptiveArchitectureConceptualFramework_MediaCity2010.pdf. Accessed 15 Mar 2015
4. Pask. https://www.researchgate.net/publication/229618136_The_architectural_relevance_of_cybernetics

# Design of Modular Re-configurable Robotic System for Construction and Digital Fabrication

Milica Vujović[✉], Aleksandar Rodić, and Ilija Stevanović

Robotics Laboratory, Mihajlo Pupin Institute,
University of Belgrade, Belgrade, Serbia
{milica.vujovic,aleksandar.rodic,
ilija.stevanovic}@pupin.rs

**Abstract.** This paper presents the design of an innovative robotic system for building constructions. The proposed robotic system has a modular structure and reconfigurability so that it can adapt to different construction requirements. The robotic system developed in this paper is applied in residential low-rise buildings (ground floor plus three floors and attic). The reconfigurable system presented in this paper implies the possibility of applying three different types of robots: the parallel SCARA, construction Delta robots and redundant, hyper articular robot for infrastructure inspection. The modular structure ensures rapid assembly and disassembly, functionality of the system even in the event of failure of one component of the module The robotic system design is conceived on the model of 3D printers with the possibility of easy replacement of various end effectors to manipulate the material in construction, assembly installation and final processing of the facade and walls. In the conclusion section of the paper a brief comparative analysis of conventional ways of constructing and discussion about the innovative approach of using robots in highly automated processes of building construction will be given.

**Keywords:** Construction robots · Digital fabrication · Robotic building cell · Modular architecture · Reconfigurable structures

## 1 Introduction

With the advent of information technology and computer science, there has been a rapid development of software tools for computer added design (CAD modelling), digitization and simulation models. This led to the development of devices for digital fabrication such as matrix and 3D printers, CNC machines etc. The above-mentioned technologies can enable very precise making even for the most complex amorphous surfaces of irregular shapes [1]. New perspectives have been thus opened in art, architecture and construction by providing additional possibilities of avant-garde design, simple fabrication and aesthetics [2–5].

On the other hand, robotic technologies are introduced in the industry to high standards of precision and quality. Today's commercial industrial robots have the precision and repeatability of up to 100 microns. This allows the creation of

sophisticated and high quality products. Today, robots are used in many industries and human activities. Most of them are applied in mechanical industry, mass production, packaging and sorting, etc., mainly because of their accuracy, repeatability, long service life (a large number of operating cycles), endurance and robustness. Robots are used to ensure high quality in production and to reduce labour costs. Robots provide clean production with minimum waste materials and scrap. When the robot is working, subjective factors of fatigue, lack of motivation, etc. are eliminated. For this reason, robots in manufacturing have increased application and effectiveness. Despite the obvious advantages brought by robotic technology in the industry, a relatively small number of robots are applied in design, construction and architecture.

Together, digitization and robotics open up new horizons for the construction and development of structures of modern avant-garde forms and structures. By coupling the CAD software tools and robotic controllers, today the most diverse and unusual forms in architecture and art can be very accurately produced. Examine their stability and stresses in critical sections, aerodynamics etc.; the problem why robots are still not enough used in the construction industry is that mainly these experiments are conducted in laboratories, to prepare exhibitions and demonstrations. Construction robots are still expensive and economically not feasible because there are no adequate, highly automated production models like those existing in the engineering industry (for example, like the flexible automated production lines in which the flow of materials, labour and energy are optimally planned). Another reason is that, for construction purpose, there are not yet commercial industrial robot manipulators, like those from ABB, Kuka or Yaskawa which are specifically designed for use in factories and not on construction sites. Robots that are experimentally used for construction in laboratories are not used at their full potential. They require careful preparation of the workspace.

In this regard, it is necessary to further adapt standard robots in a better way to the new purpose of construction of buildings. Robots in the construction of buildings can bring significant benefits in productivity and cost savings, as compared to the conventional way of construction where the main work force are people. Unlike workers, robots are tireless, can work non-stop, very precise and with reproducible precision, and economical in the use of materials. Also they cause minimum waste of construction materials, can be remotely controlled and monitored, do not depend on individual motivation and psycho-physical condition. Also, the robots are relatively easy to program and learn to perform different types of operations or tasks with no additional time for training or pre-qualification.

## 2    State-of-the-Art

Digital fabrication is a process that combines architectural design and manufacture of architectural elements. The use of 3D modelling software and computer aided design changes the way of production in architecture. Thus, the possibilities that were offered to the architects are expanded, which results in new ideas and further development of this technology. Examples of digital fabrication in the world are numerous and its application has been established at various scales. Architectural schools and architectural bureaus largely conduct research in this area and achieve significant results.

Gramazio and Kohler Architects [1] both in their work on programs at ETH Zurich and in private practice are examining methods of digital fabrication using industrial robots. Surveys are based on the use of different materials and adapting the available technology to the features and functionality of the given material. The use of bricks as building units has been developed to a large extent by connecting software and industrial robots enabling the achievement of complex structures in a way that is not possible to be carried out by human workers. In addition to bricks they use other building blocks and new liquid materials in the process of forming elements. Thus, at the end of the fabrication process, the final shape is distinct than the one generated immediately after the casting. The use of industrial robots in this manner finds wide application in digital fabrication and continues to develop in architecture too.

The centres for the development of digital fabrication are FabLabs [2], laboratories which test technologies of digital fabrication, and characteristics of the materials used for this purpose. They are widespread throughout the world and most often associated with schools of architecture, where the projects that use this technique are largely developed. FabLabs [2] are intended for testing technologies for the production of smaller objects, but the principle is still developing in the larger centres and applied to larger objects. These structures are equipped with machines such as 3D printer, 3-axis CNC machine, laser cutter, plasma cutter, water jet cutter etc.; they also features digital electronics design, assembly, and test stations where the testing and training in the field of computer technology is applied in digital fabrication.

In addition to these examples, the application of robots in digital fabrication is versatile and will rapidly develop. Due to the specific domain of architecture, it is realistic to think that in the future emphasis will be put on the design of machines specialized for the construction area, which will result in improving the production of architectural structures and developing robotics.

## 3   The Qualities of Good Construction Practices

High-quality and economically sustainable housing construction are characterized by good organization of work, adherence to norms and standards and quality control during the construction process. In this regard, the following aspects of construction are of interest to the research reported in this paper are: (i) How to optimally organize the building site including the timely supply of raw materials without undue accumulation and retention at the site? How to set up scaffolding, cranes and concrete suppliers so that the flow of materials and people be unobstructed and without delay? (ii) What are the norms of construction in terms of the number of workers and their impact in order to optimally organize jobs on site so that there would be no delays or collisions in the performance of different construction tasks (synchronizing construction work)? (iii) Which are the construction quality standards and how are they controlled?

The organization of the construction is a separate field of architecture and civil engineering and is made up of several areas which point to its complexity. The process of building the facility requires above all good preparation, starting from the beginning of the project and during the process of preparing the construction site. This is followed by the construction process which also requires constantly monitoring and proper

management. Because of the complexity of the organization and implementation of construction of the building there are certain norms that are applied and which include all the details of the construction of one building. Norms adapt to each individual case and construction technology that is used.

## 4 Robot Cell for Building Construction

Bearing in mind the characteristics of good construction practices (presented in the previous section) and the research goals (the design a one viable and efficient, highly automated robotic system for the construction of housing facilities), the paper proposes a structure for design.

This structure should meet the following criteria:

  (i)  easy to install, remove and handle,
 (ii)  manageable and open about the availability of information on the progress of works and quality,
(iii)  robust at different operating conditions, considering dust and different climatic conditions on the building site,
 (iv)  provide a uniform, continuous and smooth operation,
  (v)  flexibility in terms of its potential to change functionalities through a simple replacement of system components and/or loading a new program (application software),
 (vi)  safe for the environment and the people who are on site,
(vii)  economically viable in terms of minimizing energy costs and system maintenance.

These criteria correspond to a solution that combines the features of high automation, modularity and ability for easy reconfiguration of the system to be used for construction.

The high automation of the design process for construction involves the introduction of robotic systems for the delivery and distribution of materials to the building site, construction, assembly and setting up building installation, inspection and final internal and external processing (walls, facades, floors). The idea came from industries where automated systems (e.g., flexible manufacturing cell) are used for customized mass production in manufacturing. In the construction industry things are somewhat different in the sense that delivering raw material must be done in 3D space while the industry mainly works in 2D space using conveyor belts and handling robots.

From the types of industrial handling robots, which are widely used in the industry, and are currently available on the market, some could be successfully applied in the construction industry, due to their structure and payload: the SCARA [1] and Delta [2] robots. Due to their technical performances, SCARA robots are suitable for the tasks of installation, moving building material, final surface treatment, plastering, painting or painting, etc. Delta robots, due to their parallel structures are a very fast and accurate but have less capacity than SCARA robots. Both types of robots have reproducibility to 100 microns (Fig. 1).
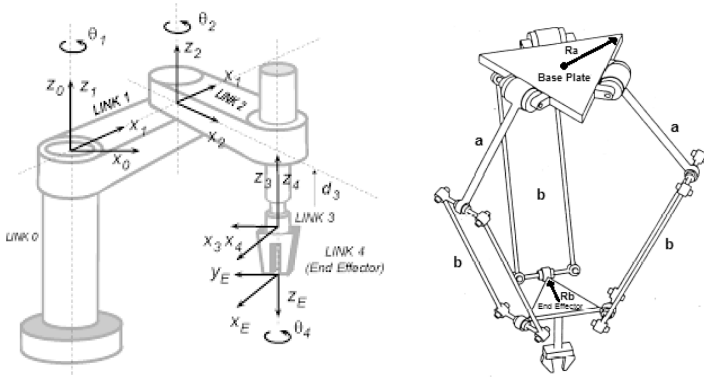
**Fig. 1.** Kinematic scheme of two manipulating standard types of robots SCARA [1] (left) and Delta [2] (right)

The above two robots can be constructed and adapted for the usage on the building site in order to feature different segment lengths depending on the size of the necessary working space, and of the specific tasks to be performed. Different from the use of these robots in manufacturing, where the precision is in the range of micrometres, in construction an accuracy of 1 mm is sufficient to meet the imposed quality standards (Fig. 2).
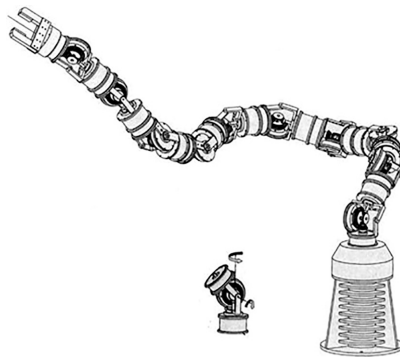


**Fig. 2.** Hyper redundant tendon-driven robot manipulator [3]

The third type of robot that is interesting for applications in the construction industry has an unconventional structure and represents a hyper redundant system that can possess many actuators. The actuators of the robot are located at the base of the mechanism and the motion is achieved by pulling and releasing the tendons (cables). The practical side of this robot is that due to its flexible structure it can be introduced in the building's openings and installations. For this reason, such a robot structure is suitable for inspection and installation of smaller parts. The payload of this type of

robot is relatively small (less than 1 kg) but his total length can be of several meters. This type of robot is used in the aviation and railway industry for the installation of electrical and sensory installations in airplanes and cars.

These three types of robots cannot be used in construction in their original appearance but must be mounted on movable mounts. Carriers are linear type of racks or threaded spindles. Linear actuators are placed at a distance of 5 m to the impact of deflection of guides to be reduced to an acceptable level. These mechanisms are macro manipulators and they are needed for the rough positioning of the robot in the workspace near the working site. In fact, these mechanisms are linear conveyors and can be mounted on all sides of the facade and the ceiling. This allows unrestricted access to the building for the distribution of materials.

The illustration of the entire robot system with linear conveyors, handling robots, gantry cranes, etc. is shown in Fig. 3. The robotic system represents a version of the mega 3D printer according to the principle of layered construction. In this case, the material used is composed from standard building materials: bricks, clay blocks, elements of prefabricated ceiling panels from insulation materials, ceramic tiles as well as binding materials like mortars, adhesives for ceramics, etc.
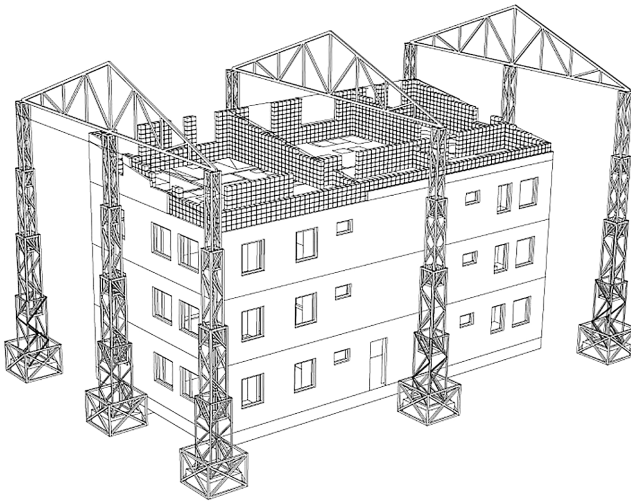


**Fig. 3.** Representation of the building with a modular frame as base for reconfigurable robot cells applied to the construction site.

The global automated construction system includes the following structural functional modules: (i) transport module, (ii) cladding system for robotic processing, (iii) robotic gantry system for incremental construction, (iv) sensing and data acquisition system, (v) site management and device control system.

The robotic system for construction shown in Fig. 4 allows applying binding material (mortar) layer-by-layer and placing brick/clay blocks row-by-row. The corresponding application program of the robot controller is generated based on the CAD

model of the building that is stored in the database of the central control system. The input data to the building system are technical drawings (plans) generated in a CAD software environment for the control of the specific cell structure for construction. Like the workers who use their two hands to perform masonry two robotic arms of handling robots are synchronized. They are managed by a master controller that distributes the tasks to each of the two individual robot controllers. One of the robots that work together (synergy) is the main robot (master) while the second is the assistant (slave). Usually the roles are divided so that the master robot is in charge of the construction task (stacking, brick laying, assembly) and the slave robot prepares the base and bonding material, applying it to a specific area (brick, wall segment). The speed of the construction operations and the amount of energy consumed depend on the synchronization between the master and slave robots. Therefore, special attention is paid to programming the robots so that they work in an optimally, with as little as possible waiting times. This robot pair is tended by a conveyor, mostly in the form of gantry crane (see Fig. 4), which brings raw materials from the lifts to the robots' working zone. The crane must be also guided by program in synchronization with the work of two robots, avoiding any delays in material supply. Considering the nature of the construction tasks and façade processing, the paper formulates a set of arguments for the utilization of dual robot cells.
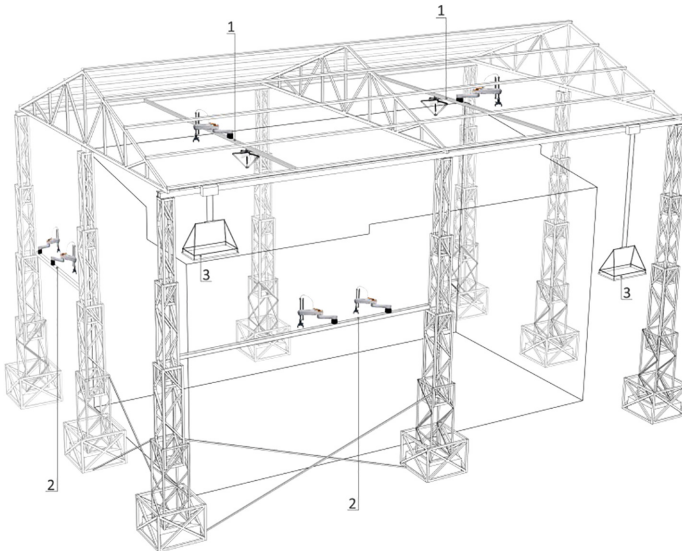


**Fig. 4.** Representation of the automated, modular and reconfigurable robotic system for building construction: (1) gantry robot cell for masonry; (2) facade robot cell for finishing tasks

For exterior masonry walls and inside walls of the building it is adequate to use one single SCARA and Delta robot. In this case, the SCARA robot would then be the master robot for precise assembly (e.g., stacking clay blocks/bricks), while the Delta

robot because of its speed, precision and less payload capacity is suitable for applying mortar or other type of binding material at the current working point. These two robots must be synchronized so that while the master robot takes a clay block or brick from the nearby pallet (which is on the crane) the assistant robot prepares the surface (applies a layer of the bonding material) in the place where the block will be placed. Alternatively, the slave robot could wait for the master to take the block, and the apply the binding materials on one side of construction block (brick) which is then placed by the master robot in its final place in the wall. While the master robot places the clay block in the current row of the wall, the auxiliary robot takes another quantity of mortar and waits to apply it on the next retrieved brick. The entire control sequence is conceived in a similar way the construction worker uses his two hands and skill to routinely perform these actions in the shortest possible time. Because bricklaying on exterior and interior walls is considered to be a monotonous work, the application of dual robot cells for these tasks is justified by efficiency and quality of work.

To create a facade of any type, robot pairs can be used, their type depending on what kind of finishing is necessary: plastered surface, panel of insulating material, putting tiles on the wall or painted the facade. If tiles or panels for insulation are placed on the facade it is necessary again to engage two robots in master-slave relationship. In this case it is recommended to use cells of two SCARA robots as they have a good payload and a satisfactory precision. The facade, as an aesthetic element, requires very precise finishing which fully justifies using of robots for this type of dexterous tasks. For façade finishing with tiles, the two robots divide their work as follows: the master robot places accurately the tiles on the façade whereas the slave robot is adding bonding material in the necessary quantity in the appropriate locations of the façade. In the case of façade plastering or painting, simpler robotic mechanisms can be used, e.g., having only translational movement up and down the surface of the façade and thus controlling the thickness of the material applied. The second robot is used in this case for refilling the paint or other facade material for the master robot from the bin located on the crane or lift (item 3 in Fig. 4).

The robotic cell for construction has a modular structure for several reasons: (i) to allow easy transport of the equipment from one construction site to another, (ii) to enable quick and easy assembly and disassembly, (iii) to ensure interchangeability of the individual modules in the event of a defect without stopping work in other sectors of construction, etc. The modular structure includes a frame with a mechanical structure consisting of several segmented trusses (Fig. 4) which resembles to the structure of a crane installed after laying the foundation of the building. Trusses or frames carry linear guides that use translational gears along the facade and above the ceiling of the building. These linear motors are used for moving the bases of the robot manipulators by cranes or lifts (on the façade) and by gantry (on the roof) as shown in Figs. 3 and 4. Robotic modules are interchangeable during construction, if required by the project.

Thus, workstations with dual robots operating synchronously are reconfigurable systems that can be adapted depending of the type of the tasks. If necessary, the entire robot cell module can be replaced with other robots or the configuration of individual robots can be changed by replacing their individual links (with longer or shorter ones) or their end effectors can be changed to perform different operations. Different types of end effectors are used in construction operations to grasp and handle materials:

standard ones, 2-fingered to transfer bricks or clay blocks, pneumatic for the transfer of ceramic or glass panels, plug handle (punch), handle with spatula for plastering, handle with syringe to apply binding material, handle for painting or polishing the façade etc.

## 5   Analysis of Proposed Concept

Before realizing the dual robotic work cell for construction tasks, it is necessary to perform simulation programs in order to test the operating modes of the robots in different scenarios. The development of such an automated system using multiple robots requires a significant investment of material resources; therefore, simulation experiments may assess the feasibility and sustainability of the proposed solutions. Considering the average lifecycle of robots and their typical capability to perform repetitive, standardized, monotonous tasks such as the operations encountered in the construction of buildings, as well as the limitations of human labour in such difficult conditions (physical effort, concentration, precision, dust, heat, a.o.), the described robotic system is economically justified.

## 6   Conclusions and Future Work

The paper presents a new concept of dual robotic cell for the construction of low-rise buildings. The innovative approach involves a high degree of automation of the modular, reconfigurable dual robot cells that are mounted on the slat support frame which surrounds the entire building. In this approach, the role of the operator consists mainly in controlling the robotic work cells, creating the application programs for the robots and the conveyors, intervention during breakdowns or malfunction of the individual modules, quality control and tuning of the sensor system within the robot cell that should provide real time information about work progress and event occurrence. Since the system is not self-configured, the operator is responsible for its adaptation to the working environment (with construction specific) and to the types of operations: bricklaying, final processing of facades, tiling, flooring, assistance in setting pipes, cables, etc.

Based on the concept presented in the paper, the development of an experimental model is planned for testing in laboratory conditions in order to confirm the feasibility of the project. The main conclusions of the paper can be summarized as follows:

(i)   Existing industrial robots for manipulation should be adapted in a better way to the construction demands. Universal robots offering the possibility of reconfiguring their link dimensions represent better solutions than conventional manipulators.

(ii)   The construction process realized by using reconfigurable and adaptive dual robot configurations has to be organized according to the 3D printing model, which assumes the use of replaceable end-effectors operating both in horizontal and vertical planes with free access to the facade and walls.

(iii)   New forms of construction bricks (smart bricks) and blocks, suitable for easier assembling by construction robots, should be considered in the future.

# References

1. Gramazio, T., Koehler, P.: http://openbuildings.com/buildings/structural-oscillations-profile-41932
2. Bock, T.: Construction robotics. Auton. Robots **22**(3), 201–209 (2007)
3. Bock, T., Linner, T.: Site Automation, Automated/Robotic On-Site Factories. Cambridge Handbooks on Construction Robotics. Cambridge University Press, Cambridge (2016). ISBN 9781107075979
4. Bock, T., Linner, T.: Robotic Industrialization, Automation and Robotic Technologies for Customized Component, Module, and Building Prefabrication. Cambridge Handbooks on Construction Robotics. Cambridge University Press, Cambridge (2015). ISBN 97811070 76396
5. Bock, T., Linner, T.: Robot-Oriented Design and Management Tools for the Deployment of Automation and Robotics in Construction. Cambridge University Press, Cambridge (2015). ISBN 9781107076389
6. Peters, S.: Introduction to Construction Robotics and the bricklaying robot SAM, Co-Founder of Construction Robotics provides an introduction to the bricklaying robot SAM (Semi-Automated Mason). SAM works side-by-side a mason for onsite masonry construction (2013). https://www.youtube.com/watch?v=OKoQMD0QZQs
7. Automatic rendering machine. https://www.youtube.com/watch?v=Pgn0ImIPJwg
8. Smart bricks - a new way to build. https://www.youtube.com/watch?v=_Yf0KEcXIYA

# Model-Based Development of Robotic Systems and Services in Construction Robotics

Christian Schlette[(✉)] and Jürgen Roßmann

Institute for Man-Machine Interaction (MMI),
RWTH Aachen University, Aachen, Germany
{schlette,rossmann}@mmi.rwth-aachen.de

**Abstract.** More and more of our indoor/outdoor environments are available as 3D digital models. In particular, digital models such as the CityGML (City Geography Markup Language) format for cities and the BIM (Building Information Modeling) methodology for buildings are becoming important standards for project management in the construction industry. In this contribution, we are proposing the combination of existing city and building models with methods from 3D simulation and 3D simulation-based system control in order to provide comprehensive geometries and semantics for the representation of large-scale working environments. In Virtual Testbeds for construction robotics, such large-scale working environments can then be systematically accessed as mental models for the model- respectively 3D simulation-based development and control of robotic systems and services.

**Keywords:** Construction robotics · Model-Based development · CityGML · BIM

## 1 Introduction

At the Institute for Man-Machine Interaction (MMI) in Aachen, we are developing the eRobotics methodology [1], where novel robotic systems and their interaction with prospective working environments are first designed, programmed, controlled and optimized in 3D simulation, before commissioning the real system (see Fig. 1). In our eRobotics projects, typical working environments are open landscapes, forests, cities, buildings, factories etc. (see Fig. 2). In consequence, CityGML (City Geography Markup Language) and BIM (Building Information Modeling) provide important standards for modelling relevant environments and simulating their interdependencies with robotic systems.

### 1.1 The eRobotics Methodology and Virtual Testbeds

The eRobotics methodology makes extensive use of 3D simulation technologies, particularly semantic world modelling techniques. A central method in eRobotics is the implementation of virtual systems, so-called Virtual Testbeds (VTBs). While typical simulations focus on specific aspects of the target system, VTBs enable engineers to examine (a) the entire target system in (b) its target environment. Thus, VTBs support
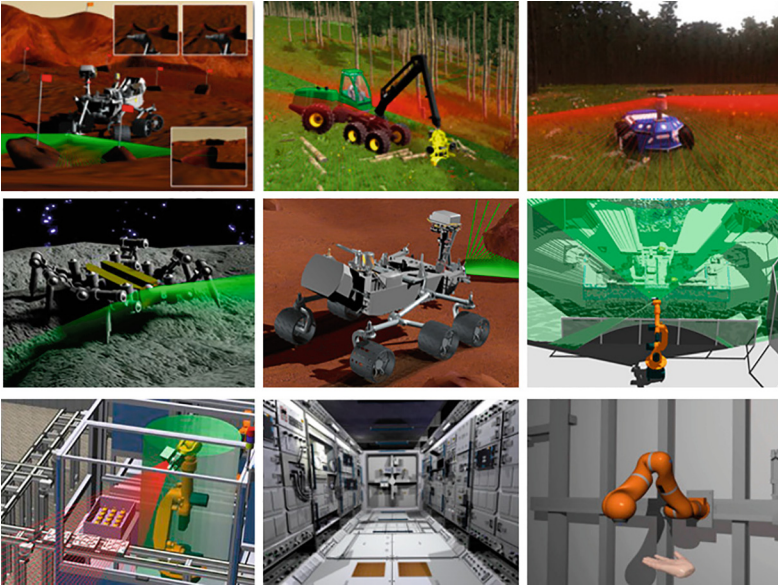
**Fig. 1.** The eRobotics methodology: Robotic systems in the fields environment, space and industry are simulated and controlled in their prospective working environments.
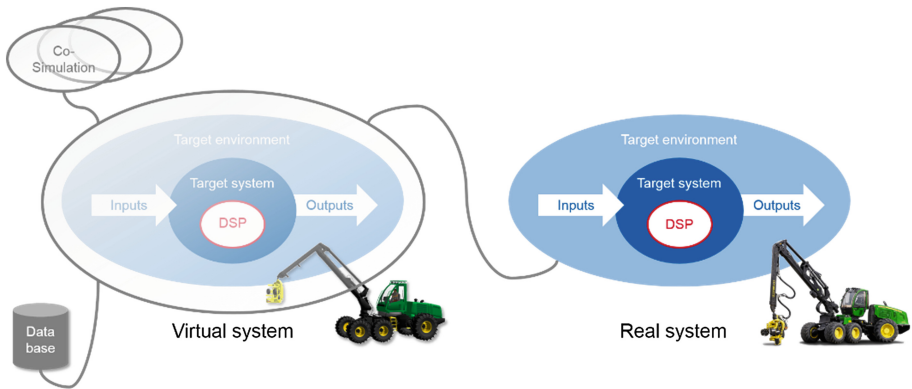


**Fig. 2.** The idea of Virtual Testbeds (VTBs): Development of data processing systems (DPSs) is carried out in a virtual system which encompasses the working environment as well.

system development by providing a replicable and observable basis to design, program and optimize the various subsystems for data processing and control (DPSs). Beyond simulation, VTBs finally allow for transferring the DSPs to the real system in modes of hardware-in-the-loop resp. software-in-the-loop – or the direct control of the real system via "simulation-based control", where the central 3D database from the VTB is wrapped into the real system as a controller (see Sect. 2).

Figure 2 depicts the idea of VTBs by the example of a harvester machine from forestry, for which we developed advanced localization and navigation DPSs first in a VTB, before transferring the development to the real system. The harvester was equipped with laser scanners and localization algorithms from robotics to generate commands for the harvester operator respectively the machine drive and crane.

Referring to this example, a systematic view on Virtual Testbeds is given in Fig. 3. VTBs combine data processing systems with a simulated environment. The simulated environment comprises the simulated target system represented by its internal system vector $\underline{s}_{sys}^{sim}(t)$ (e.g. harvester), its simulated sensors $\underline{s}_{sense}^{sim}(t)$ (e.g. laser scanners) and actuators $\underline{s}_{act}^{sim}(t)$ (e.g. machine drive and crane) and a simulated environment $\underline{s}_{env}^{sim}(t)$ (e.g. virtual forest model). The DPS processes sensor data in order to generate control commands and is represented by $\underline{s}_{impl}^{dps}(t)$ (e.g. localization algorithm), sensor input $\underline{s}_{sense}^{dps}(t)$, actuator output $\underline{s}_{act}^{dps}(t)$ and its perceived environment $\underline{s}_{env}^{dps}(t)$ (e.g. scanned trees). The simulated environment has to adequately mimic the corresponding real environment $\underline{s}_{sys}^{real}(t)$, $\underline{s}_{sense}^{real}(t)$, $\underline{s}_{act}^{real}(t)$, $\underline{s}_{env}^{real}(t)$. By turning the switches $T_{sense}^{dps}$ and $T_{act}^{dps}$, the DPS can either be used with the simulated or the real environment – a key idea of the Virtual Testbed concept. This enables development, evaluation, optimization, and productive operation in the same hardware and software environment [2].



**Fig. 3.** Systematic view on Virtual Testbeds [2]

## 1.2 Large-Scale City and Building Models

In general, Geographic Information Systems (GIS) are designed to represent the geometry, semantics and topology of 2D or 3D spaces. GIS contain 2D and 3D maps,

e.g. digital street maps and digital terrain models, which consist of raster data (bitmaps) or vector data (points, polygons and polyhedrons). A neutral, ISO-certified (ISO 19136) format for GIS modelling and exchange is Geography Markup Language (GML), standardized by the Open Geospatial Consortium (OGC) [3]. CityGML is an important application-specific extension of GML that defines GIS features, attributes and relations relevant for representing landscapes and urban environments. As CityGML builds on GML and standardized formats for modelling geospatial ontologies and topologies, OGC also adopted CityGML as an official standard [4].

The BIM methodology encompasses processes and methods to create and manage virtual 3D building models (BIMs). As a central database for construction projects, BIMs contain semantic information, parameters and geometries of all structural elements as well as tracking information to share developments, changes and comments with share- and stakeholders. An overview of BIM is given in [5, 6], which describe the BIM methodology with practical examples of projects which successfully utilized various aspects of BIM. A general approach to access BIMs independently from specific software packages is provided by the Industry Foundation Classes (IFC) [7]. IFC is a neutral, ISO-certified format standardized by buildingSMART, an international alliance of developers of the leading BIM software packages (ISO 16739).



**Fig. 4.** Consistent large-scale environment model from CityGML and BIM with detailed robot simulation [8]

### 1.3   Environment Model Access

Our approach to interact with such large-scale environment models is based on the software environment VEROSIM for robot simulation and control, which we co-design and co-develop at MMI. The general idea of VEROSIM is to provide a micro-kernel architecture for simulation, where a slim core provides the central functionality to structure and manage a database which represents the simulated scenario. Individual simulation methods, data types and UIs are added via plugins. Following the principles of Object-Oriented Modeling (OOM), the central database of VEROSIM is an active database that contains all simulation entities and information of the environment as well as extensive metadata/metatype information. The database is active, in the sense that it contains functionalities to connect and define the behaviour of simulation entities directly in the database. This behavioural information differentiates the database from simple scene graph representations. The ability to interpret and manage metadata and metatype information enables the generic import, mapping and access of external database formats, such as CityGM and IFC data [8]. As depicted in Fig. 4, the import process enables the geometries and semantics in CityGML and BIM models for rendering and interaction and further attribution and simulation in VEROSIM, e.g. kinematics, dynamics and sensor simulation.

## 2   Virtual Testbeds for Construction Robotics

The ability to map, access and interpret the semantics of a given situation and environment is accepted as an important prerequisite for advanced planning [9, 10]. In particular, Isikdag et al. extended BIM with a new data layer for (human) indoor navigation, e.g. to support emergency operations [11]. [12] gives an overview over the technologies related to model-based indoor navigation and proposes an approach based on CityGML (respectively BIMs converted to CityGML based on the conversion developed in [13]). As an important step towards semantic navigation for robots based on BIM, Siemiatkowska et al. correlated semantic information from BIMs with sensor findings from mobile robots [14, 15].

### 2.1   Central 3D Databases as Mental Models

In the context of eRobotics, we propose an approach for the use of simulation-based mental models for autonomous systems as a foundation for new approaches to prediction and AI. Based on knowledge on human behaviour, the well-known Sense-Think-Act paradigm [16] is considered as the operational definition of an autonomous robot. Humans construct mental models [17] from perception and experience. Using these models, they consider and review alternative actions and their outcomes. Thus in [18], we reproduce such mental models in robotics using the central 3D databases in VTBs, which represent the robotic system and its working environment.

Such central 3D databases respectively mental models consist of a priori models which are verified, updated and enhanced based on (simulated or real) sensor data or data from user interaction. As outlined in Sect. 1.3, we set up the a priori models from

(a) CAD data of the robotic system and (b) geometric and semantic models of its environment, such as CityGML and BIM models presented here. The imported models are then enhanced by adding components from our software environment VEROSIM in order to describe properties and functionalities of the given instances, e.g. of sensors, actuators, trees and doors. However, discrepancies between the mental models and the represented scenarios remain due to uncertainties in the original models and the fundamental lack of VTBs to describe real-world scenarios in all details.

Figure 5 depicts an example of such a mental model, where large-scale BIM data is used to analyse the floor plans for robot motion planning and strategies to avoid potential motion patterns of human co-workers [19]. Of course, a mobile robot in the given situation would need additional sensors to cope with dynamic, time-variant aspects, i.e. furniture and co-workers, and thus bridge the discrepancies between the original model and the real-world environment. Still, the mental model of the building as-is already allows for various simulations and evaluations of alternative actions and their outcomes.
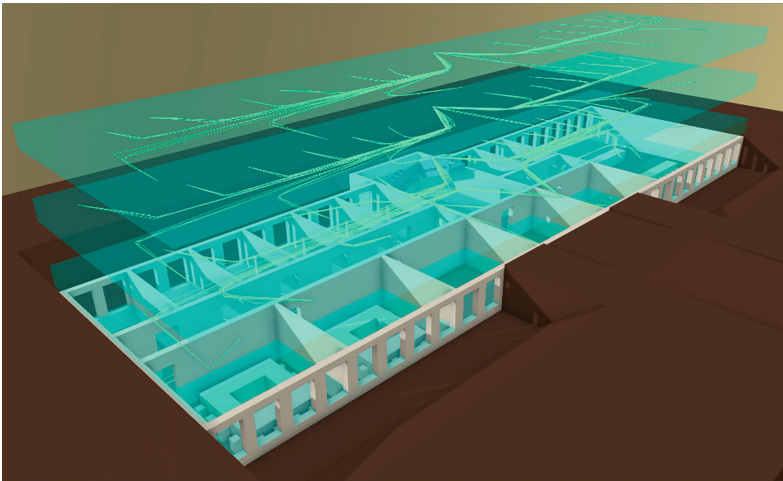


**Fig. 5.** Central 3D database from BIM geometries and semantics for robot motion planning and floor plan analysis [19]

## 2.2   Model-Based Developments in Construction Robotics

Based on Virtual Testbeds with large-scale environment models, we emphasize the following advantages for model-based developments of systems and services in construction robotics:

*Access to* a priori *knowledge of large-scale indoor/outdoor environments*. As CityGML and BIM models are applied to reflect planning data and even permanently ongoing data acquisitions, they provide detailed data in "ground truth" quality. In comparison to relying on in situ modelling and mapping only, such databases thus support large-scale navigation and localization right from the start and for the full life-time of autonomous systems.

*Consistent large-scale localization of process data.* For autonomous systems, the proposed approach allows for storing all sorts of process data with spatial respectively spatial-temporal attributes in a consistent, large-scale coordinate system. In particular, local sensor data from on board sensors can be registered consistently in these coordinates, in addition to processed data such as maps. This allows for tracking of large-scale spatial-temporal shifts and drifts in the environment and future developments of "long-term SLAM" approaches.

*Large-scale experiments in simulatable mental models.* As the geometries and semantics of the incoming environment models can be enhanced with components to describe their properties and functionalities in simulation and reality, the central 3D databases are equipped for experimenting with the instances in the environment, e.g. using dynamics simulation. For model-based robotics, such mental models thus allow for setting up and test alternative actions and their outcomes in simulation, beyond the scope of current simulations.

## 3   Conclusions

Based on our developments of the eRobotics methodology and the development and control of robotic systems in so-called Virtual Testbeds, we previously proposed to interpret the resulting central 3D databases of the robotic systems and their prospective working environment as mental models for autonomous systems. Here, we specifically present the import of environment models in standardized formats such as CityGML and BIM into the central 3D databases in order to access and interact with large-scale indoor/outdoor working environments. Due to their origin and thus their high-level realism, we then propose Virtual Testbeds for construction robotics for the 3D simulation-based development and control of robotic systems and services, particularly enabling: (a) access to a priori knowledge, (b) consistent localization of process data, and (c) large-scale experiments in simulatable mental models.

With the upcoming availability of such environment models, we expect autonomous robotic systems in the future to increasingly make use of such data sources, in addition to the well-established in situ modeling and mapping approaches available today.

## References

1. Schluse, M., Schlette, C., Waspe, R., Roßmann, J.: Advanced 3D simulation technology for eRobotics. In: IEEE International Conference on Developments in eSystems Engineering (DeSE), pp. 151–156 (2013)
2. Roßmann, J., Schluse, M., Atorf, L.: eRobotics combining electronic media and simulation technology to develop (not only) robotics applications. In: eSystems for the 21st Century: Concept, Developments, and Applications (2016). (in print)
3. Open Geospatial Consortium. http://www.opengeospatial.org/standards/gml
4. Open Geospatial Consortium. http://www.opengeospatial.org/standards/citygml

5. Eastman, C., Teicholz, P., Sacks, R.: BIM Handbook: A Guide to Building Information Modeling for Owners, Managers, Designers, Engineers and Contractors. Wiley, Hoboken (2011)

6. Hardin, B., McCool, D.: BIM and Construction Management: Proven Tools, Methods, and Workflows. Wiley, Hoboken (2015)

7. BuildingSMART International Ltd. http://www.buildingsmart-tech.org

8. Roßmann, J., Schluse, M., Hoppen, M., Losch, D., Hempe, N., Schlette, C.: Virtual BIM testbeds. In: IEEE International Conference on Developments in eSystems Engineering (DeSE) (2015). (in print)

9. Drouilly, R., Rives, P., Morisset, B.: Semantic representation for navigation in large-scale environments. In: IEEE International Conference on Robotics and Automation (ICRA), pp. 1106–1111 (2015)

10. Nüchter, A., Hertzberg, J.: Towards semantic maps for mobile robots. Robot. Auton. Syst. **56**(11), 915–926 (2008)

11. Isikdag, U., Zlatanova, S., Underwood, J.: A BIM-oriented model for supporting indoor navigation requirements. Comput. Environ. Urban Syst. **41**, 112–123 (2013)

12. Nagel. C.: Spatio-semantic modelling of indoor environments for indoor navigation. Ph.D. thesis, Technische Universität Berlin (2013)

13. Nagel, C., Stadler, A., Kolbe, T.: Conceptual requirements for the automatic reconstruction of building information models from uninterpreted 3D models. In: International Archives of the Photogrammetry, Remote Sensing and Spatial Information Sciences, vol. 34(XXX), pp. 35–46 (2009)

14. Borkowski, A., Siemiatkowska, B., Szklarski, J.: Towards semantic navigation in mobile robotics. In: Engels, G., Lewerentz, C., Schäfer, W., Schürr, A., Westfechtel, B. (eds.). LNCS, vol. 5765, pp. 719–748Springer, Heidelberg (2010). doi:10.1007/978-3-642-17322-6_30

15. Siemiatkowska, B., Harasymowicz-Boggio, B., Przybylski, M., Rozanska-Walczuk, M., Wisniowski, M., Kowalski, M.: BIM based indoor navigation system of Hermes mobile robot. In: Romansy – Robot Design, Dynamics and Control, pp. 375–382 (2013)

16. Siegel, M.: The sense-think-act paradigm revisited. In: International Workshop on Robotic Sensing (ROSE) (2003)

17. Johnson-Laird, P.: The history of mental models. In: Psychology of Reasoning: Theoretical and Historical Perspectives, pp. 179–212 (2004)

18. Roßmann, J., Kaigom, E., Atorf, L., Rast, M., Grinsphun, G., Schlette, C.: Mental models for intelligent systems: eRobotics enables new approaches to simulation-based AI. KI-Künstliche Intelligenz **28**(2), 101–110 (2014)

19. Schlette, C., Roßmann, J.: Sampling-based floor plan analysis on BIMs. In: International Symposium on Automation and Robotics in Construction (ISARC) (2016)

# Fabrication of Digital Anamorphic Sculptures with Industrial Robot

Marko Jovanović[(✉)], Jovica Tasevski, Bojan Tepavčević, Mirko Raković,
Dejan Mitov, and Branislav Borovac

Faculty of Technical Sciences, University of Novi Sad,
Trg Dositeja Obradovića 6, 21000 Novi Sad, Serbia
{markojovanovic,tasevski,tepavcevicb,rakovicm,dejan_mitov,
borovac}@uns.ac.rs

**Abstract.** The fabrication process of complex architectural designs in
the real world requires precise and complex movements in the workspace.
The robotic arms can fulfil this requirement, which makes them an excel-
lent choice for a set of digital fabrication tasks. This paper presents a
design methodology for the generation of anamorphic sculptures based
on input grayscale image. To represent pixels in real world, wooden sticks
are used. The colour of a grayscale image is represented by setting the
appropriate orientation of the wooden sticks with respect to the ini-
tial vertical position. To achieve good results a large number of sticks is
required to be placed and oriented precisely. In order to do this, the holes
are drilled at a specified angle in a wooden base. Drilling is carried out
with a driller mounted on a ABB IRB140 robot arm. After the drilling
is finished, wooden sticks are manually placed in each hole.

**Keywords:** Parametric architectural design · Robotized fabrication ·
Anamorphic images and sculptures

## 1 Introduction

In recent years integration of industrial robots in creative industry and art
increased rapidly. Design works made by robots or robot advanced motion con-
trol became part of the art performance itself [3]. As a tool for physical produc-
tion of artwork, industrial robots have been used for generating paintings with
an element of randomness [4,5]. Furthermore in recent years industrial robots
have been extensively used in manufacturing of architectural elements with novel
design solutions [6,8,9] or even full scale architectural buildings [1,14]. Industrial
robot arms has been implement in many architectural institutions as the most
advanced tool for design experiments in digital fabrication. The reason for rapid
development of robotics in architecture and design lies in the fact that inter-
play between material and digital processes in construction and fabrication with
industrial robots change the way of thinking about the design, as well as the
way we use and perceive material and material properties. One of such examples

is procedural landscapes project [12], where the robot is used to explore design possibilities that are not controlled only with robot tool path and designer's intentions, but also with emergent properties of materials.

The way we think and perceive materials is the only one of the design paradigm shifts in the digital age. The way how we perceive our surrounding and how an image can be transformed in different ways is another interesting topic that reappeared with computational design tools. Distorted and anamorphic images had been popular in the age of baroque. With new parametric and graphic design tools that enable easy manipulation with images and their transformation, interest toward raster image transformation and digital anamorphosis increases.

Interest toward perspective anamorphosis has reawakened in art, advertising, industrial design, architecture and landscape design. Moreover digital tools have been used for creating anamorphic sculptures [7,11]. However, these sculptures are designed as reversed 3D geometry, derived from the projected image.

In this paper we explore the design and fabrication possibilities in automated anamorphic sculpture generation with an industrial robot arm, by using equilateral linear elements. Similar approach has already been researched [10], where an industrial robot pushes the nails into a Styrofoam block in order to generate sculptural representation of the wind. Contrary to previously mentioned examples, complex geometry of 3D sculpture is derived from image sampling that defines the rotation angle. Thus, design of such structures can only be achieved by coupling parametric design tools and digital fabrication with industrial robot. Our goal is to utilize hole drilling prior to linear element insertion in order to generate an anamorphic image. This is achieved by changing the drilling angle in accordance with the desired image chosen for the anamorphic projection. The holes are positioned in a grid with a desired number in both directions. Viewed from a single position, the linear elements form an anamorphic image.

The paper starts by explaining the general methodology principles in Sect. 2. Section 3 explores the requirements and restrictions pertaining to the generation of anamorphic images, with all the linear elements being rotated in parallel planes. In Sect. 4 the approach is tested in simulation environment, and the drilling process with the end result is presented. Finally the paper is concluded in Sect. 5.

## 2   Methodology

For the design of the anamorphic image, a pixel colour information of a grayscale image is used. This information is used to drill the holes in a wooden base at a specific angle. In each hole linear wooden elements are placed. The linear elements' position and angle of inclination is what generates an anamorphic image in the real world.

For the design phase and for the path and target preparation, a software package Rhinoceros and Grasshopper is used, which proved its application in previous work [13]. In Rhinoceros modelling environment, first a rectangle is drawn; its dimensions correspond to the desired flat sheet element. A planar
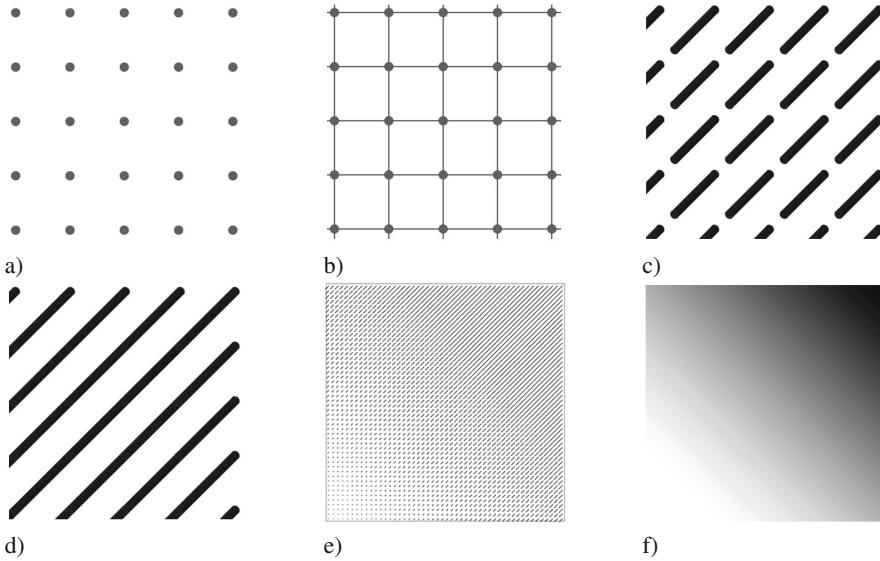
**Fig. 1.** The initial stick grid (a); square as a pixel correspondence (b); stick rotation by a desired angle (c); influence of increased stick rotation angel or length (d) general overview of the surface (e) the referential grayscale image (f)

rectangular surface is generated from it and used as a setting stage for placing a UV grid of points. The points on the edges are culled from the list, since they cannot be valid points for hole drilling afterwards. The new point list is then utilized for placing the linear cylindrical elements, i.e. sticks.

In order to construct an anamorphic image representation, stick directions are pointed towards a single viewing point positioned at 1100 mm in front of the base surface, such as the user defined eye position. As a result, when viewed from the previously defined single view point, the sticks will be viewed as very short black lines or dots in such a way to generate an anamorphic image. After setting the initial sticks grid (Fig. 1a), the surface underneath is viewed as a square grid, which corresponds to the pixel array of an image (Fig. 1b). The pixel count in X and Y direction of the grayscale image aligns to the U and V point count on the surface grid. Each pixel and square corresponds to one point on its corner, respectively. Therefore, even though a single pixel touches 4 points, it only influences one. The premise is to rotate each stick, where the rotation amount is referenced with respect to the pixel colour. In such a manner, the stick covers more or less of the square grid underneath (Fig. 1c and d) and mimics the pixel colour at the same time (Fig. 1e), generating the desired grayscale image (Fig. 1f).

## 3 Position and Orientation of the Sticks

Two parameters for determining the position and orientation of the sticks are introduced: the position of the coordinate frames (CFs) where the sticks will be
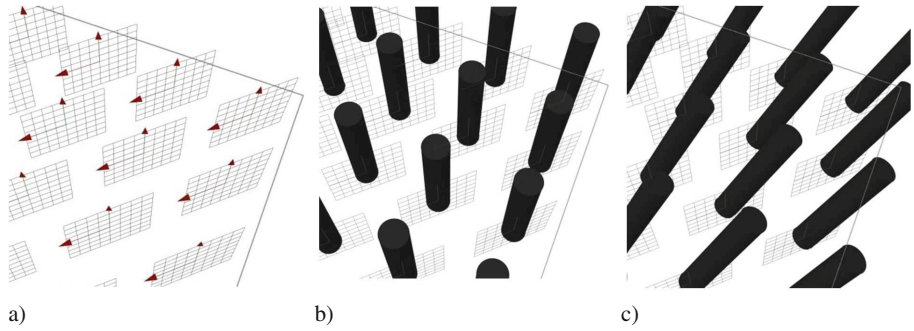
**Fig. 2.** The position of the reference CFs for the stics (a), the initial position of the sticks (b) and the position of the sticks after being rotated in accordance to the greyscale color of the corresponding pixel (c) simulated inside Rhinoceros environment

placed and the rotation off all the sticks from the vertical position in x-y plane in its reference CF. The position of each CF is defined by setting its origin in one UV point. The orientation of CFs are defined by setting the $x$ vectors to be normal to the base surface, and the $y$ and $z$ axis are user defined (Fig. 2a).

The stick's orientations are initial perpendicular to the base surface, i.e. aligned with the $x$ axis of each CF (Fig. 2b). After applying the greyscale image, stick's angle of rotation is determined from the grayscale colour of the corresponding pixel. For example, the angles of rotation of sticks representing pixels from a grayscale colours are mapped linearly from $0^o$ (representing white pixel) to $30^o$ (representing black pixel) (Fig. 2c).

This approach only abides by orthographic viewing of the image, not including the perspective distortion. The benefit of utilizing the orthographic view is determining at which perpendicular distance of the surface does the image start to blur or becomes the most clear. It shows what is the required number of elements, their thickness and rotation, in order to get the best depiction of the anamorphic image. However, the human eye generates a perspective image and therefore certain adjustments have to be made. This requires the sticks' initial position to be set differently. Instead of directing them along the $x$ axis vector of reference CF, they are directed towards the user defined eye point position. Afterwards the additional stick rotations are carried out in the same manner as described above (Fig. 3).

Afterwards, a more demanding grayscale image is chosen to check how the algorithm reacts to a more random occurrence of grayscale color (see Fig. 4a), and the end result is shown in Fig. 4(b).

The fabrication of real 3D amorphic image is carried out by drilling the holes with the pneumatic driller mounted on the industrial robot arm. Into the holes the sticks are later manually inserted. The position and orientation of the holes are determined by extracting the origin of the CFs in a global coordinate system. The orientation of a driller is defined with a vector $w$ that is connecting the top of the stick and the point of insertion i.e. the place where the stick meets the surface.
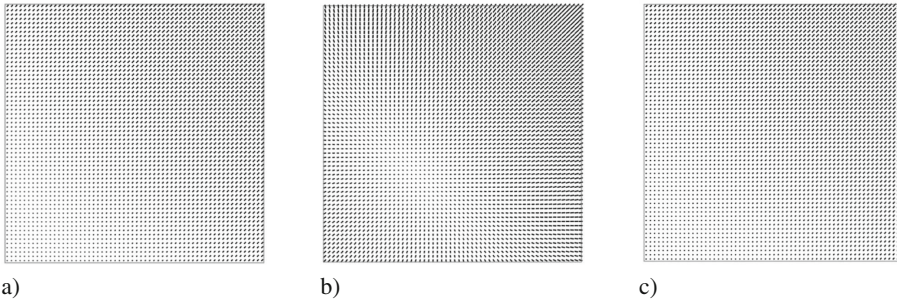
**Fig. 3.** Orthographic view with sticks perpendicular to the base surface (a), perspective view of the previous setup (b) perspective view with the initial stick direction pointed towards the eye point (c)
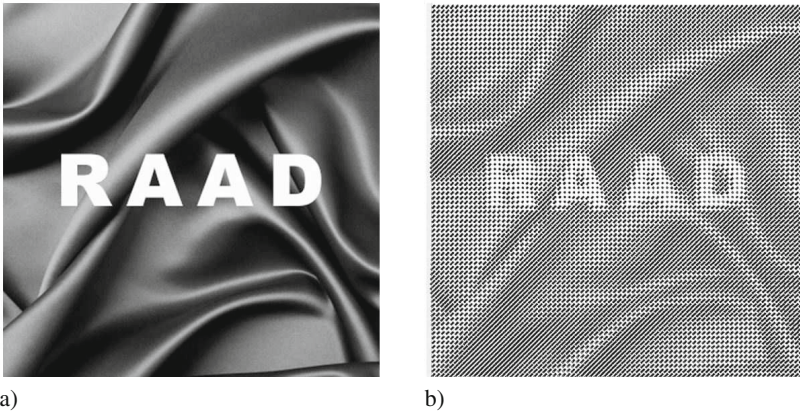


**Fig. 4.** A portrait grayscale image as a guideline (a) and a stick sculpture generating an anamorphic image of the latter (b)

## 4   Simulation Verification and Fabrication

For the simulation verification of holes drilling, the RobotStudio software, for off-line programming and simulation is used (Fig. 5a). The special concern has been devoted to the tools orientation during the drilling process.

The program data, used as input to generate the RAPID program code for ABB IRB140 robot, is organized as an array of targets where odd indexed elements represents the upper points of the sticks, and even indexed elements represents the lower points. After the targets on both ends of the sticks have been calculated, the pairs of the target as input parameters were used for generating the RAPID code. For this purpose a script for Grasshopper is developed that generates the array of targets in accordance with the RAPID syntax. To define
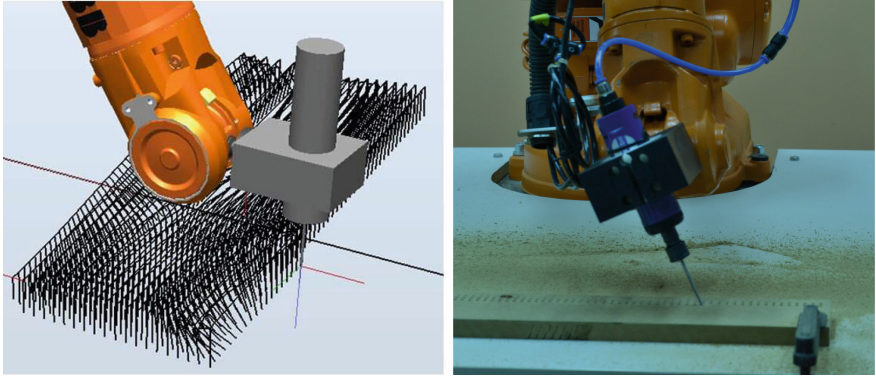
**Fig. 5.** IRB140 robot in RobotStudio simulation environment (left) and robot drilling the holes (right)
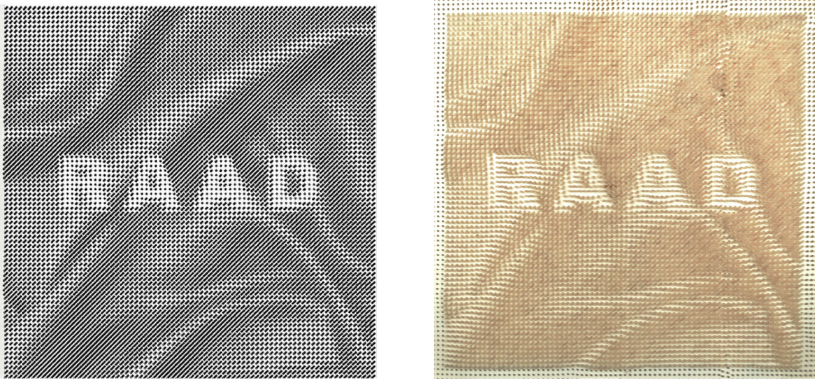


**Fig. 6.** Computer generated graphics (left) and photography of real fabricated anamorphic 3D image (right)

the position of the robot's TCP, *robtarget* (i.e. robot target) data type is used [2]. This data type has the following structure:

– the position vector **p** of the TCP with respect to the work object coordinate frame,
– the orientation vector **o** of the tool in the form of a quaternion (q1, q2, q3 and q4) with respect to the work object coordinate frame,
– the axis configuration of the robot (cf1, cf4, cf6 and cfx) and
– the position of the external axes if exists.

The calculated targets are merged into a string that is syntax correct for the RAPID programming language. When the strings for all the targets are generated, they are assembled into an array ready to be imported into the base program for the robot controller that moves the TCP through all the generated

TCP targets. After the simulation is finished successfully, the holes drilling in the real environment is performed (Fig. 5b).

For the fabrication of the computer generated anamorphic image shown left on Fig. 6 a total of 6.400 holes are drilled in a base wooden surface of dimension $60 \times 60$cm. In each hole, excluding the holes near the edge, 5476 wooden sticks with the 3 mm diameter and 25 mm length are manually placed. As a result, an anamorphic 3D image is obtained. The resulting image is shown on the right in Fig. 6(b), next to the computer generated image, for the comparison.

## 5    Conclusion

In this paper we presented a method for generation of anamorphic sculpture based on parametric design tools, robotic fabrication and stick placement. For given inputs of grayscale image, an unique rotation angle for each stick position is calculated and drilled with the use of industrial robot arm. Unlike other design approaches in creating anamorphic sculptures based on mass models, in this work it is shown that it can be also generated with linear elements but this requires advanced fabrication approach. The level of detail and quality of anamorphic sculpture are directly constrained with design parameters: number of sticks, algorithm for determining the rotation angle and size, shape and colour of the sticks. The relationship between these design parameters on perceiving sculpture will be examined in further research.

## References

1. Menges, A., Krieg, O.D., Schwinn, T.: Behavioral strategies: synthesizing design computation and robotic fabrication of lightweight timber plate structures (2015)
2. ABB Robotics Products AB, S.: RAPID reference manual (2015)
3. Abdel-Gawad, T.: Bot & dolly: box interview and behind the scenes. http://motionographer.com/2013/10/01/bot-dolly-box-interview-and-behind-the-scenes/
4. Aguilar, C., Lipson, H.: A robotic system for interpreting images into painted artwork. In: International Conference on Generative Art, vol. 11. Citeseer (2008)
5. Alkhodairy, A., Patel, S., Sobh, T.M.: Robot artist-automated picture portrait (2014)
6. Bärtschi, R., Knauss, M., Bonwetsch, T., Gramazio, F., Kohler, M.: Wiggled brick bond. In: Ceccato, C., Hesselgren, L., Pauly, M., Pottmann, H., Wallner, J. (eds.) Advances in Architectural Geometry, pp. 137–147. Springer, Vienna (2010)
7. Bärtschi, R., Knauss, M., Bonwetsch, T., Gramazio, F., Kohler, M.: A simplified procedure for anamorphic sculpture. Int. Des. J. **5**, 317–326 (2015)

8. Bonwetsch, T., Gramazio, F., Kohler, M.: Digitally fabricating non-standardised brick walls. In: ManuBuild, 1st International Conference, Rotterdam (2007)
9. Brell-Cokcan, S., Reis, M., Schmiedhofer, H., Braumann, J.: Digital design to digital production: flank milling with a 7-axis robot and parametric design. In: Proceedings of the 27th eCAADe Conference on Computation: The New Realm of Architectural Design, Istanbul, pp. 323–330 (2009)
10. CKA: Representing wind through digital fabrication and the tangible. http://cka.co/projects/representing_wind/
11. Di Paola, F., Pedone, P., Inzerillo, L., Santagati, C.: Anamorphic projection: analogical/digital algorithms. Nexus Netw. J. **17**, 253–285 (2015)
12. Gramazio, F., Kohler, M.: Procedural landscapes. www.dfab.arch.ethz.ch/web/e/lehre/208.html
13. Raković, M., Jovanović, M., Borovac, B., Tepavčević, B., Nikolić, M., Papović, M.: Design and fabrication with industrial robot as brick-laying tool and with custom script utilization. In: 2014 23rd International Conference on Robotics in Alpe-Adria-Danube Region (RAAD), pp. 1–5. IEEE (2014)
14. Schwinn, T., Krieg, O.D., Menges, A.: Behavioral strategies: synthesizing design computation and robotic fabrication of lightweight timber plate structures (2014)

# At the Crossroads of Architecture and Robotics: Control and Structural Concepts for a Reconfigurable Building

Maria Matheou[1]([✉]), Marios C. Phocas[1], Andreas Müller[2],
and Eftychios G. Christoforou[3]

[1] Department of Architecture, University of Cyprus, 75 Kallipoleos Ave.,
1687 Nicosia, Cyprus
{matheou.maria,mcphocas}@ucy.ac.cy
[2] Institute of Robotics, JKU Johannes Kepler University,
Altenbergerstr. 69, 4040 Linz, Austria
a.mueller@jku.at
[3] Department of Electrical and Computer Engineering,
University of Cyprus, 75 Kallipoleos Ave., 1687 Nicosia, Cyprus
e.christoforou@ucy.ac.cy

**Abstract.** A new generation of reconfigurable buildings will be able to provide certain advantages over traditional structures and create new architectural perspectives. One concept that has been proposed comprises a parallel arrangement of planar $n$–bar linkages to create the skeleton structure of a building. Reconfigurations of the individual planar mechanisms define the overall shape of the building. For this purpose a systematic procedure has been developed called "effective four-bar" method which is reviewed. The basic idea of this concept is to strategically lock $n - 4$ joints of the individual $n$–bar linkages so to effectively leave four-bar linkages each with 1 degree of freedom. The latter can be actuated, and thus the shape of the building changed by means of a single actuator. Two different actuation methods are discussed.

**Keywords:** Reconfigurable buildings · Adaptive architecture · Robotics in architecture

## 1 Introduction

Buildings are not merely a shelter from environmental conditions but they serve numerous functions related to aesthetics, comfort, health, culture, safety, etc. Traditional buildings have been fixed-shape structures and provide limited flexibility for adjustments to new or changing requirements. Nowadays, technological developments allow for a new generation of building structures whose form can be modified in order to better serve their purpose. Adjustments may be driven by changing needs of human activity or varying external conditions. In the latter case, adaptive structures reconfigure in response to environmental stimuli

(e.g., motion of the sun, wind conditions). This new perspective may inspire innovation and creativity in architectural design and lead to sustainable developments linked to high-efficiency buildings, improved energy performance etc.

Kinetic structures of different typologies and mechanisms have been developed in recent years, primarily in terms of deployable structures, in relation to requirements of temporary environments, aerospace and technological progress [7]. In this frame tensegrity and scissor-like systems have been proposed to provide transformability.

In particular, tensegrity structures, i.e., self-stressed systems composed of tension and compression members, are characterized by their physical properties in providing a holistic and integrated composition of embedded active control, since the members may support or replace sensors and actuators. Also, the specific typology comprises autonomous and self-supported systems in all stages of transformation, from the initial to the target ones, especially in the intermediate ones, while effectively transferring the loading [5]. In principle, the transformation of "static tensegrities" in kinetic systems, in terms of deployable systems, is based on the replacement of compression members with linear pneumatic actuators, or the implementation of tension members with variable length [1,6,9]

Elements of adaptation that can be incorporated on a building may involve adjustable surfaces, which are actively controlled to provide sun protection or internal partitioning systems for improved spatial usage. More drastic effects are possible by mechanically adjusting the overall spatial features of a building resulting to different architectural topologies. Such changes may help to meet certain objectives such as [2,3]:

- Better space utilization,
- Adjustment of the building's acoustics,
- Maximization of sun protection and optimization of lighting conditions,
- Facilitate natural ventilation,
- Relax aerodynamic loading of the structure,
- Improve energy efficiency of a photovoltaic roof,
- Shake snow off building's roof,
- Produce impressive and unique aesthetic effects.

The development of reconfigurable or adaptive buildings is a multidisciplinary approach which embraces architecture, structural and control engineering. Incorporating kinetic mechanisms constitutes adaptive buildings robotic mechanisms. Therefore, concepts from kinematics, dynamics and control of robotic systems become relevant. An adaptive structure requires a feedback control system that includes sensors as well as actuators for implementing the reconfigurations in response to the external input. In this paper a structural and reconfiguration concept for an adaptive building are reviewed. The basic element of the reconfigurable structure is the planar $n$–bar mechanism. The building envelope comprises a parallel arrangement of such mechanisms. Reconfigurations can be

realized using a concept referred to as "Effective 4–Bar" (E4B). A given reconfiguration can be realized based on stepwise motion sequences. Motion planning involves generation of alternative sequences and selection of an optimal one.

## 2    The Reconfigurable Structure and the Control Concept

The reconfigurable structure consists of a number of planar $n$–bar linkages arranged in parallel as depicted in Fig. 1. A flexible material can be attached to the structure and define the building envelope. This material is required to present appropriate mechanical properties including elasticity, strength and durability. Each individual linkage is composed of $(n-1)$ serially connected members with rotational joints between them and is linked to the ground through pivot joints on either side. The ground itself provides one member to each component linkage. Reconfigurations of the individual linkages accordingly adjust the overall shape of the building.

Considerations in the present paper focus on an individual $n$–bar mechanism. It is considered that each joint of the mechanism is installed with a brake whose operation is linked to the control system. A planar $n$–bar linkage has $(n-3)$ degrees–of–freedom (DOF) and motion control requires equal number of motion actuators. To bypass this requirement an alternative reconfiguration approach was proposed in [4] and involves stepwise adjustments. By locking $(n-4)$ joints using the available brakes the linkage is reduced to an "effective 4–bar" mechanism which has 1 DOF. This is evident in Fig. 2a,b where activated brakes are represented with a crossed circle and released brakes are represented with a dotted circle. A group of neighbouring links with locked joints between them constitutes an "effective link". The most simple actuation method involves one motion actuator (e.g., bidirectional electric motor or hydraulic cylinder) associated with one of the ground pivots, in conjunction with brakes installed at each individual joint [4], as shown in Fig. 2c. Using the motion actuator one angle is adjusted to the desired value and then remains locked until the overall reconfiguration is completed. During the next step a different set of brakes is applied and the procedure is repeated until all the joint angles are adjusted to their target value. The final E4B realization serves to simultaneously adjust the
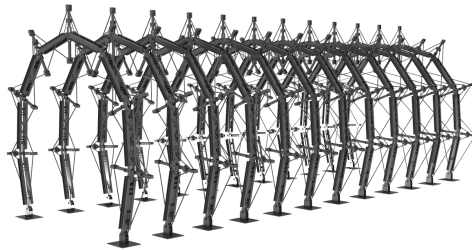


**Fig. 1.** A parallel arrangement of $n$–bar linkages generates the skeleton structure for the reconfigurable building.

position of the last remaining 4 joints. Therefore, a complete reconfiguration between an initial and a final posture of the $n$–bar requires a total of $(n − 3)$ intermediate steps. This approach was experimentally examined in [4] using a small–scale 7–bar prototype with electromagnetic brakes at the joints.

An alternative actuation concept, which was proposed in [8], is based on the tensioning of two continuous cables installed on the system in order to generate the required torques, as shown in Fig. 2d. The cables are associated with a system of pulleys and struts installed at each individual joint. A passive linkage is used for centering the struts with respect to the corresponding joint, as shown in Fig. 3. Depending on which cable is tensioned a torque is generated at the joints at a corresponding direction. A possibility for the actuation is to use electric motors and drums around which each cable is wound. Following this method the control action is distributed simultaneously at two joints of the E4B mechanism. A rule that needs to apply as part of motion planning is that brakes should be activated so that for each reconfiguration step there will be two consecutively unlocked joints, or an even number of locked joints between the two unlocked ones. This is essential so that the cable actions on the E4B system do not compete with each other.

During joint adjustments depending on the required direction of motion, the actuation task is appropriately assigned by the controller to one of the two cable systems. The cable needs to be either pulled or released depending on the tendency of the structure to move under the effect of gravity. Beyond the singularities inherent to the 4–bar mechanism, as discussed in [4], motion planning also needs to consider an additional motion limitation relevant to the specific actuation approach. This limitation is associated to the struts and pulleys system installed on each joint. During a reconfiguration step one of the unlocked joints may encounter a flattening of the cable passing through the associated strut pulleys. Practically, this state deprives the system from the ability to apply a torque at the corresponding joint. Even the vicinity of such configurations should be avoided because it corresponds to limited mechanical advantage while generating torques. Using longer struts eliminates this problem but the struts system may interfere with the internal spaces of the building. Further limitations to motion planning constitute possible envelope constraints due to neighbouring structures or internal objects that may interfere with the motion of the structure.
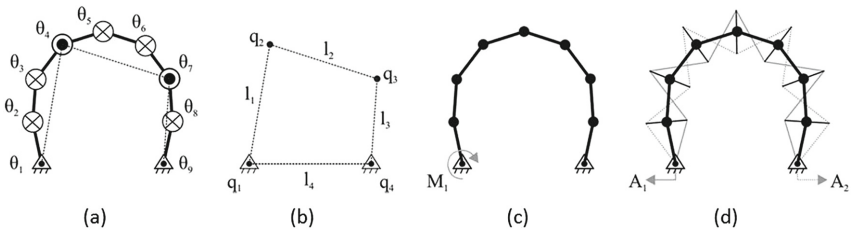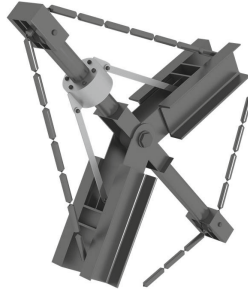


**Fig. 2.** The "Effective 4–bar Method" and the actuation approaches.

**Fig. 3.** Joint assembly for cable actuation.

## 3    Example of Control Sequences

Based on the reconfiguration and control concepts, motion planning at a basic level concerns each individual $n$–bar linkage. Each step of the reconfiguration is dedicated to the adjustment of one individual joint angle to its target value. Given the order in which the individual angles are adjusted and the alternative combinations of locked joints, different reconfiguration sequences can be defined. Here, the reconfiguration concept is demonstrated using the case of a 9–bar system. The initial $\boldsymbol{\theta}_i$ and final $\boldsymbol{\theta}_f$ configurations for the system are shown in Fig. 4 and correspond to: $\boldsymbol{\theta}_i = [102, 164, 147, 144, 147, 144, 147, 164, 102]^T$, $\boldsymbol{\theta}_f = [128, 131, 129, 160, 162, 160, 129, 131, 128]^T$ degrees. These vectors contain the angles internal to the polygon starting from the left ground pivot and moving clockwise towards the right ground pivot. Note that the above definitions of position are in fact redundant. Defining only six joint positions would have been sufficient given that the rest can be algebraically inferred from kinematics relationships.

Different alternative sequences exist for the above reconfiguration. Two examples are presented here to demonstrate the concept. The reconfiguration sequences can be effectively represented in a scheduling table form, as in Fig. 5. Symbols in gray colour represent the currently adjusted joint(s) and the dashed–line encirclements denote the "effective coupler" links. The intermediate reconfiguration steps for each sequence are depicted in Fig. 6. Both sequences finally lead to the same target configuration. Note that the specific sequences can be realized using either one of the above mentioned actuation methods (using a motor at the base or cable actuation) given that the required planning conditions are satisfied for both of them.

For a systematic selection between alternative reconfiguration sequences one appropriate criterion constitutes the size of the quasistatic actuator forces/torques and the required brake torques at the joints [4]. A static consideration is indeed appropriate given that building reconfigurations will involve slow motions and inertial effects will be negligible.
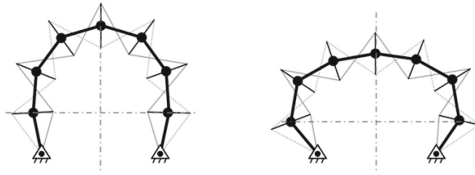
**Fig. 4.** Initial and final position for the reconfiguration example.



**Fig. 5.** Representation of two reconfiguration sequences (⊗: locked joint, ⊙: unlocked joint, △: pivoted–to–the–ground joint, shaded symbols represent the currently adjusted joint(s), the dashed–line encirclements correspond to the effective coupler links).
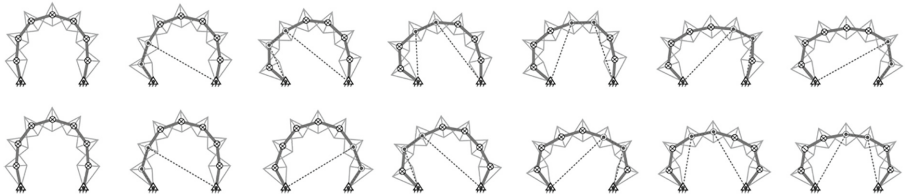


**Fig. 6.** Reconfiguration steps for the two alternative sequences.

## 4   Conclusions

A structural and control concept for a reconfigurable structure has been reviewed. The basic component of the structure is an $n$–bar planar mechanism that can assume required postures depending on the reconfiguration objective. Two actuation methods can be used for this purpose. One involves a single motion actuator installed at one of the joints. The other is based on a system of two continuous cables and the actuators corresponding to each one of them. Future work will involve further experimental investigations of this concept and its extension to adaptive architecture. In that case the structure should automatically respond to environmental stimuli in order to achieve a defined objective.

# References

1. Adam, B., Smith, I.: Active tensegrity: A control framework for an adaptive civil-engineering structure. Comput. Struct. **86**(23–24), 2215–2223 (2008)
2. Christoforou, E.G., Müller, A., Phocas, M.C.: Motion planning for shape-controlled adaptable buildings resembling topologically closed-loop robotic systems. In: 36th Mechanisms and Robotics Conference (MECH), ASME 2012 International Design Engineering Technical Conferences, Chicago, IL (2012)
3. Christoforou, E.G., Müller, A., Phocas, M.C., Matheou, M., Arnos, S.: Towards realization of shape-controlled adaptable buildings following a robotics approach. In: 37th Mechanisms and Robotics Conference (MECH), ASME 2013 International Design Engineering Technical Conferences, Portland, OR (2013)
4. Christoforou, E.G., Müller, A., Phocas, M.C., Matheou, M., Arnos, S.: Design and control concept for reconfigurable buildings. ASME J. Mech. Design **137**(4), 042302–042302-8 (2015)
5. Gantes, C.: Deployable Structures: Analysis and Design. WIT Press, Southampton (2001)
6. Hanaor, A.: Theory and application. In: Gabriel, J.F. (ed.) Beyond the Cube. John Wiley & Sons (1997)
7. Pellegrino, S.: Deployable Structures. International Center for Mechanical Sciences, vol. 412. Springer, Heidelberg (2001). CISM courses and lectures
8. Phocas, M.C., Christoforou, E.G., Matheou, M.: Design, motion planning and control of a reconfigurable hybrid structure. Eng. Struct. **101**, 376–385 (2015)
9. Tibert, G.: Deployable Tensegrity Structures for Space Applications. Ph.D. Thesis, Royal Institute of Technology, Stockholm (2002)

# On-Site Robotic Construction Assistance for Assembly Using A-Priori Knowledge and Human-Robot Collaboration

Sven Stumm[1(✉)], Johannes Braumann[2,3], Martin von Hilchen[1], and Sigrid Brell-Cokcan[1,2]

[1] Chair of Individualized Production in Architecture,
RWTH Aachen University, Aachen, Germany
`office@ip.rwth-aachen.de`
[2] Association for Robots in Architecture, Vienna, Austria
`robots@robotsinarchitecture.org`
[3] UfG Linz, Linz, Austria

**Abstract.** The programming of industrial robots is commonly static and optimized for a clearly defined surrounding. Service robotics on the other hand focuses on working in dynamic and completely unknown environments. Within construction, robotics needs to be able to adapt within dynamic and unstructured environments. However a lot of information is already available from the planning phase. Currently this information is often not used directly or efficiently on the construction site. Using force torque sensors as well as human-robot collaboration in the form of haptic programming we want to enable intuitive on-site robot programming, handle material tolerances of components and detect differences between design and reality to achieve satisfactory quality in assembly tasks.

**Keywords:** Parametric robot control · Haptic programming · Construction robotics · Human robot collaboration · Wood fabrication

## 1 Robots in Construction

The degree of automation in the construction industry is very low. Previous attempts at full automation in the construction industry failed due to the high complexity and the low degree of autonomy in the used machines. Some of these problems can now be addressed due to the developments made in recent years, as well as a paradigm shift within robotics and automation from concepts of full automation towards semi-autonomous man-machine collaboration.

However a very high number of challenges in the field of construction remain. While production lines often only fabricate a single product or a series of products with only slight variances, the construction industry deals with small lot sizes, high tolerances and variation especially when working with natural materials. Building components are therefore often fitted manually on site; this applies in particular to construction in low-wage countries where higher material tolerances are accepted practice. Current efforts in design and planning try to alleviate these discrepancies

through tighter process control and detailed modelling of material properties with concepts such as Building Information Modelling (BIM) [1]. Rather than just drawing blueprints, intelligent objects are parameterized and placed directly in a 3D environment. This results in models capable of informing construction and assembly of complex structures. However a large information gap remains between planning and realization on site due to the fact that the digital information still has to be communicated to the workers. The actual state of the site therefore only loosely correlates with the model and can be described as a highly unstructured environment, which in turn results in large efforts to ensure quality control as well as many obstacles for classical automation on site.

Therefore major challenges arise for the application of robotics in construction from working on small lot sizes in a dynamic and unstructured environment, coupled with the increased complexity of modern buildings.

Although working with natural materials exacerbates these problems due to inhomogeneity in the material they also bring a number of advantages, the most important advantage for using timber in modern fabrication and assembly being the ease with which it can be worked. This allows for uncomplicated adjustments at the construction site if necessary. However because of the anisotropic nature of wood (e.g. grain direction, variations in density), the material needs to be considered in depth to enable strong wood joints. At the same time stability is not only a relevant factor for joined elements but also for the production process itself. Nowadays milling is the easiest way of manufacturing timber-timber constructions. To enable this, the shapes of traditional joints have been adapted for mechanic processes [2]. For example it's impossible to mill squared inside corners because of the geometry of the tool.

As part of the Robotic Woodcraft project we focused on robotic fabrication of wooden components. Within this area the work of the Institute for Computational Design (ICD) of the University of Stuttgart should be mentioned [3, 4]. A first look at collaborative wood assembly was also taken within the DADA Digital Factory workshop "Robot-Assisted Assembly in Wood Construction" by the ICD. However, there the assistance of the robot was in positioning wooden parts with low variances without robotic joining operations, while parts of higher complexity were fitted manually. As part of the Project "Dynamic and Interactive Robotic Assistant for Novel Applications" (DIANA), we implemented a first demonstrator for a collaborative assembly process. Focusing on the classic assembly problem of peg-in-hole, we decided to continue the work done within the Robotic Woodcraft Project and the resulting workshops (Fig. 1(1)), which used light weight timber rods as support structures for square shaped beams to create large structures from small and lightweight parts. One of the resulting design objects and case studies can be seen in Fig. 1(2). As a result we identified a number of application scenarios for assembly tasks in construction, which previously were not addressed by the robotic fabrication via milling as can be seen in Fig. 1(3).

**Fig. 1.** Collaborative fabrication: robotic milling (1), manual assembly (2), assembled design object (3)

## 2 From Design to Production

Most construction drawings depend on a CAD (Computer Aided Design) model, which can either take the form of simple geometric objects such as lines that indicate different materials according to their width, spacing, and colour, or parametric models with intelligent objects such as walls and doors that contain their base geometry and parameters pertaining to specific dimensions, time and construction phases. In either case, one of the main challenges of any design-to-production workflow is to link the base geometry with the fabrication process [5]. These challenges motivated us to develop our own software KUKA|prc (parametric robot control) [6] that works directly within a CAD environment, and can thus be linked with native CAD geometry without any further conversion. Rather than drawing different geometries manually and planning fabrication for only this specific part, the parametric approach allows the design of a single model which can be fitted dynamically to the specific conditions. Thereby mass customization becomes manageable.

As platform we utilize the CAD software Rhinoceros, in particular its visual programming environment Grasshopper. Our software expands the capabilities of the visual programming environment beyond parametric design by integrating a series of components that allow the programming and simulation of robotic arms. Through visual programming, we are able to define our own fabrication strategies by connecting components with a variety of geometric and mathematical operations with each other, creating a parametric definition. As such, the definition has a number of inputs that define the source geometry and calculates the toolpaths based on that geometry. Finally KUKA|prc simulates and visualizes the resulting robot movements. This ensures that the process is highly interactive, as changes to the source geometry immediately propagate through the parametric model and are reflected by the simulation. Therefore, we can program and optimize processes in a very intuitive fashion by interacting with both design and production parameters at the same time. It also becomes possible to efficiently reuse existing definitions by simply replacing the geometry inputs, enabling the near immediate generation of fabrication data for an entire family of topologically similar elements, thereby facilitating mass customization with robots. Figure 2 illustrates both the model used in our case study as well as the path analysis. Through the visual programming environment, the fabrication steps can be tested and evaluated individually, and finally assembled into a single program.
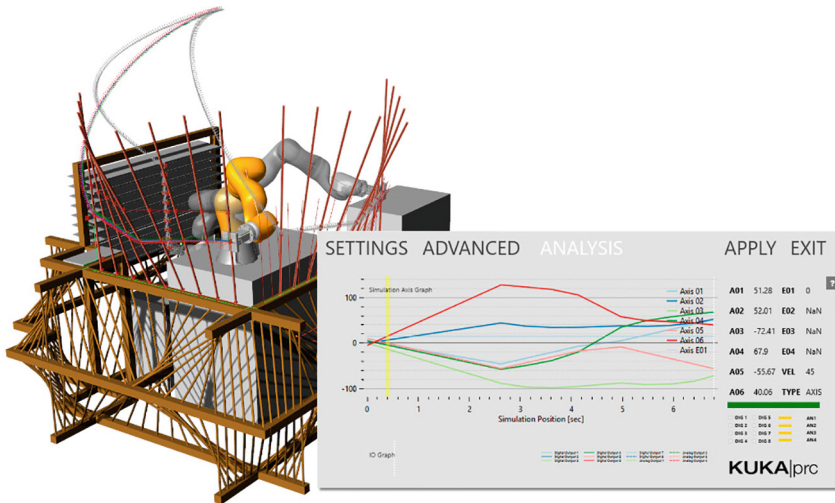
**Fig. 2.** Robotic path planning using KUKA|PRC

However, CAD environments are optimized to work with idealized data, where e.g. a NURBS (non-uniform, rational B-spline) surface uses very little information to define a free-flowing, complex geometry. Especially when working with naturally grown materials like wood, CAD cannot represent the physical, material realities. High-resolution 3D-scans may provide a high-resolution, data intensive geometric representation of a wooden part. Yet for example the anisotropic properties of wood cannot be simulated within an acceptable timeframe on a high-end workstation. This is consolidated by the fact that a complete scan of every assembly part would be necessary.

So while we are able to three dimensionally capture anything from small objects to an entire buildings, knowing the shape of an object is not sufficient to fully understand its specific behaviour in many applications. Furthermore a simple material model will also not mediate problems arising from working with natural, inhomogeneous materials. This would require a highly sophisticated physical simulation. Even an approximation of the material behaviour can be calculation expensive, because the material flexibilities need to be considered due to possible strain when performing joining operations which in turn directly affect the required motion. The resulting delay or required computational power currently clearly constitutes a hindrance for the on-site application. We therefore decided to use a different approach which is described in Sects. 4 and 5.

We also used the design shown in Fig. 2 for the fabrication of our test environment. There are several parameters affecting the quality of the result of a milled object. Often there are significant differences between the produced edges depending on the work flow direction relative to the grain, the depth of every single cut, the speed of operation and the geometry of the tool. Even the service time of the router bit impacts the joints. Wear of the bit necessitates higher tolerances to ensure that the wood joint can still be assembled.

One of the least predictable parameters is the inhomogeneity of the timber. Different types of wood lead to visible differences in the quality of the results. Variances in the material e.g. knots, cracks and resin pockets mean that even with several tests with the same kind of wood will not result in a constant quality. Ideally the local change of quality of the material demands a local adjustment of the processing parameters. One possibility is the generation of virtual 3D-models of the timber from ultrasonic and X-ray measurements. Using these models one can adapt to inhomogeneity while producing the code. An easier option is the manual regulation of the speed of operation during milling. The most precise alternative is the real-time adjustment of the processing parameters informed by sensors and software.

The rotation of the router bit generates another problem. If an un-practiced person tries to mill a straight line with a router without a fixture the result will be a curve. The forces which determine this trajectory can also have an impact on the machine tools used in modern manufacturing. Compared to an industrial robot, gantry machines are much less influenced by these forces. The position of the material relative to the robot affects the process forces and in consequence deteriorates the quality of the result. Also in this case sensor technology and dynamic real-time adjustment can be used to get a more or less constant quality.

The quality of the manufactured elements is essential for the final automated assembly. On one hand to get the wood connection easily assembled the tolerances have to be big enough but on the other hand the joint has to be strong enough to carry the load without falling apart. Usually a constant quality of the individual parts is essential for a successful automated assembly.

## 3   Design as A-Priori Knowledge for Assembly Planning

While the idealized representation of CAD is sufficient for many subtractive processes that simply remove material, further problems arise when dealing with the assembly of materials that have very high tolerances. As noted above the environment on site never completely corresponds with the digital model and is also bound to change during an active process. This can happen due to human workers on-site, but also simply through changing environmental conditions such as temperature and humidity, causing materials to deform. Although this is the case we still can use the information and positions from the digital design as a priori knowledge and plan the necessary assembly sequence in an idealized environment. However, we need to implement adaptive assembly operations, which are further described in Sect. 4.

Using this concept, assembly sequences are planned based on the parametric design data – just as we would do in regular offline programming. However, the generated positions do not accurately define the entire tool path of the robot; instead they only provide the underlying geometric data that is the basis for the adaptive assembly process.

By virtually prototyping a process we are able to optimize the best-case scenario – that does not take any tolerances into account – in a very quick and efficient manner, checking the reachability of all positions as well as avoiding axis limits and singularities. As the process is parametrically defined, we can then very easily introduce

deviations and re-evaluate the process based on the changed data. We can also use this information to define constraints for each assembly operation.

This optimization does not have to happen manually, but can be performed automatically by integrating an optimizer into the system, which then tries to reach a best-case scenario with a maximum of flexibility to accommodate the largest value of tolerances. For DIANA we used the simple genetic algorithm Galapagos, which is an existing plugin of the Grasshopper software. The geometric data of this scenario is then used to intelligently inform the adaptive parametric assembly operations. Figure 3 shows our environment for assembly testing after a collaborative fabrication of the demonstrator.
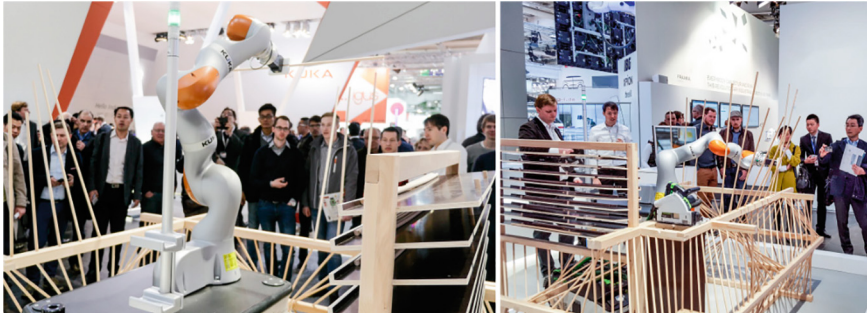


**Fig. 3.** The assembly process testing environment

The resulting assembly sequence for our test environment can be described as follows. First the robot takes a rod out of the supply station, which groups rods within a range of 50 mm. Having retrieved a rod the actual length must be determined. After this the rod is cut to length in accordance with a parameterized curve and subsequently joined to the beam at the corresponding assembly position. The challenges of working within an unstructured environment remain.

To create a reusable and dynamic solution we chose to have the robot adapt to the construction site instead of vice versa. In order to achieve this adaptability, we see the need for bringing parametric fabrication strategies directly and interactively to the construction site. We wanted to integrate fabrication strategies directly into advanced robot controllers such as the KUKA iiwa's SunriseOS so that the parameters defining the local object can be gathered on-site. By fitting a parametric model to the object the system is able to identify the corresponding manufacturing strategy. Furthermore features of the object can be identified and used as reference points within the assembly planning.

## 4 Implementing Adaptive Parametric Assembly Operations

In order to use the robot on site and to adapt to the difference between model and reality a number of sensors can be employed. However using vision system on construction sites is very difficult due to changing lighting and often dusty environment. Due to the fact that the sensors also need to be easily transportable we decided to use force torque

sensors. Instead of mounting a sensor on the flange of the robot we used a KUKA iiwa robot, which contains integrated force torque sensors in every axis. This also makes the robot well suited for human robot collaboration since contact between the human and the robot can be detected anywhere on the robot and not only at the end-effector.

The essential operations in assembly can be described as joining, handling and position adjustment. Within skill based programming these different operations are often defined as skill sets for the robot. However these skills require a parameterization which is often derived from a complete environment model. Using only force torque sensors we are however unable to scan the entire environment to complete the model. Assembly operations focus on the relative positions between assembly parts. To define these positions consistently for variations of assembly parts, they also need to be defined relative to recognizable part features. Constraint based robot programming allows for exactly that, by viewing the resulting robot path as an optimization problem that can be determined using feature based constraints, which makes it ideal for sensor based robot path planning. The main disadvantage is that solving optimization problems can require considerable calculation time in larger contexts.

In order to combine the advantages of the approaches we split up the optimizable parts into single operations and used a priori knowledge from the design to parameterize our operations. Applying on-site optimization to only simple assembly steps and not the overall assembly strategy reduces calculation time significantly. We use the force torque sensors to dynamically adapt to the current state of the environment and unexpected changes (Fig. 4).
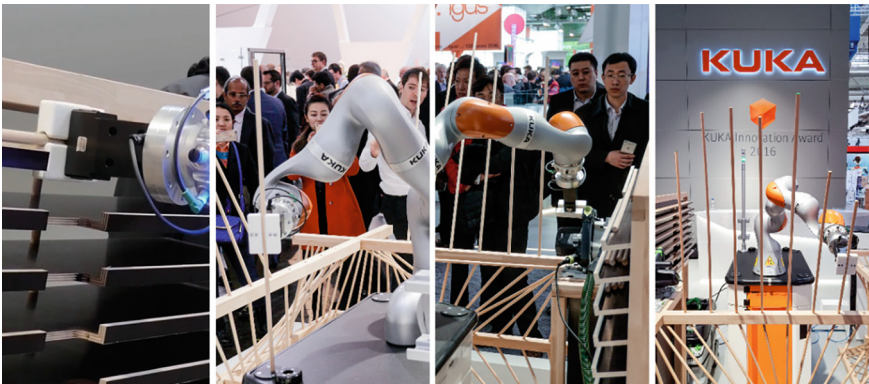


**Fig. 4.** Sensitive assembly: picking object from storage (1), measuring exact length (2), cutting (3), force-sensitive assembly (4)

Additionally each operation is parameterized by giving a source and a target position for execution as well as available tool and workpiece information as transfer parameters. The sequence of the adaptive assembly operations for our test scenario, described below, is also shown in Fig. 4.

First of all, the robot takes a rod out of the supply station. By not moving statically to the target position but slightly wiggling around the position the robot ensures successful gripping of the rod. Depending on which size range the rod was gripped from, the end frames including some tolerance are added to the gripper information to avoid collisions. To determine the exact length of the rod, the robot switches into a soft mode and moves each tip of the rod onto its transportable base (KUKA flexFELLOW). Once the force exceeds a threshold the robot stops and records the distance between the gripper fingers and the measured position. It repeats this for the other end thereby calculating the length in each direction. Using the actual length of the rod, this one is moved into the processing station. The robot then uses a circular saw to cut the rod to the required length. For the actual joining, the robot moves the rod into the approximate position of each mounting position in a soft mode. It first searches for contact with the beam. After the contact force has been detected a search movement is executed, which continuously monitors the force values along its tool axis. Once it feels a significant drop in the force value, it concludes that the rod has slipped into the mounting position. To ensure the correct angle and a good fit the Cartesian orientation axis is switched to a soft mode and the rod moved downward in a spiral pattern until a certain force threshold is reached and the joining is finished. The robot then continues with the next rod.

Should the reality however deviate too much from the model, the robot can get stuck within a search pattern. In order to be able to give the robot new commands and parameterize it for similar task directly on site without having to return to the design phase, we decided to further extend our concept. We therefore introduced the term of haptic programming, which allows us to teach the robot directly through hands on interaction.

## 5   Haptic Robot Programming

Two major elements differentiate haptic robot programming from similar means of programming especially when moving the robot's end effector in compliant mode. For one the taught motion is not used as a demonstration for imitation, but the required information is extracted in the form of parameters. Also, the robot cannot be moved around arbitrarily but instead leads the user passively. In our test scenario we use haptic programming in various ways to adjust the parametric programming on site to compensate differences between model and reality. If the robot searches for too long, the user will be informed. The operator may then move the robot within its parameter space through dynamic compliance. Following a quick confirmation the information regarding the actual target position is used to adapt the following execution of robot operations.

Another way in which we use haptic programming is the initial parametric control of the task on site. We previously mentioned that we use a parameterized curve to dictate the lengths at which the rods are cut. However we use haptic programming instead of CAD software to define the unique curves. For this the robot is in a restricted compliance mode, meaning that it will increase stiffness if the limits of the parameter space are approached. Therefore the robot can only be led on the surface whose edge the unique curve defines. For this task the user takes the iiwa robot and manually
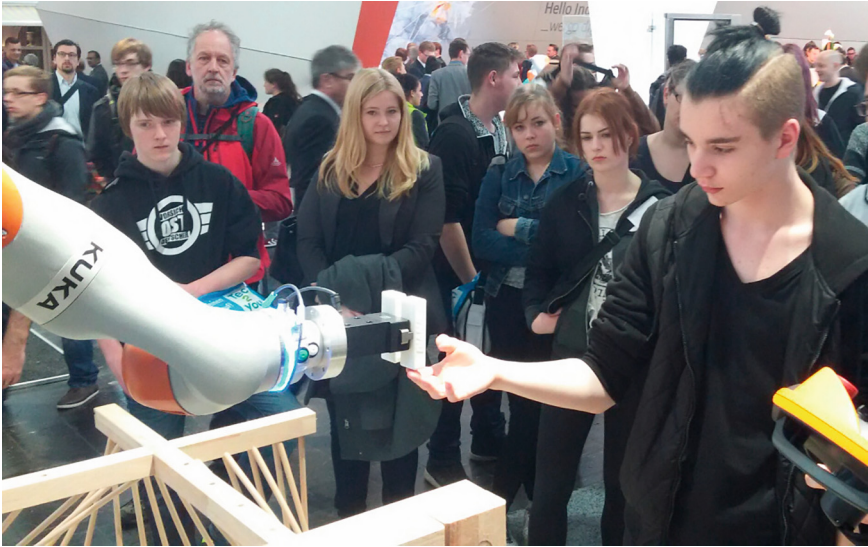
**Fig. 5.** Capturing process parameters through haptic programming

guides it from one side of the base structure to the other, which is shown in Fig. 5. By doing so, a curve is generated that informs the fabrication process, allowing each produced structure to be unique.

While executing the process a number of problems can arise due to the high material tolerances, starting from objects not being gripped correctly due to extreme bends in the rods to collision with objects that were moved. If such a problem arises the user will be asked for help. The problem can then be fixed accordingly either by haptic reprogramming the robot for later adaptation or without adaptation but a simple continuation of the process in case of false positives.

## 6   Synopsis and Future Work

At the Hannover Fair 2016, we successfully demonstrated the benefits of our approach. We were able to assemble individual curves for a week without major breaks; almost all arising problems could be fixed through human-machine collaboration. We demonstrated how modern robots are able to work as dynamic assistants, which can be programmed haptically by people without previous experience in robotics, while the context is simply provided directly out of the design required for fabrication. We extended our approach for parametric robot control by compensating material tolerances and adaptation of the planned paths through haptic programming. Our future work will focus on increasing the fields of application within the area of assembly. While we used an easily transportable robot we want to implement the approach with mobile industrial robots as well as larger kinematics in the context of higher process forces. We also want to define the operation constraints more dynamically to further

improve the adaptability of the system. Furthermore we currently only adapted some basic information for each operation. We want to extend this part to include more self-learning which will not only optimize the trajectories but also the forces used based on the current operational context.

# References

1. Eastman, C., Teicholz, P., Sacks, R., Liston, K.: BIM Handbook: A Guide to Building Information Modeling for Owners, Managers, Designers, Engineers and Contractors, 2nd edn. Wiley, Hoboken (2011)
2. Cokcan, B., Braumann, J., Winter W., Trautz, M.: Robotic production of individualised wood joints. In: Proceedings of the 21st International Conference on Computer-Aided Architectural Design Research in Asia (CAADRIA), Melbourne (2016)
3. Schwinn, T., Menges, A.: Fabrication agency – Landesgartenschau exhibition hall. Architectural Des. **85**(5), 92–99 (2015). Wiley, London
4. Menges, A., Knippers, J.: Robotic fabrication. ICD/ITKE Research pavilion 2012. In: Andia, A., Spiegelhalter, T. (eds.) Postparametric Automation in Design and Construction. Artech House, Boston (2015)
5. Brell-Cokcan, S., Braumann, J.: Robotic production immanent design: creative toolpath design in micro and macro scale. In: Proceedings of the 34th Annual Conference of the Association for Computer Aided Design in Architecture (ACADIA), Los Angeles (2014)
6. Braumann, J., Brell-Cokcan, S.: Parametric robot control: integrated CAD/CAM for architectural design. In: Proceedings of the 31st Annual Conference of the Association for Computer Aided Design in Architecture (ACADIA), Banff (2011)

# Artistic Design of the Customized Robot with Environmental, Social and Cultural Impacts to Human Society

Biljana Vicković[1(✉)], Svemir Popić[2], Miloš D. Jovanović[2], and Aleksandar Rodić[2]

[1] The Association Octopus, Belgrade, Serbia
`b.vickovic@oktopus.org`
[2] Mihajlo Pupin Institute, Robotics Laboratory Belgrade,
University of Belgrade, Belgrade, Serbia
`{svemir.popic,milos.jovanovic,`
`aleksandar.rodic}@pupin.rs`

**Abstract.** The paper presents a sculpture realized with the basic idea of using robotic technology. The robot bird is an artistic creation that captivates with its striking appearance, with its surreal form, but also because its send a message about some common, everyday activities, such as material recycling. The robot bird sends a message to take care about our environmental protection together with raising our sociological, cultural and technological awareness and education. By its appearance it makes us to think a little bit about the problems of task scheduling and according to our action to be rewarded. This is an ideal way to think about our environment, about the life education of the coming generation, which will, throughout the game, become aware of their actions.

**Keywords:** Robots in art · High-tech artistic expression · Advanced design · Biologically inspired robots

## 1 Introduction

In our modern society with high-technology impact on daily life and work of people, artistic research is in symbiosis with other scientific disciplines, such as the area of robotics etc. The above mentioned aspect has proven to be an important sociological and cultural approach in terms of incentive for the development of future generations.

The main goal of scientific and technological research in the area of art and architecture is to keep existing cultural and historical values of urban space and through this implementation make them publicly visible and well known. The subject here is the influence of this approach on the public urban space which contains social and cultural transformation trough time.

Thus we intend to expand the existing borders of Art. The essence of this art work within technology illuminates new horizons of interaction with direct consumers.

Exactly this interactive change with consumers where contemplation is replaced by action is given to a robot because of its numerous operating options. It can do it in a

way to become a big, dear friend and buddy that children love to hug, endlessly happy with unbelievable freedom and achieved closeness as a result of their interactions. The focus here is on the results consumers benefit from, and monitoring the registered data. The consumer is involved in this relationship; therefore his passive involvement is no longer an authentic state. With this we get a new platform which becomes a part of collective experience. It is an open space for acting and thinking with the purpose of upgrading the mind level of the consumers; we can call it a Cyber sign of possibilities that are ahead of us.

The basic idea of the placement of the Robot Bird, whose author is Biljana Biba Vicković, is to develop the urban space with interactive sculpture and its purpose is to culturally revitalize the public space.

The idea introduced by this change is determined by a spatial and temporal concept that transforms a common monumental sculpture, reconsidering the visual momentum. This robot, "fed" with tins by the citizens, proves that an artistic artefact is an active factor which discovers new possibilities with interactive and kinetic characteristics, using artificial intelligence obviously to reshape it.

Placing the Robot Bird in other European cities (Barcelona, Ljubljana) opens the possibility for the realization of an international communication strategy, aimed at contributing to the process of changing the cultural policy in public areas and the environmental one at the local level, according to EU standards.

The project tasks are related to the achievement of one of the objectives of the Europe 2020 Strategy, the one for improving conditions for research and development of innovations, because it has multiple "levers" for achieving a complete strategy. Innovation is the key "lever" for development, based on knowledge, and it doesn't have a substitute when it is related to European development.

## 2   State-of-the-Art

The visual identity of the work contains an evolutionary aspect formed by the impression from dream from which the author's reflecting vision is represented by four dragon bodies placed in the deep bowels of the universe, connected through a knot in the middle of the space. This vision is descriptively very close to Ouroboros which opens and raises the question of eternity and infinity, expressing visually the primary function of this artistic robot through the process of recycling aluminium cans that takes place countless times [1].

"Eternity and infinity are the same". Only for those who seek eternity trough the infinity and not for "the end", infinity is it the same as eternity [2]. This resembles to the endless process of city appearing and disappearing with its cultural history, in which we are all constant and inevitable participants.

The foothold of Birds Robot entertainment character is partly inspired by Leonardo da Vinci's "mechanical lion" [3].

This artistic structure is not the first robotic device made in Mihajlo Pupin Institute. One of them has already been made and presented at a prestigious art exhibition in Berlin, while the other one is designed in two versions and variants of its forthcoming production. The first represents the robotic tree, the Dancing Tree, with one degree of

freedom of movement, while the other one, the Robot Flower, has two degrees of freedom of movement around two axes of rotation, and a synchronized performance is the result of selection of different axes of rotation [4].
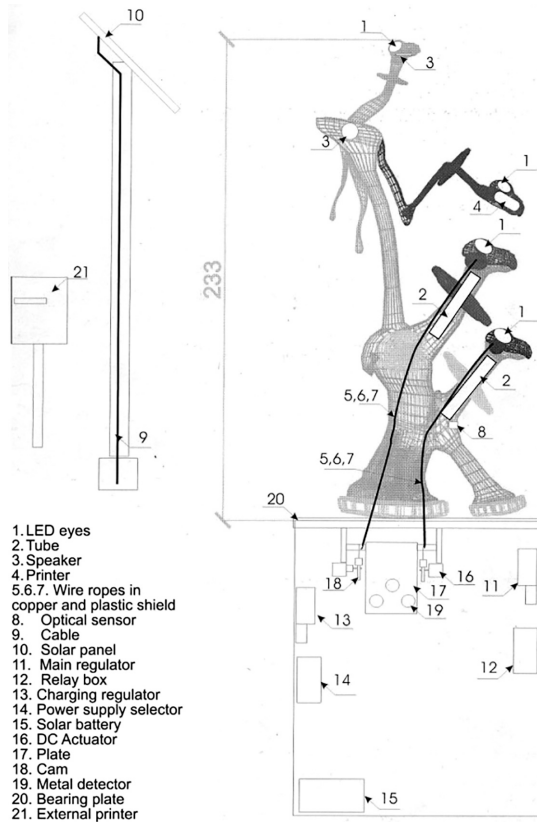
## 3   General Design Presentation

The Robot Bird is a mechatronic form that by its appearance draws the attention of passers by suggesting or imposing a contact from which the pleasure of communication results, in addition to fulfilling its primary purpose; the piece of art is interesting and above all represents an instructive and educational way to collect recyclable materials while preserving the environmental awareness of citizens, especially of young users – the children. The piece of art expresses the idea implemented using well known principles of mechanics, e.g. the bird robot's mouth, opens and closes at the request under the command of a control unit. As with almost all robotic systems, a propulsion system can be placed in the vicinity of the main body or near it. Each of these principles brings its own advantages and disadvantages. Due to the control unit placed close to the Robot Bird's beak, some structural changes in the shape and dimensions of the piece of art might be caused, as well as the increase of the system's inertia; it was therefore decided to place the actuators at a reasonable distance to the form, i.e. in a location where their deployment would not affect the shape and dimensions and thus be mechanically acceptable. Structurally, the transmission of force or torque is always accompanied by side effects of the uncontrolled friction, elasticity system in full and strokes in the joints. But as the conceived system does not require an excessive accuracy except for a reliable opening or closing of the beak, pre or post loading the used cans, a mechanism composed from steel cables as basic gear movement was chosen (Fig. 1).



TEHNIČKI CRTEŽI ZA NOSEĆU KONSTRUKCIJU

**Fig. 1.** Final form of the Robot Bird with open and closed beak

Generally speaking, the mechatronic form is a recycling system for collecting used aluminium cans that can be found in our markets. On this basis, the beak is designed together with an appropriate pipe channel to carry the can, reliably and without jamming in a landfill - bunker, which was buried in the ground. In simple cases this warehouse is a metal basket which is periodically emptied. The version with a small automatic press system providing higher storage capacity is also planned (Fig. 2).



1. LED eyes
2. Tube
3. Speaker
4. Printer
5.6.7. Wire ropes in copper and plastic shield
8. Optical sensor
9. Cable
10. Solar panel
11. Main regulator
12. Relay box
13. Charging regulator
14. Power supply selector
15. Solar battery
16. DC Actuator
17. Plate
18. Cam
19. Metal detector
20. Bearing plate
21. External printer

**Fig. 2.** Cross section of the Robot Bird and listing of main parts

Electrical motors with gearboxes 12VDC, 50 W are the basic actuators of the system (Fig. 3). On the shafts of both motors, two eccentrics from duralumin are mounted, whose circumferences lie on the shorter lever arms. At the ends of the longer lever arm a steel cable is attached which, through plastic tubes, reaches both of the moving beak heads. The ratio of free length of the steel cable and output speed of the motor gear unit define the opening and closing times of the beak, which are 0.5 s to open or 2:55 s to close the beak. This is done for security reasons, and because slowing down at beak closing allows the user to promptly extract his hand after loading the cans into the beak. Of course it is the same reason for which a second security system is

**Fig. 3.** DC motor as beak's actuating device

applied that exclude the possibility of injury. The final positions of the active parts of beaks are not only limited by mechanical hard stops but also use micro switches at the end positions.

Plastic guiding tubes for passing of well-oiled steel cables must be attached in places along the wall of the conduction channel in order to avoid scuffing the can in the channel, while the cable must be optimally applied to avoid empty strokes and achieve optimum angles of beak opening - closing in the two receiving heads.

The control system of the described mechatronic device capable of artistic audio-visual performances named Robot Bird has a modular structure, the block diagram of which is shown in Fig. 4.
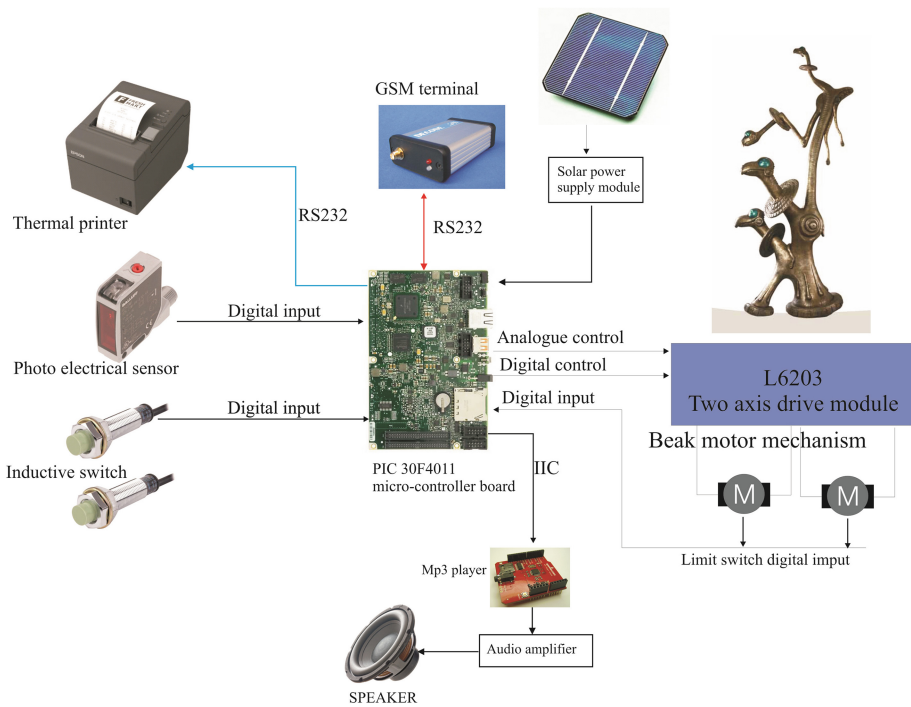


**Fig. 4.** Block diagram of the control system.

The main part of the control structure is the microcontroller circuit board based on the PIC microcontroller PIC30F4011. Through a special motor driver based on the L6203 driver component, the microcontroller circuit board can control the two motors that open and close the beaks of the mechanical system. The mechanical system is equipped with two limit switches which can detect when its moving parts reach some physical limits so that no mechanical damage occurs. Protecting the mechanics is double secured. The direction of movement of each mechanism possesses a double security protection installed as micro switches. If the first level of protection (digital sensor reading and command issued by the controller) fails, then the second level of protection interrupts the power supply for the motors, preventing thus that the movement in the direction of interest. In this way, a cheap and effective protection against mechanical damage of the entire system during operation is provided. The control system can receive SMS messages from the user via GSM terminal (GT900 allows receiving SMS messages). The control system can provide a printed receipt about recycled material through a built-in thermal printer system. There has been implemented a MP3 player that is capable to create voice messages that are uploaded into the memory and reproduced through the speakers built into the head of the bird.

The microcontroller system checks also the status of the built-in photoelectric sensor that detects whether a person came close to the exhibited mechanism. If it detects that someone approached the mechanic system, it open the mechanisms of both beaks, activates the traffic lights embedded in the eyes of the bird's head and reproduces the voice signal message for recycling. If a metal can is placed inside the bird open mechanism, this one will fall into an appropriate container due to the effect of gravitational forces at the interior of the mechanism. The passage of the thrown cans is detected by a built-in inductive sensor. The control system increments the counter for recycled process in its memory, closes the beak mechanism, activates the ticket print of the thermal printers and the voice message thanking the person for environmental protection.

The system continuously monitors the status of the photoelectric to detect if a person departed from the recycling mechanism; if this situation occurs the whole mechanism is set in the initial state, the bird's beak mechanisms are closed and the device is place in the waiting state for a new recycling event. Periodically, while the mechanism is in the waiting (quiet) mode, the control system activates an appropriate voice message in order to attract the attention of people around. The control system of the supervision centre can send appropriate control signals to the robot bird controller and receives status signals of the entire device through SMS messages.

The system has an independent solar power supply. Through solar panel it collects solar energy and accumulates it in a battery having an independent power supply from the power greed of the city too. This enables a continuous autonomy of the whole system for a time period of 36 h. This entire system works in a completely independent and autonomous mode and does not make the environment pollutant. The system can be easily connected to the city power greed. In this way, the mechatronic recycling device can take energy from the city grid when the battery charge drops below 30 % of its full load state.

## 4  Technological Solution as an Incentive for Upgrading Artistic Expression and Culture

This project is designed as a high-tech innovative prototype and interactive web portal system for the international exchange of cultural and historical knowledge of the participants on a daily basis. This project intensively uses the principle of innovative multi-sectoral combination determining the most important human activities: socialization, social relations, art, technology and science, in order to stimulate and intensify thinking about their effects on everyday lives of the project's beneficiaries. Robot Bird reconstructs the identity of a work of art through interaction, providing one with numerous interpretations (each encounter is particular). The robot's cybernetic characteristic includes an option of upgrading ad infinitum.

In developing the new tendencies opened by this project, a series of programs are envisaged that are oriented towards the cultural history of the city. This cultural history of the city, as well as its database, will undergo the processing of storing and exchanging large amounts of contents and knowledge via internet platforms, with clear causal links and potentiating the critical thinking of individuals in the form of decentralized networking [5].

## 5  Technological Solution as an Incentive for Upgrading Social Frameworks

Each user gets a numeric code on a ticket by inserting tins in the Robot Bird. The code on the ticket can be used to apply for the prize on the international on-line competition "Target Art". During the competition the participants have to enter a new code from the ticket after inserting a new tin, in order to continue the contest. This stimulates the continuity of the recycling initiative.

The competition's program will be designed for all creative groups of talented individuals, as well for journalists, and it is divided into two categories:

1. **"Target Art" competition in the development of intelligent sculptures for public space (the ecological functions and web connection).** The task of competing groups will be designing creative proposals for intelligent sculpture for a public space with ecological functions and web connection possibilities. The toy sculptures will be, as a permanent value and interest of the competition, placed in public spaces.
2. **"Target Art" competition for journalists.** An international competition for journalists is based on the exchange of knowledge on cultural sites, cultural and historical events of participating countries. Journalists will receive the task to explore the urban space of the city, especially those parts where differences among the cultural history are most visible. Spaces such as those where it is most probable that urban fabrics will perpetually emerge and disappear (especially in urban underground zones as focal points of pop culture, which are the creative engine of thought tendency of each new generation) are of interest. Students should choose to explore and analyse their own city with which they have a special relationship. It can be a

space of cultural heritage in which the participant has grown up, or an area that borders real and imaginary worlds. Through audio or video and the photo-documentation, journalists will set up materials on a project website. The web portal will be used as a dynamic showcase, to give all participants the opportunity of gaining insight and criteria for the establishment of their profile. One of the goals of this approach is to stimulate the creative competition that web space allows.

Results of journalistic competitions and collected cans are part of the "challenges" between the friendly competitions. On the other hand, the on-line competition "Target Art" will enable the development of competitive cultural and historical educational programs.

## 6   Technological Solution as an Incentive for Mind Upgrading for the Purpose of Preserving the Environment

The mechanization of Robot Bird is powered by solar energy (solar concentrator), thus providing promotional activities for sustainable development during and after the project; the citizens' environmental awareness is enhanced as well as the use of renewable energy in daily life.

The Robot Bird project is designed as an innovative socially-useful robotic work of art, with tin recycling function, and it is used to influence the environmental awareness of citizens. During one year, about 50.000 people insert cans in the bunker of the Robot Bird. The average quantity of collected cans is from 670 to 750 kg annually. The revenue from the collected cans can be used for charity.

## 7   Conclusions and Future Work

Ambient artistic robots have the important role to control the behaviour of the consumers' society to prevent the creation of a fairground of temporary values using the new scientific inventions for that purpose. This type of robots and robotized architectural systems has a multifunctional influence expressed as follows:

- in a way which is typical for a robot, they can be an incentive for the creative potential of consumers;
- robots have impact on the mind creation and development of a consumer about the knowledge of historical and cultural value in public spaces;
- the above impact on the citizens is to protect the environment in an entertaining and humoristic way;
- robots of this type contribute to the development of the economic capacity of city spaces through investments on the market, bringing profit.

Robotics opens the possibilities of artificial intelligence, a world within a world - the network space, the space of signs, simulations, manipulations and introduces interaction as an inner space of meta existence. Robotics involves supreme

technological ranges which makes it possible for numerous tasks to be accomplished and which are yet to be discovered.

With the ROBOMEM project ("Unravelling layers of memory with new technology in public space") we will explore the potential of robotic technology in unravelling layers of memory of particular contested public spaces. The project ROBOMEM is inspired by the recent practices of using new technologies and means of communication for the purpose of social protest/activism, in which memory is often used as a symbolic capital. Social memory is used as basis for arguing various political stances, and as source for legitimating various social actors.

In the context of democratization of social memory, traditional (monopolistic) modes of recording and transmitting memory are outdated. This project explores potentials of robotic technology in unravelling layers of memory of particular contested public spaces. Using mobile robots, these spaces will be used as a stage for examining layers of history that a public space entails, while revealing both official and marginalized memories, and contemplating relation to the public space as a public good. Using interactive web platforms and smart-phone mobile applications, the project will invite citizens to contribute with their own memories and experiences of the particular public space, thus co-creating public exhibition and regaining citizens' symbolic ownership of the public space.

Robots will be artefacts that will have post-project life. They could be regarded as artistic objects, they could be purchased by a company and used for promotional and other purposes, and/or they could be adapted for regular use in cultural exhibition venues [6].

# References

1. https://en.wikipedia.org/wiki/Ouroboros
2. Mayrink, G.: The White Dominican (Beli Dominikanac), Ultimatum.rs (2015). ISBN 978-86-80274-01-0
3. https://www.youtube.com/watch?v=xNWE2AdfNuo&feature=player_embedded

4. Popić, S., Jovanović, M., Miloradović, B., Dodig, L.: Robotics in art. Robot Flower, INFOTEH-JAHORINA **11**, 1015–1018 (2012)
5. http://www.ted.com/talks/manuel_lima_a_visual_history_of_human_knowledge?utm_source=newsletter_weekly_2015-08-21&utm_campaign=newsletter_weekly&utm_medium=email&utm_content=talk_of_the_week_image
6. http://selfiecity.net/selfiexploratory/

# Evolution, Education, Legal and Social Issues of Robotics

# Legal Issues for Mobile Servant Robots

Eduard Fosch Villaronga[1,2(✉)] and Gurvinder S. Virk[3]

[1] Joint International Ph.D. Erasmus Mundus in Law,
Science and Technology Coordinated by CIRSFID,
University of Bologna, Bologna, Italy
eduard.fosch@unibo.it
[2] IDT-UAB, Universitat Autònoma de Barcelona, Barcelona, Spain
[3] Professor of Robotics, University of Gävle,
KTH Royal Institute of Technology, Stockholm, Sweden
gurvinder.virk@hig.se

**Abstract.** This paper identifies key legal issues which are emerging for Mobile Servant Robots (MSRs), a sub-type of Personal Care Robots (PCR) defined in ISO 13482. New cases are likely to be introduced in the market soon even though appropriate and specific binding legal regulations regarding MSRs are missing and several questions need to be carefully considered. The main issues of concern are the need for a concrete and holistic definition of MSR, clarification on the confusion among new emerging ISO/IEC robot categories (especially between boundaries and gaps in machinery with medical device regulations), unclear liability scenarios (avoiding harm, prospective liability, butterfly effect), defining and regulating human-robot collaborations and relationships, ethical issues (mass surveillance, post-monitoring personal data), autonomy (from the robot but also from the user perspective), isolation scenarios, etc. Despite the recent technical advances, there is still a long way ahead and further research is needed to overcome a variety of associated legal and ethical issues which are emerging.

**Keywords:** Social robots · Legal aspects · Human-Robot Interaction (HRI) · Personal care robot · Mobile servant robots · ISO 13482:2014

## 1 Introduction

Current industrial robot standards cannot give appropriate answers to all the questions that new service robots pose on the legal layer. However, "ignorance of the law, excuses not" is a clear and factual statement which must be addressed to ensure there is clarity in these uncertain times. Consider the following use case:

> "Duško has just bought a cloud-based personalized mobile servant robot. He calls him Duško. Duško reminds him to take medication at appropriate times, does online grocery shopping based on Duško's preferences and regularly checks his health status. Duško is a vegetarian and is concerned about taking pharmaceutical drugs. As he cannot sleep at night, he asks Duško for help. The following day, and after checking with other robots and the Internet, a green box arrives home. Duško has bought marihuana on the Internet".

This use case, which is inspired by the Random Darknet Shopper [1], a human-centred social robot for elderly care [2] and the Patent of Google on Robot Personality [3], raises the question of what is the impact that assistive technology poses to users on legal/ethical aspects: who would be liable for the acquisition of drugs illegally on the Internet? How can a robot respect the autonomy of the person? How can privacy be preserved after the insertion of a robot to the market?

Traditionally only industrial robot standards and regulations were available for ensuring human safety via ISO 10218-1, -2 and recently new service robot safety requirements have been published for personal care robots in ISO 13482. The industry robot regulations are concerned mainly with ensuring human safety by separating humans from operational robotics. The new service robot regulations focus on physical human-robot interaction (HRI) hazards by stipulating safety requirements on various design factors; these include the following: robot shape, robot motion, energy supply and storage or incorrect autonomous decisions. However, the state of the art confirms that robot capabilities go beyond the mere physical HRI, especially if the robot is used in social applications [4]. Thus, questions concerning other hazards such as cognitive HRI hazards, robot personality, understanding human commands, whether robots should be granted agenthood, what is the acceptable level of autonomy in the robot decision-making process (in legal transactions on the Internet for instance, which consequences could not physically harm a human) or simply the respect for private life are still disregarded by current standards. Some initiatives to ethically design robots and robotic system are under development [5], but at the same time that these machinery safety regulations are being developed, supra-/national and state laws are needed to provide citizens a fully legal coverage, not only in privacy matters [6].

The main objective of the paper is to highlight growing wider concerns in adopting service robots in new settings to provide some guidelines for the creation of a possible future regulatory framework for MSRs, which includes legal and ethical aspects [7]. Law is always some steps behind reality and new technology can create new scenarios not already covered in the legal framework. Although some MSRs have already entered the market, there are no specific laws addressing their use and appropriate management, no judge is specifically trained to deal with the legal consequences arising from the use of these new technologies, and end-users are not aware of what the possible consequences of adopting the new service robots could be to them. In fact, although the identification of safety principles regarding robots is a great step towards a future robotics policy [8], a specialist in robotics may still encounter a two-fold problem, namely, (1) the identification of the wider principles and impacts that their particular technology involves and brings to society; and (2) a deep understanding of the implications of adopting the new technology (e.g. does an encrypted data communication channel from the robot to the cloud offer sufficient data protection capabilities?).

First, the definition of "mobile servant robots" presented in ISO 13482 used to develop an application scenario robot at the Institut Mihajlo Pupin in the University of Belgrade is presented in Sect. 2 [2]. Second, some legal and/or ethical issues concerning, inter alia, privacy, autonomy, agenthood, final say/free will, surveillance or robotic empathy arising from the deployment of such service robots possessing a degree of autonomy is presented in Sect. 3. Section 4 introduces the conclusions and future direction of this research.

## 2   Mobile Servant Robots: The Serbian Case Study

Sometimes called companion robots, sometimes called care robots, ISO 13482:2014 safety standard for personal care robots included Mobile Servant Robots (MSR) together with Person Carrier (PCaR, for example intelligent wheelchairs) and Physical Assistant Robots (PAR, inter alia wearable exoskeletons) [9]. This is the first ISO standardization project aimed at addressing the shift from industrial to service robotics for Activities of the Daily Living (ADL) and how the new safety requirements for close human-robot interaction shall be accommodated. The terminology is still developing and currently is not consistent across research and regulatory stakeholders [11]; various definitions of service robot, personal care robot and MSR can be found in different ISO or Institute of Federal Robotics (IFR) corpuses:

– IFR and ISO 8373:2012 define the *service robot* as "a robot that performs useful tasks for humans or equipment excluding industrial automation applications".
– *Personal care robots* (PCR) are a sub-type of service robots and are defined by ISO 13482:2014 as "service robots that perform actions contributing directly towards improvement in the quality of life of humans, excluding medical applications".
– ISO 13482:2014 defines the *mobile servant robot* (MSR) as "personal care robot that is capable of travelling to perform serving tasks in interaction with humans, such as handling objects or exchanging information".

The robot from the Institut Mihajlo Pupin is a "human-centric, social, care-robot for elderly people and persons with reduced ability to improve their quality of their life and to create conditions for more independent living at their homes […] by providing companionship" [2]. To work, this robot complements its features with ambient assisted living technologies (AAL) and wearable body devices for the humans that can measure, among others, their blood pressure, heart pulse and motion accelerations. Within its capabilities, this robot has communication capabilities (for tele-visits by medical staff or for making emergency calls), ability to collect and fuse all data into a cloud system accessible by authorized people such as family members or the medical team, and performs several caregiver tasks such as assisting, nursing, monitoring, amusing or communicating with the elderly and disabled people. According to the above-mentioned definitions, the Serbian robot is a mobile servant robot.

Three very important aspects can easily be derived from this use case:

(1)  Although service robots are intended to allow close human-robot interactions as well as human-robot contact for performing ADL, there are fundamental differences in their human-robot interaction (HRI) capabilities even if they are in the same corpus [12]. PCaR and PAR, although differing largely on their technical functions, are non-social assistive technologies. As a matter of fact, either sporadically (PCaR) or in a symbiotic manner (PAR), both interact physically with their users. MSRs on the other hand do not interact physically with their users, but cognitively. In Rodić et al. words, it is important to establish a "mental communication [and] emotional contact" with elderly people, something that goes beyond the physical HRI. Indeed, there is no "contact" understood as the "zero distance between the robot and an object in its external environment" between

humans and MSRs. And in spite of the fact that "mental stress" is mentioned in section 5.9.3 or "non-contact sensing" in section 6.5.2.1 in ISO 13482:2014, the standard disregards the cognitive aspects related to the above-mentioned caregiver tasks. The article 3 of the European Charter of Fundamental Rights (EU CFR) on the contrary protects both the physical and the mental integrity of the persons, something that should be addressed by machinery-type service robot standards, especially because care robots "will not only communicate but play important roles in their user's emotional life" [13].

(2) The standard is concerned with HRIs, while actually these interactions are going to turn into a "life-long relationship" once MSRs will end up in personal environments [14]. This challenges the current categorization of these robots provided by the ISO robot standardization process, which focuses only on the safety issues. The "sophisticated presence" that social assistive technologies as MSRs offer in companionship contexts goes far beyond single sporadic HRIs [15]. Indeed, MSRs aim at creating affective meaningful relationships with their users [13, 16]. As relationships are "long-term built up over time through many interactions" as well as "social, emotional, persistent and personalized" [17], the shift from interaction to relationship will require reciprocity, trustworthiness, empathy, social awareness and tones of personal sensitive data from the user [18–20]. In this respect, Google has already patented some of these characteristics such as the use of cloud robotics to support robot personality [3]. This may hinder further research on this domain.

(3) Although the definition of PCR excludes expressly medical applications, the Serbian carebot "monitors" the patient and uses wearable technology to measure the user's vital signs. Here there are two issues to note. First, it is true that the first main goal of the carebot is not to perform medical tasks such as "diagnosis, prevention, monitoring, treatment or alleviation of disease" [21]; however it is "keeping the human under surveillance" as if he/she is a patient and is able to call medical services or relatives in case of emergency. If the robot monitors/keeps-under-surveillance a person in this way with any particular and well-known disease (which is likely to happen if used in elderly care), the robot should be considered a medical device under the Council Directive 93/42/EEC of 14 June 1993 concerning medical devices. In any case, the "intention of use" is what will prime before the Court [22, 23]. The issue is regarding whether the medical device category of the wearable technology used to complement the robot functionalities could be extended to the robot itself. The Serbian carebot happens to work within a robotic system that includes a cloud platform, an AAL environment and a range of wearable devices that monitor the vital signs of the human in a patient-like manner (making it a medical device). If the robot works accordingly to the vital medical signs collected by the wearable sensors (e.g. to call to an ambulance) and if this information is processed together in the cloud platform, then it is not clear whether the robot is by extension a medical device. In fact, this pictures an Internet-of-Things (IoT) scenario where the robot will be just one of the devices connected to the system. Of course, privacy and security issues but also other concerns regarding this new phenomenon are still not clear from the legal perspective (see *infra*).

## 3   Legal Aspects Concerning Mobile Servant Robots

Besides their compliance with the technical safety requirements, MSR need to be compliant with the current existing legal framework. In 2014, the RoboLaw project claimed the respect for the fundamental rights as well as for the safety, responsibility, autonomy, independence, enablement, privacy, social connectedness and justice when developing care robots [8].

Concerning safety, there is a difference between the certified safety, gained by the obtaining of certifications (which forces specialists in robotics to correctly categorize their creations); and the perceived safety in the planned intended use scenarios, i.e. the reliance that a person has over the robot which normally relates to the robot's physical safety and the trust of not only the robot's behaviour but also the robot's intention [19]. This is important because "robotics combines […] the promiscuity of information with the capacity to do physical harm" [24] but also they can be involved in psychological risk scenarios if "mental communication" [2] is the only channel of communication, e.g. depression due to decrease on human-human interaction, overreliance on the robot, frustration when the robot does not understand human commands, or increasing feeling of presence (FoP) [25].

Responsibility refers to who should be held responsible if harm occurs. Clause 7 e) Directive 85/374/EEC in theory prevents manufacturers from being held responsible for defective products if "the state of scientific and technical knowledge at the time when they put the product into circulation was not such as to enable the existence of the defect to be discovered" [26]. The problem is that nowadays we are within a butterfly-effect moment: we do not know which are the consequences of these machines on long-term. The degree of autonomy of the robot will play a major role in the allocation of responsibility: in teleoperated robots, the American Federal Trade Commission (FTC) is already working on "unfair and deceptive" robots so as to protect the expectations of citizens when robots work in WoZ [27]; and in autonomous robots, the National Highway Traffic Safety Administration (NHTSA) recently identified the artificial intelligent system of the Google's driverless car as the driver of the vehicle [28]. This is the first time in history that some sort of agenthood has been given to a robot, the consequences of which are still unknown for the relationship between an autonomous robot and its responsibility.

The use of social robots in elderly care also poses questions concerning privacy, freedom as well as the deception and the infantilization of the elderly [29]. Privacy refers to the respect for the private and family life (Art. 7 EU CFR) but also to the protection of personal data (Art. 8 EU CFR). The robotic system needs to ensure that privacy is protected in balance with other competing interests such as the wellness of elderly people at their own homes. With regard to data protection, the use of cloud computing capabilities for sensor fusion challenges the current data protection framework. Similar to what happens with applications on smart devices, the Serbian carebot would be subject to the data protection laws of the country where the user would be, including non-European countries [30]. In the European Union there are strict rules concerning the explicit consent of the involved subject, something difficult to obtain in dementia patients and in long-standing relationships; also on the relationships between data

controllers and data processors, something aggravated by the IoT structure. The upcoming General Data Protection Regulation will toughen all these requirements and will introduce new principles and rights such as the privacy-by-design principle, the right to be forgotten and data portability right which will oblige the data controllers to collect the information in a "structured and commonly used and machine-readable format" so as to "transmit those data to another controller without hindrance from the controller to which the data have been provided" [31].

The autonomy, independence as well as the free will of the elderly and disabled people are recognized in [32]. The RoboLaw project states that this autonomy "is no longer a lack of dependence from others […] rather it should mean the relational capability of a person to take care of his/her own forms of dependence". This independence and free will need to be carefully addressed in companionship contexts, especially when the robot will have a role in the decision-making process (autonomously or tele-operated). The Serbian carebot includes an embedded personality on the system that could help ease the relationship between the human and the robot. Until now, there has been research on proxemics and social awareness (and the swift from one to the other one [33]), as well as from the recognition/exposure of emotions from the robot perspective [34]. Yet, there are some researchers that think more social and emotional behaviour could lead to a poorer perception of the social robot [35].

In any case, the robot should avoid any discrimination contexts, e.g. when interacting with elderly people with impaired hearing/speaking. In addition, it should be made accessible and affordable to the general public according to the Article 35 EU CFR and the principle of justice.

## 4   Conclusions

This article has highlighted that current machinery-type standards governing service robots focus on the physical HRI are inadequate when social robots are used in elderly care where they work more on the cognitive layer. This challenges the current legal regulatory system which is supposed to protect the physical and mental integrity of the persons; both these aspects are not often taken sufficiently into account. In addition, other legal aspects such as privacy, data protection or autonomy are also not adequately addressed. Although there are no current specific laws governing them, users of these robots are a part of the society vulnerable that need special protection. Because of that, future robot technology will have to pay attention to all the cognitive aspects involved in human-robot relationships as well as to promote the human-human interaction as it is found of vital importance.

## References

1. Power, M.: What Happens When a Software Bot Goes on a Darknet Shopping Spree? The Guardian (2014). www.theguardian.com/technology/2014/dec/05/software-bot-darknet-shopping-spree-random-shopper

2. Rodić, A., Vujović, M., Stevanović, I., Jovanović, M.: Development of human-centered social robot with embedded personality. In: Wenger, P., Chevallereau, C., Pisla, D., Bleuler, H., Rodić, A. (eds.) New Trends in Medical and Service Robots. Human Centered Analysis, Control and Design. Mechanisms and Machine Science, vol. 39, pp. 223–247. Springer, Switzerland (2016)

3. Google, Methods and systems for robot personality development, U.S. Patent 8 996 429 B1, 31 March 2015

4. Robinson, H., et al.: The role of healthcare robots for older people at home: a review. Int. J. Soc. Robot. **6**(4), 575–591 (2014)

5. BS 8611 Robots and robotic devices — Guide to the ethical design and application of robots and robotic systems. standardsdevelopment.bsigroup.com/Home/Project/201500218

6. Wang, Y., Kobsa, A.: Privacy enhancing technologies. In: Gupta, M., Sharman, R. (eds.) Handbook of Research on Social and Organizational Liabilities in Information Security, pp. 203–227. IGI Global, Hershey (2008)

7. Salvini, P.: On ethical, legal and social issues of care robots. In: Mohammed, S., Moreno, Juan C., Kong, K., Amirat, Y. (eds.) Intelligent Assistive Robots. STAR, vol. 106, pp. 431–445. Springer, Heidelberg (2015). doi:10.1007/978-3-319-12922-8_17

8. Palmerini, E., et al.: Guidelines on Regulating Robotics. EU RoboLaw Project, Deliverable 6.2 (2014)

9. ISO 13482:2014, Robots and Robotics Devices – Safety Requirements for Personal Care Robots (2014)

10. ISO 8373:2012 Robots and robotic devices – Vocabulary (2012)

11. Robotics 2020 Multi-Annual Roadmap. For Robotics in Europe. Call 2 ICT 24 Horizon 2020, SPARC, p. 287 (2015)

12. Fosch-Villaronga, E.: Personal care robots: between social and non-social robots. In: Casanovas, P., Moreso, J.J. (eds.) Anchoring Institutions. Springer (2016)

13. Collins, E.C., et al.: Saying it with light: a pilot study of affective communication using the MIRO Robot. In: Biomimetic and Biohybrid Systems, pp. 243–255 (2015)

14. Borenstein, J., Arkin, R.: Robotic nudges: the ethics of engineering a more socially just human being. Sci. Eng. Ethics **22**(1), 31–46 (2016)

15. Sorell, T., Heather, D.: Robot carers, ethics, and older people. Ethics Inf. Technol. **16**(3), 183–195 (2014)

16. McColl, D., et al.: A survey of autonomous human affect detection methods for social robots engaged in natural HRI. J. Intell. Robot. Syst., 1–33 (2015)

17. Benyon, D., Mival, O.: From human-computer interaction to human-companion relationships. In: IITM 2010, Allahabad, UP, India. ACM (2010)

18. Lim, A., Okuno, H.G.: A recipe for empathy. IJSR **7**(1), 35–49 (2015)

19. Salem, M., Lakatos, G., Amirabdollahian, F., Dautenhahn, K.: Towards safe and trustworthy social robots: ethical challenges and practical issues. In: Tapus, A., André, E., Martin, J.-C., Ferland, F., Ammi, M. (eds.) ICSR 2015. LNCS (LNAI), vol. 9388, pp. 584–593. Springer, Heidelberg (2015). doi:10.1007/978-3-319-25554-5_58

20. Baddoura, R., Venture, G.: This robot is sociable: close-up on the gestures and measured motion of a human responding to a proactive robot. IJSR **7**(4), 489–496 (2015)

21. Council Directive 93/42/EEC of 14 June 1993 concerning medical devices

22. Gamerman, G.E.: Intended use and medical devices: distinguishing nonmedical devices from medical devices under 21 USC 321 (h). Geo. Wash. L. Rev. **6**, 806 (1992)

23. Food and Drug Administration General Wellness: Policy for Low Risk Devices (2015). www.fda.gov/downloads/medicaldevices/deviceregulationandguidance/guidancedocuments/ucm429674.pdf

24. Calo, R.: Robotics and the lessons of cyberlaw. Cal Law Rev. **103**, 101–148 (2015)

25. Blanke, O., et al.: Neurological and robot-controlled induction of an apparition. Curr. Biol. **24**(22), 2681–2686 (2014)
26. Art. 7e) Council Directive 85/374/EEC of 25 July 1985 on the approximation of the laws, regulations and administrative provisions of the Member States concerning liability for defective products
27. Hartzog, W.: Unfair and Deceptive Robots (2015). We Robot at: www.werobot2015.org/wp-content/uploads/2015/04/Hartzog-Unfair-Deceptive-Robots.pdf
28. Shepardson, D., Lienert, P.: Exclusive: In boost to self-driving cars, U.S. tells Google computers can qualify as drivers. Technology, Reuters (2016). www.reuters.com/article/us-alphabet-autos-selfdriving-exclusive-idUSKCN0VJ00H
29. Sharkey, A., Sharkey, N.: Granny and the robots: ethical issues in robot care for the elderly. Ethics Inf. Technol. **14**(1), 27–40 (2012)
30. Article 29 Working Party (2013) Opinion 02/2013 on Apps on Smart Devices (2013). ec.europa.eu/justice/data-protection/article-29/documentation/opinion-recommendation/files/2013/wp202_en.pdf
31. Council of Europe 15039/2015 on the Proposal for a Regulation of the European Parliament and of the Council on the protection of individuals with regard to the processing of personal data and on the free movement of such data (General Data Protection Regulation)
32. UN Convention on the Rights of Persons with Disabilities, Art. 3. www.un.org/disabilities/documents/convention/convoptprot-e.pdf
33. Rios-Martinez, J.: From proxemics theory to socially-aware navigation: a survey. Int. J. Soc. Robot. **7**, 137–153 (2015)
34. Koschate, M., et al.: Overcoming the uncanny valley: displays of emotions reduce the uncanniness of humanlike robots. In: International Conference on Human-Robot Interaction. IEEE/ACM (2016)
35. Petisca, S., Dias, J., Paiva, A.: More social and emotional behaviour may lead to poorer perceptions of a social robot. In: Tapus, A., André, E., Martin, J.-C., Ferland, F., Ammi, M. (eds.) ICSR 2015. LNCS (LNAI), vol. 9388, pp. 522–531. Springer, Heidelberg (2015). doi:10.1007/978-3-319-25554-5_52

# Robot and Robotics: The Origin and Beyond

Eftychios G. Christoforou[1]([✉]) and Andreas Müller[2]

[1] Department of Electrical and Computer Engineering, University of Cyprus,
75 Kallipoleos Ave., 1687 Nicosia, Cyprus
`e.christoforou@ucy.ac.cy`
[2] Institute of Robotics, JKU Johannes Kepler University,
Altenbergerstr. 69, 4040 Linz, Austria
`a.mueller@jku.at`

**Abstract.** The words "Robot" and "Robotics" originate from the theatrical play "Rossum's Universal Robots" (R.U.R.) by Karel Čapek and the short science fiction story "Runaround" by Isaak Asimov, respectively. While reading these works one realizes that beyond their historical value they also express many ideas that are pertinent to modern robotics and deserve the attention of the robotics community.

**Keywords:** Rossum's universal robots · Runaround · Social impact of robots · Roboethics · History of robotics

## 1  Introduction

In robotics textbooks it is common that the introduction briefly refers to the origin of the words *"Robot"* and *"Robotics"*, which were introduced in the works of the Czechoslovak writer Karel Čapek and the American (of Russian descent) science fiction writer Isaak Asimov, respectively. Chronologically, the relevant works of Čapek and Asimov were published years before the first industrial robot was created. However, they pose many issues that constitute research topics for contemporary robotics. Some of these issues are identified and discussed in this paper. Quoted italics text represents extracts from the original texts.

One of the most famous works of Karel Čapek (1890–1938) is *"Rossum's Universal Robots"* (R.U.R.) [13]. It was written and published in 1920 and first staged in Prague in 1921. It is known for the first use of the word *"Robot"*, which was derived from the archaic Czech word *"robota"* (drudgery) describing the serf's obligatory work [6]. To better understand the play one needs to consider the era and the sociological framework that gave birth to R.U.R. At that time Europe was living the consequences of World War I, during which technology was used systematically in warfare. It was also a time of industrialization and introduction of the production lines. These developments nourished scepticism towards technology, which was epitomized by the robots in R.U.R.: *"Upon my soul we might have known that some day or other the Robots would be stronger than human beings, and that this was bound to happen."* [13, p. 42].

Another sociological element that played a role is religion. Culture in the "West" is dominated by elements of Christian and Jewish religious beliefs according to which life originates from God and any attempt to create life constitutes a "punishable blasphemy": *"All these new–fangled things are an offense to the Lord. It's downright wickedness. Wanting to improve the world after He has made it."* [13, p. 29] (All quotations of the R.U.R. play in this paper refer to the English translation [13] by Selver and Playfair). A more recent expression of this perception is linked to Honda's Asimo. Before it was revealed engineers consulted the Catholic church fearing that its opposition to human cloning could probably extend to androids [15]. Interestingly, the response was that "by building a robot, you're using your imagination to make something useful, not playing God" and that "any robot that helps people, especially the sick or handicapped, would be welcomed."

The writings of Asimov (1920–1992) have been a source of inspiration for robotics. In historical notes about robotics it is often quoted that Joseph F. Engelberger was discussing together with George C. Devol about the works of Asimov when they conceived the idea and pursued with the development of the first industrial manipulator, which was first put in service in 1961 in the automotive industry. In his short story *"Runaround"* Asimov introduced the word *"Robotics"*. It was written in 1941 and appeared in different published collections [2]. Therein, Asimov also stated the *"Fundamental Rules of Robotics"*, which are *"built most deeply into a robot's positronic brain"*. Note that their weight is hierarchical and the story unfolds around the three laws. Later Asimov himself added a Zeroth Law which was a logical extension to the previous ones. This appeared in the novel *"Robots and Empire"* that was published in 1985 and it is an extrapolation of the original three laws to a preceding hierarchical level.

**Law 0:** A robot may not injure humanity, or, through inaction, allow humanity to come to harm.

**Law 1:** A robot may not injure a human being, or, through inaction, allow a human being to come to harm.

**Law 2:** A robot must obey the orders given it by human beings except where such orders would conflict with the First Law.

**Law 3:** A robot must protect its own existence as long as such protection does not conflict with the First or Second Laws.

## 2   R.U.R. and the Origins of "Robot"

### 2.1   Summary of R.U.R

The story takes place in the island of the factory of Rossum's Universal Robots, a successful business producing robots, a kind of artificial people. Helena, the president's daughter, visits the factory and meets Domin, the general manager. Helena is a member of the *"Humanity League,"* which supports the robots' rights. Domin explains to Helena the origins and the nature of the robots. It all started with Old Rosuum, an eccentric genius: *"His sole purpose was nothing more nor*

*less than to prove that God was no longer necessary."* [13, p. 5]. His experimentation with chemical synthesis led to the discovery of a substance which behaved alike living matter (in the year 1932). His efforts remained unconcluded until the Young Rossum continued following a more practical "engineer's approach". With robots employed as labour the prices of goods drop, while at the same time social implications emerge including a rising unemployment. Robots are also used as soldiers. Helena's visit to the factory leads to her marriage with Domin.

The robot population continues to increase while the human population dramatically drops until finally humans are outnumbered by the robots. Ten years later the course of the story changes after some robots had been further developed and acquired a soul! It follows their revolution against humans until they were ready to completely wipe out the human race. Surrounded by menacing robots a last hope for the few remaining humans barricaded in the factory was the possession of *"Rossum's Manuscript"*, with the details of robot manufacture that could perhaps be traded with the robots. This last hope vanishes upon finding out that the well–kept secret had already been intentionally destroyed by Helena. It follows the invasion of the robots in the factory and the killing of all but one human. The only human who survived the robots' menace was Alquist (the builder), because according to the robots he *"works with his hands like the robots"*. Then the robots become desperate about the continuation of their existence and they put all their hope on Alquist who is proved unable to help them recover Rossum's formula. Rather unexpectedly, at the conclusion of the story, two Robots begin to express human qualities in their behaviour towards one another, appearing ready to assume roles equivalent to Adam and Eve. The curtains fall with a revived hope for the survival of "humanity."

## 2.2   R.U.R. and Today's Robots

It is interesting that many issues raised in R.U.R. constitute research topics in engineering, social science and philosophy today [5–7]. Some issues pertinent to modern robotics are discussed here. An extensive presentation of these topics can be found in Christoforou and Müller [4]. An interesting element is that R.U.R. robots were produced through a chemical synthesis contrary to today's robots that are engineered systems. Perhaps this signals that a systematic use of biological sciences in robotics constitutes a direction not yet explored. Of relevance here is the notion of "bioinspired robots" and "biomimetics". This concept is not about replicating nature as in the Rossums' case, but rather getting ideas from the nature's paradigm. Rossum's intention was to create a human, but today's research towards humanoid robots is about creating more useful and human–friendlier service robots. Despite the perfect resemblance of R.U.R. robots to humans these were manufactured rather than reproduced which was perceived strangely: *"They don't have any young, and a dog has young, every one has young."* [13, p. 20]. A relevant issue often raised in public discussions on robotics concerns the possibility of robots independently manufacturing more robots. Philosophically, this is indeed a most worrying scenario. In R.U.R. this

didn't finally happen since robots never got access to the robot formula. One characteristic of R.U.R. robots is that after production they were ready for work which is also true for today's robots. As expressed by Pratt [12]: "Human beings take decades to learn enough to add meaningfully to the compendium of common knowledge. However, robots not only stand on the shoulders of each other's learning, but can start adding to the compendium of robot knowledge almost immediately after their creation."

Today's manufacturing businesses are required to use automation in order to maintain a competitive advantage. In the words of R.U.R. business manager: *"The cost of labour has fallen. All factories will go pop like chestnuts if they don't at once buy Robots to lower the cost of production."* [13, p. 15]. However, the result was an increase of unemployment. Idealistically, even though workers were left unemployed, robots would produce so much to lower the prices of goods and eliminate poverty so that everybody would *"live only to perfect himself."* The concerns in R.U.R. about robots depriving workers of their job are also echoed in today's societies. It is a fact, however, that many of the jobs in production undertaken by robots are repetitive and unhealthy. Moreover, increased production output due to robotization requests for more people in downstream activity.

The play shows the consequences of an unrestrained use of robots. Today, it is perceived as an appeal for setting up and imposing ethical standards in order to prevent them. Existing regulations regarding the use of robots mainly concern safety issues but efforts towards addressing ethical concerns arising from the use of robots are more recent [14]. Interestingly, isolated references to ethical issues also extend to the "rights of robots" an issue which was also raised in the play through the *"Humanity League"*. One question that is often posed today regards the use of robots in military applications [1]. This is also expressed in R.U.R.: *"...governments turned the Robots into soldiers, and there were so many wars,"* *"It was criminal of old Europe to teach the Robots to fight. ...It was a crime to make soldiers of them."* [13, p. 23, 39]. Ethical and social responsibility questions directly concern the involvement of engineers. An attitude of indifference and blindness to morality was also expressed in R.U.R. When Helena was asked the question: *"Why do you keep selling thousands and thousands of these heathens as soldiers?"* her answer was: *"Domin can't know what they're to be used for. When an order comes for them he must just send them."* [13, p. 24].

The R.U.R. robots have a close resemblance to humans in terms of appearance and behaviour: *"You wouldn't know that she's made of different material from us, would you?"* [13, p. 8]. There exist both male and female R.U.R. robots but this is irrelevant to reproduction. It has to do with human friendliness and acceptance, i.e., it would be perceived more natural for humans if jobs traditionally performed by men/women were assigned to a robot/robotess, respectively: *"There's a certain demand for them, you see. Servants, saleswomen, stenographers. People are used to it."* [13, p. 17]. The physical appearance of robots is often directly attributed to human friendliness and deemed beneficial for human–robot interaction as required by service robots. However, it is difficult to cross

the "uncanny valley" [9]. A current trend that also exists is to make service robots appear clearly as a technical system a user has control of. But in different cultures there are different attitudes towards human likeness.

Technological issues are also raised in R.U.R. Methodologically, we see that two different approaches were followed by the two Rossums towards creating the robots. Old Rossum was a physiologist and he tried to *"manufacture everything as in the human body," "The old crank wanted to actually make people."* [13, p. 5]. Young Rossum pursued a more practical, engineer's approach upon realizing that Old Rossum's process had been a rather long one: *"It's absurd to spend ten years making a man. If you can't make him quicker than nature, you might as well shut up shop."* [13, p. 5]. He identified what could be omitted or simplified from the human anatomy given that a human does many things that are unnecessary for a good working machine. Young Rossum effectively *"he rejected man and made the Robot."* [13, p. 6]. In analogy, today's robots are engineered systems where complexity adding little value to the system is usually discarded.

Robots are tireless workers as implied by their given name. Their effectiveness was advocated by the factory management: *"- One Robot can replace two and a half workmen. The human machine, Miss Glory, was terribly imperfect. It had to be removed sooner or later. - It was too expensive. - It was not effective. It no longer answers the requirements of modern engineering."* [13, p. 13].

An idea expressed for the further development of the R.U.R. robots was to build *"pain–nerves"* as *"an automatic protection against damage."* [13, p. 14]. It was proposed in order to protect the robot's existence and well–being, as in the case of humans or animals. For an engineered robot of today introducing suffering sounds an interesting but also absurd idea since the same result can be achieved simply as a programmed reaction of the system to sensory input.

The possession of a soul and consciousness is seen as the dividing line between humans and robots but conflicting views exist relevant to this issue [8,10,11]. When Helena posed the question *"- Why don't you create a soul for them?"* she received three answers from the factory directors [13, p. 15]: *"- That's not on our power. - That's not in our interest. - That would increase the cost of production."* It was after the acquisition of a soul that the robots' mental potency was augmented and their rebelion was ignited. From that point on robots appeared with deeper consciousness, emotions and initiative. Among their emotions was hostility and ambition: *"I want to be master over people."* [13, p. 27], but also anxiety regarding the continuation of their "species": *"Teach us to multiply or we perish!"* [13, p. 53]. At the epilogue of the story robots exhibited a wider range of emotions (empathy, altruism, etc.) which signified a transformation towards humans. In [3] it is explained that from a Buddhist perspective empathy is a key aspect of interaction between humans which will be important in human–robot relations.

Today, anthropomorphic robots are probably perceived as the technological product most close to humans and this realization is important for service robotics. Towards the end of the story an element that emerges is the notion of duality

between human and robot, a most vivid expression of which comes from Alquist when he desperately tries to recover the reproduction formula. He prays to God to help the robots: *"Lord - I pray to you - if there are no human beings left, at least let there be Robots! - At least the shadow of man!"* [13, p. 51].

## 3   Runaround and the Origins of "Robotics"

### 3.1   Summary of Runaround

In the year 2015 Powel and Donovan arrive to Mercury to restart operations at a mining station which had been abandoned ten years before. They were accompanied by *"Speedy"*, a technologically advanced robot. Upon arrival they realize that the photocells that were vital for the operation of the station and the occupants' survival were short of selenium and they were close to fail. The conditions outside the station were not suitable for humans and Speedy was sent to the nearest selenium pool to bring selenium. When Speedy was late to return the two men were anxious about finding selenium but also how to recover Speedy. Using the antiquated equipment available from the previous expedition they managed to track Speedy's position who had been circling the pool.

Their first idea was to use the old robots from the previous expedition, which were less developed *"subrobotic"* machines with primitive *"positronic"* brain. They were oversized and could not operate autonomously; only with a rider on their shoulders. Wearing their special *"insosuits"* (suits designed to withstand extreme heat) the two men used the old robots to approach Speedy's location. Speedy was not responsive to their instructions (as one would expect on the basis of Law 2) while behaving strangely - something perceived as a robotic equivalence of drunkenness. Puzzled about the robot's behaviour they started reasoning based on the Three Laws of Robotics and the corresponding *"positronic potentials"* in the robot's brain until they identified the source of the problem: Speedy was a highly developed and expensive robot and for this reason Law 3 was strengthened in order to better protect it. As a result, Law 2 was setting up a potential driving the robot towards the selenium pool. Upon approaching to the danger a counterpotential was emerging from Law 3 driving the robot backwards until a potential equilibrium is obtained. Speedy was then moving on the locus of points of potential equilibrium resulting to a "runaround".

Their next idea was to increase the potential of Law 3 by multiplying the danger at the pool which would drive Speedy backwards and allow them to capture him. To implement this idea they used the old robots to throw oxalic acid at the pool, which on heating produces more carbon monoxide. Speedy's motion was then disturbed until finally settled to a new equilibrium by opening up the path; but recovering him was not successful. Within their desperation they thought about Law 1 and decided that one of them should risk his life by approaching the pool to get the selenium, hoping that Speedy will realize the situation and come to rescue. Powel who attempted this finally found himself in a dramatic situation while Speedy would not intervene. It was only until Powel was fully exhausted when Speedy became aware of the situation, came to his rescue

and both returned to the station. After the hierarchy of the Laws was restored in Speedy's brain the robot was sent again to bring the selenium. Following this development the operation of the station was ready to begin.

## 3.2    Runaround and Today's Robotics

It is interesting that Runaround had foreseen many issues regarding robotics. In the story, Speedy participates in a space operation. This application for robotics was in fact considered a few years after the story was published, during the Cold War era for the exploration of the moon and more recently with the rovers for the exploration of Mars. Speedy was sent to the selenium pool for a task that humans were unable to do because of the environmental conditions. Today's analogy is that modern robotics undertake operations that are difficult or dangerous for humans, such as fire fighting and explosives disposal. In the case of Speedy it was mentioned: *"You know he's perfectly adapted to a Mercurian environment. Heat doesn't mean anything to him and he's built for the light gravity and the broken ground. He's foolproof."*

There exist other descriptions in Runaround that also applied to robotics a few decades after its publication. The developments in robotic technology have been tremendous. As also described in the story: *"Even ten years, technologically speaking, meant so much. Compare Speedy with the type of robot they must have had back in 2005.", "You mean six robots from the First Expedition. Are you sure? They may be subrobotic machines. Ten years is a long time as far as robot-types are concerned, you know."* Another difference between Speedy and the robots from the first expedition was their physical size: *"They were large, extremely so, and even though they were in a sitting position on the floor, legs straddled out before them, their heads were a good seven feet in the air."* Speedy was also faster when compared to the older models. The same applies to modern–times robotics. Consider for example industrial robots of the 60's or 70's and the latest models of today. Clearly, the former were bulkier and slow–moving.

The introduction of robots is sometimes confronted with skepticism and this particularly applies to service robotics. Some people may even feel threatened by robots and afraid that one day robots can take control and destroy humanity (as in the R.U.R. scenario). In the story, after the old–model robot responded to the orders with a *"Yes, Master!"*, Powell commented humorously at Donovan: *"Did you get that? Those were the days of the first talking robots when it looked as if the use of robots on Earth would be banned. The makers were fighting that and they built good, healthy slave complexes into the damned machines."*

Speedy was a modern robot characterized by autonomy but the robots from the first expedition would require a rider in order to move. A drive towards more autonomy is a characteristic of modern robotics. Originally, robotics was dealing with well–defined problems and structured environments. Nowadays, robotics is increasingly confronted with ill–defined and unstructured problems. Today, safety has become a key issue. The approach to safety for the old generation robots in the station was to eliminate autonomy: *"We've got to ride him? Like a*

*horse?", "I told you they were playing up robot–safety in those days. Evidently, they were going to sell the notion of safety by not allowing them to move about, without a mahout on their shoulders all the time."*

## 4    Concluding Remarks

Both R.U.R. and Runaround deserve the attention of roboticists primarily because of their historical value but also because they express ideas that are pertinent to our times. It is both interesting and stimulating to (re)consider R.U.R. and Runaround, as it is for robots in science fiction in general. It is inevitable that the use of robots will expand and in the future people will be living and working alongside robots. Today, it is considered unlikely that robots will revolt against humans, as in the case of R.U.R. However, R.U.R. may be seen as a call for regulation to prevent any unwanted consequences from a large–scale use of robotics. At the core of the Runaround story have been the Three Laws of Robotics. Admittedly, Asimov's Laws have not been at the epicenter of Robotics but they may be perceived as an ethical foundation for the field. It is interesting that the above two works that named our scientific field have left us as a legacy the obligation for an ethical foundation which today we refer to as "Roboethics."

## References

1. Arkin, R.: Governing Lethal Behavior in Autonomous Robots. CRC Press, Boca Raton (2009)
2. Asimov, I.: The Complete Robot. Voyager, London (1982)
3. Barua, R., Sraman, S., Heerink, M.: Empathy, compassion and social robots: an approach from Buddhist philosophy. In: Proceedings of New Friends 2015–1st International Conference on Social Robots in Therapy and Education. Almere, The Netherlands (2015)
4. Christoforou, E., Müller, A.: R.U.R. revisited: perspectives and reflections on modern robotics. Int. J. Soc. Robot. **8**, 237–246 (2016)
5. Hoffmann, M., Brom, C.: Agents vs. Rossum's robots: towards intelligent living machines. In: Proceedings of 1st Czech - Argentine Biennale Workshop "e - Golems", Prague, Czech Republic, pp. 87–96 (2005)
6. Horáková, J., Kelemen, J.: Artificial living beings and robots: one root, variety of influences. Artif. Life Robot. **13**, 555–560 (2009)
7. Horáková, J., Kelemen, J.: Some impacts of Karel Čapek's concept of robots as artificial organisms. In: Proceedings of 4th International Conference on Emerging Trends in Engineering & Technology, Port Louis, Mauritius, pp. 49–54 (2011)
8. Metzler, T.: Viewing assignment of moral status to service robots from the theological ethics of Paul Tillich: some hard questions. Technical report WS-07-07 15–20, AAAI Press, Menlo Park, California (2007)

9.  Mori, M.: The uncanny valley. Energy **7**(4), 33–35 (1970)
10. Mori, M.: The Buddha in the Robot. Kosei Publishing Co., Tokyo (2005)
11. Pope, L., Metzler, T.: Has a robotic dog the Buddha-nature? Mu! Technical report WS-08-05 23–26. AAAI Press, Menlo Park, California (2008)
12. Pratt, G.: Is a Cambrian explosion coming for robotics? J. Econ. Perspect. **29**, 51–60 (2015)
13. Čapek, K.: Rossum's Universal Robots. Dover Publications Inc., Mineola (2001)
14. Veruggio, G., Operto, F.: Roboethics: social and ethical implications of robotics. In: Siciliano, B., Khatib, O. (eds.) Handbook of Robotics. Springer, Berlin (2008)
15. Zaun, T.: Why did Honda build a humanoid robot that meets with the Vatican's approval? Wall Street J. (2001)

# Development of Virtual Laboratory for Mechatronic Systems

Vladimir M. Petrović[1(✉)], Branko Nikolić[2], Kosta Jovanović[1], and Veljko Potkonjak[1]

[1] School of Electrical Engineering, University of Belgrade, Belgrade, Serbia
{vpetrovic,kostaj}@etf.bg.ac.rs, potkonjak@yahoo.com
[2] S Technology, Šabac, Serbia
brankonikolic2004@yahoo.com

**Abstract.** E-learning and distance learning systems developed rapidly in the last decade. However, it can be noticed that the concept of distance education is far more implemented in social sciences than it is in engineering. The main reason lies in the fact that engineering disciplines require laboratory exercises. In other words, if we want to develop fully functional e-learning and distance learning for engineering students, we must provide them with skill acquisition. In order to overcome this problem we present a concept of software based laboratory – VLMS (Virtual Laboratory for Mechatronic Systems). VLMS currently consists of two parts – the robotics module and the hydraulics module. Detailed description of each will be provided in this paper. The virtual user interface of the particular device is identical to the real one. Simulation models are used in order to emulate system dynamics. Finally, 3D CAD graphics provides realistic and attractive visualization.

**Keywords:** Virtual laboratory · Robotics · Mechatronics

## 1 Introduction

In the last few decades we have witnessed increased efforts to globalize education and make it more available. E-learning and distance learning appeared as efficient responses to this challenge. Significant developments in this direction (driven by the rapid growth of information and communication technologies) have been made – including Internet-based universities, MOOCs, etc. However, compared to social sciences, engineering disciplines are still a few steps behind in exploiting all the possibilities that these concepts have to offer [1, 2]. The main constraint for the full realization of distance education in engineering disciplines comes from the fact that laboratory exercises must be provided at certain moments of the learning process. Conducting experiments in a well-equipped laboratory is one of the most important issues for students of engineering and STE (Science, Technology, Engineering) in general [3]. Experimental work gives them the possibility to test hypotheses and observe and explore real-world applications of fundamental theories and laws. This allows them to get a deeper understanding of theoretical lessons they learned, in that way discovering

and relating various scientific aspects. Hence, it may be concluded that the role of experimentation is one of the crucial concepts in the engineering education.

However, if we consider some multidisciplinary engineering field such as mechatronics, one could notice that laboratory exercises require significant amount of resources and infrastructure: lab. space, quality equipment, specialized and well trained personnel, etc. Following technological advances that have created new frontiers in education - two different research directions emerged, as an attempt to substitute a classical laboratory exercises. Developing a physical (real) laboratory with distance access is one option and large number of "remote laboratory" projects was initiated on a national and international level in the last two decades [4–6]. Although "remote access" approach solves some issues considering distance learning, it has several drawbacks. It can often be quite complex, especially if we take into account the hardware and software that is required for such systems. Financial aspect, considering the overall cost of the equipment and maintenance of the system, can be problematic too. One could also notice relative inefficiency considering the accessibility – only one student/trainee can access a particular workplace at a time. The second option (that authors of this paper prefer) is a fully software-based virtual laboratory, which has numerous advantages and can avoid some of the mentioned drawbacks [1, 2]. At this point, it should be noticed that some hybrid solutions of the mentioned approaches are also reported [7].

The aim of our work is to exploit the full potential of computer-based virtual experiments, in order to improve the current state in a complex multidisciplinary engineering field – Mechatronics. Hence, in this paper we present the Virtual Laboratory for Mechatronic Systems (VLMS). Some general foundations will be described in Sect. 2 of this paper. Section 3 will present the virtual robotics module. The hydraulics module will be presented in Sect. 4. Finally, concluding remarks will be given in Sect. 5, followed by the list of references. Due to conference rules and constraints in number of pages, at the same time followed by our idea to focus (as much as it can be done) on presenting VLMS features that we find important, we will not describe mathematical models in this paper. The mathematical background along with some other details will be subject of the separate publication.

## 2 General Foundations

Software based virtual laboratories gained large attention during the last decade and more [8, 9]. By analyzing numerous solutions that emerged [1, 2], one could find a connecting thread between the existing virtual laboratories. However, specific features depend on the particular field to which the laboratory belongs.

The development of the VLMS starts from one crucial principle described in [1, 2]: the user of a virtual laboratory must feel like he is working with real authentic devices in a real authentic space.

In order to provide a realistic perception, some requirements must be fulfilled. The virtual user interface must be identical (or similar as much as possible) to the real one. This is particularly important if we want to perform training of the system operators. The behaviour of the virtual system must be identical to the behaviour of the real

system under the same conditions. This means that dynamics must be included, as the presence of the full dynamics represents a precondition of the realistic system behaviour. At this point, it should be noticed that mathematical models of system dynamics represent the key principle of the VLMS. Finally, realistic visualization through sophisticated 3D CAD models of all the elements of the particular system must be provided. Most of the existing virtual laboratories do not fulfil these requirements in full measure [1, 2].

VLMS was developed by strictly following the previously defined principles. The library of objects is organized in the form of cabinets (further in the text we will call them modules) which consists out of shelves with akin objects/devices. The general framework that was built currently consists out of two modules (robotics and hydraulics) which will be described further in the paper. Pneumatics and CNC module are expected to be soon integrated into the VLMS. The idea of modular approach is to allow for gradually supply of virtual laboratory with new devices. In this way (as a final goal), at one point large flexible manufacturing systems could be created. The general logic behind the virtual laboratory is shown in Fig. 1. Every object selected from the library has a unique user interface, graphical model, and mathematical model of dynamics. Internal connections between each of them are predefined and can be applied to every object selected from the library.
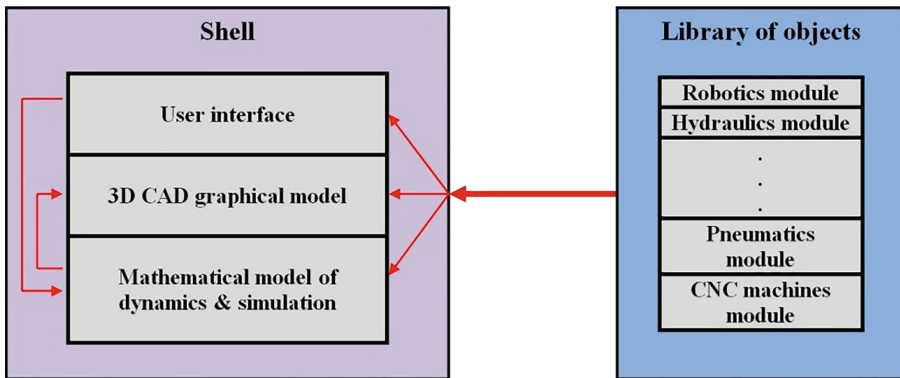


**Fig. 1.** Working principles of the VLMS

## 3   Virtual Robotics Module

A number of simulators in different branches of robotics emerged in the last decade and more [10–13]; a detailed analysis and comparison can be found in [1, 2]. Bearing in mind the constant expansion of robotics research, it is not surprising that the development of virtual robotics laboratories was in the scope of scientific interest.

In this section we will present the virtual robotics module, as a part of VLMS. Development of the robotics module started few years ago [14], while in the meanwhile several modifications were implemented resulting in current upgraded versions. The idea was to demonstrate the main features of robotic manipulators. In the current

version of the system, the user can choose one of the five manipulators that represent most common robotic configurations (Fig. 2). Expanding the virtual laboratory with several industrial manipulators is in progress.

As was stated before, the notion of dynamics is of key relevance in the virtual laboratory concept and mathematical models of the dynamics [15, 16] are at the essence of the software system. Manipulator dynamics plays a fundamental role in motion simulation and control algorithm synthesis. The robot's motion and all the other variables relevant for monitoring the robot's behaviour can be calculated by numerically integrating the appropriate differential equations. Several useful options are provided in the virtual robotics module. Among other things, the user has an option to change control parameters, as well as to make a choice between appropriate control schemes. By developing "custom blocks" in the control scheme, one can define his own controller and then perform the testing. Actuators and other parameters can be easily changed too [14]. Thus, the user can do the experiments and observe the behaviour of the robot in several scenarios, thus gaining the knowledge about the way how the parameters influence the system.
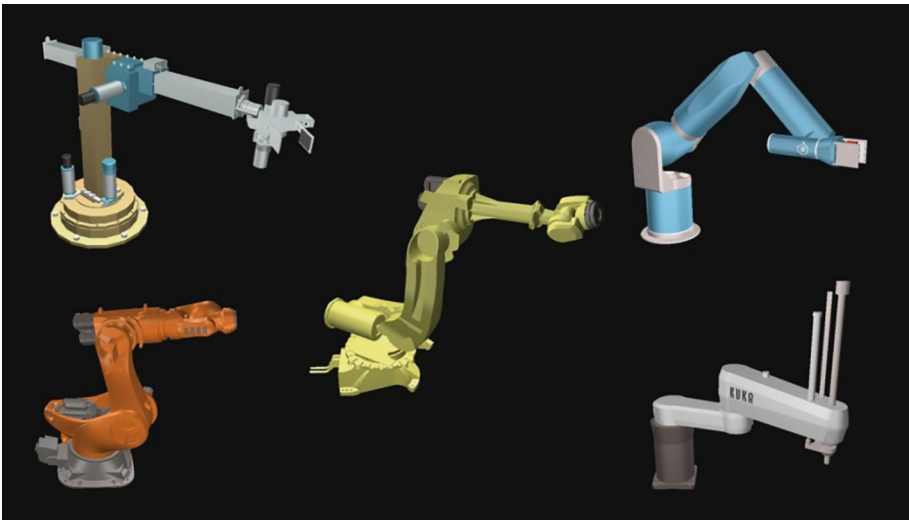


**Fig. 2.** Robotic manipulators currently available in the VLMS: UMS2 (top left corner), STÄUBLI RX270 (in the middle), ETF configuration (top right corner), Kuka KR 1000 Titan (bottom left corner), Kuka R850 (bottom right corner)

Special attention was paid to 3D graphical representation and animation based on virtual reality, in order to make the system more realistic and attractive. Precise and detailed robot models are provided. Different lighting (Fig. 3) and different viewpoints enhance the user's experience. Further on, the graphical representation includes all the inner mechanisms: transmission systems (gears in a gearbox, belts, etc.), the encoder inner structure, the motor elements (rotor, stator), etc. The motion of all of these inner

mechanisms is in complete accordance with the defined kinematics and dynamics laws. The user can remove the covers and take a look at inner structures of the particular robotic manipulator, thus having the possibility to examine the behaviour and the role of each of the inner elements. A virtual robot has several advantages compared to the real one. For example, thanks to the features of computer animation, the manipulator can leave a trace during its movement. Several options exist: the trace may be a line that shows the trajectory of the tip, it may represent the entire robot arm, the trace may be permanent showing thus the complete motion or it may be temporary (being deleted with a certain delay), etc. [14].
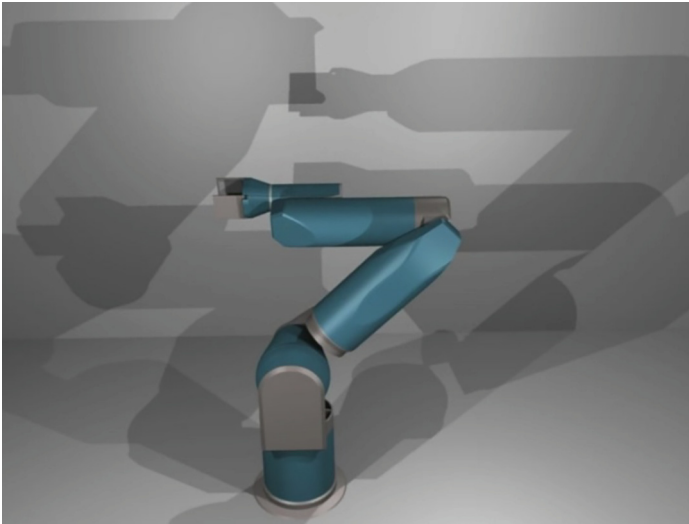


**Fig. 3.** ETF configuration under specific lighting

## 4   Virtual Hydraulic Systems Module

In this section the Virtual Hydraulic Systems Module of the VLMS will be presented. The idea was to thoroughly demonstrate the working principles and control strategy of one complex hydraulic system, which is a good mechatronic example.

The user interface of the hydraulics module offers numerous options. The student / trainee could change all relevant coefficients, PID parameters, etc. After inserting parameter values, the simulation can be started. The results of the simulation can be analysed by appropriate diagrams (showing time histories of the relevant variables). Also, 3D graphical animation is also provided in order to make more intuitive visualization of the attempted experiment. All features of the user interface highlight the possibility of using the VLMS for various exercises and experiments. Hence, it can be used for training of the future operators, as well as for helping students to learn hydraulics theory.
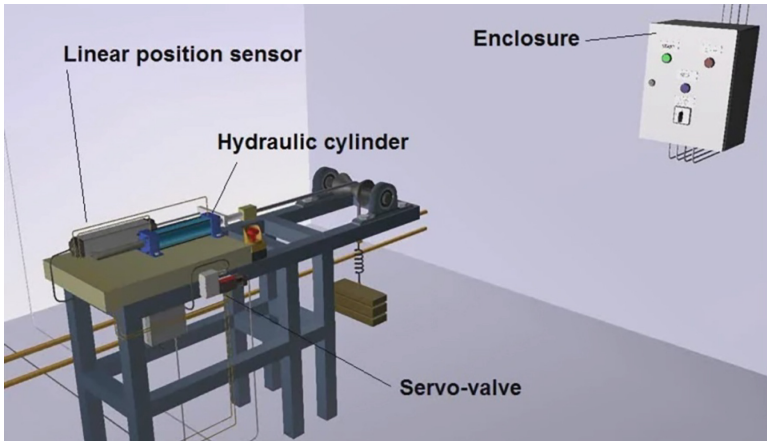
**Fig. 4.** Hydraulic system
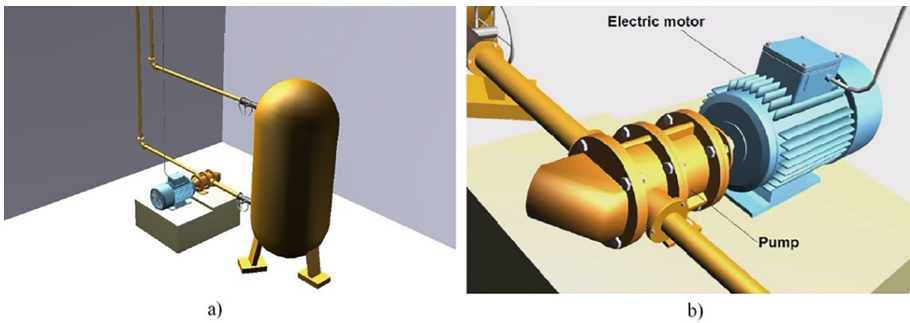


**Fig. 5.** (a) Oil reservoir, motor and pump (b) Closer look at the motor and pump

All system elements move in a complete accordance with the system dynamics [17, 18]. In other words, in order to provide realistic behaviour of the virtual system, the real system is substituted with its mathematical model – the set of differential equations that describe its dynamics. In that way, integration of differential equations provides the information that real systems gets through appropriate sensors.

The graphical representation of the equipment faithfully resembles the actual real world system. In the upper right corner of the Fig. 4 one could see the electrical cabinet (consisting of the control unit and low voltage electrical components). On the left side of Fig. 4, the working surface is placed with all its components (servo valve, hydraulic cylinder, linear position sensor, load, etc.).

The entire virtual area is covered with 7 cameras, which allows for a user to see any part of the system that he is interested in. Cameras can move in all four directions (left, right, up and down), as well as to rotate or accelerate.
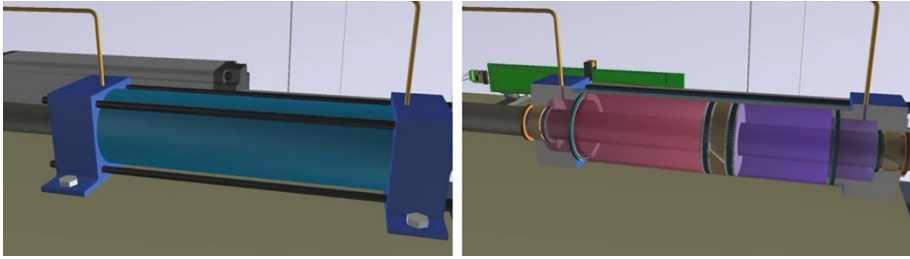
**Fig. 6.** Hydraulic cylinder (left), uncovered cylinder (right)

Figure 5a shows the oil reservoir, electric motor and butterfly pump. Using the camera options (such as different angles, and zooming) can provide a closer look at the system components that might be of interest (Fig. 5b).

The user can remove the covers and have an inside view in internal structures of some system elements (Fig. 6), thus having a possibility to obtain deeper knowledge about the role and working principles of the particular part of the mechatronic system. Figure 6b shows different pressure levels that are highlighted in different colours.

## 5    Conclusion and Final Remarks

STE sciences are yet to implement all the potentials of distance learning. The main constraint is represented by the fact that these sciences require laboratory exercises. Software based virtual laboratories have emerged as a solution, and shown great potential in teaching and learning. Although the final goal of the virtual lab is to replace the real one, it can have another important role – serving for training before the experimentation in the real laboratory.

In this paper we have presented VLMS (Virtual Laboratory for Mechatronic Systems), which is part of our efforts to enhance the current state in mechatronics education and research. The virtual laboratory has some advantages, as compared to the real one. This refers mainly to the features that are almost impossible to observe in the real system, but which can be for many reasons useful for users. For example, almost all the parameters can be changed in the virtual system. This gives the possibility to simulate a collision with the environment, or overload the system. In other words, users can learn by mistake, which can be very important, but in most cases is not very desirable in the real world (because the equipment can be damaged or even destroyed). Also, easily removing of the covers (that protect the system elements from outside influences) is another important feature, allowing students to observe the behaviour of the complex mechanisms.

Despite all the benefits and advanced features that are currently available, the full potential of the virtual laboratories in education has still to be reached. In our opinion, in order to develop a total virtual replacement of a real laboratory, 3D ambience must be created in order to allow the communication and collaboration among users and the lab supervisor (through avatars). The last aspect actually means that we need to

integrate virtual laboratories into the multi-user virtual environments [1, 2]. Fulfilling of the mentioned criteria has yet to be done, and with the rapid progress in computer science technology, the boundary between what can only be done in the real world and what can be done in the virtual system is reducing. Therefore, new directions for scientific research are emerging.

# References

1. Potkonjak, V., Petrović, V.M.: Survey of virtual laboratories and virtual environments with emphasis on applications in robotics. In: Proceedings of the 1st International Conference on Electrical, Electronic and Computing Engineering (IcETRAN 2014), p. ROI3.1.1-6. Vrnjačka Banja, Serbia (2014)
2. Potkonjak, V., Gardner, M., Callaghan, V., Mattila, P., Guetl, C., Petrović, V.M., Jovanović, K.: Virtual laboratories for education in science, technology, and engineering: a review. Comput. Educ. **95**, 309–327 (2016)
3. Wankat, P.C., Oreovicz, F.S.: Teaching Engineering. McGraw-Hill, New York (1993)
4. Ko, C.C., Chen, B.M., Chen, J., Zhuang, Y., Tan, K.C.: Development of a web-based laboratory for control experiments on a coupled tank apparatus. IEEE Trans. Educ. **44**(1), 76–86 (2001)
5. Bellmunt, O.G., Miracle, D.M., Arellano, S.G., Sumper, A., Andreu, A.S.: A distance PLC programming course employing a remote laboratory based on a flexible manufacturing cell. IEEE Trans. Educ. **49**(2), 278–284 (2006)
6. Besada-Portas, E., Lopez-Orozco, J.A., de la Torre, L., de la Cruz, J.M.: Remote control laboratory using EJS applets and TwinCAT programmable logic controllers. IEEE Trans. Educ. **56**(2), 156–164 (2013)
7. Abdulwahed, M., Nagy, Z.K.: Developing the TriLab, a triple access mode (hands-on, virtual, remote) laboratory, of a process control Rig Using LabVIEW and Joomla. Comput. Appl. Eng. Educ. **21**(4), 614–626 (2013)
8. Richter, T., Boehringer, D., Jeschke, S.: LiLa: a European project on networked experiments. In: Proceedings of the 6th International Conference on Remote Engineering and Virtual Instrumentation (REV 2009), pp. 41–46, Bridgeport, CT, USA (2009)
9. De Jong, T., Sotirou, S., Gillet, D.: Innovations in STEM education: the Go-Lab federation of online labs. Smart Learn. Environ. **1**(3), 1–16 (2014)
10. Jaramillo-Botero, A., Matta-Gomez, A., Correa-Caicedo, J.F., Perea-Castro, W.: ROBOtics modeling and simulation platform. IEEE Robot. Autom. Mag. **13**(4), 62–73 (2006)
11. Noguez, J., Noguez, J.: Intelligent virtual laboratory and project oriented learning for teaching mobile robotics. Int. J. Eng. Educ. **22**(4), 743–757 (2006)
12. Carpin, S., Lewis, M., Wang, J., Balakirsky, S., Scrapper, C.: USARSim – a robot simulator for research and education. In: Proceedings of the 2007 IEEE International Conference on Robotics and Automation (ICRA 2007), pp. 1400–1405, Rome, Italy (2007)
13. Jara, C., Candelas, F., Puente, S., Torres, F.: Hands on experiences of undergraduate students in automatics and robotics using a virtual and remote laboratory. Comput. Educ. **57**(4), 2451–2461 (2011)
14. Potkonjak, V., Vukobratović, M., Jovanović, K., Medenica, M.: Virtual mechatronic/robotic laboratory – a step further in distance education. Comput. Educ. **55**, 465–475 (2010)
15. Vukobratović, M., Potkonjak, V., Matijević, V.: Dynamics of Robots with Contact Tasks. Kluwer Academic Publishers, Boston (2003)

16. Siciliano, B., Sciavicco, L., Villani, L., Oriolo, G.: Robotics – Modelling, Planning and Control. Springer-Verlag, London (2009)
17. Merritt, H.E.: Hydraulic Control Systems. Wiley, New York (1967)
18. Jelali, M., Kroll, A.: Hydraulic Servo-systems – Modelling, Identification and Control. Springer-Verlag, London (2003)

# Serbia Robotics Hall of Fame: The Impact of the Past

Branko Karan[✉]

Institute of Technical Sciences of the Serbian Academy of Sciences and Arts,
Belgrade, Serbia
branko.karan@itn.sanu.ac.rs

**Abstract.** The paper presents a list of the most influential works in Serbian robotics. The list has been synthesized using document citation data from the Elsevier Scopus database and it shows that the impact of Serbia, compared to neighbouring countries, has been highly disproportional and outperforming having in mind the Serbian economic and general scientific strength. However, the analysis also reveals that Serbia's contribution has been significantly weakened during the last ten years and that Serbian robotics has been declining with respect to the neighbouring countries.

**Keywords:** Serbian robotics · Scientific impact · Robotics paper

## 1   Introduction

Scientific strength of a nation has many dimensions. It can be expressed by the number of researchers, the number of scientific articles produced, of patents, of defended dissertations, etc. Yet, it is commonly agreed that the main attribute reflecting the scientific merit is the number of citations in works published in refereed journals, conference proceedings, and other renowned sources. Here, highly cited works are of special importance. Having in mind that the distribution of citations has a characteristic skewed shape with a relatively small number of high-impact documents and large numbers of documents of minimal impact, the key measure of scientific performance is the capability of producing or supporting highly cited works [1].

Using a scientific metrics, G. Mester recently presented a list of top scientists in robotics in Serbia based on citations in Google Scholar [2]. Here, a slightly different goal has been posed, that is to identify the top impact works originating from the research institutions of Serbia, and to highlight research fields in which these top results have been achieved. At the same time, a comparison between Serbia and its neighbouring countries has been made in order to determine the relative differences in contribution as well as to emphasize possible issues in scientific production.

## 2    Methodology Remarks

At the first glance, once it has been agreed that the number of citations is an appropriate measure of impact, the task of finding the most influential works of national robotics seems straightforward. Yet, there are few subtle details that deserve more attention. Here, the issues that are connected to the actual measurement of the influence, country of origin, and the field of the influence are presented.

### 2.1    Number of Citations

For many practical reasons, determining the number of citations is performed by modern standards using data from publicly available citation indexing services. Today, the citation indexing databases that are most commonly used in scientific community are Thomson Reuters Science Citation Index (SCI), Elsevier Scopus, and Google Scholar, all providing online retrieval features. This analysis was conducted using only Scopus data. The reason to choose Scopus rather than SCI was simple: in the Serbian academy network, there was no access to SCI records for years prior 1996.

Clearly, different citations may have different importance, depending e.g. on the context of citation or the impact of the journal or other source in which the citing work has been published. Yet, for practical reasons, the citations were in this work simply counted, albeit being aware of limited value of such a simplification. The counts were calculated without self-citations because only the proper citations could serve as a measure of influence; at best, a large number of self-citations may signal the self-influence or a constancy and dedication to research subject.

When identifying the list of top cited works, only the works with 20 or more citations have been considered. This number was arbitrary chosen in order to make the list compact – for a more advanced and influential research environment than Serbia, a limit of 50 or even 100 citations could be more suitable.

Data in Scopus database are divided in two groups: *primary sources*, for which the lists of references are retrieved and indexed by Scopus, and *secondary sources*, which may appear in Scopus only as referenced documents. In this work, when investigating the database, both primary and secondary sources were considered, because references to both kinds of sources were properly indexed by Scopus.

### 2.2    Country of Origin

Information on the authors' affiliation is available for each document appearing in Scopus database and this information was used to determine the country of origin of the published work. In the case of a document with several affiliations, only the first enlisted affiliation was regarded as relevant, because it normally identifies an organization or institution in which the research was organized or conducted.

## 2.3   Importance to the Robotics Community

Robotics is by its nature an interdisciplinary field of research, combining knowledge from many diverse disciplines. It is hard to find any scientific field without some influence to robotics, from operations research to psychology and from material engineering to ergonomy. The border between robotics and other relevant fields is often fuzzy and a question of whether a research belongs to robotics is, to a great extent, a matter of personal taste.

However, while it is extremely difficult to filter-out "truly" robotic papers in efficient and bias-free manner, the task of determining papers with significant influence in robotics is much easier. Namely, we can easily adopt as the most influencing those papers that have received the greatest attention in renowned robotic journals.

In this work, the list of high-impact robotic journals provided by Thomson Reuters (SCIROB hereafter) was used for this purpose. Still, the question remained on the number of citations in SCIROB journals that signalled the high influence. To answer it, a diagram for a sample of highly-cited journals was prepared (see Fig. 1). The diagram shows clear clustering of highly cited works in two parts: the works that were only occasionally cited in SCIROB journals (those with 1–4 SCIROB citations) and the works for which there was a strong correlation between the total number of citations and citations in SCIROB journals, with a trend of having a portion of SCIROB citations ranging from about 25% for papers with 20 citations down to 10% for highly cited papers with 100 or more citations.
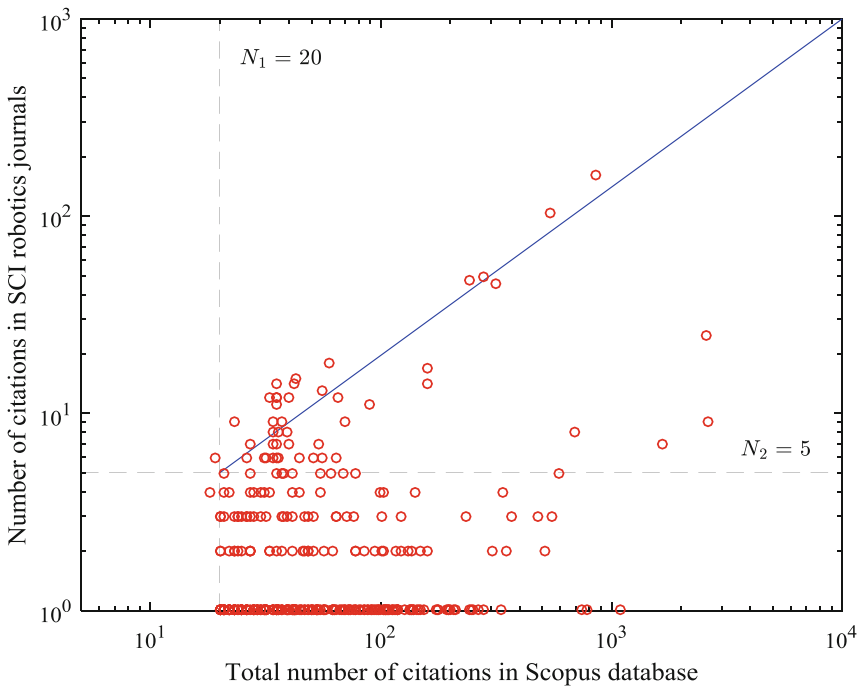


**Fig. 1.** Citation data for a sample of 344 highly cited works referenced in SCI robotics journals

Applying a linear function is a bit impractical, so for the purpose of this analysis a simpler criterion of minimum 5 citations in SCIROB was adopted as a signal of significant impact in robotics.

## 3    The List of Most Influencing Works

Following the described 20 + 5 criterion, the list of the most cited robotics works was synthesized from Scopus database starting from all the documents cited by SCIROB journals (totally about 450,000 documents cited by some 25,000 SCIROB papers), then by extracting the subset with affiliation from Serbia/Yugoslavia, sorting afterward the extracted documents by the number of citations and finally by examining the documents with 20 or more citations: for each document, a check was made of whether the affiliation of the first author was an institution from Serbia, and for each such a document, the database was again queried for a total number of citations and the number of citations in SCIROB journals. The process resulted in a list of 17 Serbian works with 5 or more SCIROB citations. The list is presented in Table 1 which also contains, for each document, the number of citations in all journals indexed in Scopus.

What immediately catches the eye in Table 1 is the absolute prevalence of works of Miomir Vukobratović, who authored 13 out of 17 documents (and also co-authored 2 additional documents). The remaining 4 papers were authored by D. Katić [9], R. Tomović [10], M. Gavrilović [15] and B. Karan [16]. Aside from M. Vukobratović, the most successful in producing high-impact works were B. Borovac and M. Kirćanski, each with 3 works, and Y. Stepanenko, D. Juričić, and V. Potkonjak, each with 2 works.

Manja Kirćanski, who collaborated with Prof. Vukobratović in three highly cited works on trajectory generation for manipulation robots [11, 14, 18], rightfully deserves the title of the first lady of the Serbian robotics.

It is interesting to note that all the documents from the list were produced at the institutions from the University of Belgrade: Mihajlo Pupin Institute and the School of Electrical Engineering. For 16 out of 17 works, the affiliation of the first author was Mihajlo Pupin Institute, the house of famous "Belgrade school of robotics" headed and promoted by M. Vukobratović, a long-time director of its Robotics Centre. The only exception was the paper by R. Tomović et al. [10] that was made while the author was with the School of Electrical Engineering.

There is no room here for a detailed analysis of subjects of these works. However, few comments can be made. All the works mainly belong to the so called classical robotics, dealing with modelling and motion control of robotic and robotized mechanisms, including various complex active orthotic and prosthetic devices. The top impact, with more than 200 citations per document, is exhibited by the works on biped locomotion [3–7]. Bipedal walk is also the main subject of several other top cited documents [8, 9, 12, 13]. Besides two papers concerning active orthoses and prostheses [8, 15], focal points of all other papers are related to manipulation robots, including dynamic modelling [19], trajectory synthesis [11, 14, 18], contact tasks [17], grasping [10], calibration and accuracy [16].

An issue that should concern today is the age of the works. The last work in Table 1 was published in 2006 and it is now already 10 years old. However, despite the

**Table 1.** Serbian works with highest impact in robotics

| | Year | Document | Citations in Scopus database | Citations in Scopus-indexed journals | Citations in SCI Robotics journals |
|---|---|---|---|---|---|
| 1 | 2004 | Vukobratović, M., Borovac, B.: Zero-moment point – thirty five years of its life [3] | 860 | 348 | 163 |
| 2 | 1990 | Vukobratović, M., Borovac, B., Surla, D., Stokić, D.: Biped locomotion: dynamics, stability, control, and application [4] | 543 | 256 | 104 |
| 3 | 1972 | Vukobratović, M., Stepanenko, Y.: On the stability of anthropomorphic systems [5] | 322 | 118 | 45 |
| 4 | 1969 | Vukobratović, M., Juričić, D.: Contribution to the synthesis of biped gait [6] | 309 | 115 | 49 |
| 5 | 1970 | Vukobratović, M., Frank, .A., Juričić, D.: On the stability of biped locomotion [7] | 243 | 114 | 47 |
| 6 | 1974 | Vukobratović, M., Hristić, D., Stojiljković, Z.: Development of active anthropomorphic exoskeletons [8] | 90 | 47 | 11 |
| 7 | 2003 | Katić, D., Vukobratović, M.: Survey of intelligent control techniques for humanoid robots [9] | 54 | 23 | 7 |
| 8 | 1987 | Tomović, R., Bekey, G., Karplus, W. J.: A strategy for grasp synthesis with multi-fingered robot hands [10] | 51 | 40 | 15 |
| 9 | 1984 | Vukobratović, M., Kirćanski, M.: A dynamic approach to nominal trajectory synthesis for redundant manipulators [11] | 43 | 32 | 14 |
| 10 | 2006 | Vukobratović, M., Borovac, B., Potkonjak, V.: ZMP: A review of some basic misunderstandings [12] | 40 | 23 | 12 |
| 11 | 1973 | Vukobratović, M., Stepanenko, Y.: Mathematical models of general anthropomorphic systems [13] | 38 | 27 | 9 |
| 12 | 1982 | Vukobratović, M., Kirćanski, M.: Method for optimal synthesis of manipulation robot trajectories [14] | 37 | 33 | 12 |

<div align="right">(<em>continued</em>)</div>

**Table 1.** (*continued*)

|    | Year | Document | Citations in Scopus database | Citations in Scopus-indexed journals | Citations in SCI Robotics journals |
|----|------|----------|------|------|------|
| 13 | 1969 | Gavrilović, M., Marić, M.: Positional servo-mechanism activated by artificial muscles [15] | 36 | 20 | 8 |
| 14 | 1994 | Karan, B., Vukobratović, M.: Calibration and accuracy of manipulation robot models—an Overview [16] | 34 | 24 | 9 |
| 15 | 1999 | Vukobratović, M., Potkonjak, V., Dynamics of contact tasks in robotics. Part I: General model of robot interacting with environment [17] | 34 | 20 | 5 |
| 16 | 1986 | Vukobratović, M., Kirćanski, M.: Kinematics and trajectory synthesis of manipulation robots [18] | 29 | 23 | 9 |
| 17 | 1985 | Vukobratović, M., Kirćanski, N.: Real-time dynamics of manipulation robots [19] | 28 | 23 | 6 |

old age, these works still have a large frequency of citation: notably, they received 195 citations in Scopus database only in the course of the last year; out of these, 101 were the citations of the top Vukobratović and Borovac paper [3].

Related to the question of the age of works is the age of their authors. Currently, the only active roboticists in Serbia with their papers enlisted in the Table 1 are B. Borovac, V. Potkonjak and B. Karan, all well in the middle sixties. Here, it is worth noting that the last years witnessed strong expansion of robotic centres in Mihajlo Pupin Institute, Belgrade School of Electrical Engineering, and Faculty of Technical Sciences in Novi Sad. They have engaged talented young people, but their time is yet to come. They still do not have top achievements that would be possibly reflected in high impact.

## 4   Comparison to Neighbouring Countries

To get a better insight into the actual impact of Serbia robotics, a comparison was made to the neighbouring countries having similar geographic position and more-or-less similar human and economic potentials (similar in the sense of being on the same order of magnitude). To this end, the process of extracting the articles with the top impact in robotics was repeated for all Serbian neighbours plus Slovenia (hereafter, the neighbouring region), which has been traditionally seen in Serbia as a desired model of organization in many fields.

Importantly, this analysis has shown that the influence of the regional robotics should not be exaggerated: out of some 450,000 references found in SCIROB journals, only a bit less than 2,700 or 0.6% have been identified as the citations of the works from the region. However, out of these 2,700 references, almost 20% are citations to works from the Table 1.

The analysis resulted in extracting 57 highly cited papers from the region. Distribution of papers among countries is displayed in Fig. 2, which shows that the countries with the largest number of high-impact robotic papers are Slovenia, Serbia, and Hungary, which together contribute to more than three-quarters of all papers. This result should be regarded as more than satisfactory, having in mind that technology research and development in Serbia has been regularly weakly funded. Compared to
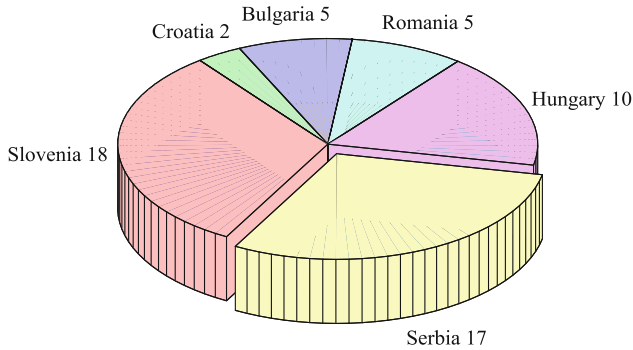


**Fig. 2.** Serbia share in highly cited robotic works from the region
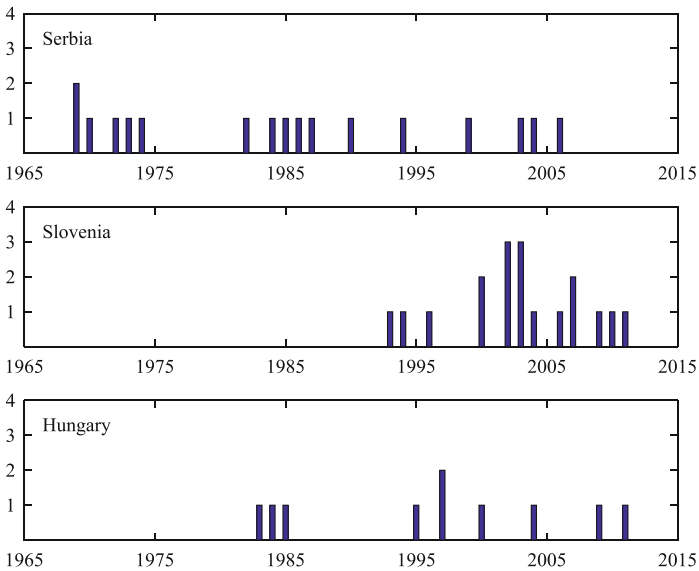


**Fig. 3.** Timeline of highly cited robotic works in Serbia and neighbouring countries

Slovenia, the total expenditure for research and development in Serbia was about 3.4 (in 2010) to 4.6 (in 2000) times smaller [20].

However, the picture changes when considering the time of production of high-impact works. Figure 3, which displays the timeline of highly cited works for three leading countries from the region, evidently shows a decrease in frequency of publication from Serbia. Here, it is interesting to note that the majority of high-impact works from Slovenia and Hungary in the last ten years come from non-traditional robotic fields, such as high-level pattern recognition, control of mobile robots, learning by imitation, bioinspired vision, and fuzzy logic-based swarm coordination.

## 5   Instead of Conclusion

This paper repeats more-or-less known facts that robotics research in Serbia was for a long time concentrated in Belgrade Mihajlo Pupin Institute, thanks to the enormous energy of Miomir Vukobratović to explore new horizons and to gather and motivate talented engineers. However, the list of top published works presented here offers details that might be new to many researchers.

To the author's best knowledge, this is the first time that such a list has been published. It may have errors, both at methodological and technical levels. To provide a space for discussion and improvements, the page http://www.danuberobotics.org/srhf shall be established after the RAAD 2016 conference. The site shall also contain additional data that could not be presented here due to the limited space.

## References

1. Narin, F., Hamilton, K.S.: Bibliometric performance measures. Scientometrics **36**(3), 293–310 (1996)
2. Mester, G.: Indexes in scientific metrics – application in robotics (in Serbo-Croatian.) In: Proceedings of 2015 ETRAN Conference, Srebrno Jezero, Serbia (2015)
3. Vukobratović, M., Borovac, B.: Zero-moment point - thirty five years of its life. Int. J. Humanoid Robot. **1**(1), 157–173 (2004)
4. Vukobratović, M., Borovac, B., Surla, D., Stokić, D.: Biped Locomotion: Dynamics, Stability, Control, and Application. Communications and Control Engineering Series, vol. 7. Springer, Berlin, Heidelberg (1990)
5. Vukobratović, M., Stepanenko, Y.: On the stability of anthropomorphic systems. Math. Biosci. **15**(1), 1–37 (1972)
6. Vukobratović, M., Juričić, D.: Contribution to the synthesis of biped gait. IEEE Trans. Biomed. Eng. **16**(1), 1–69 (1969)
7. Vukobratović, M., Frank, A., Juričić, D.: On the stability of biped locomotion. IEEE Trans. Biomed. Eng. **17**(1), 25–36 (1970)

8. Vukobratović, M., Hristić, D., Stojiljković, Z.: Development of active anthropomorphic exoskeletons. Med. Biol. Eng. **12**(1), 66–80 (1974)

9. Katić, D., Vukobratović, M.: Survey of intelligent control techniques for humanoid robots. J. Intell. Robot. Syst. **37**(2), 117–141 (2003)

10. Tomović, R., Bekey, G., Karplus, W.J.: A strategy for grasp synthesis with multi-fingered robot hands. In: Proceedings of 1987 IEEE International Conference on Robotics and Automation, vol. 4, pp. 83–89. IEEE (1987)

11. Vukobratović, M., Kirćanski, M.: A dynamic approach to nominal trajectory synthesis for redundant manipulators. IEEE Trans. Syst. Man Cybern. **14**(4), 580–586 (1984)

12. Vukobratović, M., Borovac, B., Potkonjak, V.: ZMP: a review of some basic misunderstandings. Int. J. Humanoid Robot. **3**(2), 153–175 (2006)

13. Vukobratović, M., Stepanenko, Y.: Mathematical models of general anthropomorphic systems. Math. Biosci. **17**(3), 191–242 (1973)

14. Vukobratović, M., Kirćanski, M.: Method for optimal synthesis of manipulation robot trajectories. J. Dyn. Syst. Meas. Control **104**(2), 188–193 (1982)

15. Gavrilović, M., Marić, M.: Positional servo-mechanism activated by artificial muscles. Med. Biol. Eng. **7**(1), 77–82 (1969)

16. Karan, B., Vukobratović, M.: Calibration and accuracy of manipulation robot models—an overview. Mech. Mach. Theor. **29**(3), 479–500 (1994)

17. Vukobratović, M., Potkonjak, V.: Dynamics of contact tasks in robotics. Part I: general model of robot interacting with environment. Mech. Mach. Theor. **34**(6), 923–942 (1999)

18. Vukobratović, M., Kirćanski, M.: Kinematics and Trajectory Synthesis of Manipulation Robots. Communications and Control Engineering Series, vol. 3. Springer, Berlin, Heidelberg (1986)

19. Vukobratović, M., Kirćanski, N.: Real-Time Dynamics of Manipulation Robots. Communications and Control Engineering Series, vol. 4. Springer, Berlin, Heidelberg (1985)

20. World Bank Data. http://data.worldbank.org/

# Building Remote Lab for Robot SLAM Algorithm Testing

Nikola Jović[(✉)], Radomir Mitrović, and Milan Matijević

Faculty of Engineering, University of Kragujevac, Kraujevac, Serbia
nikolajovic@live.com, radomir.mitrovic3@gmail.com,
matijevic@kg.ac.rs

**Abstract.** This paper describes the development of a remote laboratory at the University of Kragujevac, with examples on testing robot SLAM algorithms. The laboratory is built with the scope of engineering education, but it can be also used by scientist and developers for quick testing of SLAM, maze solving or similar algorithms on real robots. The main goal is to build a remote lab whose price is as low as possible, while still having the necessary functionality, allowing users to access it at any time, and to be sustainable and maintainable for a long period of time.

**Keywords:** Remote laboratory · SLAM · Node.JS · Engineering education

## 1 Introduction

Simultaneous Localization and Mapping (SLAM) is one of fundamental challenges of robotics. It is a process by which a mobile robot can build a map of the environment and at the same time use this map to deduce its location [1]

It is of interest to build a remote laboratory environment for testing SLAM algorithms on real robots. One of the reasons for building this remote lab is to include robot SLAM in engineering education. In this sense motivations for building remote laboratory can reduce time of engineering education in developing countries [2], enable carrying out experiments during lectures, and for preparation of hands-on experiments [3], while reducing costs of equipment and manpower by help of hands-on training in laboratory exercises. There is no significant difference in the effects and benefits of hands-on and remote laboratory for engineering education [4] so it is worth pursuing the remote lab initiative.

Our intention is to build a remote laboratory in which the user would be able to perform tests for a SLAM problem and solve related algorithms. In that respect there are two problems: building the remote laboratory interface which is capable of communicating the user's algorithm to the robot, and sending relevant data back to the user and the robot that can perform all that mechanical and electrical tasks, for example in construction. We propose the solution to build first the remote lab interface using Pioneer P3-DX as a test robot, and then in the future to build customized and more affordable robots for particular applications.

From [5] it can be seen that a poorly developed remote laboratory is in danger of not permanent functioning due to costly maintenance. Because of that, remote lab is developed with ease of maintenance in mind and programmed with caution (every user command is checked before execution) which makes impossible for the user to damage the hardware equipment or software systems.

The first part of this paper describes the Pioneer P3-DX robot. This robot is used currently as a test robot, but any other affordable solution could be used. The second part describes two WiFi communication options that are currently available, Lantronix 2100E and ESP8266, and some comparative analysis is included. The third part of the paper describes the remote lab server and its basic operation and the client web interface for the remote lab.

## 2  Pioneer P3-DX Robot

Pioneer P3-DX robot is a very robustly built multipurpose research robot. Its complete documentation can be found in [6]. What makes it suitable for utilisation in the remote lab testing processes is its sensory system composed by eight ultrasonic sensors and two encoders for the wheels drives. It is recommended that the ultrasonic sensors be paired with some other odometer [1] devices in order to compensate their lack of precision.

Some of robot's disadvantages are its weight and cost. The robot weights 9 kg which requires powerful DC motors, which, due to their high power consumption, need an adequate battery set. The robot's weight can increase up to 23 kg when fully equipped, but extra options were not considered for the remote lab application, mainly because of the possibility of endangering the environment (the maze) in case of failure of the ultrasonic sensors. This is also the reason for its high price, which represents a drawback for equipping the remote lab with multiple robots, planned for future projects.

For the above mentioned reasons the robot is used only for testing purposes whilst the software part of the remote lab is developed. It will be replaced in the future with another robot with the same number of sensors and actuators, but much lighter.

## 3  Communication Between Pioneer P3-DX and the Remote Lab Server

Communication with the P3-DX robot is performed via RS232 serial channel. Commands related to desired motor movements are sent from the computer to the robot through 5–8 byte long serial messages, and complete information about the robots' current settings, ultrasonic and odometer measurements are returned.

The remote communication between the robot and WEB lab server was tested with the Lantronix 2100e wireless device server, and ESP8266 WiFi to UART interface. Lantronix 2100e was an out-of-the-box ready solution, while ESP8266 requires an additional UART to RS232 interface which was built around the MAX232 transceiver.

### 3.1    Lantronix 2100e Wireless Device Server

From [7] can be seen that Lantronix (Fig. 1) is adequate for establishing remote serial communications. It is well documented and straightforward to set up. During testing it kept connection to a wireless router at a distance of 20 m through wall, which is more than enough for remote lab applications.



**Fig. 1.** The Lantronix 2100e wireless device server

On the other hand, its price is still too high for remote labs in which a number of robots should be involved. Also, it has two RS232 ports and one Ethernet port which is quite sufficient for applications where it is expected to transform wireless signals into serial and vice versa.

### 3.2    ESP8266

The Espressif Systems' Smart Connectivity Platform (ESCP) is a set of high performance, highly integrated wireless SOCs, designed for space and power constrained mobile platform designers. It provides a very important characteristic to embed WiFi capabilities within other systems or to function as a standalone application, with the lowest possible cost and minimal space requirement [8].

The advantage of ESP8266 over Lantronix 2100e is its cost which is almost hundred times lower. The main disadvantage is the necessity of having programmer for uploading HEX file, writing flash program and building TTL to RS232 interfaces (Fig. 2) for each ESP8266 unit.

Programs were written in the programing language LUA that bridges WiFi and UART signals. This allows connecting to local WiFi network connected to the internet. It can receive commands through IP address and port assigned in the program.
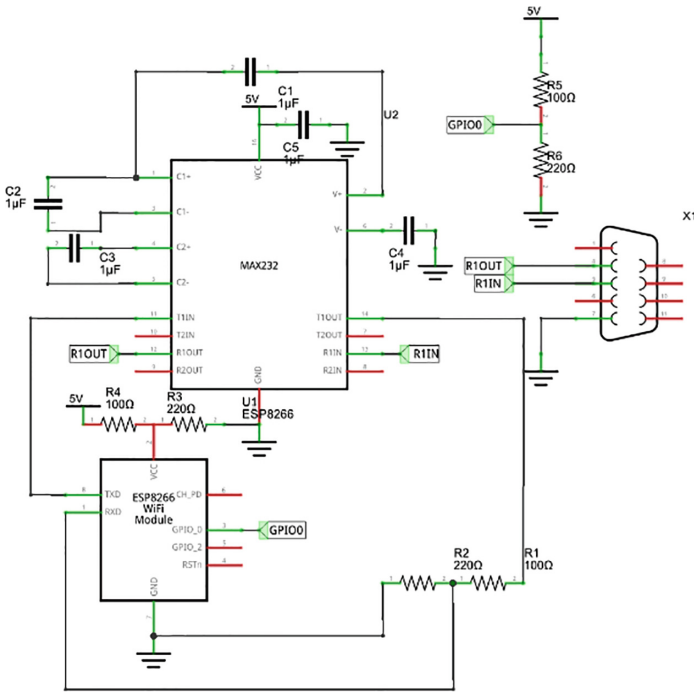
**Fig. 2.** Connection of ESP8266 to RS232 port

## 4   Remote Lab Server

The remote lab server was written in Node.JS; its task is to communicate with the robot via virtual serial port or web socket. Using a virtual port creates a longer delay between the command issued to a robot and the execution of that command by the robot. The second task of Node.JS server is importing the user created Python script which contain the algorithm for the robot behaviour (client script) into a script used for direct communication with the robot (server script).

A server script contains functions for opening and closing connection with the robot and functions for looped execution of the algorithm for a particular robot behavior. Here safety constraints for the robot movement are implemented, so no matter how user defines control algorithm there is no possibility for damaging the equipment.

The safety procedure when connection with the robot is lost is also defined here. P3-DX has a watchdog timer implemented that will stop the robot if no command is received for a period of time. Despite that, if a command is received by the robot, but not sent due to temporary connection failure, the server does not update the robot sonar and odometer data, and thus it operates with wrong data. This problem is solved by issuing a stop command to the robot by the server and requesting continuously state update. Once the robot successfully sends data, algorithm execution is immediately

resumed. The client script contains the definition of the robot control algorithm in one function; this function takes as parameters sonar and odometer readings, and as output issues robot rotational and forward speed.

Finally, concerning the remote lab server serves client web page (Fig. 3), the interface shown is the test interface. The complete remote lab will be publically available when the user documentation is completed.
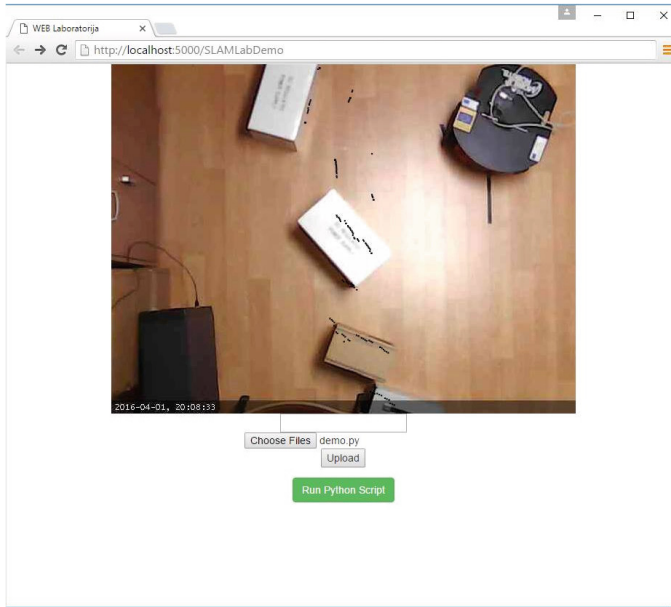


**Fig. 3.** Web lab GUI with test data

## 5   Conclusion

In this paper we have discussed the reasons for building a robot SLAM remote laboratory, and some of our hardware and software solutions that were used for this purpose. This is the first remote robot laboratory at University of Kragujevac, and it awaits its first implementation in higher engineering education (HEE) next academic year when its effects in hands-on training engineering education will be observed. Until then, there is much to be done. First of all, a new robot platform needs to be built and to replace Pioneer P3-DX in the remote lab. The preliminary estimation is that it is possible to build a fully functional robot with all necessary characteristics for up to 5 % of the cost of P3-DX.

Second, complete documentation must be done in order to enable users to exploit the full potential of the remote laboratory. Documentation is also necessary for the maintenance of the remote lab.

During the final preparation period we do not believe that the software solution will change much. A similar approach was already used for an RC circuit remote lab which was set up at the Faculty of Engineering, University of Kragujevac for the course Measurement and Control, and it performed well [9].

# References

1. Aulinas, J., Petillot, Y., Salvi, J., Llado, X.: The SLAM problem: a survey. In: Proceedings of the 2008 Conference on Artificial Intelligence Research and Development: Proceedings of the 11th International Conference of the Catalan Association for Artificial Intelligence, The Netherlands, pp. 363–371 (2008)
2. Garcia-Guzman, J., Villa-Lopez, F.H., Silva-Del-Rosario, F.H., Ramirez-Ramirez, A., Enriquez, J.V., Alvarez-Sanchez, E.J.: Virtual environment for remote access and automation of an AC motor in a web-based laboratory. Procedia Technol. **3**, 224–234 (2012)
3. Abdulwahed, M., Nagy, Z.K.: Systematic evaluation of the use of remote and virtual laboratories in engineering education. In: 21th European Symposium on Computer aided Process engineering – ESCAPE21 (2011)
4. Farrokhnia, M.R., Esmailpour, A.: A study on the impact of real, virtual and comprehensive experimenting on students' conceptual understanding of DC electric circuits and their skills in undergraduate electricity laboratory. Procedia Soc. Behav. Sci. **2**, 5474–5482 (2010)
5. Kara, A., Ozbek, M.E., Cagiltay, N.E., Aydin, E.: Maintenance, sustainability and extendibility in virtual and remote laboratories. Procedia Soc. Behav. Sci. **28**, 722–728 (2011)
6. Mobile Robots, Pioneer 3 Operations Manual (2003). http://www.inf.ufrgs.br/~prestes/Courses/Robotics/manual_pioneer.pdf. Accessed 29 Mar 2016
7. WiBox Dual Port – Wireless Device Server – Lantronix. http://www.lantronix.com/products/wibox-dual-port/. Accessed 29 Mar 2016
8. Esspressif Systems, 2015, ESP8266EX Datasheet http://espressif.com/en/file/397/download?token=oVtCENmg. Accessed 29 Mar 2016
9. Mitrović, R., Jović, N., Cvjetković, V., Nedeljković, M., Matijević, M.: Udaljene laboratorije sa pristupom internetu u inženjerskom obrazovanju. In: Proceedings of 22nd Conference TREND, Serbia (2016)

# Author Index